# IMPROVEMENT OF SEISMIC BEHAVIOUR OF RETAINING WALLS BY USING CUSHIONS

by

Gözde Sezgin Tunçay

B.S., Civil Engineering, Çukurova University, 2005

M.S., Earthquake Engineering, İstanbul Technical University, 2008

Submitted to Kandilli Observatory and Earthquake Research Institute

in partial fulfillment of requirements for the degree of

Doctor of Philosophy

Graduate Program in Earthquake Engineering

Boğaziçi University

2023

***To my precious husband, Onur Tunçay,***

# ACKNOWLEDGEMENTS

I would like to express my gratitude and respect to my thesis advisor, Prof. Dr. Ayşe Edinçliler, who never withheld her knowledge, expertise, and support while guiding me in the right direction and providing me with her valuable time during my thesis study. I would like to sincerely thank her for her persistence, tolerance, and optimistic attitude throughout the challenging parts of my doctoral study process. I also appreciate her unique personality, who always academically and socially guided me.

I would also like to thank my committee members, Prof. Dr. Ali Pınar and Prof. Dr. Musaffa Ayşen Lav, Prof. Dr. Ayfer Erken, Doç. Dr. Gülüm Tanırcan for their contributions and valuable guidance during my thesis progress processes.

I would like to thank Destech Müşavirlik, Mühendislik ve Proje A.Ş. for their financial support for the retaining wall model. I thank BU-BAP for the laminar box designed and produced in collaboration with the Boğaziçi University Research Fund (Project No: BU-BAP8084). I want to thank the experts and technicians who supported me during my experiments in Kandilli Observatory and Earthquake Research Institute Shake Table Laboratory at Boğaziçi University. Also, I would like to thank my friends Dr. Aytaç Yaşargün and Ph.D. candidate Yasin Sait Toksoy, who supported me during this intensive thesis study.

I want to express my gratitude to my beloved husband, Onur Tunçay, who has always stood by me and treated me with respect, love, kindness, and compassion. I could not have succeeded without his excellent contribution, dedication, exertion, and encouragement during my Ph.D. I am grateful to my father, mother, precious nieces, beloved siblings and their husbands, mother-in-law, and aunts who have been with me throughout my life, supporting me with love, respect, and understanding.

# ABSTRACT

## IMPROVEMENT OF SEISMIC BEHAVIOUR OF RETAINING WALLS BY USING CUSHIONS

Damages and collapses of retaining walls that occur after earthquakes cause loss of life and property and huge economic losses. The use of lightweight material as a cushion behind the retaining wall is one of the improvement methods. The main aim of this thesis is to evaluate the effectiveness and efficiency of a new proposed cushion layer as EPS beads and sand mixture (EPSB) for retaining structures. This cushion material placed behind the retaining wall was used for the first time in the literature. The effects of the mixture ratio and thickness of the EPSB cushion layer under different input motions were investigated. The other cushion layers as EPS geofoam and tire waste and sand mixture (TW) were also used. The performances of three cushion materials were compared with each other under the same input motions. In the experiments, a 1/15 scaled retaining wall model was designed to investigate the effectiveness of the cushion materials on the seismic performance of the retaining wall. Firstly, the experiments for the retaining wall model without cushion material were carried out on the shake table in the laminar box. In the second part, three different types of cushion materials were placed behind the retaining wall by changing thickness, density, and mixture ratios. EPS geofoam was found to provide the highest improvement performance compared to the TW and the EPSB cushions. Evaluation of the test results showed that the cushion type is significantly effective in improving the retaining wall model. Additionally, changes in thickness, density/mixing ratio, and input motions affect the results.

# ÖZET

## İSTİNAT DUVARLARININ SİSMİK DAVRANIŞININ YASTIK MALZEMELERİ KULLANILARAK İYİLEŞTİRİLMESİ

İstinat duvarı hasarları ve göçmeleri can ve mal kayıplarına ve çok büyük ekonomik kayıplara neden olmaktadır. İstinat duvarının arkasında yastık malzemesi olarak hafif malzeme kullanılması istinat duvarı iyileştirme yöntemlerinden biridir. Bu çalışmanın başlıca amacı, istinat yapıları için yeni yastık malzemesi olarak önerilen EPS boncuk ve kum karışımının etkinliğinin ve verimliliğinin değerlendirilmesidir. İstinat duvarının arkasına yerleştirilen bu yastık malzemesi literatürde ilk kez kullanılmıştır. EPS boncuk ve kum karışımı yastık malzemesinin kalınlık ve karışım oranı etkileri farklı girdi (input) hareketleri altında incelenmiştir. Ayrıca EPS geofoam ve atık lastik-kum karışımı da yastık malzemesi olarak kullanılmıştır. İncelenen üç yastık malzemesinin aynı girdi (input) hareketleri altında performansları birbirleriyle kıyaslanmıştır. İstinat duvarı iyileştirme yöntemlerinin araştırılması amacıyla 1/15 ölçekli istinat duvarı modeli tasarlanmıştır. Öncelikli olarak iyileştirilme yapılmamış olan, yani yastık malzemesi kullanılmayan model deneyi sarsma masasında laminar kutu içinde gerçekleştirilmiştir. Daha sonra ise istinat duvarı arkasına üç farklı yastık malzemesi, kalınlık, yoğunluk ve karışım oranı değiştirilerek yerleştirilmiştir. EPS geofoam, atık lastik ve kum karışımı ve EPS boncuk ve kum karışımı ile oluşturulan yastık modelleri kıyaslandığında en yüksek iyileştirme performansını EPS Geofoam yastığın gösterdiği tespit edilmiştir. Deney sonuçları değerlendirildiğinde, yastık tipinin istinat duvarının iyileştirilmesinde önemli ölçüde etkili olduğu görülmektedir. Ayrıca, kalınlık, yoğunluk/karışım oranı ve girdi (input) hareketlerindeki değişiklikler sonuçları etkilemektedir.

# TABLE OF CONTENTS

ACKNOWLEDGEMENTS ..... iv
ABSTRACT ..... v
ÖZET ..... vi
TABLE OF CONTENTS ..... vii
LIST OF FIGURES ..... xii
LIST OF TABLES ..... xxxvii
LIST OF SYMBOLS ..... xxxix
LIST OF ACRONYMS/ABBREVIATIONS ..... xlii
1. INTRODUCTION ..... 1
1.1. General ..... 1
1.2. Problem Statement ..... 2
1.3. The objective of the Thesis ..... 3
1.4. Organization of the Thesis ..... 3
2. LITERATURE REVIEW ..... 5
2.1. Retaining Structures ..... 5
2.1.1. Retaining Wall Analysis under Static Conditions ..... 7
2.1.2. Retaining Structures Analysis under Dynamic Conditions ..... 10
2.2. Failure of Retaining Walls ..... 15
2.3. Case Studies on Failure of Retaining Walls under Earthquakes ..... 19
2.4. Improvement of Retaining Walls ..... 24
2.5. Lightweight Materials ..... 27
2.5.1. EPS Geofoam ..... 27
2.5.2. Tire Waste and Sand Mixtures ..... 38
2.5.3. EPS Beads and Sand Mixtures ..... 45
2.6. Effects of Soil Improvement for the Retaining Walls under Static and Seismic Loading ..... 52

2.6.1. Numerical Modelling of Retaining Walls ..... 53
2.6.2. Experimental Studies on Retaining Walls ..... 61
2.6.3. Field Studies on Retaining Walls ..... 69
3. EXPERIMENTAL STUDY ..... 76
3.1. Materials and Methods ..... 76
3.1.1. Backfill Material ..... 77
3.1.2. EPS Geofoam Material ..... 78
3.1.3. Tire Waste and Sand Mixture ..... 79
3.1.4. EPS Beads and Sand Mixture ..... 81
3.1.5. Laminar Box ..... 84
3.1.5.1. Inertia Effect ..... 86
3.1.5.2. Friction Effect ..... 86
3.1.5.3. Membrane Effect ..... 88
3.1.5.4. Boundary Effect of the Laminar Box ..... 88
3.1.6. Shake Table ..... 91
3.2. Experimental Study ..... 92
3.2.1. Design of the Retaining Wall Model ..... 93
3.2.2. Input Motions ..... 98
3.2.3. Experimental Program ..... 109
3.2.4. Preperation of the Experimental Studies ..... 111
3.2.4.1. Instrumentation of the Experimental Set-up ..... 111
3.2.4.2. Preparation of the Control Case ..... 115
3.2.4.3. Preparation of the EPS Geofoam Cushioned Cases ..... 118
3.2.4.4. Preparation of the Tire Waste and Sand Mixture Cushion Models ..... 122
3.2.4.5. Preparation of the EPS Beads and Sand Mixture Cushion Models ..... 126
4. RESULTS OF THE EXPERIMENTAL STUDY ..... 131
4.1. Results of Case 1 – Control Case ..... 132
4.2. Results of Case 2 - EPS10-4cm ..... 137

4.3. Results of Case 3 - EPS20-4cm ..... 143
4.4. Results of Case 4 - EPS30-4cm ..... 149
4.5. Results of Case 5 - EPS10-8cm ..... 155
4.6. Results of Case 6 - EPS20-8cm ..... 161
4.7. Results of Case 7 - EPS30-8cm ..... 167
4.8. Results of Case 8 - TW10-4cm ..... 173
4.9. Results of Case 9 - TW20-4cm ..... 179
4.10. Results of Case 10 - TW30-4cm ..... 185
4.11. Results of Case 11 - TW10-8cm ..... 191
4.12. Results of Case 12 - TW20-8cm ..... 197
4.13. Results of Case 13 - TW30-8cm ..... 203
4.14. Results of Case 14 - EPSB10-4cm ..... 209
4.15. Results of Case 15 - EPSB20-4cm ..... 215
4.16. Results of Case 16 - EPSB30-4cm ..... 221
4.17. Results of Case 17 - EPSB10-6cm ..... 227
4.18. Results of Case 18 - EPSB20-6cm ..... 233
4.19. Results of Case 19 - EPSB30-6cm ..... 239
4.20. Results of Case 20 - EPSB10-8cm ..... 245
4.21. Results of Case 21 - EPSB20-8cm ..... 251
4.22. Results of Case 22 - EPSB30-8cm ..... 257

5. DISCUSSION ..... 263

5.1. The Effects of EPS Geofoam Cushion on the Seismic Performance of the Retaining Wall Model ..... 264

5.1.1. The Effects of Thickness and Density of EPS Geofoam Cushion ..... 264

5.1.1.1. Comparison of Improvement Efficiency under Far Field and Near Field Earthquake Motions ..... 265
5.1.1.2. Comparison of Maximum Spectral Accelerations under Far Field and Near Field Earthquake Motions ..... 269
5.1.1.3. Comparison of Improvement Efficiency under Sinusoidal Motions ... 277

5.1.1.4. Comparison of Maximum Spectral Accelerations under Sinusoidal Motions ..... 281

5.1.2. The Effects of Acceleration Response for EPS Geofoam Cushion under Different Input Motions ..... 287

5.1.2.1. Maximum Acceleration Comparison at 4 cm Thickness ..... 287

5.1.2.2. Maximum Acceleration Comparison at 8 cm Thickness ..... 289

5.1.3. Maximum Lateral Displacements for EPS Geofoam Cushion Cases under All Input Motions ..... 291

5.2. The Effects of Tire Waste and Sand Mixture Cushion on the Seismic Performance of the Retaining Wall Model ..... 296

5.2.1. The Effects of Thickness and Mixture Ratio of Tire Waste and Sand Mixture Cushion ..... 296

5.2.1.1. Comparison of Improvement Efficiency under Far Field and Near Field Earthquake Motions ..... 297

5.2.1.2. Comparison of Maximum Spectral Accelerations under Far Field and Near Field Earthquake Motions ..... 301

5.2.1.3. Comparison of Improvement Efficiency under Sinusoidal Motions ... 310

5.2.1.4. Comparison of Maximum Spectral Accelerations under Sinusoidal Motions ..... 313

5.2.2. The Effects of Acceleration Response for Tire Waste and Sand Mixture Cushion under Different Input Motions ..... 318

5.2.2.1. Maximum Acceleration Comparison at 4 cm Thickness ..... 318

5.2.2.2. Maximum Acceleration Comparison at 8 cm Thickness ..... 320

5.2.3. Maximum Lateral Displacements for Tire Waste and Sand Mixture Cushion Cases under All Input Motions ..... 322

5.3. The Effects of EPS Beads and Sand Mixture Cushion on the Seismic Performance of the Retaining Wall Model ..... 326

5.3.1. The Effects of Thickness and Mixture Ratio of EPS Beads and Sand Mixture Cushion ..... 326

5.3.1.1. Comparison of Improvement Efficiency under Far Field and Near Field Earthquake Motions ..... 327

5.3.1.2. Comparison of Maximum Spectral Accelerations under Far Field and Near Field Earthquake Motions ..... 331

5.3.1.3. Comparison of Improvement Efficiency under Sinusoidal Motions ... 339

5.3.1.4. Comparison of Maximum Spectral Accelerations under Sinusoidal Motions ..... 342

5.3.2. The Effects of Acceleration Response for EPS Beads and Sand Mixture Cushion under Different Input Motions..... 347

5.3.2.1. Maximum Acceleration Comparison at 4 cm Thickness ..... 347

5.3.2.2. Maximum Acceleration Comparison at 6 cm Thickness ..... 348

5.3.2.3. Maximum Acceleration Comparison at 8 cm Thickness ..... 350

5.3.3. Maximum Lateral Displacements for EPS Beads and Sand Mixture Cushion Cases under All Input Motions ..... 352

5.4. Comparison of Maximum Spectral Acceleration of the Backfill and the Top of the Retaining Wall Model ..... 356

5.5. Discussion on the Effects of Different Cushion Types ..... 362

5.5.1. Comparison of EPS Geofoam, Tire Waste and Sand Mixture, EPS Beads and Sand Mixture Cushioned Cases for t=4cm Thickness..... 362

5.5.2. Comparison of EPS Geofoam, Tire Waste and Sand Mixture, EPS Beads and Sand Mixture Cushioned Cases for t=8cm Thickness..... 370

6. CONCLUSIONS ..... 379

7. REFERENCES ..... 391

# LIST OF FIGURES

Figure 2.1. Common retaining wall types include a) gravity walls, b) cantilever walls, c) counterfort, d) crib walls, e) semi-gravity walls, f) bridge abutments (Day, 2012). .....6

Figure 2.2 Active earth pressure development through wall movement (Murthy, 2002). .....7

Figure 2.3 Passive earth pressure development through wall movement (Murthy, 2002). .....8

Figure 2.4 Forces in the Mononobe-Okabe analysis acting on the active wedge and a force polygon showing their equilibrium (Day, 2002). .....12

Figure 2.5 Forces in the Mononobe-Okabe analysis acting on the passive wedge and a force polygon showing their equilibrium (Day, 2002). .....13

Figure 2.6 Retaining wall movements to reach the active state (Das, 2006).....14

Figure 2.7 Retaining wall movements to reach the passive state (Das, 2006). .....14

Figure 2.8. Retaining wall failure modes induced by earthquakes (Day, 2002).....16

Figure 2.9. The gravity wall shifted outward at the construction joint after the 1999 Chi-Chi Earthquake (Fang et al., 2003).....20

Figure 2.10. Overturning of gravity wall after the 1999 Chi-Chi Earthquake (Fang et al., 2003). .....20

Figure 2.11. Overturning and sliding of retaining wall after the 1999 Chi-Chi Earthquake (Fang et al., 2003). .....21

Figure 2.12. Concrete gravity retaining wall with a trapezoidal shape rotated outward due to the failure of the slope during the 1999 Chi-Chi earthquake in Taiwan (Sitar et al., 2012). .....22

Figure 2.13. Reinforced retaining wall failure in the 2008 Wenchuan Earthquake (Changwei et al., 2015). .....22

Figure 2.14. Retaining wall failure in the 1995 Kobe Earthquake (Zamiran et al., 2016). .....23

Figure 2.15. Failure of retaining wall in the Mid-Nigata Prefecture Earthquake in 2004 (Zamiran et al., 2016). .....23

Figure 2.16 Construction of a geogrid-reinforced retaining wall: (a) Excavate the area for the retaining wall; (b) Install the geogrid layers; (c) Place the geotextile filter layer close to the wall's face; (d) Connect the folded geogrid sheet to the next sheet; (e) Observe the finished retaining wall (Shukla, 2016).....25

Figure 2.17 A schematic example of a retaining wall with EPS geofoam backfill (Alliance, 2012). .....29

Figure 2.18 The model's cross-section for the centrifuge test for the wall with EPS inclusion (Athanasopoulos-Zekkos et al., 2011). .....32

Figure 2.19 Young's modulus of the initial tangent and EPS density correlation (Horvart, 1994). .....34

Figure 2.20 Time-varying stress-strain behaviour under axial compression of EPS 23.5 kg/m$^3$ (Horvart, 1994). .....35

Figure 2.21 Correlation between EPS density and compressive strength (Horvart, 1994). .....35

Figure 2.22. Lightweight fill used as backfill to retaining structures (Hylands and Shulman, 2003). .....39

Figure 2.23. Proven applications for post-consumer tires in highway and related engineering applications (Hylands and Shulman, 2003). .....39

Figure 2.24 Sand backfills, EPS geofoam buffer, and boundary conditions (Zarnani and Bathurst, 2009).....54

Figure 2.25. Reinforced quay wall with tire chips cushion (Abdullah et al., 2017). .....57

Figure 2.26. Finite element mesh generated in the reinforced quay wall (Abdullah et al., 2017). .....57

Figure 2.27. FEM Model used during Numerical Analyses (Edinçliler and Toksoy, 2017)....58

Figure 2.28. Model of retaining wall and backfill for static condition with and without EPS geofoam (Yadav et al., 2018).....59

Figure 2.29. Experimental study (Zarnani et al., 2005). .....62

Figure 2.30 Input dynamic motion (Zarnani et al., 2005).....62

Figure 2.31 Cross-section of test model (Hazarika et al., 2008). .....65

Figure 2.32. Schematic diagram of retaining wall model with compressible inclusion (Reddy and Krishna, 2017).....67

Figure 2.33. Typical abutment cross section (facing perpendicular to centerline) (Lutenegger and Ciufetti, 2009). .....71

Figure 2.34. Full-scale test retaining wall a) plan view, b) cross section (Tweedie et al., 1998). .....72

Figure 2.35. Locations of the earth pressure cells (center panel, retaining wall, and detailed locations of the cells) (Hazarika et al., 2004). .....73

Figure 2.36. Test conditions. .....74

Figure 2.37. Distribution of earth pressure (15 cm thick EPS layer and 25 cm thick EPS layer) (Hazarika et al., 2004).....74

Figure 2.38. Performance comparison of the cushion (Hazarika et al., 2004). .....74

Figure 3.1. Silivri Sand. .....77

Figure 3.2. The grain size distribution of Silivri Sand.....78

Figure 3.3 The EPS Geofoam cushion material .....79

Figure 3.4 The grain size distribution of tire waste material. .....80

Figure 3.5. Tire crumb and sand mixture pictures a) TW10, b) TW20, and c) TW30 respectively. .....80

Figure 3.6. EPS Beads. .....81

Figure 3.7. EPS beads and sand mixture pictures a) EPSB10, b) EPSB20, and c) EPSB30, respectively. .....83

Figure 3.8. Laminar box installation process. .....85

Figure 3.9 Perform of static pull-out tests. .....87

Figure 3.10 The static forces measured from pull-out tests for each layer. .....87

Figure 3.11 The Acceleration-Time Histories of A9, A10, and A11 under sinusoidal motion at 0.3g amplitude with 1 Hz frequency. .....89

Figure 3.12 The Acceleration-Time Histories of A9, A10, and A11 under sinusoidal motion at 0.6g amplitude with 3 Hz frequency. .....90

Figure 3.13 The Acceleration-Time Histories of A9, A10, and A11 under sinusoidal motion at 0.6g amplitude with 3 Hz frequency. .....90

Figure 3.14. Laminar Box on the Shake Table at Boğaziçi University Kandilli Observatory and Earthquake Research Institute ShakeTable Laboratory. .....91

Figure 3.15 Illustration of the shake table, laminar box and the retaining wall model. .....92

Figure 3.16. a) The dimensioning of the retaining wall (TS7994/February 1990), b) The design of retaining walls (Azizi, 1999), c) Retaining wall preliminary dimensions (The Reinforced Concrete Design_ACI 318-14, 2016), d) The design of reinforced concrete retaining walls (TBEC, 2018).....93

Figure 3.17. The prototype retaining wall (the dimensions are in cm). ..... 94

Figure 3.18. 1/15 scaled retaining wall model (the dimensions are in cm). ..... 96

Figure 3.19 The ACCTH and FAS of the scaled 1999 Kocaeli EQ Motion-İznik Station (FF). ..... 105

Figure 3.20. The ACCTH and FAS of the scaled 2014 Gökçeada EQ Motion-Çanakkale Station (FF). ..... 105

Figure 3.21. The ACCTH and FAS of the scaled 2020 İzmir EQ Motion-Kuşadası Station (FF). ..... 106

Figure 3.22. The ACCTH and FAS of the scaled 1999 Kocaeli EQ Motion-İzmit Station (NF). ..... 106

Figure 3.23. The ACCTH and FAS of the scaled 1940 Imperial Valley EQ El Centro Station (NF). ..... 107

Figure 3.24. The ACCTH and FAS of the scaled 1995 Kobe EQ (NF). ..... 107

Figure 3.25. a) The ACCTH of sinusoidal motion at 0.3g amplitude with 8 Hz frequency b) The ACCTH of sinusoidal motion at 0.4g amplitude with 8 Hz frequency c) The ACCTH of sinusoidal motion at 0.5g amplitude with 8 Hz frequency d) The ACCTH of sinusoidal motion at 0.4g amplitude with 12 Hz frequency e) The ACCTH of sinusoidal motion at 0.4g amplitude with 14 Hz frequency. ..... 108

Figure 3.26. Experimental Study Program. ..... 110

Figure 3.27. The cross-section of the instrumentation of the control case. ..... 112

Figure 3.28. Front view of the instrumentation of the control case. ..... 112

Figure 3.29. The cross-section of the instrumentation of the cushioned cases. ..... 113

Figure 3.30. Front view of the instrumentation of the cushioned cases. ..... 113

Figure 3.31. Instrumentation of the experimental study a-e) positioning of laser displacement sensors and placement of accelerometers on the retaining wall, f-g) placement of accelerometers and laser displacement sensors in the foundation backfill and on the laminar box and view of the set-up. ..... 114

Figure 3.32 Retaining wall model without cushion (Control Case). ..... 116

Figure 3.33 The illustrations of the control case experimental setup a) placement of A13, b) placement of A15, c-f) placement of retaining wall model, accelerometers, and positioning of the laser displacement sensor. ..... 117

Figure 3.34 The illustrations of the EPS geofoam cushioned cases experimental setup a-b) placement of EPS Geofoam, c) placement of backfill, d-e-f) positioning of accelerometers and laser displacement sensors. ..... 120

Figure 3.35 EPS Geofoam cushioned cases of the study a) Case 2, b) Case 3, c) Case 4, d) Case 5, e) Case 6, f) Case 7. ..... 121

Figure 3.36 The illustrations of the tire waste and sand mixture cushioned cases experimental setup a) emptying the laminar box, b) mixture preparation, c) placement of cushion, d) placement of backfill, e-f) positioning of accelerometers and laser displacement sensors. ... 124

Figure 3.37 Tire waste and sand mixture cushioned cases of the study a) Case 8, b) Case 9, c) Case 10, d) Case 11, e) Case 12, f) Case 13. ..... 125

Figure 3.38 EPS beads and sand mixture cushioned cases experimental setup a-b) mixture preparation, c) unloading process, d-e) placement of cushion and placement of backfill, f) positioning of accelerometers and laser displacement sensors. ..... 128

Figure 3.39 EPS beads and sand mixture cushioned cases of the study a) Case14, b) Case 15, c) Case 16, d) Case 17, e) Case 18, f) Case 19, g) Case 20, h) Case 21, i) Case 22. ..... 130

Figure 4.1. The ACCTH, FAS, Response Spectrum at the top of the RWM (A7) and in the backfill (A16) for Case 1 compared to input motion (A1) under the scaled 2020 İzmir EQ Motion-Kuşadası Station record (FF). ..... 133

Figure 4.2. The DISTH at the top of the RWM (D19) for Case 1 compared to input motion (D17) under the scaled 2020 İzmir EQ Motion-Kuşadası Station record (FF). ..... 133

Figure 4.3. The ACCTH, FAS, Response Spectrum at the top of the RWM (A7) and in the backfill (A16) for Case 1 compared to input motion (A1) under the scaled 1940 Imperial Valley EQ-El Centro Station record (NF). ..... 135

Figure 4.4. The DISTH at the top of the RWM (D19) for Case 1 compared to input motion (D17) under the scaled 1940 Imperial Valley EQ-El Centro Station record (NF). ..... 135

Figure 4.5. The ACCTH, FAS, Response Spectrum at the top of the RWM (A7) and in the backfill (A16) for Case 1 compared to input motion (A1) under sinusoidal motion at 0.4g amplitude with 8 Hz frequency. ..... 136

Figure 4.6. The DISTH at the top of the RWM (D19) for Case 1 compared to input motion (D17) under sinusoidal motion at 0.4g amplitude with 8 Hz frequency. ..... 136

Figure 4.7. The ACCTH, FAS, Response Spectrum at the top of the RWM (A7) and in the backfill (A16) for Case 2 compared to Case 1 under the scaled 2020 İzmir EQ Motion-Kuşadası Station record (FF). ..... 138

Figure 4.8. The DISTH at the top of the RWM (D19) for Case 2 compared to Case 1 under the scaled 2020 İzmir EQ Motion-Kuşadası Station record (FF). ..... 138

Figure 4.9. The ACCTH, FAS, Response Spectrum at the top of the RWM (A7) and in the backfill (A16) for Case 2 compared to Case 1 under the scaled 1940 Imperial Valley EQ-El Centro Station record (NF). ..... 140

Figure 4.10. The DISTH at the top of the RWM (D19) for Case 2 compared to Case 1 under the scaled 1940 Imperial Valley EQ-El Centro Station record (NF). ..... 140

Figure 4.11. The ACCTH, FAS, Response Spectrum at the top of the RWM (A7) and in the backfill (A16) for Case 2 compared to Case 1 under sinusoidal motion at 0.4g amplitude with 8 Hz frequency. ..... 142

Figure 4.12. The DISTH at the top of the RWM (D19) for Case 2 compared to Case 1 under sinusoidal motion at 0.4g amplitude with 8 Hz frequency. ..... 142

Figure 4.13. The ACCTH, FAS, Response Spectrum at the top of the RWM (A7) and in the backfill (A16) for Case 3 compared to Case 1 under the scaled 2020 İzmir EQ Motion-Kuşadası Station record (FF). ..... 144

Figure 4.14. The DISTH at the top of the RWM (D19) for Case 3 compared to Case 1 under the scaled 2020 İzmir EQ Motion-Kuşadası Station record (FF). ..... 144

Figure 4.15. The ACCTH, FAS, Response Spectrum at the top of the RWM (A7) and in the backfill (A16) for Case 3 compared to Case 1 under the scaled 1940 Imperial Valley EQ-El Centro Station record (NF). ..... 146

Figure 4.16. The DISTH at the top of the RWM (D19) for Case 3 compared to Case 1 under the scaled 1940 Imperial Valley EQ-El Centro Station record (NF). ..... 146

Figure 4.17. The ACCTH, FAS, Response Spectrum at the top of the RWM (A7) and in the backfill (A16) for Case 3 compared to Case 1 under sinusoidal motion at 0.4g amplitude with 8 Hz frequency. ..... 148

Figure 4.18. The DISTH at the top of the RWM (D19) for Case 3 compared to Case 1 under sinusoidal motion at 0.4g amplitude with 8 Hz frequency. ..... 148

Figure 4.19. The ACCTH, FAS, Response Spectrum at the top of the RWM (A7) and in the backfill (A16) for Case 4 compared to Case 1 under the scaled 2020 İzmir EQ Motion-Kuşadası Station record (FF). ..... 150

Figure 4.20. The DISTH at the top of the RWM (D19) for Case 4 compared to Case 1 under the scaled 2020 İzmir EQ Motion-Kuşadası Station record (FF). ..... 150

Figure 4.21. The ACCTH, FAS, Response Spectrum at the top of the RWM (A7) and in the backfill (A16) for Case 4 compared to Case 1 under the scaled 1940 Imperial Valley EQ-El Centro Station record (NF). ..... 152

Figure 4.22. The DISTH at the top of the RWM (D19) for Case 4 compared to Case 1 under the scaled 1940 Imperial Valley EQ-El Centro Station record (NF). ..... 152

Figure 4.23. The ACCTH, FAS, Response Spectrum at the top of the RWM (A7) and in the backfill (A16) for Case 4 compared to Case 1 under sinusoidal motion at 0.4g amplitude with 8 Hz frequency. ..... 154

Figure 4.24. The DISTH at the top of the RWM (D19) for Case 4 compared to Case 1 under sinusoidal motion at 0.4g amplitude with 8 Hz frequency. ..... 154

Figure 4.25. The ACCTH, FAS, Response Spectrum at the top of the RWM (A7) and in the backfill (A16) for Case 5 compared to Case 1 under the scaled 2020 İzmir EQ Motion-Kuşadası Station record (FF). ..... 156

Figure 4.26 The DISTH at the top of the RWM (D19) for Case 5 compared to Case 1 under the scaled 2020 İzmir EQ Motion-Kuşadası Station record (FF). ..... 156

Figure 4.27. The ACCTH, FAS, Response Spectrum at the top of the RWM (A7) and in the backfill (A16) for Case 5 compared to Case 1 under the scaled 1940 Imperial Valley EQ-El Centro Station record (NF). ..... 158

Figure 4.28. The DISTH at the top of the RWM (D19) for Case 5 compared to Case 1 under the scaled 1940 Imperial Valley EQ-El Centro Station record (NF). ..... 158

Figure 4.29. The ACCTH, FAS, Response Spectrum at the top of the RWM (A7) and in the backfill (A16) for Case 5 compared to Case 1 under sinusoidal motion at 0.4g amplitude with 8 Hz frequency. ..... 160

Figure 4.30. The DISTH at the top of the RWM (D19) for Case 5 compared to Case 1 under sinusoidal motion at 0.4g amplitude with 8 Hz frequency. ..... 160

Figure 4.31. The ACCTH, FAS, Response Spectrum at the top of the RWM (A7) and in the backfill (A16) for Case 6 compared to Case 1 under the scaled 2020 İzmir EQ Motion-Kuşadası Station record (FF). ..... 162

Figure 4.32. The DISTH at the top of the RWM (D19) for Case 6 compared to Case 1 under the scaled 2020 İzmir EQ Motion-Kuşadası Station record (FF). ..... 162

Figure 4.33. The ACCTH, FAS, Response Spectrum at the top of the RWM (A7) and in the backfill (A16) for Case 6 compared to Case 1 under the scaled 1940 Imperial Valley EQ-El Centro Station record (NF). ..... 164

Figure 4.34. The DISTH at the top of the RWM (D19) for Case 6 compared to Case 1 under the scaled 1940 Imperial Valley EQ-El Centro Station record (NF). ..... 164

Figure 4.35. The ACCTH, FAS, Response Spectrum at the top of the RWM (A7) and in the backfill (A16) for Case 6 compared to Case 1 under sinusoidal motion at 0.4g amplitude with 8 Hz frequency. ..... 166

Figure 4.36. The DISTH at the top of the RWM (D19) for Case 6 compared to Case 1 under sinusoidal motion at 0.4g amplitude with 8 Hz frequency. ..... 166

Figure 4.37. The ACCTH, FAS, Response Spectrum at the top of the RWM (A7) and in the backfill (A16) for Case 7 compared to Case 1 under the scaled 2020 İzmir EQ Motion-Kuşadası Station record (FF). ..... 168

Figure 4.38. The DISTH at the top of the RWM (D19) for Case 7 compared to Case 1 under the scaled 2020 İzmir EQ Motion-Kuşadası Station record (FF). ..... 168

Figure 4.39. The ACCTH, FAS, Response Spectrum at the top of the RWM (A7) and in the backfill (A16) for Case 7 compared to Case 1 under the scaled 1940 Imperial Valley EQ-El Centro Station record (NF). ..... 170

Figure 4.40. The DISTH at the top of the RWM (D19) for Case 7 compared to Case 1 under the scaled 1940 Imperial Valley EQ-El Centro Station record (NF). ..... 170

Figure 4.41. The ACCTH, FAS, Response Spectrum at the top of the RWM (A7) and in the backfill (A16) for Case 7 compared to Case 1 under sinusoidal motion at 0.4g amplitude with 8 Hz frequency. ..... 172

Figure 4.42. The DISTH at the top of the RWM (D19) for Case 7 compared to Case 1 under sinusoidal motion at 0.4g amplitude with 8 Hz frequency. ..... 172

Figure 4.43. The ACCTH, FAS, Response Spectrum at the top of the RWM (A7) and in the backfill (A16) for Case 8 compared to Case 1 under the scaled 2020 İzmir EQ Motion-Kuşadası Station record (FF). ..... 174

Figure 4.44. The DISTH at the top of the RWM (D19) for Case 8 compared to Case 1 under the scaled 2020 İzmir EQ Motion-Kuşadası Station record (FF). ..... 174

Figure 4.45. The ACCTH, FAS, Response Spectrum at the top of the RWM (A7) and in the backfill (A16) for Case 8 compared to Case 1 under the scaled 1940 Imperial Valley EQ-El Centro Station record (NF). ..... 176

Figure 4.46. The DISTH at the top of the RWM (D19) for Case 8 compared to Case 1 under the scaled 1940 Imperial Valley EQ-El Centro Station record (NF). ..... 176

Figure 4.47. The ACCTH, FAS, Response Spectrum at the top of the RWM (A7) and in the backfill (A16) for Case 8 compared to Case 1 under sinusoidal motion at 0.4g amplitude with 8 Hz frequency. ..... 178

Figure 4.48. The DISTH at the top of the RWM (D19) for Case 8 compared to Case 1 under sinusoidal motion at 0.4g amplitude with 8 Hz frequency. ..... 178

Figure 4.49. The ACCTH, FAS, Response Spectrum at the top of the RWM (A7) and in the backfill (A16) for Case 9 compared to Case 1 under the scaled 2020 İzmir EQ Motion-Kuşadası Station record (FF). ..... 180

Figure 4.50. The DISTH at the top of the RWM (D19) for Case 9 compared to Case 1 under the scaled 2020 İzmir EQ Motion-Kuşadası Station record (FF). ..... 180

Figure 4.51. The ACCTH, FAS, Response Spectrum at the top of the RWM (A7) and in the backfill (A16) for Case 9 compared to Case 1 under the scaled 1940 Imperial Valley EQ-El Centro Station record (NF). ..... 182

Figure 4.52. The DISTH at the top of the RWM (D19) for Case 9 compared to Case 1 under the scaled 1940 Imperial Valley EQ-El Centro Station record (NF). ..... 182

Figure 4.53. The ACCTH, FAS, Response Spectrum at the top of the RWM (A7) and in the backfill (A16) for Case 9 compared to Case 1 under sinusoidal motion at 0.4g amplitude with 8 Hz frequency. ..... 184

Figure 4.54. The DISTH at the top of the RWM (D19) for Case 9 compared to Case 1 under sinusoidal motion at 0.4g amplitude with 8 Hz frequency. ..... 184

Figure 4.55. The ACCTH, FAS, Response Spectrum at the top of the RWM (A7) and in the backfill (A16) for Case 10 compared to Case 1 under the scaled 2020 İzmir EQ Motion-Kuşadası Station record (FF). ..... 186

Figure 4.56. The DISTH at the top of the RWM (D19) for Case 10 compared to Case 1 under the scaled 2020 İzmir EQ Motion-Kuşadası Station record (FF). ..... 186

Figure 4.57. The ACCTH, FAS, Response Spectrum at the top of the RWM (A7) and in the backfill (A16) for Case 10 compared to Case 1 under sinusoidal motion at 0.4g amplitude with 8 Hz frequency. ..... 188

Figure 4.58. The DISTH at the top of the RWM (D19) for Case 10 compared to Case 1 under sinusoidal motion at 0.4g amplitude with 8 Hz frequency. ..... 188

Figure 4.59. The ACCTH, FAS, Response Spectrum at the top of the RWM (A7) and in the backfill (A16) for Case 10 compared to Case 1 under sinusoidal motion at 0.4g amplitude with 8 Hz frequency. ..... 190

Figure 4.60. The DISTH at the top of the RWM (D19) for Case 10 compared to Case 1 under sinusoidal motion at 0.4g amplitude with 8 Hz frequency. ..... 190

Figure 4.61. The ACCTH, FAS, Response Spectrum at the top of the RWM (A7) and in the backfill (A16) for Case 11 compared to Case 1 under the scaled 2020 İzmir EQ Motion-Kuşadası Station record (FF). ..... 192

Figure 4.62. The DISTH at the top of the RWM (D19) for Case 11 compared to Case 1 under the scaled 2020 İzmir EQ Motion-Kuşadası Station record (FF). ..... 192

Figure 4.63. The ACCTH, FAS, Response Spectrum at the top of the RWM (A7) and in the backfill (A16) for Case 11 compared to Case 1 under the scaled 1940 Imperial Valley EQ-El Centro Station record (NF). ..... 194

Figure 4.64. The DISTH at the top of the RWM (D19) for Case 11 compared to Case 1 under the scaled 1940 Imperial Valley EQ-El Centro Station record (NF). ..... 194

Figure 4.65. The ACCTH, FAS, Response Spectrum at the top of the RWM (A7) and in the backfill (A16) for Case 11 compared to Case 1 under sinusoidal motion at 0.4g amplitude with 8 Hz frequency. ..... 196

Figure 4.66. The DISTH at the top of the RWM (D19) for Case 11 compared to Case 1 under sinusoidal motion at 0.4g amplitude with 8 Hz frequency. ..... 196

Figure 4.67. The ACCTH, FAS, Response Spectrum at the top of the RWM (A7) and in the backfill (A16) for Case 12 compared to Case 1 under the scaled 2020 İzmir EQ Motion-Kuşadası Station record (FF). ..... 198

Figure 4.68. The DISTH at the top of the RWM (D19) for Case 12 compared to Case 1 under the scaled 2020 İzmir EQ Motion-Kuşadası Station record (FF). ..... 198

Figure 4.69. The ACCTH, FAS, Response Spectrum at the top of the RWM (A7) and in the backfill (A16) for Case 12 compared to Case 1 under the scaled 1940 Imperial Valley EQ-El Centro Station record (NF). ..... 200

Figure 4.70. The DISTH at the top of the RWM (D19) for Case 12 compared to Case 1 under the scaled 1940 Imperial Valley EQ-El Centro Station record (NF). ..... 200

Figure 4.71. The ACCTH, FAS, Response Spectrum at the top of the RWM (A7) and in the backfill (A16) for Case 12 compared to Case 1 under sinusoidal motion at 0.4g amplitude with 8 Hz frequency. ..... 202

Figure 4.72. The DISTH at the top of the RWM (D19) for Case 12 compared to Case 1 under sinusoidal motion at 0.4g amplitude with 8 Hz frequency. ..... 202

Figure 4.73. The ACCTH, FAS, Response Spectrum at the top of the RWM (A7) and in the backfill (A16) for Case 13 compared to Case 1 under the scaled 2020 İzmir EQ Motion-Kuşadası Station record (FF). ..... 204

Figure 4.74. The DISTH at the top of the RWM (D19) for Case 13 compared to Case 1 under the scaled 2020 İzmir EQ Motion-Kuşadası Station record (FF). ..... 204

Figure 4.75. The ACCTH, FAS, Response Spectrum at the top of the RWM (A7) and in the backfill (A16) for Case 13 compared to Case 1 under the scaled 1940 Imperial Valley EQ-El Centro Station record (NF). ..... 206

Figure 4.76. The DISTH at the top of the RWM (D19) for Case 13 compared to Case 1 under the scaled 1940 Imperial Valley EQ-El Centro Station record (NF). ..... 206

Figure 4.77. The ACCTH, FAS, Response Spectrum at the top of the RWM (A7) and in the backfill (A16) for Case 13 compared to Case 1 under sinusoidal motion at 0.4g amplitude with 8 Hz frequency. ..... 208

Figure 4.78. The DISTH at the top of the RWM (D19) for Case 13 compared to Case 1 under sinusoidal motion at 0.4g amplitude with 8 Hz frequency. ..... 208

Figure 4.79. The ACCTH, FAS, Response Spectrum at the top of the RWM (A7) and in the backfill (A16) for Case 14 compared to Case 1 under the scaled 2020 İzmir EQ Motion-Kuşadası Station record (FF). ..... 210

Figure 4.80. The DISTH at the top of the RWM (D19) for Case 14 compared to Case 1 under the scaled 2020 İzmir EQ Motion-Kuşadası Station record (FF). ..... 210

Figure 4.81. The ACCTH, FAS, Response Spectrum at the top of the RWM (A7) and in the backfill (A16) for Case 14 compared to Case 1 under the scaled 1940 Imperial Valley EQ-El Centro Station record (NF). ..... 212

Figure 4.82. The DISTH at the top of the RWM (D19) for Case 14 compared to Case 1 under the scaled 1940 Imperial Valley EQ-El Centro Station record (NF). ..... 212

Figure 4.83. The ACCTH, FAS, Response Spectrum at the top of the RWM (A7) and in the backfill (A16) for Case 14 compared to Case 1 under sinusoidal motion at 0.4g amplitude with 8 Hz frequency. ..... 214

Figure 4.84. The DISTH at the top of the RWM (D19) for Case 14 compared to Case 1 under sinusoidal motion at 0.4g amplitude with 8 Hz frequency. ..... 214

Figure 4.85. The ACCTH, FAS, Response Spectrum at the top of the RWM (A7) and in the backfill (A16) for Case 15 compared to Case 1 under the scaled 2020 İzmir EQ Motion-Kuşadası Station record (FF). ..... 216

Figure 4.86. The DISTH at the top of the RWM (D19) for Case 15 compared to Case 1 under the scaled 2020 İzmir EQ Motion-Kuşadası Station record (FF). ..... 216

Figure 4.87. The ACCTH, FAS, Response Spectrum at the top of the RWM (A7) and in the backfill (A16) for Case 15 compared to Case 1 under the scaled 1940 Imperial Valley EQ-El Centro Station record (NF). ..... 218

Figure 4.88. The DISTH at the top of the RWM (D19) for Case 15 compared to Case 1 under the scaled 1940 Imperial Valley EQ-El Centro Station record (NF). ..... 218

Figure 4.89. The ACCTH, FAS, Response Spectrum at the top of the RWM (A7) and in the backfill (A16) for Case 15 compared to Case 1 under sinusoidal motion at 0.4g amplitude with 8 Hz frequency. ..... 220

Figure 4.90. The DISTH at the top of the RWM (D19) for Case 15 compared to Case 1 under sinusoidal motion at 0.4g amplitude with 8 Hz frequency. ..... 220

Figure 4.91. The ACCTH, FAS, Response Spectrum at the top of the RWM (A7) and in the backfill (A16) for Case 16 compared to Case 1 under the scaled 2020 İzmir EQ Motion-Kuşadası Station record (FF). ..... 222

Figure 4.92. The DISTH at the top of the RWM (D19) for Case 16 compared to Case 1 under the scaled 2020 İzmir EQ Motion-Kuşadası Station record (FF). ..... 222

Figure 4.93. The ACCTH, FAS, Response Spectrum at the top of the RWM (A7) and in the backfill (A16) for Case 16 compared to Case 1 under the scaled 1940 Imperial Valley EQ-El Centro Station record (NF). ..... 224

Figure 4.94. The DISTH at the top of the RWM (D19) for Case 16 compared to Case 1 under the scaled 1940 Imperial Valley EQ-El Centro Station record (NF). ..... 224

Figure 4.95. The ACCTH, FAS, Response Spectrum at the top of the RWM (A7) and in the backfill (A16) for Case 16 compared to Case 1 under sinusoidal motion at 0.4g amplitude with 8 Hz frequency. ..... 226

Figure 4.96. The DISTH at the top of the RWM (D19) for Case 16 compared to Case 1 under sinusoidal motion at 0.4g amplitude with 8 Hz frequency. ..... 226

Figure 4.97. The ACCTH, FAS, Response Spectrum at the top of the RWM (A7) and in the backfill (A16) for Case 17 compared to Case 1 under the scaled 2020 İzmir EQ Motion-Kuşadası Station record (FF). ..... 228

Figure 4.98. The DISTH at the top of the RWM (D19) for Case 17 compared to Case 1 under the scaled 2020 İzmir EQ Motion-Kuşadası Station record (FF). ..... 228

Figure 4.99. The ACCTH, FAS, Response Spectrum at the top of the RWM (A7) and in the backfill (A16) for Case 17 compared to Case 1 under the scaled 1940 Imperial Valley EQ-El Centro Station record (NF). ..... 230

Figure 4.100. The DISTH at the top of the RWM (D19) for Case 17 compared to Case 1 under the scaled 1940 Imperial Valley EQ-El Centro Station record (NF). ..... 230

Figure 4.101. The ACCTH, FAS, Response Spectrum at the top of the RWM (A7) and in the backfill (A16) for Case 17 compared to Case 1 under sinusoidal motion at 0.4g amplitude with 8 Hz frequency. ..... 232

Figure 4.102. The DISTH at the top of the RWM (D19) for Case 17 compared to Case 1 under sinusoidal motion at 0.4g amplitude with 8 Hz frequency. ..... 232

Figure 4.103. The ACCTH, FAS, Response Spectrum at the top of the RWM (A7) and in the backfill (A16) for Case 18 compared to Case 1 under the scaled 2020 İzmir EQ Motion-Kuşadası Station record (FF). ..... 234

Figure 4.104. The DISTH at the top of the RWM (D19) for Case 18 compared to Case 1 under the scaled 2020 İzmir EQ Motion-Kuşadası Station record (FF). ..... 234

Figure 4.105. The ACCTH, FAS, Response Spectrum at the top of the RWM (A7) and in the backfill (A16) for Case 18 compared to Case 1 under the scaled 1940 Imperial Valley EQ-El Centro Station record (NF). ..... 236

Figure 4.106. The DISTH at the top of the RWM (D19) for Case 18 compared to Case 1 under the scaled 1940 Imperial Valley EQ-El Centro Station record (NF). ..... 236

Figure 4.107. The ACCTH, FAS, Response Spectrum at the top of the RWM (A7) and in the backfill (A16) for Case 18 compared to Case 1 under sinusoidal motion at 0.4g amplitude with 8 Hz frequency. ..... 238

Figure 4.108. The DISTH at the top of the RWM (D19) for Case 18 compared to Case 1 under sinusoidal motion at 0.4g amplitude with 8 Hz frequency. ..... 238

Figure 4.109. The ACCTH, FAS, Response Spectrum at the top of the RWM (A7) and in the backfill (A16) for Case 19 compared to Case 1 under the scaled 2020 İzmir EQ Motion-Kuşadası Station record (FF). ..... 240

Figure 4.110. The DISTH at the top of the RWM (D19) for Case 19 compared to Case 1 under the scaled 2020 İzmir EQ Motion-Kuşadası Station record (FF). ..... 240

Figure 4.111. The ACCTH, FAS, Response Spectrum at the top of the RWM (A7) and in the backfill (A16) for Case 19 compared to Case 1 under the scaled 1940 Imperial Valley EQ-El Centro Station record (NF). ..... 242

Figure 4.112. The DISTH at the top of the RWM (D19) for Case 19 compared to Case 1 under the scaled 1940 Imperial Valley EQ-El Centro Station record (NF). ..... 242

Figure 4.113. The ACCTH, FAS, Response Spectrum at the top of the RWM (A7) and in the backfill (A16) for Case 19 compared to Case 1 under sinusoidal motion at 0.4g amplitude with 8 Hz frequency. ..... 244

Figure 4.114. The DISTH at the top of the RWM (D19) for Case 19 compared to Case 1 under sinusoidal motion at 0.4g amplitude with 8 Hz frequency. ..... 244

Figure 4.115. The ACCTH, FAS, Response Spectrum at the top of the RWM (A7) and in the backfill (A16) for Case 20 compared to Case 1 under the scaled 2020 İzmir EQ Motion-Kuşadası Station record (FF). ..... 246

Figure 4.116. The DISTH at the top of the RWM (D19) for Case 21 compared to Case 1 under the scaled 2020 İzmir EQ Motion-Kuşadası Station record (FF). ..... 246

Figure 4.117. The ACCTH, FAS, Response Spectrum at the top of the RWM (A7) and in the backfill (A16) for Case 20 compared to Case 1 under the scaled 1940 Imperial Valley EQ-El Centro Station record (NF). ..... 248

Figure 4.118. The DISTH at the top of the RWM (D19) for Case 20 compared to Case 1 under the scaled 1940 Imperial Valley EQ-El Centro Station record (NF). ..... 248

Figure 4.119. The ACCTH, FAS, Response Spectrum at the top of the RWM (A7) and in the backfill (A16) for Case 20 compared to Case 1 under sinusoidal motion at 0.4g amplitude with 8 Hz frequency. ..... 250

Figure 4.120. The DISTH at the top of the RWM (D19) for Case 20 compared to Case 1 under sinusoidal motion at 0.4g amplitude with 8 Hz frequency. ..... 250

Figure 4.121. The ACCTH, FAS, Response Spectrum at the top of the RWM (A7) and in the backfill (A16) for Case 21 compared to Case 1 under the scaled 2020 İzmir EQ Motion-Kuşadası Station record (FF). ..... 252

Figure 4.122. The DISTH at the top of the RWM (D19) for Case 22 compared to Case 1 under the scaled 2020 İzmir EQ Motion-Kuşadası Station record (FF). ..... 252

Figure 4.123. The ACCTH, FAS, Response Spectrum at the top of the RWM (A7) and in the backfill (A16) for Case 21 compared to Case 1 under the scaled 1940 Imperial Valley EQ-El Centro Station record (NF). ..... 254

Figure 4.124. The DISTH at the top of the RWM (D19) for Case 21 compared to Case 1 under the scaled 1940 Imperial Valley EQ-El Centro Station record (NF). ..... 254

Figure 4.125. The ACCTH, FAS, Response Spectrum at the top of the RWM (A7) and in the backfill (A16) for Case 21 compared to Case 1 under sinusoidal motion at 0.4g amplitude with 8 Hz frequency. ..... 256

Figure 4.126. The DISTH at the top of the RWM (D19) for Case 21 compared to Case 1 under sinusoidal motion at 0.4g amplitude with 8 Hz frequency. ..... 256

Figure 4.127. The ACCTH, FAS, Response Spectrum at the top of the RWM (A7) and in the backfill (A16) for Case 22 compared to Case 1 under the scaled 2020 İzmir EQ Motion-Kuşadası Station record (FF). ..... 258

Figure 4.128. The DISTH at the top of the RWM (D19) for Case 22 compared to Case 1 under the scaled 2020 İzmir EQ Motion-Kuşadası Station record (FF). ..... 258

Figure 4.129. The ACCTH, FAS, Response Spectrum at the top of the RWM (A7) and in the backfill (A16) for Case 22 compared to Case 1 under the scaled 1940 Imperial Valley EQ-El Centro Station record (NF). ..... 260

Figure 4.130. The DISTH at the top of the RWM (D19) for Case 22 compared to Case 1 under the scaled 1940 Imperial Valley EQ-El Centro Station record (NF). ..... 260

Figure 4.131. The ACCTH, FAS, Response Spectrum at the top of the RWM (A7) and in the backfill (A16) for Case 22 compared to Case 1 under sinusoidal motion at 0.4g amplitude with 8 Hz frequency. ..... 262

Figure 4.132. The DISTH at the top of the RWM (D19) for Case 22 compared to Case 1 under sinusoidal motion at 0.4g amplitude with 8 Hz frequency. ..... 262

Figure 5.1. Improvement efficiencies for all EPS Geofoam cushioned cases with respect to A7 under a) the scaled 1999 Kocaeli EQ Motion-İznik Station Record-FF, b) the scaled 2014 Gökçeada EQ Motion-Çanakkale Station Record-FF, c) the scaled 2020 İzmir EQ Motion-Kuşadası Station Record-FF, d) the scaled 1999 Kocaeli EQ Motion-İzmit Station Record-NF, e) the scaled 1940 Imperial Valley EQ-El Centro Station record-NF, f) the scaled 1995 Kobe EQ Record-NF. ..... 268

Figure 5.2 Response Spectrums of all EPS Geofoam cushioned cases with respect to A7 under a-b-c) the scaled 1999 Kocaeli EQ Motion-İznik Station Record-FF, d-e-f) the scaled 2014 Gökçeada EQ Motion-Çanakkale Station Record-FF, g-h-i) the scaled 2020 İzmir EQ Motion-Kuşadası Station Record-FF. ..... 272

Figure 5.3 Response Spectrums of all EPS Geofoam cushioned cases with respect to A7 under a-b-c) the scaled 1999 Kocaeli EQ Motion-İzmit Station Record-NF, d-e-f) the scaled 1940 Imperial Valley EQ-El Centro Station record-NF, g-h-i) the scaled 1995 Kobe EQ Record-NF. ..... 276

Figure 5.4. Improvement efficiencies for all EPS Geofoam cushioned cases with respect to A7 under a) sinusoidal motion at 0.3g amplitude with 8 Hz frequency, b) sinusoidal motion at 0.4g amplitude with 8 Hz frequency, c) sinusoidal motion at 0.5g amplitude with 8 Hz frequency, d) sinusoidal motion at 0.4g amplitude with 12 Hz frequency, e) sinusoidal motion at 0.4g amplitude with 14 Hz frequency. ..... 280

Figure 5.5 Response Spectrums of all EPS Geofoam cushioned cases with respect to A7 under a-b-c) sinusoidal motion at 0.3g amplitude with 8 Hz frequency, d-e-f) sinusoidal motion at 0.4g

amplitude with 8 Hz frequency, g-h-i) sinusoidal motion at 0.5g amplitude with 8 Hz frequency. .....285

Figure 5.6 Response Spectrums of all EPS Geofoam cushioned cases with respect to A7 under a-b-c) sinusoidal motion at 0.4g amplitude with 12 Hz frequency, d-e-f) sinusoidal motion at 0.4g amplitude with 14 Hz frequency. .....286

Figure 5.7 Variation of maximum accelerations at the top of the RWM for EPS Geofoam cases with t=4cm compared to the control case under all input motions. .....288

Figure 5.8 Variation of maximum accelerations at the top of the RWM for EPS Geofoam cases with t=8cm compared to the control case under all input motions. .....290

Figure 5.9. Maximum lateral displacements measured from D19 under all input motions a) Case 1, b) Case 2, c) Case 3, d) Case 4, e) Case 5, f) Case 6, g) Case 7. .....292

Figure 5.10. Improvement efficiency for all Tire Waste and Sand Mixture cushioned cases with respect to A7 under a) the scaled 1999 Kocaeli EQ Motion-İznik Station Record-FF, b) the scaled 2014 Gökçeada EQ Motion-Çanakkale Station Record-FF, c) the scaled 2020 İzmir EQ Motion-Kuşadası Station Record-FF, d) the scaled 1999 Kocaeli EQ Motion-İzmit Station Record-NF, e) the scaled 1940 Imperial Valley EQ-El Centro Station record-NF, f) the scaled 1995 Kobe EQ record-NF. .....300

Figure 5.11 Response Spectrums of all Tire Waste and Sand Mixture cushioned cases with respect to A7 under a-b-c) the scaled 1999 Kocaeli EQ Motion-İznik Station Record-FF, d-e-f) the scaled 2014 Gökçeada EQ Motion-Çanakkale Station Record-FF, g-h-i) the scaled 2020 İzmir EQ Motion-Kuşadası Station Record-FF. .....305

Figure 5.12 Response Spectrums of all Tire Waste and Sand Mixture cushioned cases with respect to A7 under a-b-c) the scaled 1999 Kocaeli EQ Motion-İzmit Station Record-NF, d-e-f) the scaled 1940 Imperial Valley EQ-El Centro Station record-NF, g-h-i) the scaled 1995 Kobe EQ Record-NF. .....309

Figure 5.13. Improvement efficiency for all Tire Waste and Sand Mixture cushioned cases with respect to A7 under a) sinusoidal motion at 0.3g amplitude with 8 Hz frequency, b) sinusoidal motion at 0.4g amplitude with 8 Hz frequency, c) sinusoidal motion at 0.5g amplitude with 8 Hz frequency, d) sinusoidal motion at 0.4g amplitude with 12 Hz frequency, e) sinusoidal motion at 0.4g amplitude with 14 Hz frequency. .....312

Figure 5.14 Response Spectrums of all Tire Waste and Sand Mixture cushioned cases with respect to A7 under a-b-c) sinusoidal motion at 0.3g amplitude with 8 Hz frequency, d-e-f) sinusoidal motion at 0.4g amplitude with 8 Hz frequency, g-h-i) sinusoidal motion at 0.5g amplitude with 8 Hz frequency.....316

Figure 5.15 Response Spectrums of all Tire Waste and Sand Mixture cushioned cases with respect to A7 under a-b-c) sinusoidal motion at 0.4g amplitude with 12 Hz frequency, d-e-f) sinusoidal motion at 0.4g amplitude with 14 Hz frequency. .....317

Figure 5.16 Variation of maximum accelerations at the top of the RWM for Tire Waste and Sand Mixture cases with t=4cm compared to the control case under all input motions.....319

Figure 5.17 Variation of maximum accelerations at the top of the RWM for Tire Waste and Sand Mixture cases with t=8cm compared to the control case under all input motions.....321

Figure 5.18. Maximum lateral displacements measured from D19 under all input motions a) Case 8, b) Case 9, c) Case 10, d) Case 11, e) Case 12, f) Case 6, g) Case 13. .....323

Figure 5.19. Improvement efficiency for all EPS Beads and Sand Mixture cushioned cases with respect to A7 under a) the scaled 1999 Kocaeli EQ Motion-İznik Station Record-FF, b) the scaled 2014 Gökçeada EQ Motion-Çanakkale Station Record-FF, c) the scaled 2020 İzmir EQ Motion-Kuşadası Station Record-FF, d) the scaled 1999 Kocaeli EQ Motion-İzmit Station Record-NF, e) the scaled 1940 Imperial Valley EQ-El Centro Station record-NF, f) the scaled 1995 Kobe EQ Record-NF. .....330

Figure 5.20 Response Spectrums of all EPS Beads and Sand Mixture cushioned cases with respect to A7 under a-b-c) the scaled 1999 Kocaeli EQ Motion-İznik Station Record-FF, d-e-f)

the scaled 2014 Gökçeada EQ Motion-Çanakkale Station Record-FF, g-h-i) the scaled 2020 İzmir EQ Motion-Kuşadası Station Record-FF. .....334

Figure 5.21 Response Spectrums of all EPS Beads and Sand Mixture cushioned cases with respect to A7 under a-b-c) the scaled 1999 Kocaeli EQ Motion-İzmit Station Record-NF, d-e-f) the scaled 1940 Imperial Valley EQ-El Centro Station record-NF, g-h-i) the scaled 1995 Kobe EQ Record-NF. .....338

Figure 5.22. Improvement efficiency for all EPS Beads and Sand Mixture cushioned cases with respect to A7 under a) sinusoidal motion at 0.3g amplitude with 8 Hz frequency, b) sinusoidal motion at 0.4g amplitude with 8 Hz frequency, c) sinusoidal motion at 0.5g amplitude with 8 Hz frequency, d) sinusoidal motion at 0.4g amplitude with 12 Hz frequency, e) sinusoidal motion at 0.4g amplitude with 14 Hz frequency. .....341

Figure 5.23 Response Spectrums of all EPS Beads and Sand Mixture cushioned cases with respect to A7 under a-b-c) sinusoidal motion at 0.3g amplitude with 8 Hz frequency, d-e-f) sinusoidal motion at 0.4g amplitude with 8 Hz frequency, g-h-i) sinusoidal motion at 0.5g amplitude with 8 Hz frequency.....345

Figure 5.24 Response Spectrums of all EPS Beads and Sand Mixture cushioned cases with respect to A7 under a-b-c) sinusoidal motion at 0.4g amplitude with 12 Hz frequency, d-e-f) sinusoidal motion at 0.4g amplitude with 14 Hz frequency. .....346

Figure 5.25 Variation of maximum accelerations at the top of the RWM for EPS Beads and Sand Mixture cases with t=4cm compared with the control case under all input motions.....348

Figure 5.26 Variation of maximum accelerations at the top of the RWM for EPS Beads and Sand Mixture cases with t=6cm compared with the control case under all input motions.....350

Figure 5.27 Variation of maximum accelerations at the top of the RWM for EPS Beads and Sand Mixture cases with t=8cm compared with the control case under all input motions.....351

Figure 5.28. Maximum lateral displacements measured from D19 under all input motions a) Case 1, b) Case 14, c) Case 15, d) Case 16, e) Case 17, f) Case 18, g) Case 19, h) Case 20, i) Case 21, j) Case 22. .....353

Figure 5.29 The maximum spectral acceleration variation ratio (A16 by A7) for all cushion cases under a) the scaled 1999 Kocaeli EQ Motion-İznik Station Record-FF, b) the scaled 2014 Gökçeada EQ Motion-Çanakkale Station Record-FF, c) the scaled 2020 İzmir EQ Motion-Kuşadası Station Record-FF, d) the scaled 1999 Kocaeli EQ Motion-İzmit Station Record-NF, e) the scaled 1940 Imperial Valley EQ-El Centro Station record-NF, f) the scaled 1995 Kobe EQ Record-NF. .....358

Figure 5.30 The maximum spectral acceleration variation ratio (A16 by A7) for all cushion cases under a) sinusoidal motion at 0.3g amplitude with 8 Hz frequency, b) sinusoidal motion at 0.4g amplitude with 8 Hz frequency, c) sinusoidal motion at 0.5g amplitude with 8 Hz frequency, d) sinusoidal motion at 0.4g amplitude with 12 Hz frequency, e) sinusoidal motion at 0.4g amplitude with 14 Hz frequency.....361

Figure 5.31 Improvement efficiency comparison for all cushion types with t=4cm thickness under far field earthquake input motions.....363

Figure 5.32 Improvement efficiency comparison for all cushion types with t=4cm thickness under near field earthquake input motions. .....365

Figure 5.33 Improvement efficiency comparison for all cushion types with t=4cm thickness under sinusoidal input motions.....367

Figure 5.34 Improvement efficiency comparison for all cushion types with t=4cm thickness under all input motions. .....369

Figure 5.35 Improvement efficiency comparison for all cushion types with t=8cm thickness under far field earthquake input motions.....371

Figure 5.36 Improvement efficiency comparison for all cushion types with t=8cm thickness under near field earthquake input motions. .....373

Figure 5.37 Improvement efficiency comparison for all cushion types with t=8cm thickness under sinusoidal input motions. .....375

Figure 5.38 Improvement efficiency comparison for all cushion types with t=8cm thickness under all input motions. .....377

# LIST OF TABLES

Table 2.1 The horizontal wall movements required to reach the active and passive states (Coduto, 2001; Das, 2006).....13

Table 2.2 Physical properties of EPS geofoam (ASTM D6817) (Alliance, 2012).....29

Table 2.3. Application of scrap tire-derived (STD) materials in geo-engineering applications (Reddy and Krishna, 2017).....40

Table 2.4 Physical properties of Sand- EPS-1, EPS-2, and EPS-3 (Edinçliler and Özer, 2013). .....46

Table 2.5 Test configurations (Bathurst et al., 2007). .....63

Table 3.1. EPS Geofoam cushion material density and dimensions used in the study. .....79

Table 3.2. Tire crumb and sand mixture cushion material content and dimensions used in the study.....81

Table 3.3. EPS beads and sand mixture cushion material content and dimensions used in the study.....83

Table 3.4. The factor of safety under static and seismic conditions of the prototype wall (Kramer, 1996; Day, 2002). .....95

Table 3.5. The scale factors of the retaining wall model (Iai, 1989; Wood et al., 2002 and Wood, 2004). .....95

Table 3.6. The factor of safety under static and seismic conditions of the 1/15 scaled wall (Kramer, 1996, Day, 2002).....97

Table 3.7 The $f/f_n$ values for the input motions conducted in the experimental studies.....98

Table 3.8 The selected earthquake records. ..... 102

Table 3.9 The selected earthquake input motions executed in the experimental study (1/15 scaled). ..... 102

Table 3.10. The sinusoidal input motions in the experimental study. ..... 104

Table 3.11. Experimental cases considered in the study. ..... 109

# LIST OF SYMBOLS

| | |
|---|---|
| $H$ | Height of the wall |
| $\Delta H$ | Amount of wall movement |
| $W$ | Weight of the soil wedge |
| $\varphi$ | Friction angle of the backfill soil |
| $\beta$ | Angle of the inclined back face of the wall |
| $i$ | Slope of the backfill surface relative to the horizontal |
| $\delta$ | Angle of the wall friction |
| $\gamma$ | Unit weight of the backfill soil |
| $\alpha$ | Angle of the inclined surface of the backfill soil |
| $\theta$ | Angle of the failure surface |
| $R$ | The resultant force |
| $c$ | Cohesion of backfill soil |
| $P_a$ | Active force per unit length |
| $\sigma_a$ | Active earth pressure |
| $\sigma_p$ | Passive earth pressure |
| $\sigma_h$ | Lateral earth pressure acting on the retaining wall |
| $K_{AE}$ | Coefficients of active earth pressure under seismic loading |
| $K_{PE}$ | Coefficients of passive earth pressure under seismic loading |
| $P_{AE}$ | Total active earth pressure under seismic loading |
| $P_{PE}$ | Total passive earth pressure under seismic loading |
| $\Delta P_{AE}$, $\Delta P_{PE}$ | Additional component of dynamic lateral force due to earthquake |
| $K_A$ | Coefficients of static active pressure |
| $K_P$ | Coefficients of static passive pressure |
| $\Delta K_{AE}$ | Coefficients of dynamic pressure increments for active condition |

| | |
|---|---|
| $\Delta K_{PE}$ | Coefficients of dynamic pressure increments for passive condition |
| $a_h$ | Horizontal acceleration of the earthquake. |
| $a_v$ | Vertical acceleration of the earthquake |
| $k_h$ | Factor of horizontal acceleration |
| $k_v$ | Factor of vertical acceleration |
| g | Acceleration due to gravity |
| q | Surcharge loading |
| $V_s$ | Shear wave velocity |
| G | Shear modulus of the backfill soil |
| ρ | Density of the backfill soil |
| ν | Poisson's ratio |
| $\omega_1$ | Fundamental frequency of the system |
| $a_{max}$ | Maximum ground acceleration |
| $V_{max}$ | Maximum ground velocity |
| E | Young's modulus |
| ρs | Density of soil |
| $\rho_{dmin}$ | Minimum dry density |
| $\rho_{dmax}$ | Maximum dry density |
| $e_{min}$ | Void ratio of the soil in the densest state |
| $e_{max}$ | Void ratio of the soil in the loosest state |
| $D_{50}$ | Mean diameter of soil particles |
| $D_{10}$ | Effective particle size |
| $D_{30}$ | Particle corresponding to 30% |
| $D_{60}$ | Particle corresponding to 60% |
| $C_u$ | Coefficient of uniformity |
| $C_c$ | Coefficient of curvature |
| $t_m$ | Thickness of the model wall, |
| $t_p$ | Thickness of the prototype wall, |

| | |
|---|---|
| $E_m$ | Young's modulus of the model wall, |
| $E_p$ | Young's modulus of the prototype wall. |
| $f_{11}$ | Fundamental frequency |
| $f_1$ | Frequency of infinitely long and uniform soil (1D approach) |
| t | Thickness of wall |
| t/H | Cushion thickness ratio |
| $P_p$ | Passive earth pressure |
| $P_A$ | Active earth pressure |
| $a_h$ | Acceleration of horizontal earthquake component |
| $a_v$ | Acceleration of horizontal earthquake component |
| $G_s$ | Spesific Gravity |
| $K_0$ | Coefficieny of earth pressure at rest |

# LIST OF ACRONYMS/ABBREVIATIONS

| | |
|---|---|
| EPS | Expanded Polystyrene |
| FLAC | Fast Lagrangian Analysis of Continua |
| 2D | Two dimensional |
| 3D | Three dimensional |
| SAFETY | Stability and flexibility of structures during earthquake using tyres |
| M-O | Mononobe-Okabe method |
| FS | Factor of safety |
| USCS | United Soil Classification System |
| SP | Poorly graded sand |
| TW | Tire waste and sand mixture |
| EPSB | EPS beads and sand mixture |
| A | Accelerometers |
| D | Laser displacement sensors |
| FF | The far field recording |
| NF | The near field recording |
| PGA | Peak ground acceleration |
| PGV | Peak ground velocity |
| PGD | Peak ground displacement |
| Hz | Hertz |
| ACCTH | Acceleration-time histories |
| FAS | Fourier amplitude spectra |
| SA | Spectral acceleration |
| NS | North-South component of earthquake recording |
| EW | East-West component of earthquake recording |
| ELM | Equivalent-linear method |

| | |
|---|---|
| TDA | Tire derived aggregate |
| VOL | Volume |
| STMC | Scrap Tire Management Council |
| STB | Sand-tire buffing |
| STC | Sand-tire crumb |
| TCS | Tire-crumb sand |
| TBS | Tire-buffer sand |
| TBEC | Turkish Building Earthquake Code |
| MLR | Multiple Linear Regression |
| FEM | Finite Element Analysis |
| ACC | Acceleration |
| ASTM | American Society for Testing and Materials |
| MSE | Mechanically Stabilized Earth |
| PMMA | Polymethyl methacrylate |
| $R_{epi}$ | Epicentral distance |
| $R_{rup}$ | Rupture distance |
| $R_{jb}$ | Joyner-Boore distance |
| Sec | Second |
| RWM | Retaining wall model. |
| DISTH | Displacement-Time History |
| EQ | Earthquake |
| SDOF | Single Degree of Freedom System |

# 1. INTRODUCTION

## 1.1. General

Retaining walls are built to resist the lateral pressure of soil. Sand, liquid pressure, earth filling, and other granular materials may also contribute to the lateral force behind the retaining wall construction. Retaining walls are subjected to increasing earth pressure during seismic activity. Behind retaining wall systems, compressible materials are known to reduce static and dynamic forces (Kramer, 1996; Day, 2012).

In order to improve the retaining structures' stability in seismic areas, it may be possible to use vertical compressible layers, often known as cushion layers. Two alternative compressible materials, such as tire waste and sand mixtures, EPS geofoam are investigated in the literature to reduce dynamic earth pressures caused by earthquakes against retaining walls (Edinçliler and Toksoy, 2018; Hazarika et al., 2008; Karpurapu and Bathurst, 1992; Horvath, 1997; Partos and Kazaniwsky, 1987).

EPS geofoam, a cushion placed behind retaining walls, is an excellent lightweight alternative material. Because it is so light, using it as a backfill, the lateral pressures decrease significantly in these structures. Despite being lightweight, it has a naturally high compressive strength. In contrast to conventional retaining wall materials like soil, sand, and stone, geofoam blocks weigh 100 times less (Hazarika et al., 2001; Bathurst et al., 2007).

The weight of the backfill used directly relates to the horizontal force applied to a retaining wall. Cushions made of tire waste and sand mixture or EPS Geofoam behind retaining walls can reduce the potential horizontal earthquake forces.

EPS geofoam or tire waste and sand mixtures placed behind retaining walls or below-grade walls can offer lower settlements, less lateral pressure, improved waterproofing, and

improved insulation. The main idea behind using EPS geofoam as a retaining structure backfill is to completely replace as much soil in the active or at-rest wedge with geofoam (Khushefati et al. 2015).

The aim of this thesis is to evaluate the effectiveness and efficiency of a new cushion layer for retaining structures, which consists of EPS beads and sand mixtures. The study investigates the effects of thickness, mixture ratio, and input motions on the retaining wall with the cushion layer. The cushion layers EPS geofoam and tire waste and sand mixture were also used as cushion materials, and their performances were compared with the EPS beads and sand mixture cushion under the same input motions. The study is the first to use EPS beads and sand mixture cushion behind the retaining wall. The effects of cushion type were also investigated. The experimental studies were implemented in the shake table laboratory with retaining wall models by using cushions behind the retaining walls to reduce the seismic effects of the retaining wall. The shake table experiments were executed in the laminar box. A 1/15 scaled retaining wall was used after the retaining wall was modeled and developed while taking the shake table and laminar box facilities into consideration. This parametric study is executed by using different thicknesses and densities of EPS geofoam, by using different thicknesses and mixture ratios of tire waste and sand mixture, and by using different thicknesses and mixture ratios of EPS beads and sand mixture, by applying selected far field and near field earthquake motions and sinusoidal motions at different input motion characteristics.

## 1.2. Problem Statement

Retaining walls are one of the most important geotechnical structures due to their widespread use and high demand. Under static and dynamic stresses, retaining walls are susceptible to bearing capacity failure, sliding, or overturning. Consequently, retaining wall degradation and collapse result in the loss of lives and significant financial losses in the world. Therefore, retaining wall improvement techniques become more important as a result. As a solution to this problem, numerical, experimental, and field investigations have been carried on using cushions behind the retaining wall. In order to make a new contribution to the solutions that have been worked out for this problem, a new cushion material of EPS beads and sand

mixture that has never been placed as a cushion material behind the retaining wall was proposed in this thesis study. The retaining wall was modeled and designed considering the laminar box conditions; a 1/15 scaled retaining wall model was used. EPS geofoam material and tire waste and sand mixture were used as cushions for comparison. The performances of each of these cushion materials were compared to one another under the same input motions. The effects of cushion material, thickness, mixture ratio, and the specified input motion were evaluated on the performance of the retaining wall model by conducting a series of shake table experiments.

### 1.3. The objective of the Thesis

The main objective of the thesis is to improve the seismic performance of the retaining wall by using cushion materials depending on the types and some factors affecting the results to sustain the retaining structure's stability in a variety of seismic conditions by performing shake table tests. For this purpose, the aim of the experimental study in the thesis is to define a new proposed cushion layer consisting of EPS Beads and sand mixture and investigate the effects of cushion on the retaining wall model seismic performance under various input motions. This study is the first experimental study in the literature to evaluate the validity of the proposed EPS beads and sand mixture cushion. Under the same input motions, EPS geofoam, tire waste and sand mixture cushions were also used as cushion materials, and their performances were compared with those of the EPS beads and sand mixture cushion. The experimental studies include the purpose of the effects of cushion types with different thicknesses, densities, and mixture ratios on the retaining wall model performance under the same input motions.

### 1.4. Organization of the Thesis

In this thesis study, a series of shake table tests were performed to investigate the seismic performance of the retaining wall model by using three different cushion materials under various input motions. Considering the shake table and laminar box facilities, the retaining wall model was designed and constructed as 1/15 scaled and was used to perform experimental studies in the laminar box on the shake table. Firstly, the literature review consisting of numerical, experimental, and field studies with cushion materials was summarized. The experimental study

including materials and methods, retaining wall model, input motions, experimental program, and the preperation of the experimental studies were explained in detail. Afterward, the shake table tests were conducted for 22 different cases under the same input motions, and the results of the cushioned cases were compared with the model without cushion. The influence of the cushion type considering cushion thickness, density/mixture ratio under different earthquake motions and various sinusoidal motions on the seismic performance of control and cushioned retaining wall models were evaluated and compared with each other.

# 2. LITERATURE REVIEW

This part of the thesis consists of a detailed literature survey, including laboratory and field experiments and numerical studies that are related to the failure mechanisms of retaining wall structures and how to improve their static and dynamic performances. Improvement methods include the use of geosynthetics, EPS geofoam blocks, EPS beads and sand mixtures, tire waste and sand mixtures.

## 2.1. Retaining Structures

In general definition, structures that provide a vertical transition between slopes with sudden level differences are called retaining walls. They are structures that are built to prevent slipping and erosion of the ground they hold behind them and provide a vertical transition between slopes with sudden level differences. The purpose of the construction of the retaining wall is to provide the required stability against the lateral thrust increasing from the backfill soil behind the retaining wall. Gravity walls, counterfort walls, cantilevered walls, and crib walls are among the most typical retaining wall types and are represented in Figure 2.1 (Day, 2012).

Retaining walls are commonly categorized based on their mass, flexibility, and anchorage conditions. The simplest and the oldest type of retaining wall is gravity walls, which are thick and rigid enough to resist bending, and their movement primarily occurs through rigid-body translation and/or rotation. Some composite wall systems, like crib walls and mechanically stabilized walls, are also designed as gravity walls due to their minimal bending characteristics, although internal stability is taken into account. Cantilever walls, on the other hand, rely on their flexural strength to withstand lateral earth pressures and exhibit both bending and translation/rotation movements. The stiffness of the wall and the soil's deformation both have an impact on how the lateral earth pressure on a cantilever wall is distributed. Both of these factors are interrelated and affect the overall behaviour of the wall and the soil. Braced walls are supported by external bracing elements, which restrict certain types of movement. The

supporting structures can limit the sideways movements of the top of walls in situations such as basement walls and bridge abutment walls. Tieback walls and anchored bulkheads, on the other hand, are prevented from lateral movement by anchors buried in the backfill soil. By incorporating lateral support at various points along a braced wall, it becomes feasible to minimize bending moments to a level that permits the utilization of comparatively flexible structural sections (Kramer, 1996).

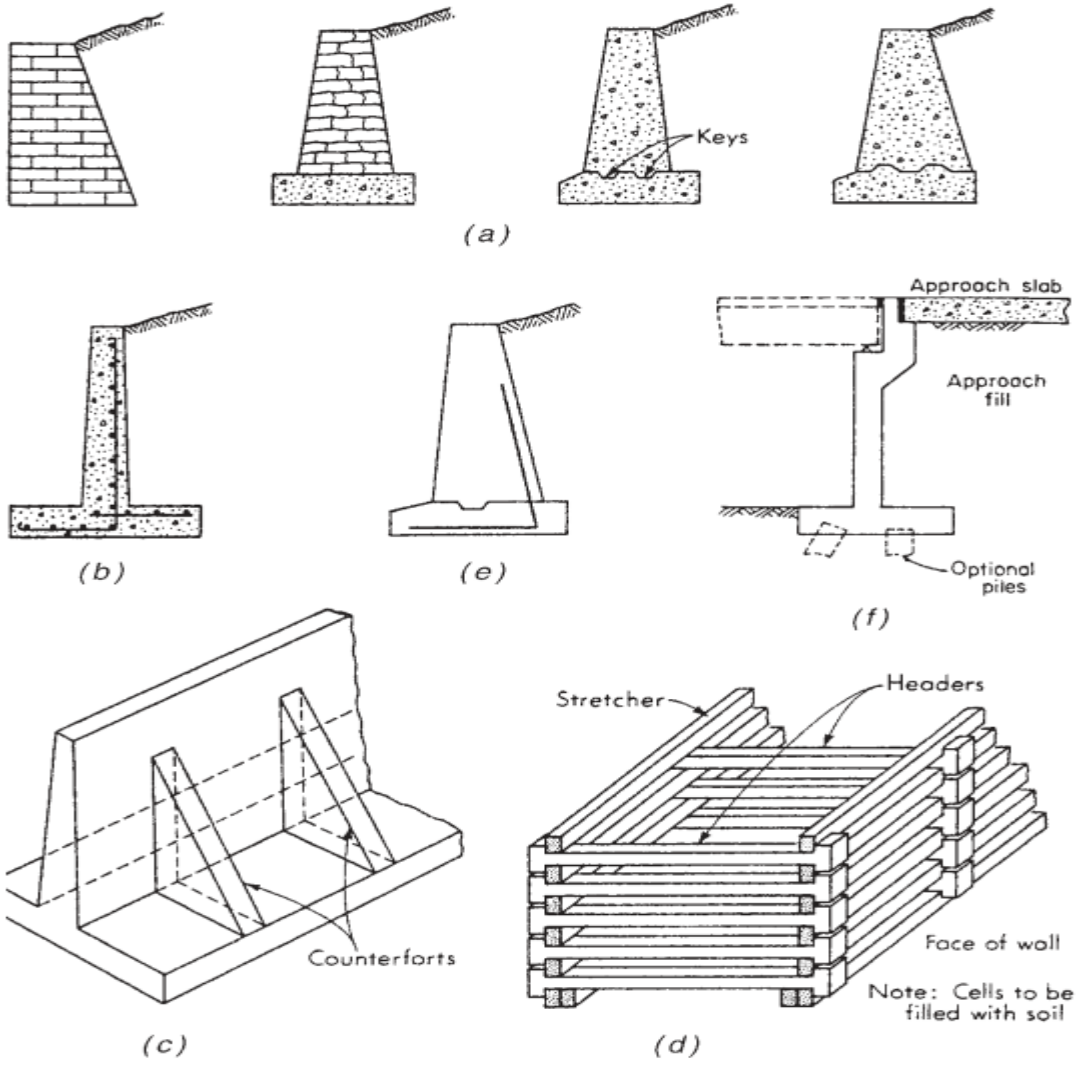


Figure 2.1. Common retaining wall types include a) gravity walls, b) cantilever walls, c) counterfort, d) crib walls, e) semi-gravity walls, f) bridge abutments (Day, 2012).

### 2.1.1. Retaining Wall Analysis under Static Conditions

In order to understand how retaining walls behave, it is important to discuss static earth pressures. The movements of the wall and soil greatly influence the static earth pressures on retaining structures. When a retaining wall moves away from the soil it is holding back, active earth pressures develop, causing the soil to undergo extensional lateral strain (Figure 2.2). Minimum active earth pressures are exerted on the wall when the wall movement is enough to fully utilize the strength of the soil. Retaining walls that are not attached to any other structure are usually based on minimum active earth pressures. However, if the wall's ability to move sideways is limited, minimum active pressures may be exceeded by static earth pressures. Passive earth pressures develop when a retaining wall moves towards the soil, causing the soil to undergo compressive lateral strain (Figure 2.3). When the soil's strength is completely mobilized, the wall is subjected to the highest levels of passive earth pressures. The stability of numerous retaining walls that are not attached to any other structure is often achieved through a balance between active forces, which mainly operate on one side of the wall, and passive pressures, which primarily act on the other side (Kramer, 1996).

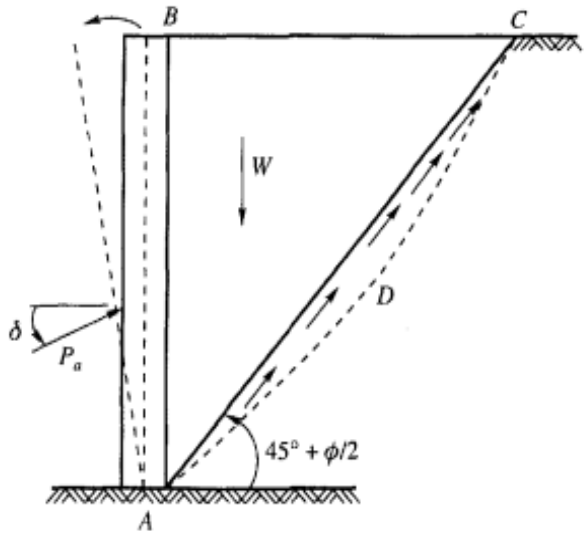


Figure 2.2 Active earth pressure development through wall movement (Murthy, 2002).

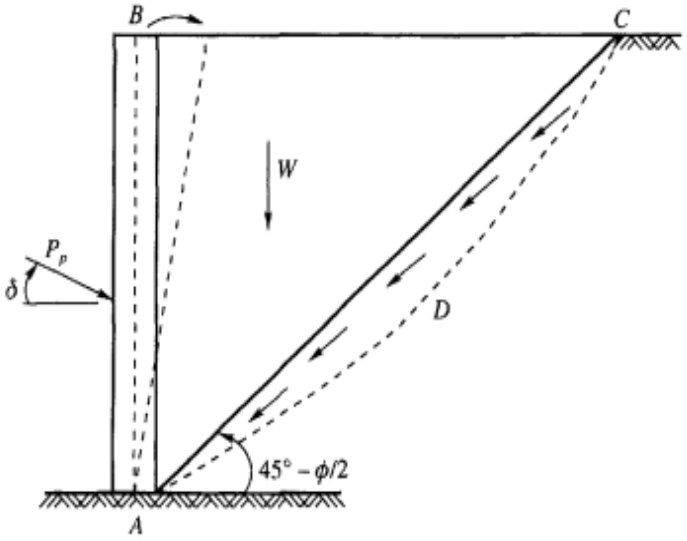


Figure 2.3 Passive earth pressure development through wall movement (Murthy, 2002).

Soil-structure interaction in predicting the deformations and the actual forces of retaining walls is a complex problem, even under static conditions. In design, the focus is usually on estimating the forces on a wall and designing it to withstand those forces with a sufficient factor of safety to limit deformations. There are several simplified methods available to assess static loads on retaining walls (Kramer, 1996).

In 1776, Coulomb conducted an initial investigation into the effects of horizontal earth pressures on retaining structures. In his suggestion, he proposed that the force exerted on the rear of a retaining wall was caused by the mass of a soil wedge situated above a flat surface that is prone to failure. Coulomb utilized the principle of force equilibrium to calculate the soil pressure on the wall, taking into account the minimum active forces and maximum passive forces. However, since the problem is indeterminate, it is necessary to analyze multiple potential failure surfaces to identify the critical failure surface that generates the highest active thrust, or the lowest passive thrust.

In 1857, Rankine developed a groundbreaking method for determining the minimum active and maximum passive earth pressures. By making certain assumptions about the stress conditions and strength envelope of the soil behind a retaining wall, Rankine was able to convert

the problem of lateral earth pressure into a problem that could be solved directly, allowing for the calculation of the static pressures exerted on retaining walls. Rankine's procedure provided a fundamental framework for analyzing and designing retaining structures, laying the groundwork for further advancements in geotechnical engineering (Kramer, 1996).

In the Rankine theory, the active pressure distribution for dry, homogeneous, cohesionless backfill is determined to be triangular in shape and parallel to the surface of the backfill. This triangular distribution represents the pressure exerted by the soil against a wall. The resultant active earth pressure, denoted as $P_A$, is applied at a location that is one-third of the wall's height (H) above its bottom. The theory also introduces the $K_A$ coefficient, which represents the minimum active earth pressure, and γ, which represents the unit weight of the soil.

$$P_A = \frac{1}{2} K_A \gamma H^2 \tag{2.1}$$

where,

$$K_A = \frac{1-sin\Phi}{1+sin\Phi} = tan^2(45 - \frac{\Phi}{2}) \tag{2.2}$$

According to Rankine's theory, a dry homogeneous backfill is expected to have a triangular passive pressure distribution that is across the backfill surface. The resultant passive earth pressure, also known as the passive thrust, or $P_p$ acts at a point situated H/3 above the base of a wall that is H in height, defining the $K_p$ coefficient of maximum passive earth pressure and γ as the unit weight of the soil.

$$P_P = \frac{1}{2} K_P \gamma H^2 \tag{2.3}$$

where,

$$K_P = \frac{1+sin\Phi}{1-sin\Phi} = tan^2(45 + \frac{\Phi}{2}) \tag{2.4}$$

### 2.1.2. Retaining Structures Analysis under Dynamic Conditions

The behaviour of retaining walls during seismic activity is a complex phenomenon, as described by Kramer (1996). Using laboratory experiments and examinations of gravity walls exposed to seismic forces, researchers have made several key observations:

- Walls can undergo movement in the form of translation (horizontal displacement) and/or rotation. The extent of rotation and translation depends on the wall's design, with some walls predominantly experiencing one type of movement and others exhibiting a combination of both (Siddharthan et al., 1992; Nadim and Whitman, 1984).

- The way a wall moves can impact the intensity and pattern of dynamic pressures it experiences. The type of movement, whether it's a linear translation, rotation around the base, or rotation around the top, can affect the dynamic pressures that are applied to the wall (Sherif and Fang, 1984a, b, Sherif et al., 1982).

- The highest amount of soil pressure on a wall usually happens when the wall has moved or turned towards the backfill. On the other hand, the lowest amount of soil pressure occurs when the wall has moved or turned away from the backfill (Day, 2002).

- The pressure distribution of an earthquake on the back of a wall changes as the wall moves, causing the point of application of the soil thrust to move up and down along the back of the wall. When the wall moves toward the soil, the location of the soil thrust is maximum, and when the wall moves outward, the location of the soil thrust is minimum (Kramer, 1996).

- The dynamic pressures exerted on a wall are impacted by the dynamic response of both the wall and the backfill. These pressures can increase considerably when the wall-backfill system's natural frequency is approached, as noted by Steedman and Zeng in 1990. Furthermore, in 1982, Nadim noted that when the frequency of the wall-backfill

system approaches its natural frequency, the permanent displacements of the wall tend to increase. This is because of dynamic response effects, which can cause different parts of the wall to deflect out of phase. This phenomenon is especially evident in walls that penetrate into the foundation soils, where the backfill soils move out of phase with the foundation soils.

- After a period of intense shaking has passed, higher residual pressures could still be present on the wall (Whitman, 1990).

These findings highlight the complicated behaviour of retaining walls during earthquakes and provide valuable insights for designing and analyzing these structures to enhance their seismic performance.

The Mononobe—Okabe (M-O) approach was created as the foundation for a pseudo-static study of seismic earth pressures upon retaining structures by Okabe (1926) and Mononobe and Matsuo (1929). The static Coulomb theory is directly extended to pseudo-static situations using the M-O approach. Pseudo-static accelerations are introduced to a Coulomb active (or passive) wedge in a M-O analysis. The wedge's force equilibrium is then used to determine the pseudostatic soil thrust.

Figure 2.4 illustrates the forces acting on an active wedge in a dry, cohesionless backfill. Apart from the forces present under static conditions, the wedge is also subjected to horizontal and vertical pseudo-static forces. The magnitudes of these forces are determined by the mass of the wedge and are related to the pseudo-static accelerations $a_h=k_h.g$ for the accelerations of the earthquake's horizontal components and $a_v = k_v.g$ for the accelerations of the earthquake's vertical components. The coefficient of dynamic active earth pressure is denoted as $K_{AE}$, the backfill soil unit weight as $\gamma$, the wall height as H, the friction angle of the backfill soil as $\phi$, the angle of wall friction as $\delta$, the slope of the backfill surface relative to the horizontal as i, and the slope of the wall back relative to the vertical as $\beta$. The total active thrust, $P_{AE}$, can be expressed in a similar form to that derived for static conditions.

$$P_{AE} = \frac{1}{2} K_{AE} \gamma H^2 (1 - k_v) \tag{2.5}$$

$$K_{AE} = \frac{\cos^2(\Phi - \theta - \beta)}{\cos\theta \cos^2\beta \cos(\delta + \beta + \theta)\left[1 + \sqrt{\frac{\sin(\Phi + \delta)\sin(\Phi - \theta - i)}{\cos(i - \beta)\cos(\delta + \beta + \theta)}}\right]^2} \tag{2.6}$$

$$\theta = \tan^{-1}\left(\frac{k_h}{1 - k_v}\right) \tag{2.7}$$

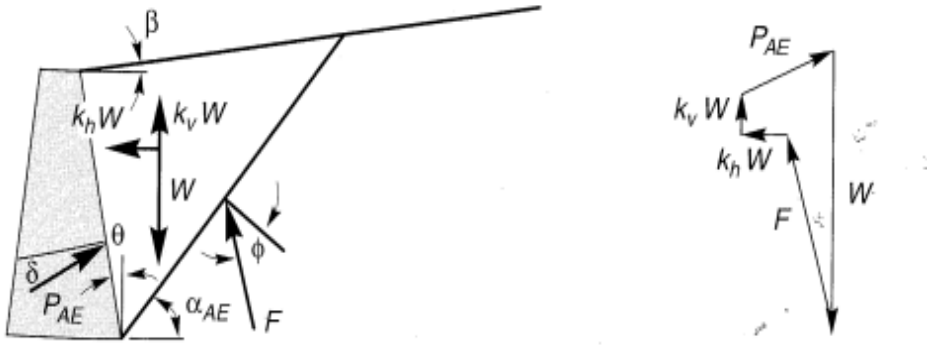


Figure 2.4 Forces in the Mononobe-Okabe analysis acting on the active wedge and a force polygon showing their equilibrium (Day, 2002).

The forces acting on a passive wedge in a dry, cohesionless backfill are shown in Figure 2.5. The coefficient of dynamic passive earth pressure is denoted as $K_{PE,}$ and the total passive thrust, $P_{PE}$, can be expressed in a similar form to that derived for static conditions.

$$P_{PE} = \frac{1}{2} K_{PE} \gamma H^2 (1 - k_v) \tag{2.8}$$

$$K_{PE} = \frac{\cos^2(\Phi - \theta + \beta)}{\cos\theta \cos^2\beta \cos(\delta - \beta + \theta)\left[1 - \sqrt{\frac{\sin(\Phi - \delta)\sin(\Phi - \theta + i)}{\cos(i - \beta)\cos(\delta - \beta + \theta)}}\right]^2} \tag{2.9}$$

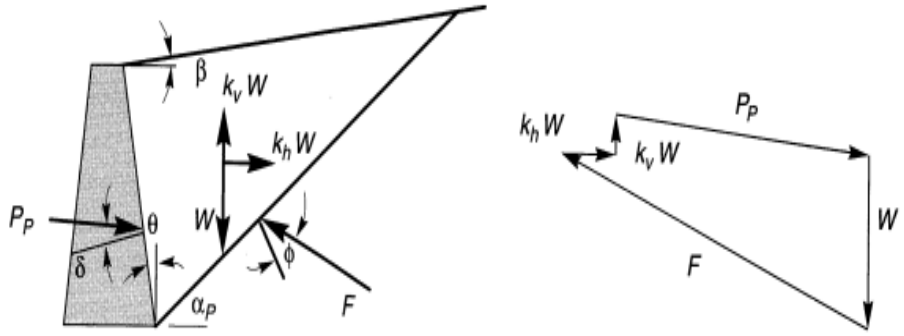


Figure 2.5 Forces in the Mononobe-Okabe analysis acting on the passive wedge and a force polygon showing their equilibrium (Day, 2002).

The type of earth pressure experienced by retaining walls depends on the movement of the wall and the soil it holds. There are two conditions that can occur: active and passive. Active earth pressure occurs when the retaining wall moves away from the soil it holds, causing the soil mass to stretch. This happens when the wall rotates away from the soil mass (Figure 2.6). Passive earth pressure occurs when the retaining wall moves towards the soil it holds, causing the soil to compress horizontally (Figure 2.7). This happens when the wall rotates into the retaining soil. As the wall moves, the lateral pressure against it increases until it reaches the maximum passive earth pressure. The horizontal wall movements required to reach the active and passive states are given in Table 2.1 (Coduto, 2001; Das, 2006).

Table 2.1 The horizontal wall movements required to reach the active and passive states (Coduto, 2001; Das, 2006).

| Soil Type | Horizontal Movement Required to Reach the Active State | Horizontal Movement Required to Reach the Passive State |
|---|---|---|
| **Loose Sand** | 0.001–0.002H | 0.01H |
| **Dense Sand** | 0.0005–0.001H | 0.005H |
| **Soft Clay** | 0.02H | 0.04H |
| **Stiff Clay** | 0.01H | 0.02H |

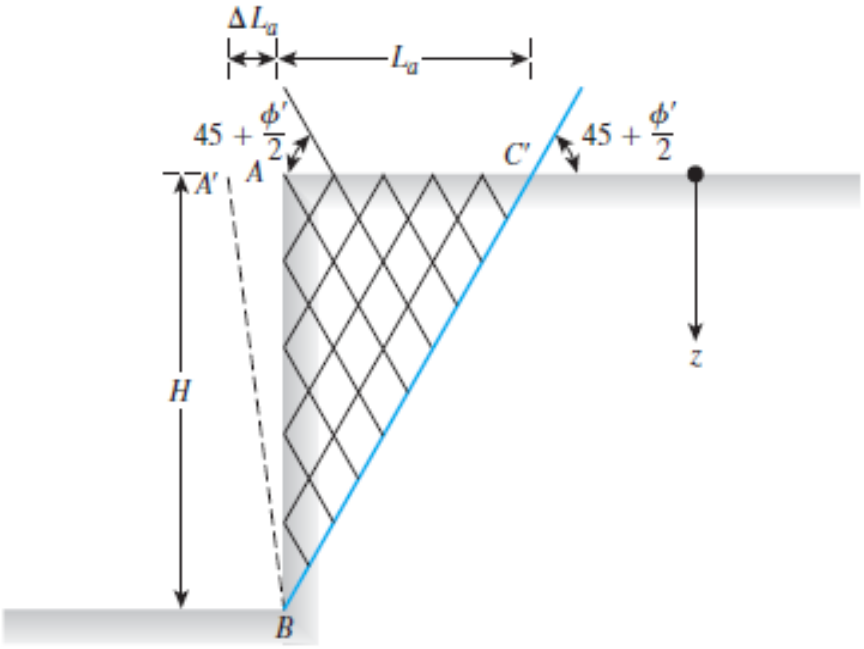


Figure 2.6 Retaining wall movements to reach the active state (Das, 2006).

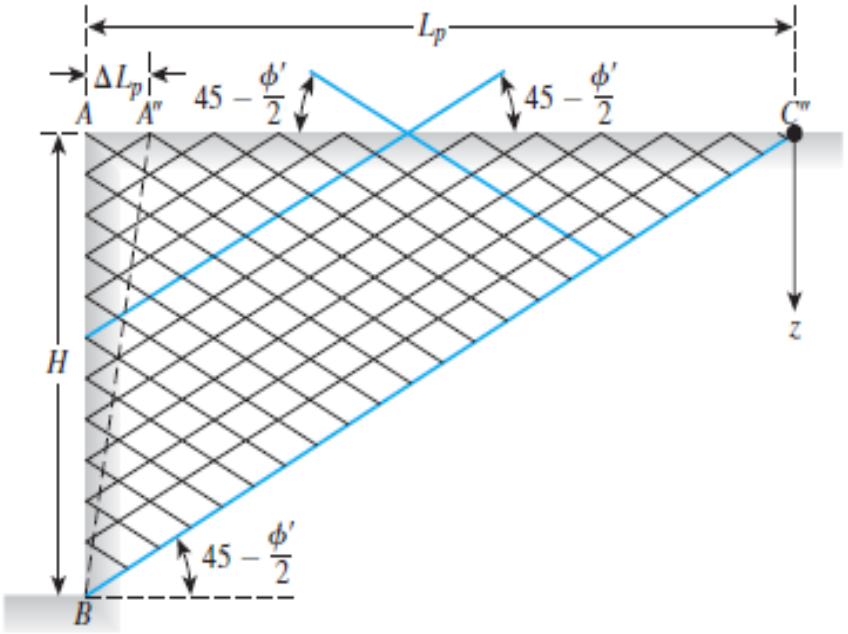


Figure 2.7 Retaining wall movements to reach the passive state (Das, 2006).

## 2.2. Failure of Retaining Walls

Retaining walls are structures specifically designed to provide lateral support for soil or rock and can also bear vertical loads. They come in different types, including gravity walls, cantilever walls, counterfort walls, basement walls, and bridge abutments. The design of a retaining wall requires a thorough understanding of the concept of "failure" and how these structures can fail. A retaining wall experiences internal forces from its weight, soil pressures, and external forces transmitted by braces when it is in a static state. A properly designed retaining wall will balance these forces without causing shear stresses that exceed the soil's shear strength. In an earthquake, the wall can experience forces and changes in soil strength that disturb its balance and cause permanent displacement. Failure can happen when these movements exceed certain limits, like sliding, tilting, bending, or other actions. The assessment of what amount of deformation is considered excessive relies on different factors and needs to be evaluated for each specific location (Kramer, 1996).

The behaviour of retaining walls during an earthquake is complicated. When subjected to seismic forces, walls can undergo both translational and rotational movements, which depend on their design. The intensity and distribution of dynamic pressure on the wall are affected by the specific mode of wall movement. When a wall translates or rotates towards the backfill, it experiences the maximum soil thrust. Conversely, when the wall translates or rotates away from the backfill, the soil thrust is minimized. As the wall moves, the shape of the earthquake pressure distribution and the point where the resultant force is applied also change. During an earthquake, the natural frequency of the wall backfill system causes a significant increase in both dynamic wall pressure and permanent wall displacement. Additionally, even after the strong shaking has ended, there may be an increase in residual pressure on the wall (Kramer, 1996; Day, 2002).

It has been suggested that the allowed bearing and passive pressure during seismic analysis should be increased by a factor of one-third. This increase is considered suitable in certain circumstances, such as when the retaining wall-bearing material and the soil in front of the wall are made of stable, massive crystalline bedrock and sedimentary rock that are not impacted by seismic activity. Additionally, it applies to soils that exhibit dilation during an

earthquake, soils that demonstrate little reduction in shear strength with strain, soils located above the water table, and clay with low sensitivity. Nevertheless, it is advised against increasing the load-bearing capacity in certain soil conditions. These conditions include foliated rock that tends to fracture during earthquakes, loose soil situated below the water table, as well as sensitive and soft clays. The first group of soils retains its shear strength even during seismic shaking, whereas the second group experiences a loss of shear strength during such events (Kumar, 2008).

Retaining walls fail in many different forms under different conditions. The most common types of retaining wall failure modes can be seen in Figure 2.10. Retaining wall failure modes and case studies that indicate some of the retaining wall failures induced by earthquakes are shown in Figure 2.8.

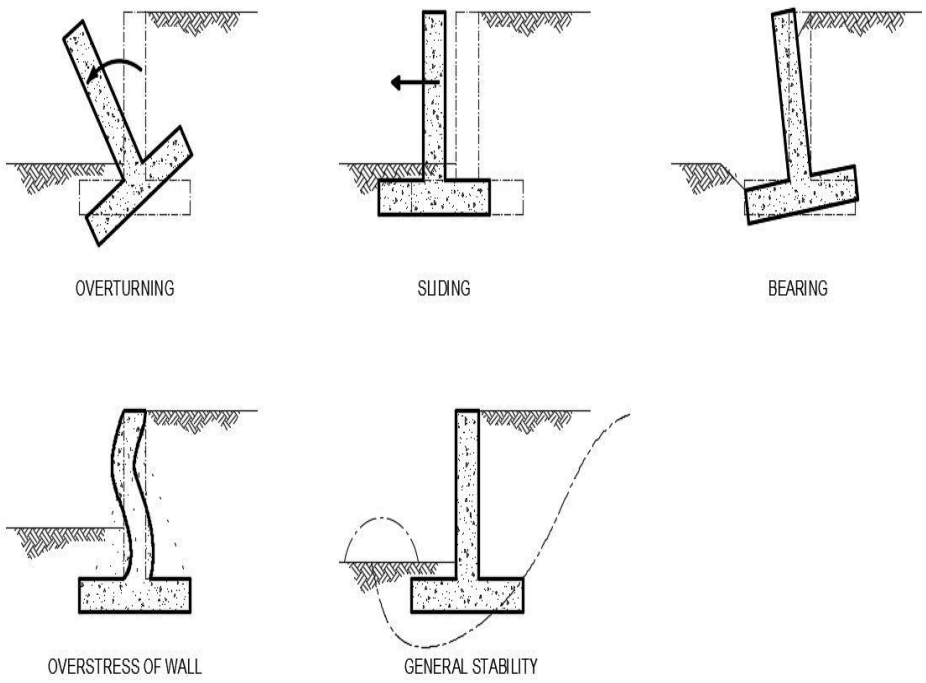


Figure 2.8. Retaining wall failure modes induced by earthquakes (Day, 2002).

The main reasons for the collapse of the retaining walls are the insufficiency of the drainage behind the wall, the incomplete foundation, and faulty production issues. These collapses, which cause loss of life and property, occur due to incorrect engineering application and negligence.

The stability of a retaining wall can be influenced by various factors. It is crucial to consider the following requirements to ensure the stability of the wall during construction, as highlighted by Kramer in 1996:

- Overturning Failures: This occurs when the lateral forces acting on the wall exceed its resistance, causing it to rotate or overturn.

- Sliding Failures: Sliding failures happen when the wall is unable to resist the horizontal forces acting on it, leading to movement along the base.

- Bearing Failure of Soil: This refers to the failure of the soil beneath the wall to support the applied loads, resulting in settlement or collapse.

- Slope Stability Failures: These failures occur when the stability of the soil slopes adjacent to the wall is compromised, leading to slope movement and potential damage to the wall.

- Lack of Reinforcements: Inadequate or improper reinforcement can weaken the retaining wall, reducing its ability to withstand the applied loads and compromising its stability.

- Excessive Pore Water Development: The presence of excessive water negatively affects the strength and stability of the wall.

- Incorrect Estimation of Earth Pressure Coefficients: Incorrect estimation of the lateral earth pressure acting on the wall can lead to inadequate design and potential stability issues.

- Shallow Foundations: Insufficient depth or inadequate design of the wall's foundation can result in settlement and instability.

- Excessive Settlement: Excessive settlement of the soil supporting the wall can cause differential movement and compromise its stability.

- Unexpected Loads: Unforeseen or unaccounted loads, such as additional surcharge or impact loads, can exceed the wall's capacity and lead to instability.

- Seismic Loads: Earthquakes or seismic events can subject the retaining wall to dynamic forces, which may cause failure if not properly considered in the design.

- Reinforcement Detailing Issues: Poor detailing or improper installation of reinforcement can weaken the wall's structural integrity and compromise its stability.

Considering and addressing these factors is essential to ensure the stability and safety of retaining walls during construction and throughout their lifespan.

There are some points to be considered while building retaining walls (Kramer, 1996):

- Analysis of the construction site should be made, and after this analysis, it should be decided what kind of retaining wall will be built.

- The materials used should be durable and correctly selected in accordance with the area of use.

- Necessary precautions should be taken by calculating the possibility of the water that may collect behind the retaining wall to destroy the wall.

- The foundation depth and height of the wall must be calculated correctly. The foundation should not go below the freezing level, the effect of its height on the flexibility of the structure should be calculated.

- If the land on which the retaining wall will be built is sloping, the wall should be built gradually.

### 2.3. Case Studies on Failure of Retaining Walls under Earthquakes

Recently, many different retaining walls failed due to the destructive effects of earthquakes worldwide.

As can be seen in Figure 2.9, Figure 2.10, Figure 2.11, and Figure 2.12, gravity-type retaining walls failed as a result of the outward movement and overturning due to the seismic motions of Chi-Chi Earthquake.

The upper parts of the whole structure progressively separated from the backfill at the construction joints during the Chi-Chi earthquake. As seen in Figure 2.9, the top two blocks eventually fell into the side ditch of the highway. The length of the damaged area was around 20 meters. It was observed from the field that the frictional resistance at the flat construction joint was insufficient to withstand both the upward force of the wall and the dynamic earth pressure (Fang et al., 2003).

The retaining wall severely shifted and displaced around its toe following the Chi-Chi earthquake, as seen in Figure 2.10. The active soil wedge that was behind the wall fell, while the majority of the wall's body was undamaged. The beetle-nut planting on the hillside was unaffected by the earthquake. The wall has 2.5 m height, 1.25 m thickness at the base, and 0.5m

thickness at the top. The wall was constructed with horizontal weep holes spaced 0.25 meters apart. The affected area was about 40 meters long. It's conceivable that the damage was mostly caused by the unexpectedly severe ground motion (Fang et al., 2003).

Figure 2.9. The gravity wall shifted outward at the construction joint after the 1999 Chi-Chi Earthquake (Fang et al., 2003).

Figure 2.10. Overturning of gravity wall after the 1999 Chi-Chi Earthquake (Fang et al., 2003).

Different types of failure modes can be observed in retaining walls under earthquake effects. As given in Figure 2.11, a retaining wall experienced sliding and overturning after Chi-Chi Earthquake and depicts the collapse of a gravity wall at the Taiwan Cinema Culture Town, which is close to the Wu-Fung township. The CheLung-Pu fault was just above the wall when it was built. The wall slipped and overturned due to the fault rupture during the earthquake. The power pole leaned with the retaining wall. However, the body of the retaining wall was undamaged; the ground shift in front of the toe is clearly seen in Figure 2.11. Ground deformation and intense ground shaking caused the backfill behind the wall to crack, severely damaging the structures built on the backfill (Fang et al., 2003).

Figure 2.11. Overturning and sliding of retaining wall after the 1999 Chi-Chi Earthquake (Fang et al., 2003).

Chi Chi Earthquake had a significant impact on the stability of retaining walls. Another example given in Figure 2.12 is a trapezoidal concrete gravity wall that rotated outward. In central Taiwan, there was a gravity retaining system built along a road cut that collapsed partially during the Chi-Chi earthquake in 1999. This retaining wall was constructed in the typical trapezoid shape. The failure of the steep slope above the wall was more significant, and although it was caused by seismic activity, it was not solely due to the ground vibrations caused by the earthquake (Figure 2.12). Similar failures were observed during the 1995 Hyogoken-

Nambu earthquake in Japan, where older structures supporting poorly compacted embankments and/or on sloped land were the leading cause of failure (Sitar et al., 2012).

Figure 2.12. Concrete gravity retaining wall with a trapezoidal shape rotated outward due to the failure of the slope during the 1999 Chi-Chi earthquake in Taiwan (Sitar et al., 2012).

Figure 2.13. Reinforced retaining wall failure in the 2008 Wenchuan Earthquake (Changwei et al., 2015).

Figure 2.13 shows the failure of the reinforced retaining wall in the 2008 Wenchuan Earthquake in China. Similarly, many retaining walls failed in Japan due to the 1995 Kobe Earthquake (Figure 2.14) and the 2004 Mid-Nigata Prefecture Earthquake (Figure 2.15).

Figure 2.14. Retaining wall failure in the 1995 Kobe Earthquake (Zamiran et al., 2016).

Figure 2.15. Failure of retaining wall in the Mid-Nigata Prefecture Earthquake in 2004 (Zamiran et al., 2016).

## 2.4. Improvement of Retaining Walls

For retaining walls to be secure and stable, it is necessary to take various precautions to prevent distress and failure. There are several factors related to construction, design, and detailing that can influence the safety and stability of retaining walls. In order to avoid retaining wall collapse and damage, improvement can be employed, as suggested by Kramer (1996) and Yewalekar et al. (2020). These methods include addressing surface drainage problems, reducing the height of the retaining wall, extending the footing, using tie-backs, replacing backfill materials, reinforcing the front of the wall, adding a key, using cantilevered soldier beams, obtaining a building permit, and pushing the wall back to plumb. However, it is essential to note that demolishing the wall should only be considered as a last resort and after careful evaluation of all other options.

Geosynthetics are used for the improvement of retaining walls. The types of geosynthetics commonly used in retaining walls are geotextiles, geogrids, geocells, geofoams, and geocomposites. According to Saran et al. (1992), the application of reinforcement in soil can decrease the pressure caused by backfill and surcharge loading by approximately 50%. Additionally, the use of soil-reinforcement interface friction and bearing can almost eliminate lateral thrust on the wall. Geosynthetic Reinforced Wall is the most cost-effective option among all types of walls, as stated by Koerner (2000). These walls are also simple to construct, saving time during the construction process.

The primary function of geogrids is soil reinforcement. Geogrids, due to their grid-like structure, allow for the passage of soil through their voids. This enables the development of passive resistance in the transverse grids by facilitating the formation of normal forces within the soil. In the longitudinal strips, tensile forces and friction forces arise due to the compression of the soil. Geogrids are a popular choice for enhancing the performance and lifespan of retaining walls. These geosynthetic materials are typically made from polymers and come in the form of a grid or mesh. Geogrids are placed within the soil to provide reinforcement, improving the load-bearing capacity and shear strength of the soil. By distributing lateral forces and reducing pressure on the wall, geogrids help to prevent wall failure. They also enhance the

overall stability of retaining walls by preventing soil movement and reducing the potential for wall settlement. Geogrids enable engineers to design taller walls with thinner cross-sections, reducing material and construction costs while maximizing available space. Additionally, geogrids enhance the drainage capabilities of retaining walls by allowing water to flow through the apertures, preventing the buildup of hydrostatic pressure and reducing the risk of water-related damage. Geogrids are made from high-strength polymers that resist degradation from environmental factors, ensuring their durability and long-term performance. They are also lightweight and easy to handle, making installation convenient and saving time and labor costs (Koerner, 2005). The construction of a geogrid-reinforced retaining wall is seen in Figure 2.16.

Figure 2.16 Construction of a geogrid-reinforced retaining wall: (a) Excavate the area for the retaining wall; (b) Install the geogrid layers; (c) Place the geotextile filter layer close to the wall's face; (d) Connect the folded geogrid sheet to the next sheet; (e) Observe the finished retaining wall (Shukla, 2016).

Geotextile walls are designed for both internal and exterior stability. The internal stability is used to determine the fabric length, lift thickness, and overlap. The external stability prevents foundation collapse, overturning, and sliding. In more detail, internal stability refers to the ability of the wall to withstand the forces acting on it from the soil it is retaining. External stability, on the other hand, refers to the ability of the wall to resist sliding and overturning due to the forces acting on it from the retained soil and other external factors (Koerner, 2005).

Soil nailing is a method used to enhance the stability of retaining walls. It involves increasing the normal force and soil shear resistance along potential slip surfaces in frictional soils while also reducing the driving force along potential slip surfaces in both frictional and cohesive soils. This technique is aimed at improving the overall strength and stability of the retaining wall. The process of soil nailing involves inserting slender reinforcing elements, such as rebar or proprietary bars, into unstable natural or man-made soil slopes to create a gravity retaining wall for excavation support. The reinforcing bars are grouted in place, and the soil nail walls are constructed from the top down in three to six-foot stages. Once each section is excavated, near-horizontal holes are drilled into the visible surface, and tension-resistant steel bars are inserted and fixed in place with grout. A drainage system is then installed on the surface, and either reinforced shotcrete wall facing or precast face panels are applied. Soil nailing can be used for various purposes, including slopes, excavations, and retaining walls. There are two types of soil nailing methods: passive and driven. However, soil nailing is not suitable for all soil conditions, such as dry, poorly graded cohesion-less soils, highly corrosive soils, and loess.

Lightweight materials are used behind the wall as cushion material. These materials can be EPS geofoam and tire waste materials mixed with sand. The seismic performance of the retaining structure is improved by the cushion material (Karpurapu and Bathurst, 1992; Partos and Kazaniwsky, 1987; Horvath, 1997). The use of tire chips is an innovative and cost-effective technique for mitigating disasters and enhancing the seismic performance of geotechnical structures. By embedding tire chips in the foundation material, the impact of earthquakes and liquefaction can be minimized. Studies have shown that recycled tire chips are effective in reducing dynamic earth pressure and absorbing earthquake vibrations. This method is a new way of utilizing scrap tires for infrastructure protection (Hazarika et al., 2008).

According to Shukla (2016), EPS geofoams are offered in either slab or block form and are a type of geosynthetic product that is extremely lightweight, with a unit weight that ranges from 0.11 to 0.48 kN/m$^3$. These materials can be utilized as a highway fill over compressible subgrade soils and frost-sensitive soils, as well as a backfill material for retaining walls to decrease the lateral earth pressure. Essentially, they act as a cushion.

## 2.5. Lightweight Materials

The cushion materials are used to investigate the potential to reduce seismic-induced dynamic earth pressures against retaining structures. The use of cushions behind the retaining wall can result in a significant reduction of earth pressures under both static and dynamic loading conditions, which can help to prevent damage to the retaining wall and improve its overall stability. The lightweight materials can be used as cushions behind the retaining wall. This section will provide an explanation of the material characteristics of the cushions used in this study. The material properties of EPS geofoam, tire waste, and sand mixtures, and the proposed cushion material in this study, EPS beads and sand mixtures are explained.

### 2.5.1. EPS Geofoam

EPS geofoam, invented in the 1950s, is inherently multi-functional, which makes it optional to use in a wide variety of applications. It has unique benefits for retaining walls, stabilizing slopes, and building on soft ground. In order to prevent ground freezing and heaving, EPS geofoam has been utilized under refrigerated storage facilities, sports stadiums, and storage tanks.

Density is an important property to distinguish between EPS products. The elastic modulus and strength of these materials increase as the density increases. These materials behave linearly elastic up to 1% strain based on rapid cyclic compression loading (BASF 1997). Horvath (1995) is the first study in the literature to propose the elastic modulus of EPS. It has also been used in below-ground construction segments to lower seasonal heating and cooling

needs. It reduces the stress caused by vertical overburden on pipes. With its strength and flexibility, EPS geofoam also provides creative solutions to a variety of issues, such as seismic shock absorption and noise and vibration dampening.

EPS geofoam is a material that can be utilized as a backfill behind buried and retaining structures to significantly decrease the lateral pressures exerted on the structure. The weight of the backfill is directly proportional to the horizontal pressure acting on a retaining wall. By replacing the backfill soil in the active zone behind the retaining wall with EPS geofoam, a less robust retaining structure can be used. Additionally, the use of EPS geofoam backfill behind buried and retaining structures can reduce the horizontal forces that may occur during earthquakes.

The EPS geofoam material reduces the static and dynamic lateral earth pressures on retaining structures (Zarnani and Bathurst 2007,2008). It gives flexibility to the wall. This flexibility prevents it from collapsing. The geofoam is a feasible option for impact and vibration isolation because of its damping characteristics. It makes improvements in the stability of slopes and also embankments. EPS geofoam also absorbs better at high frequencies and reduces accelerations better.

The ASTM requirements of EPS geofoam and schematic drawing of retaining wall with EPS geofoam backfill from EPS Geofoam Application and Technical Data are shown in Table 2.2 and Figure 2.17 (Alliance, 2012).

Table 2.2 Physical properties of EPS geofoam (ASTM D6817) (Alliance, 2012).

| ASTM D6817 Compliance, Type | | EPS12 | EPS15 | EPS19 | EPS22 | EPS29 | EPS39 | EPS46 |
|---|---|---|---|---|---|---|---|---|
| Density, min. | $kg/m^3$ | 11.2 | 14.4 | 18.4 | 21.6 | 28.8 | 38.4 | 45.7 |
| Compressive Resistance, min. (1% deformation) | *kPa* | 15 | 25 | 40 | 50 | 75 | 103 | 128 |
| Elastic Modulus | *kPa* | 1500 | 2500 | 4000 | 5000 | 7500 | 10300 | 12800 |
| Flexural Strength | *kPa* | 69 | 172 | 207 | 240 | 345 | 414 | 517 |
| Water Absorbtion by Total Immersion, max. | *vol. %* | 4 | 4 | 3 | 3 | 2 | 2 | 2 |
| Oxygen Index, min. | *vol. %* | 24 | 24 | 24 | 24 | 24 | 24 | 24 |
| Buoyancy Force | $kg/m^3$ | 990 | 980 | 980 | 980 | 970 | 960 | 950 |

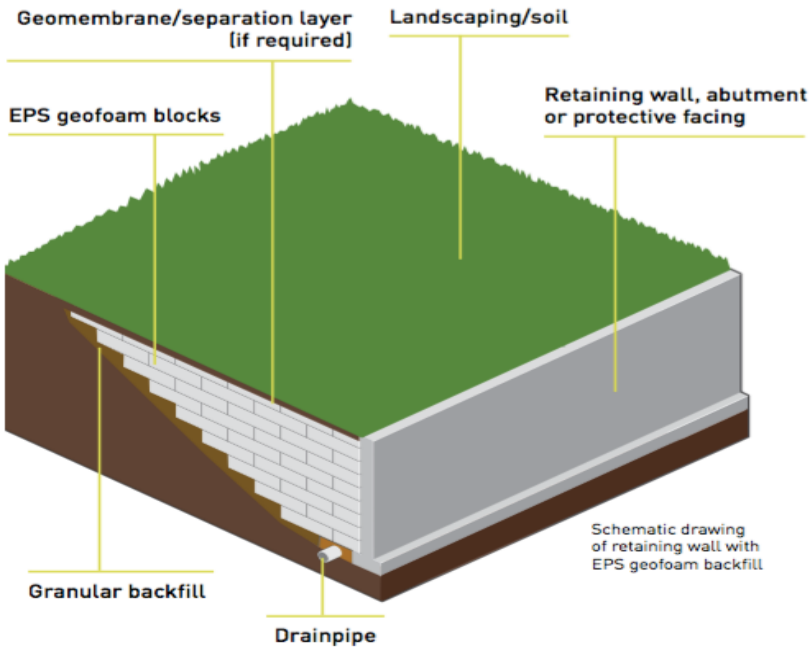


Figure 2.17 A schematic example of a retaining wall with EPS geofoam backfill (Alliance, 2012).

Athanasopoulos et al., 1999 conducted experiments to study the dynamic characteristics of two types of EPS geofoam materials. The researchers conducted tests on EPS geofoam samples that were molded into blocks with average densities of 12.4 and 17.1 kg/m3. These tests included torsional resonant column tests and cyclic uniaxial tests and were performed without applying any confining pressure to the specimens. By integrating the findings from the two different types of experiments, the behaviour of geofoam for strains ranging from 5×10-4 to 8.0% was examined. It was discovered that EPS geofoam acts linearly for strain levels up to 0.1%, but for stresses larger than 1%, a considerable nonlinearity emerges. The density of the geofoam significantly affected the dynamic moduli values, with the moduli increasing as the density increased. However, the density did not have an appreciable effect on damping ratio values. For strains less than 0.1%, the damping ratio values were very low (~1%) and increased to 10% for strains larger than 1%. Based on the findings of the experiments, the nonlinear characteristics of EPS geofoam were presented. It was also shown that the damping ratio values decreased with increasing frequency ranges between 0.01 and 2.00 Hz, the moduli values were not significantly impacted by the frequency of loading.

The elastic properties and damping ratio of EPS geofoam are significantly affected by the cyclic strain amplitude. As the strain increases, the elastic moduli values decrease, particularly for strains greater than 1%. However, the damping ratio values increased up to 15% for the highest strain values tested in the current experiment, which was around 8%. The resonant column and cyclic uniaxial test results were used to propose an "equivalent" Poisson's ratio value for both EPS geofoams within their overlap value strain range through back-calculation. This process resulted in negative Poisson's ratio values for EPS-1 and EPS-2 geofoam, respectively, $\nu$ = -0.75 and = -0.50 (Athanasopoulos et al., 1999).

Based on the results of the study by Athanasopoulos et al., 1999 on EPS geofoam, the following findings were observed:

*Linear and Nonlinear Behaviour:* The EPS geofoam demonstrates a linear stress-strain relationship when subjected to strains up to 0.1%. However, once the strain exceeds this limit,

the geofoam exhibits non-linear behaviour, which becomes increasingly noticeable for strains exceeding 1%.

*Damping Ratio:* The EPS geofoam exhibits low damping ratio values, specifically less than 1.5% when subjected to strains below 1%. However, as the strains increase, the material's ability to absorb energy becomes more prominent, with the damping ratio reaching a value of 10% for strains around 10%.

*Effect of Density:* The density of the EPS geofoam does not affect its damping ratio, which distinguishes its behaviour from that of other geomaterials.

*Loading Frequency:* The dynamic characteristics of EPS geofoam are impacted differently by loading frequency compared to viscoelastic materials. The loading frequency has a negligible effect on the elastic moduli values, but decreasing the loading frequency results in a significant increase in the damping ratio.

*Elastic Moduli and Strain:* The EPS geofoam experiences a significant reduction in its elastic moduli values as the strains increase, particularly for strains that exceed 1%.

*Negative Poisson's Ratio:* It was proposed to derive an "equivalent" Poisson's ratio value through back-calculation for the EPS geofoam. This approach led to the determination of negative Poisson's ratio values.

Athanasopoulos-Zekkos et al., 2011 studied the seismic isolation efficiency of EPS geofoam compressible inclusions for retaining walls by conducting centrifuge tests under horizontal cyclic shaking. Two experiments were performed, one using a uniform-density sand model and the other using the EPS Geofoam inclusion between the retaining walls and the backfill soil. The retaining walls being tested were fully equipped with instruments, having a prototype height of 4m, and supported cohesionless backfill. Additionally, they were seismically isolated with EPS compressible inclusions and were exposed to horizontal sinusoidal shaking

of different intensities. The experiments involved measuring the lateral earth pressures on a wall and the accelerations across the model.

The first experiment was conducted on a sand model with uniform density. The subsequent centrifuge experiment followed the same setup, with one key variation: the inclusion of EPS geofoam, a compressible material, between the retaining walls and the backfill soil. In this case, the EPS inclusion has a normalized thickness of 10% of the wall height in the prototype scale and 40 cm in thickness. The model's cross-section for the centrifuge test for the wall with EPS inclusion is shown in Figure 2.18 (Athanasopoulos-Zekkos et al., 2011).

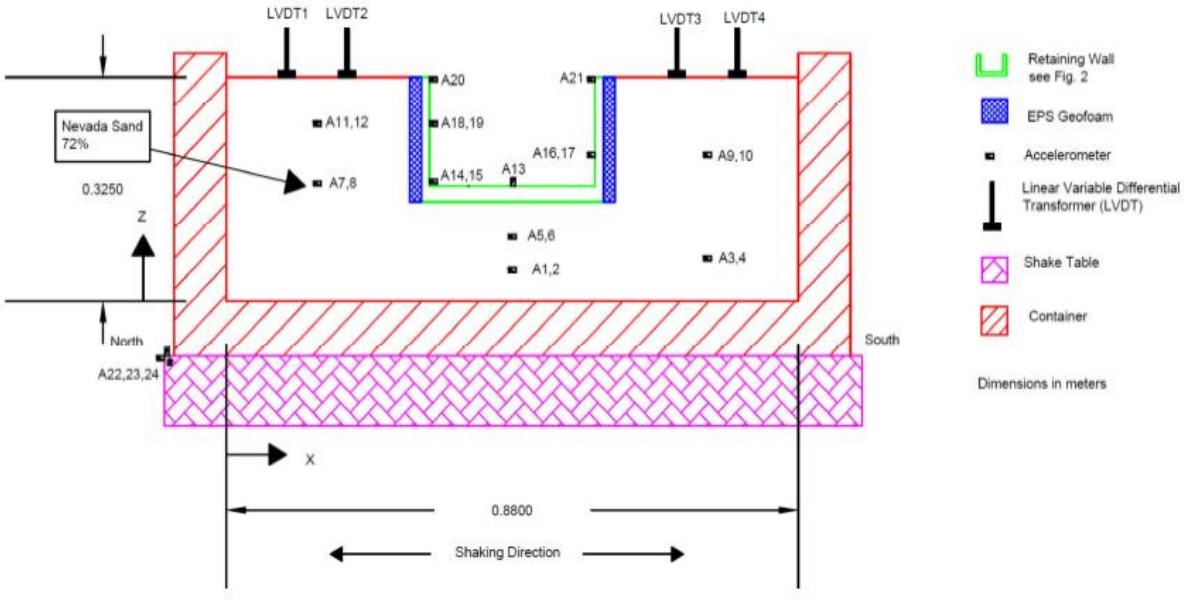


Figure 2.18 The model's cross-section for the centrifuge test for the wall with EPS inclusion (Athanasopoulos-Zekkos et al., 2011).

The static lateral pressures are considerably reduced as a result of the EPS's existence. In the case with EPS geofoam, a decrease in the overall lateral pressures is noticed, along with a smaller fluctuation in the earth pressures during the loading half-cycle. The decrease fluctuates across the vertical span of the wall, ranging from 5% at one end to 50% near the middle height of the wall. In regard to the overall force $P_{AE}$, the tests showed an average decrease of 27.7% across the entire tactile pressure pad. The decrease ranges between 5% and 30% along the wall's

height. The results of the tests showed that the EPS-geofoam inclusion significantly improved the seismic isolation efficiency of the retaining walls. In the initial findings and analysis of the centrifuge tests, it was observed that the inclusion of an EPS-geofoam layer in the second model served as a protective barrier. This layer effectively mitigated the seismic pressures exerted on the retaining wall, resulting in a reduction of their impact. The isolation efficiency of EPS was found to vary between 10% and 50% along the height of the wall for an input motion of 0.2g at a frequency of 2 Hz (Athanasopoulos-Zekkos et al., 2011).

Horvart, 1994 presented an overview of the engineering properties of expanded polystyrene (EPS), a type of rigid plastic foam used in geotechnical applications. EPS is commonly used as thermal insulation and ultra-lightweight fill due to its low density compared to soil. The most common form of EPS used in geotechnical applications is a prismatic block, which is a rectangular parallelepiped shape. These blocks are produced by a block molder using expandable polystyrene beads, which consist of polystyrene and pentane, which is a dissolved blowing agent. The density of EPS blocks can vary within a range of approximately 10 kg/m$^3$ to 40 kg/m$^3$, with densities between 15 kg/m$^3$ and 30 kg/m$^3$ being most common, having a density of nearly 1% of the soil density. The engineering properties of EPS, such as its linear-elastic behaviour, compressive strength, and post-yield behaviour, are influenced by its density.

EPS geofoam does not decompose in nature and does not react chemically with soil or water. It can be treated with additives to prevent infestation. Although EPS geofoam has a closed-cell form that prevents water absorption, water can still enter the tiny pores in the material without affecting its mechanical properties. However, EPS geofoam should not be exposed to UV radiation for extended periods as it can cause the surface to become yellow and brittle. EPS geofoam may dissolve in certain liquids, such as gasoline and diesel fuel, so it may need to be protected with geomembrane or other materials (Horvart, 1994).

There is a linear relationship between the initial tangent Young's modulus and the density of EPS shown in Figure 2.19. The elastic limit and compressive strength decrease as the density of EPS decreases. An increase in creep effect can result from a decrease in EPS or an increase in temperature at a specified EPS density. Creep data can be used to generate stress-strain curves

for EPS with different densities and durations of loading. Samples subjected to an initial strain of up to 0.5% exhibit minimal further deformation over time. Samples that were subjected to a 1% strain initially showed only a slight increase in deformation after 10,000 hours. However, samples that were initially strained between 1.5 and 2% experienced a significant increase in deformation over time (Figure 2.20). Figure 2.21 illustrates the correlation between EPS density and compressive stress measured at 1% compressive strain. As the density of EPS increases, its compressive strength also increases. Additionally, the point at which yield occurs is not a single point but rather a range (Horvart, 1994).

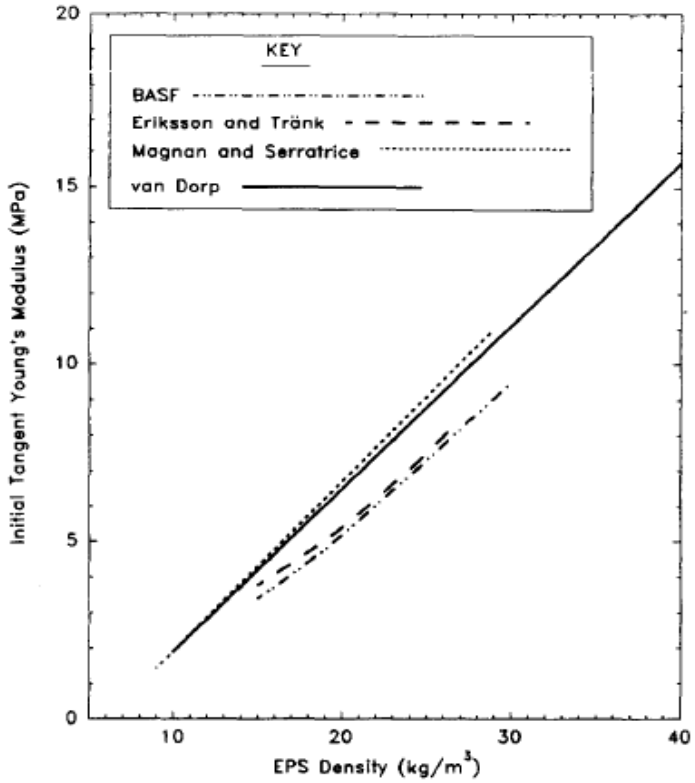


Figure 2.19 Young's modulus of the initial tangent and EPS density correlation (Horvart, 1994).

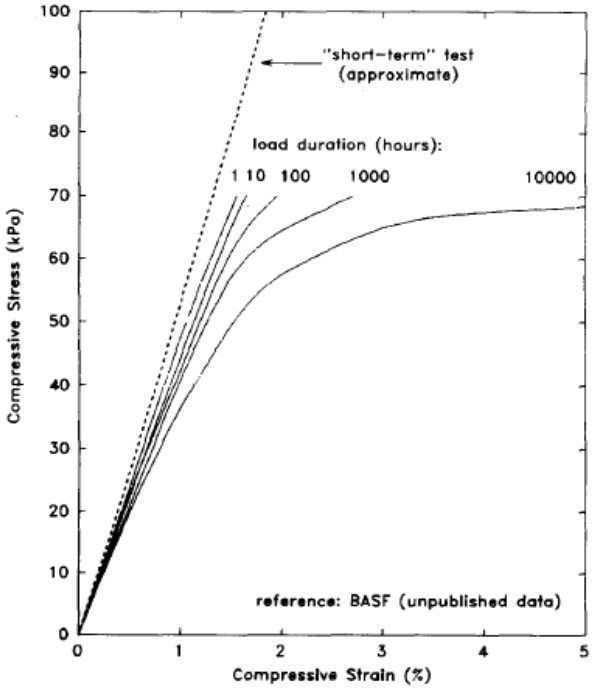


Figure 2.20 Time-varying stress-strain behaviour under axial compression of EPS 23.5 kg/m$^3$ (Horvart, 1994).

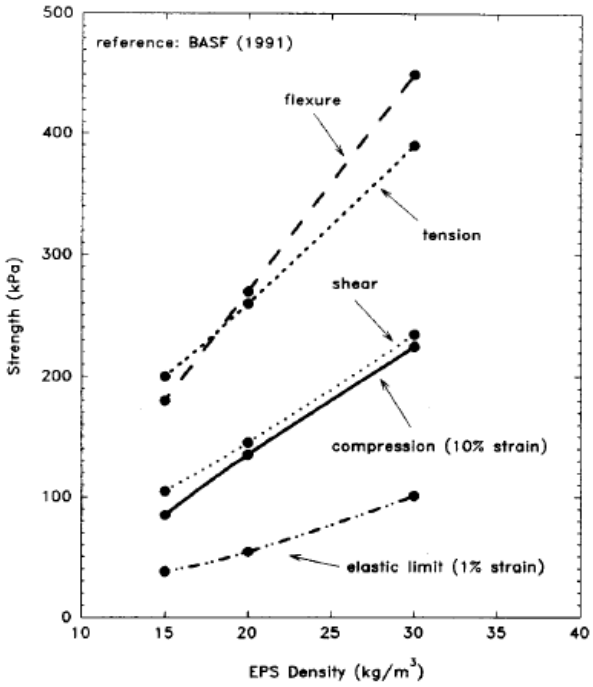


Figure 2.21 Correlation between EPS density and compressive strength (Horvart, 1994).

The study by Chun et al., 2004 aimed to investigate the stress-strain behaviour of EPS geofoam blocks under short-term loading conditions. The researchers conducted triaxial tests on EPS geofoam samples of densities 15, 20, 25, and 30 kg/m$^3$, subjected to varying levels of confining stress (0, 20, 40, and 60 kPa). It is indicated in the study that the major principal stress-strain behaviour of EPS geofoam is nonlinear and relies on both the density and confining stress, and as the density and confining stress increase, the compressive strength also increases. EPS geofoam undergoes directional deformation along the major principal strain axis without any expansion in volume, and the resulting axial and volumetric strains have a linear relationship that is influenced by the density and confining stress. The researchers proposed a hyperbolic model that captures the stress-strain behaviour of EPS geofoam, taking into account both the applied confining stress and the material's density. The model allows for the determination of the tangent modulus and Poisson's ratio values, which vary with the applied strain. The study provides practical insights into the behaviour of EPS geofoam under varying conditions and presents a useful model for its stress-strain characteristics.

The study focuses on the response of EPS geofoam to varying conditions and presents a practical construction model that captures its stress-strain characteristics. Experimental data indicates that an increase in EPS geofoam density leads to a corresponding increase in both compressive strength and initial tangent elastic modulus. EPS geofoam experiences the highest deformation in the major principal strain direction while experiencing minimal deformation in the lateral direction. In contrast, the soil experiences either contraction or dilation processes that are influenced by various factors such as soil properties, confining stress, and deviator stress. According to the results obtained from Chun et al. (2004), EPS geofoam exhibits a nonlinear stress-strain behaviour that is influenced by both its density and the level of confining stress it experiences during triaxial loading conditions. Higher density results in higher ultimate strength, and increasing confining stress leads to an increase in ultimate strength. It is observed a direct relationship between the volumetric and axial strain, and this relationship is affected by both density and confining stress.

Zarnani and Bathurst (2009) introduced two constitutive models to simulate seismic buffer shake table tests on expanded polystyrene (EPS). In a subsequent study (Zarnani and

Bathurst, 2009b), the authors compared a linear-elasto-plastic model with a Mohr-Coulomb failure criterion to an equivalent linear method that incorporated hysteretic loading-unloading cycles. Both models were used to simulate shake table tests on the performance of EPS seismic buffers, which were previously conducted by Zarnani and Bathurst (2007). These models were applied to both the geofoam buffer and sand backfill in the tests. The researchers utilized the finite difference numerical program FLAC to carry out the simulations.

The paper discusses two models used to simulate the stress-strain behaviour of EPS geofoam. The first model is a linear elastic-plastic model that includes the Mohr-Coulomb criterion for plasticity and Rayleigh damping. The second model is known as the equivalent-linear method (ELM), which uses Masing-type functions to incorporate hysteretic load-unload cycles and strain-dependent shear modulus and damping ratio functions. The FLAC finite difference model was used to implement both models. When the accelerations and total wall forces of the model are at their maximum, the predictions from the advanced ELM model are more accurate than the observed findings for the seismic buffer test with the most compressible EPS. However, the linear elastic-plastic model, which is simpler, is considered accurate enough for practical use when only the dynamic force increment is being considered. The results from simulations using both models show similar trends to the measured data during base excitation, but the ELM model tends to provide higher numerical predictions as time progresses. Both models accurately captured the general patterns observed in the recorded load-time history of the walls, and in many cases, they closely matched the measured data in terms of numerical values. However, the ELM method tended to provide higher estimates of total peak wall forces, especially at higher levels of excitation. The advanced ELM model produced predictions that were more in line with the measured results for the seismic buffer test, particularly when the EPS material with the highest compressibility was used, and the model experienced the greatest accelerations and total wall forces. However, the simpler model can be considered sufficiently accurate for practical purposes for a significant portion of the load-time history of the systems.

### 2.5.2. Tire Waste and Sand Mixtures

Tire waste material has been effectively utilized in various interdisciplinary engineering applications due to its favorable engineering characteristics, including thermal insulation, permeability, compressibility, stiffness, and high damping properties. The availability of different sizes and shapes of tire waste material also contributes to its versatility. Tire waste materials have suddenly become more widely employed as a soil-reinforcing material in a variety of constructions, including landfill construction and operations, alternative daily covers, leachate collection systems, landfill closures, gas venting systems, subgrade fill and embankments, pavement, septic system drain fields, backfill for retaining walls and bridge abutments, subgrade insulation for roads, and vibration dampening layers, etc. The increasing potential for recycled tires for use in the construction field gives us a good idea of the potential that can be explored in this area. It is ideal for reinforcing material due to its lightweight and durability. The use of tire waste materials has the benefit of being inexpensive and of providing for the utilization of waste resources. Numerous studies using soil reinforced with tire chips show that it is a feasible alternative in the form of reinforcing material or in the form of aggregate (STMC, 2010; Lepcha et al., 2014).

The use of tire chips in retaining wall backfill, vulnerable to earthquake action, has also been successful. Tire Derived Aggregate (TDA), a recycled lightweight construction material, is created by cutting up used tires into pieces that range in size from 25 to 305 mm. TDA has been utilized in a variety of civil engineering applications over the past 20 years, such as lateral edge drains, retaining walls, bridge abutments, subgrade insulation to prevent frost penetration, and embankment and subgrade fill (Lepcha et al., 2014; Ahn et al., 2015).

Due to the technical characteristics, such as thermal insulation, permeability, compressibility, stiffness, and high damping, tire wastes (TW) are favored in a wide range of engineering applications (Figure 2.22, Figure 2.23). Tire waste addition is used as lightweight fill, embankment fill, retaining wall backfill, subgrade insulation for highways, and vibration-dampening layers in geotechnical applications and highway applications. Tire trash has recently been recommended as a novel seismic buffer material since it has superior damping and stiffness

properties compared to sand. By absorbing the seismic energy, the protective cushion layer would enable the buildings to be flexible and stable during earthquakes (Hylands and Shulman, 2003). In different areas of geotechnical engineering, there has been a growing trend in utilizing materials derived from scrap tires, such as tire shreds, chips, and tire crumbs. Table 2.3 provides a summary of multiple studies that have explored the use of these scrap tyre-derived (STD) materials in various geo-engineering applications.

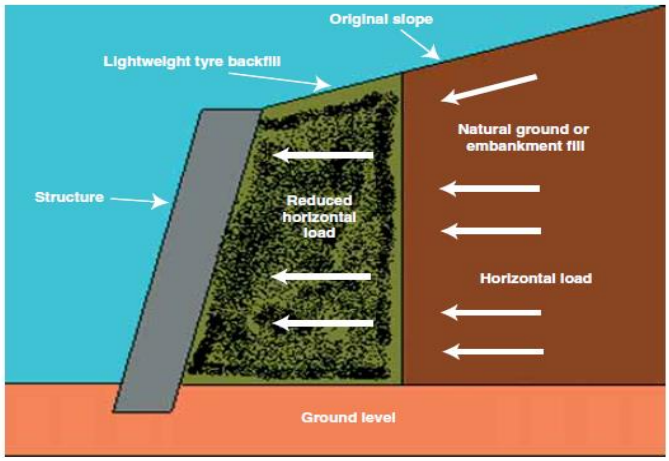


Figure 2.22. Lightweight fill used as backfill to retaining structures (Hylands and Shulman, 2003).

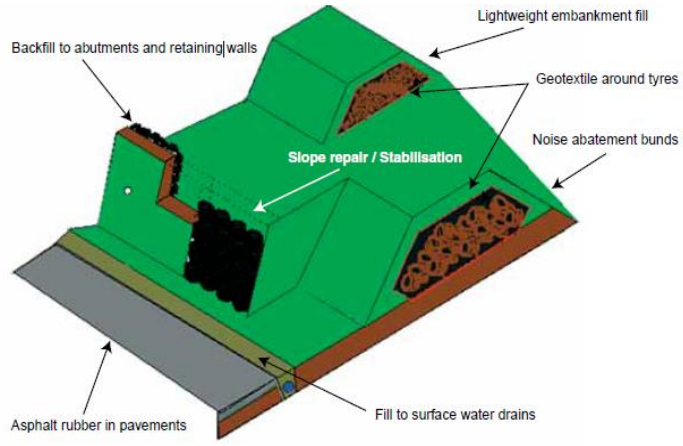


Figure 2.23. Proven applications for post-consumer tires in highway and related engineering applications (Hylands and Shulman, 2003).

Table 2.3. Application of scrap tire-derived (STD) materials in geo-engineering applications (Reddy and Krishna, 2017)

| Reference | STD material | Application | Remarks |
|---|---|---|---|
| Cecich et al. (1996) | Tyre chips | Retaining structures | Cost analysis was presented to retaining wall using tyre chips in backfill |
| Tweedie et al. (1998) | Tyre shreds | Field retaining wall model | Reduction of lateral earth pressures were backfill reported |
| Yang et al. (2002) | Shredded tyres | — | Mechanical properties of shredded tyres were found |
| Salgado and Prezzi (2004)<br>Lee and Roh (2006)<br>Rao and Dutta (2006) | Tyre shreds<br>Recycled tyre chips<br>Sand–tyre chip mixtures | Embankment<br>Retaining wall backfill | Field model study was done using tyre shreds<br><br>Compressibility and strength behaviour were evaluated |
| Yoon et al. (2006)<br>Hazarika and Yasuhara (2007) | Sand–tyre shred mixture<br>STD materials | Embankment<br>Different geo-applications | Applications such as foundations, slopes, retaining wall, seismic isolation, liquefaction mitigation and so on were discussed |
| Anbazhagan et al. (2011) | Tyre crumbs soil mixture | — | Dynamic properties such as damping, shear modulus and so on were studied |
| Hazarika et al. (2012) | STD materials | Different geo-engineering applications | STD materials were used as ground improving geomaterials |
| Sheikh et al. (2013) | Sand–tyre crumb mixtures | | Shear and compressibility behaviour was determined |
| Ahn and Cheng (2014) | TDA | Retaining wall backfill | Dynamic response of retaining wall was studied |
| Balunaini et al. (2014) | Tyre chip–sand and tyre shred–sand mixtures | | Shear strength properties were found |
| Ayothiraman and Soumya (2015) | Tyre chips | Stone columns | Tyre chips using as aggregate in stone |
| Boominathan et al. (2015) | Soil–rubber tyre scrap mixture | Foundations | This study was focused on seismic base isolator for foundations |
| Dammala et al. (2015)<br>Reddy and Krishna (2015)<br>Reddy et al. (2016a, 2016b) | Sand–tyre chips mixtures | Retaining wall backfill | Focused on optimum mixture ratio of sand–tyre chips using mechanical properties and retaining wall model studies |

Feng and Sutter, 2000 studied the properties of granulated tire rubber/sand mixtures, specifically focusing on the shear modulus and damping ratio. In the study, a torsional resonant column was utilized to construct specimens with varying percentages of Ottawa sand and granulated tire rubber. These tests were conducted on materials prepared under different conditions, such as air-dried or with a small amount of moisture, using dry spooning or under-compaction to replicate real-world scenarios. The results clarified the minimum damping ratio and the maximum shear modulus associated with each percentage of granulated rubber. It is discovered in the study that normalizing the shear modulus using a reference strain reduced the variability in the data for granulated rubber/sand mixtures. This approach proved effective in bringing the normalized shear modulus reduction for mixtures containing 50% granulated rubber closer to that of a typical saturated cohesive soil.

The elasticity of tire rubber allows for a more elastic response in mixtures with granulated rubber or sand as the rubber content increases. The small degradation of shear modulus with increasing shear strain for samples containing 49% and 76% rubber is due to the high elasticity of rubber. Particle deformation and friction from particle interactions lead to damping in a rubber-sand mixture. Rubber absorbs energy when its particles are deformed, but sand particles are rigid and disperse little energy. The damping ratio slightly increases as the confinement pressure increases, which is contrary to the behaviour of typical soils. The percentage of rubber in the mixtures has a significant impact on the shear modulus. The damping ratio for 100% rubber increased slightly with confinement pressure, which is contrary to the response observed in soil. This could be attributed to the presence of rubber causing an increase in the size of interparticle contacts between particles as the confining stress increases. The study demonstrates that the reference strain concept is applicable to mixtures of rubber and sand, and the behaviour of the mixture is similar to that of cohesive soil and wheat (Feng and Sutter, 2000).

Edinçliler et al., 2014 conducted a study on the behaviour of recycled materials for highways. The static and dynamic behaviour of tire buffings was studied using large-scale direct shear and dynamic triaxial testing. The inclusion of tire buffings in the sand had an impact on how the mixture deformed, resulting in increased stiffness at low strains and decreased stiffness at high strains. When tire buffings were combined with sand, the resulting mixtures exhibited

higher shear modulus and damping values compared to tire buffings alone. To determine the shear strength properties of the lightweight aggregates as tire buffings, a large-scale direct shear test equipment with dimensions 300mm×300 mm was designed and manufactured at Boğazici University.

The addition of tire buffings to medium-dense sand altered tire buffings and sand mixture's dynamic and deformation behaviour. At low strains, the mixture exhibited rigid behaviour, but the addition of tire buffings increased the displacement at failure values by three to seven times. When mixed with sand, the dynamic shear modulus of tire buffings increased significantly. However, adding 10% by weight of tire buffings to sand decreased the shear modulus while significantly increasing damping. In order to enhance the strength-deformation and dynamic characteristics of sand, it is possible to utilize tire buffings, given their accessibility and cost-effectiveness (Edinçliler et al., 2014).

Edinçliler, 2008 performed a study to evaluate the shear strength properties of tire buffings and mixtures of tire buffings and sand with different compositions. The purpose of the study was to investigate the potential uses for these mixtures. The experiments were conducted on various mixtures of medium-density sand and tire buffings under three vertical stresses: 20 kPa, 40 kPa, and 80 kPa, respectively. A large-scale direct shear testing instrument was used to assess the shear strength characteristics and deformation behaviour of tire buffings and their mixtures. Different weight percentages of tire buffings were added in the mixtures, namely 5%, 10%, 20%, and 30% (referred to as STB5, STB10, STB20, and STB30), with relative densities of 15.19 kN/$m^3$, 14.89 kN/$m^3$, 14.22 kN/$m^3$, and 13.56 kN/$m^3$, respectively.

The study found that adding tire buffings to sand had a significant impact on the deformation behaviour and shear strength values of the mixture. Specifically, the addition of tire buffings resulted in an increase in strength at low confinement stresses. The laboratory tests showed that adding ten percent by weight of tire buffings to sand altered the deformation behaviour of the mixture, making it stiffer at low strains but softer at large strains. Additionally, adding tire buffings to the top one to two meters of highway embankments can improve their performance under traffic load. The tire buffings stiffen the composites at low strains and soften

them at large strains, improving support under the pavement structure. It is indicated that adding tire buffings to sand can enhance the mixture's shear strength, suggesting that tire buffings can serve as effective fiber reinforcement components. Even at low concentrations of tire buffings, such as 10 percent, the mixture's deformation is significantly modified under the test conditions used in the study (Edinçliler, 2008).

The main aim of the study conducted by Edinçliler et al. (2010) is to evaluate various processing techniques used to enhance the mechanical properties of soil by incorporating mixtures of sand and recycled tires. The summary of existing literature on the mechanical properties of different processed tire materials, including tire shreds, tire chips, tire buffings, and their combinations with sand was explained to compare the results of the large-scale direct shear tests conducted to determine the shear strength of sand-tire crumb mixtures. Direct shear tests were conducted on various samples using three different normal stresses of 20 kPa, 40 kPa, and 80 kPa, respectively. Medium-dense and uniformly graded sand, with a dry unit weight of 13.8 $kN/m^3$ was used in the experiments. The tire crumb used in the tests had dimensions ranging from 1 to 3 mm, and the unit weight of the tire crumb was 5.4 $kN/m^3$. Only sand and tire crumb sand mixtures with weight percentages of 5% (STC5), 10% (STC10), 20% (STC20), and 30% (STC30) having densities of 13.38 $kN/m^3$, 13.02 $kN/m^3$, 12.38 $kN/m^3$, and 11.85 $kN/m^3$, respectively.

The test results for tire crumb mixtures are compared with those of other processed tire-sand mixtures. It is found that sand-tire mixtures have higher shear strength compared to sand alone, and this shear strength is dependent on the processing conditions of the recycled tires. Mechanical properties of materials are significantly affected by three factors: normal stress, processing techniques, and the content of recycled tires. The shear strength of the mixtures is influenced by factors such as the content of recycled tires, aspect ratio, compaction, and normal stress. These studies indicate that by-products of recycled tires, such as tire shreds, tire chips, and tire buffings, have the potential to improve the mechanical properties of sand. The inclusion of used tires in sand mixtures has been found to increase the shear strength, indicating their potential as fiber reinforcement elements. Even at low inclusion levels, such as 10% by weight, the deformation behaviour of the mixture is considerably altered by the presence of processed

used tires, considering the specific tire specimens and test conditions. It is indicated in the study that when tire crumbs are added to sand, the peak shear strengths increase for all tire crumb percentages. This change in the deformation behaviour of the mixture involves making the material stiffer at small horizontal displacements and softer at larger horizontal displacements, except for cases with low tire crumb content (STC5). The results showed that the processing technique, processed used tire content, and normal stress were the most important factors that influenced shear strength (Edinçliler et al., 2010).

Edinçliler and Yıldız, 2022 conducted an experimental study to investigate the effects of processing type on the shear modulus and damping ratio of waste tire-sand mixtures. The study aimed to analyze the impact of two distinct processing techniques on the damping ratio and the shear modulus of the mixtures and to investigate the outcomes of comparable tests utilizing various processed waste tires by combining the literature and the findings of this study. The sand-tire crumb and sand-tire buffing specimens, referred to as TCS and TBS, respectively, with tire additive proportions of 10%, 20%, and 30% were used. The results showed that sand-rubber mixtures consistently exhibited lower shear modulus compared to clean sand specimens, regardless of the tire content and confining pressure. The highest shear modulus value was obtained when 10% rubber was added to the sand. The study also found that the shear modulus decreased as the tire content ratio increased, and this decrease became more pronounced under higher confining pressure. The damping ratio increased as the rubber content increased, with the highest damping ratio achieved at 30% waste tire inclusion.

The study investigated the relationship between confining pressure and shear modulus in specimens subjected to increasing shear strain. The results showed that the shear modulus decreases as the confining pressure increases for a given rubber ratio with the same properties. However, specimens subjected to higher confining pressures exhibited higher shear modulus values. The study also found that the shear modulus of all mixtures decreased under various confining pressures, irrespective of the type of waste tire inclusion. An increase in confining pressure led to a decrease in the damping ratio. The introduction of rubber materials enhanced the damping ratio, and the highest damping ratio was measured for the TCS30 specimen under a confining pressure of 40 kPa. The study also evaluated the impact of the processing method

on the shear modulus for TCS and TBS specimens with the same rubber content. The results showed that both tire crumb and tire buffing mixtures exhibited reduced shear modulus compared to the clean sand specimen. TBS specimens tended to have higher shear modulus values than TCS specimens due to their higher additive contents. The tire-sand mixture created frictional resistance at the surface of the tire buffing material, increasing friction angles and shear modulus values. Tire polishing stiffened when confining pressure was raised, increasing the frictional resistance along the tire buffing surface, resulting in higher values for shear modulus (Edinçliler and Yıldız, 2022).

The percentage of tire crumb/tire buffing inclusions and confining pressures had a significant impact on the damping ratio of the mixtures. The tire crumb specimens consistently displayed higher damping ratios than tire buffing specimens under all three confining pressures. This is due to the particle deformation and friction along particle contacts, which consume more energy in tire crumbs having granular shape. The damping behaviour becomes more pronounced as the rubber content increases for both tire buffing and tire crumb specimens. However, at higher confining pressures, both specimens dissipate less energy. The mixtures with granulated rubber have significantly higher damping ratios than specimens with fiber-shaped tire buffing due to the different deformability, contact surface, and dimensions of the materials. The study also found that incorporating waste tire inclusions can increase the damping ratio, making the mixtures an excellent material for mitigating earthquake hazards (Edinçliler and Yıldız, 2022).

### 2.5.3. EPS Beads and Sand Mixtures

Many civil engineering projects in the world have utilized lightweight fill solutions. In locations where the soil conditions are poor, traditional fill materials for lightweight construction can be substituted with expanded polystyrene (EPS) geofoam, tire wastes, and wood chip. These materials are added to the soil as an additive. The type, content, and aspect ratio of the mixtures all have an impact on their mechanical and dynamic properties.

Edinçliler and Özer, 2013 conducted a series of triaxial compression tests at different confining pressures (40kPa, 100kPa, 200kPa) to investigate how the gradation of EPS beads affects the stress-strain behaviour of lightweight materials made of EPS beads and sand mixtures. Three different types of EPS beads as EPS-1, EPS-2, and EPS-3 given properties in Table 2.4 were mixed with sand, each with a different unit weight and varied the content of EPS beads.

Table 2.4 Physical properties of Sand- EPS-1, EPS-2, and EPS-3 (Edinçliler and Özer, 2013).

| Material | Specific gravity ($G_s$) | Dry unit weight ($kN/m^3$) | Effective size $D_{10}$ (mm) | Mean grain size $D_{50}$ (mm) | Uniformity coefficient $C_u$ | Coefficient of curvature $C_c$ |
|---|---|---|---|---|---|---|
| Sand | 2.65 | 14.2-16.4 | 0.2 | 0.6 | 2.7 | 1.2 |
| EPS-1 | 0.02 | 0.14 | 2.2 | 3.5 | 1.6 | 1 |
| EPS-2 | 0.03 | 0.19 | 2 | 2.8 | 1.6 | 1 |
| EPS-3 | 0.05 | 0.3 | 1.2 | 2.4 | 2.2 | 0.8 |

The initial modulus of elasticity reduces linearly as the volumetric EPS bead content increases assuming all other factors (EPS bead type in EPS-sand) remain constant. Therefore, compared to the sand-only specimen, the highest deviatoric stress of the EPS-sand was not increased by the addition of EPS beads. The study suggested multiple linear regression (MLR) equations based on the number of EPS beads, the amount of confining pressure, and the type of EPS beads to calculate the preliminary undrained elastic modulus of EPS-sand, saving time and money compared to the usual laboratory testing. In geotechnical applications, these materials can be used as lightweight fill materials according to the stress-strain behaviour of EPS-sand mixtures (Edinçliler and Özer, 2013).

It is revealed that the initial undrained elastic modulus of EPS-sand decreases in a linear manner as the volumetric content of EPS beads increases. However, this decrease is influenced by the type of EPS beads used. When smaller EPS beads are added to the mixture, the deviatoric stresses and initial undrained modulus increase. Under low confining pressure, EPS-sand behaves like loose sand, but under high confining pressure, it exhibits strain-hardening behaviour. Selecting smaller-sized EPS beads results in higher stiffness properties, allowing for

the creation of lightweight fills without considerably compromising stiffness. Based on the EPS type, volumetric EPS bead concentration, and confining pressure, an MLR equation is suggested to estimate the elastic modulus derived from EPS-sand samples, which can reduce the cost and time associated with laboratory testing. The unit weight of EPS-sand fill is greatly reduced when the volumetric EPS bead content is increased, but determining the optimum bead content and type is crucial to compromise the loss of stiffness. Despite reducing deviatoric stress and initial elastic modulus, EPS bead addition to sand may be utilized as a lightweight fill in conjunction with other techniques, such as geotextiles, to boost stability when used for embankment fills (Edinçliler and Özer, 2013).

The aim of the study conducted by Fard et al., 2015 was to assess the shear strength properties of a sand-EPS beads mixture through large direct shear tests. The tests were conducted under six different vertical stresses to investigate the effect of EPS bead content on the mixture's properties. The experiments were performed by using the sand particles having properties gray in color and having a uniform distribution. These spherical EPS beads range in size from 2 to 7 mm. EPS-sand specimens were created by mixing EPS beads with sand at different dry mass ratios. This ratio, denoted as η, represents the proportion of EPS beads to sand and is considered a crucial factor influencing the unit weight, strength, and deformation characteristics of the mixtures. The investigated ratios ranged from 0 to 0.125% by weight. Adequate water was added to ensure proper bonding between the EPS beads and sand, thus preventing segregation during mixing. The rest of the experiments were carried out using the EPS-sand specimens. Each series of tests comprised six specimens subjected to six distinct overburden pressures (5 kPa, 10 kPa, 20 kPa, 40 kPa, 80 kPa, and 160 kPa).

Control tests using only sand indicated that the shear strength findings obtained by the large-scale direct test apparatus were equivalent. In most cases, the EPS content was low enough to allow for the observation of peak shear strength resistance. The results showed no significant differences among the various deformation levels, suggesting that selecting design parameters for EPS-sand mixtures is not a challenging task. The analyses indicated that the shear strength of the EPS-sand mixture is primarily governed by frictional behaviour, with intercept cohesion values being relatively small. Notably, the obtained results demonstrated a decrease in the

internal friction angle with increasing EPS content, attributed to the replacement of sand particles with EPS beads (Fard et al., 2015).

Chenari et al., 2016 conducted a study on the use of Expanded Polystyrene (EPS) beads mixed with sand in geotechnical engineering applications. They used a newly designed and fabricated large-scale oedometer apparatus to measure and calculate various parameters such as permeability, coefficient of earth pressure at rest, and volume compressibility coefficient for different EPS bead contents. It was also investigated that important deformation and strength characteristics parameters such as the internal friction angle, constraint modulus, and the drained 3-D elasticity modulus. The results showed that the addition of EPS beads led to a reduction in the overall stiffness of composites. The researchers submitted predictive models in the form of MLR simulations and evaluated their performances. The study found that while the volume compressibility coefficient and the $K_0$ coefficient showed opposing trends, the permeability, internal friction angle, constraint modulus, and 3-D Young modulus all decreased with inclusion content. Overall, the study provides valuable insights into the hydraulic and mechanical behaviour of non-conventional materials in geotechnical engineering applications. The obtained results showed that the addition of EPS beads led to a reduction in the overall stiffness of composites. Due to the replacement of sand particles with impermeable EPS beads, the addition of EPS beads to composites decreased their overall stiffness and permeability. Increasing overburden pressure further decreased permeability by inducing more compression in EPS beads. The inclusion of EPS beads led to an increase in the coefficient of earth pressure "at rest" ($K_0$) initially, but this effect diminished with higher effective stress. The internal friction angle decreased with increasing EPS inclusion but increased with overburden pressure. The volume compressibility coefficient of EPS-sand mixtures depended on the rigidity of the mixture, which decreased with EPS inclusion and increased with overburden pressure. The elasticity modulus decreased with increasing EPS content up to 0.5% by weight. Predictive models using MLR were used successfully to simulate these parameters. While the decrease in permeability, internal friction angle, and constraint modulus may not be desirable in geotechnical applications, EPS beads offer benefits due to their low unit weight and specific gravities compared to quartz sand.

El-Sherbiny et al. 2017 conducted a study to evaluate the dynamic properties of sand-EPS bead mixtures through a series of consolidated undrained cyclic triaxial tests and resonant column tests. The tests were conducted to determine the small and large strain dynamic properties, specifically the shear modulus and the damping ratio. The influence of two main factors, EPS bead content, and confining pressure, on the dynamic behaviour of the mixtures was studied. The mixtures were prepared with varying EPS bead content by weight, ranging from 0.0% to 2.5%. The confining pressure was also varied, with tests conducted at 50 kPa, 100 kPa, and 200 kPa. This increase in confining pressure resulted in the compression of air voids and EPS particulates, leading to a denser and stiffer specimen. The damping ratio showed a decrease with increasing beads content. The influence of confining pressure on the damping ratio followed a similar trend to the bead content. Higher confining pressures resulted in less absorption of energy and a lower damping ratio. The shear modulus degradation curves showed a reduction in shear modulus as the EPS bead content increased, particularly at low to medium shear strain levels. The degradation curves also changed with the addition of EPS beads. The confining pressure had a similar effect on the shear modulus, with higher pressures resulting in higher shear modulus. The damping curves showed that the damping ratio increased with the increase in bead content at high strain levels. The confining pressure had a limited effect on the damping ratio. The results showed that increasing the confining pressure led to a higher shear modulus for all bead content. The inclusion of EPS beads decreased the unit weight of the mixture significantly, and increased bead content resulted in a reduction in shear strength. It was seen that the small-strain shear modulus increases with respect to the confining pressure as expected because EPS bead particles lost their sphere shape and crushed. The inclusion of EPS beads increased the damping of the mixture, and confining pressure was found to have little effect on the damping ratio at high strain levels of the study. The addition of EPS beads to the sand mixture affected the dynamic properties. Increasing the confining pressure develops a higher shear modulus and lower damping ratio. Shear modulus, damping ratio, and shear modulus degradation were all affected by the EPS beads' composition.

Alaie et al. 2021, performed shake table experiments to obtain the dynamic properties of these mixtures under medium to large strain levels. During the experiments, the effect of the EPS bead ratio and amplitude of the input motion on the shear modulus, damping ratio, and

stress-strain response were achieved. Five different EPS bead contents of 0%, 0.5%, 1%, 1.5%, and 2% by weight were studied. Shake table experiments were performed using different displacement amplitudes from 0.5 mm to 4 mm, which corresponds to 0.05g to 0.4g, at a constant 5 Hz frequency and during 15 cycles. Increased EPS bead ratio resulted in lower surface fractions of the samples under high intensity shaking as the damping ratio increased. Also, displacement amplification factors on the surface increased with respect to the input acceleration, and it decreased with increased EPS bead content. Moreover, peak acceleration values of Sand-EPS bead mixtures at a surface level were less than only sand samples with increased damping and decreased shear modulus levels. The stiffness behaviour of mixtures was higher for smaller size beads.

The results showed that for all sand-EPS bead mixtures, the horizontal displacements increased from the lowest to the highest layers. With an increase in the input base acceleration, the rigid base movement and the relative maximum horizontal displacement increased. The mixtures with 0% and 1% had very small maximum horizontal displacement values under input base accelerations of 0.05g, 0.1g, and 0.2g. The maximum horizontal displacement of the sand model with 0% was higher than the sand-EPS composite model with 1% mixture ratio. Even at an input acceleration of 0.4g, the horizontal displacement was considerably decreased by adding more EPS content to the mixture. With respect to differing EPS contents and input base accelerations, the amplification levels varied. In the sand-EPS mixtures, high shaking intensities (0.4g or higher) can result in significant displacements and surface cracks. Under all input base accelerations, the sand-EPS mixture surface acceleration amplification values were lower than those of the pure sand models. The peak acceleration amplification value decreased as the input base acceleration increased, demonstrating the impacts of the deposit non-linearity (Alaie et al. 2021).

Alaie and Chenari, 2018 evaluated the dynamic properties of mixtures of EPS beads and sand using cyclic triaxial and Bender element tests. It is found that as the EPS content increased, the values of shear wave velocity and maximum shear modulus obtained from the Bender element tests decreased. The weight percentage of EPS was also shown to have a significant impact on the damping and shear modulus of the samples, with an increase in EPS content

resulting in an increase in the ratio of damping under constant confining pressure. The dynamic characteristics of EPS beads were covered in the study as this material behaves differently under cyclic pressure than clean sands or clays do. The material's shear modulus increases depending on the increases in EPS density but has no appreciable impact on the damping ratio. Through a series of strain-controlled cyclic compression experiments, it is evaluated that as EPS bead content increases, the interface shear stiffness decreases, and the damping ratio increases. The Poisson's ratio of the samples was measured using a large-scale oedometer apparatus.

The results showed that increasing EPS content led to a significant decrease in unit weight and equivalent void ratio. Shear wave velocity decreased with increasing EPS content while shear modulus increased. The shear modulus of sand decreased with increasing cyclic shear strain amplitude, while the shear modulus of EPS-sand mixtures decreased with increasing confining pressure. The damping behaviour of EPS-modified sand mixtures depended on the EPS content, with lower EPS content exhibiting friction mechanism damping and higher EPS content exhibiting viscoelastic and viscoelasto-plastic behaviour. The study also investigated the use of EPS-sand mixtures as isolators to reduce dynamic loads on geotechnical structures. EPS is a lightweight and inexpensive material that can be used to improve the seismic isolation properties of low-to-medium-rise buildings (Alaie and Chenari, 2018).

Edinçliler and Yıldız (2022) conducted a study on the use of EPS beads and sand mixtures as a seismic isolation material for medium-rise buildings. To evaluate the effectiveness of this material, they performed shake table tests on a scaled model of a five-story building. The foundation of the model was surrounded by layers of sand-EPS beads mixtures of varying thickness to simulate seismic isolation. The study examined a number of factors, such as the thickness of the isolation layer, the content of the EPS beads, and the characteristics of seismic motions. In the experiment, isolation layers were created using mixtures of EPS beads and sand, with varying percentages of EPS beads 5%, 20%, and 40% by weight, respectively. The isolation layers, with thicknesses of 10 and 15 cm, were applied around the foundation of a 1/10 scaled building model. The model was subjected to different earthquake excitations to investigate the enhancement of its seismic performance.

Models with EPS beads-sand mixtures exhibited significant absorption of seismic energy and reduced transmitted accelerations under the Kocaeli Earthquake, Kobe Earthquake, and El Centro Earthquake excitations. On average, a response reduction between 30 to 34% in acceleration could be achieved for the top of the building and 11 to 16% for the first-floor level. The energy absorption capacity increased with a higher content of EPS beads in the mixture, resulting in improved seismic performance of the structure. Notably, the highest seismic performance was achieved with EPS40, which showed a 33% reduction in transmitted acceleration. Increasing the thickness of the EPS beads-sand isolation layer enhanced the seismic reduction effect, albeit to a lesser extent compared to increasing the percentage of EPS beads in the mixtures. The percentage decrease in inter-story drifts differs between the first and top floors, ranging from 10% to 31%. The isolated models with EPS beads-sand layers experienced a significant reduction in lateral displacements compared to the non-isolated scenario. The addition of the EPS beads-sand isolation layer led to reductions of up to 35% in inter-story drifts, as the compressibility of EPS beads helped absorb transitional forces and decrease relative displacements between floors. The spectral accelerations showed amplified values in the higher period ranges for the isolated case under the Kocaeli earthquake. The reduction in spectral accelerations under the scaled Kobe and El Centro earthquakes was 31% and 30%, respectively. The corresponding period lengthening ratios were calculated as 1.1% and 1.07%, respectively. The study showed that the proposed EPS beads-sand mixture material is susceptible to changes in content and earthquake characteristics. These findings highlighted the potential of EPS beads-sand mixtures as a reliable seismic isolation material (Edinçliler and Yıldız, 2022).

## 2.6. Effects of Soil Improvement for the Retaining Walls under Static and Seismic Loading

This section is based on numerical, experimental, and field studies related to the effects of soil improvement for the retaining walls under static and seismic loading.

### 2.6.1. Numerical Modelling of Retaining Walls

In a study by Ayuluri and Ramulu (2017), case studies and related numerical analyses were presented about reinforced soil retaining walls. The static behaviour of models was investigated numerically using the finite element modeling program Plaxis. It is well known that using FEM analyses provides relevant information on the mechanical behaviour of such structures, which is quite difficult to obtain from the limit equilibrium analyses. The aim of the paper was to analyze the behaviour of reinforced soil retaining walls under static load through a parametric analysis and to determine the impact of changes in soil parameters (dense and loose soil) and applied load on the performance of the retaining walls. The numerical analyses were conducted to determine the appropriate loads and geometry for a reinforced soil retaining wall and to determine the appropriate selection of geogrid stiffness for the reinforced soil retaining wall. The performance of the wall is influenced by various factors, including the surcharge load, geogrid length, geogrid stiffness, and geogrid spacing. The displacement behaviour of loose sand is similar to that of dense sand when compared. Both loose and dense sands exhibit higher degrees of instability when used as foundation and backfill materials in reinforced soil retaining walls. This study suggests that the geogrids play a significant role in enhancing the wall's stability. The behaviour of the wall is similar in both loose and dense soil conditions, indicating that the performance of the wall is not significantly affected by the soil type. To ensure stability, a state of equilibrium must be achieved between the stiffness of the geogrids and the soil's angle of internal friction.

Notash and Dabiri (2018) performed numerical analyses to explore the effectiveness of geofoam panels in improving the static performance of cantilever retaining walls. During the analyses, FLAC 2D finite difference software was used. The variables were the height of the wall (3m, 6m, 9m), geofoam panel densities (15 kg/m$^3$, 20 kg/m$^3$, 25 kg/m$^3$) and relative thicknesses t/H (0.05, 0.2 and 0.4). Also, four-panel spacing of 50, 100, 150, and 200 cm were also evaluated. It was obtained that EPS15 (15 kg/m$^3$), having the lowest density of all other geofoam panels, is quite successful in the reduction of lateral stresses. Soil lateral displacements are directly, and acting forces are reversely proportional to the geofoam thickness. Moreover, soil lateral displacements are inversely proportional, and acting forces are directly proportional

to the geofoam density. Two of the geofoam panels had a negligible effect on the lowering of static forces. Trapezoidal geofoam performs better than rectangular geofoam panels in increasing the soil lateral displacements and reducing the forces on retaining walls. It was also seen that using EPS geofoam behind the retaining walls with a relative thickness of up to 0.05H increases their overturning safety factor. However, because of the possibility of overturning, it was not advised to use geofoam in yielding cantilever retaining walls with a relative thickness greater than 0.2H. When the thickness ratio is 0.4 H, the yielding retaining wall's overturning safety factor is reduced by fifty percent. The impact of EPS geofoam on reducing the acting forces is greater for nonyielding cantilever retaining walls compared to yielding walls.

A numerical study by Zarnani and Bathurst, 2009 investigates the performance of seismic buffers affected by wall height, EPS geofoam type, thickness, stiffness, and dynamic excitation. FLAC was used for the numerical analysis (Figure 2.24). The variables of the study were wall height and backfill width (1mx5m, 3mx15m, 6mx30m, 9mx45m), EPS geofoam types as EPS19, EPS22, EPS29, thickness of the EPS geofoam buffer changing t/H ratios of 0, 0.025, 0.05, 0.1, 0.2, 0.4, EPS geofoam stiffness and frequency ratios of 0.3, 0.5, 0.85, 1.2, 1.4 under various input motions.

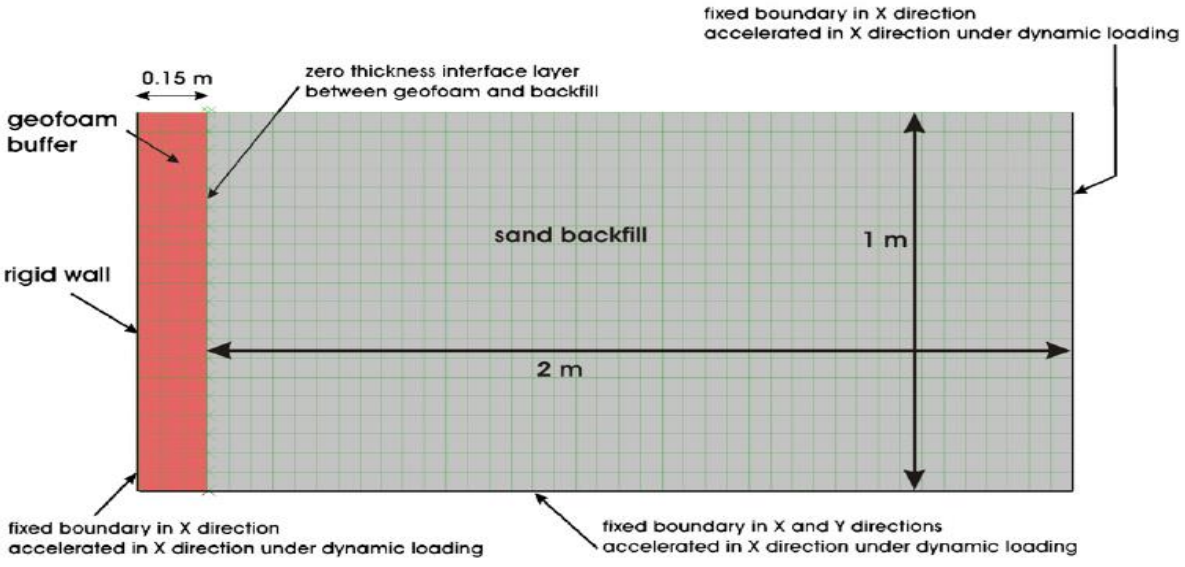


Figure 2.24 Sand backfills, EPS geofoam buffer, and boundary conditions (Zarnani and Bathurst, 2009).

In consideration of the results, the introduction of a vertical layer of EPS seismic buffer at the back of retaining walls resulted in a significant reduction in seismic loads. As the thickness of the buffer increased, the attenuation of the load also increased. When the wall height ratio was t/H= 0.4, up to 55% load reduction was achieved compared to the control case. Seismic load attenuation increases as EPS geofoam modulus decreases under controlled conditions. The fundamental frequency of rigid wall–sand systems with/out EPS buffer is quite similar due to the fact that the volume of the EPS buffer is very small when compared to the volume of the backfill. The total wall forces increase when the resonance phenomenon occurs. Isolation efficiency increases when the wall height exceeds 3m with t/H ratios greater than 0.05. Buffer stiffness, which is defined as K = E/t, was selected as a practical parameter to observe a design range to attenuate seismic loads. It was found to be applicable when $K \leq 50$ kN/m$^3$. Results show that the transient peak buffer compressive strains are directly proportional to the wall height and the dynamic excitation frequency and inversely proportional to the modulus and thickness of the buffer (Zarnani and Bathurst, 2009).

With the aim of increasing the seismic performance of retaining walls, Edinçliler and Toksoy (2018) performed FEM analyses to determine the optimum seismic cushion thickness/height ratio (t/H). The selected cushion material was tire crumb-sand mixture. Wall height, cushion thickness, and dynamic motion were the parameters of the study, which was performed using PLAXIS software. The t/H ratios were selected as 0.3 and 0.4 with wall heights of 5m and 7m. The 1995 Kobe earthquake record was used for the dynamic analysis. The results showed that reducing the (t/H) ratio led to increased total displacements and rotations for Models 1 and 2 with a 5m wall height, while it led to decreased total displacements and rotations for Models 3 and 4 with a 7m wall height. However, reducing the (t/H) ratio increased earthquake-induced forces on the retaining wall for all cases. Model 4 showed deamplification at the top of the wall, and a t/H ratio of 0.3 presented a higher factor of safety values. Overall, the study suggests that selecting a t/H ratio of 0.3 instead of 0.4 can considerably increase the stability of retaining structures.

Bathurst and Zarnani (2011) conducted a summary of recent research on the use of EPS geofoam buffers for seismic load attenuation against rigid soil retaining walls. A series of

physical tests were carried out on different walls constructed with EPS seismic buffers, which demonstrated up to a 40% reduction in peak dynamic loads using vertical EPS buffer layers. The authors also developed and verified displacement-based and numerical models, which were used to develop preliminary design charts for selecting a suitable seismic buffer based on the characteristics of the design earthquake accelerogram. It also includes data from laboratory testing of EPS specimens, which are important for developing advanced non-linear hysteretic constitutive models for EPS seismic buffers.

In a study by Zarnani and Bathurst (2007) and Bathurst et al. (2007a), the EPS geofoam material was modeled as a linear elastic-plastic material in the FLAC simulations. The modulus values were estimated using measured buffer forces and deformations in the physical tests through back-calculation. These results of the experimental studies were verified using a FLAC numerical model showing that the EPS buffer reduced the peak dynamic loads by up to 40%. Buffer stiffness value of $K \leq 50$ MN/m$^3$ was observed to be an applicable range for the design of such structures to attenuate seismic loads against rigid retaining walls.

A numerical study by Zarnani and Bathurst (2005) was performed to validate the obtained results of an experimental study about a reduced scale retaining wall with EPS geofoam buffer. Using the FLAC code, shake table experiments of five physical tests were simulated. Models differ in bulk density and stiffness values of EPS buffers and include a rigid wall (control) model with no buffer. The height of each model was maintained at 1 meter, while the backfill width remained at 2 meters. The thickness of the geofoam used in the experiments was set at 15 cm to align with the physical tests. In this study, the findings of two numerical simulations employing geofoam densities of 12 kg/m$^3$ and 16 kg/m$^3$, respectively, are presented. Additionally, a control test without the presence of a geofoam buffer is included for comparison. The FLAC code was successful in capturing the differences in earth forces with increasing base acceleration for all models. Later, Zarnani and Bathurst (2006) described how a numerical FLAC code was developed and verified in order to simulate those reduced-scale shake table experiments. A performed numerical study showed that the use of vertical EPS geofoam buffers reduces the earthquake-induced dynamic earth forces up to 36%, which is quite relevant to the obtained results from experimental studies.

Finite element analyses were carried out by Abdullah et al. (2017) to find out the potential use of tire chip cushions to mitigate the seismic response of waterfront retaining walls as given in Figure 2.25 and Figure 2.26. The numerical analyses were performed using PLAXIS 2D software, and the real earthquake record of the 1995 Hyogo-ken Nanbu earthquake was used. To model the concrete quay wall, a nonporous linear elastic model was used with a modulus of elasticity of 30 MPa and Poisson's ratio of 0.2. The unit weight of the wall was 24 kN/m$^3$. A Mohr-Coulomb model was used to simulate the bedrock, and a linear elastic model was used to simulate the tire chip material. The hardening soil model was used to simulate the rubble mound. Numerical results were presented in terms of horizontal and vertical displacements of the wall and the settlement of the backfill. In comparison to an unreinforced quay wall, the usage of a cushioned quay wall reinforced with tire chips cushion was found to minimize displacement in both horizontal and vertical directions. Additionally, the tire chip cushion was effective in minimizing soil settlement. However, there are several aspects of the research that require improvement, such as input parameters and analysis methods.

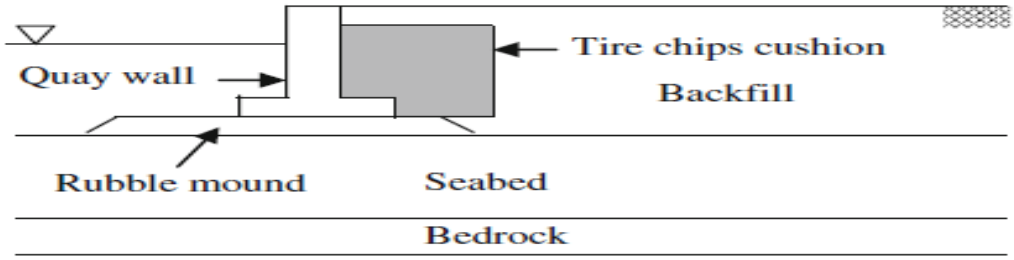


Figure 2.25. Reinforced quay wall with tire chips cushion (Abdullah et al., 2017).

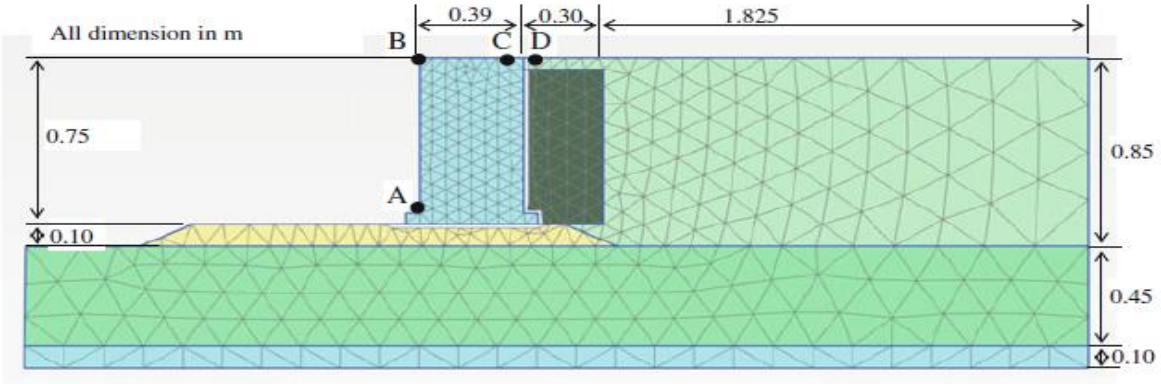


Figure 2.26. Finite element mesh generated in the reinforced quay wall (Abdullah et al., 2017).

Edinçliler and Toksoy (2017) conducted a series of FEM analyses in order to investigate the effect of ground motion parameters on the seismic performance of cantilever-type retaining walls using tire waste-sand mixture as a cushion material (Figure 2.27). The purpose of this study is to examine the seismic performance of the retaining wall with the proposed cushion affected by ground motions. Therefore, a finite element program, PLAXIS is used to simulate a cantilever-type retaining wall with a TW cushion and subjected to various input motions.

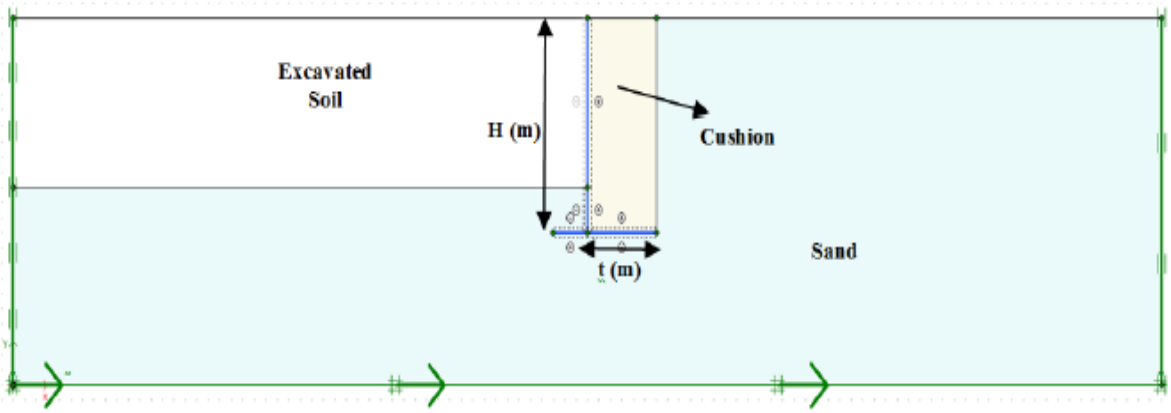


Figure 2.27. FEM Model used during Numerical Analyses (Edinçliler and Toksoy, 2017).

In the numerical investigation, Model 1 represents a retaining wall without a cushion layer, while Model 2 includes a cushion layer. The dimensions of the cantilever retaining wall are H:7m (height) and L:4.5m (length). Dynamic analyses were conducted using two distinct real earthquake records. These records are the El Centro earthquake, which had a peak ground acceleration (PGA) of 0.36g, and the Kobe Earthquake, which had a PGA of 0.68g. The predominant frequencies of the earthquake records were 2.1 Hz for the Kobe Earthquake and 4 Hz for the El Centro Earthquake. The results showed that the inclusion of the cushion layer successfully reduced the peak acceleration values and improved the distribution of acceleration along the wall model. The maximum acceleration on the retaining wall model decreased from 2.23g to 1.25g, resulting in a reduction ratio of 44%. The obtained results show that the axial stress values acting on the retaining wall were reduced by up to 21%, considering static and dynamic cases. Similarly, shear stresses were reduced by up to 17% in case a tire waste sand cushion was introduced to the wall. Depending on the selected earthquake motions, bending moments were decreased by up to 20% in the static case and up to 10% under earthquake-

induced conditions. Additionally, in both static and dynamic movements, lateral stress levels were successfully reduced by up to 19% and 4%, respectively (Edinçliler and Toksoy, 2017).

Yadav et al., 2018 carried out an analysis of the static and seismic behaviour of the retaining wall and backfill soil. The study of a retaining wall under static and seismic conditions was accomplished using Plaxis 2D software (Figure 2.28). The study involved utilizing EPS geofoam, a compressive material, at the interface between the retaining wall and the backfill material. The purpose of the EPS geofoam was to act as an absorber and reduce the lateral earth pressures on the retaining wall. The retaining wall plate has a height of 6 meters, with 2 meters embedded in the foundation soil and a thickness of 0.85 meters. Additionally, a backfill material was placed 12 meters behind the wall to demonstrate the appropriate failure pattern in the backfill. Variables of the parametric study were selected as the density and thickness of the EPS geofoam. The study utilized EPS geofoam with varying thicknesses of 0.5m, 1m, and 2m. The analysis considered EPS geofoam with densities of 15 kg/m$^3$, 20 kg/m$^3$, and 22 kg/m$^3$. The proposed cushion reduces the lateral earth pressures by up to 78.06% and reduces the dynamic lateral earth pressures by up to 42.07%. It was found that as the thickness of the geofoam increases, the lateral pressures on the retaining wall reduce.

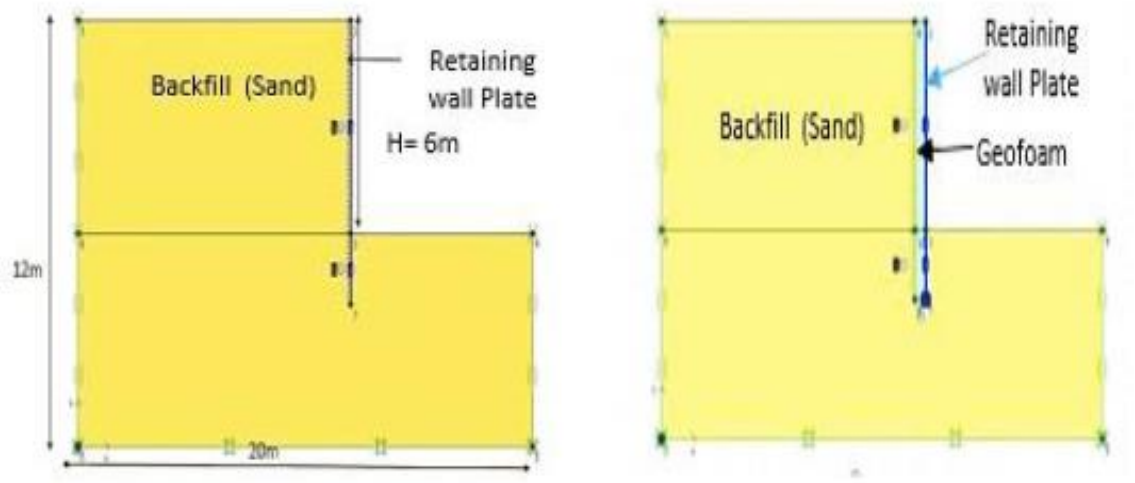


Figure 2.28. Model of retaining wall and backfill for static condition with and without EPS geofoam (Yadav et al., 2018).

In a study conducted by Khan and Meguid in 2021, a finite element model was developed to examine the effectiveness of using a geofoam buffer behind a rigid retaining wall in reducing the seismic lateral thrust caused by backfill material. The parametric study considered different densities of geofoam, specifically EPS15, EPS22, EPS29, and EPS39. Additionally, three different ratios of EPS thickness "t" to wall height "H" (t/H) were examined, namely 0.1, 0.2, and 0.3, and four different backfill materials with friction angles ranging from 30° to 45°. A variable amplitude sinusoidal base acceleration record with a frequency of 5 Hz and peak accelerations of 0.8g was applied as horizontal base excitation. The acceleration amplitude was increased in increments of 0.05g, with each increment maintained for 5 seconds. According to Iai scaling rules, a 5 Hz frequency, which has a period of 0.2 seconds, is equivalent to a 2 Hz frequency, which has a period of 0.5 seconds, at a 1/6 scale model. The effectiveness of EPS geofoam as a seismic buffer is influenced by its density, relative thickness, and the frictional properties of the backfill soil, according to the findings. Geofoam with lower density is better at absorbing seismic waves and provides improved performance. Additionally, increasing the thickness of the geofoam block significantly reduces the total thrust on the wall.

Dabiri and Notash (2020) conducted a numerical study to investigate the impact of a geofoam installed behind a cantilever wall under static and dynamic earth pressure. The study considered various parameters such as wall height, wall type, and geofoam characteristics. The unit weight of the geofoams are 0.5 $kN/m^3$ and 0.2 $kN/m^3$, respectively. The thicknesses of the geofoam are 0.1H and 0.2H, with wall heights of 6m and 9m. FLAC software was used for the analysis, and two earthquake recordings were used for the dynamic analysis. The earthquake recordings used were the scaled far field 1989 Loma Prieta Earthquake and scaled near field 1999 Kocaeli Earthquake. Results show that increasing the thickness of the geofoam reduces the relative stiffness of the geofoam inclusion, making it more compressible against forces on a retaining wall. This leads to increased lateral displacements of the soil and decreased lateral forces on the wall. However, in dynamic conditions, there is no clear relationship between the relative stiffness of the geofoam and its isolation efficiency for yielding retaining walls. Under static and dynamic loading conditions, geofoam inclusion generally performs well in reducing the load on non-yielding retaining walls. It is more effective in reducing static forces compared to dynamic forces. The efficiency of geofoam in load reduction is influenced by the near field

earthquake records. The study also found that geofoam inclusion does not always reduce permanent displacements of cantilever retaining walls. However, it can significantly reduce displacements for yielding retaining walls, depending on factors such as excitation frequency, peak acceleration amplitude, geofoam relative thickness, relative frequency, and wall height. Further studies are needed to determine the appropriate thickness of geofoam to prevent negative efficiency.

A parametric study by Shrestha and Ravichandran, 2018 represents the results of FEM analyses of a retaining wall model backfilled with tire aggregates in comparison with the same model backfilled with conventional backfill material. Numerical analyses were performed under static and dynamic conditions. Results were evaluated in terms of maximum shear force and bending moments and the construction cost. It was found out that the structural demand was significantly reduced with the application of tire aggregates. Also, it was highlighted that the design cost of retaining walls with tire aggregates is much more economical than retaining walls with conventional backfill materials under both static and dynamic conditions.

### 2.6.2. Experimental Studies on Retaining Walls

An experimental study by Zarnani et al. (2005) was conducted to examine how the density of EPS geofoam material affects the response of geofoam buffers when used as a protective layer behind rigid walls and to investigate the impact of EPS density on the load-deformation behaviour of these buffers when subjected to simulated earthquake loading using a shake table. The shake table was designed to hold granular soil, which extended 2 meters behind a compressible layer. In all the tests, a stiff bulkhead, consisting of a six mm-thick aluminum plate with aluminum stiffeners, was constructed to serve as a rigid wall.

Sand material was used as a backfill material, and several geofoam inclusions with different moduli were implemented in the experiments. The experimental study is illustrated in Figure 2.29. The shake table experiments utilized a stepped amplitude base excitation of up to 0.9g, with a horizontal base excitation history of a stepped amplitude sinusoidal record at a

frequency of 5Hz. This frequency corresponds to a period of 0.2 seconds at a 1/6 model scale, which is equivalent to 2 Hz or a period of 0.5 seconds at a prototype scale, as per the scaling laws proposed by Iai in 1989 (Figure 2.30). During the experiments, lateral displacements and total wall forces were measured. The test findings clearly demonstrate that reducing geofoam modulus decreased dynamic lateral earth forces. The best-case scenario reveals that the acting earth pressures to the wall were effectively reduced by up to 60% with the inclusion of the compressible vertical buffer (Zarnani et al., 2005).

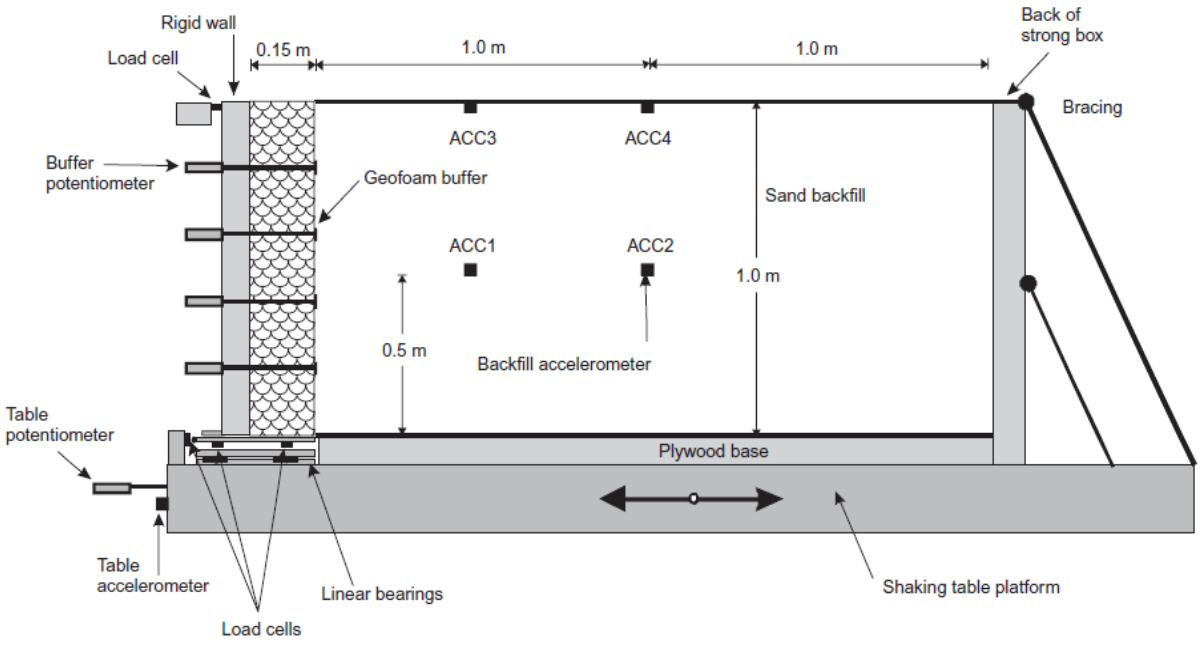


Figure 2.29. Experimental study (Zarnani et al., 2005).

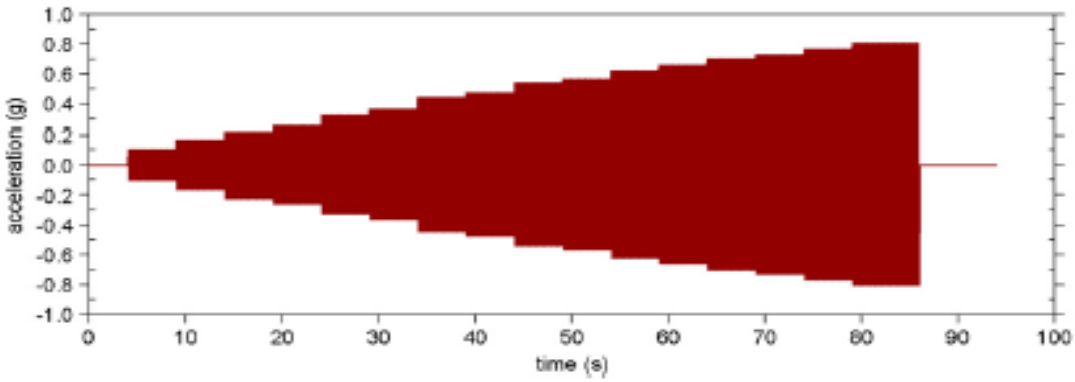


Figure 2.30 Input dynamic motion (Zarnani et al., 2005).

Bathurst et al., 2007 conducted experiments to test the effectiveness of using compressible EPS geofoam seismic buffers to reduce dynamic loads on rigid retaining wall structures during earthquakes. The study involved a detailed experimental program that quantitatively examined the concept of using geofoam compressible inclusions to reduce earthquake-induced dynamic forces against rigid earth retaining wall structures. The experiments were conducted on 1-meter-high models on a large shake table measuring 2.7m by 2.7m. The models were filled with dry synthetic olivine sand as backfill material, and three different types of geofoam buffers with densities of 16kg/m$^3$, 12kg/m$^3$, and 14kg/m$^3$ were used to retain the sand soil. The models were subjected to a displacement-time history that matched a target stepped-amplitude sinusoidal accelerogram with a frequency of 5Hz. The researchers used scaling laws proposed by Iai (1989) to determine that a 5 Hz frequency at a 1/6 model scale corresponds to 2 Hz at the prototype scale. It was found that there was acceleration amplification through the backfill. The stiffness of the geofoam buffer material decreased, causing an increase in vertical toe forces. The study suggests that as the modulus of the geofoam decreased, the average horizontal compression increased. During base shaking, structures with a geofoam inclusion generated less horizontal load than the rigid structure. The findings indicate that the reduction in dynamic load increased as the density of the seismic buffer decreased. For tests 2, 4, and 6, shown in Table 2.5, the reduction in lateral earth forces from the rigid wall case at a common peak base acceleration of 0.7g was 16%, 20%, and 31%, respectively. The greatest reduction occurred in Test 6, which used the lowest density geofoam inclusion and the lowest stiffness. The maximum reduction in dynamic force reached 31% at a peak base acceleration of 0.7g in the best-case scenario.

Table 2.5 Test configurations (Bathurst et al., 2007).

| Wall | Geofoam thickness (mm) | Geofoam Type (ASTM-C578-06) | Geofoam Density (kg/m$^3$) | Initial Tangent Elastic Modulus (MPa) |
|---|---|---|---|---|
| 1 (control) | 0 | | | 0.6 |
| 2 | 150 | I | 16 | 3.5 |
| 4 | 150 | Elasticized | 14 | 2.8 |
| 6 | 150 | XI | 6 | 2.4 |

Zarnani and Bathurst, 2007 present the results of six shake table experiments with 1/6 reduced scale retaining walls with geofoam buffer. During the experiments, the density and stiffness of the geofoam buffers differed, which of the experimental program has been described in detail by Bathurst et al. (2007a). It was revealed that as the geofoam density and stiffness decrease, the interface shear strength increases based on the back calculation results. EPS buffer that was compressed further than their elastic limit results in large dynamic force attenuations. Amplification factors of the backfill increase when geofoam stiffness decreases. Performed experiments with the highest geofoam stiffness showed a 15% reduction in dynamic load, and the experiment with the lowest stiffness showed a 40% reduction in dynamic load when compared to the model with no geofoam buffer.

In the study of Xiao et al., 2012, the dynamic response of Mechanically Stabilized Earth (MSE) walls with tire-derived aggregates (TDA) backfill was reported under shake table conditions. Two dimensionally identical MSE walls, which are 1.6 m high, 1.5 m deep, and 1.5 m long, were built in a box that is fixed to the shake table. The models differ in backfill material as one model has TDA backfill, whereas the other one has poorly graded sand. The reinforcement material of the MSE wall was selected as geogrid. Real earthquake records were used during the experiments. A detailed instrumentation plan includes the measurement of accelerations, displacements, strain, and stresses. The outcomes of the experiments are that the seismic performance of MSE walls can be enhanced by using TDA backfill instead of conventional ones. According to the search results, the reinforced TDA wall performs better than the conventional MSE wall under the same seismic conditions and wall configurations. The advantages of TDA backfill over sand include lower lateral displacements, settlements, acceleration measurements, and static and dynamic stresses in the MSE wall.

Hazarika et al. (2008) conducted an experimental study on a gravity-type caisson quay wall model that was backfilled with tire chips. The study aimed to investigate the dynamic response of the model using a large-scale underwater shake table. The model used in the testing had a scale ratio of 1/10. The study utilized various measuring devices, including load cells, earth pressure cells, pore-water pressure cells, accelerometers, and displacement gauges, which were located at different points in the model. Tire chip backfill was introduced as a cushion to

the model to reduce the load and displacements. The study used two real earthquake records and one synthetic record as input motions. The input motions selected were the Port Island Earthquake, the Hachinohe Earthquake, and the Ohta Ward Earthquake. Two series of tests were conducted, namely Case A and Case B. In Case A, a conventional sandy backfill was used, while in Case B, a 0.3 m thick layer of tire chips with an average grain size of 20 mm was placed vertically down as a buffer cushion behind the caisson. The cross-section of the soil box, the model caisson, and the locations of the various measuring devices are shown in Figure 2.31. Due to the nature of the tire chips cushion, earthquake-induced forces and displacements were successfully reduced. The stiffness of tire chips remains constant even after repeated loading, indicating that the cushion's protective performance remains intact even after severe and repeated earthquake loading.

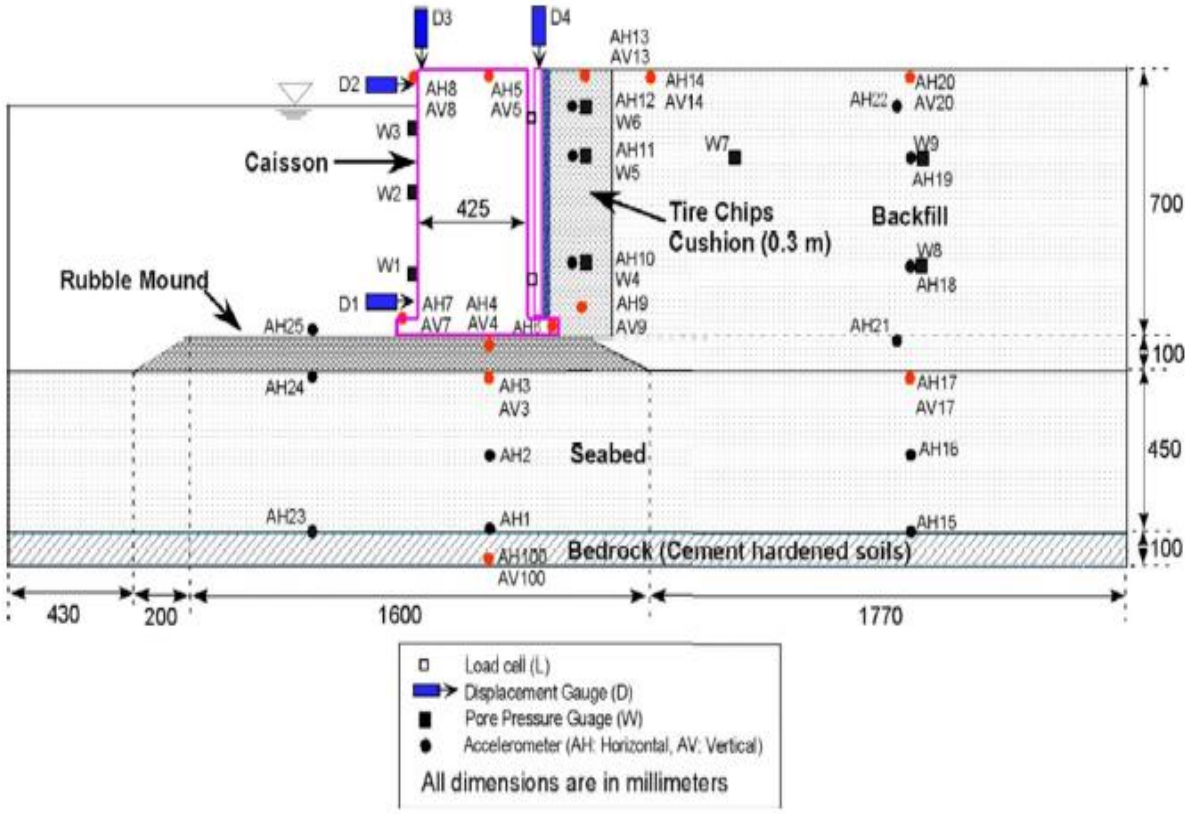


Figure 2.31 Cross-section of test model (Hazarika et al., 2008).

Shake table experiments were conducted by Reddy and Krishna, 2017 to investigate the seismic response of the retaining wall with recycled tire chip backfill. The retaining wall model was 60cm high and constructed in a PMMA container. The retaining wall model with a compressible layer is given in Figure 2.32. The detailed instrumentation plan included pressure sensors, displacement sensors, and accelerometers. The input motion characteristics were also discussed. The unit weight of the sand in the model was kept at approximately 15.57 $kN/m^3$. The tire chips used in the model were 10x10 mm in size and about 20 mm long, with a unit weight of 6.45 $kN/m^3$. The unit weight of the compressible tire chip inclusions in the model wall was around 6.35 $kN/m^3$. The compressible cushion thicknesses used in the model were 0mm, 90mm, and 180mm, and the dynamic motions were 0.1g, 0.2g, and 0.3g with a frequency of 3 Hz.

Incorporating compressible inclusions made of waste tire chips in wall models leads to a significant reduction of approximately 60-75% in the maximum horizontal displacement compared to the control test wall. Additionally, the incremental earth pressure is reduced by around 68-83% compared to the control tests. These findings indicate that the use of recycled tire chips as a compressible inclusion material enhances the dynamic performance of the retaining wall. It was stated that using recycled tire chip backfills improves the dynamic performance of such structures and enables lower design requirements as the lateral earth pressure and displacements are significantly reduced. It was observed that displacements are significantly increased with the increasing acceleration of the input motion (Reddy and Krishna, 2017).

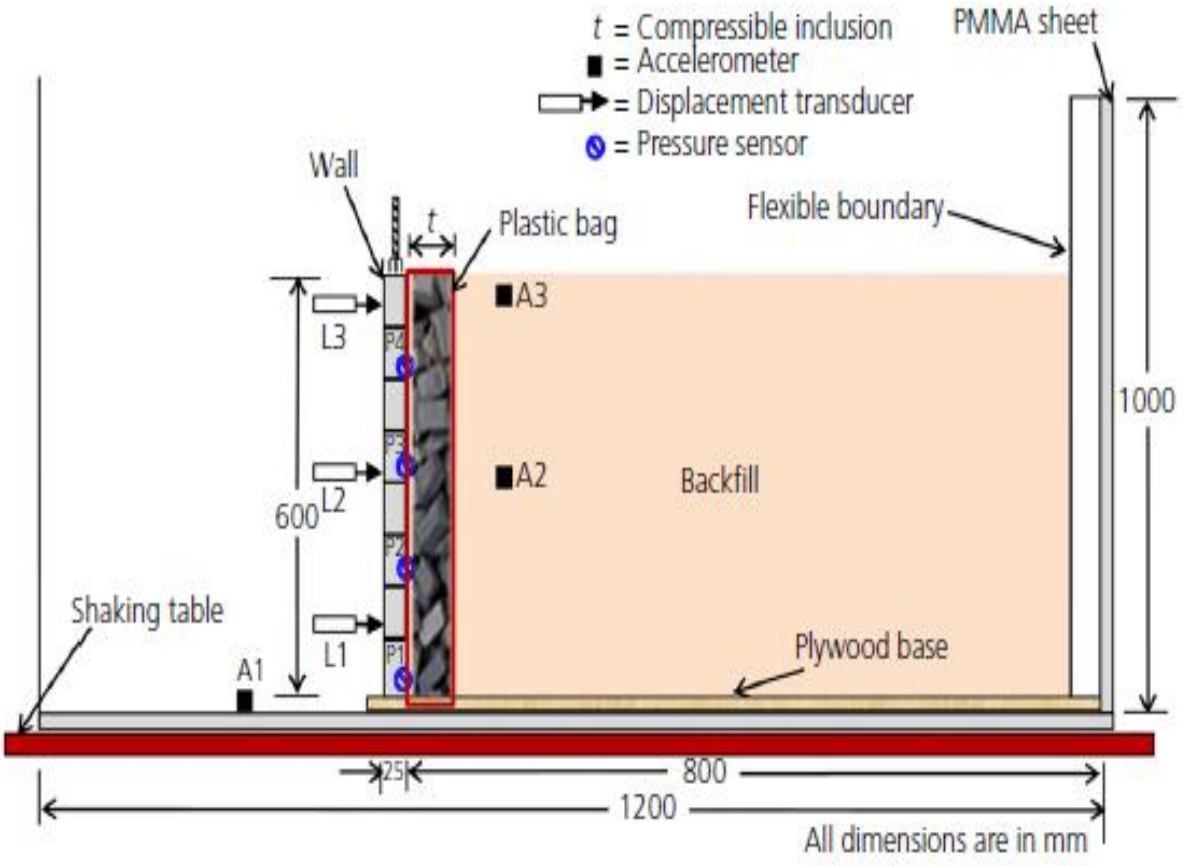


Figure 2.32. Schematic diagram of retaining wall model with compressible inclusion (Reddy and Krishna, 2017).

Reddy and Krishna, 2019 conducted a study on the response of retaining wall models backfilled with different mixtures of sand and tire chips (STC) using shake table tests. The study aimed to compare the dynamic responses of retaining walls with STC mixtures to those filled with traditional granular backfill under the same base excitations. The researchers used different proportions of tire chips in the sand, including STC10, STC20, STC30, STC40, STC50, and STC0 (control test), as backfill materials. They built a 600 mm retaining wall in a box anchored on a shake table to execute dynamic excitations. The study found that the higher the tire chips content in the sand, the greater the reduction in wall displacements and dynamic earth pressures. They observed up to 50% to 65% reduction in wall displacements and 70% to 80% lowering of dynamic earth pressures. The study also revealed that a retaining wall with STC30 backfill had better seismic performance compared to a retaining wall with a conventional backfill. The

researchers conducted model tests at three different accelerations of 0.1 g, 0.2 g, and 0.3 g amplitude with frequencies of 3 Hz and 5 Hz.

Based on the shake table tests conducted, several conclusions can be drawn. Firstly, it was observed that acceleration and displacement responses were amplified with height. Secondly, using the STC30 mixture as a backfill resulted in a reduction of displacements by around 60% compared to the control test or conventional backfill. Thirdly, dynamic-induced pressures were reduced by 70% to 80% compared to the control test or conventional backfill model wall. Finally, the acceleration amplifications decreased when the STC mixtures were increased, even with the addition of up to 30% tire chips to the sand mixture. This is due to the lower unit weight and more shear strength property of STC materials compared to conventional materials. These results demonstrate that the seismic performance of retaining walls with STC mixtures as backfill materials is significant and that STC materials have the capacity to absorb earthquake-induced forces. The model walls with STC30 mixtures exhibited higher resilience behaviour. Therefore, the STC mixture can be used as a backfill material for retaining walls to enhance their seismic resilience (Reddy and Krishna, 2019).

An experimental study performed by Demirtaş (2022) investigated the effect of different cushion types on the seismic performance of retaining walls via shake table tests. The experiments were performed on a 1/25 scaled model of a retaining wall with and without a cushion layer. The cushions used in the study were EPS geofoam and a mixture of tire crumb and sand. The study evaluated various parameters, such as cushion thicknesses, EPS geofoam densities, mixture ratios of sand-tire crumb mixture, and input characteristics. The results were analyzed by comparing the cases with a cushion layer to the case without a cushion layer based on the mentioned parameters. The study investigated the use of EPS geofoam with densities of 10, 20, and 30 kg/m$^3$, named EPS10, EPS20, and EPS30, respectively, with thicknesses of 2 and 4 cm. The tire waste-sand mixture as a cushion material was placed behind a scaled wall at a thickness of 2 and 4 cm, corresponding to 50 and 100 cm at the scaled wall. The tire contents of mixtures were selected as 10%, 20%, and 30% by weight. The first group of experiments involved varying acceleration amplitudes (0.3g - 0.5g) with frequencies of 5 Hz – 15Hz, while

the second group used actual earthquake recordings, including the Kocaeli Earthquake, El-Centro Earthquake, Kobe Earthquake, and İzmir Earthquake motions.

It was found that adding a cushion layer behind a retaining wall can significantly improve its seismic performance. The cushion layer, made of EPS geofoam and a mixture of sand-tire crumb, can reduce the transmitted acceleration, spectral acceleration, and displacement values of the wall during an earthquake. The thickness and density of the cushion layer, as well as the characteristics of the input motions, were found to be important factors in the wall's seismic behaviour. Additionally, using a cushion layer with a greater thickness can be an effective solution to enhance the seismic performance of the retaining wall, prevent future failure of the retaining structure, and mitigate earthquake hazards. The study also showed that the type of cushion material used is the most important parameter affecting the seismic performance of the retaining wall. The EPS geofoam cushions were found to be more effective than the sand-tire crumb mixtures in improving the seismic performance of the wall. Overall, the inclusion of a cushion layer behind a retaining wall can be an effective method for mitigating earthquake-induced damages (Demirtaş, 2022).

### 2.6.3. Field Studies on Retaining Walls

The characteristics of the earth pressure acting on a retaining wall were studied by Matsuo et al. (1978) on field conditions. In these large-scale experiments, a concrete, 10m high retaining wall model was constructed, and silty sand material with slags was used as a backfill. The results show the measured earth pressure at rest, as well as changes in the active and passive states. The study also examined the influence of wall displacement on the magnitude and distribution of earth pressure in the vertical direction. The experimental study found that after the construction of a backfill, the earth pressure gradually increased and eventually reached a stable state at rest, indicating that the backfill settled and achieved equilibrium over time. The distribution of earth pressure in the vertical direction did not form a triangular shape, with relatively higher pressures measured at the lower part of the wall in both the state at rest and the active state. The earth pressure rapidly decreased when the retaining wall experienced

displacement towards the outside direction, and the backfill transitioned into the active state of plastic equilibrium under certain displacement conditions. The angle of wall friction at the active state was approximately 50°, which was higher than expected, indicating higher frictional resistance between the retaining wall and the backfill. The study also found that the earth pressure, which was initially in the active state, gradually recovered over time, highlighting the importance of considering the long-term behaviour and stability of retaining walls in design considerations.

The first geosynthetic reinforced wall was constructed, instrumented, and tested in Turkey by Güler and İsmeik (1996). As a backfill material, lime-stabilized cohesive clay was used, and the wall was designed to have an FOS value of less than one. The addition of lime to the clay significantly improved the workability with clay with improved shear resistance. The instrumentation plan included sensors to measure the horizontal and vertical movement of the backfill and the vertical and horizontal stresses. The constructed wall's height was 5.25m, and it has a trapezoidal face with inclinations of 46° and 50° from the right and left sides, respectively. During the study, the contribution of the wall rigidity to the overall stability of the MSE wall was investigated experimentally. The MSE wall was inspected for more than two years with/out surcharge conditions and subjected to all weather conditions in the meantime. The obtained results show that the facing rigidity clearly affects the stability and design costs directly. In addition, vertical stress distributions were found not to be constant, which indicates the nonlinear behaviour. Also, weather conditions were not found to be affecting the stability under given conditions.

A study conducted by Lutenegger and Ciufetti (2009) aimed to evaluate the lateral earth pressures resulting from using geofoam blocks in place of traditional backfill by obtaining earth pressure measurements on the back face of the concrete abutments. During the long-term study, which took 16 months, the concrete bridge abutments were monitored to assess the effect of Geofoam on the lateral and vertical stresses, as given in Figure 2.33. It was highlighted that the use of Geofoam instead of conventional granular backfill significantly reduced the measured earth pressures in both directions. It was found that substituting conventional granular backfill with EPS Geofoam resulted in noteworthy reductions in both horizontal and vertical earth

pressures behind the bridge abutments. The lateral pressures measured at the boundary between the Geofoam blocks and the overlying fill were insignificant, ranging from 2 to 6 kPa. However, at the mid-depth of the Geofoam blocks, the lateral pressures were slightly higher in magnitude.

The study found that the EPS geofoam blocks have a pressure-spreading effect, with higher pressures measured at the top of the blocks than at the base. This suggests that the blocks are effective at dissipating vertical stresses. The study used various loading conditions to estimate lateral pressures based on $K_0$ values of 0.1 and 0.5, but in all cases, the estimated lateral pressures exceeded the measured lateral pressures. Based on the final measurements of vertical and lateral pressures, $K_0$ values were found to be between 0.02 and 0.05 (Lutenegger and Ciufetti, 2009).

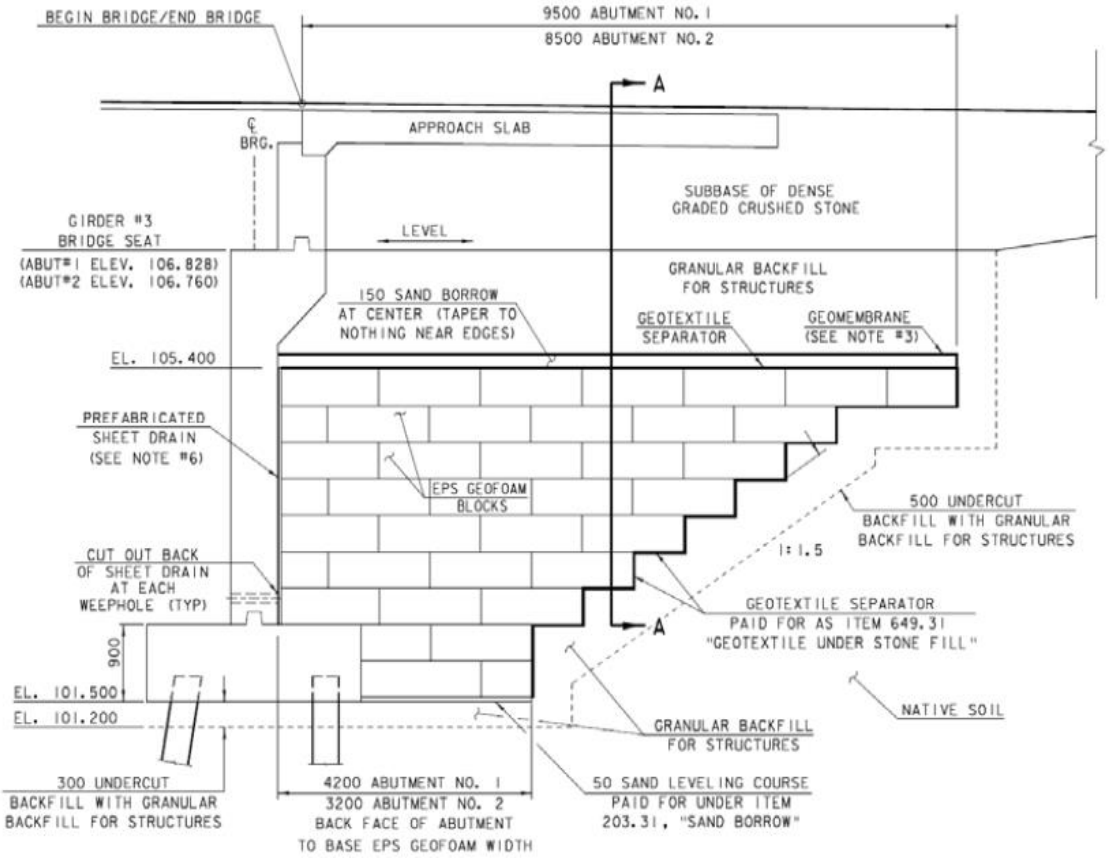


Figure 2.33. Typical abutment cross section (facing perpendicular to centerline) (Lutenegger and Ciufetti, 2009).

Another experimental study was performed by Tweedie et al. (1998) in order to assess the effect of different tire shreds (from three different suppliers) on at-rest horizontal stresses as a backfill material of a 4.88m full-scale retaining wall. The plan view and cross-section of the wall are given in Figure 2.34. To study the effectiveness of using tire shreds as backfill for conventional retaining walls, a full-scale test facility was built, measuring 4.88 meters. The facility was designed to test the backfill under both at-rest and active conditions and to measure horizontal stress and interface shear. The study tested tire shreds from three different suppliers, which were placed in 200-mm lifts and compacted using a walk-behind vibratory tamping foot roller.

It was found that the horizontal stress increases with increasing surcharge but becomes nearly constant with depth as the surcharge increases. The at-rest horizontal stress for tire shreds is 45% less than that of typical granular fill. The coefficient of lateral earth pressure at rest, $K_0$, decreases with depth at each surcharge and decreases as the surcharge increases until 23.9 kPa and remains constant from 23.9 kPa to 35.9 kPa. The value of $K_0$ is not dependent on the tire shred size and the amount of steel belts. Reloading tire shreds does not increase the horizontal stress. The angle of wall friction for tire shreds from the three suppliers ranged from 30° to 32°, determined by the horizontal and shear forces acting on the concrete face of the wall (Tweedie et al., 1998).

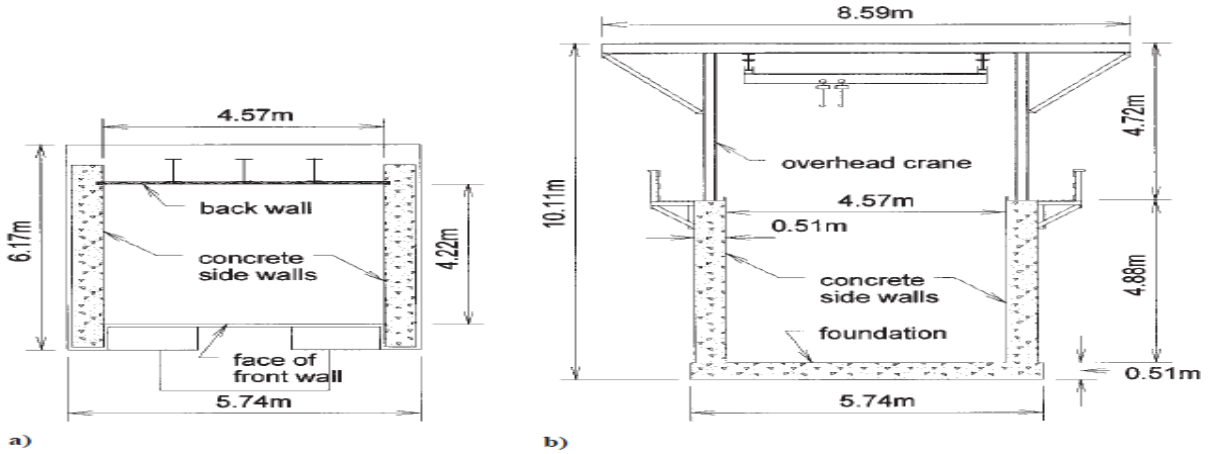


Figure 2.34. Full-scale test retaining wall a) plan view, b) cross section (Tweedie et al., 1998).

Extensive field scale tests were performed by Hazarika et al. (2004) to investigate the effect of EPS Geofoam thickness, which was used instead of conventional backfill, on load reduction acting on the retaining wall. Pressure cells were used for instrumentation, as shown in Figure 2.35. During the tests, a constant-thickness layer of tire chips was used behind the EPS blocks for drainage purposes. The wall had dimensions of 1.6 m height and 2 m width with three panels to the front. The wall was designed as rigid enough to prevent yielding and to ensure that the wall remained at rest state. The backfill zone was 2.6 m long and 2.0 m wide in plan. The testing procedure consists of several sequential steps. First, compressible EPS blocks are positioned behind the wall. Next, the area is backfilled with sand in three layers, utilizing the free-falling technique. The density and water content of each backfilled layer are closely monitored. To gradually develop earth pressure on the wall-backfill system, a surcharge load is applied. This is done by placing sandbags at the top of the backfill in increments of 2 kPa, with ten stages in total. The earth pressures against the wall are continuously monitored for a duration of six days under each experimental condition. During the testing process, the density and water content of each layer were monitored. The EPS blocks used in the testing are expanded polystyrene formed into large lightweight blocks, often used as a soil substitute for engineering and construction projects. Test conditions were schematically illustrated in Figure 2.36.

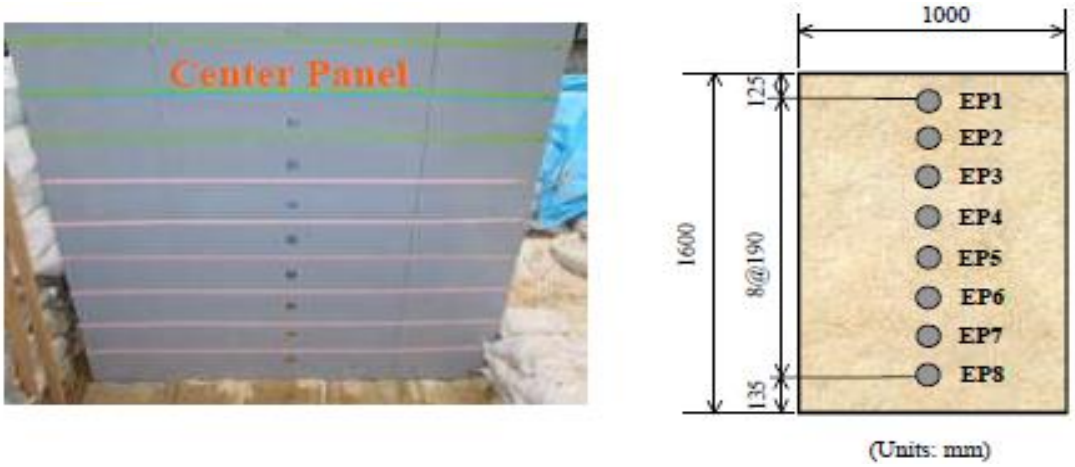


Figure 2.35. Locations of the earth pressure cells (center panel, retaining wall, and detailed locations of the cells) (Hazarika et al., 2004).

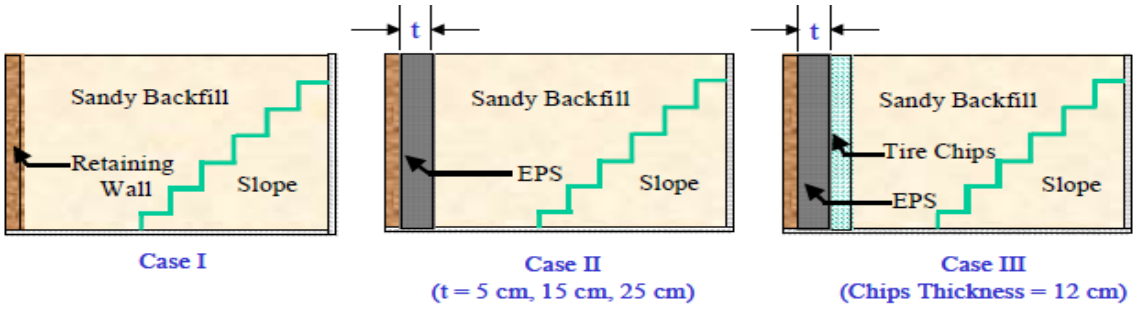


Figure 2.36. Test conditions.

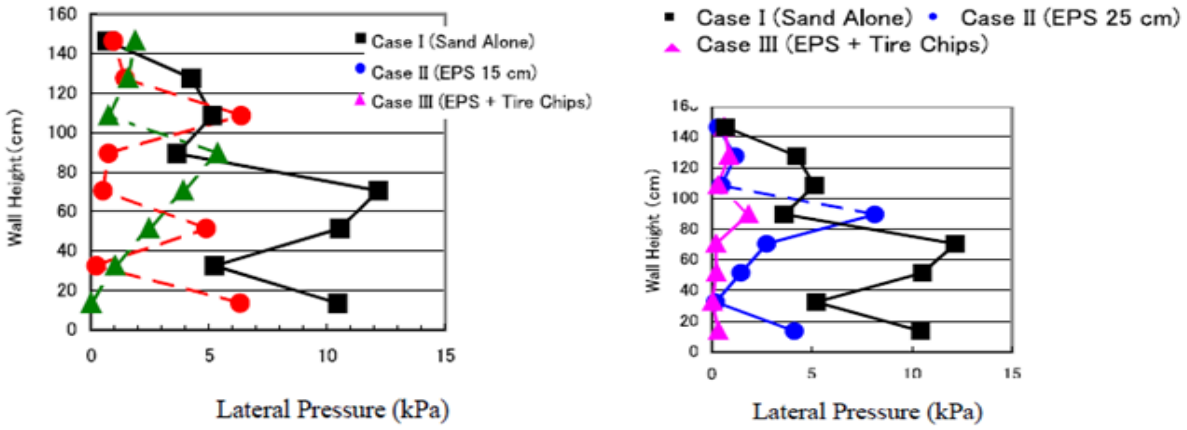


Figure 2.37. Distribution of earth pressure (15 cm thick EPS layer and 25 cm thick EPS layer) (Hazarika et al., 2004).

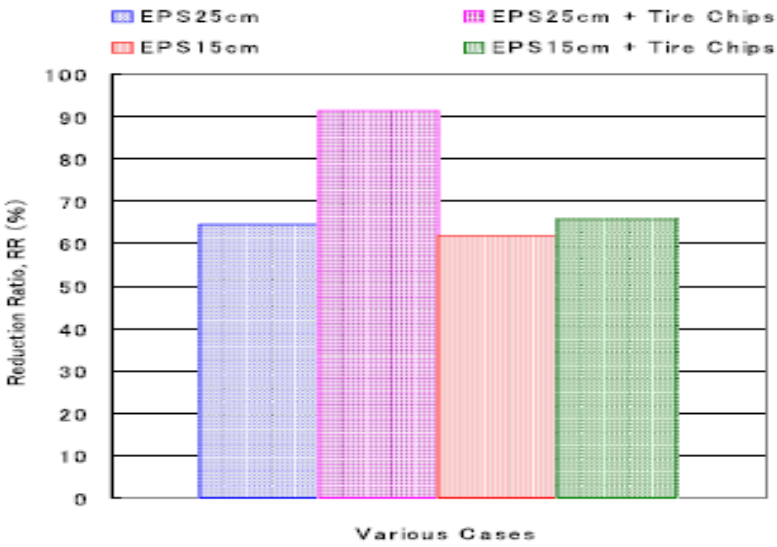


Figure 2.38. Performance comparison of the cushion (Hazarika et al., 2004).

In Figure 2.37, increasing EPS geofoam layer thickness negatively affects the measured lateral pressures on the retaining wall. Apart from that, the use of EPS geofoam instead of conventional granular backfill material significantly reduces imposed loads at different heights. Another important finding of this study is that apart from its usage as a drainage material, tire chips also acted as a lightweight, compressible buffer, which contributed to the reduction of earth pressures (Figure 2.38) (Hazarika et al., 2004).

# 3. EXPERIMENTAL STUDY

This thesis study consists of experimental studies on the shake table executed with EPS geofoam, tire waste, and sand mixtures and EPS beads and sand mixtures as cushion material behind the 1/15 scaled retaining wall as the prototype wall height of 6 m to evaluate the cushion efficiency in order to improve the seismic performance of the retaining wall. In these experiments, a novel cushion material consisting of a mixture of EPS beads and sand was utilized for the first time as a cushion material behind the retaining wall.

Firstly, shake table experiments for the retaining wall model were carried out without any cushion material. Subsequently, further experiments were conducted on the shake table by placing three different types of cushion materials behind the retaining wall. These cushion materials varied in terms of their thickness, density/mixture ratio by applying the same input motions.

The experimental study of the thesis includes materials and methods, design of the retaining wall model, input motions, experimental cases of the study, instrumentation of the experimental set-up, preperation of the experimental studies, and the performing of the shake table tests.

## 3.1. Materials and Methods

This section includes information on materials such as Silivri sand backfill, EPS geofoam, tire waste, sand, and EPS beads as well as cushion materials and laminar box, shake table, accelerometers, and laser displacement sensors.

### 3.1.1. Backfill Material

The backfill material was used as “Silivri Sand”. The sand is from the Silivri Region, İstanbul (Figure 3.1). Figure 3.2 displays the results of analyzing the grain-size distribution of the sand using the American Standard Test Method of D422. The sieve analysis was performed at the Boğaziçi University Kandilli Observatory Geotechnical Earthquake Engineering Research Center Laboratory. The Silivri sand is classified as SP (poorly graded sand) and has a coefficient of curvature of 0.98, and the coefficient of uniformity as $C_u$ = 2.70 ($C_u$=$D_{60}$/$D_{10}$) according to the United Soil Classification System.

The specific gravity of sand was calculated to be $G_s$ = 2.67, and the bulk unit weight is 16.5 kN/m$^3$. The maximum void ratio of the sand is obtained as 0.73, and the minimum void ratio of the sand is obtained as 0.37.

Figure 3.1. Silivri Sand.

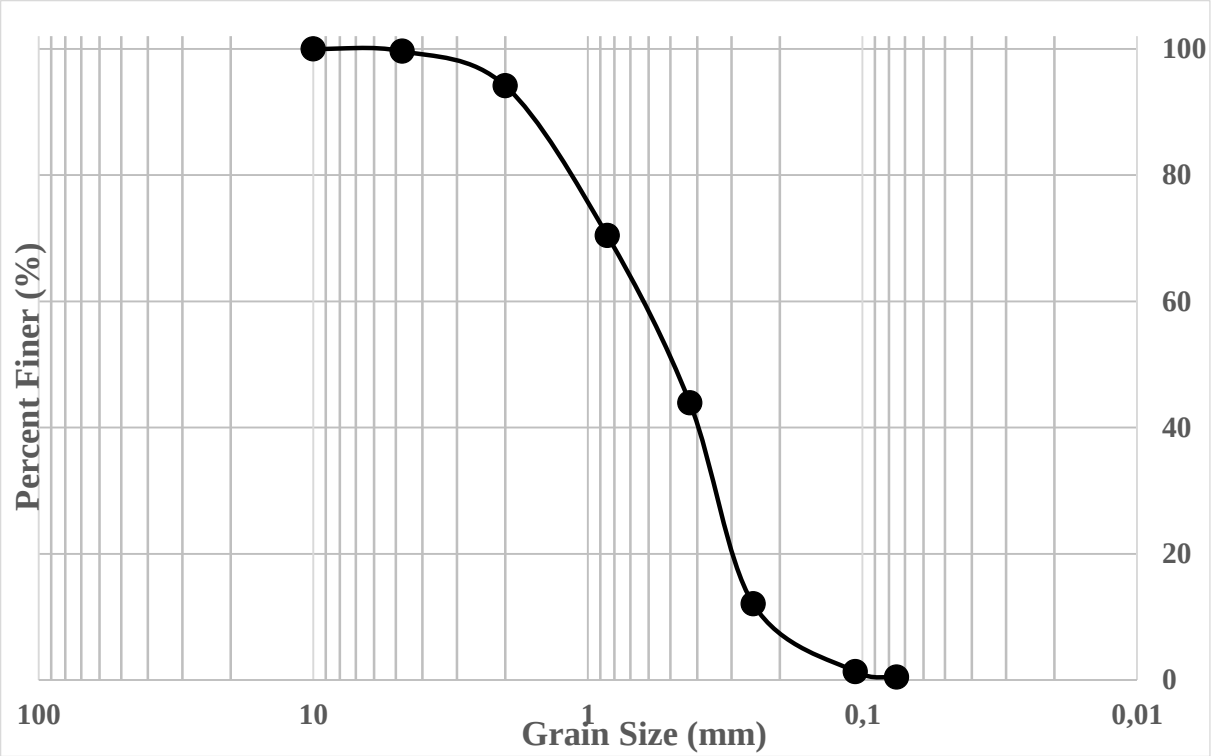


Figure 3.2. The grain size distribution of Silivri Sand.

### 3.1.2. EPS Geofoam Material

The first cushion material utilized in the experimental studies is EPS geofoam. Table 3.1 provides a list of the properties of the EPS Geofoam materials, and Figure 3.3 provides the illustrations used in the experimental tests. The height of the retaining wall model is 41 cm, the height of the stem is 40 cm, and the height of the cushion is as the same as the stem. The thicknesses of the EPS geofoam cushion placed behind the retaining wall as a cushion material in the experimental studies are 4cm and 8cm, and the t/H ratios are 0.1 and 0.2, respectively.

Table 3.1. EPS Geofoam cushion material density and dimensions used in the study.

| EPS Geofoam Materials | Density (kN/m$^3$) | Dimensions (height*length*thickness) | Abbreviation |
|---|---|---|---|
| EPS10 | 0.10 kN/m$^3$ | 40*110*4cm | EPS10-4cm |
| EPS20 | 0.20 kN/m$^3$ | 40*110*4cm | EPS20-4cm |
| EPS30 | 0.30 kN/m$^3$ | 40*110*4cm | EPS30-4cm |
| EPS10 | 0.10 kN/m$^3$ | 40*110*8cm | EPS10-4cm |
| EPS20 | 0.20 kN/m$^3$ | 40*110*8cm | EPS20-8cm |
| EPS30 | 0.30 kN/m$^3$ | 40*110*8cm | EPS30-8cm |

Figure 3.3 The EPS Geofoam cushion material

### 3.1.3. Tire Waste and Sand Mixture

The tire crumb and sand mixture is the second cushion material used in this thesis. The diameter of the tire crumb varies from 0.5-2mm. The grain size distribution of tire waste material can be seen in Figure 3.4. The tire waste and sand mixtures are termed as TW10 for 10% tire waste mixture ratio, TW20 for 20% tire waste mixture ratio, and TW30 for 30% tire waste mixture ratio by weight. The densities of TW10, TW20, and TW30 were obtained as 12,50

kN/m$^3$, 11,10 kN/m$^{3,}$ and 10,40 kN/m$^{3,}$ respectively, and samples of the mixtures are shown in Figure 3.5. For all cushion mixtures, the weight of the sand and tire waste materials were calculated and mixed uniformly.

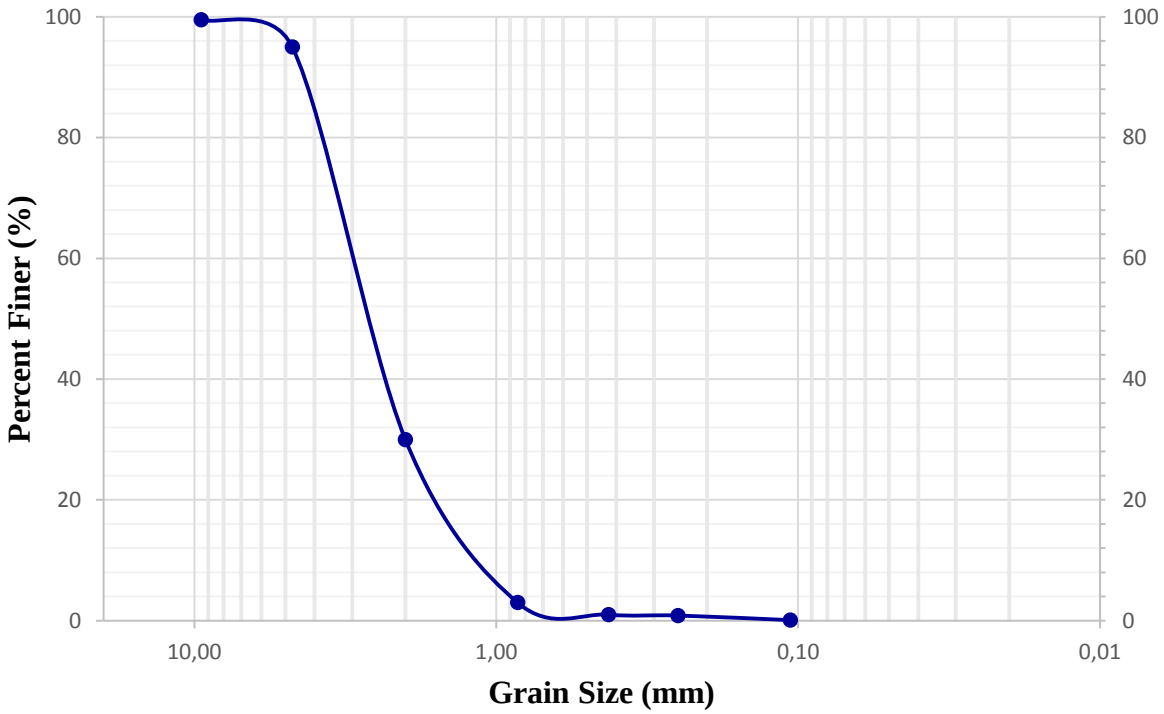


Figure 3.4 The grain size distribution of tire waste material.

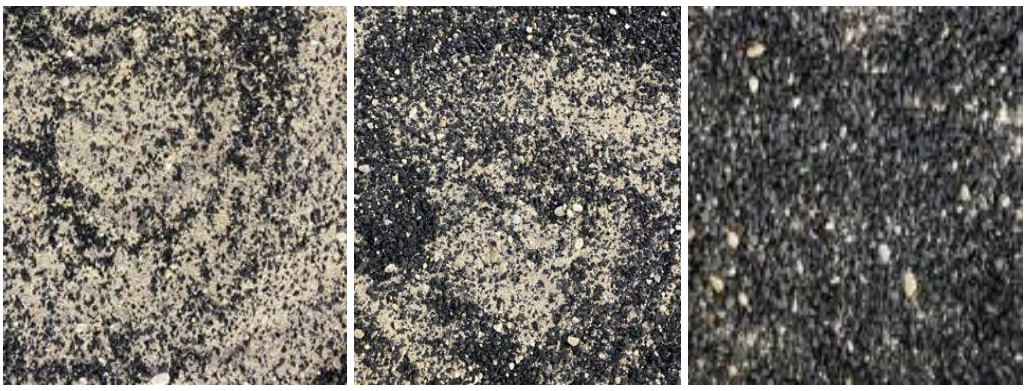

a) b) c)

Figure 3.5. Tire crumb and sand mixture pictures a) TW10, b) TW20, and c) TW30 respectively.

The properties of tire waste and sand mixtures used in the experimental studies are listed in Table 3.2. The height of the retaining wall model is 41 cm, and the t/H ratios are 0.1 and 0.2 for tire waste and sand mixture (TW) cushion, respectively.

Table 3.2. Tire crumb and sand mixture cushion material content and dimensions used in the study.

| **Tire Waste and Sand Mixture** | **Density (kN/m$^3$)** | **Dimensions (height*length*thickness)** | **Abbreviation** |
|---|---|---|---|
| TW10 | 12.50 kN/m$^3$ | 40*110*4cm | TW10-4cm |
| TW20 | 11.10 kN/m$^3$ | 40*110*4cm | TW20-4cm |
| TW30 | 10.40 kN/m$^3$ | 40*110*4cm | TW30-4cm |
| TW10 | 12.50 kN/m$^3$ | 40*110*8cm | TW10-8cm |
| TW20 | 11.10 kN/m$^3$ | 40*110*8cm | TW20-8cm |
| TW30 | 10.40 kN/m$^3$ | 40*110*8cm | TW30-8cm |

### 3.1.4. EPS Beads and Sand Mixture

Expandable polystyrene EPS bead is a lightweight, rigid, plastic foam insulation material produced from solid particles of polystyrene (Figure 3.6).

Figure 3.6. EPS Beads.

EPS beads can be mixed with sand to create lightweight fill materials, which reduces the overall weight of the fill material due to the lightweight nature of the EPS beads. This material can be utilized for various purposes, such as preventing excessive settlement over soft clay sites, construction of embankments, reducing horizontal driving forces as backfill for retaining and basement walls, increasing the factor of safety for slopes as fill material, and acting as seismic buffers to reduce seismic forces ((Alaie and Chenari, 2018; Somantri and Febriansya, 2019).

In this study, the EPS beads material was provided by the EPS block company. The EPS bead material has a dry unit weight of 0.30 $kN/m^3$. The effective size $D_{10}$ (mm) of EPS beads material is 1.2 mm, and mean grain size $D_{50}$ (mm) of EPS beads material is 2.4 mm.

EPS beads and sand mixtures were prepared by mixing EPS beads with sand and adding a water content of 10% to ensure that the EPS beads and sand particles were in contact with each other (Edinçliler and Özer, 2013). The water provides both compaction and contact between the EPS beads and sand materials. When EPS beads and sand are mixed without water, the EPS beads, being lighter, tend to remain suspended in the mixture. By adding water, adhesion was created between the EPS beads and sand, preventing segregation. The EPS beads and sand were bonded together by the additional water without separating. EPS beads, sand and water were mixed into a big plastic bowl and thoroughly mixed until a uniform mixture was obtained. The illustrations of EPS beads and sand mixture samples for 10%, 20%, and 30% by volume are shown in Figure 3.7.

The volume of the EPS beads cushion was calculated, and the mixtures were prepared as 10%, 20%, and 30% mixture ratios by volume. The mixtures were prepared as 4 cm, 6cm, and 8cm cushion thicknesses. The EPS beads and sand mixtures are termed as EPSB10 for 10% EPS beads mixture ratio, EPSB20 for 20% EPS beads mixture ratio, and EPSB30 for 30% EPS beads mixture ratio.

a) b) c)

Figure 3.7. EPS beads and sand mixture pictures a) EPSB10, b) EPSB20, and c) EPSB30, respectively.

The properties of EPS beads and sand mixtures used in the experimental studies are listed in Table 3.3. The density of the mixtures is consistent with the results obtained in the experimental study of Edinçliler and Özer, 2013. The height of the retaining wall model is 41 cm, and the t/H ratios are 0.1, 0.15, and 0.2 for EPS beads and sand mixture (EPSB) cushion, respectively.

Table 3.3. EPS beads and sand mixture cushion material content and dimensions used in the study.

| **EPS Beads and Sand Mixture** | **Density (kN/m$^3$)** | **Dimensions (height*length*thickness)** | **Abbreviation** |
|---|---|---|---|
| EPSB10 | 10.10 kN/m$^3$ | 40*110*4cm | EPSB10-4cm |
| EPSB20 | 8.20 kN/m$^3$ | 40*110*4cm | EPSB20-4cm |
| EPSB30 | 6.30 kN/m$^3$ | 40*110*4cm | EPSB30-4cm |
| EPSB10 | 10.10 kN/m$^3$ | 40*110*6cm | EPSB10-6cm |
| EPSB20 | 8.20 kN/m$^3$ | 40*110*6cm | EPSB20-6cm |
| EPSB30 | 6.30 kN/m$^3$ | 40*110*6cm | EPSB30-6cm |
| EPSB10 | 10.10 kN/m$^3$ | 40*110*8cm | EPSB10-8cm |
| EPSB20 | 8.20 kN/m$^3$ | 40*110*8cm | EPSB20-8cm |
| EPSB30 | 6.30 kN/m$^3$ | 40*110*8cm | EPSB30-8cm |

### 3.1.5. Laminar Box

The laminar box, which was designed and manufactured in conjunction with the Boğaziçi University Research Fund (Project No. BU-BAP8084), has inner dimensions of 130 cm (length) x 110 cm (width) x 100 cm (height) and outer dimensions as 150 cm (length) x 130 cm (width) x 100 cm (height).

The laminar box works like a soil model with flexible sides that allow the soil to move and change shape freely, as the behaviour of natural ground during seismic activity. Since the layers are more mobile, the restriction of the boundaries is eliminated. Laminar box which has ideal boundary conditions that will enable the correct modeling of dynamic retaining wall and soil and structure analysis to form the same deformed shape as its prototype. Rigid and flexible walls have limitations in this respect. Earthquake waves are reflected in the rigid box, and the boundary conditions are more prominent. The earthquake waves hit the boundary and reflect back, and grease is used to reduce the boundary condition and reflection parts.

The laminar box is composed of eighteen steel sliding layers, roller bearings, a base plate, side guides, and a membrane. The roller bearings and rubber stoppers minimized friction forces between the laminates. Each laminate layer was equipped with six sets of roller bearings, resulting in a total of 324 roller bearings facilitating smooth sliding motion. The rubber strips were positioned at both ends of the bearing houses to ensure stability and durability for the roller bearings. The steel tube sections were utilized as side guides as a safety measure against unforeseen accidents. To prevent soil leakage that may occur between the two laminates of the box, the membrane was affixed to the inner surface of the laminar box (BU-BAP8084, Sekman, 2016).

In order to prepare for the experiments, the layers of the laminar box, roller bearings were cleaned to ensure they were free of any contaminants. Once the cleaning was complete, the laminar box was placed on a shake table, and performance tests were conducted to evaluate the performance of the empty box. The membrane was cleaned, and grease was applied between the membrane and the laminar box to prevent any additional friction forces (Figure 3.8).

Figure 3.8. Laminar box installation process.

To examine how inertia, friction, membrane, and boundary affect the performance of the laminar box, various performance tests were conducted on it, as described in studies by Prasad et al. (2004), Jafarzadeh (2004), and Whitman and Lambe (1986). These tests evaluate how inertia, friction, membrane, and boundary impact the performance of a laminar box.

### 3.1.5.1. Inertia Effect

The inertia effect is caused by the mass of the laminar box. When measuring acceleration inside the soil, it is possible for it to be lower than the acceleration of the table due to the inertia of the laminar box. To account for this, a correction factor should be applied to the recorded acceleration in order to eliminate the inertia effect. Accounting a is acceleration, $m_1$ is the mass of the soil in the laminar box, and $m_2$ is the mass of the layers of the laminar box; the total dynamic force can be expressed as:

$$F_d = (m_1 + m_2)a \tag{3.1}$$

Nonetheless, the goal is to completely transfer the force onto the soil. Consequently, if the desired acceleration in the soil is considered without the influence of the box,

$$F_d = (m_1)a' \tag{3.2}$$

According to the two equations,

$$a' = \left(\frac{m_1+m_2}{m_1}\right)a \tag{3.3}$$

$$a' = \left(\frac{25.96+8.04}{25.96}\right)a \tag{3.4}$$

When the container is not affecting the soil, the acceleration of the soil (a') is 1.31 times greater than the measured acceleration (a). The influence coefficient is calculated to be around 1.31, and this coefficient is considered normal up to 1.5.

### 3.1.5.2. Friction Effect

The procedure depicted in Figure 3.9 was utilized to conduct static pullout tests. The static pullout tests performed using a load cell with a 50kg load capacity attached to each layer

is to determine the friction forces required to initiate the motion of a laminate. The results showed that the required maximum force was 68 N from the bottom layer, with an average friction force of about 33 N, as shown in Figure 3.10.

Figure 3.9 Perform of static pull-out tests.

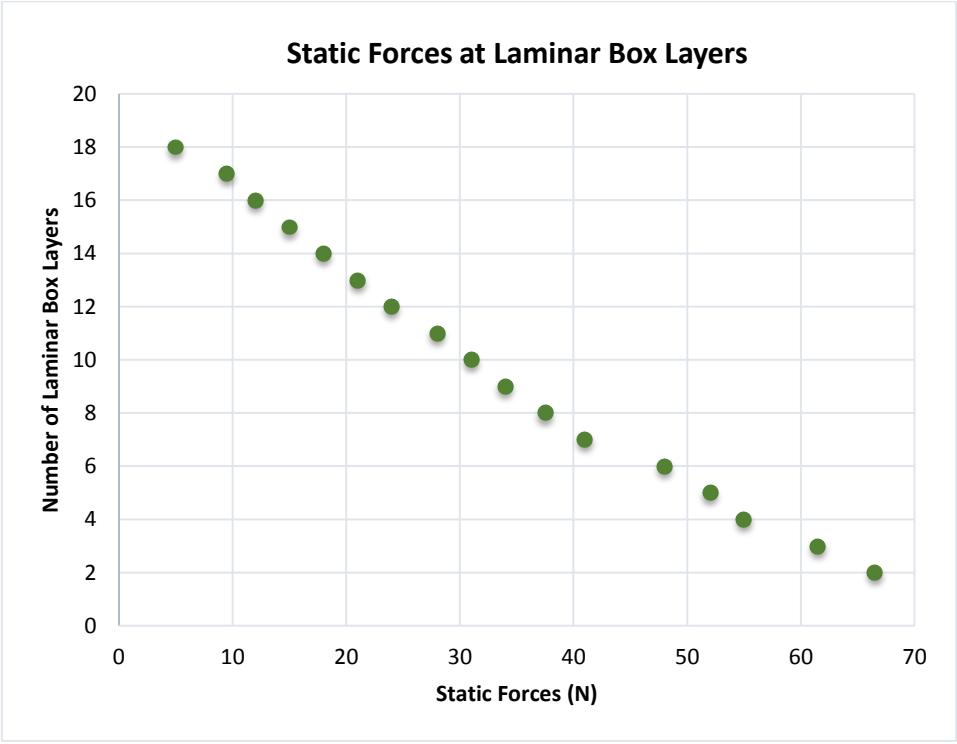


Figure 3.10 The static forces measured from pull-out tests for each layer.

#### 3.1.5.3. Membrane Effect

A rubber membrane with a thickness of 1 mm was used to prevent soil leakage between the layers of the laminates during the performance tests. The membrane was sufficiently flexible compared to the soil stiffness and did not affect the performance of the soil mass significantly. The shake table tests were performed to investigate the effect of the laminar box boundaries on its performance criteria, both with an empty box and a box filled with soil.

#### 3.1.5.4. Boundary Effect of the Laminar Box

The sinusoidal motions at 0.05g amplitude with 0.5 Hz frequency, sinusoidal motion at 0.3g amplitude with 1 Hz frequency, sinusoidal motion at 0.5g amplitude with 2 Hz frequency, sinusoidal motion at 0.75g amplitude with 2 Hz frequency, sinusoidal motion at 0.6g amplitude with 3 Hz frequency, sinusoidal motion at 0.75g amplitude with 3 Hz frequency, sinusoidal motion at 0.7g amplitude with 4 Hz frequency, sinusoidal motion at 0.8g amplitude with 4 Hz frequency, sinusoidal motion at 0.8g amplitude with 5 Hz frequency, sinusoidal motion at 1g amplitude with 5 Hz frequency were applied to the empty laminar box and the laminar box was subjected to shake table tests.

The sand was filled in four equal layers through compaction. After that, the filled laminar box was used to conduct shake table tests to evaluate how the laminar box boundary affected the behaviour of the soil. The same sinusoidal motions conducted on the empty laminar box were applied to the laminar box filled with sand. In addition to sinusoidal motions, real earthquake records as the scaled 1999 Kocaeli EQ Motion-İzmit Station acceleration record, the scaled 1940 Imperial Valley EQ-El Centro Station record, and the scaled 1995 Kobe EQ record were applied to the laminar box.

To investigate the impact of box boundaries on soil behaviour, the acceleration data from accelerometers A9, A10, and A11 were analyzed and compared in Figures 3.11, 3.12, and 3.13. These accelerometers were positioned at the height of 30 cm within the laminar box and were

located in close proximity to each other on the same horizontal plane. Since they are placed nearby at the same horizontal plane in a relatively homogenous soil, it is expected that the measured acceleration values are identical. Figure 3.11 shows the Acceleration-Time Histories of A9, A10, and A11 under sinusoidal motion at 0.3g amplitude with 1 Hz frequency. Additionally, the Acceleration-Time Histories of A9, A10, and A11 under sinusoidal motion at 0.6g amplitude with 3 Hz frequency sinusoidal motion and 0.8g amplitude with 4 Hz frequency sinusoidal motion are shown in Figure 3.12 and Figure 3.13, respectively. There is no significant difference among A9, A10, and A11 under different shake table motions.

The results of various performance tests indicated that the laminar box and its flexible boundaries were functioning correctly. Overall, the results suggest that the laminar box's flexible boundaries were effective in operating properly.

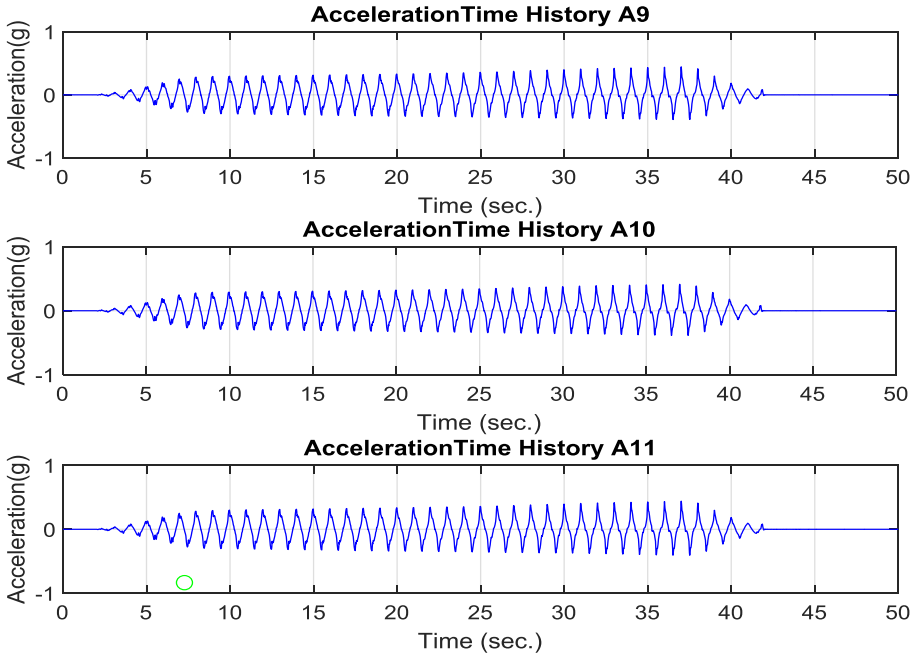


Figure 3.11 The Acceleration-Time Histories of A9, A10, and A11 under sinusoidal motion at 0.3g amplitude with 1 Hz frequency.

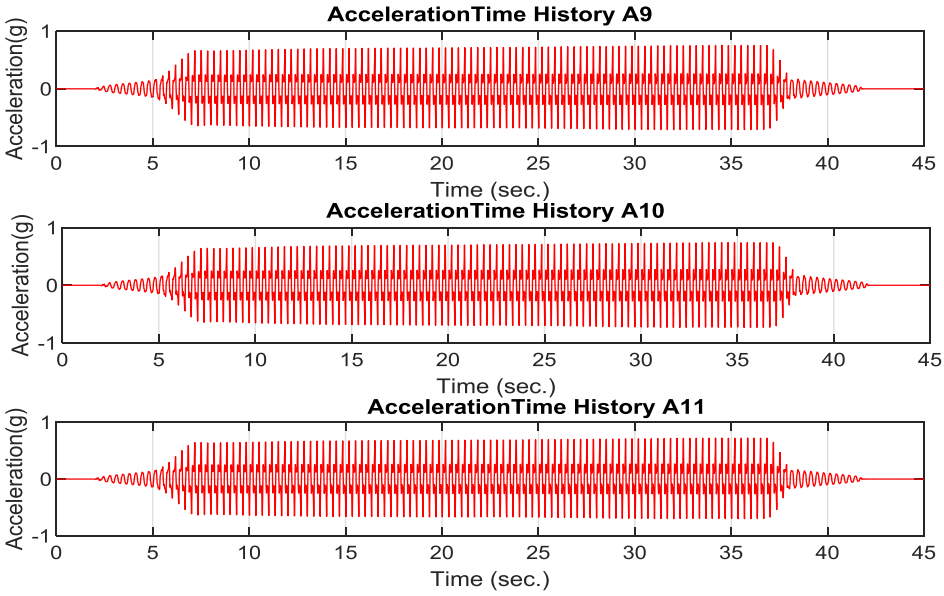


Figure 3.12 The Acceleration-Time Histories of A9, A10, and A11 under sinusoidal motion at 0.6g amplitude with 3 Hz frequency.

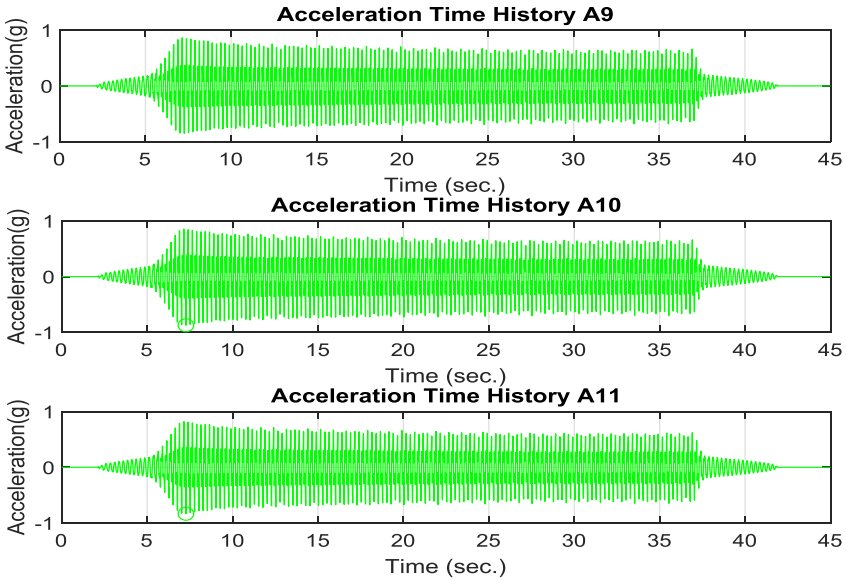


Figure 3.13 The Acceleration-Time Histories of A9, A10, and A11 under sinusoidal motion at 0.6g amplitude with 3 Hz frequency.

### 3.1.6. Shake Table

In order to examine the seismic behaviour of model structures and structural components, Department of Earthquake Engineering at Kandilli Observatory and Earthquake Research Institute of Bogazici University acquired three shake tables of various sizes. The shake tables are maintained at the shake table laboratory, a 300 square meter structure close to the Department of Earthquake Engineering, together with the related sensors and control systems.

The uniaxial shake table, which has plan dimensions of 3 m by 3 m, is the largest of the three shake tables. The table's payload capacity is 10 tons, and the top height for test specimens is 6.5 meters. With accelerations of up to 2g and displacements of +/- 12 cm, the table can simulate the motions of real or scenario earthquakes (total stroke 24 cm). A 3-stage servo-valve is used as the actuator for the shake table, and it is managed by analog inner-loop (displacement-based) and digital outer-loop (acceleration feedback-based) control systems.

The shake table facilities at Boğaziçi University Kandilli Observatory and Earthquake Institute and the laminar box on the shake table are shown in Figure 3.14.

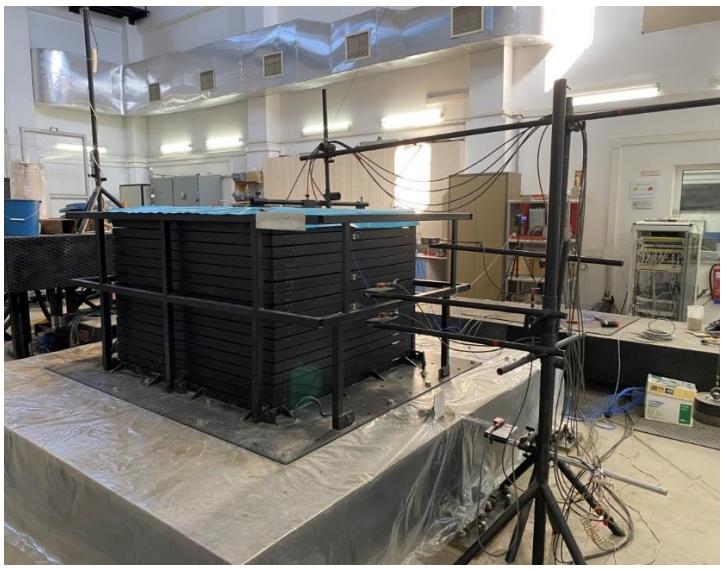

Figure 3.14. Laminar Box on the Shake Table at Boğaziçi University Kandilli Observatory and Earthquake Research Institute ShakeTable Laboratory.

## 3.2. Experimental Study

The experiments were performed on the shake table, where the variables changed as the types of cushions, thicknesses, densities, mixture ratios of cushions, and characteristics of input motions. The laminar box was placed on the shake table. The retaining wall model is a 1/15 scaled model. This scaling was deemed appropriate to the dimensions of the laminar box, and all calculations were based on this scale. The 1/15 scaled retaining wall model is made of aluminum.

The illustration of the shake table, the laminar box and the retaining wall model of the experimental study is shown in Figure 3.15.

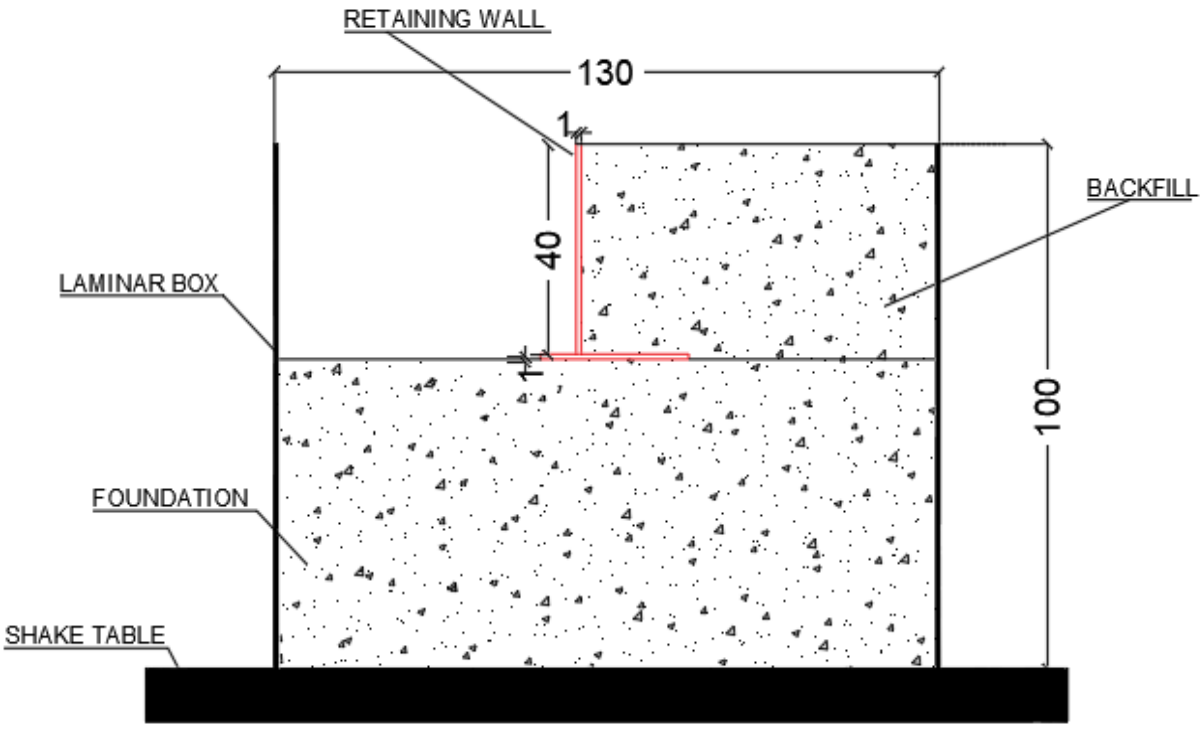


Figure 3.15 Illustration of the shake table, laminar box and the retaining wall model.

### 3.2.1. Design of the Retaining Wall Model

The dimensioning of the prototype retaining wall was calculated taking into account the retaining wall's preliminary dimensions accepted in the literature (Figure 3.16.a-3.16.d).

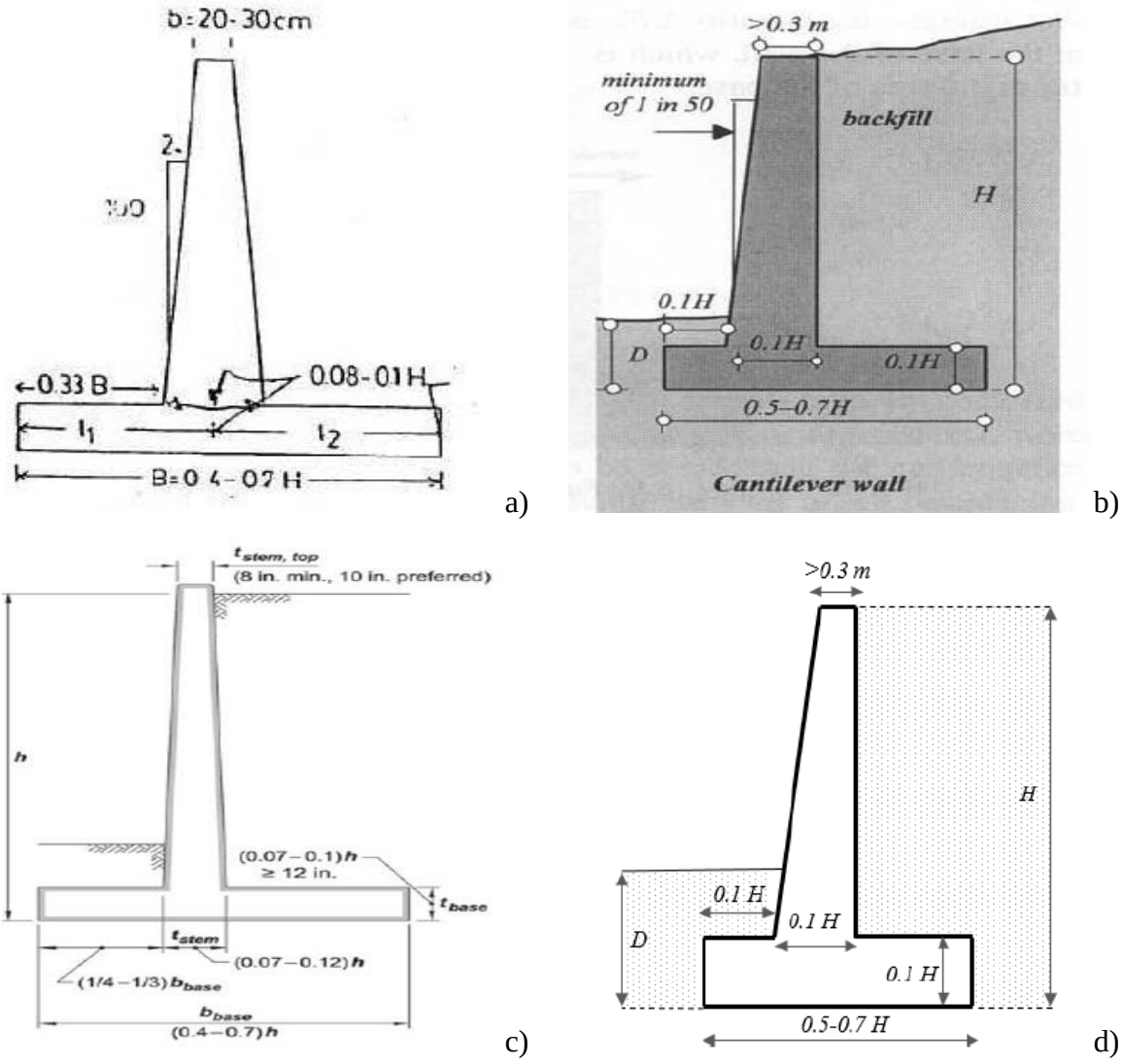


Figure 3.16. a) The dimensioning of the retaining wall (TS7994/February 1990), b) The design of retaining walls (Azizi, 1999), c) Retaining wall preliminary dimensions (The Reinforced Concrete Design_ACI 318-14, 2016), d) The design of reinforced concrete retaining walls (TBEC, 2018).

Regarding the dimensioning rules given in Figures 3.16.a-d, the dimensions were selected as shown in Figure 3.17 as the prototype cantilever wall. Preliminary dimensions of the prototype wall are the height of the stem is 600 cm, the thickness of the stem and the base is 35 cm, the width of the base in front of the stem is 60 cm, and the width of the base behind the stem is 295 cm as seen in Figure 3.17.

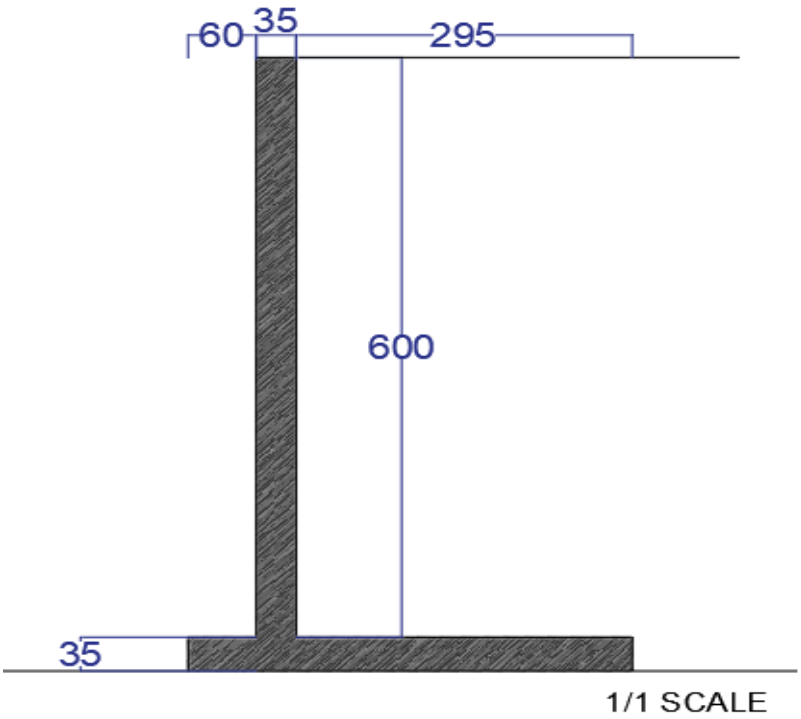


Figure 3.17. The prototype retaining wall (the dimensions are in cm).

The wall dimensions were carefully designed to ensure stability under both static and seismic conditions. Analytical solutions were used to determine the appropriate dimensions using the Coulomb, Rankine Methods for static analysis and Mononobe-Okabe Methods for dynamic analysis. Table 3.4 shows the safety factors against overturning and sliding for each method for the prototype retaining wall. According to the Coulomb and Rankine Methods, the safety factors should be at least 1.5 for both overturning and sliding. However, the M-O method requires a minimum safety factor of 1.3 for overturning and 1.1 for sliding. The wall dimensions were found to meet these requirements, as shown in Table 3.4.

Table 3.4. The factor of safety under static and seismic conditions of the prototype wall (Kramer, 1996; Day, 2002).

| **Static Analysis** | | | | **Seismic Analysis** | |
|---|---|---|---|---|---|
| **Coulomb** | | **Rankine** | | **M-O Method** | |
| **(FS)overturning** | 4.29 > 1.5 | **(FS)overturning** | 3.88 > 1.5 | **(FS)overturning** | 3.66 > 1.3 |
| **(FS)sliding** | 1.71 > 1.5 | **(FS)sliding** | 1.52 > 1.5 | **(FS)sliding** | 1.11 > 1.1 |

The scaling rules were followed when scaling the model (Table 3.5). In this study, the prototype wall was scaled to a 1/15 model retaining wall. Many variables of the prototype wall can be scaled, as well. These relations were obtained from the similitude method proposed by Iai (1989) and developed by Wood et al. (2002) and Wood (2004). The value of n is the scale factor.

Table 3.5. The scale factors of the retaining wall model (Iai, 1989; Wood et al., 2002 and Wood, 2004).

| **Parameter** | **Prototype - 1/15 Scaled Model** | |
|---|---|---|
| Length | n | 1/15 |
| Time | $\sqrt{n}$ | $1/\sqrt{15}$ |
| Frequency | $1/\sqrt{n}$ | $\sqrt{15}$ |
| Displacement | n | 1/15 |
| Acceleration | 1 | 1 |
| Velocity | $\sqrt{n}$ | $1/\sqrt{15}$ |
| Stress | n | 1/15 |
| Strain | 1 | 1 |
| Density | 1 | 1 |
| Stiffness | $\sqrt{n}$ | $1/\sqrt{15}$ |
| Mass | $n^2$ | $1/15^2$ |
| Force | $n^2$ | $1/15^2$ |

The concrete prototype retaining wall was scaled as aluminum in order to conduct a shake table test on a 1/15 scaled model. According to Wood (2004), the thickness of the aluminum model was calculated by using the following scaling correlation.

$$t_m = t_p \left( \frac{E_p}{E_m} \frac{1}{n^{7/2}} \right)^{\frac{1}{3}} \tag{3.5}$$

$t_m$ = the thickness of the model wall,

$t_p$ = the thickness of the prototype wall,

$E_m$ = Young's modulus of the model wall,

$E_p$ = Young's modulus of the prototype wall.

Young's modulus of the prototype concrete wall is equal to 20 GPa, and Young's modulus of the model aluminum wall is equal to 70 GPa (Wood, 2004). Additionally, the value of $t_p$ was selected as 0.35. When the equation is solved, $t_m$ (the thickness of the model wall) for aluminum is calculated as 10 mm. The 1/15 scaled retaining wall model is shown in Figure 3.18.

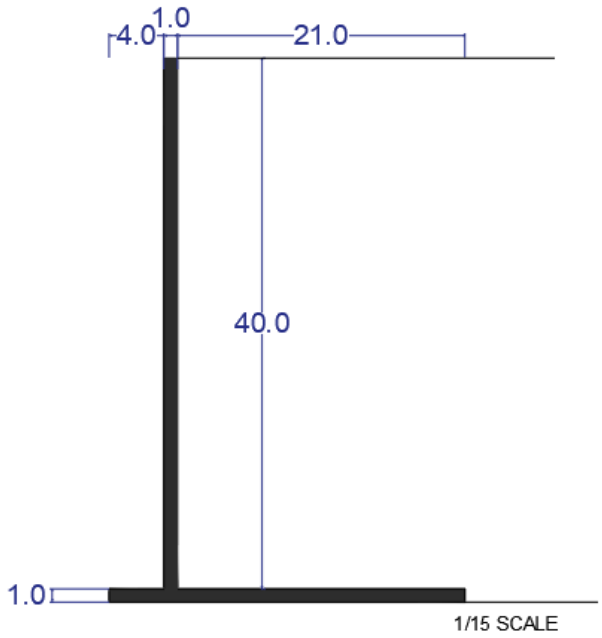


Figure 3.18. 1/15 scaled retaining wall model (the dimensions are in cm).

The analytical solutions were used to check the scaled dimensions using the Coulomb and Rankine Methods for static analysis and the Mononobe-Okabe Methods for dynamic analysis. Table 3.6 shows the safety factors against overturning and sliding for each method for the 1/15 scaled retaining wall.

Table 3.6. The factor of safety under static and seismic conditions of the 1/15 scaled wall (Kramer, 1996, Day, 2002).

| **Static Analysis** | | | | **Seismic Analysis** | |
|---|---|---|---|---|---|
| **Coulomb** | | **Rankine** | | **M-O Method** | |
| **(FS)overturning** | 4.57 > 1.5 | **(FS)overturning** | 4.09 > 1.5 | **(FS)overturning** | 4.04 > 1.3 |
| **(FS)sliding** | 1.73 > 1.5 | **(FS)sliding** | 1.55 > 1.5 | **(FS)sliding** | 1.12 > 1.1 |

The fundamental frequency of vibration for a two-dimensional, linear elastic medium of width B and height H contained by two rigid vertical boundaries and a rigid base and subject to horizontal base excitation is given by Wu (1994) and (Bathurst and Hatami, 1998).

$$f_{11} = \frac{1}{4H}\sqrt{\frac{G}{\rho}}\sqrt{1+\left(\frac{2}{1-\nu}\right)\left(\frac{H}{B}\right)^2} \tag{3.6}$$

The $f_{11}$ = frequency in Hz corresponding to the first mode shape of the medium in both the horizontal and vertical directions; G= shear modulus; ρ = density; and $\nu$ =Poisson's ratio of the elastic medium.

The fundamental frequency of the prototype retaining wall system was calculated as 5.9 Hz, and the fundamental frequency of the scaled retaining wall was calculated as 22.8 Hz. Earthquakes with medium-to-high frequencies usually have predominant frequencies that range from 2 to 3Hz. Furthermore, Table 3.7 presents the $f/f_n$ values computed for the input motions. These values correspond to the dominant frequency of the earthquakes (f) and the fundamental frequency of the retaining wall ($f_n$).

Table 3.7 The $f/f_n$ values for the input motions conducted in the experimental studies.

| Input Motion | Predominant Frequency (Hz) | $f_n$ (Hz) | $f/f_n$ |
|---|---|---|---|
| "Kocaeli_ Turkey" 17 August 1999 “İznik" Station | 2.58 | 22.8 | 0.113 |
| "Kocaeli_ Turkey" 17 August 1999 “İzmit" Station | 12.91 | 22.8 | 0.566 |
| "Kobe_ Japan" 17 January 1995 “KJMA" Station | 5.73 | 22.8 | 0.251 |
| "Imperial Valley-02" 18 May 1940 “El Centro Array #9" Station | 5.96 | 22.8 | 0.261 |
| "İzmir-Turkey" 30 October 2020 "Kuşadası 0905" Station | 24.44 | 22.8 | 1.072 |
| "Gökçeada-Turkey" 24 May 2014 "Çanakkale Merkez 1701" Station | 3.22 | 22.8 | 0.141 |
| Sinusoidal Motion at 0.3g Amplitude with 8Hz Frequency | 8 | 22.8 | 0.351 |
| Sinusoidal Motion at 0.4g Amplitude with 8Hz Frequency | 8 | 22.8 | 0.351 |
| Sinusoidal Motion at 0.5g Amplitude with 8Hz Frequency | 8 | 22.8 | 0.351 |
| Sinusoidal Motion at 0.4g Amplitude with 12Hz Frequency | 12 | 22.8 | 0.526 |
| Sinusoidal Motion at 0.4g Amplitude with 12Hz Frequency | 14 | 22.8 | 0.614 |

### 3.2.2. Input Motions

This thesis study involved conducting shake table tests. The tests were performed using different cushions by changing the types of cushions and by varying the thickness and density of the cushions under input motions having different earthquake characteristics and various sinusoidal motions. The 1/15 scaled model was designed to withstand the physical environment of a laminar box.

Near field earthquakes are seismic events that occur in close proximity to the site or structure of interest. They are characterized by ground motions with high amplitude and low frequency. In contrast, far field earthquakes occur at a significant distance from the site or structure of interest and are characterized by ground motions with low amplitude and high frequency. Compared to far field earthquakes, near field earthquakes exhibit higher acceleration and a narrower frequency range, but they have lower frequencies overall. The distinction between the far field and near field is determined by the distance from the earthquake source, including the epicenter and fault. Near field earthquakes occur within a few kilometers of the earthquake source, and far field earthquakes occur at a distance greater than a few kilometers from the earthquake source. Near field earthquakes have a greater impact on structures in terms of hysteresis energy and relative displacement of steel moment-resisting frame structures when compared to far field earthquakes. However, it is important not to overlook the potential seismic disasters that can occur in far field areas as a result of strong earthquakes (Davoodi et al., 2012; Heydari and Mousavi, 2015)

The far field earthquakes conducted in this study are the scaled 1999 Kocaeli Earthquake Motion-İznik Station acceleration record, the scaled 2014 Gökçeada Earthquake Motion-Çanakkale Station acceleration record and the scaled 2020 İzmir Earthquake Motion-Kuşadası Station acceleration record.

The near field earthquakes conducted in this study are the scaled 1999 Kocaeli Earthquake Motion-İzmit Station acceleration record, the scaled 1940 El Centro Station acceleration record, and the scaled 1995 Kobe EQ acceleration record.

The sinusoidal motions conducted in this study are sinusoidal motion at 0.3g amplitude with 8 Hz frequency, sinusoidal motion at 0.4g amplitude with 8 Hz frequency, sinusoidal motion at 0.5g amplitude with 8 Hz frequency, sinusoidal motion at 0.4g amplitude with 12 Hz frequency, sinusoidal motion at 0.4g amplitude with 14 Hz frequency.

The selected input motions, far field earthquakes, near field earthquakes, and sinusoidal motions conducted in this thesis study are shown in Tables 3.8, 3.9, and 3.10. The earthquake

input motions used for the shake table tests are given in Table 3.9, and the sinusoidal input motions are given in Table 3.10.

The frequencies of sinusoidal motions 8 Hz and 12 Hz of the 1/15 scaled model correspond to 2.1-3.1 Hz, respectively, in the prototype scale model, while the earthquakes within the medium-to-high frequency range usually have predominant frequencies that range from 2 to 3 Hz.

The earthquake input motion characteristics are given in Table 3.8. Two different records of the 1999 Kocaeli Earthquake ($M_w$: 7.51) are used. İznik Station record (E-W) has PGA, PGV, and PGD values of 0.12g, 25.3 cm/s and 18.6cm. The Joyner-Boore distance ($R_{jb}$) is 30.7km. İznik Station is located on a site with $V_{s30}$ of 476.6 m/s. The duration of the record is 30s, and the significant duration is 19.5s. The predominant frequency and the lowest usable frequency values are 0.67 Hz and 0.125 Hz. İzmit Station record (E-W) has PGA, PGV, and PGD values of 0.22g, 29.8 cm/s and 17.1cm. The Joyner-Boore distance ($R_{jb}$) is 3.6km. İzmit Station is located on a site with $V_{s30}$ of 811 m/s. The duration of the record is 30s, and the significant duration is 15.1s. The predominant Frequency and the lowest usable frequency values are 3.33 Hz and 0.125 Hz. The pulse period of the record is 5.3s (AFAD, KOERI, PEER).

The 1995 Kobe Earthquake ($M_w$: 6.9) KJMA Station record (N-S) has PGA, PGV, and PGD values of 0.82g, 81.3 cm/s and 17.6cm. The Joyner-Boore distance ($R_{jb}$) is 0.94km. KJMA Station is located on a site with $V_{s30}$ of 312 m/s. The duration of the record is 48s, and the significant duration is 9.5. The predominant frequency and the lowest usable frequency values are 1.48 Hz and 0.0625 Hz. The pulse period of the record is 1.09s (AFAD, KOERI, PEER).

The 1940 Imperial Valley-02 Earthquake ($M_w$: 6.95) El Centro Array #9 Station record (N-S) has PGA, PGV, and PGD values of 0.32g, 36.2 cm/s, and 21.3cm. The Joyner-Boore distance ($R_{jb}$) is 6.09km. El Centro Array #9 Station is located on a site with $V_{s30}$ of 213.4 m/s. The duration of the record is 31.2s, and the significant duration is 24.2. The predominant frequency and the lowest usable frequency values are 1.53 Hz and 0.25 Hz (AFAD, KOERI, PEER).

The 2020 Izmir Earthquake ($M_w$: 6.6) Kuşadası 0905 Station record (N-S) has PGA, PGV, and PGD values of 0.18g, 7.8 cm/s and 1.5cm. The Joyner-Boore distance ($R_{jb}$) is 59.6km. Kuşadası 0905 Station is located on a site with $V_{s30}$ of 369 m/s. The duration of the record is 68.6s, and the significant duration is 15.7. The predominant frequency of the record is 6.31 Hz (AFAD, KOERI, PEER).

The 2014 Gökçeada Earthquake ($M_w$: 6.5) Çanakkale Merkez 1701 Station record (N-S) has PGA, PGV, PGD values of 0.14g, 12.7 cm/s and 7.8cm. The epicentral distance ($R_{epi}$) is 93.1km. Çanakkale Merkez 1701 Station is located on a site with $V_{s30}$ of 192 m/s. The duration of the record is 200s, and the significant duration is 27.4. The predominant frequency of the record is 0.83 Hz (AFAD, KOERI, PEER).

Table 3.8 The selected earthquake records.

| Earthquake | Date | Station | Mw | Component | PGA (g) | PGV (cm/s) | PGD (cm) | Sampling Interval | $R_{epi}$ (km) | $R_{jb}$ (km) | $V_{s30}$ (m/s) | Significant Duration (sec) | Duration (sec) | Predominant Frequency (Hz) | Lowest Useable Frequency (Hz) | Pulse Period (sec) |
|---|---|---|---|---|---|---|---|---|---|---|---|---|---|---|---|---|
| "Kocaeli-Turkey" | 17 August 1999 | "Iznik" | 7.51 | E-W | 0.12 | 25.26 | 18.58 | 0.001 | - | 30.73 | 477 | 19.5 | 30 | 0.67 | 0.125 | - |
| "Kocaeli-Turkey" | 17 August 1999 | "Izmit" | 7.51 | E-W | 0.22 | 29.79 | 17.11 | 0.001 | - | 3.62 | 811 | 15.1 | 30 | 3.33 | 0.125 | 5.369 |
| "Kobe-Japan" | 17 January 1995 | "KJMA" | 6.9 | N-S | 0.82 | 81.30 | 17.64 | 0.001 | - | 0.94 | 312 | 9.5 | 48 | 1.48 | 0.0625 | 1.092 |
| "Imperial Valley-02" | 18 May 1940 | "El Centro Array #9" | 6.95 | N-S | 0.32 | 36.33 | 21.33 | 0.001 | - | 6.09 | 213 | 24.2 | 31.2 | 1.53 | 0.25 | - |
| "İzmir-Turkey" | 30 October 2020 | "Kuşadası 0905" | 6.6 | N-S | 0.18 | 7.83 | 1.50 | 0.001 | 49.38 | 59.57 | 369 | 15.7 | 68.6 | 6.31 | - | - |
| "Gökçeada-Turkey" | 24 May 2014 | "Çanakkale Merkez 1701" | 6.5 | N-S | 0.14 | 12.66 | 7.85 | 0.001 | 93.11 |  | 192 | 27.4 | 200 | 0.83 | - | - |

Table 3.9 The selected earthquake input motions executed in the experimental study (1/15 scaled).

| Earthquake | Date | Station | Component | PGA (g) | PGV (cm/s) | PGD (cm) | Sampling Interval | Significant Duration (sec) | Duration (sec) | Predominant Frequency (Hz) |
|---|---|---|---|---|---|---|---|---|---|---|
| "Kocaeli_ Turkey" | 17 August 1999 | "Iznik" | E-W | 0.12 | 6.52 | 1.24 | 0.001 | 5.03 | 7.74 | 2.58 |
| "Kocaeli_ Turkey" | 17 August 1999 | "Izmit" | E-W | 0.22 | 7.69 | 1.14 | 0.001 | 3.90 | 7.74 | 12.91 |
| "Kobe_ Japan" | 17 January 1995 | "KJMA" | N-S | 0.82 | 21.10 | 1.18 | 0.001 | 2.45 | 12.40 | 5.73 |
| "Imperial Valley-02" | 18 May 1940 | "El Centro Array #9" | N-S | 0.32 | 9.38 | 1.42 | 0.001 | 6.25 | 8.05 | 5.96 |
| "İzmir-Turkey" | 30 October 2020 | "Kuşadası 0905" | N-S | 0.18 | 2.03 | 0.10 | 0.001 | 4.05 | 17.72 | 24.44 |
| "Gökçeada-Turkey" | 24 May 2014 | "Çanakkale Merkez 1701" | N-S | 0.14 | 3.27 | 0.52 | 0.001 | 7.07 | 50 | 3.22 |

While conducting the experimental study, the 1/15 scaled earthquake input motions were executed. The scaled earthquake input motion characteristics are represented in Table 3.9. Two different records of the 1999 Kocaeli Earthquake are used as a 1/15 scaled input. The scaled İznik Station record (E-W) has PGA, PGV, and PGD values of 0.12g, 6.5 cm/s, and 1.2cm, respectively. The duration of the scaled record is 7.7s, and the predominant frequency of the scaled record is 2.58 Hz. The scaled İzmit Station record (E-W) has PGA, PGV, and PGD values of 0.22g, 7.7 cm/s and 1.1cm. The duration of the scaled record is 7.7s, and the predominant frequency of the scaled record is 12.91 Hz (AFAD, KOERI, PEER).

The scaled 1995 Kobe EQ KJMA Station record (N-S) has PGA, PGV, and PGD values of 0.82g, 21.1 cm/s, and 1.2cm. The duration of the scaled record is 12.4s, and the predominant frequency of the scaled record is 5.73 Hz (AFAD, KOERI, PEER).

The scaled 1940 Imperial Valley-02 Earthquake El Centro Array #9 Station record (N-S) has PGA, PGV, and PGD values of 0.32g, 9.4 cm/s, and 1.4cm. The duration of the scaled record is 8.05s, and the predominant frequency of the scaled record is 5.96 Hz (AFAD, KOERI, PEER).

The scaled 2020 Izmir Earthquake Kuşadası 0905 Station record (N-S) has PGA, PGV, and PGD values of 0.18g, 2.03 cm/s, and 0.1cm. The duration of the scaled record is 17.7s, and the predominant frequency of the scaled record is 24.4 Hz (AFAD, KOERI, PEER).

The scaled 2014 Gökçeada Earthquake Çanakkale Merkez 1701 Station record (N-S) has PGA, PGV, PGD values of 0.14g, 3.3 cm/s, and 0.5cm. The duration of the scaled record is 50s, and the predominant frequency of the record is 3.22 Hz (AFAD, KOERI, PEER).

Table 3.10. The sinusoidal input motions in the experimental study.

| Record | PGA | Frequency |
|---|---|---|
| Sinusoidal Motion | 0.30 g | 8 Hz |
| Sinusoidal Motion | 0.40 g | 8 Hz |
| Sinusoidal Motion | 0.50 g | 8 Hz |
| Sinusoidal Motion | 0.40 g | 12 Hz |
| Sinusoidal Motion | 0.40 g | 14 Hz |

The scaled earthquakes regarding Iai (1989) scaling laws as the Acceleration-Time Histories (ACCTH) and the Fourier Amplitude Spectrums (FAS) of the far field (FF) earthquakes as the scaled 1999 Kocaeli Earthquake (EQ) Motion-İznik Station, the scaled 2014 Gökçeada Earthquake (EQ) Motion-Çanakkale Station, the scaled 2020 İzmir Earthquake (EQ) Motion-Kuşadası Station records and the near field (NF) earthquakes as the scaled 1999 Kocaeli Earthquake (EQ) Motion-İzmit Station, the scaled 1940 Imperial Valley Earthquake (EQ) El Centro Station, the scaled 1995 Kobe EQ (EQ) records are given in Figures 3.19-3.24.

The Acceleration-Time Histories (ACCTH) of sinusoidal motions for 30 seconds as sinusoidal motion at 0.3g amplitude with 8 Hz frequency, sinusoidal motion at 0.4g amplitude with 8 Hz frequency, sinusoidal motion at 0.5g amplitude with 8 Hz frequency, sinusoidal motion at 0.4g amplitude with 12 Hz frequency, sinusoidal motion at 0.4g amplitude with 14 Hz frequency are given Figure 3.25.a-e.

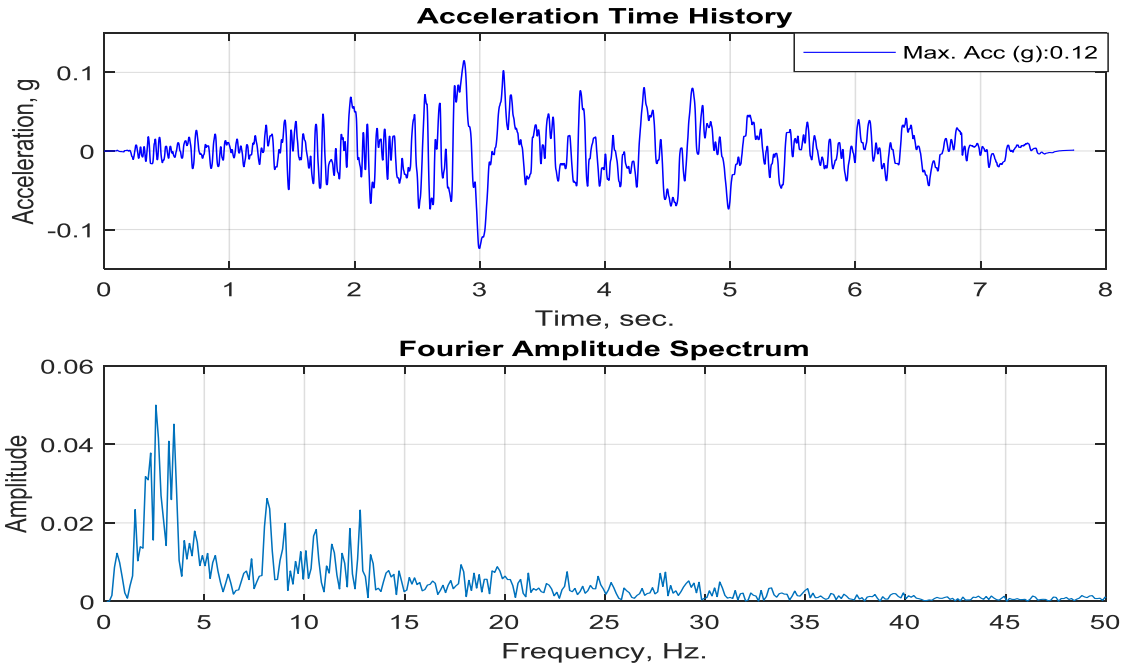


Figure 3.19 The ACCTH and FAS of the scaled 1999 Kocaeli EQ Motion-İznik Station (FF).

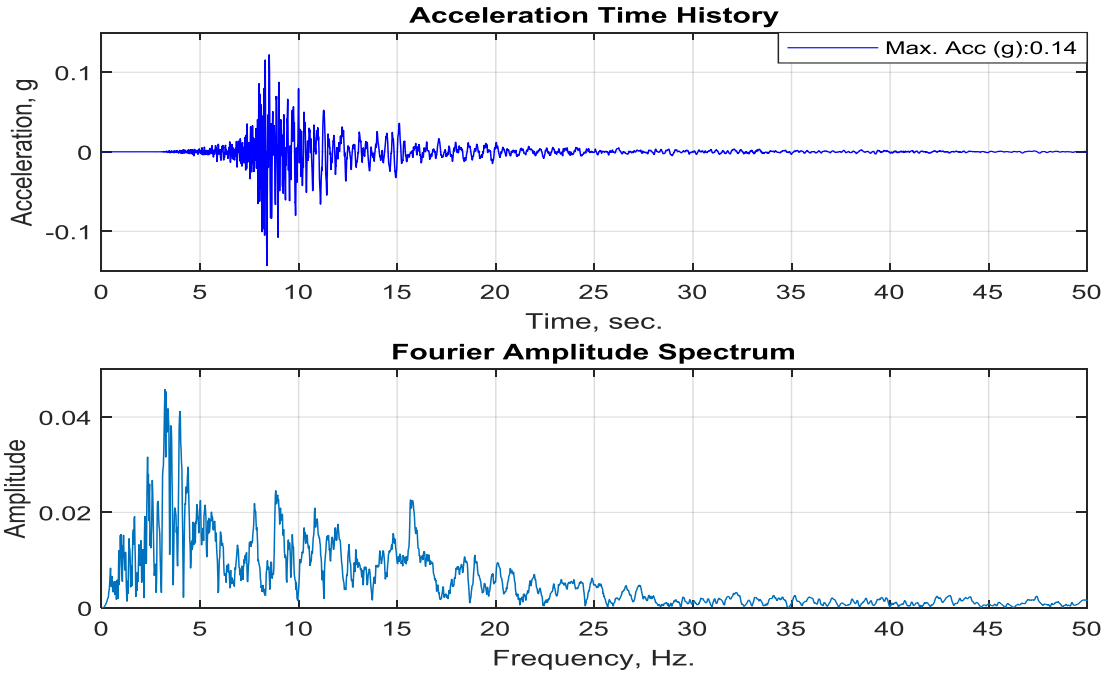


Figure 3.20. The ACCTH and FAS of the scaled 2014 Gökçeada EQ Motion-Çanakkale Station (FF).

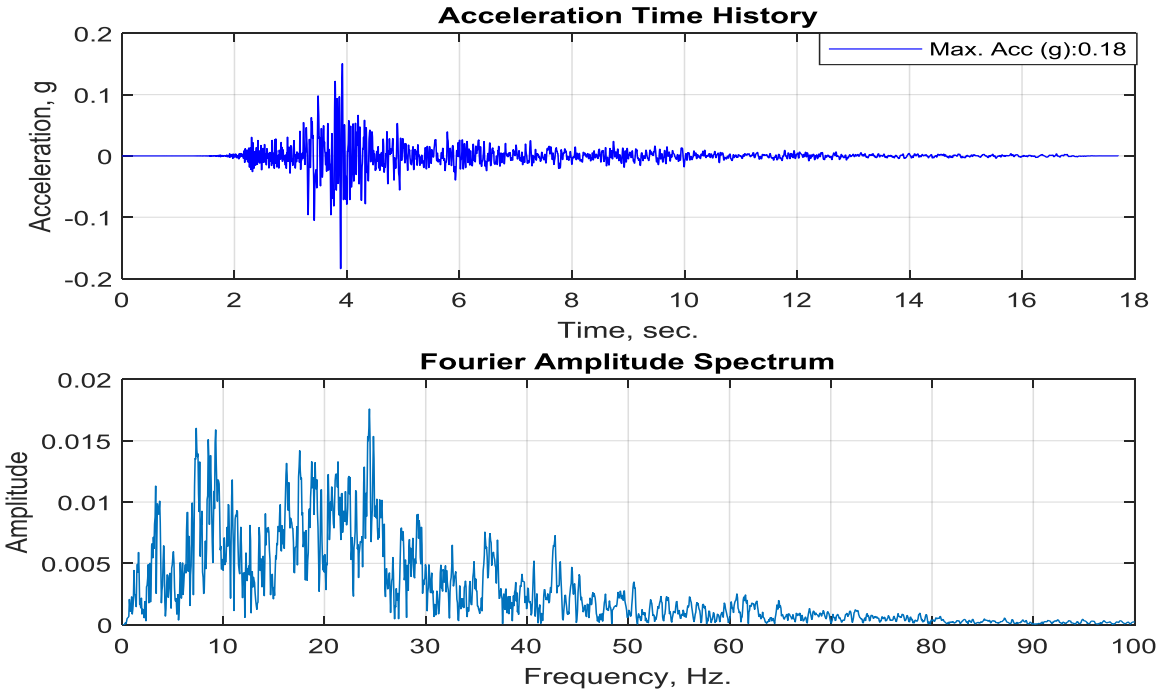


Figure 3.21. The ACCTH and FAS of the scaled 2020 İzmir EQ Motion-Kuşadası Station (FF).

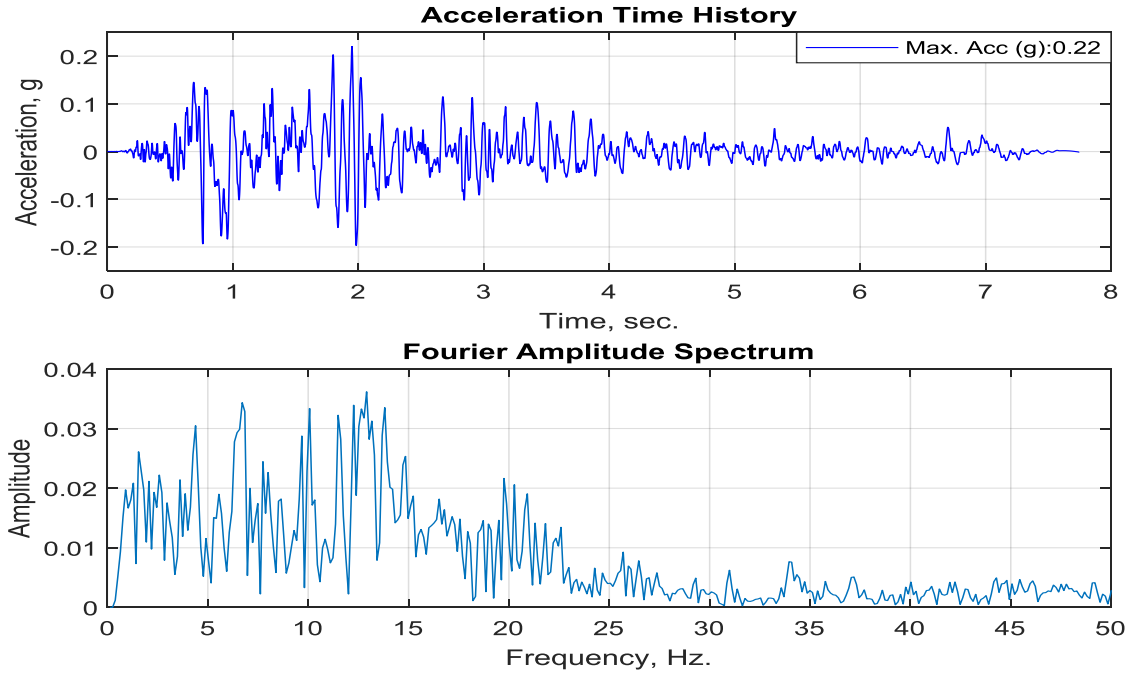


Figure 3.22. The ACCTH and FAS of the scaled 1999 Kocaeli EQ Motion-İzmit Station (NF).

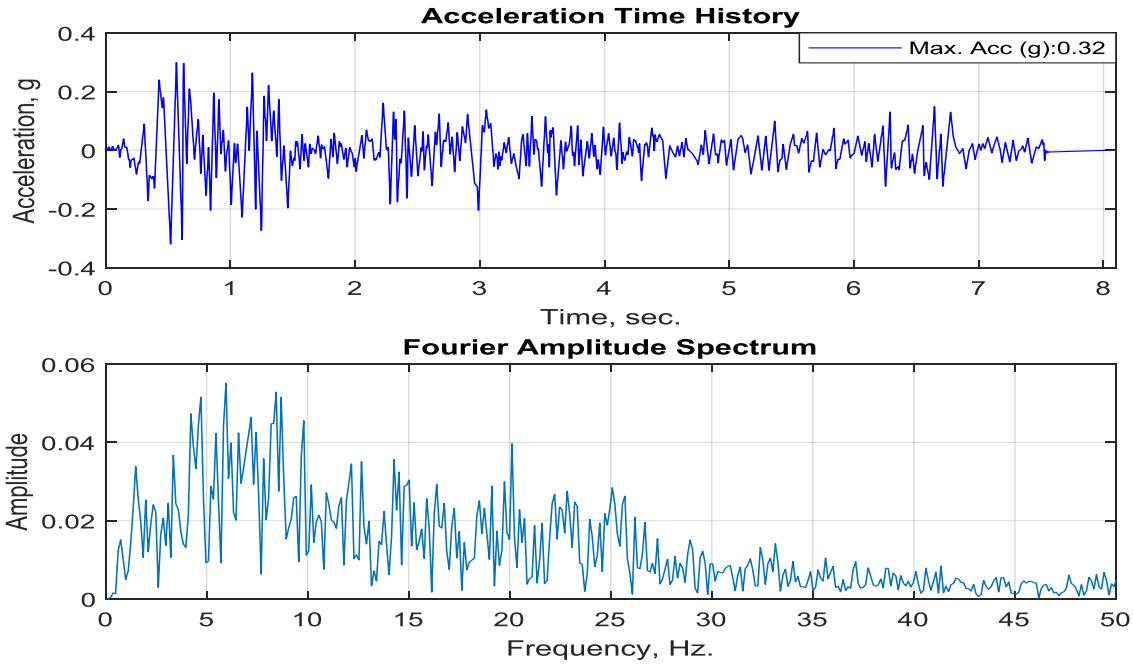


Figure 3.23. The ACCTH and FAS of the scaled 1940 Imperial Valley EQ El Centro Station (NF).

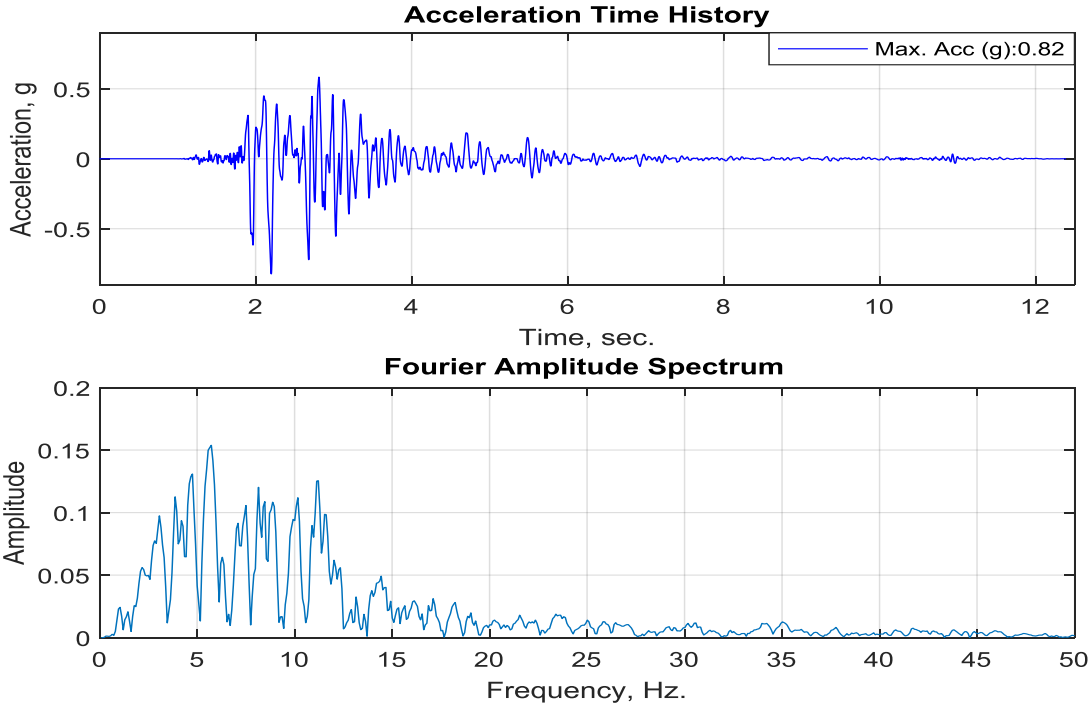


Figure 3.24. The ACCTH and FAS of the scaled 1995 Kobe EQ (NF).

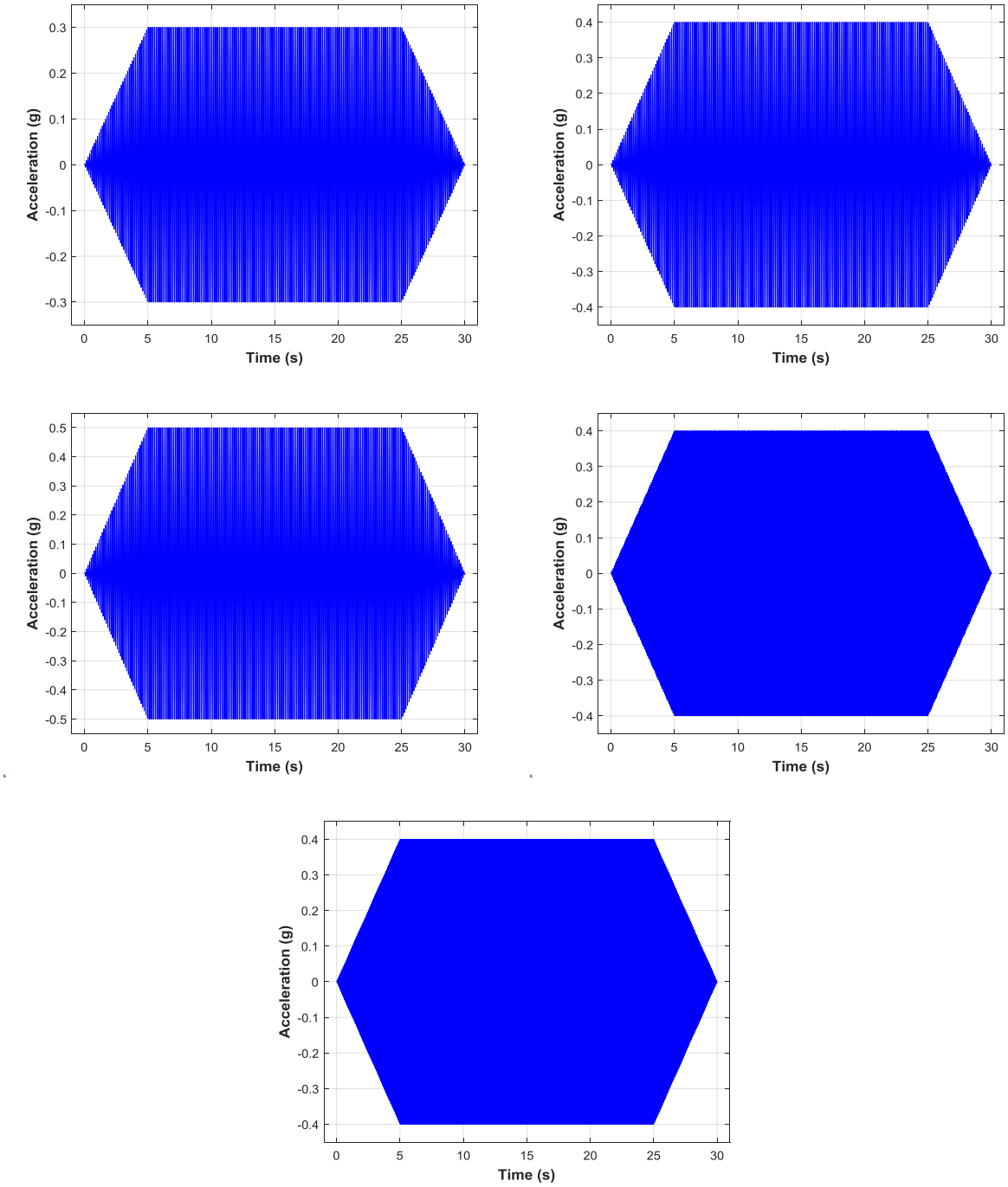


Figure 3.25. a) The ACCTH of sinusoidal motion at 0.3g amplitude with 8 Hz frequency b) The ACCTH of sinusoidal motion at 0.4g amplitude with 8 Hz frequency c) The ACCTH of sinusoidal motion at 0.5g amplitude with 8 Hz frequency d) The ACCTH of sinusoidal motion at 0.4g amplitude with 12 Hz frequency e) The ACCTH of sinusoidal motion at 0.4g amplitude with 14 Hz frequency.

### 3.2.3. Experimental Program

This thesis study consists of 22 experimental cases (Table 3.11). The first case is the control case containing only sand backfill. The other cases include three different cushion materials as EPS geofoam material, tire waste and sand mixtures, EPS Beads and sand mixtures with different thicknesses, densities, and mixture ratios under the same input motions.

Table 3.11. Experimental cases considered in the study.

| Cases | Cushion Material | Cushion Thickness | t/H Ratio | Input Motions (PGA, Frequency) for Each Case |
|---|---|---|---|---|
| **Case 1** | None | - | - | The scaled 1999 Kocaeli EQ İznik Station Record-FF (0.12g, 2.58 Hz)<br>The scaled 2014 Gökçeada EQ Çanakkale Station Record-FF (0.14g, 3.22 Hz)<br>The scaled 2020 İzmir EQ Kuşadası Station Record-FF (0.18g, 24.44 Hz)<br>The scaled 1999 Kocaeli EQ İzmit Station Record-NF (0.22g, 12.91 Hz)<br>The scaled 1940 El Centro Station Record-NF (0.32g, 5.96 Hz)<br>The Scaled Kobe Earthquake Record-NF (0.82g, 5.73 Hz)<br>Sinusoidal Motion (0.30g. 8Hz)<br>Sinusoidal Motion (0.40g. 8Hz)<br>Sinusoidal Motion (0.50g. 8Hz)<br>Sinusoidal Motion (0.40g. 12Hz)<br>Sinusoidal Motion (0.40g. 14Hz) |
| **Case 2** | EPS10 | 4cm | 0.1 | |
| **Case 3** | EPS20 | 4cm | 0.1 | |
| **Case 4** | EPS30 | 4cm | 0.1 | |
| **Case 5** | EPS10 | 8cm | 0.2 | |
| **Case 6** | EPS20 | 8cm | 0.2 | |
| **Case 7** | EPS30 | 8cm | 0.2 | |
| **Case 8** | TW10 | 4cm | 0.1 | |
| **Case 9** | TW20 | 4cm | 0.1 | |
| **Case 10** | TW30 | 4cm | 0.1 | |
| **Case 11** | TW10 | 8cm | 0.2 | |
| **Case 12** | TW20 | 8cm | 0.2 | |
| **Case 13** | TW30 | 8cm | 0.2 | |
| **Case 14** | EPSB10 | 4cm | 0.1 | |
| **Case 15** | EPSB20 | 4cm | 0.1 | |
| **Case 16** | EPSB30 | 4cm | 0.1 | |
| **Case 17** | EPSB10 | 6cm | 0.15 | |
| **Case 18** | EPSB20 | 6cm | 0.15 | |
| **Case 19** | EPSB30 | 6cm | 0.15 | |
| **Case 20** | EPSB10 | 8cm | 0.2 | |
| **Case 21** | EPSB20 | 8cm | 0.2 | |
| **Case 22** | EPSB30 | 8cm | 0.2 | |

The experimental study program with the selected input motions is given in Figure 3.26.

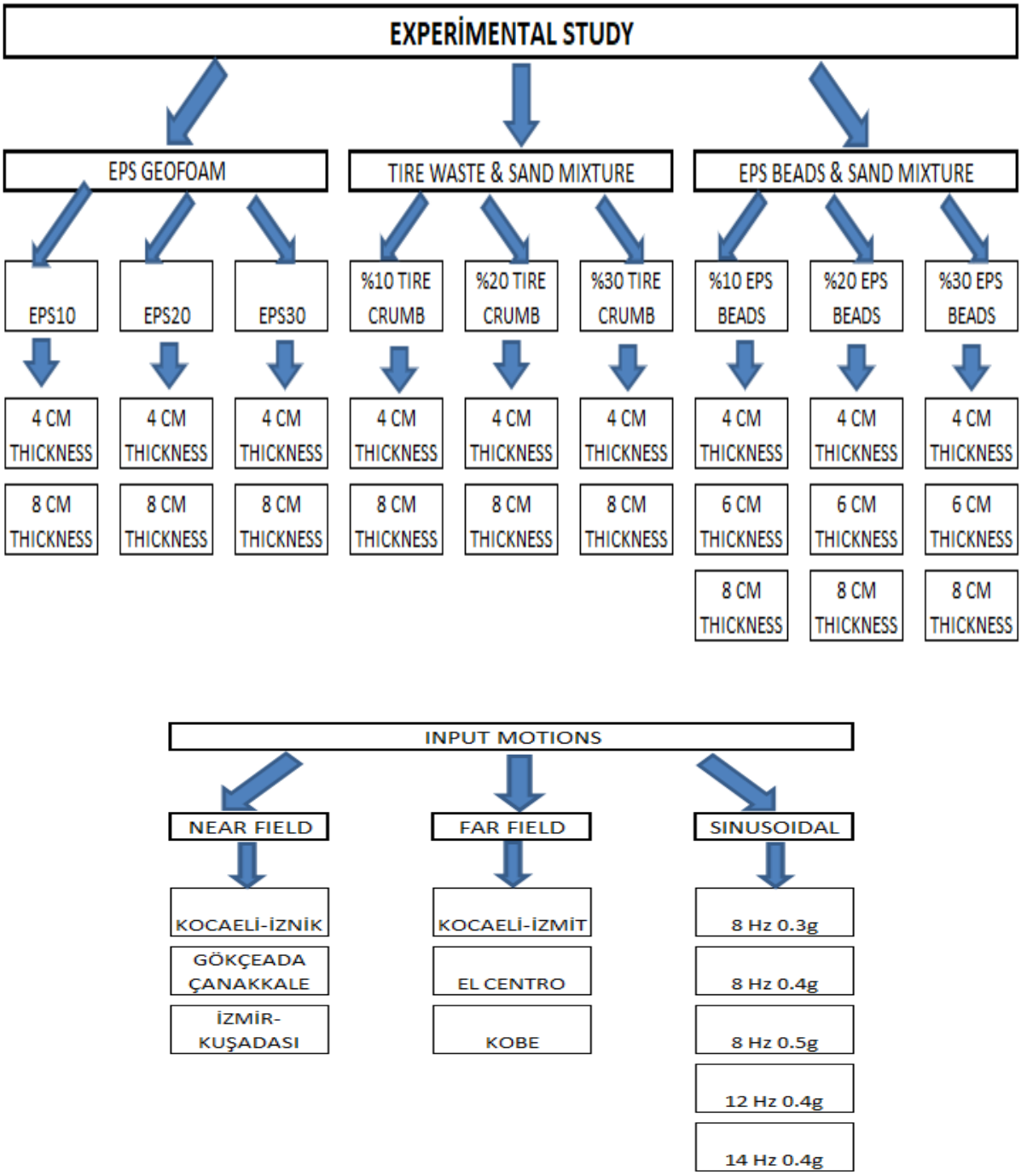


Figure 3.26. Experimental Study Program.

### 3.2.4. Preperation of the Experimental Studies

The 22 experimental cases were carried out in the laminar box on the shake table, starting with the control case (Case 1) followed by 6 experimental studies of EPS Geofoam cushioned cases with different thickness and density under the same input motions, 6 experimental studies of tire waste and sand mixture cushion cases with different thickness and mixture ratio under the same input motions, and 9 experimental studies of EPS Beads and sand mixture cushion cases with different thickness and mixture ratio under the same input motions. Three far field earthquakes, three near field earthquakes and five sinusoidal motions were applied as input motions during the shake table tests for each case.

#### 3.2.4.1. Instrumentation of the Experimental Set-up

In this part of the study, the instrumentation of the 1/15 scaled retaining wall model was configured for the experimental studies. The accelerometers were placed on the shake table, on laminar box layers, on the retaining wall, in the foundation, and backfill. Linear Displacement Transducers (LVDTs) were placed on the shake table, on the laminar box layer, and on the retaining wall.

The cross-section and the front view of the instrumentations of the control case and the cushioned cases are shown in Figure 3.27, Figure 3.28, Figure 3.29, and Figure 3.30, respectively. The A3, A4, A5, A6, A7, and A10 are accelerometers, and D18, D19, D20, and D21 are laser displacement sensors on the retaining wall, as seen in Figures 3.28 and 3.30. In Figures 3.27 and 3.29, the A1 and the D17 are on the shake table. The A2 and D24 are on the laminar box layer sixteen, the A25 and D22 are on the laminar box layer nine, and the A26 and D23 are on the laminar box layer twelve as shown in Figure 3.28 and Figure 3.30; also pictures of them are given in Figure 3.31.f and 3.31.g. The accelerometers A3, A4, A5, A6, A7, and A8 and the laser displacement sensors D18 (middle-middle of the retaining wall), D19 (top middle of the retaining wall), D20 (top right of the retaining wall), D21 (top left of the retaining wall) are on the retaining wall (Figure 3.28 and Figure 3.30). The illustrations of the accelerometers

and laser displacement sensors are shown in Figures 3.31.a-e. The A9, A10 and A11 are the accelerometers in the foundation, and the A12, A13, A14, A15 and A16 are the accelerometers in the backfill shown in Figure 3.27 and Figure 3.29.

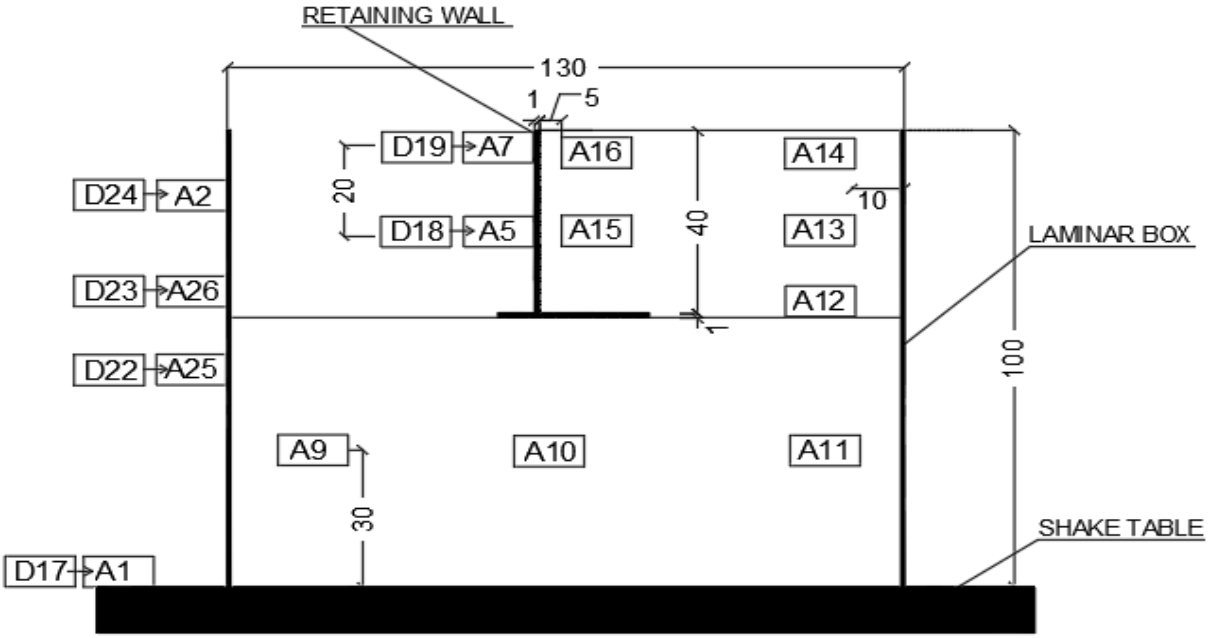


Figure 3.27. The cross-section of the instrumentation of the control case.

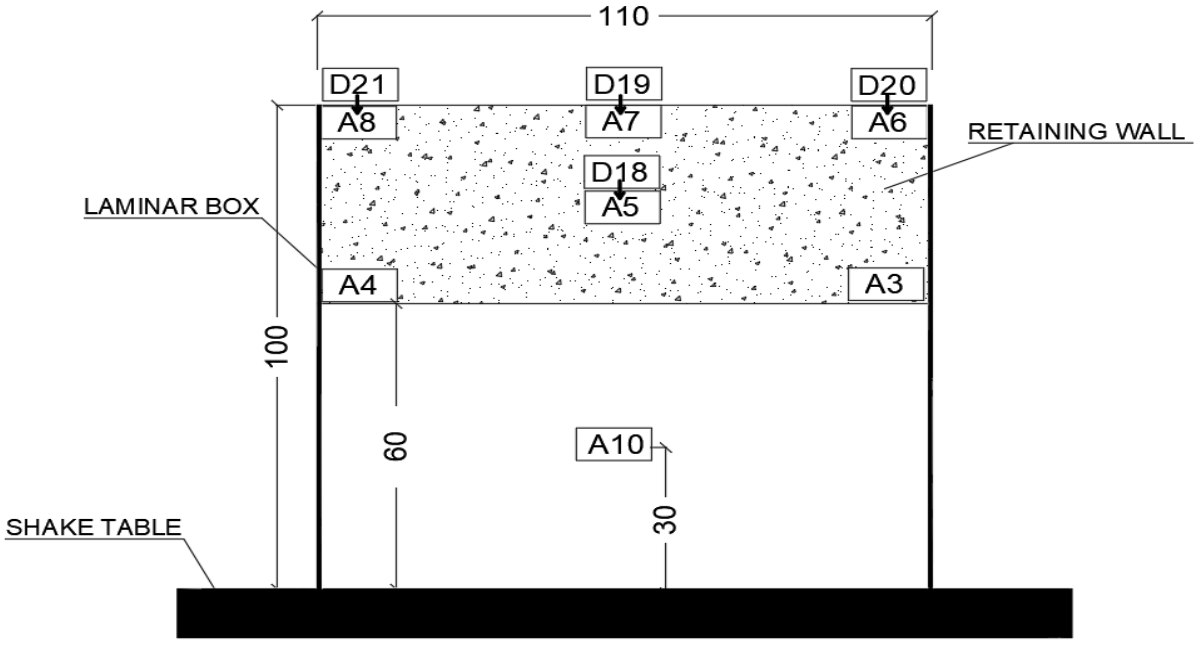


Figure 3.28. Front view of the instrumentation of the control case.

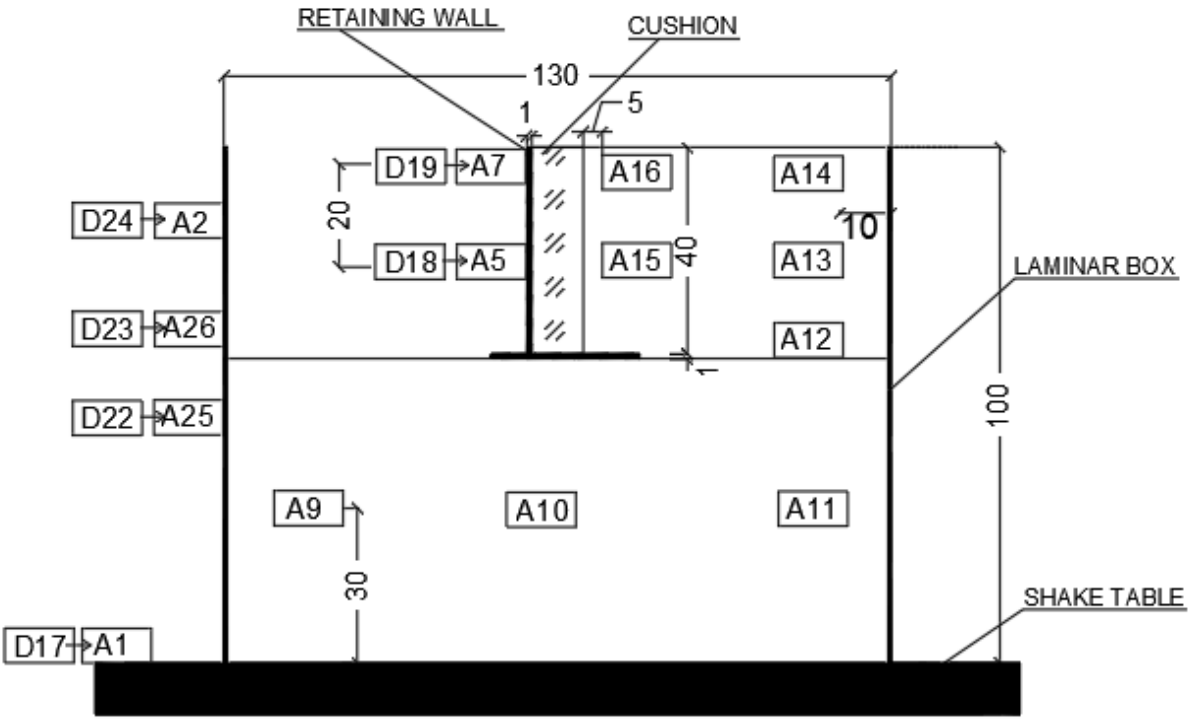


Figure 3.29. The cross-section of the instrumentation of the cushioned cases.

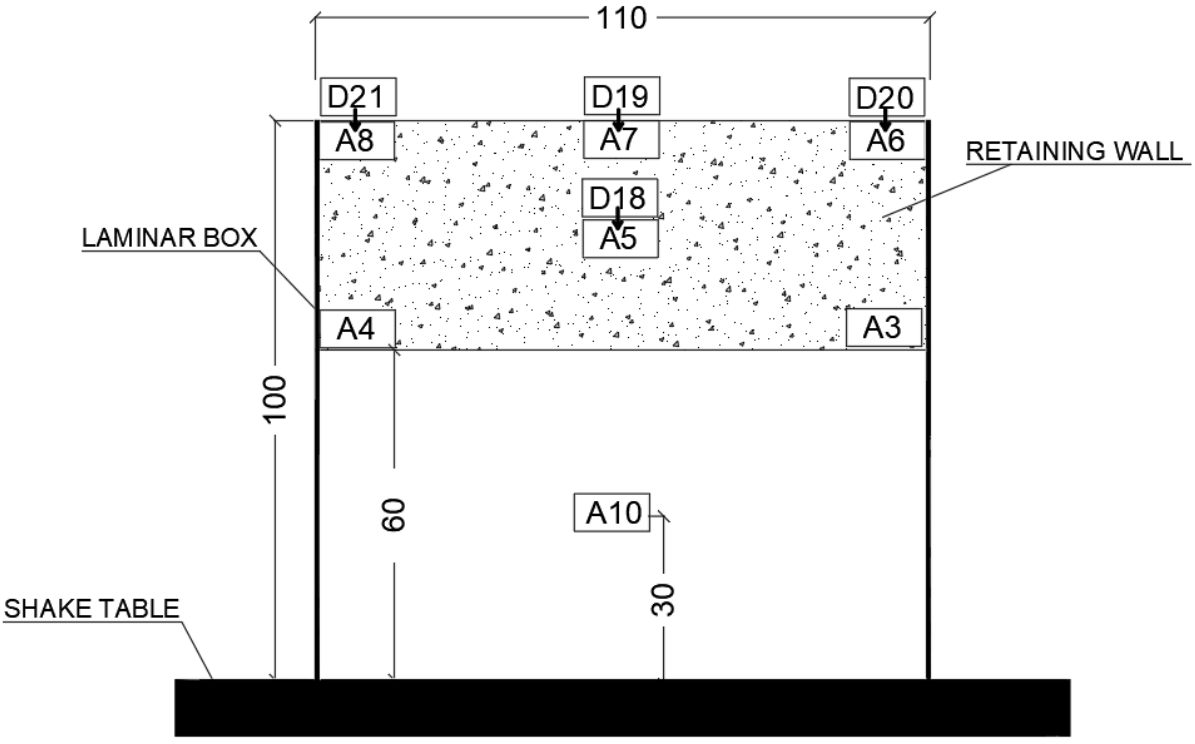


Figure 3.30. Front view of the instrumentation of the cushioned cases.

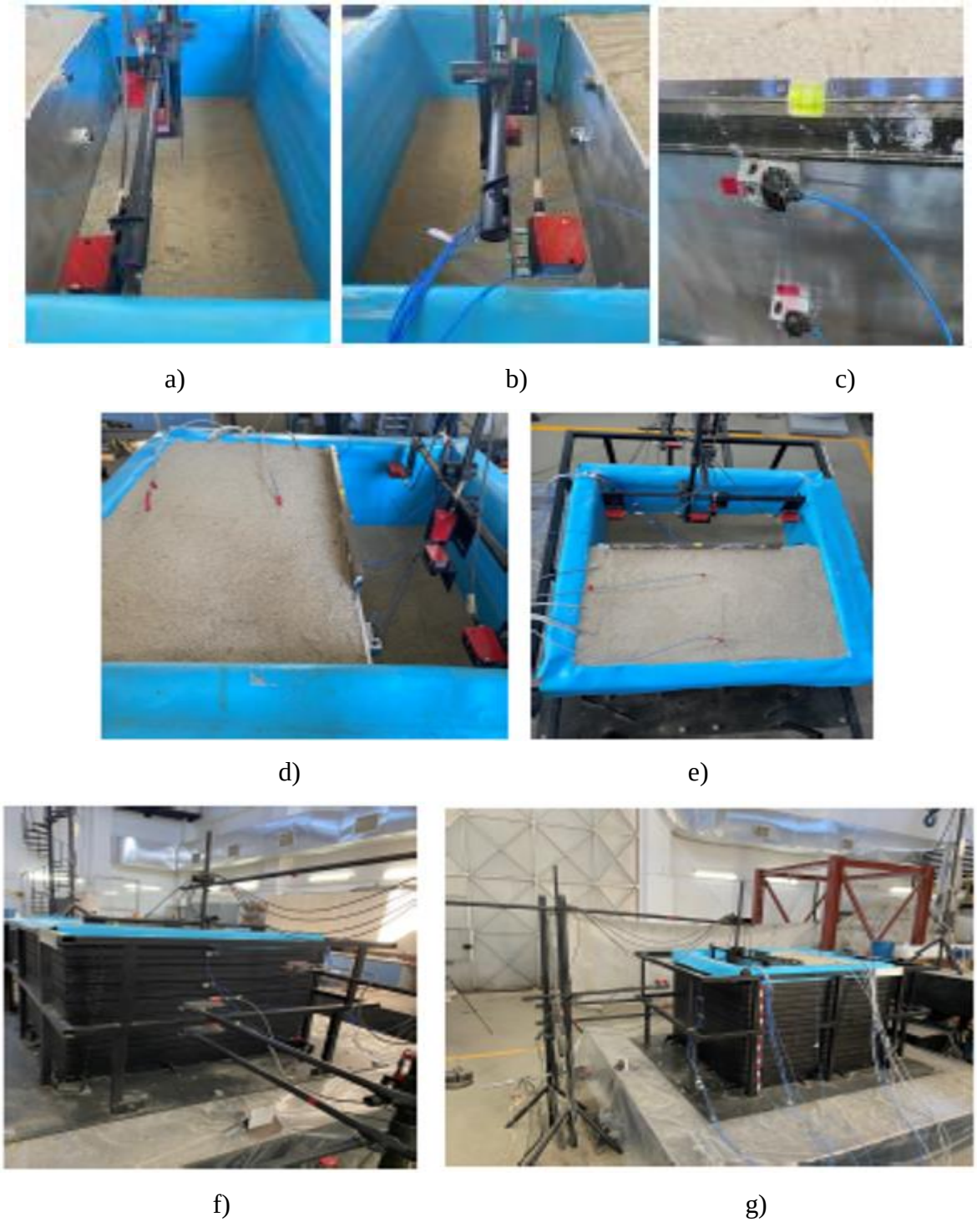

Figure 3.31. Instrumentation of the experimental study a-e) positioning of laser displacement sensors and placement of accelerometers on the retaining wall, f-g) placement of accelerometers and laser displacement sensors in the foundation backfill and on the laminar box and view of the set-up.

3.2.4.2. Preparation of the Control Case

The control case was prepared without cushion, and experimental tests were conducted for comparison with the cushioned cases. Firstly, the laminar box was securely placed on the shake table, and the layers inside the laminar box were coated with grease to eliminate the friction between the laminar box and the membrane. Following the application of grease, the membrane was positioned in place. The membrane was marked at regular intervals for each 10 cm of height. The dry sand was poured into the laminar box, and the compaction process began. The dry sand in the foundation layer and in the backfill was compacted until it reached the density of 16.5kN/$m^3$ and a relative density of 65%. Each layer of sand was manually compacted with hand compaction. The sand layer was placed and compacted into 3 layers, each 10 cm high, up to the 30 cm height of the foundation layer. Accelerometers A9, A10, and A11 were positioned in the middle of the foundation layer. Then, the next sand layer was placed and compacted into 3 layers, each 10 cm high, up to the 60 cm height of the foundation. Accelerometers A3, A4, A5, A6, A7, and A8 were placed on the retaining wall (Figure 3.31.c). A3 on the bottom right of the retaining wall, A4 on the bottom left of the retaining wall, A5 on the middle-middle of the retaining wall, A6 on the top right of the retaining wall, A7 on the top middle of the retaining wall, A8 on the top left of the retaining wall. After the foundation layer was completed, the retaining wall model was placed on top of the foundation layer.

After the retaining wall was installed, the backfill was compacted into three layers of 15 cm thickness, and accelerometers A12, A13, A14, A15, and A16 were placed during this process. Specifically, A12 was placed at a height of 60 cm from the backfill, A13 at the height of 75 cm, which is shown in Figure 33.a, and A14 at the height of 90 cm. All three accelerometers were positioned 10 cm away from the inner surface of the laminar box. Additionally, A15 was placed at the height of 75 cm, and A16 at the height of 90 cm, both positioned 5 cm close to the retaining wall (Figure 33.b). Furthermore, Figures 3.33.d-f depict the placement of accelerometers in the backfill, foundation, and retaining wall, along with the positioning of the laser displacement sensor. The laser displacement sensor system was then installed, positioning D18 in the middle of the retaining wall, D19 in the middle of the top of the retaining wall, D20 on the upper right corner, and D21 on the upper left corner. The backfill

surface and the sand surface in front of the retaining wall have been leveled. Figure 3.32 illustrates the experimental setup for the control case. The vibro-compaction was used to compact each case, and a sinusoidal motion at 0.2g amplitude with 9 Hz frequency for 90 seconds was applied during the vibro-compaction. After the setup for the control case was completed, experiments were performed by executing selected input motions. These experimental setups were conducted to investigate the behaviour of the control case, likely referring to the seismic behaviour of the retaining wall system without cushion.

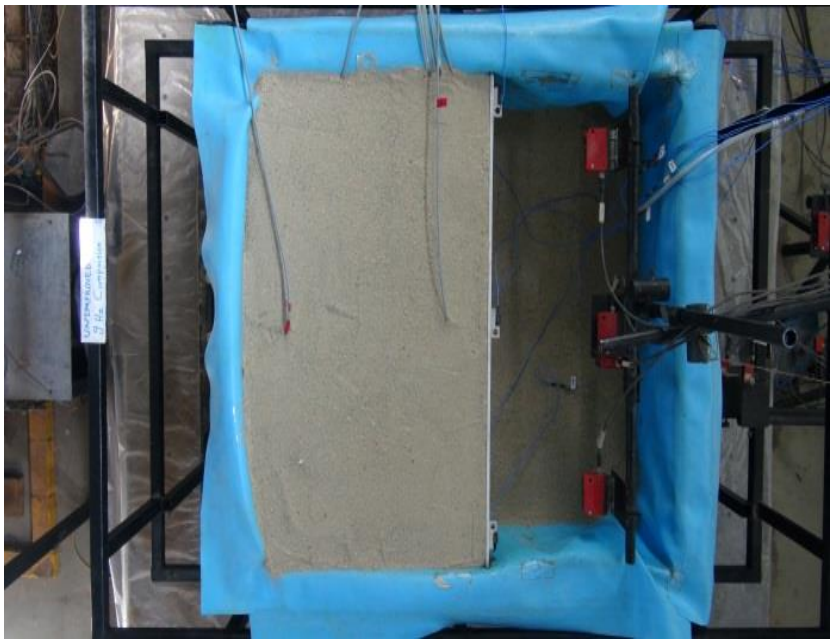

***Case 1 Control Case***

Figure 3.32 Retaining wall model without cushion (Control Case).

a) b)

c) d)

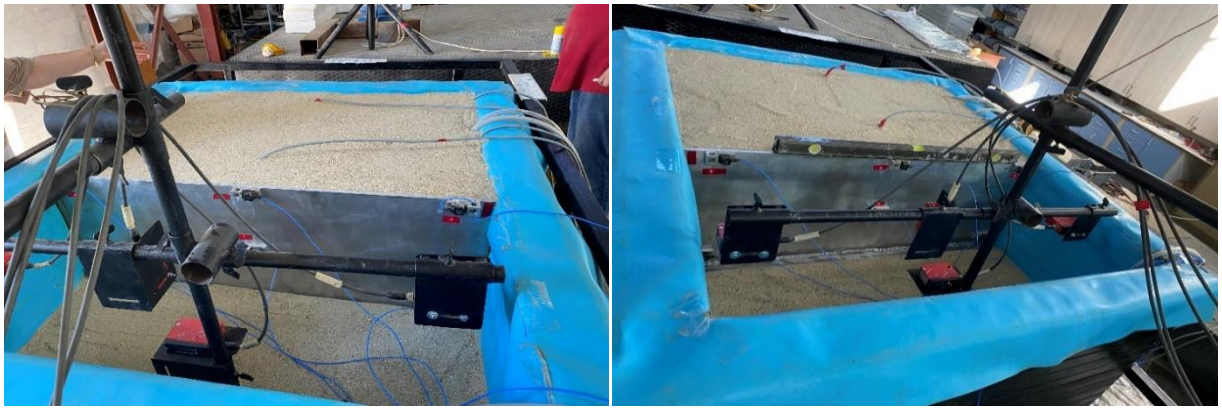

e) f)

Figure 3.33 The illustrations of the control case experimental setup a) placement of A13, b) placement of A15, c-f) placement of retaining wall model, accelerometers, and positioning of the laser displacement sensor.

3.2.4.3. Preparation of the EPS Geofoam Cushioned Cases

The study involved experimenting with 6 different variations of EPS geofoam, which had varying thicknesses and densities. Each of these variations was installed behind the retaining wall in 6 different cases, which were referred to as Case 2, Case 3, Case 4, Case 5, Case 6, and Case 7. The properties of EPS geofoam cushion material used for the cushioned cases are explained as Case 2 with a density of 10kN/$m^3$ and 4cm thickness (EPS10-4cm), Case 3 with a density of 20kN/$m^3$ and 4cm thickness (EPS20-4cm), Case 4 with a density of 30kN/$m^3$ and 4cm thickness (EPS30-4cm), Case 5 with a density of 10kN/$m^3$ and 8cm thickness (EPS10-8cm), Case 6 with a density of 20kN/$m^3$ and 8cm thickness (EPS20-8cm), Case 7 with a density of 30kN/$m^3$ and 8cm thickness (EPS30-8cm).

All procedures for the preparation of the foundation layer are as the same as the control case. Preparation of the EPS geofoam cushioned case is given in Figure 3.34. After the retaining wall was installed, the EPS geofoam cushion material was placed behind the retaining wall (Figure 3.34.a and Figure 3.34.b). The process was repeated for each case of the EPS geofoam cushioned cases, with the only difference being the substitution of the EPS geofoam cushion density and thickness.

Once the installation of the EPS geofoam cushion material, the backfill was poured and hand compacted into three layers of 15 cm thickness, and accelerometers A12, A13, A14, A15, and A16 were placed during this process (Figure 3.34.c). Specifically, A12 was placed at a height of 60 cm in the backfill, A13 at the height of 75 cm, and A14 at the height of 90 cm. All three accelerometers were positioned 10 cm away from the inner surface of the laminar box. Additionally, A15 was placed at the height of 75 cm and A16 at the height of 90 cm, both positioned 5 cm close to the EPS geofoam cushion material. The laser displacement sensor system was then positioned as the same as the control case. In addition, Figures 3.34.d-f illustrate the arrangement of accelerometers within the backfill, foundation, and retaining wall, as well as the location of the laser displacement sensor. The backfill surface and the sand surface in front of the retaining wall have been leveled. The vibro-compaction was utilized, which involved applying a sinusoidal motion at 0.2g amplitude with 9 Hz frequency and a duration of

90 seconds. Following the vibro-compaction, experiments were conducted by executing selected input motions. The experimental setup for the EPS Geofoam cushioned cases is depicted in Figure 3.35. The figure includes several sub-figures, with Figure 3.35.a displaying Case 2, Figure 3.35.b displaying Case 3, Figure 3.35.c displaying Case 4, Figure 3.35.d displaying Case 5, Figure 3.35.e displaying Case 6, and Figure 3.35.f displaying Case 7.

a) b)

c) d)

e) f)

Figure 3.34 The illustrations of the EPS geofoam cushioned cases experimental setup a-b) placement of EPS Geofoam, c) placement of backfill, d-e-f) positioning of accelerometers and laser displacement sensors.

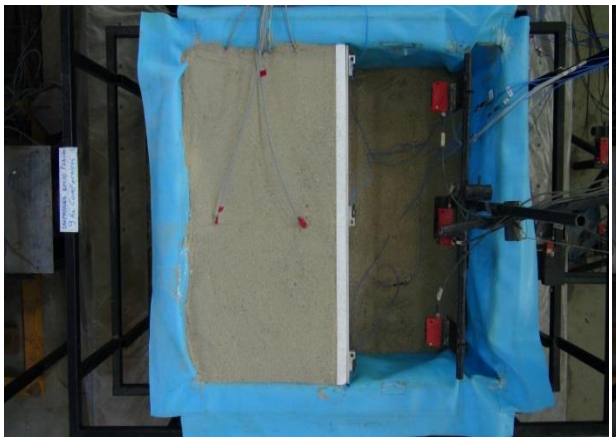

***Case 2 EPS10-4cm*** a)

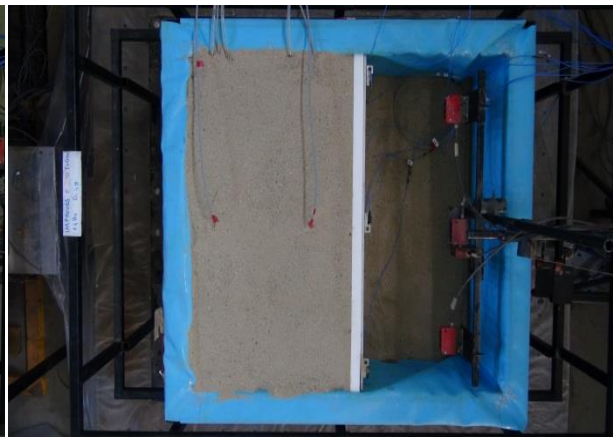

***Case 3 EPS20-4cm*** b)

***Case 4 EPS30-4cm*** c)

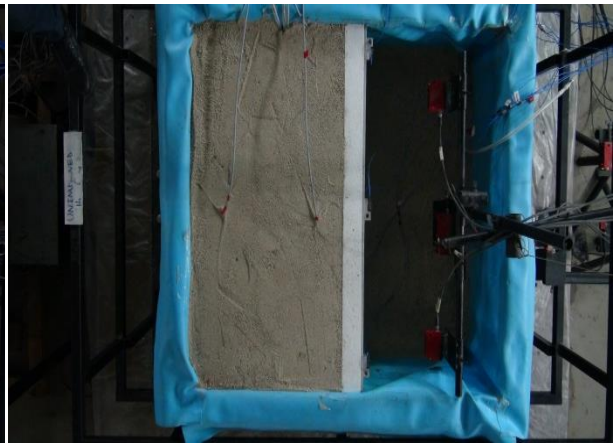

***Case 5 EPS10-8cm*** d)

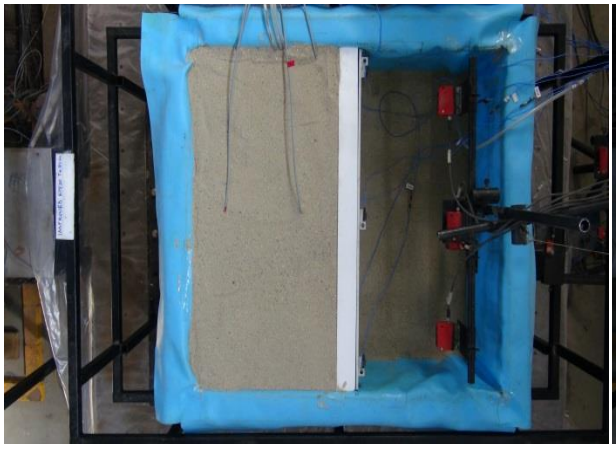

***Case 6 EPS20-8cm*** e)

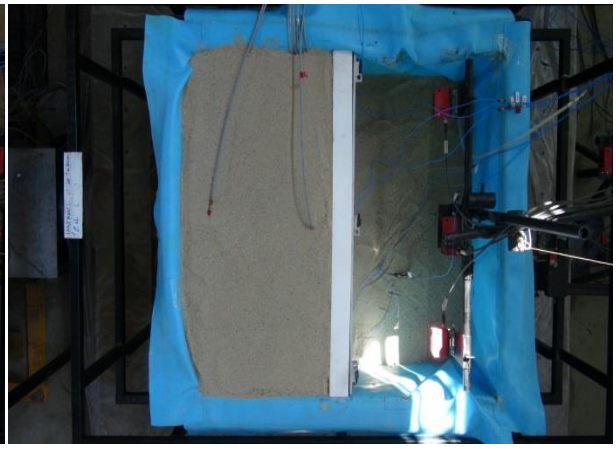

***Case 7 EPS30-8cm*** f)

Figure 3.35 EPS Geofoam cushioned cases of the study a) Case 2, b) Case 3, c) Case 4, d) Case 5, e) Case 6, f) Case 7.

3.2.4.4. Preparation of the Tire Waste and Sand Mixture Cushion Models

The study involved the experimental study consisting of 6 different variations of tire waste and sand mixture, which had varying thicknesses and mixture ratios. Each of these cushion materials was installed behind the retaining wall in 6 different cases, which were referred to as Case 8, Case 9, Case 10, Case 11, Case 12, Case 13. The mixture was prepared for different contents, and for all mixture ratios of TW cushions, the weight of the sand and tire waste materials were calculated and mixed uniformly in a big bowl, as shown in Figure 3.36.b. The properties of TW cushion material used for the cushioned cases are explained as Case 8 with density of 12.50kN/$m^3$ and 4cm thickness (TW10-4cm), Case 9 with density of 11.10kN/$m^3$ and 4cm thickness (TW20-4cm), Case 10 with density of 10.40kN/$m^3$ and 4cm thickness (TW30-4cm), Case 11 with density of 12.50kN/$m^3$ and 8cm thickness (TW10-8cm), Case 12 with density of 11.10kN/$m^3$ and 8cm thickness (TW20-8cm), Case 13 with density of 10.40kN/$m^3$ and 8cm thickness (TW30-8cm). TW cushions were compacted until they reached the specified density and relative density of 65% for each case.

Before the preparation of the experimental setups, all the sand in the laminar box is emptied (Figure 3.36.a). After that, all procedures for the foundation layer are as the same as the control case. In order to place the tire waste and sand mixture behind the retaining wall, galvanized sheet metal in the same dimensions as the stem was produced as an auxiliary material. After the retaining wall was installed carefully on the compacted foundation layer, the TW cushion was placed behind the retaining wall, as shown in Figure 3.36.c. and Figure 3.36.d. To ensure the correct thickness of the TW cushion during placement, styrofoam was cut to the thickness of the TW cushion and placed between the retaining wall and the galvanized sheet at specific intervals. As the TW cushion was added and compacted to obtain the unit weight of the cushion material, the styrofoam was pulled up, and when the TW cushion was fully placed, the styrofoam was removed.

At the same time, the cushion material was placed and compacted every 10cm, the backfill material was placed and compacted into three layers of 15 cm thickness, and accelerometers A12, A13, A14, A15, and A16 were placed during this process. A15 was placed

at the height of 75 cm, and A16 at the height of 90 cm, both positioned 5 cm close to the TW cushion material. The laser displacement sensor system was then installed. The placement of accelerometers in the backfill, foundation, and retaining wall, along with the positioning of the laser displacement sensor, are depicted in Figures 3.36.d-e. The backfill surface and the sand surface in front of the retaining wall have been smoothed. The TW cushioned cases were compacted using vibro-compaction, which involved applying a sinusoidal motion at 0.2g amplitude with 9 Hz frequency and a duration of 90 seconds. After the vibro-compaction, shake table experiments were performed by applying the selected input motions. The process was repeated for each case of the TW cushioned cases, with the only difference of the tire waste and sand mixture content. The experimental setup for the TW cushioned cases is depicted in Figure 3.37 where Figure 3.37.a exhibits Case 8, Figure 3.37.b exhibits Case 9, Figure 3.37.c exhibits Case 10, Figure 3.37.d exhibits Case 11, Figure 3.37.e exhibits Case 12, and Figure 3.37.f exhibits Case 13.

a) b)

c) d)

e) f)

Figure 3.36 The illustrations of the tire waste and sand mixture cushioned cases experimental setup a) emptying the laminar box, b) mixture preparation, c) placement of cushion, d) placement of backfill, e-f) positioning of accelerometers and laser displacement sensors.

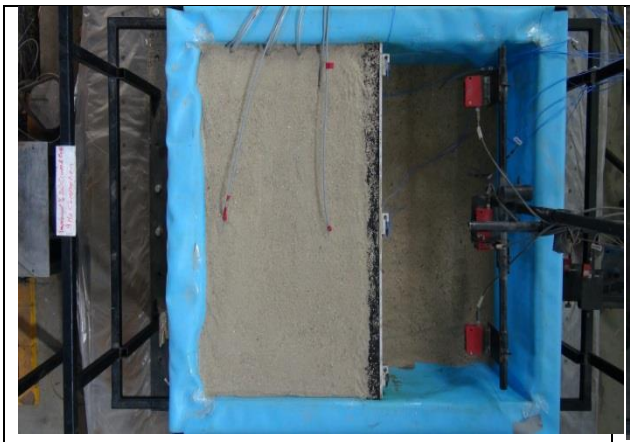

***Case 8 TW10-4cm*** a)

***Case 9 TW20-4cm*** b)

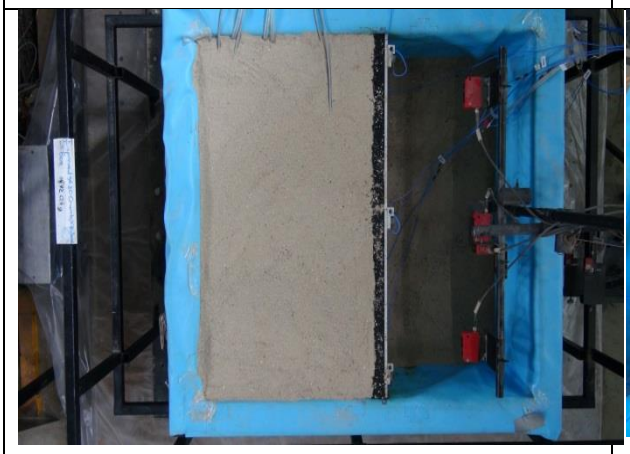

***Case 10 TW30-4cm*** c)

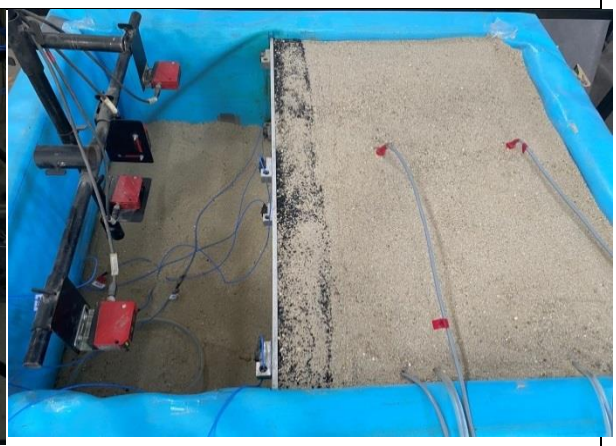

***Case 11 TW10-8cm*** d)

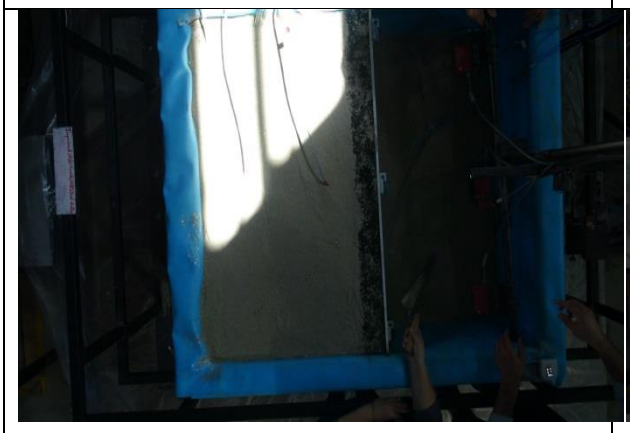

***Case 12 TW20-8cm*** e)

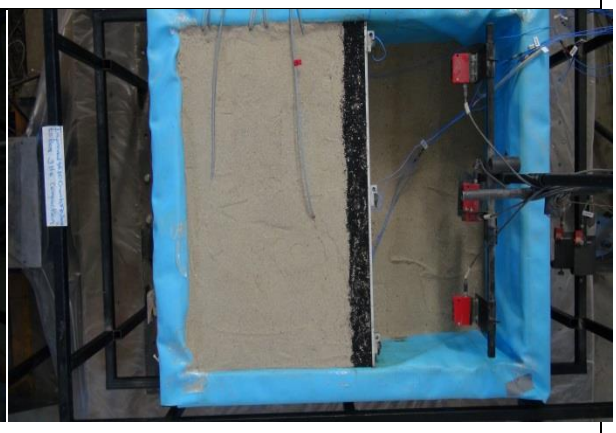

***Case 13 TW30-8cm*** f)

Figure 3.37 Tire waste and sand mixture cushioned cases of the study a) Case 8, b) Case 9, c) Case 10, d) Case 11, e) Case 12, f) Case 13.

3.2.4.5. Preparation of the EPS Beads and Sand Mixture Cushion Models

The experimental study involved 9 different variations of EPS beads and sand mixture, which had varying thicknesses and mixture ratios. Each of these variations was installed behind the retaining wall in 9 different cases, which were referred to as Case 14, Case 15, Case 16, Case 17, Case 18, Case 19, Case 20, Case 21 and Case 22. The EPS beads and sand were bonded together by the additional water without segregation. EPS beads, sand, and water with 10% by volume were mixed into a big plastic bowl and thoroughly mixed until a uniform mixture was obtained, as shown in Figure 3.38.a and Figure 3.38.b. The properties of EPSB cushion material used for the cushioned cases are explained as Case 14 with density of 10.10kN/$m^3$ and 4cm thickness (EPSB10-4cm), Case 15 with density of 8.20kN/$m^3$ and 4cm thickness (EPSB20-4cm), Case 16 with density of 6.30kN/$m^3$ and 4cm thickness (EPSB30-4cm), Case 17 with density of 10.10kN/$m^3$ and 6cm thickness (EPSB10-6cm), Case 18 with density of 8.20kN/$m^3$ and 6cm thickness (EPSB20-6cm), Case 19 with density of 6.30kN/$m^3$ and 6cm thickness (EPSB30-6cm), Case 20 with density of 10.10kN/$m^3$ and 8cm thickness (EPSB10-8cm), Case 21 with density of 8.20kN/$m^3$ and 8cm thickness (EPSB20-8cm), Case 22 with density of 6.30kN/$m^3$ and 8cm thickness (EPSB30-8cm). EPSB cushions were compacted until they reached the specified density and relative density of 65% for each case.

To prepare the setups, the sand in the laminar box is emptied beforehand, as shown in Figure 3.38.c. The test procedure for the preparation of the foundation layer is the same for the control case. In order to place the EPSB cushion material behind the retaining wall, galvanized sheet metal in the same dimensions of the stem was produced as an auxiliary material. After the retaining wall was installed carefully on the compacted foundation layer, the EPSB cushion were placed behind the retaining wall, as shown in Figure 3.38.d. and Figure 3.38.e. To make sure that the EPSB cushion was placed with the proper thickness, styrofoam was cut to the thickness of the EPSB cushion and placed between the retaining wall and the galvanized sheet at specific intervals. As the EPSB cushion material was added and compacted to obtain the unit weight of the cushion material, the styrofoam was pulled up, and when the EPSB cushion was fully placed, the styrofoam was removed.

At the same time, the EPSB cushion material was placed and compacted every 10cm, the backfill was poured and compacted into three layers of 15 cm thickness, and accelerometers A12, A13, A14, A15, and A16 were placed during this process. A15 was placed at the height of 75 cm, and A16 at the height of 90 cm, both positioned 5 cm close to the EPSB cushion material. The laser displacement sensor system was then installed. The placement of accelerometers in the backfill, foundation, and retaining wall, along with the positioning of the laser displacement sensor, are depicted in Figure 3.38.f. The backfill surface and the sand surface in front of the retaining wall have been leveled. The EPSB cushioned cases were compacted through vibro-compaction, which utilized a sinusoidal motion at 0.2g amplitude with 9 Hz frequency and lasted for a duration of 90 seconds. Following the vibro-compaction, experiments were carried out using far field, near field, and sinusoidal input motions. The process was repeated for each case of the EPSB cushioned cases, with the only difference of the EPS beads and sand mixture content and thickness. The process of conducting experiments on EPSB cushioned cases is illustrated in Figure 3.39. Each subfigure within Figure 3.39 represents a different case. Specifically, Figure 3.39.a corresponds to Case 14, Figure 3.39.b corresponds to Case 15, Figure 3.39.c corresponds to Case 16, Figure 3.39.d corresponds to Case 17, Figure 3.39.e corresponds to Case 18, Figure 3.39.f corresponds to Case 19. Figure 3.39.g corresponds to Case 20, Figure 3.39.h corresponds to Case 21 and Figure 3.39.i corresponds to Case 22.

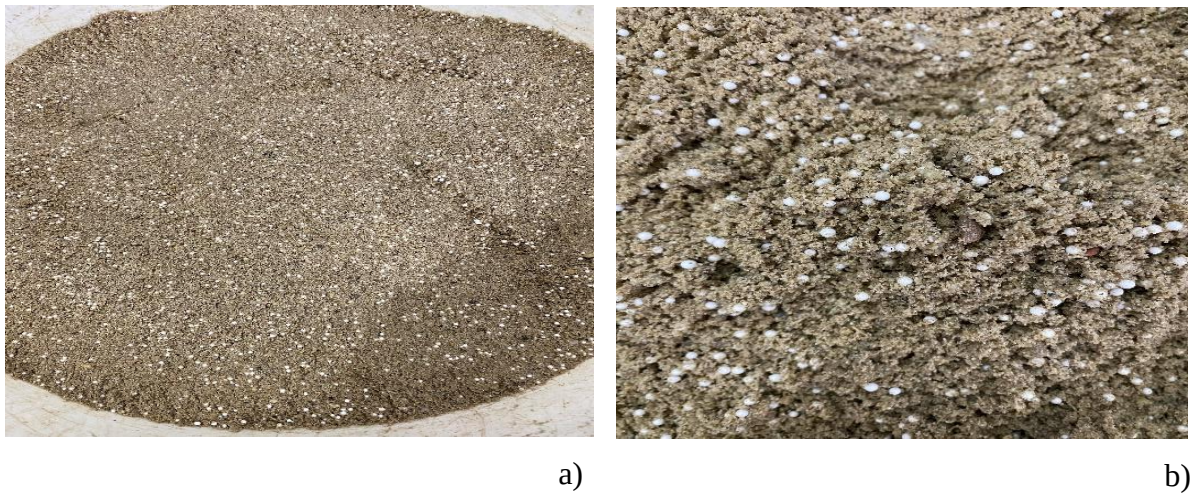

a) b)

c) d)

e) f)

Figure 3.38 EPS beads and sand mixture cushioned cases experimental setup a-b) mixture preparation, c) unloading process, d-e) placement of cushion and placement of backfill, f) positioning of accelerometers and laser displacement sensors.

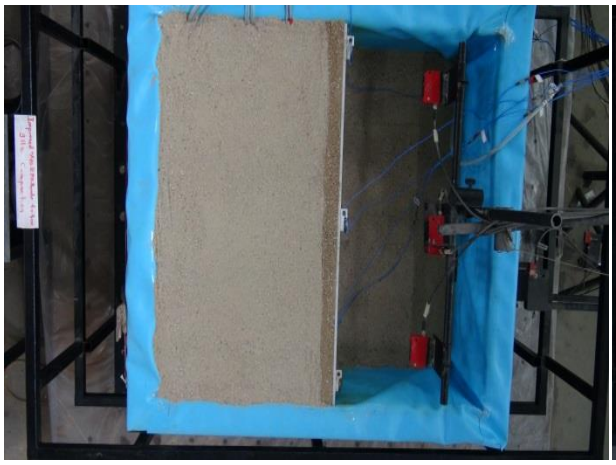

***Case 14 EPSB10-4cm*** a)

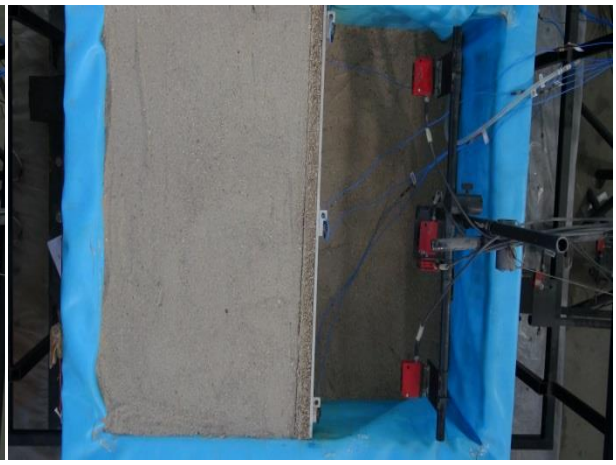

***Case 15 EPSB20-4cm*** b)

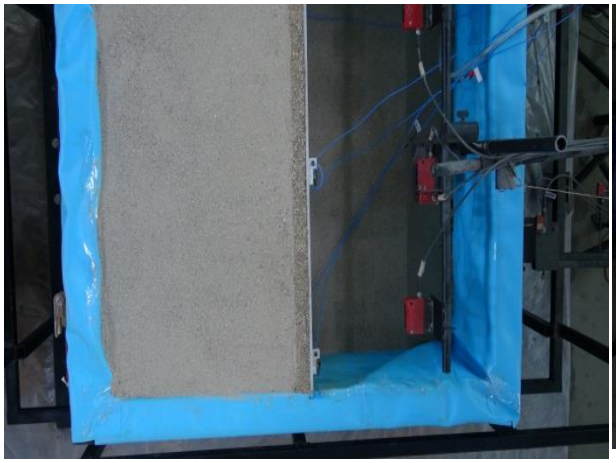

***Case 16 EPSB30-4cm*** c)

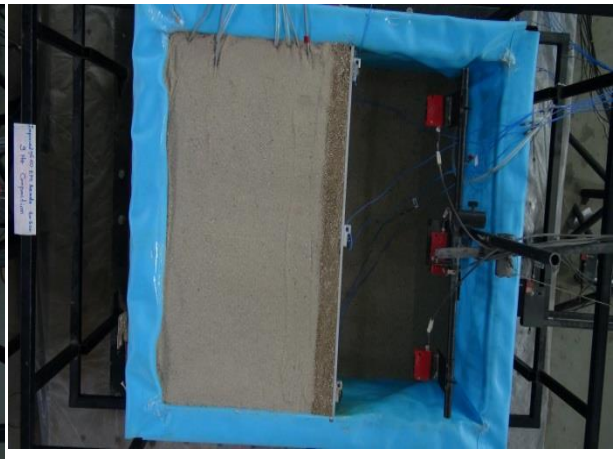

***Case 17 EPSB10-6cm*** d)

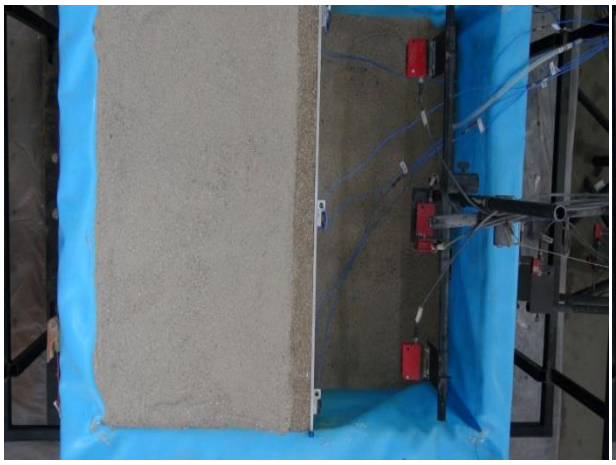

***Case 18 EPSB20-6cm*** e)

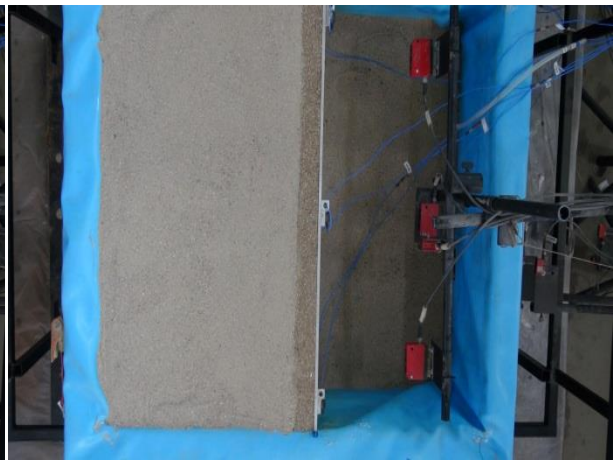

***Case 19 EPSB30-6cm*** f)

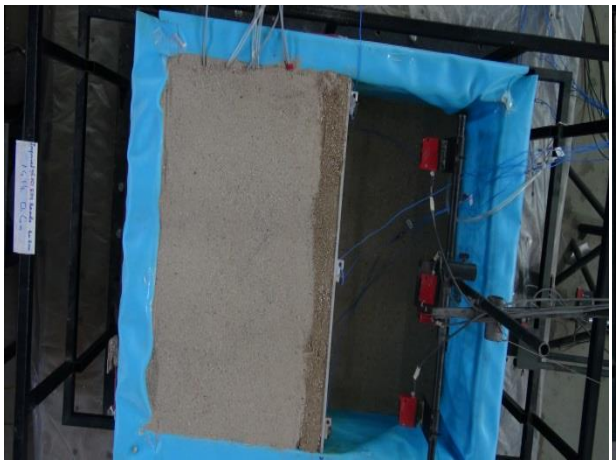

***Case 20 EPSB10-8cm*** g)

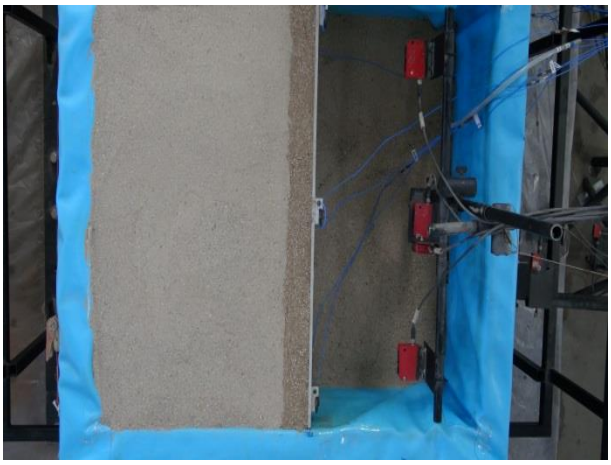

***Case 21 EPSB20-8cm*** h)

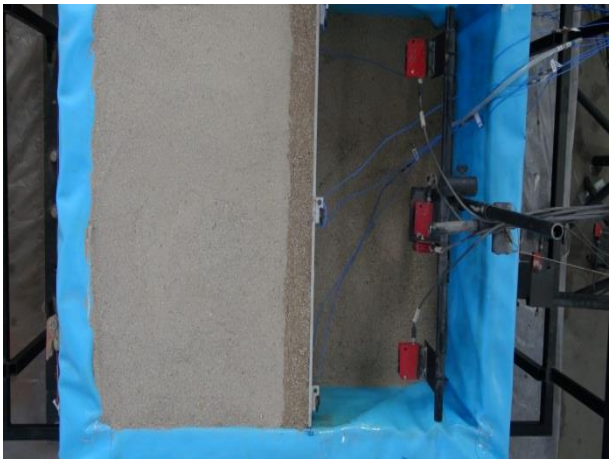

***Case 22 EPSB30-8cm*** i)

Figure 3.39 EPS beads and sand mixture cushioned cases of the study a) Case14, b) Case 15, c) Case 16, d) Case 17, e) Case 18, f) Case 19, g) Case 20, h) Case 21, i) Case 22.

# 4. RESULTS OF THE EXPERIMENTAL STUDY

This thesis study consists of experimental studies executed with EPS geofoam, tire waste and sand mixture, and EPS beads and sand mixture as cushions behind the retaining wall to compare the seismic performance of the retaining wall.

The ultimate aim of this study is to compare all the results of the seismic performance tests of the retaining wall. EPS beads and sand mixture is used for the first time as a cushion material in this experimental study. The efficiency and effectiveness of a new cushion layer for retaining structures composed of sand and EPS beads mixture are assessed. The study examines the impact of mixture ratio and thickness on the cushion layer. Under the same input motions, the performances of the cushion layers made of EPS geofoam, tire waste and sand mixture (TW), and EPS beads and sand mixture (EPSB) cushion were compared to those of the control case (unimproved case).

The far field earthquakes, near field earthquakes, and sinusoidal input motions were executed for 22 cases in Table 3.6. The Acceleration-Time Histories (ACCTH), Fourier Amplitude Spectrums (FAS), Response Spectrums, and Displacement-Time Histories (DISTH) of all 22 cases are presented for far field earthquake as the scaled 2020 İzmir EQ Motion-Kuşadası Station record, near field earthquake as the scaled 1940 Imperial Valley EQ-El Centro Station record and sinusoidal motion at 0.4g amplitude with 8 Hz frequency acquired from the sensor A7 accelerometer and D19 laser displacement sensor at the top of the retaining wall model (RWM) and A16 accelerometer in the backfill.

## 4.1. Results of Case 1 – Control Case

The control case (Case 1) is the only case without any cushion layer. The results under two different earthquake motions and one sinusoidal motion acquired from accelerometer A7, laser displacement sensor D19 at the top of the retaining wall model (RWM), and accelerometer A16 in the backfill are given in comparison with the control case in Figure 4.1, Figure 4.2, Figure 4.3, Figure 4.4, Figure 4.5 and Figure 4.6.

Figure 4.1 shows the Acceleration-Time Histories, Fourier Amplitude Spectrums, and Response Spectrums under the scaled 2020 İzmir EQ Motion-Kuşadası Station excitations. It was measured maximum acceleration of 0.27g at the top of the RWM, and 0.19g in the backfill for the control case. Fourier amplitudes peaked around 9.25 Hz at the top of the RWM and in the backfill for the input and control case. The maximum spectral accelerations were at 0.05 sec and 0.13 sec period ranges. The maximum spectral accelerations were at 0.05 sec and 0.15 sec period ranges and 0.98g at the top of the RWM and 0.76g in the backfill for the control case, respectively. The maximum spectral accelerations increased from A16 to A7 at a ratio of 29%.

As represented in Figure 4.2, the maximum displacement of the control case was measured 0.37cm at the top of the RWM acquired from D19 under the scaled 2020 İzmir EQ Motion-Kuşadası Station record.

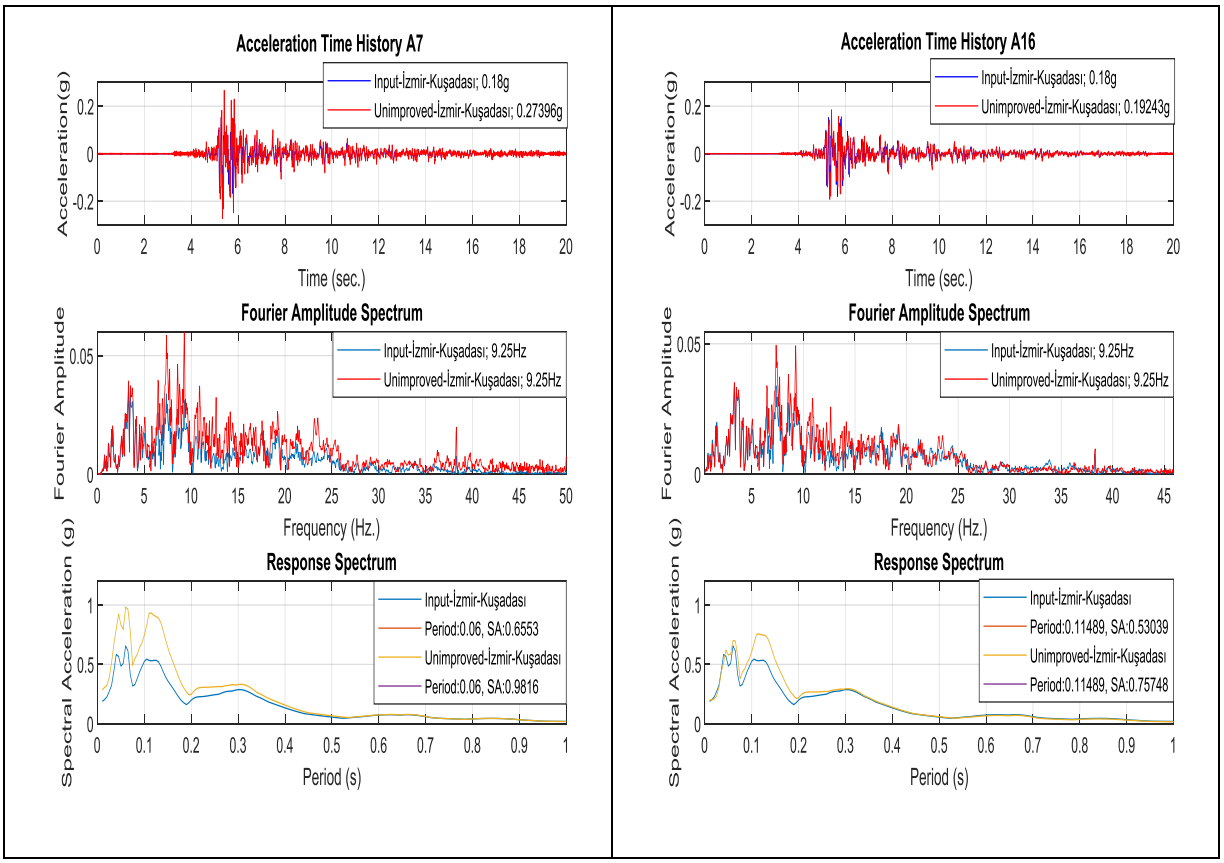


Figure 4.1. The ACCTH, FAS, Response Spectrum at the top of the RWM (A7) and in the backfill (A16) for Case 1 compared to input motion (A1) under the scaled 2020 İzmir EQ Motion-Kuşadası Station record (FF).

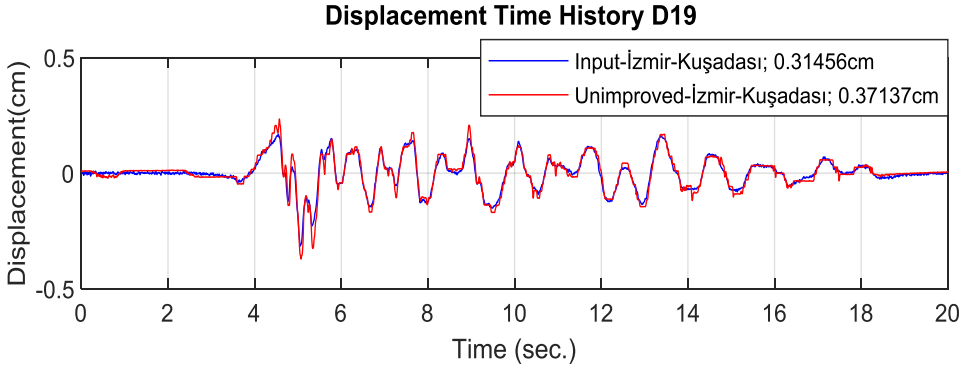


Figure 4.2. The DISTH at the top of the RWM (D19) for Case 1 compared to input motion (D17) under the scaled 2020 İzmir EQ Motion-Kuşadası Station record (FF).

Under the scaled 1940 Imperial Valley EQ-El Centro Station record (NF), the Acceleration-Time Histories, Fourier Amplitude Spectrums, and Response Spectrums are shown in Figure 4.3. The A7 measured 0.52g maximum acceleration, and the A16 measured 0.32g maximum acceleration for the control case. Fourier amplitudes peaked around 4.58 Hz from A7 and A16. The maximum spectral accelerations were at 0.05 sec and 0.22 sec period ranges. The maximum spectral accelerations were 1.48g at 0.055 sec period at the top of the RWM and 1.26g at 0.22 sec period in the backfill measured from A16.

Figure 4.4 presents the displacement time history of the control case compared to the input motion under the scaled 1940 Imperial Valley EQ-El Centro Station record. The maximum displacement of the control case was measured as 1.88 cm at the top of the RWM acquired from D19.

The Acceleration-Time Histories, Fourier Amplitude Spectrums, and Response Spectrums under the sinusoidal motion at 0.4g amplitude with 8 Hz frequency are shown in Figure 4.5. It was measured 0.47g from the A7, and the A16 measured 0.36g of maximum accelerations for the control case, respectively. The Fourier amplitude peaks were 8 Hz at the top of the RWM in the backfill for the input motion and the control case. The maximum spectral accelerations were at 0.12 sec period, 4.7g at the top of the RWM, and 3.81g in the backfill for the control case, respectively.

Figure 4.6 presents the displacement time history of the control case compared to the cushioned case under sinusoidal motion at 0.4g amplitude with 8 Hz frequency. Maximum displacement was measured as 0.20 cm acquired from D19.

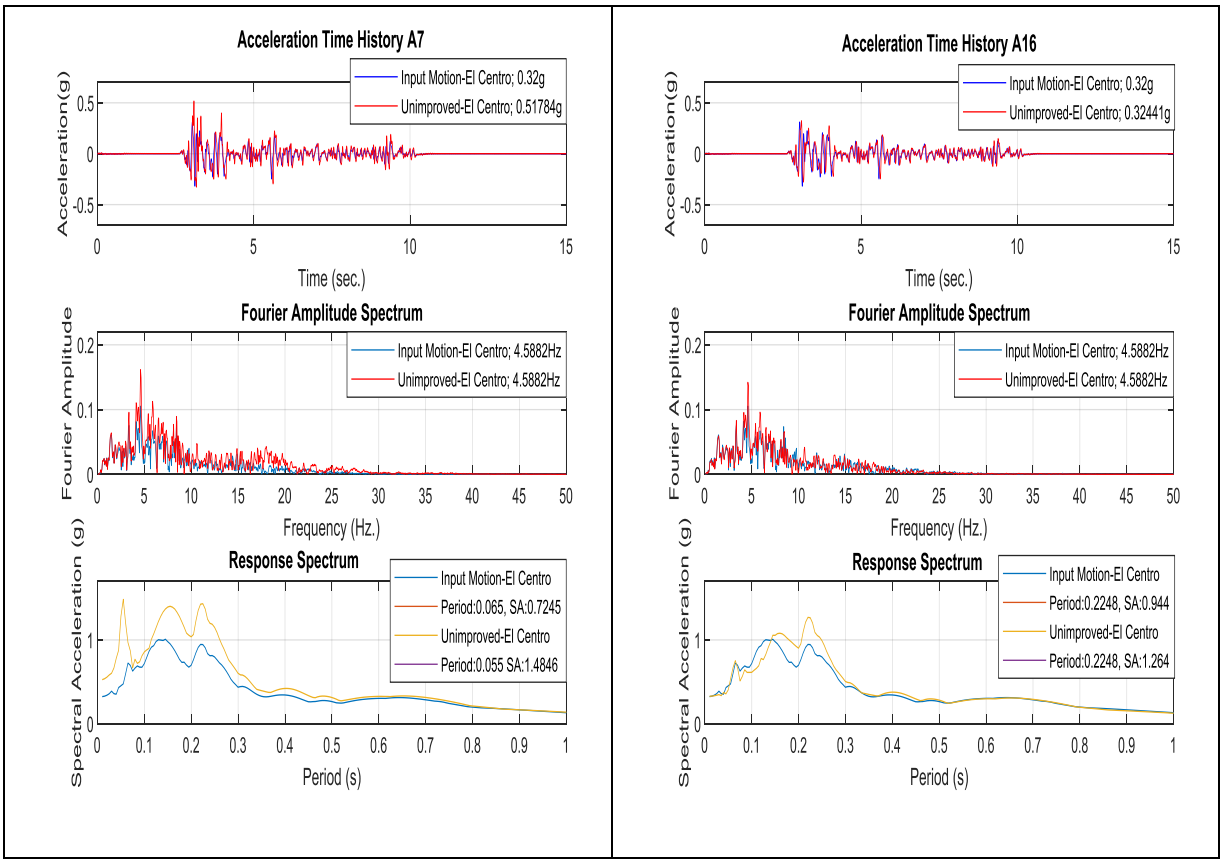


Figure 4.3. The ACCTH, FAS, Response Spectrum at the top of the RWM (A7) and in the backfill (A16) for Case 1 compared to input motion (A1) under the scaled 1940 Imperial Valley EQ-El Centro Station record (NF).

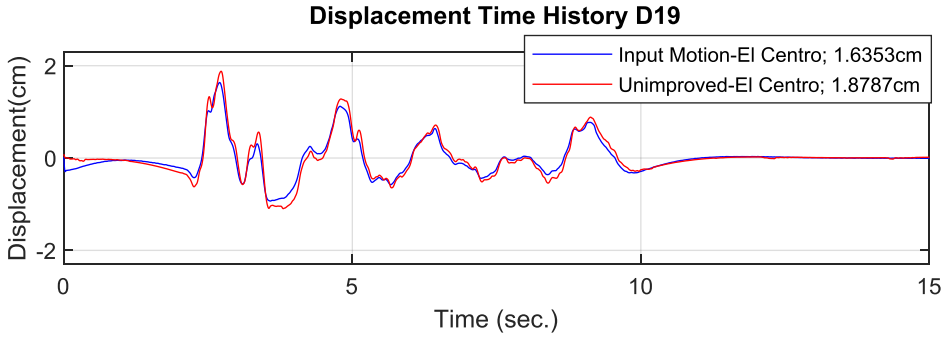


Figure 4.4. The DISTH at the top of the RWM (D19) for Case 1 compared to input motion (D17) under the scaled 1940 Imperial Valley EQ-El Centro Station record (NF).

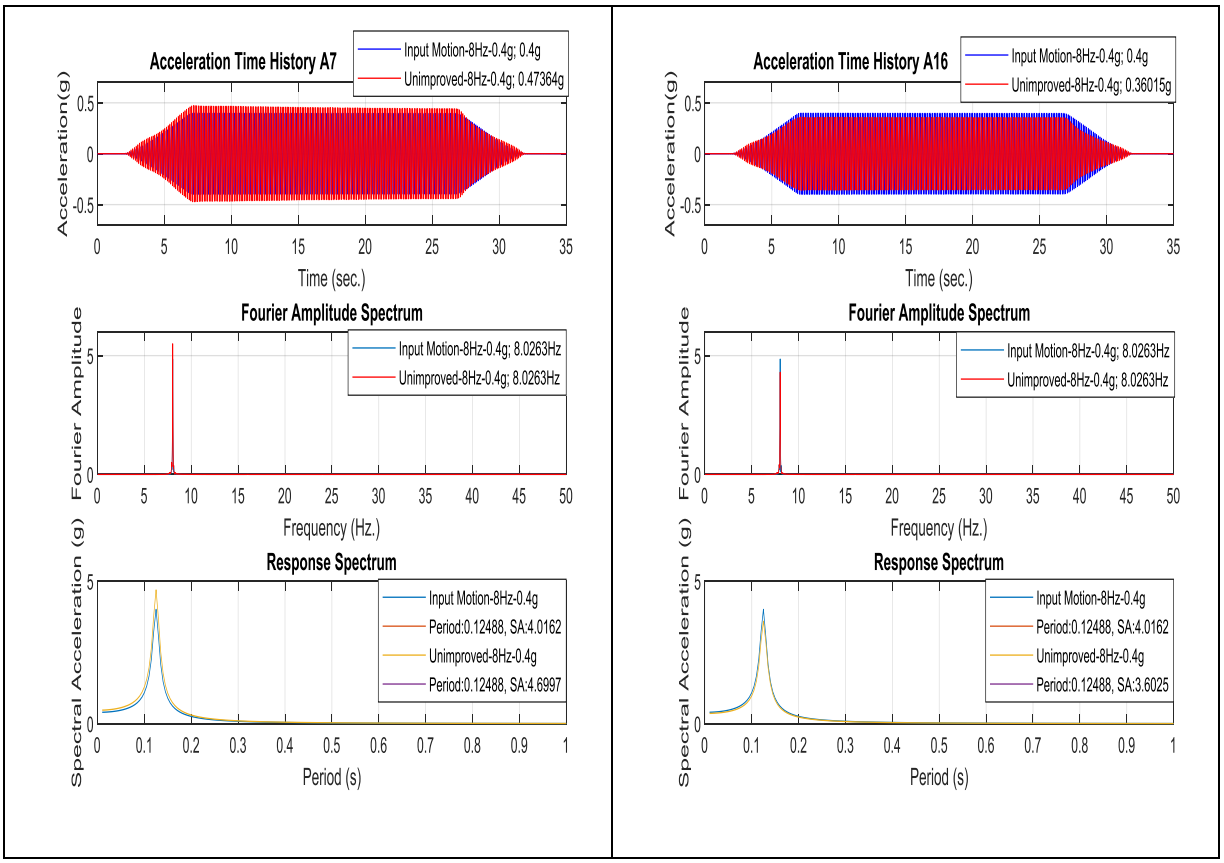


Figure 4.5. The ACCTH, FAS, Response Spectrum at the top of the RWM (A7) and in the backfill (A16) for Case 1 compared to input motion (A1) under sinusoidal motion at 0.4g amplitude with 8 Hz frequency.

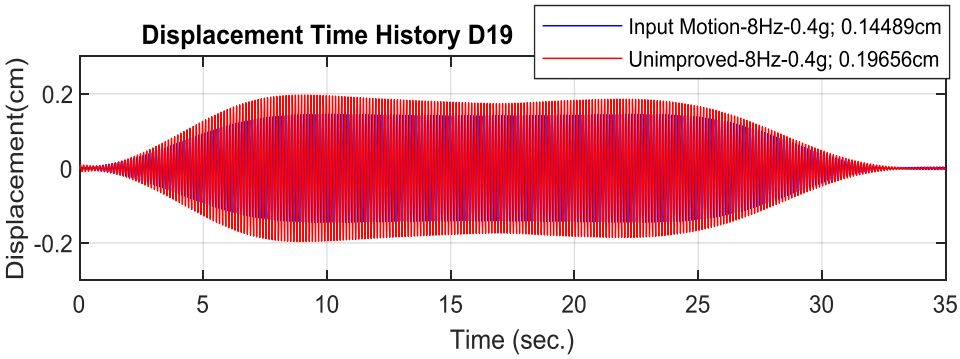


Figure 4.6. The DISTH at the top of the RWM (D19) for Case 1 compared to input motion (D17) under sinusoidal motion at 0.4g amplitude with 8 Hz frequency.

## 4.2. Results of Case 2 - EPS10-4cm

Case 2 in this thesis study consists of EPS Geofoam cushion with a density of 0.10 $kN/m^3$ and 4 cm thickness (EPS10-4cm) behind the RWM. The results under two different earthquake motions and one sinusoidal motion acquired from accelerometer A7, laser displacement sensor D19 at the top of the retaining wall model (RWM), and accelerometer A16 in the backfill are given in comparison with the control case in Figure 4.7, Figure 4.8, Figure 4.9, Figure 4.10, Figure 4.11, Figure 4.12.

Figure 4.7 shows the Acceleration-Time Histories, Fourier Amplitude Spectrums, and Response Spectrums under the scaled 2020 İzmir EQ Motion-Kuşadası Station (FF) excitations for Case 2 in comparison with the control case Case 1. The A7 recorded maximum acceleration values of 0.27g and 0.24g, while the A16 measured 0.19g and 0.18g for the control case (Case 1) and cushioned case (Case 2), respectively. It can be noticed that the maximum acceleration values decreased at the top of the RWM and in the backfill when the EPS10-4cm cushion was implemented. Fourier amplitudes decreased from 9.25 Hz to 7.35 Hz at the top of the RWM and in the backfill for the cushioned case compared to the control case, respectively. The maximum spectral accelerations were at 0.05 sec and 0.13 sec period ranges. The maximum spectral accelerations ($S_a$) of 0.98g decreased to 0.70g at the top of the RWM at a period of 0.06 sec, and 0.76g decreased to 0.69g in the backfill at a period of 0.11 sec for the cushioned case compared to the control case, respectively.

As represented in Figure 4.8, the control case deforms around 0.37cm, whereas the EPS10-4cm cushioned model deforms 0.36cm under the scaled 2020 İzmir EQ Motion-Kuşadası Station record.

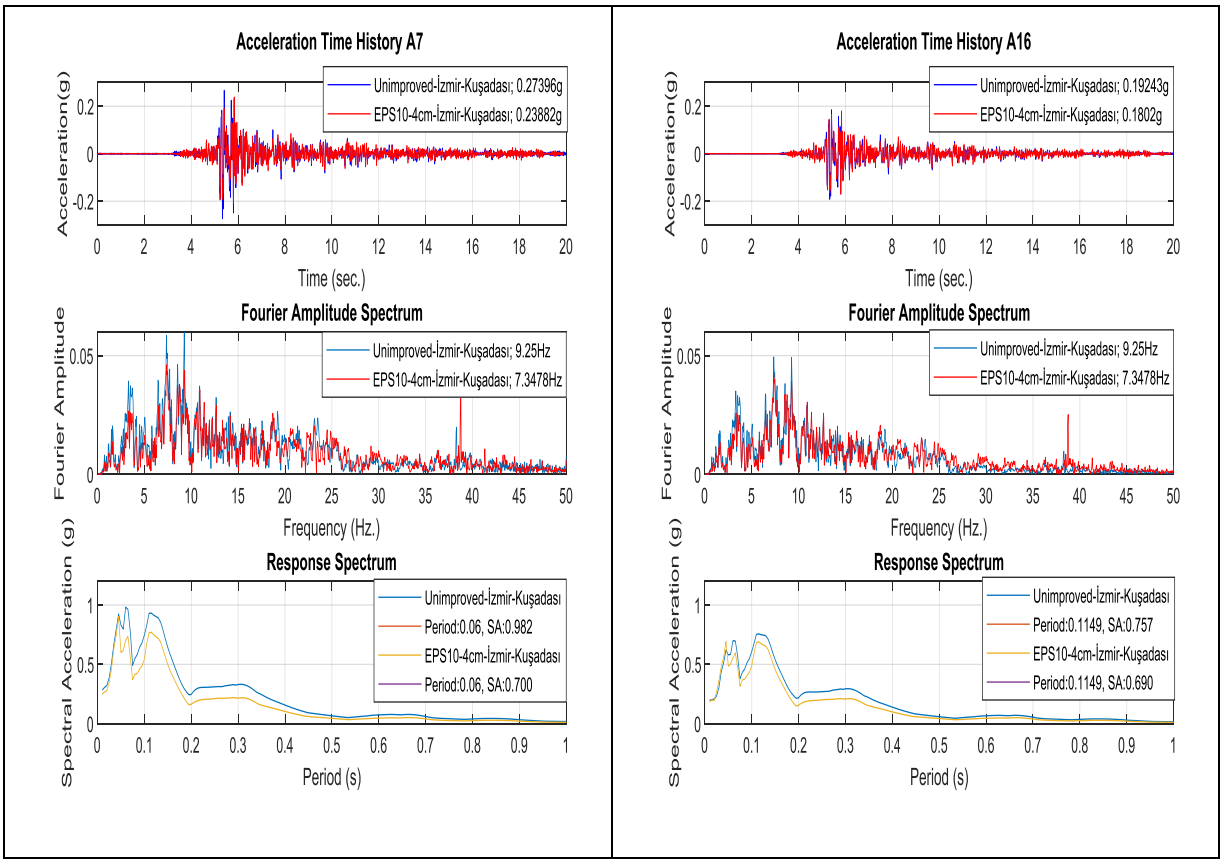


Figure 4.7. The ACCTH, FAS, Response Spectrum at the top of the RWM (A7) and in the backfill (A16) for Case 2 compared to Case 1 under the scaled 2020 İzmir EQ Motion-Kuşadası Station record (FF).

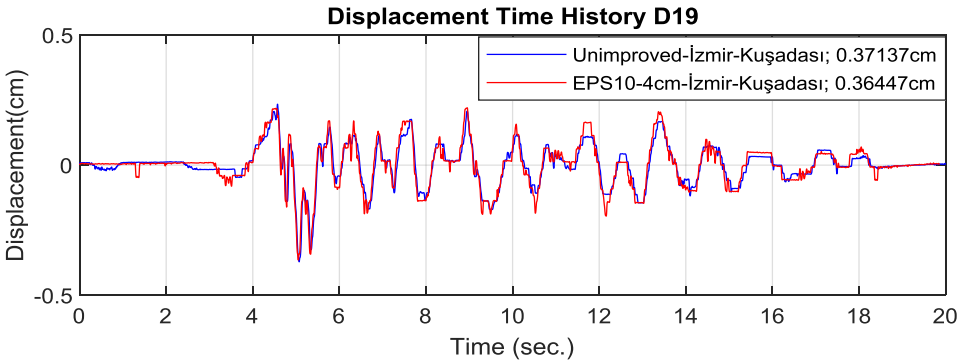


Figure 4.8. The DISTH at the top of the RWM (D19) for Case 2 compared to Case 1 under the scaled 2020 İzmir EQ Motion-Kuşadası Station record (FF).

Under the scaled 1940 Imperial Valley EQ-El Centro Station record (NF) the Acceleration-Time Histories, Fourier Amplitude Spectrums, and Response Spectrums are shown in Figure 4.9. It was measured 0.52g maximum acceleration from the A7 for the control case and decreased to 0.45g maximum acceleration for the EPS10-4cm cushioned case. The A16 measured 0.32g maximum acceleration for the control case and 0.39g for the cushioned case. Fourier amplitudes peaked around 4.62 Hz and 4.59 Hz at the top of the RWM and in the backfill for the control and cushioned cases, respectively. The maximum spectral accelerations were at 0.05 sec and 0.22 sec period ranges. The maximum spectral accelerations ($S_a$) were 1.48g at 0.055 sec period at the top of the RWM, decreasing to 1.27g and increasing from 1.26g to 1.34g at the same periods of 0.22 sec in the backfill for the control case and EPS10-4cm cushioned cases, respectively.

Figure 4.10 presents the displacement time history of the control case compared to the cushioned case under the scaled 1940 Imperial Valley EQ-El Centro Station record. The maximum displacement of the EPS10-4cm cushioned model decreased to 1.79 cm, while the control case was measured as 1.88 cm at the top of the RWM. The peak displacement decreased when the cushioned case EPS10-4cm cushion was installed behind the retaining wall model.

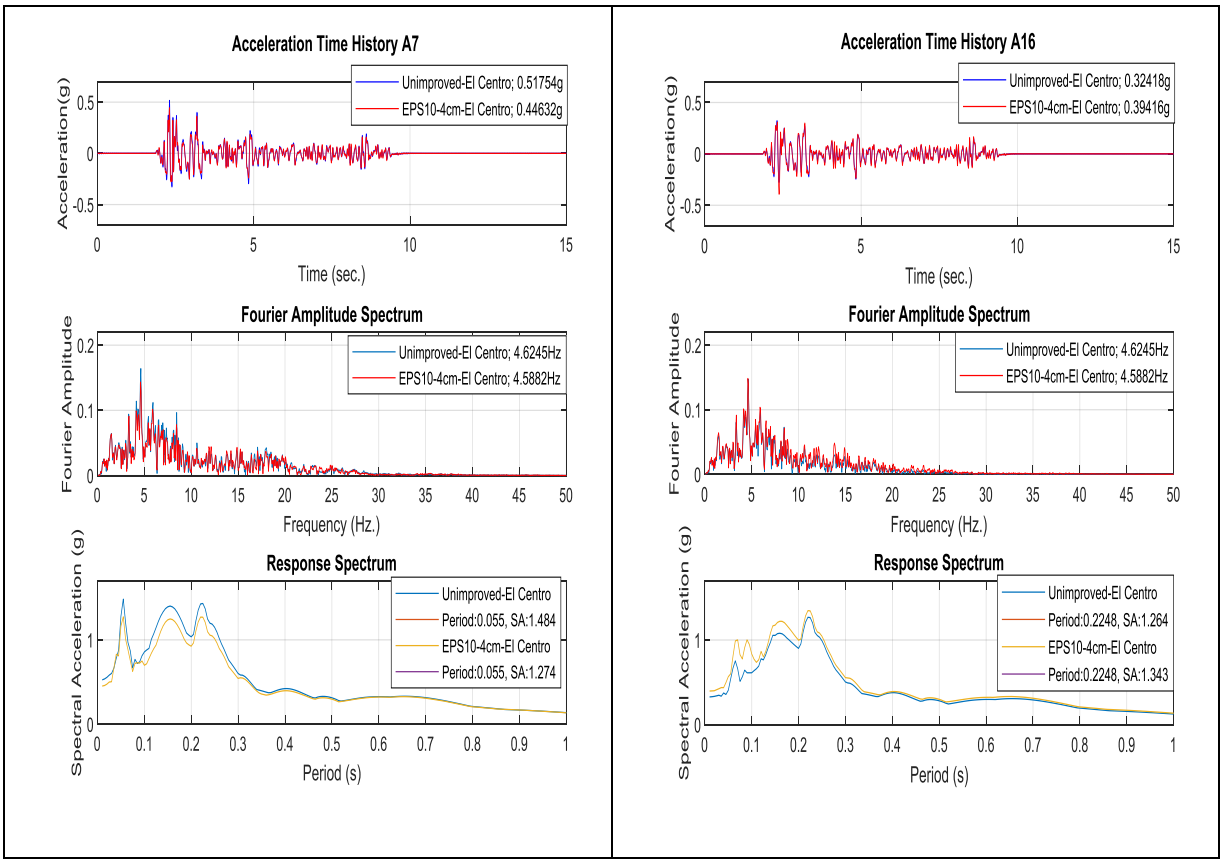


Figure 4.9. The ACCTH, FAS, Response Spectrum at the top of the RWM (A7) and in the backfill (A16) for Case 2 compared to Case 1 under the scaled 1940 Imperial Valley EQ-El Centro Station record (NF).

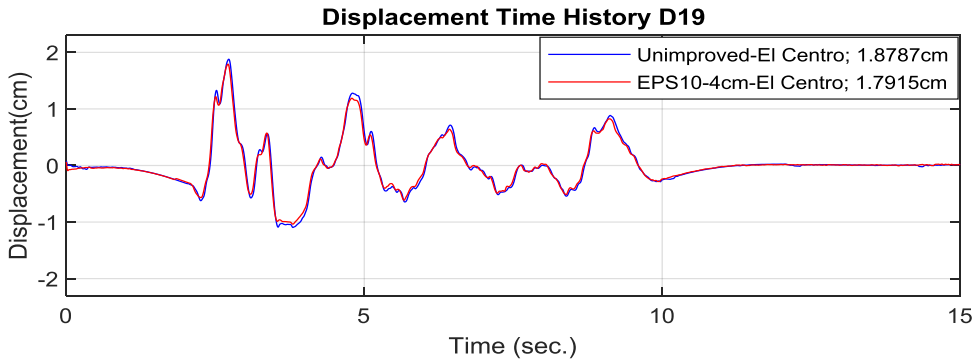


Figure 4.10. The DISTH at the top of the RWM (D19) for Case 2 compared to Case 1 under the scaled 1940 Imperial Valley EQ-El Centro Station record (NF).

The Acceleration-Time Histories, Fourier Amplitude Spectrums, and Response Spectrums under the sinusoidal motion at 0.4g amplitude with 8 Hz frequency are shown in Figure 4.11. Maximum acceleration for the EPS10-4cm cushioned case was measured as 0.42g at the top of the RWM and 0.47g for the control case. The A16 measured a maximum acceleration of 0.40g for the cushioned case and 0.36g for the control case. The Fourier amplitude peaks were 8.03 Hz and 8.02 Hz at the top of the RWM and in the backfill for the cushioned and control cases, respectively. The maximum spectral accelerations ($S_a$) were at 0.12 sec period, decreasing from 4.7g to 4.14g at the top of the RWM and increasing from 3.81g to 3.96g in the backfill for the control case and cushioned cases, respectively.

Figure 4.12 presents the displacement time history of the control case compared to the cushioned case. A reduction was observed in displacement measurement under the sinusoidal motion at 0.4g amplitude with 8Hz. Maximum displacement was measured as 0.15 cm at the top of the RWM for the cushioned case, whereas it was measured as 0.20 cm for the control case.

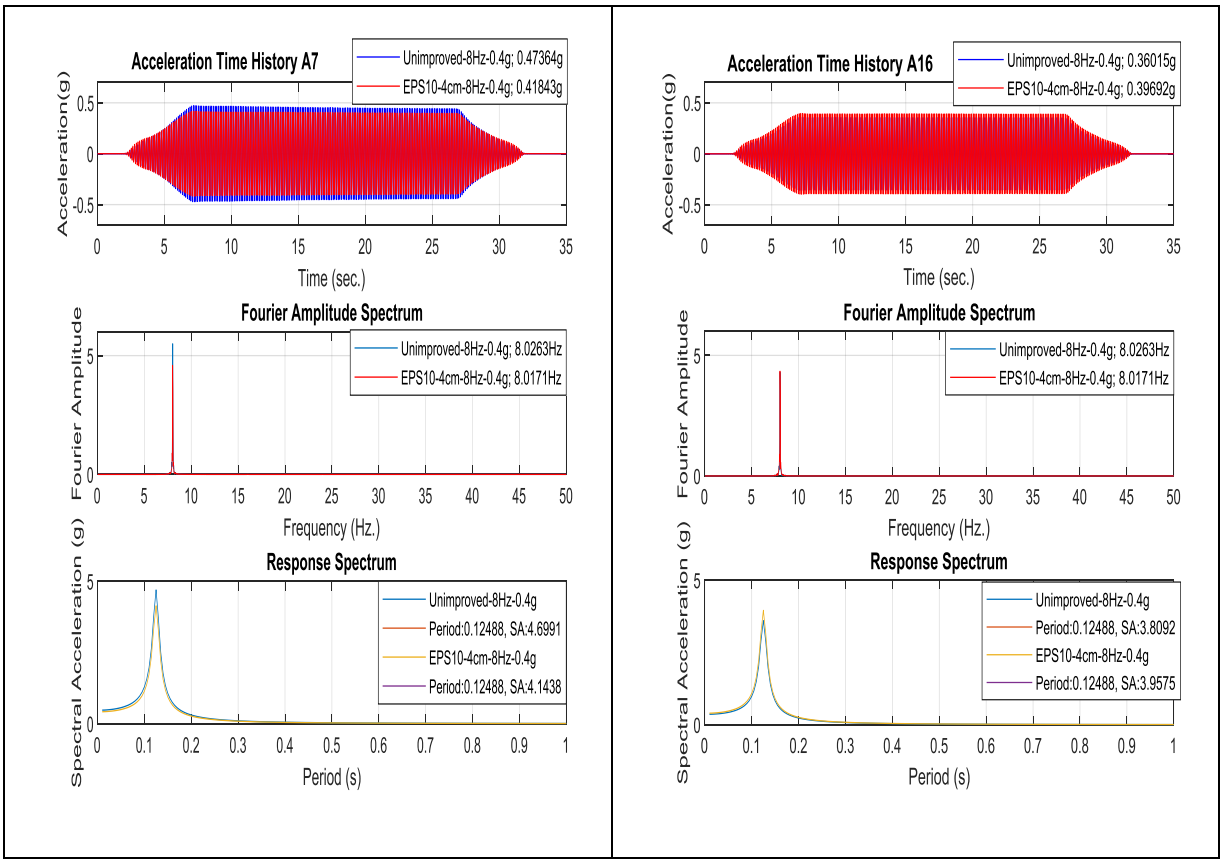


Figure 4.11. The ACCTH, FAS, Response Spectrum at the top of the RWM (A7) and in the backfill (A16) for Case 2 compared to Case 1 under sinusoidal motion at 0.4g amplitude with 8 Hz frequency.

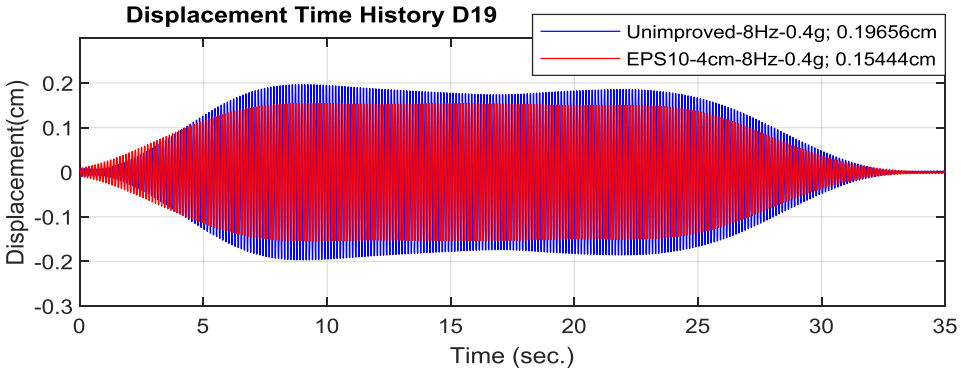


Figure 4.12. The DISTH at the top of the RWM (D19) for Case 2 compared to Case 1 under sinusoidal motion at 0.4g amplitude with 8 Hz frequency.

### 4.3. Results of Case 3 - EPS20-4cm

The study investigated the effects of using an EPS Geofoam cushion with a density of 0.20 kN/m$^3$ and 4 cm thickness (EPS20-4cm) behind the RWM in Case 3, compared to the control case. The results were measured by accelerometer A7, laser displacement sensor D19 at the top of the retaining wall model (RWM), and accelerometer A16 in the backfill, shown in Figures 4.13-4.18.

Figure 4.13 shows the Acceleration-Time Histories, Fourier Amplitude Spectrums, and Response Spectrums under the scaled 2020 İzmir EQ Motion-Kuşadası Station excitations for Case 3 compared to the control case. The A7 measured maximum acceleration values as 0.27g and 0.29g, and the A16 measured 0.19g and 0.28 for the control and cushioned Case 3, respectively. It can be noticed that the maximum acceleration values increased at the top of the RWM and in the backfill when the EPS20-4cm cushion was implemented. The Fourier amplitudes decreased from 9.25 Hz to 7.36 Hz at the top of the RWM and in the backfill for Case 3 compared to the control case. The maximum spectral accelerations were at 0.05 sec and 0.13 sec period ranges. The maximum spectral acceleration ($S_a$) values were 0.98g and 1.004g at the top of the RWM at a period of 0.06 sec, and 0.76g and 0.91g in the backfill at a period of 0.11 sec for the cushioned Case 3 compared to the control case.

Figure 4.14 shows the control case displaced a maximum of 0.37 cm and 0.31 cm for the cushioned model EPS20-4cm when subjected to the dynamic motions of the scaled 2020 İzmir EQ Motion-Kuşadası Station.

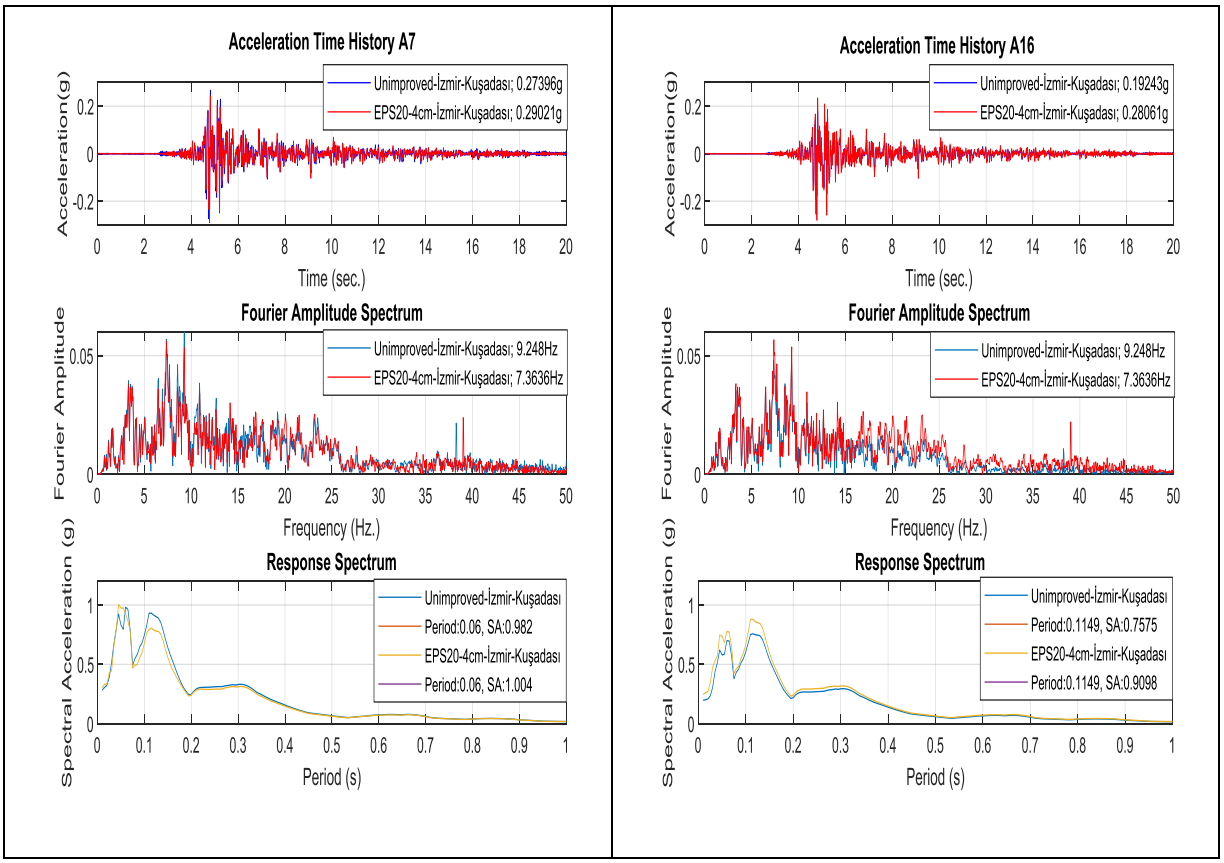


Figure 4.13. The ACCTH, FAS, Response Spectrum at the top of the RWM (A7) and in the backfill (A16) for Case 3 compared to Case 1 under the scaled 2020 İzmir EQ Motion-Kuşadası Station record (FF).

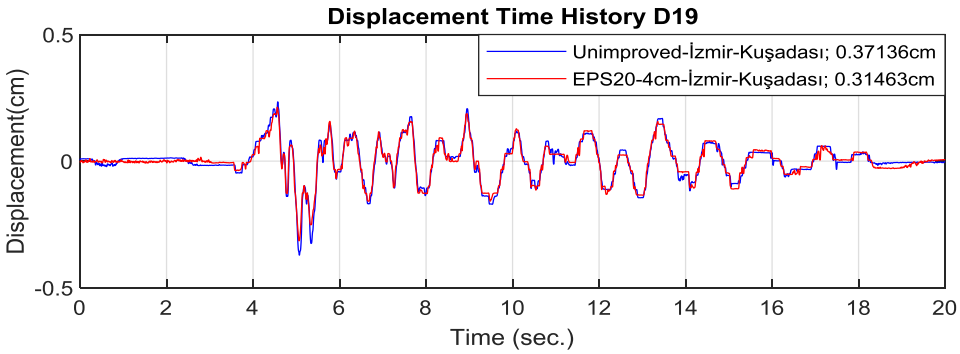


Figure 4.14. The DISTH at the top of the RWM (D19) for Case 3 compared to Case 1 under the scaled 2020 İzmir EQ Motion-Kuşadası Station record (FF).

In Figure 4.15, the Acceleration-Time Histories, Fourier Amplitude Spectrums, and Response Spectrums are displayed under the scaled 1940 Imperial Valley EQ-El Centro Station record. The A7 recorded a maximum acceleration of 0.52g for the control case, which decreased to 0.40g maximum acceleration for the EPS20-4cm cushioned case. Similarly, the A16 measured 0.32g maximum acceleration for the control case and 0.29g maximum acceleration for the cushioned case. The Fourier amplitudes peaked around 4.62 Hz and 4.65 Hz at the top of the RWM and in the backfill for the control case and cushioned cases, respectively. The maximum spectral accelerations were at 0.05 sec and 0.22 sec period ranges. The maximum spectral accelerations ($S_a$) were 1.48g at 0.055 sec period at the top of the RWM for the control case, decreasing to 1.027g at 0.070 sec period for the EPS20-4cm cushioned case. The maximum spectral accelerations were shifted to the higher period ranges for the EPS20-4cm cushioned case. Accordingly, a 31% reduction in seismic demand was calculated as the spectral acceleration decreased from 1.48g to 1.027g, shifting the periods from 0.055 sec to 0.070 sec. EPS Geofoam cushion extends the period of the retaining wall caused by the earthquake, and the damping of the system increases. Similarly, spectral accelerations in the backfill were 1.26g and 1.43g at the same periods of 0.22 sec for the control case and EPS20-4cm cushioned cases, respectively.

The information presented in Figure 4.16 shows the displacement for the control case in comparison to the cushioned case under the scaled 1940 Imperial Valley EQ-El Centro Station record. The maximum displacement of the EPS20-4cm cushioned model was 2.05 cm, while the control case was 1.88 cm at the top of the RWM.

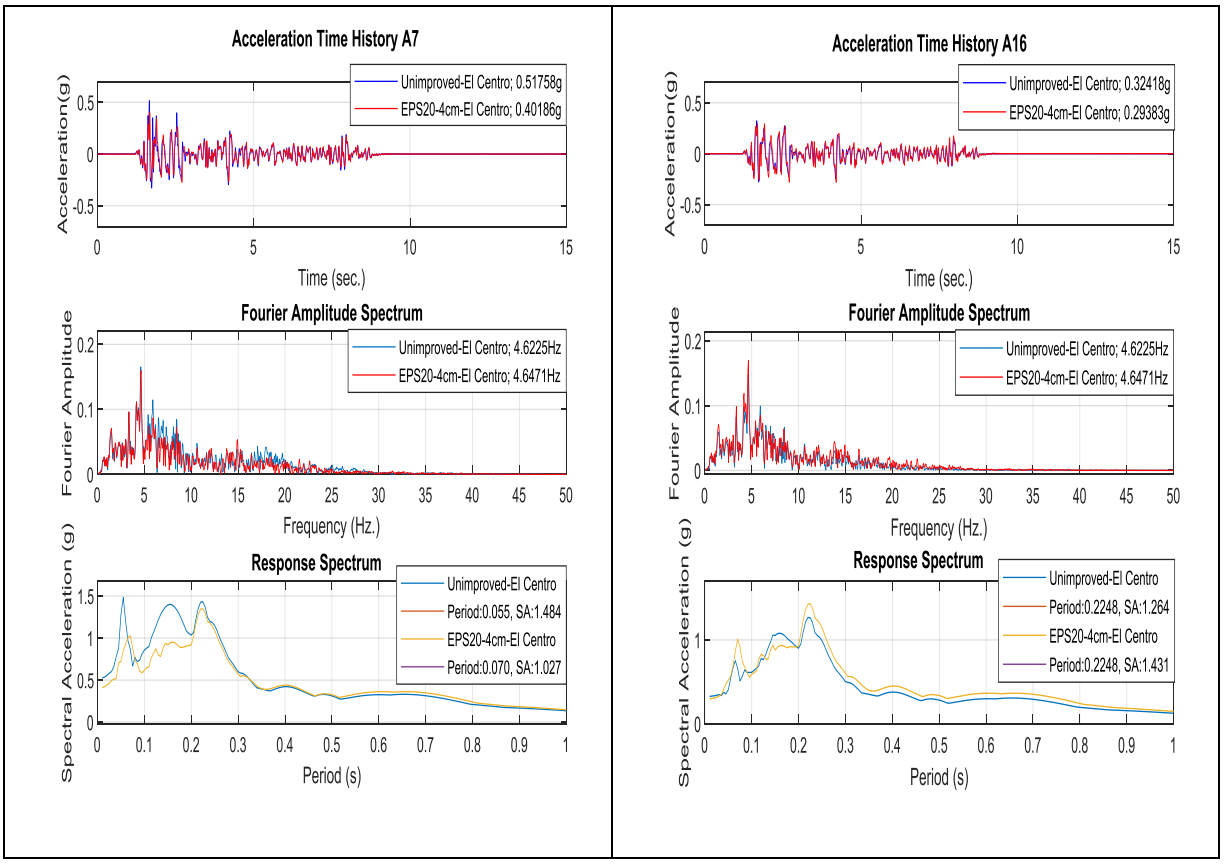


Figure 4.15. The ACCTH, FAS, Response Spectrum at the top of the RWM (A7) and in the backfill (A16) for Case 3 compared to Case 1 under the scaled 1940 Imperial Valley EQ-El Centro Station record (NF).

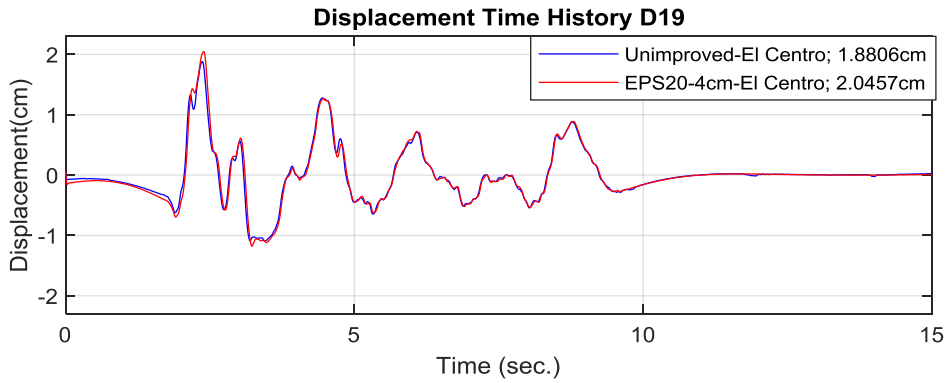


Figure 4.16. The DISTH at the top of the RWM (D19) for Case 3 compared to Case 1 under the scaled 1940 Imperial Valley EQ-El Centro Station record (NF).

The graphs in Figure 4.17 show the Acceleration-Time Histories, Fourier Amplitude Spectrums, and Response Spectrums under a sinusoidal motion at 0.4g amplitude with 8 Hz frequency. When this motion was applied, A7 measured a maximum acceleration of 0.38g at the top of the RWM for the cushioned case with EPS20-4cm, while it was measured as 0.47g for the control case. Similarly, A16 measured a maximum acceleration of 0.40g for the cushioned case compared to 0.36g for the control case. The Fourier amplitude peaks were 8.03 Hz at the top of the RWM and in the backfill for both the cushioned and control cases. The maximum spectral accelerations ($S_a$) were observed at a period of 0.12 seconds, decreasing from 4.7g to 3.81g at the top of the RWM and increasing from 3.60g to 4.01g in the backfill for the control case and cushioned cases, respectively.

Figure 4.18 shows the displacement-time graph for the control case in comparison to the cushioned case under the sinusoidal motion at 0.4g amplitude with 8 Hz frequency. The cushioned case reduced displacement measurement, with a peak displacement of 0.17 cm measured at the top of the RWM, compared to 0.20 cm for the control case.

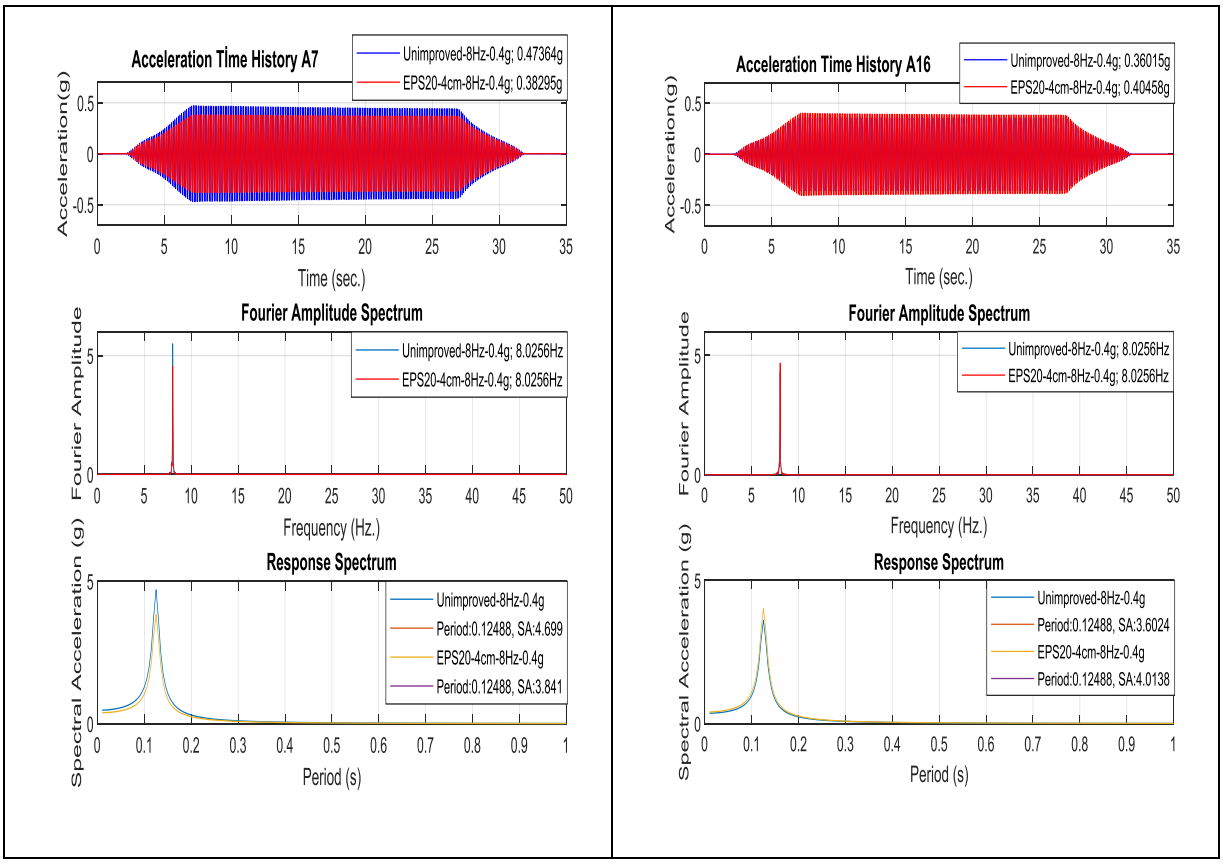


Figure 4.17. The ACCTH, FAS, Response Spectrum at the top of the RWM (A7) and in the backfill (A16) for Case 3 compared to Case 1 under sinusoidal motion at 0.4g amplitude with 8 Hz frequency.

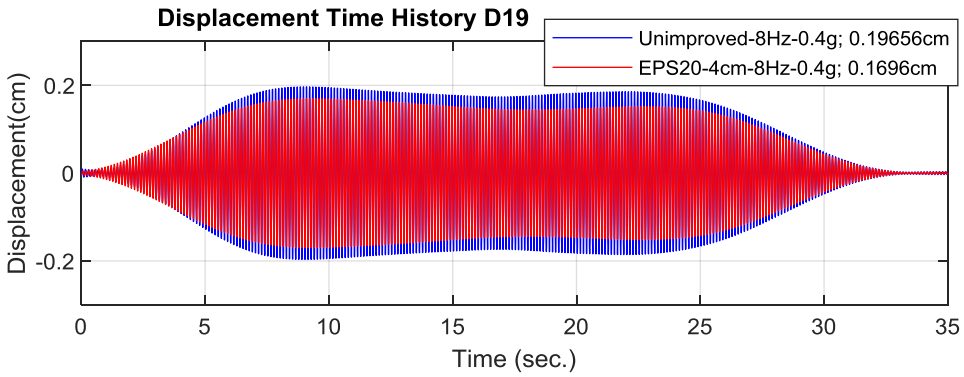


Figure 4.18. The DISTH at the top of the RWM (D19) for Case 3 compared to Case 1 under sinusoidal motion at 0.4g amplitude with 8 Hz frequency.

### 4.4. Results of Case 4 - EPS30-4cm

The study used a cushion made of EPS Geofoam with a density of 0.30 kN/m$^3$ and a thickness of 4 cm (EPS30-4cm) behind the RWM for Case 4. Figures 4.19-4.24 show the results for two different earthquake motions and one sinusoidal motion as measured by accelerometer A7, laser displacement sensor D19 at the top of the retaining wall model (RWM), and accelerometer A16 in the backfill, in comparison to the control case.

The comparison between Case 1 and Case 4 under the scaled 2020 İzmir EQ Motion-Kuşadası Station excitations is shown in Figure 4.19. The figure illustrates the Acceleration-Time Histories, Fourier Amplitude Spectrums, and Response Spectrums. It was measured maximum acceleration values as 0.27g and 0.23g at the top of the RWM, while the A16 measured maximum acceleration values as 0.19g and 0.32g for the control case and Case 4, respectively. Implementing the EPS30-4cm cushion resulted in a decrease in maximum acceleration values at the top of the RWM. The Fourier amplitudes decreased from 9.25 to 7.38 Hz at the top of the RWM and in the backfill for the control and cushioned cases, respectively. The maximum spectral accelerations were at 0.05 sec and 0.13 sec period ranges. The comparison of the control case and cushioned cases shows that the maximum spectral acceleration ($S_a$) values decreased from 0.98g to 0.73g at the top of the RWM at a period of 0.06 sec. The spectral accelerations were 0.76g and 1.05g in the backfill at a period of 0.11 sec for the control case and Case 4, respectively.

Figure 4.20 shows that the control case displaced a maximum of 0.37 cm compared to 0.38 cm for the EPS30-4cm when subjected to the dynamic motions of the scaled 2020 İzmir EQ Motion-Kuşadası Station.

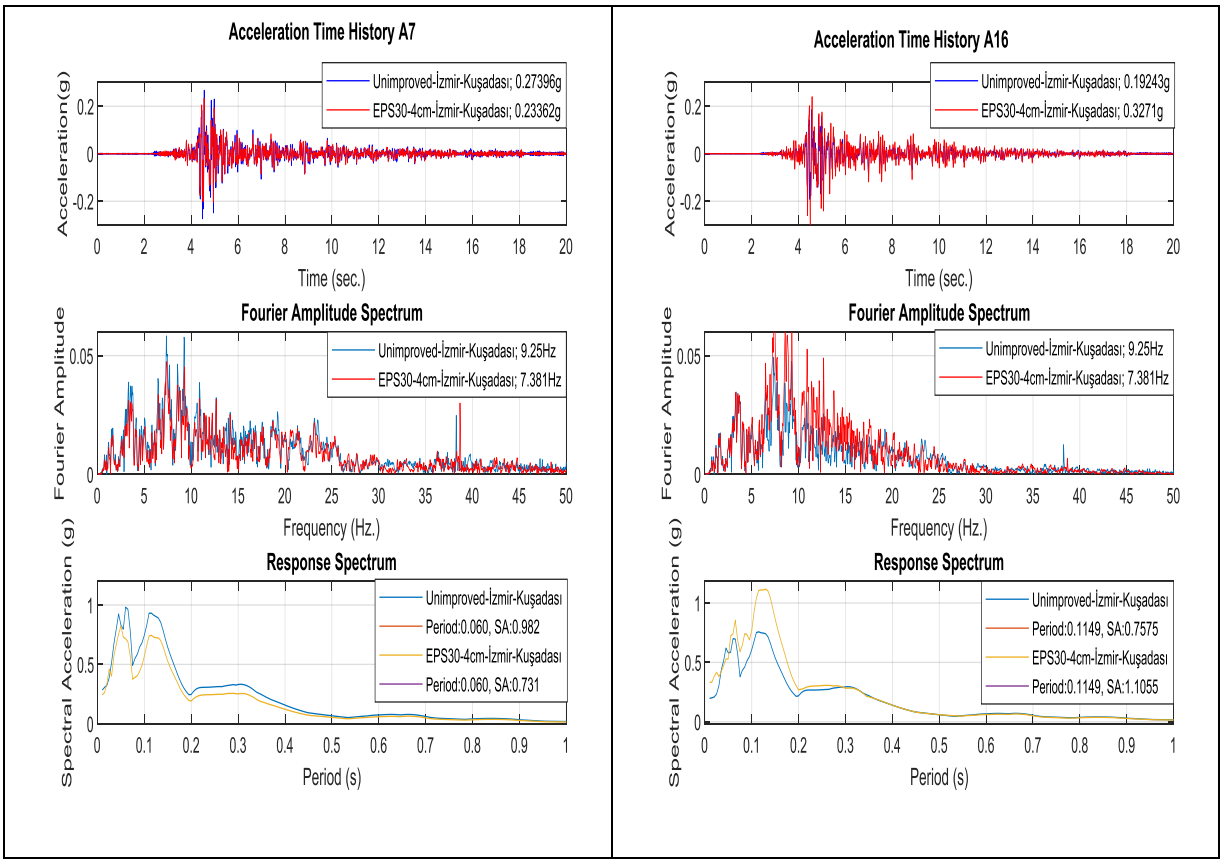


Figure 4.19. The ACCTH, FAS, Response Spectrum at the top of the RWM (A7) and in the backfill (A16) for Case 4 compared to Case 1 under the scaled 2020 İzmir EQ Motion-Kuşadası Station record (FF).

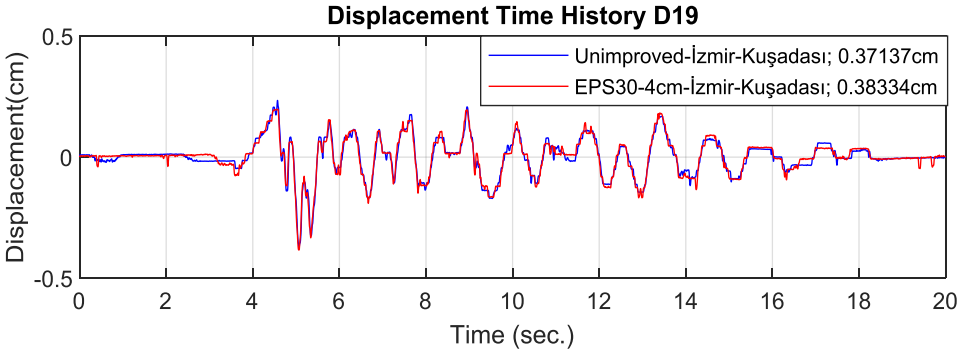


Figure 4.20. The DISTH at the top of the RWM (D19) for Case 4 compared to Case 1 under the scaled 2020 İzmir EQ Motion-Kuşadası Station record (FF).

The Acceleration-Time Histories, Fourier Amplitude Spectrums, and Response Spectrums are illustrated in Figure 4.21 under the scaled 1940 Imperial Valley EQ-El Centro Station record. It was measured 0.52g maximum acceleration for the control case at the top of the RWM and decreased to 0.46g maximum acceleration for the EPS30-4cm cushioned case. The A16 measured 0.32g maximum acceleration for the control case and 0.48g for the cushioned case. Fourier amplitudes peaked around 4.64 Hz and 4.58 Hz at the top of the RWM for the control and cushioned cases, respectively, and 4.64 Hz in the backfill. The maximum spectral accelerations were at 0.05 sec and 0.22 sec period ranges. The maximum spectral accelerations ($S_a$) were 1.48g at 0.055 sec period at the top of the RWM for the control case, decreasing to 1.285g for the EPS30-4cm cushioned case. The spectral accelerations in the backfill were 1.27g and 2.02g at the same periods of 0.22 sec for the control case and EPS30-4cm cushioned cases, respectively.

The displacement time history of the control case in comparison to the cushioned case during the scaled 1940 Imperial Valley EQ-El Centro Station record is shown in Figure 4.22. The peak displacement at the top of the RWM of the EPS30-4cm cushioned model was measured to be 1.85 cm, while the control case was measured to be 1.88 cm at the top of the RWM. No significant change is observed in displacement time histories of the control and cushioned cases.

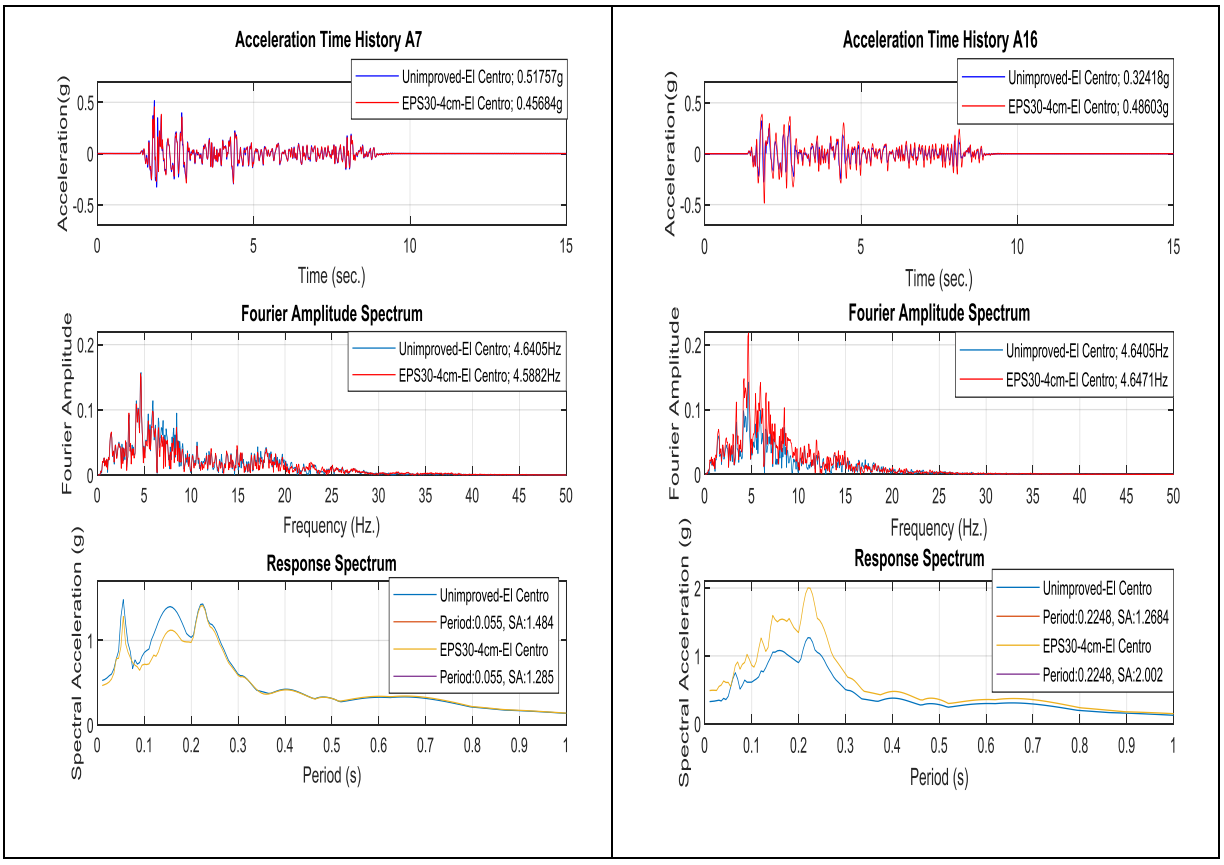


Figure 4.21. The ACCTH, FAS, Response Spectrum at the top of the RWM (A7) and in the backfill (A16) for Case 4 compared to Case 1 under the scaled 1940 Imperial Valley EQ-El Centro Station record (NF).

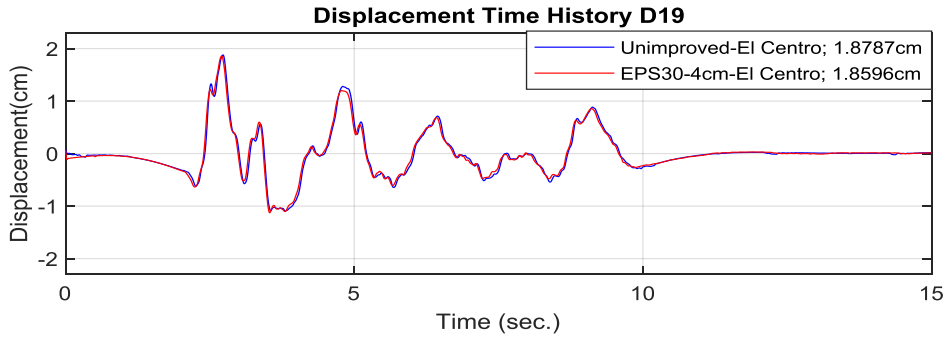


Figure 4.22. The DISTH at the top of the RWM (D19) for Case 4 compared to Case 1 under the scaled 1940 Imperial Valley EQ-El Centro Station record (NF).

Figure 4.23 displays the Acceleration-Time Histories, Fourier Amplitude Spectrums, and Response Spectrums under a sinusoidal motion at 0.4g amplitude with 8 Hz frequency. A maximum acceleration of 0.35g was measured at the top of the RWM for the EPS30-4cm cushioned case, which was lower than the control case measurement of 0.47g. Similarly, A16 measured a maximum acceleration of 0.46g for the cushioned case, higher than the control case measurement of 0.36g. The Fourier amplitude peaks were 8.04 Hz and 8.03 Hz at the top of the RWM and in the backfill for both the cushioned and control cases. The maximum spectral accelerations ($S_a$) were observed at a period of 0.12 seconds, decreasing from 4.7g to 3.50g at the top of the RWM and increasing from 3.60g to 4.51g in the backfill for the control case and cushioned cases, respectively.

Figure 4.24 presents the displacement time history of the control case compared to the cushioned case under sinusoidal motion at 0.4g amplitude with 8 Hz frequency. The measurement of displacement showed a reduction. For the cushioned case, maximum displacement was measured as 0.18 cm at the top of the RWM acquired from D19, while for the control case, it was measured as 0.20 cm.

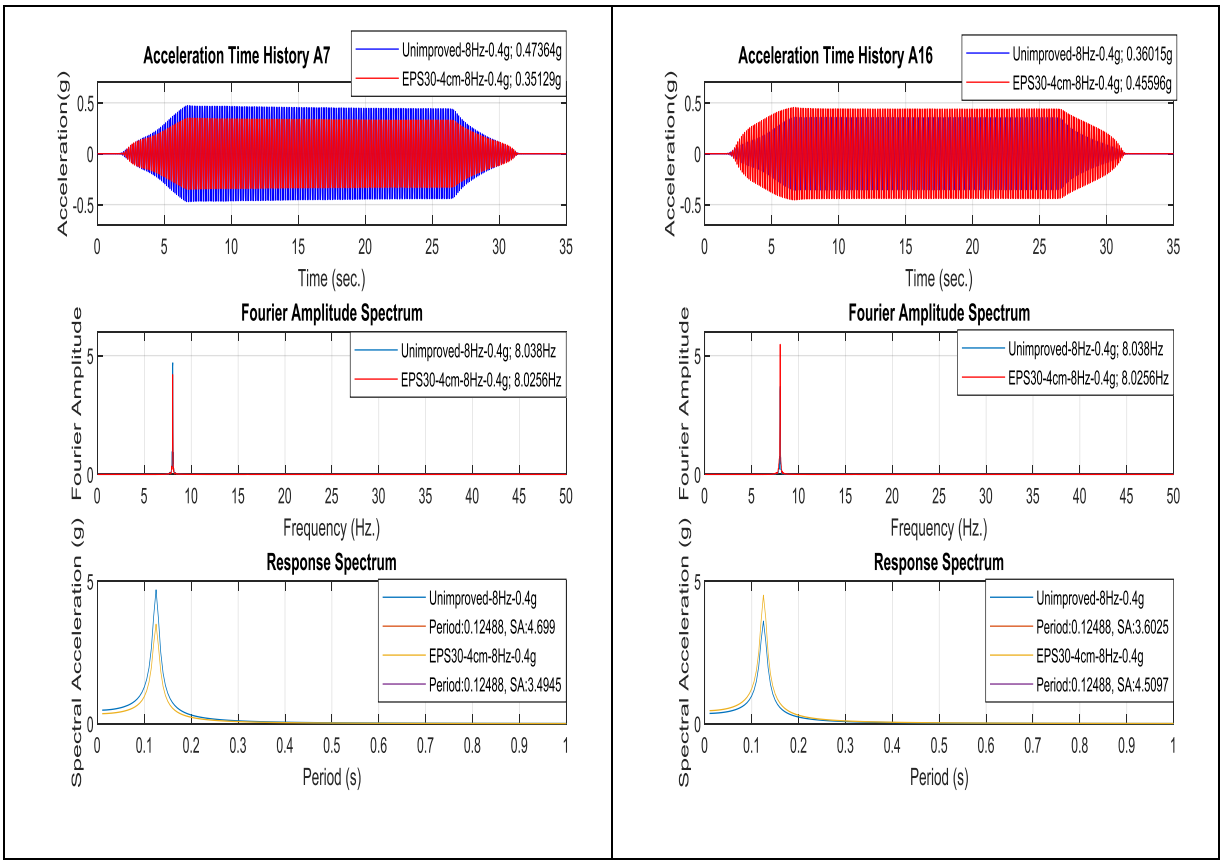


Figure 4.23. The ACCTH, FAS, Response Spectrum at the top of the RWM (A7) and in the backfill (A16) for Case 4 compared to Case 1 under sinusoidal motion at 0.4g amplitude with 8 Hz frequency.

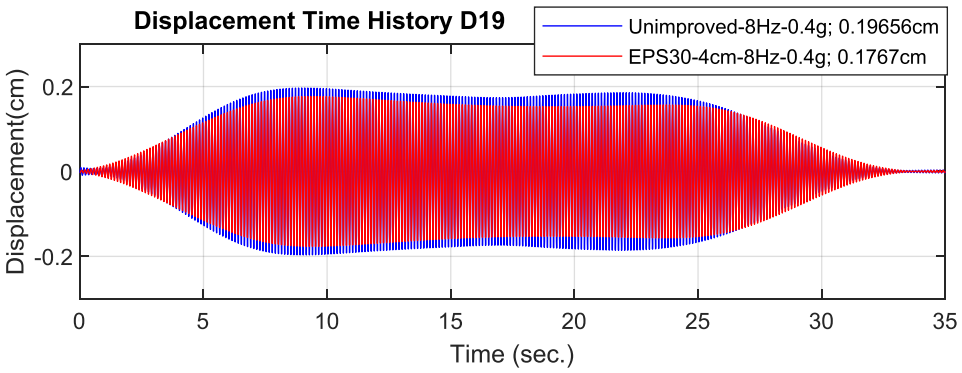


Figure 4.24. The DISTH at the top of the RWM (D19) for Case 4 compared to Case 1 under sinusoidal motion at 0.4g amplitude with 8 Hz frequency.

## 4.5. Results of Case 5 - EPS10-8cm

In this study, Case 5 involved using an EPS Geofoam cushion with a density of 0.10 kN/m$^3$ and a thickness of 8 cm (EPS10-8cm) behind the RWM. The results of the study are presented in Figures 4.25 - 4.30, which show the measurements taken by accelerometer A7, laser displacement sensor D19 at the top of the retaining wall model (RWM), and accelerometer A16 in the backfill. These measurements were compared to the control case.

Figure 4.25 displays the Acceleration-Time Histories, Fourier Amplitude Spectrums, and Response Spectrums for Case 5 compared to the control case under the excitations of the scaled 2020 İzmir EQ Motion-Kuşadası Station record. The maximum acceleration values of 0.27g and 0.22g were measured at the top of the RWM, while A16 measured maximum acceleration values of 0.19g and 0.20g for the control case and Case 5, respectively. It was observed that the maximum acceleration values decreased at the top of the RWM when the EPS10-8cm was implemented. The Fourier amplitudes were 9.24 Hz and 7.36 Hz at the top of the RWM and in the backfill for the control and cushioned cases, respectively. The maximum spectral accelerations were at 0.05 sec and 0.13 sec period ranges. Comparing the control case and the cushioned case, it was observed that the maximum spectral acceleration ($S_a$) decreased from 0.98g to 0.86g at a period of 0.060 sec at the top of the RWM. In the backfill, the spectral accelerations were 0.76g and 0.80g at a period of 0.11 sec for the cushioned case, compared to the control case, respectively.

Figure 4.26 illustrates the displacements of the control case and the EPS10-8cm under the dynamic motions of the scaled 2020 İzmir EQ Motion-Kuşadası Station. The control case displaced 0.37 cm, while the cushioned model displaced 0.39 cm.

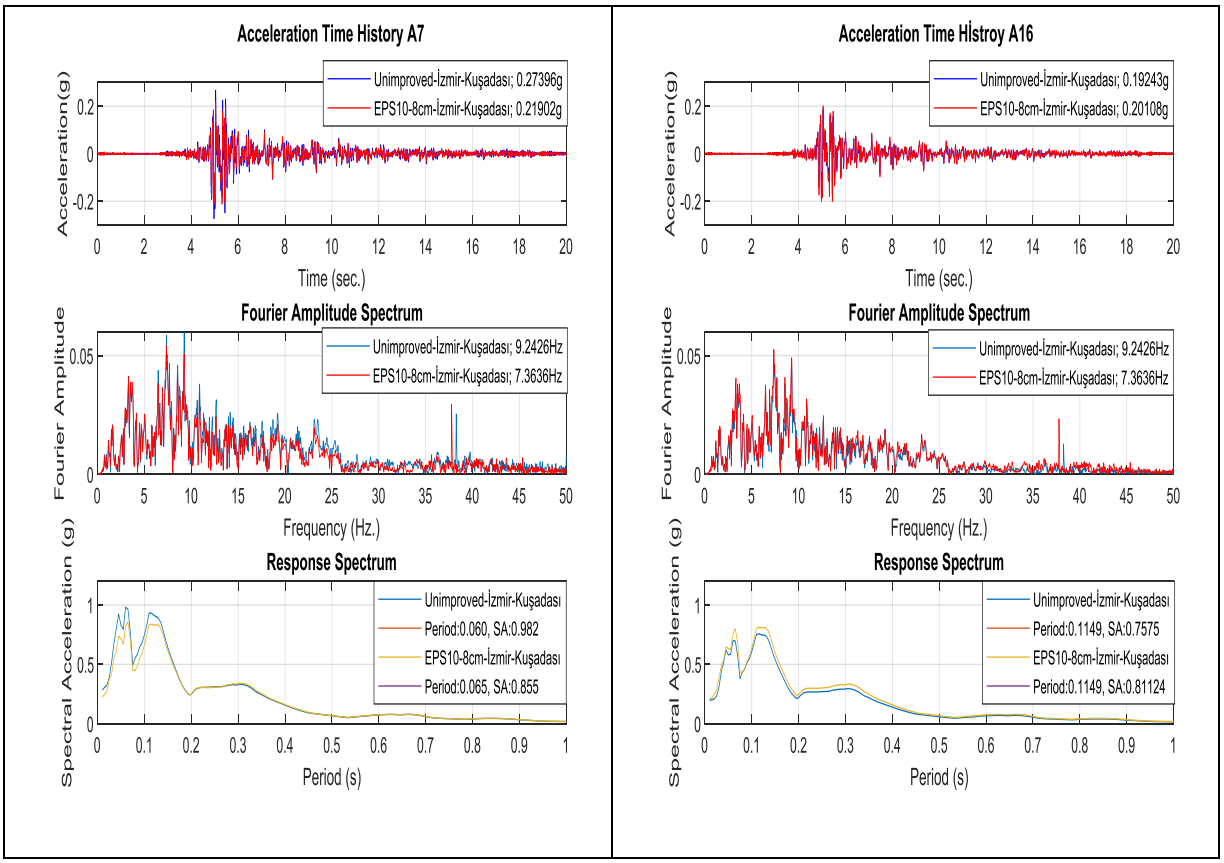


Figure 4.25. The ACCTH, FAS, Response Spectrum at the top of the RWM (A7) and in the backfill (A16) for Case 5 compared to Case 1 under the scaled 2020 İzmir EQ Motion-Kuşadası Station record (FF).

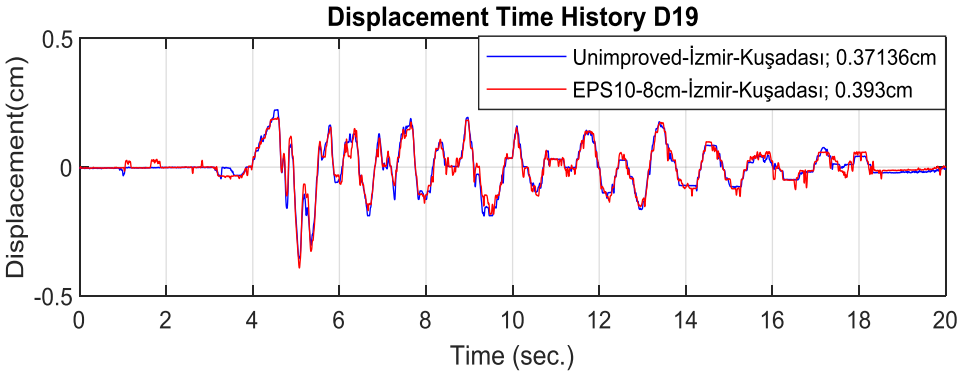


Figure 4.26 The DISTH at the top of the RWM (D19) for Case 5 compared to Case 1 under the scaled 2020 İzmir EQ Motion-Kuşadası Station record (FF).

Figure 4.27 illustrates the Acceleration-Time Histories, Fourier Amplitude Spectrums, and Response Spectrums under the scaled 1940 Imperial Valley EQ-El Centro Station record. The A7 recorded a maximum acceleration of 0.52g for the control case. However, this value decreased to 0.45g maximum acceleration for the EPS10-8cm cushioned case. Similarly, the A16 measured a maximum acceleration of 0.32g for the control case and 0.33g maximum acceleration for the cushioned case. The Fourier amplitudes peaked at approximately 4.62 Hz and 4.59 Hz for both at the top of the RWM and in the backfill for the control and cushioned cases, respectively. The maximum spectral accelerations were at 0.05 sec and 0.22 sec period ranges. The maximum spectral accelerations ($S_a$) were 1.48g at 0.055 sec period at the top of the RWM for the control case, decreasing to 1.058g at 0.065 sec period for the EPS10-8cm cushioned case. The maximum spectral accelerations were shifted to the higher period ranges for the EPS10-8cm cushioned case. Accordingly, a 29% reduction in seismic demand was calculated as the spectral acceleration decreased from 1.48g to 1.058g, shifting the periods from 0.055 sec to 0.065 sec. EPS Geofoam cushion extends the period of the retaining wall caused by the given earthquake record, and damping of the system increases. The spectral accelerations in the backfill were 1.27g and 1.37g at the same periods of 0.22 sec for the control case and EPS10-8cm cushioned cases, respectively.

Figure 4.28 shows a comparison of the displacement time history between the control case and cushioned cases under the scaled 1940 Imperial Valley EQ-El Centro Station record. In the cushioned model, which utilized EPS10-8cm, the maximum displacement was measured as 1.90 cm at the top of the RWM. On the other hand, the control case recorded a peak displacement of 1.88 cm.

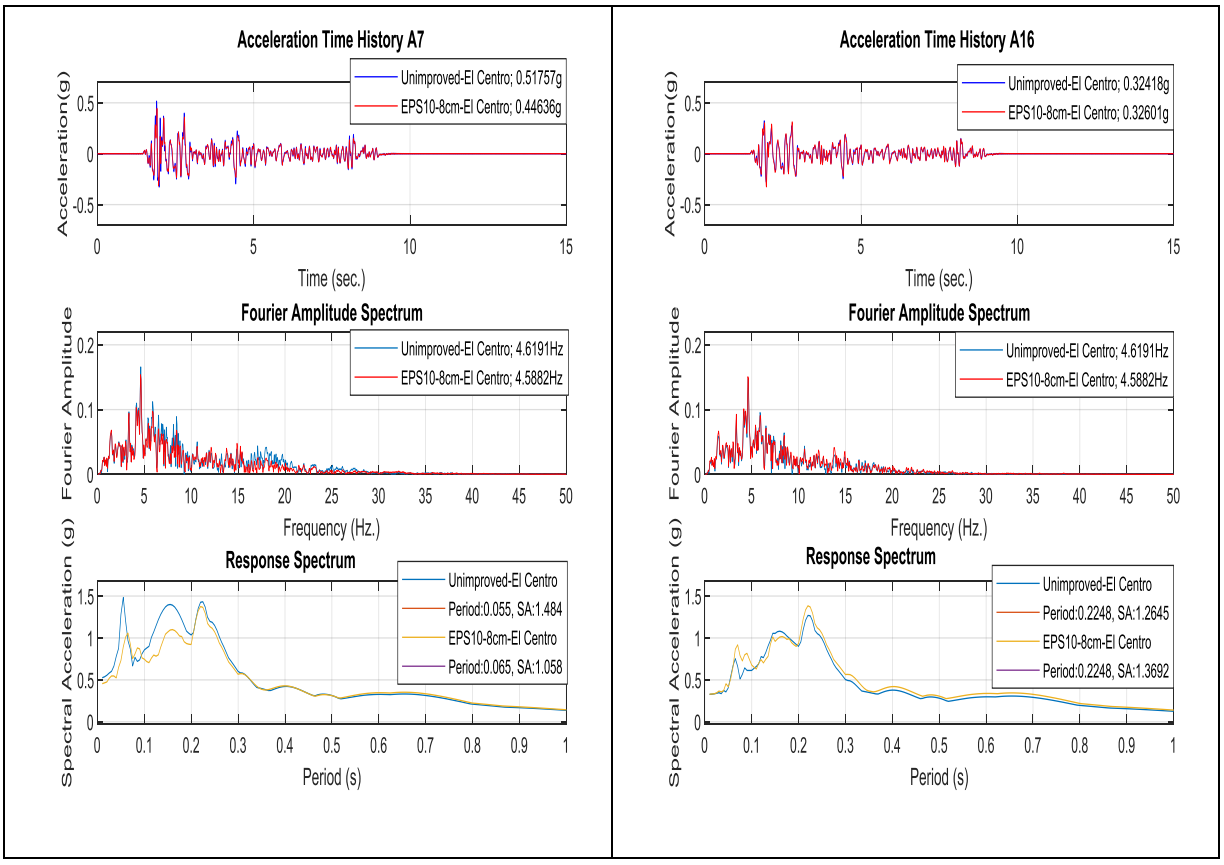


Figure 4.27. The ACCTH, FAS, Response Spectrum at the top of the RWM (A7) and in the backfill (A16) for Case 5 compared to Case 1 under the scaled 1940 Imperial Valley EQ-El Centro Station record (NF).

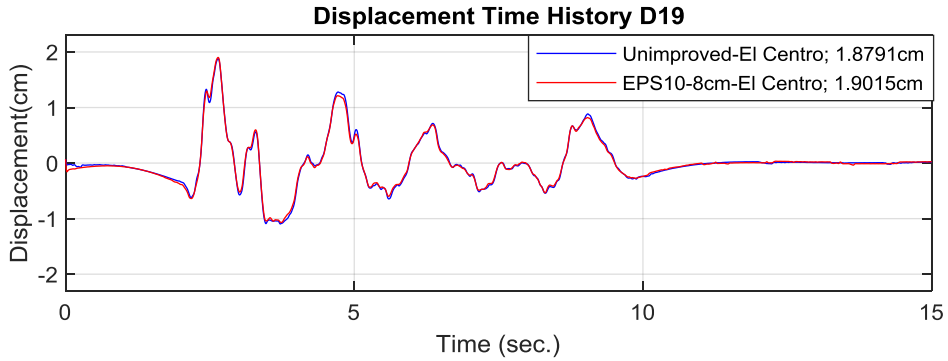


Figure 4.28. The DISTH at the top of the RWM (D19) for Case 5 compared to Case 1 under the scaled 1940 Imperial Valley EQ-El Centro Station record (NF).

Figure 4.29 displays the Acceleration-Time Histories, Fourier Amplitude Spectrums, and Response Spectrums under a sinusoidal motion at 0.4g amplitude with 8 Hz frequency. In the cushioned case, the A7 recorded a peak acceleration of 0.29g at the top of the RWM, whereas the control case recorded a higher maximum acceleration of 0.47g. Additionally, the A16, located in the backfill, measured a maximum acceleration of 0.31g for the cushioned case, while the control case recorded a slightly higher maximum acceleration of 0.36g. The cushioned and control cases exhibited Fourier amplitude peaks of 8.03 Hz at the top of the RWM and in the backfill. Furthermore, the maximum spectral accelerations ($S_a$) occurred at 0.12 sec period. For the control case, $S_a$ decreased from 4.7g to 2.86g at the top of the RWM and from 3.60g to 3.10g in the backfill in the cushioned case.

Figure 4.30 illustrates a comparison of the displacement time history between the control case and cushioned cases under the sinusoidal motion at 0.4g amplitude with 8 Hz frequency. It shows a reduction in displacement measurement in the cushioned case. Specifically, the maximum displacement was 0.12 cm for the cushioned case, whereas it was 0.20 cm for the control case.

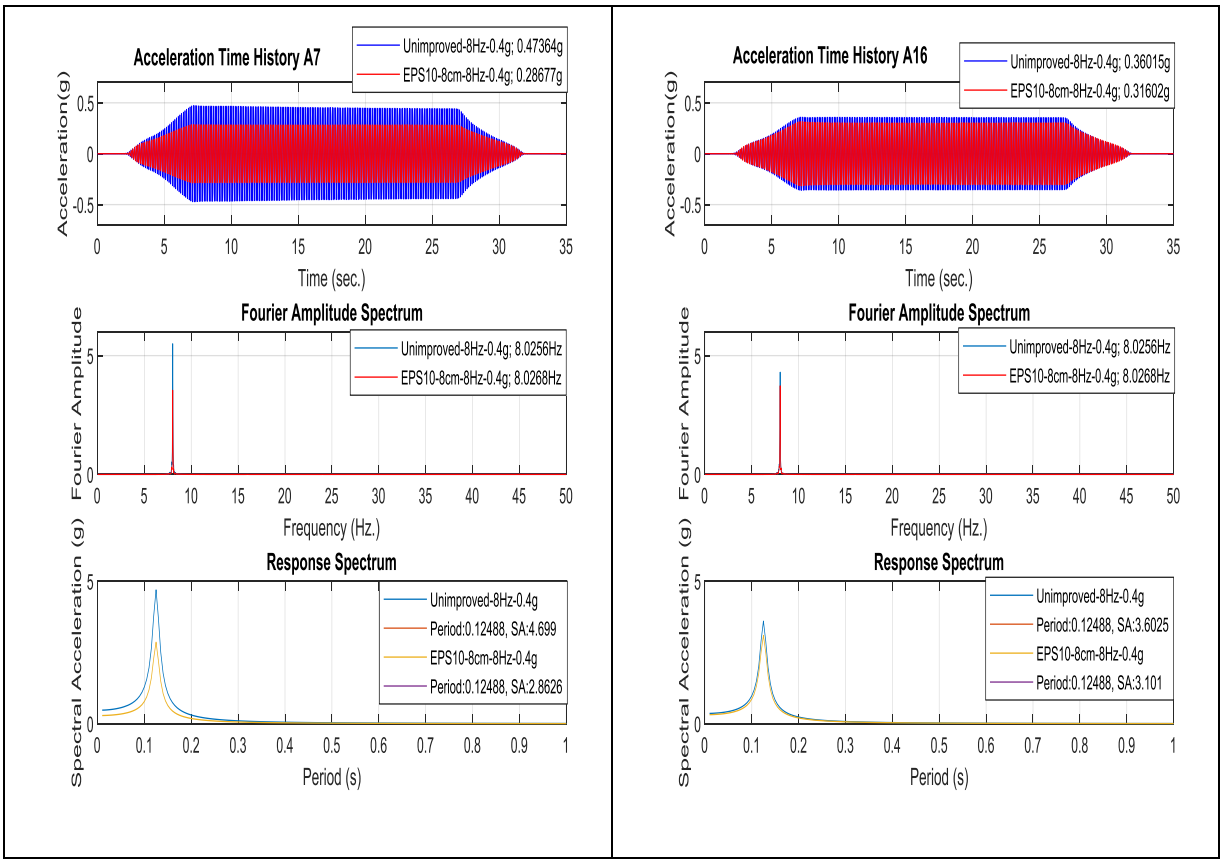


Figure 4.29. The ACCTH, FAS, Response Spectrum at the top of the RWM (A7) and in the backfill (A16) for Case 5 compared to Case 1 under sinusoidal motion at 0.4g amplitude with 8 Hz frequency.

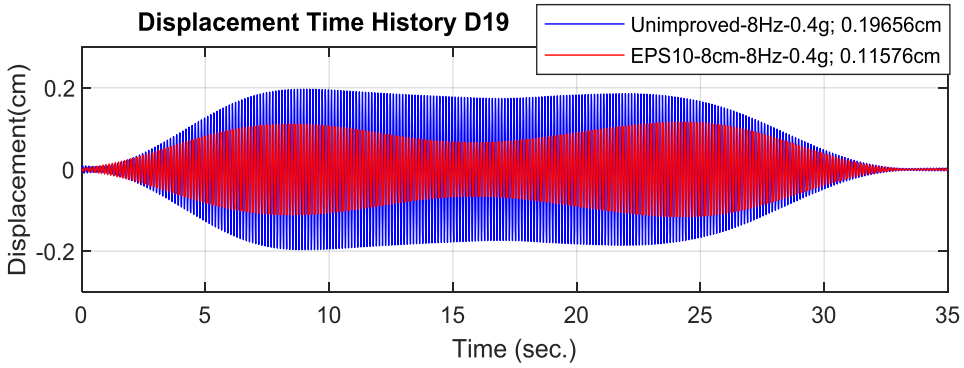


Figure 4.30. The DISTH at the top of the RWM (D19) for Case 5 compared to Case 1 under sinusoidal motion at 0.4g amplitude with 8 Hz frequency.

## 4.6. Results of Case 6 - EPS20-8cm

In this study, Case 6 consists of EPS Geofoam cushion with a density of 0.20 kN/m$^3$ and 8 cm thickness (EPS20-8cm) behind the RWM. Figures 4.31, 4.32, 4.33, 4.34, 4.35, and 4.36 show the results for two different earthquake motions and one sinusoidal motion as measured by accelerometer A7, laser displacement sensor D19 at the top of the retaining wall model (RWM) and accelerometer A16 in the backfill in comparison to the control case.

Figure 4.31 illustrates the Acceleration-Time Histories, Fourier Amplitude Spectrums, and Response Spectrums under the scaled 2020 İzmir EQ Motion-Kuşadası Station excitations for Case 6 in comparison with the control case Case 1. It was measured maximum acceleration values as 0.27g and 0.20g at the top of the RWM, and the A16 measured maximum acceleration values as 0.19g and 0.18 for the control case and Case 6, respectively. It can be noticed that the maximum acceleration values deceased at the top of the RWM and in the backfill when the EPS20-8cm cushion was implemented. Fourier amplitudes were 9.23 Hz and 7.36 Hz at the top of the RWM and in the backfill for the control and cushioned cases. The maximum spectral accelerations were at 0.05 sec and 0.13 sec period ranges. Compared to the control case and cushioned cases, the maximum spectral acceleration (Sa) values decreased from 0.98g to 0.61g at the top of the RWM at a period of 0.06 sec. The spectral accelerations were 0.76g and 0.72g in the backfill at a period of 0.11 sec for the cushioned and control cases, respectively.

Figure 4.32 shows that, when subjected to the dynamic motions of the scaled 2020 İzmir EQ Motion-Kuşadası Station, the control case displaced a maximum of 0.37 cm and 0.31 cm for the EPS20-8cm.

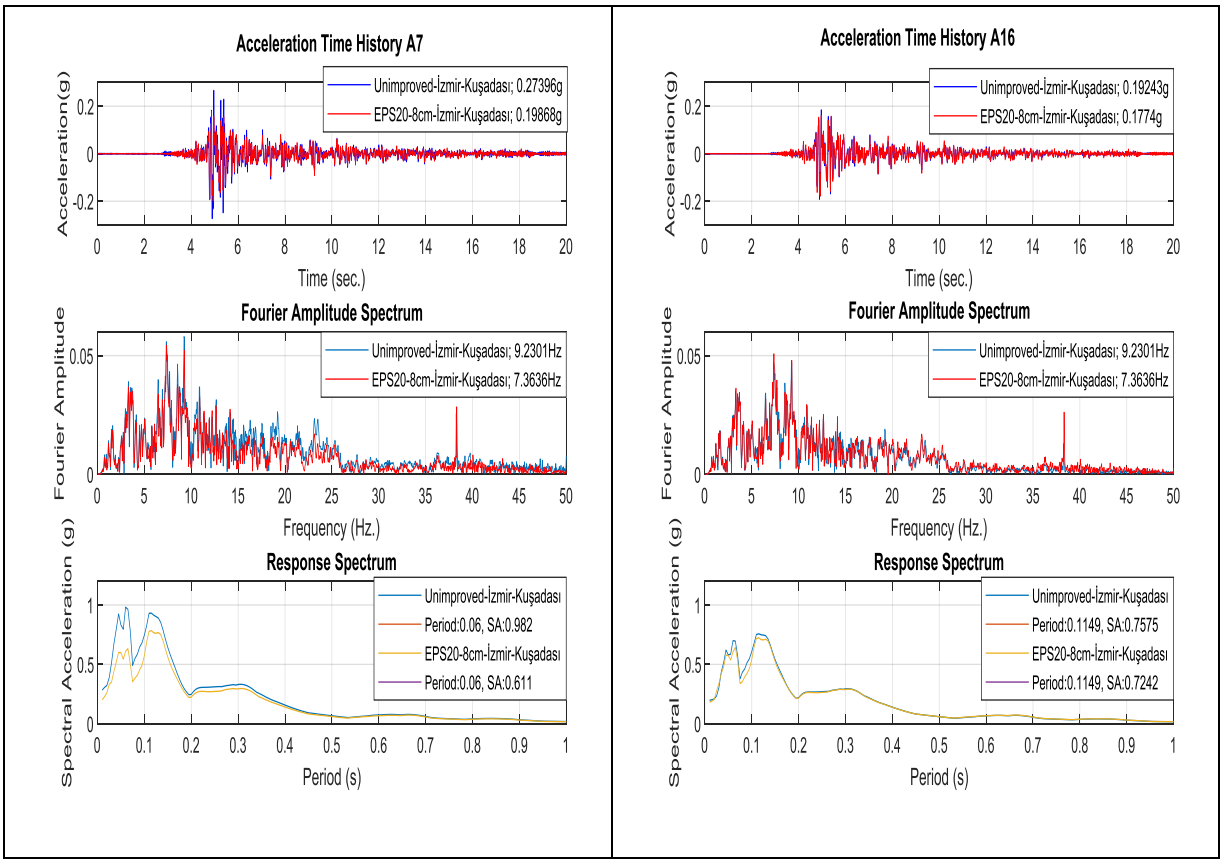


Figure 4.31. The ACCTH, FAS, Response Spectrum at the top of the RWM (A7) and in the backfill (A16) for Case 6 compared to Case 1 under the scaled 2020 İzmir EQ Motion-Kuşadası Station record (FF).

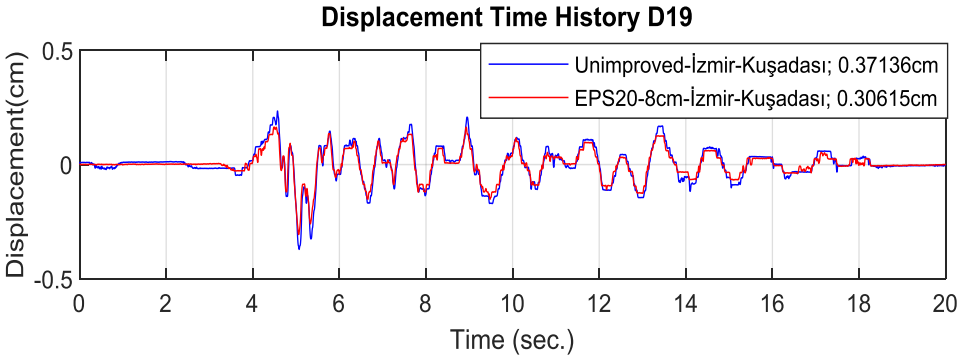


Figure 4.32. The DISTH at the top of the RWM (D19) for Case 6 compared to Case 1 under the scaled 2020 İzmir EQ Motion-Kuşadası Station record (FF).

The Acceleration-Time Histories, Fourier Amplitude Spectrums, and Response Spectrums are illustrated in Figure 4.33 under the scaled 1940 Imperial Valley EQ-El Centro Station record. It was measured 0.52g maximum acceleration for the control case at the top of the RWM decreased to 0.40g maximum acceleration for the EPS20-8cm cushioned case. The A16 measured 0.32g maximum acceleration for the control case and 0.33g for the cushioned case. Fourier amplitudes peaked around 4.61 Hz and 4.58 Hz at the top of the RWM and in the backfill for the control and cushioned cases. The maximum spectral accelerations were at 0.05 sec and 0.22 sec period ranges for the cushioned and control cases. The maximum spectral accelerations ($S_a$) were 1.48g at 0.055 sec period at the top of the RWM for the control case, decreasing to 0.885g at 0.065 sec period for the EPS20-8cm cushioned case. The maximum spectral accelerations were shifted to the higher period ranges for the EPS20-8cm cushioned case. Accordingly, a 40% reduction in seismic demand was calculated as the spectral acceleration decreased from 1.48g to 0.885g, shifting the periods from 0.055 sec to 0.065 sec. EPS Geofoam cushion extends the period of the retaining wall caused by the earthquake, and the damping of the system increases. The spectral accelerations in the backfill were 1.27g and 1.40g at the same periods 0.22 sec for the control case and EPS20-8cm cushioned case, respectively.

Figure 4.34 presents the displacement time history of the control case compared to the cushioned case under the scaled 1940 Imperial Valley EQ-El Centro Station record. The maximum displacement of the EPS20-8cm cushioned model was measured as 1.91 cm, while the control case was measured as 1.88 cm at the top of the RWM.

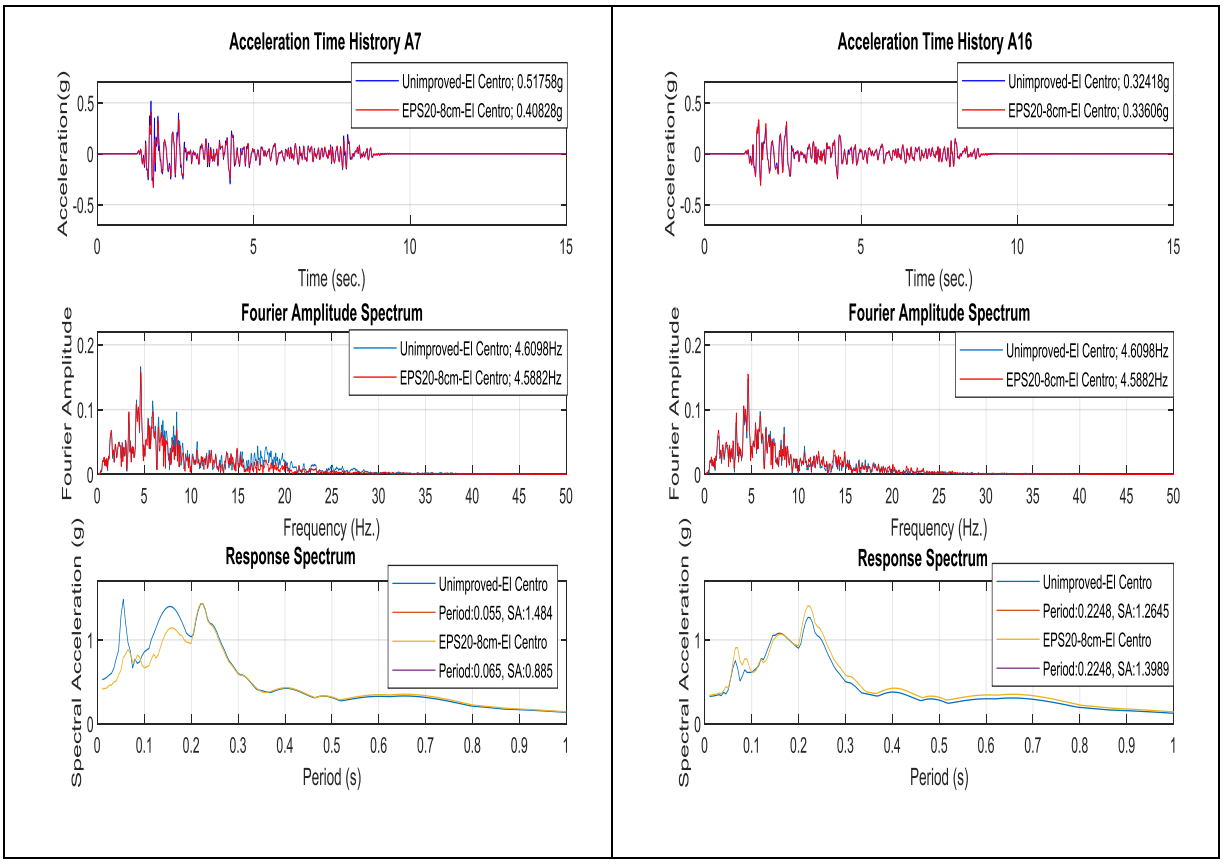


Figure 4.33. The ACCTH, FAS, Response Spectrum at the top of the RWM (A7) and in the backfill (A16) for Case 6 compared to Case 1 under the scaled 1940 Imperial Valley EQ-El Centro Station record (NF).

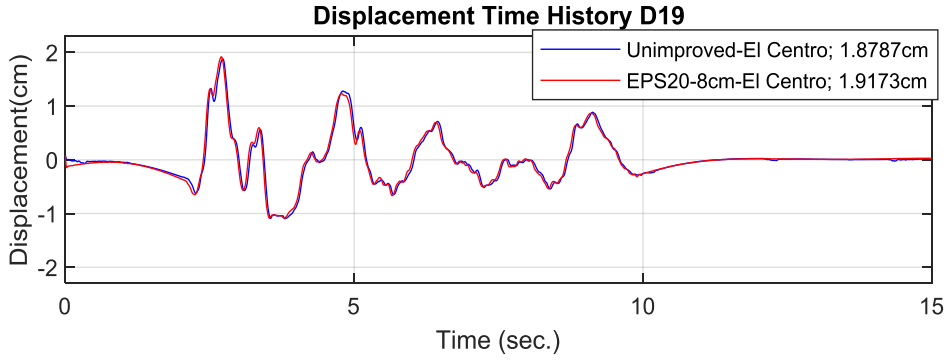


Figure 4.34. The DISTH at the top of the RWM (D19) for Case 6 compared to Case 1 under the scaled 1940 Imperial Valley EQ-El Centro Station record (NF).

The Acceleration-Time Histories, Fourier Amplitude Spectrums, and Response Spectrums under the sinusoidal motion at 0.4g amplitude with 8 Hz frequency are shown in Figure 4.35. It was measured 0.33g maximum acceleration at the top of the RWM for the EPS10-8cm cushioned case compared to the control case of 0.47g, and the A16 measured 0.34g maximum acceleration for the cushioned case compared to the control case of 0.36g. The Fourier amplitude peaks were 8.03 Hz at the top of the RWM and in the backfill both for the cushioned case and control case with respect to the measurements taken from A7 and A16. The maximum spectral accelerations ($S_a$) were at 0.12 sec period, decreasing from 4.7g to 3.31g at the top of the RWM and decreasing from 3.60g to 3.45g in the backfill for the control case and cushioned cases, respectively.

Figure 4.36 presents the displacement time history of the control case compared to the cushioned case under sinusoidal motion at 0.4g amplitude with 8 Hz frequency. A reduction was observed in displacement measurement. Maximum displacement was measured as 0.13 cm at the top of the RWM for the cushioned case, whereas it was measured as 0.20 cm for the control case.

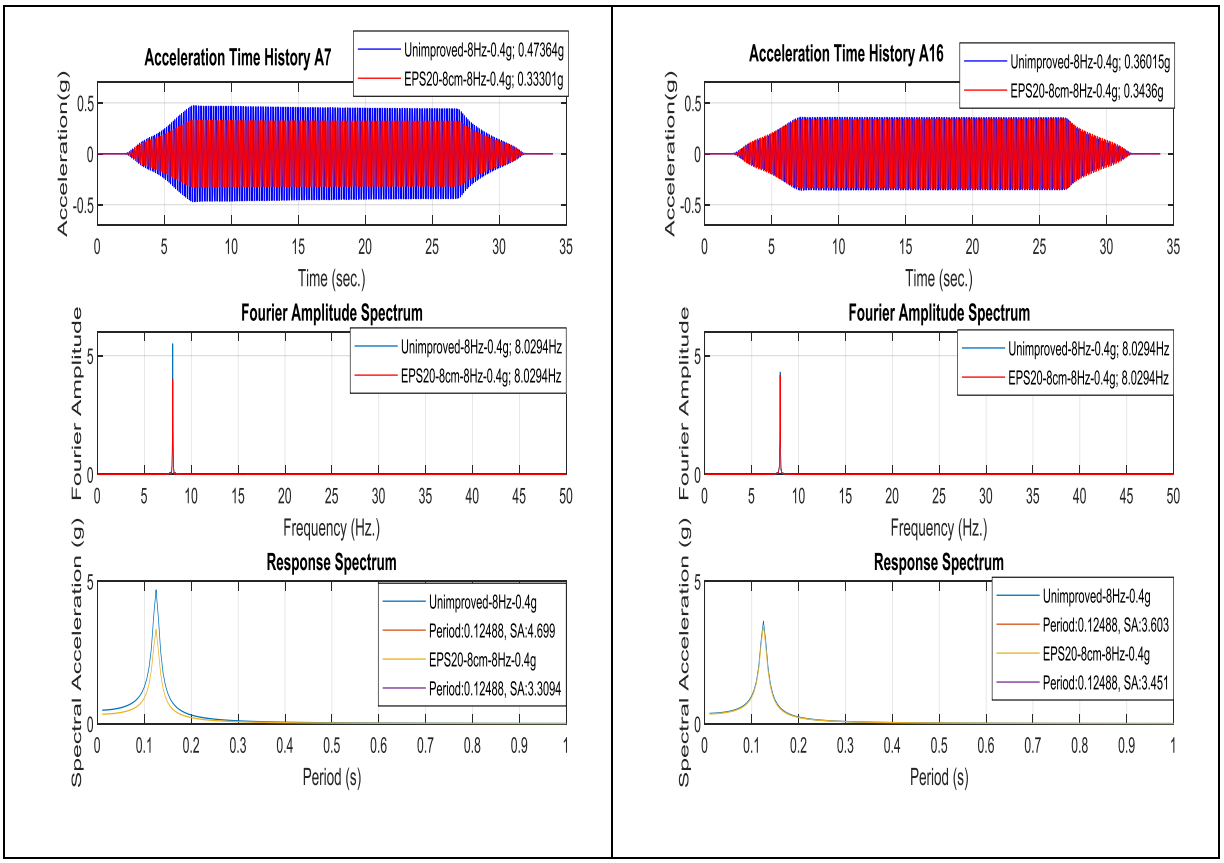


Figure 4.35. The ACCTH, FAS, Response Spectrum at the top of the RWM (A7) and in the backfill (A16) for Case 6 compared to Case 1 under sinusoidal motion at 0.4g amplitude with 8 Hz frequency.

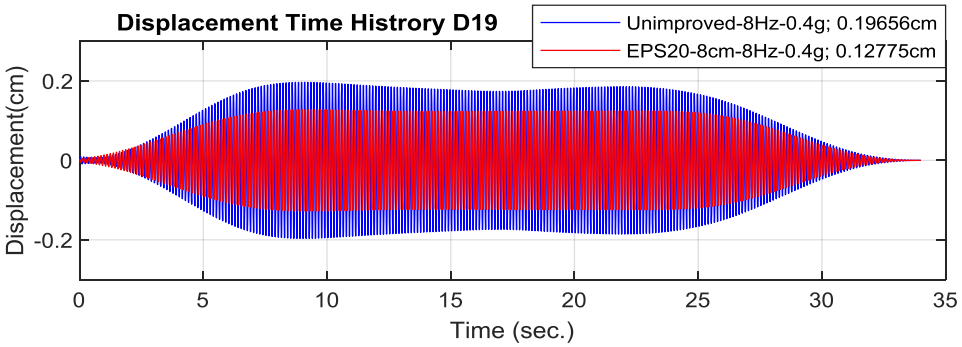


Figure 4.36. The DISTH at the top of the RWM (D19) for Case 6 compared to Case 1 under sinusoidal motion at 0.4g amplitude with 8 Hz frequency.

## 4.7. Results of Case 7 - EPS30-8cm

In this study, Case 7 involved using an EPS Geofoam cushion with a density of 0.30 kN/m$^3$ and an 8 cm thickness (EPS30-8cm) behind the RWM. The results for two different earthquake motions and one sinusoidal motion, as measured by accelerometer A7, laser displacement sensor D19 at the top of the retaining wall model (RWM), and accelerometer A16 in the backfill, are presented in Figures 4.37, 4.38, 4.39, 4.40, 4.41, and 4.42. These results are compared to the control case.

Figure 4.37 showcases the Acceleration-Time Histories, Fourier Amplitude Spectrums and Response Spectrums for Case 7 under the scaled 2020 İzmir EQ Motion-Kuşadası Station excitations, compared to the control case (Case 1). The maximum acceleration values at the top of the RWM were 0.27g and 0.22g for the control and cushioned cases, respectively. For the A16, the maximum acceleration values were 0.19g for the control case and 0.18g for the cushioned case. It can be noticed that the implementation of EPS30-8cm cushion resulted in a decrease in maximum acceleration values at both the top of the RWM and in the backfill. For the control and cushioned cases, the Fourier amplitudes at the top of the RWM and in the backfill were 9.26 Hz and 7.36 Hz. The maximum spectral accelerations occur at 0.05 sec and 0.13 sec period ranges. Comparing the control and cushioned cases, the maximum spectral acceleration ($S_a$) values decreased from 0.98g to 0.69g at the top of the RWM at a period of 0.060 sec. The spectral accelerations were 0.76g and 0.72g in the backfill at a period of 0.11 sec, for the cushioned case compared to the control case, respectively.

Figure 4.38 shows that under the dynamic motions of the 2020 İzmir Earthquake Motion-Kuşadası Station, the control case displaced a maximum of 0.37 cm and 0.34 cm for the EPS30-8cm cushioned model.

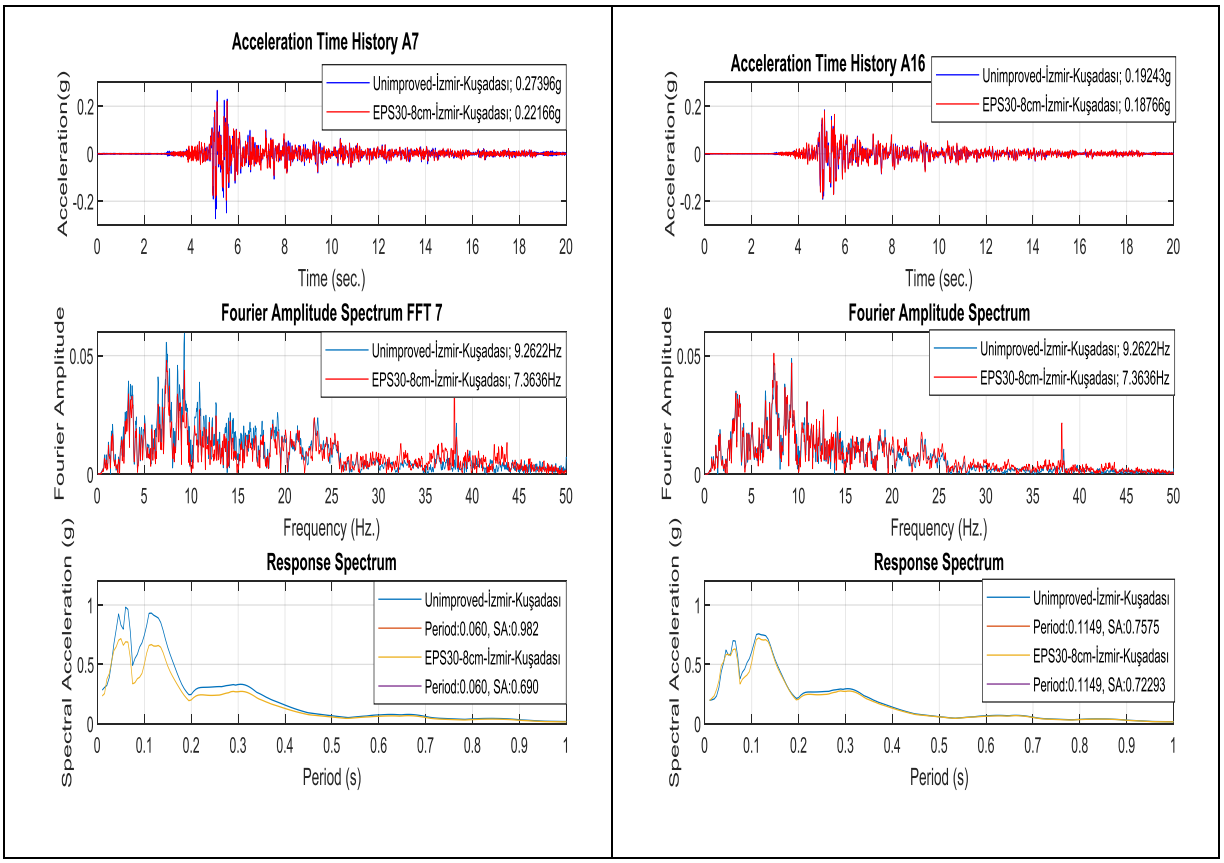


Figure 4.37. The ACCTH, FAS, Response Spectrum at the top of the RWM (A7) and in the backfill (A16) for Case 7 compared to Case 1 under the scaled 2020 İzmir EQ Motion-Kuşadası Station record (FF).

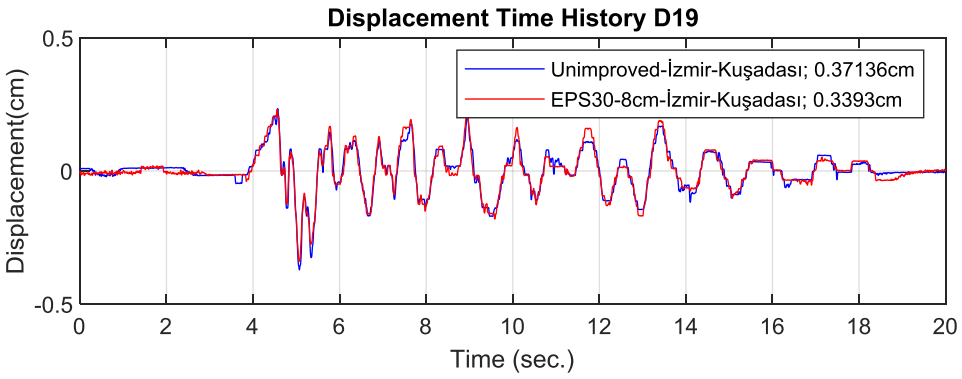


Figure 4.38. The DISTH at the top of the RWM (D19) for Case 7 compared to Case 1 under the scaled 2020 İzmir EQ Motion-Kuşadası Station record (FF).

Figure 4.39 illustrates the Acceleration-Time Histories, Fourier Amplitude Spectrums and Response Spectrums under the scaled 1940 Imperial Valley EQ-El Centro Station record. For the control case, the A7 measured a maximum acceleration of 0.52g, which decreased to 0.49g for the EPS30-8cm cushioned case. The A16 measured a maximum acceleration of 0.32g for the control case and 0.36g for the cushioned case. The Fourier amplitudes peaked at around 4.61 Hz for both the control and cushioned cases, measured by A7 and A16. The maximum spectral accelerations occurred at 0.05 sec and 0.22 sec period ranges for both the cushioned and control cases. At the top of the RWM, the maximum spectral accelerations ($S_a$) decreased from 1.48g to 1.189g for the EPS30-8cm cushioned case. In the backfill, the spectral accelerations were 1.27g for the control case and 1.46g for the cushioned case at the same periods of 0.22 sec.

Figure 4.40 displays the displacement time history of the control case compared to the cushioned case under the scaled 1940 Imperial Valley EQ-El Centro Station record. The maximum displacement of the cushioned model with EPS30-8cm was measured as 1.85 cm, while the control case was measured as 1.88 cm at the top of the RWM.

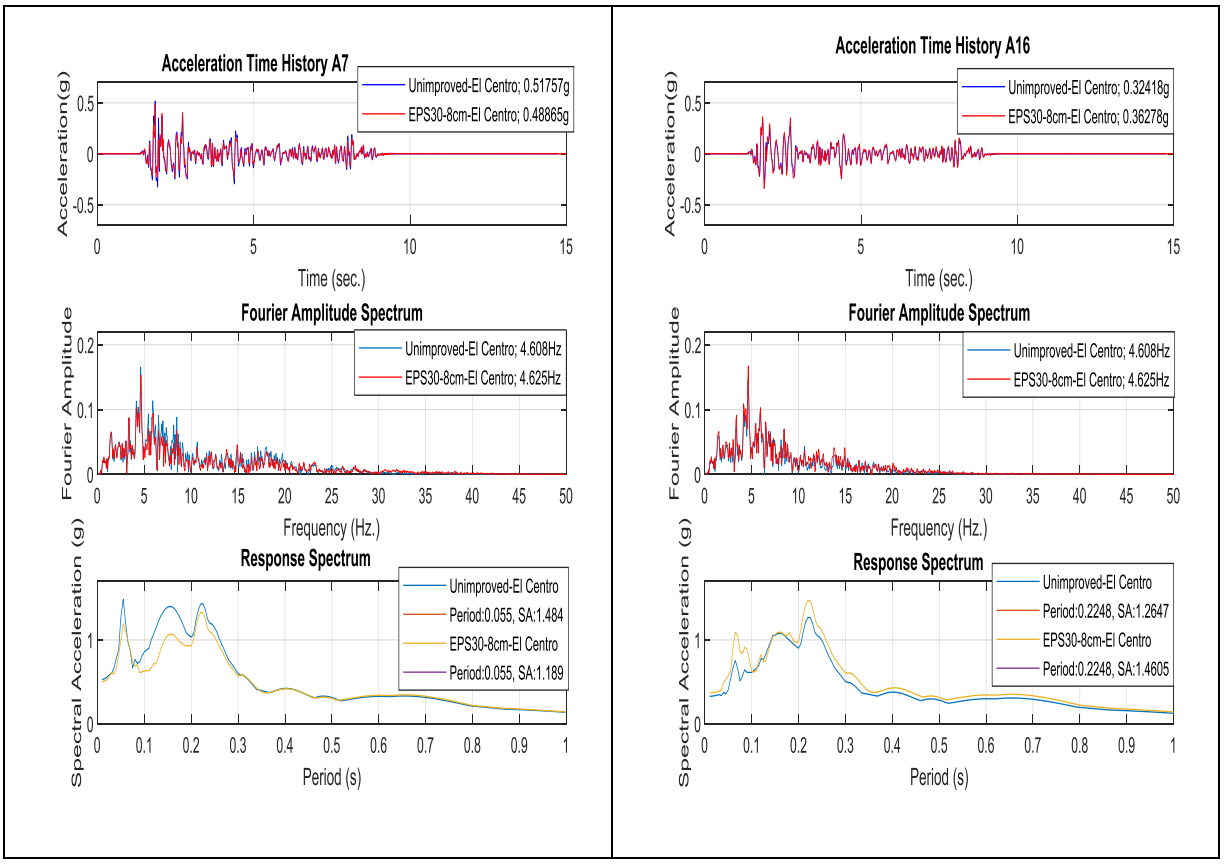


Figure 4.39. The ACCTH, FAS, Response Spectrum at the top of the RWM (A7) and in the backfill (A16) for Case 7 compared to Case 1 under the scaled 1940 Imperial Valley EQ-El Centro Station record (NF).

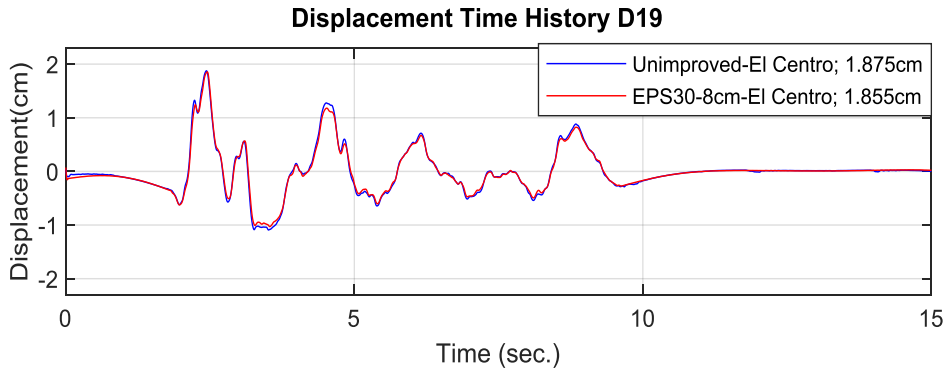


Figure 4.40. The DISTH at the top of the RWM (D19) for Case 7 compared to Case 1 under the scaled 1940 Imperial Valley EQ-El Centro Station record (NF).

For the sinusoidal motion at 0.4g amplitude with 8 Hz frequency, Figure 4.41 presents the Acceleration-Time Histories, Fourier Amplitude Spectrums, and Response Spectrums. The cushioned case with EPS10-8cm measured a maximum acceleration of 0.28g at the top of the RWM, compared to 0.47g for the control case. The A16 recorded a maximum acceleration of 0.31g for the cushioned case and 0.36g for the control case. The Fourier amplitude peaks were 8.03 Hz at the top of the RWM and in the backfill for both the cushioned and control cases. The maximum spectral accelerations ($S_a$) were at 0.12 sec period, decreasing from 4.7g to 2.72g at the top of the RWM and decreasing from 3.60g to 3.07g in the backfill for the control and cushioned cases, respectively.

Figure 4.42 presents the displacement time history of the control case compared to the cushioned case under sinusoidal motion at 0.4g amplitude with 8 Hz frequency. A reduction was observed in displacement measurement. Maximum displacement was measured as 0.10 cm at the top of the RWM for the cushioned case, whereas it was measured as 0.20 cm for the control case.

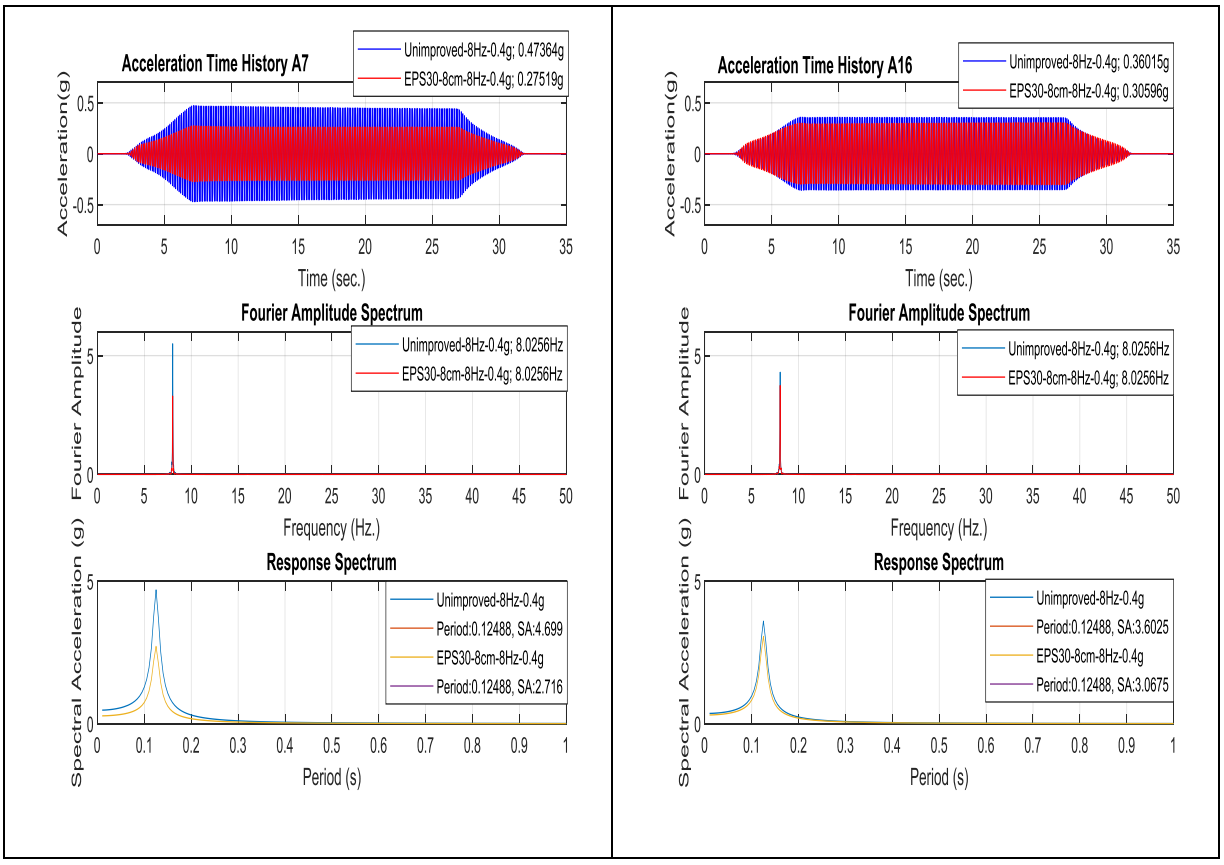


Figure 4.41. The ACCTH, FAS, Response Spectrum at the top of the RWM (A7) and in the backfill (A16) for Case 7 compared to Case 1 under sinusoidal motion at 0.4g amplitude with 8 Hz frequency.

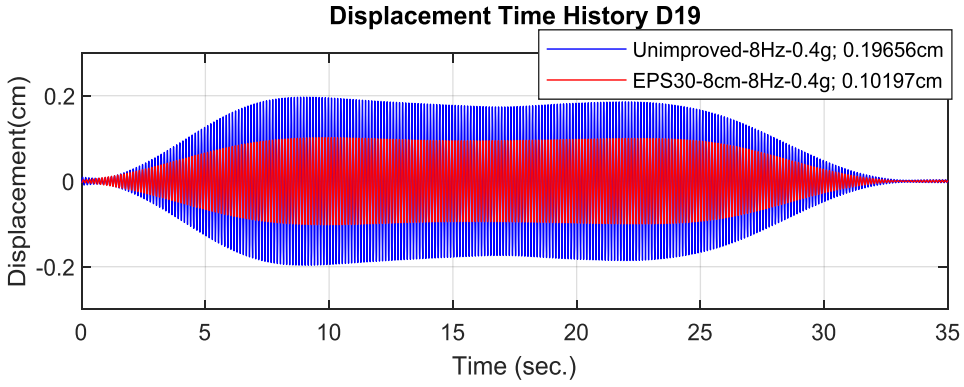


Figure 4.42. The DISTH at the top of the RWM (D19) for Case 7 compared to Case 1 under sinusoidal motion at 0.4g amplitude with 8 Hz frequency.

## 4.8. Results of Case 8 - TW10-4cm

This study focuses on Case 8, which involves a mixture of tire waste and sand cushion with a 10% mixture ratio and a thickness of 4 cm (TW10-4cm) behind the RWM. The results for two different earthquake motions and one sinusoidal motion are presented in Figures 4.43, 4.44, 4.45, 4.46, 4.47, and 4.48. These figures compare the measurements taken by accelerometer A7, laser displacement sensor D19 at the top of the retaining wall model (RWM), and accelerometer A16 in the backfill for the cushioned case (Case 8) to the control case.

In Figure 4.43, the Acceleration-Time Histories, Fourier Amplitude Spectrums, and Response Spectrums are depicted under the scaled 2020 İzmir EQ Motion-Kuşadası Station record for Case 8, compared to the control case (Case 1). The A7 recorded maximum acceleration values of 0.27g and 0.28g, and the A16 measured maximum acceleration values of 0.19g and 0.23g for the control case and TW10-4cm, respectively. The Fourier amplitudes for the control and cushioned cases were 9.24 Hz and 7.36 Hz at the top of the RWM and in the backfill. The maximum spectral accelerations occur at 0.05 sec and 0.13 sec period ranges. Comparing the control case and cushioned cases, the maximum spectral acceleration ($S_a$) values increased from 0.98g to 1.09g at a period of 0.060 sec at the top of the RWM and increased from 0.75g to 0.9g at a period of 0.11 sec in the backfill for the cushioned case compared to the control case.

Figure 4.44 demonstrates that under the dynamic motions of the scaled 2020 İzmir EQ Motion-Kuşadası Station, the control case displaced 0.37 cm, while the cushioned model TW10-4cm displaced 0.39 cm.

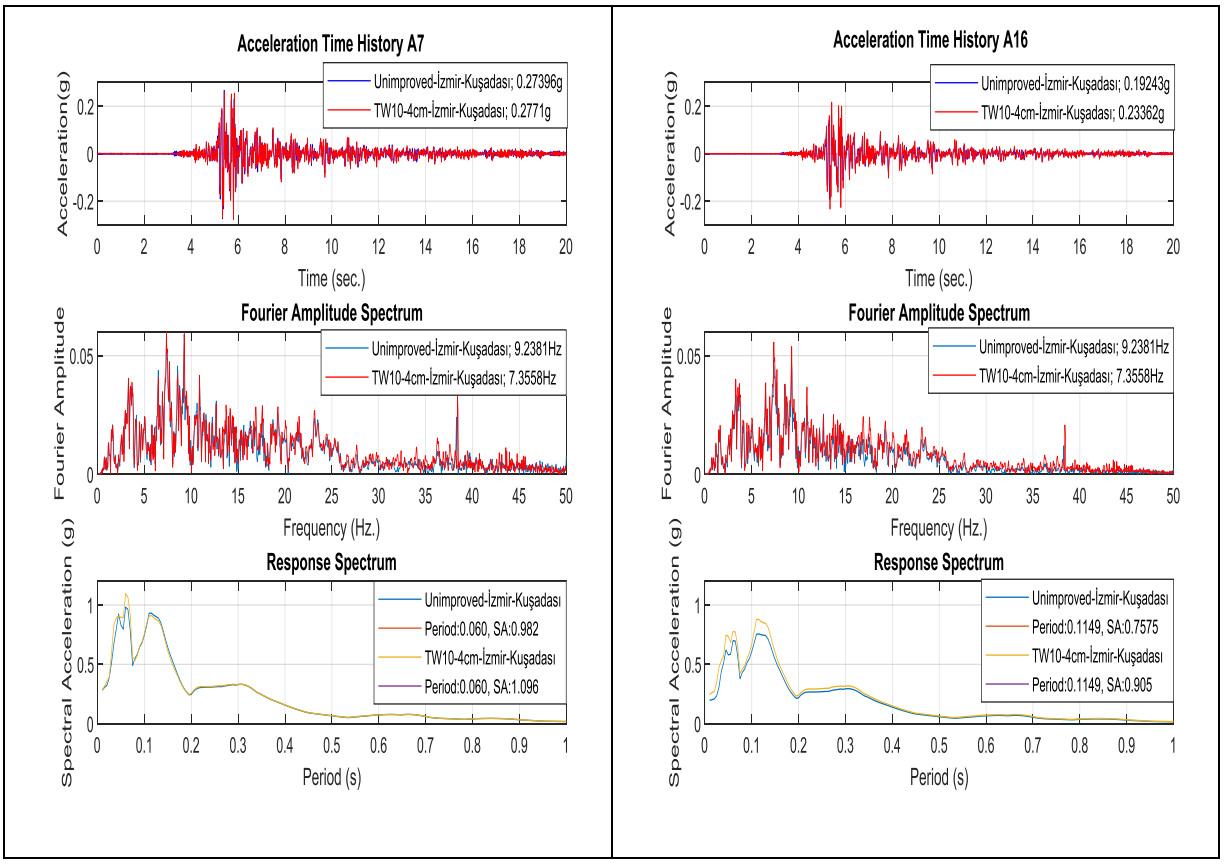


Figure 4.43. The ACCTH, FAS, Response Spectrum at the top of the RWM (A7) and in the backfill (A16) for Case 8 compared to Case 1 under the scaled 2020 İzmir EQ Motion-Kuşadası Station record (FF).

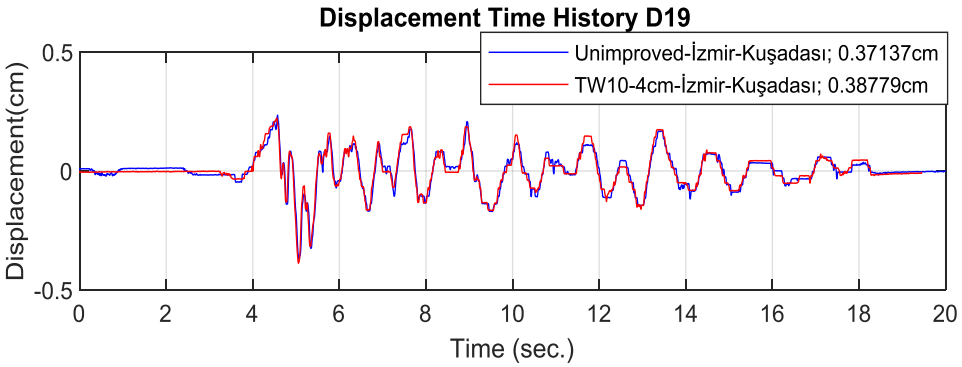


Figure 4.44. The DISTH at the top of the RWM (D19) for Case 8 compared to Case 1 under the scaled 2020 İzmir EQ Motion-Kuşadası Station record (FF).

Figure 4.45 presents the Acceleration-Time Histories, Fourier Amplitude Spectrums and Response Spectrums under the scaled 1940 Imperial Valley EQ-El Centro Station record. For the control case, it was recorded a maximum acceleration of 0.52g at the top of the RWM, which decreased to 0.50g for the cushioned case TW10-4cm. The A16 measured a maximum acceleration of 0.32g for both the control and cushioned cases. The Fourier amplitudes peaked around 4.61 Hz and 4.59 Hz at the top of the RWM and 4.61 Hz and 4.65 Hz in the backfill for the control case and cushioned case. The maximum spectral accelerations occur at 0.05 sec and 0.22 sec period ranges for both the cushioned and control cases. The maximum spectral accelerations ($S_a$) were 1.48g at 0.055 sec period at the top of the RWM for the control case, decreasing to 1.24g at 0.60 sec period for the TW10-4cm cushioned case. The maximum spectral accelerations were shifted to the higher period ranges for the TW10-4cm cushioned case. Accordingly, a 19% reduction in seismic demand was calculated as the spectral acceleration decreased from 1.48g to 1.20g, shifting the periods from 0.055 sec to 0.060 sec. TW cushion extends the period of the retaining wall caused by the earthquake, and the damping of the system increases. The spectral accelerations in the backfill were 1.26g and 1.44g at the same periods 0.22 sec for the control case and TW10-4cm cushioned case, respectively.

Figure 4.46 presents the displacement time history of the control case compared to the cushioned case under the scaled 1940 Imperial Valley EQ-El Centro Station record. The maximum displacement of the TW10-4cm cushioned model was measured as 1.93 cm, while the control case was measured as 1.88 cm at the top of the RWM.

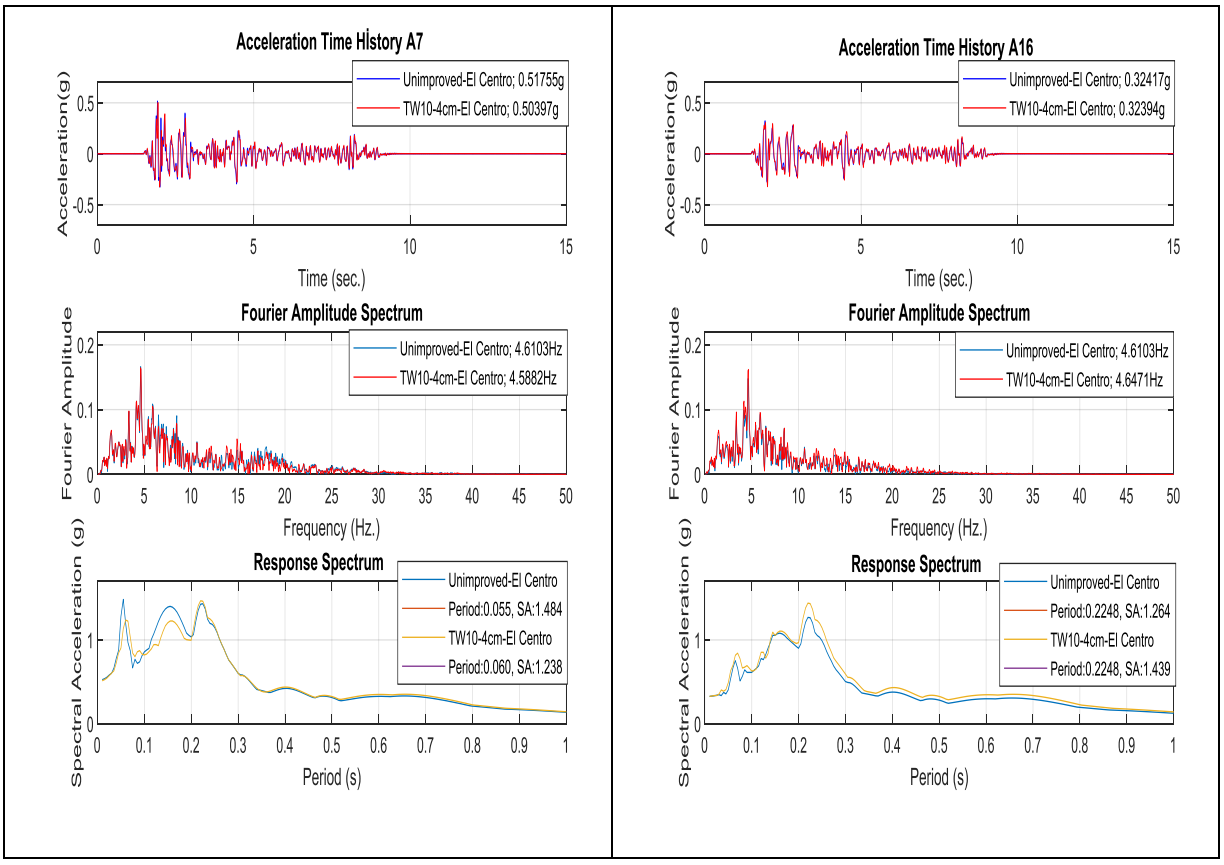


Figure 4.45. The ACCTH, FAS, Response Spectrum at the top of the RWM (A7) and in the backfill (A16) for Case 8 compared to Case 1 under the scaled 1940 Imperial Valley EQ-El Centro Station record (NF).

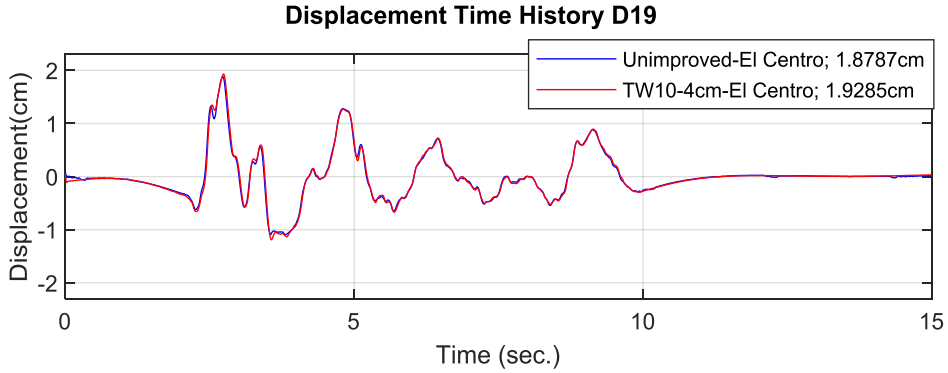


Figure 4.46. The DISTH at the top of the RWM (D19) for Case 8 compared to Case 1 under the scaled 1940 Imperial Valley EQ-El Centro Station record (NF).

The Acceleration-Time Histories, Fourier Amplitude Spectrums, and Response Spectrums under the sinusoidal motion at 0.4g amplitude with 8 Hz frequency are shown in Figure 4.47. The maximum acceleration of 0.45g was measured at the top of the RWM for the TW10-4cm cushioned case compared to the control case as 0.47g, and the A16 measured 0.44g maximum acceleration for the cushioned case compared to the control case as 0.36g. The Fourier amplitude peaks were 8.02 Hz at the top of the RWM and in the backfill for both the cushioned and control cases. The maximum spectral accelerations ($S_a$) were at 0.12 sec period, decreasing from 4.7g to 4.45g at the top of the RWM and increasing from 3.60g to 4.44g in the backfill for the control and cushioned cases, respectively.

Figure 4.48 presents the displacement time history of the control case compared to the cushioned case under sinusoidal motion at 0.4g amplitude with 8 Hz frequency. A reduction was observed in displacement measurement. Maximum displacement was measured as 0.16 cm at the top of the RWM for the cushioned case, whereas it was measured as 0.20 cm for the control case.

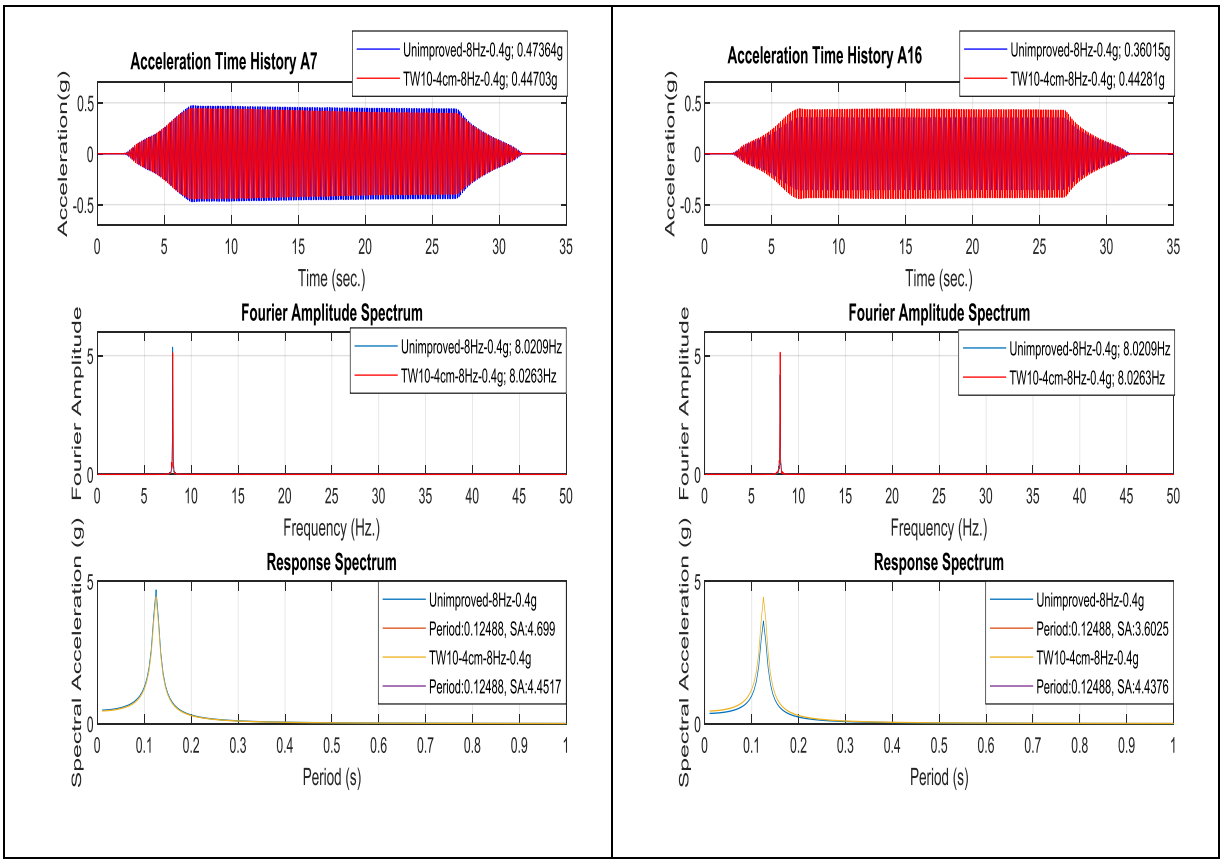


Figure 4.47. The ACCTH, FAS, Response Spectrum at the top of the RWM (A7) and in the backfill (A16) for Case 8 compared to Case 1 under sinusoidal motion at 0.4g amplitude with 8 Hz frequency.

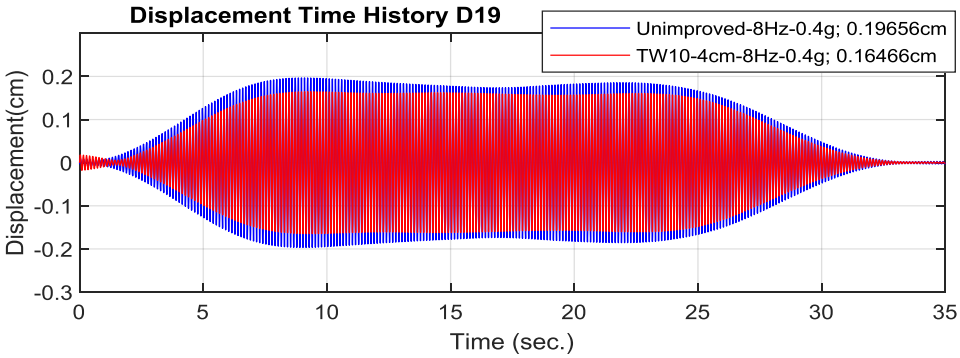


Figure 4.48. The DISTH at the top of the RWM (D19) for Case 8 compared to Case 1 under sinusoidal motion at 0.4g amplitude with 8 Hz frequency.

## 4.9. Results of Case 9 - TW20-4cm

Case 9 consists of tire waste and sand mixture cushion with a 20% mixture ratio and 4 cm thickness (TW20-4cm) behind the RWM. Figures 4.49, 4.50, 4.51, 4.52, 4.53, and 4.54 show the results for two different earthquake motions and one sinusoidal motion as measured by accelerometer A7, laser displacement sensor D19 at the top of the retaining wall model (RWM) and accelerometer A16 in the backfill in comparison to the control case.

Figure 4.49 demonstrates the Acceleration-Time Histories, Fourier Amplitude Spectrums, and Response Spectrums for Case 9 compared to the control case under the scaled 2020 İzmir EQ Motion-Kuşadası Station excitations. The maximum acceleration values were measured as 0.27g and 0.29g at the top of the RWM, while the maximum acceleration values were measured as 0.19g and 0.24g in the backfill for the control case and Case 9, respectively. The Fourier amplitudes at the top of the RWM and in the backfill were 9.26 Hz and 7.36 Hz for the control and cushioned cases. The maximum spectral accelerations occur in the 0.05 and 0.13 sec period ranges. Comparing the control and cushioned cases, the maximum spectral acceleration ($S_a$) values increased from 0.98g to 1.02g at the top of the RWM for a period of 0.06 sec. In the backfill, the maximum spectral acceleration ($S_a$) values increased from 0.75g to 0.89g at a period of 0.11 sec for the control and cushioned cases, respectively.

Figure 4.50 depicts the displacement comparison between the control case and the cushioned model TW20-4cm under the dynamic motions of the scaled 2020 İzmir EQ Motion-Kuşadası Station. The control case displaced 0.37 cm, whereas the cushioned model displaced 0.38 cm.

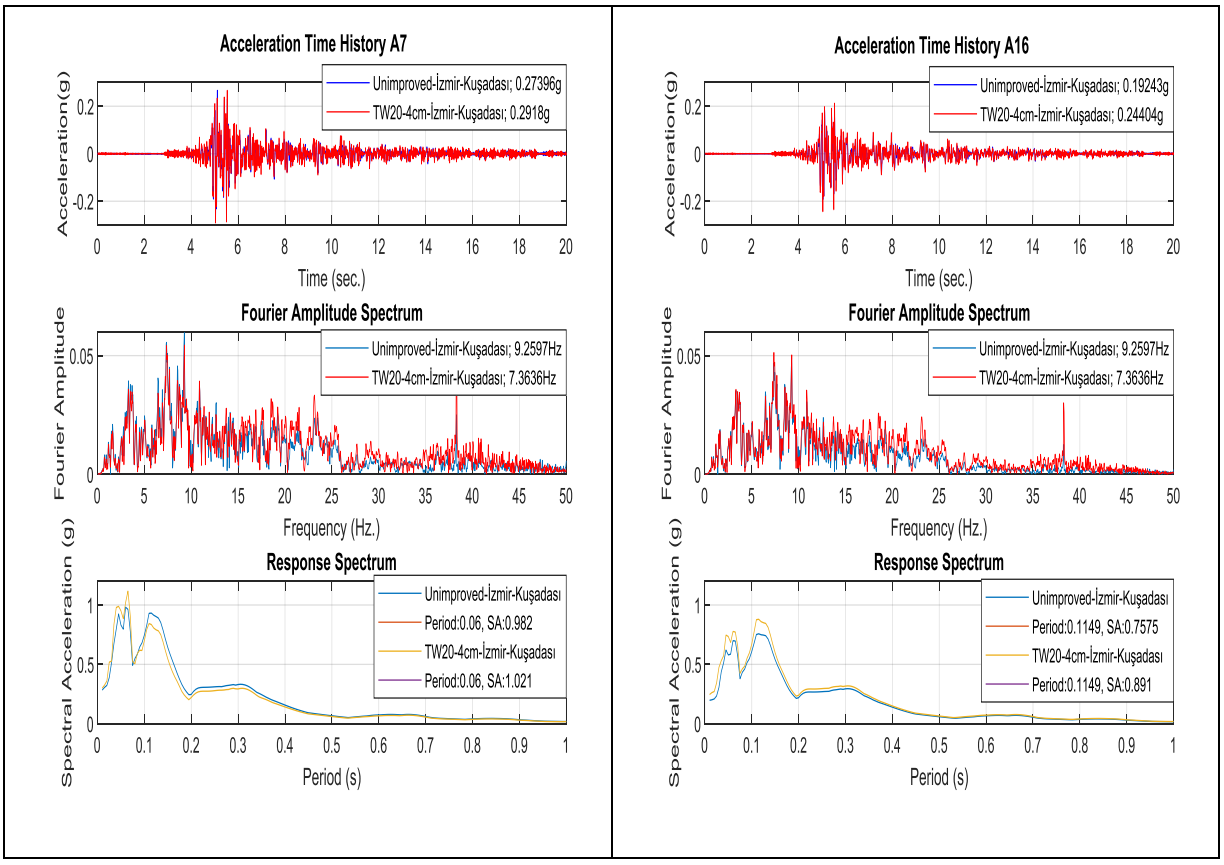


Figure 4.49. The ACCTH, FAS, Response Spectrum at the top of the RWM (A7) and in the backfill (A16) for Case 9 compared to Case 1 under the scaled 2020 İzmir EQ Motion-Kuşadası Station record (FF).

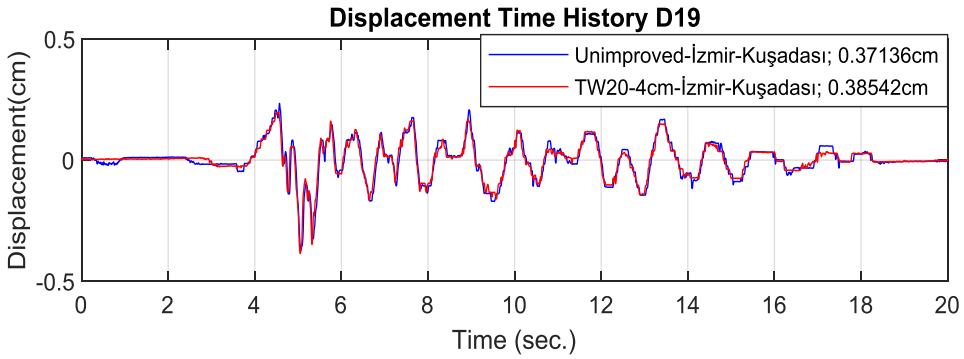


Figure 4.50. The DISTH at the top of the RWM (D19) for Case 9 compared to Case 1 under the scaled 2020 İzmir EQ Motion-Kuşadası Station record (FF).

Figure 4.51 shows the Acceleration-Time Histories, Fourier Amplitude Spectrums and Response Spectrums under the scaled 1940 Imperial Valley EQ-El Centro Station record. For the control case, the A7 recorded a peak acceleration of 0.52g, which decreased to 0.46g for the cushioned case TW20-4cm. Similarly, the A16 measured a maximum acceleration of 0.32g for the control case and 0.33g for the cushioned case. It is worth noting that the maximum acceleration values decreased at the top of the RWM when the TW20-4cm was implemented. The Fourier amplitudes peaked around 4.61 Hz and 4.59 for the control and cushioned cases, measured from A7 and A16. The maximum spectral accelerations occurred in the 0.05 and 0.22 sec period ranges for both the cushioned and control cases. The maximum spectral accelerations ($S_a$) were 1.48g at 0.055 sec period at the top of the RWM for the control case, decreasing to 1.18g at 0.60 sec period for the TW20-4cm cushioned case. The maximum spectral accelerations were shifted to the higher period ranges for the TW20-4cm cushioned case. Accordingly, a 20% reduction in seismic demand was calculated as the spectral acceleration decreased from 1.48g to 1.18g, shifting the periods from 0.055 sec to 0.06 sec. TW cushion extends the period of the retaining wall caused by the earthquake, and the damping of the system increases. In the backfill, the spectral accelerations were 1.26g and 1.33g for the control and cushioned cases, respectively, at the same 0.22 sec periods.

Figure 4.52 displays the displacement time history of the control case compared to the cushioned case under the scaled 1940 Imperial Valley EQ-El Centro Station record. The maximum displacement for the cushioned model was 1.93 cm at the top of the RWM, while the control case recorded a peak displacement of 1.88 cm.

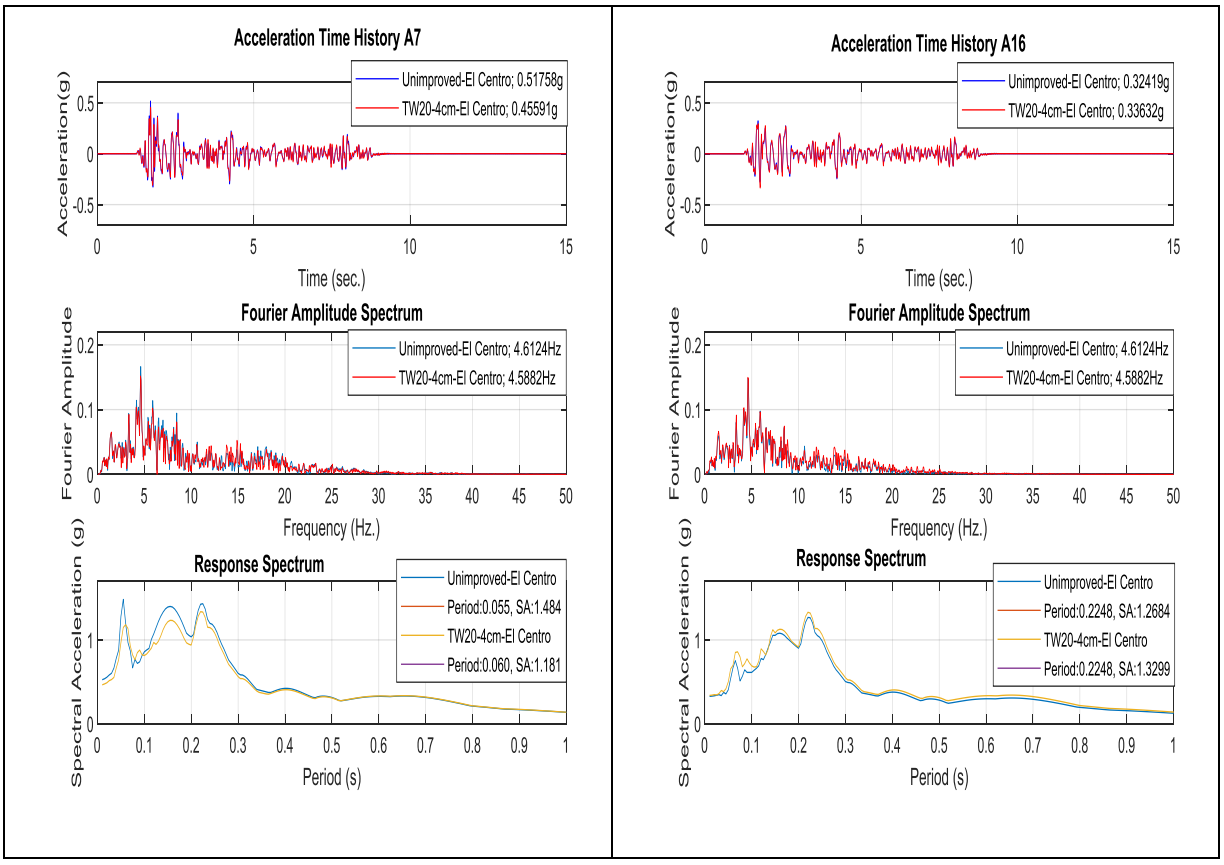


Figure 4.51. The ACCTH, FAS, Response Spectrum at the top of the RWM (A7) and in the backfill (A16) for Case 9 compared to Case 1 under the scaled 1940 Imperial Valley EQ-El Centro Station record (NF).

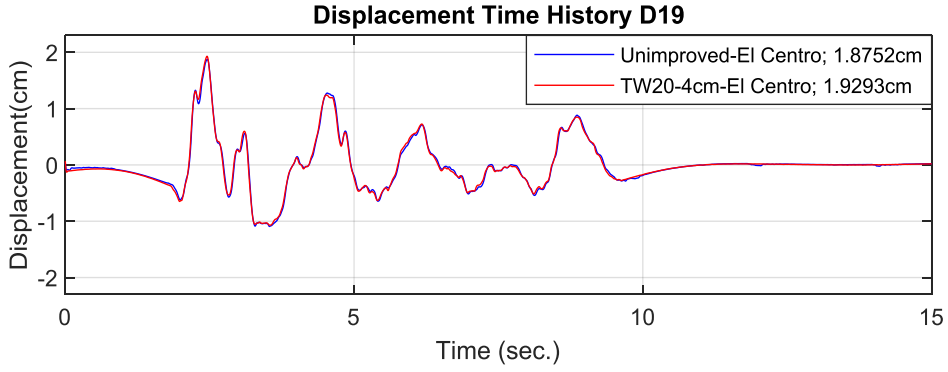


Figure 4.52. The DISTH at the top of the RWM (D19) for Case 9 compared to Case 1 under the scaled 1940 Imperial Valley EQ-El Centro Station record (NF).

Figure 4.53 presents the Acceleration-Time Histories, Fourier Amplitude Spectrums, and Response Spectrums under the sinusoidal motion at 0.4g amplitude with 8 Hz frequency. For the cushioned case, the A7 recorded a peak acceleration of 0.45g at the top of the RWM, compared to 0.47g for the control case. Similarly, the A16 measured a maximum acceleration of 0.48g for the cushioned case and 0.36g for the control case. The peaks of the Fourier amplitudes were observed at 8.03 Hz at the top of the RWM and in the backfill for both the cushioned and control cases, based on measurements from A7 and A16. The maximum spectral accelerations ($S_a$) occurred at a period of 0.12 sec. For the control case, the $S_a$ decreased from 4.7g to 4.44g at the top of the RWM and increased from 3.60g to 4.80g in the backfill, compared to the cushioned case.

Figure 4.54 compares the displacement time history of the control case to the cushioned case under sinusoidal motion at 0.4g amplitude with 8 Hz frequency. The cushioned case exhibited a reduced displacement, with a peak displacement of 0.18 cm at the top of the RWM, whereas the control case had a peak displacement of 0.20 cm.

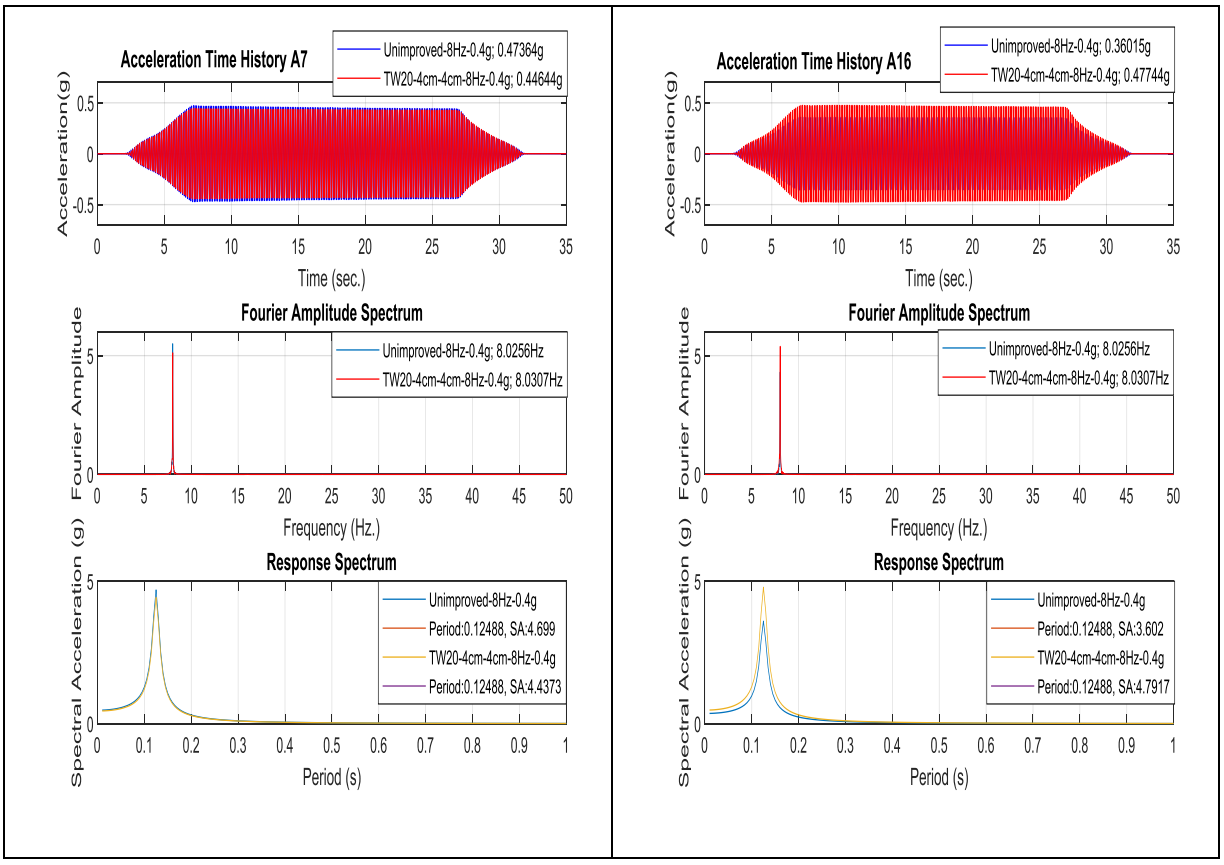


Figure 4.53. The ACCTH, FAS, Response Spectrum at the top of the RWM (A7) and in the backfill (A16) for Case 9 compared to Case 1 under sinusoidal motion at 0.4g amplitude with 8 Hz frequency.

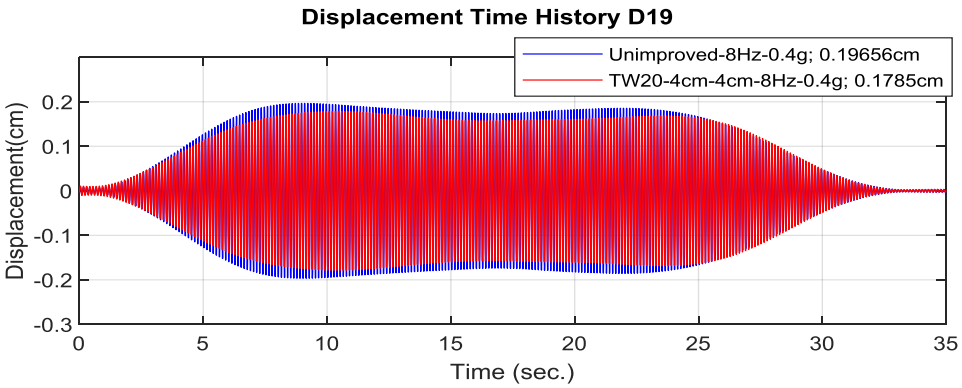


Figure 4.54. The DISTH at the top of the RWM (D19) for Case 9 compared to Case 1 under sinusoidal motion at 0.4g amplitude with 8 Hz frequency.

## 4.10. Results of Case 10 - TW30-4cm

Case 10 involves a mixture of tire waste and sand cushion with a ratio of 30% and a thickness of 4 cm (TW30-4cm) behind the RWM. The results obtained from the sensors as accelerometer A7, laser displacement sensor D19 at the top of the retaining wall model (RWM), and accelerometer A16 in the backfill are compared to the control case for two different earthquake motions and one sinusoidal motion. Figures 4.55, 4.56, 4.57, 4.58, 4.59, and 4.60 showcase these results.

Figure 4.55 displays the Acceleration-Time Histories, Fourier Amplitude Spectrums, and Response Spectrums for Case 10 and the control case (Case 1) under the scaled 2020 İzmir EQ Motion-Kuşadası Station excitations. The A7 recorded maximum acceleration values of 0.27g and 0.26g, while the A16 measured maximum acceleration values of 0.19g and 0.16g for the control and cushioned cases, respectively. The Fourier amplitudes for the control and cushioned cases were 9.23 Hz and 7.36 Hz at the top of the RWM and in the backfill. The response spectrums show that the maximum spectral accelerations occurred within the 0.05 and 0.13 sec period ranges. Comparing the control case and cushioned cases, the maximum spectral acceleration ($S_a$) decreased from 0.98g to 0.88g at the top of the RWM at a period of 0.06 sec. In the backfill, the spectral accelerations were 0.76g and 0.70g at a period of 0.11 sec for the cushioned and control cases, respectively.

Figure 4.56 indicates that under the dynamic motions of the scaled 2020 İzmir EQ Motion-Kuşadası Station, the maximum displacement of the control case was 0.37 cm, while the cushioned model TW30-4cm displaced a maximum of by 0.36 cm.

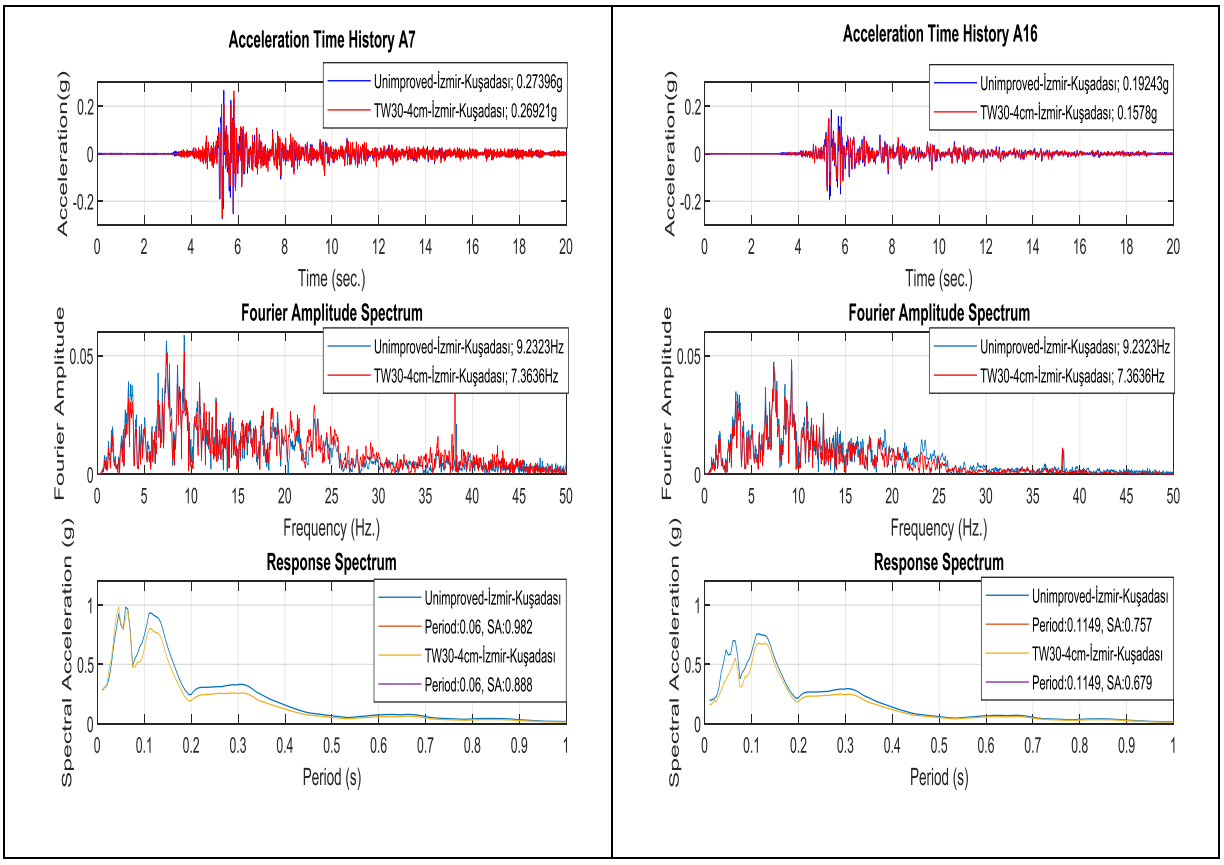


Figure 4.55. The ACCTH, FAS, Response Spectrum at the top of the RWM (A7) and in the backfill (A16) for Case 10 compared to Case 1 under the scaled 2020 İzmir EQ Motion-Kuşadası Station record (FF).

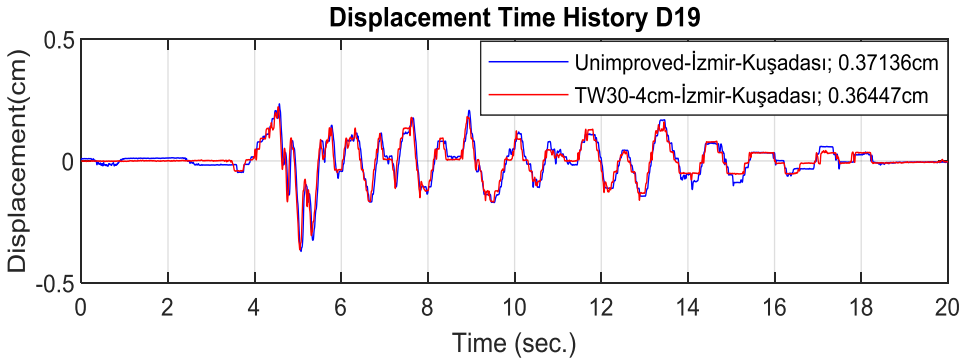


Figure 4.56. The DISTH at the top of the RWM (D19) for Case 10 compared to Case 1 under the scaled 2020 İzmir EQ Motion-Kuşadası Station record (FF).

Figure 4.57 presents the Acceleration-Time Histories, Fourier Amplitude Spectrums, and Response Spectrums under the scaled 1940 Imperial Valley EQ-El Centro Station record. The A7 recorded a maximum acceleration of 0.52g for the control case, which decreased to 0.48g for the cushioned case. Similarly, the maximum acceleration values measured by the A16 were 0.32g for the control case and 0.37g for the cushioned case. The Fourier amplitudes peaked around 4.60 Hz at the top of the RWM and in the backfill for both the control and cushioned cases. The response spectrums show that the maximum spectral accelerations occurred within the 0.05 sec and 0.22 sec period ranges. At the top of the RWM, the control case recorded a maximum spectral acceleration ($S_a$) of 1.48g at a period of 0.055 sec, which decreased to 1.39g for the cushioned case. In the backfill, the spectral accelerations were 1.26g for the control case and 1.30g for the cushioned case at the same period of 0.22 sec.

Figure 4.58 illustrates the displacement time history of the control case compared to the cushioned case under the scaled 1940 Imperial Valley EQ-El Centro Station record. The cushioned case with the TW cushion had a measured maximum displacement of 1.77 cm, while the control case had a peak displacement of 1.88 cm at the top of the RWM.

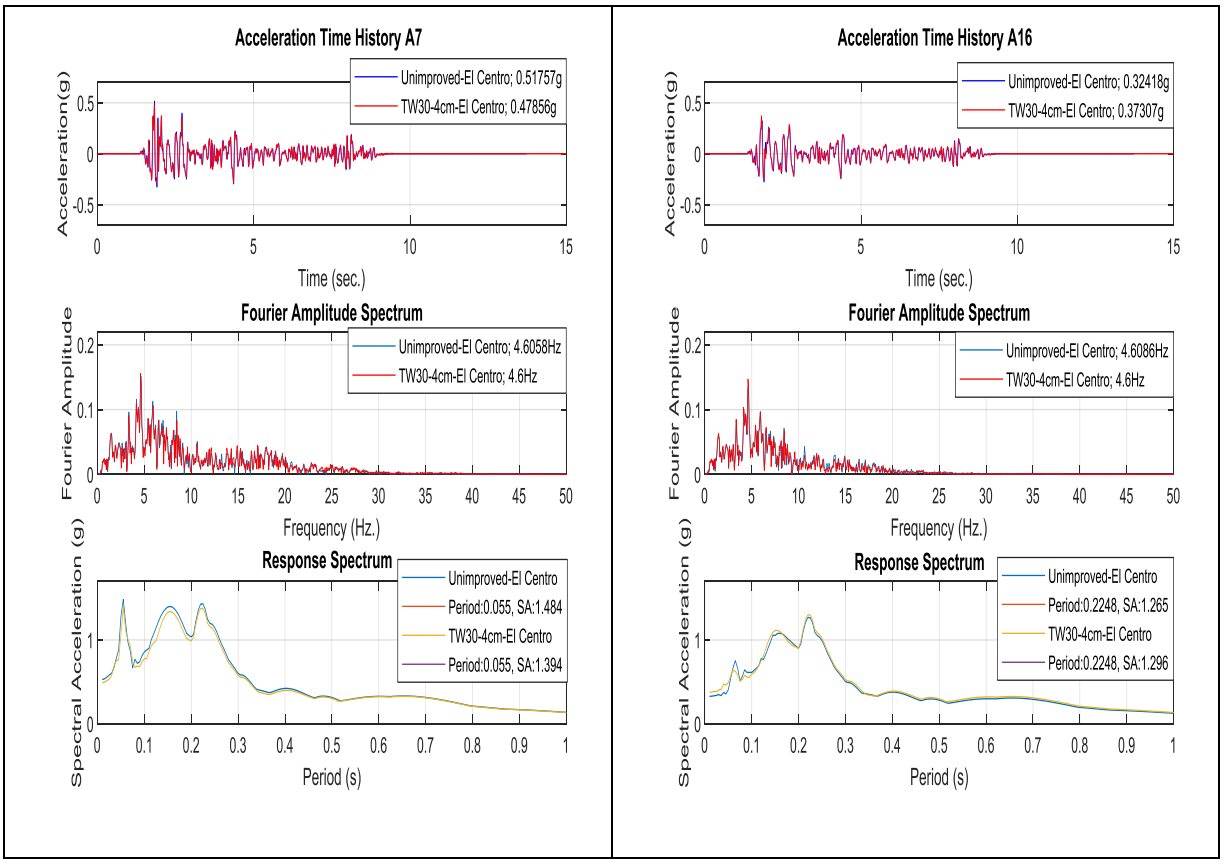


Figure 4.57. The ACCTH, FAS, Response Spectrum at the top of the RWM (A7) and in the backfill (A16) for Case 10 compared to Case 1 under sinusoidal motion at 0.4g amplitude with 8 Hz frequency.

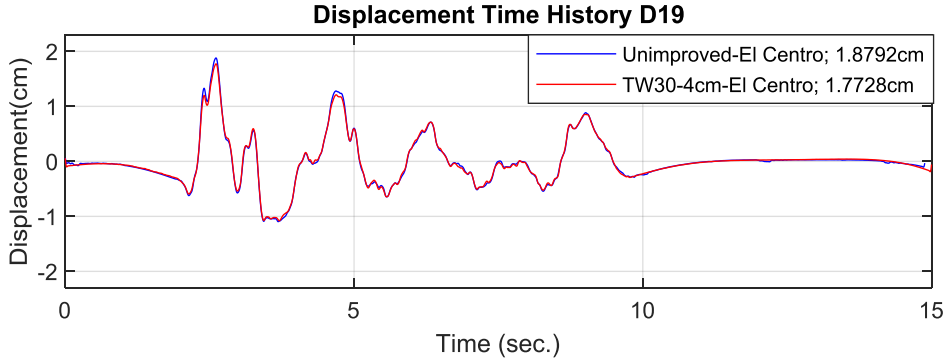


Figure 4.58. The DISTH at the top of the RWM (D19) for Case 10 compared to Case 1 under sinusoidal motion at 0.4g amplitude with 8 Hz frequency.

Figure 4.59 shows the Acceleration-Time Histories, Fourier Amplitude Spectrums, and Response Spectrums under sinusoidal motion at 0.4g amplitude with 8 Hz frequency. For the cushioned case, it was measured a maximum acceleration of 0.45g at the top of the RWM, compared to 0.47g for the control case. The A16 recorded a maximum acceleration of 0.31g for the cushioned case and 0.36g for the control case. The peak Fourier amplitudes were 8.02 Hz at the top of the RWM and in the backfill for both cases. The response spectrums demonstrate that the maximum spectral accelerations occurred at a period of 0.12 sec, decreasing from 4.7g to 4.42g at the top of the RWM and from 3.60g to 3.10g in the backfill for the control case and cushioned cases, respectively.

Figure 4.60 presents the displacement time history of the control case compared to the cushioned case under sinusoidal motion at 0.4g amplitude with 8 Hz frequency. A reduction was observed in displacement measurement. Maximum displacement was measured as 0.17 cm at the top of the RWM for the cushioned case, whereas it was measured as 0.20 cm for the control case.

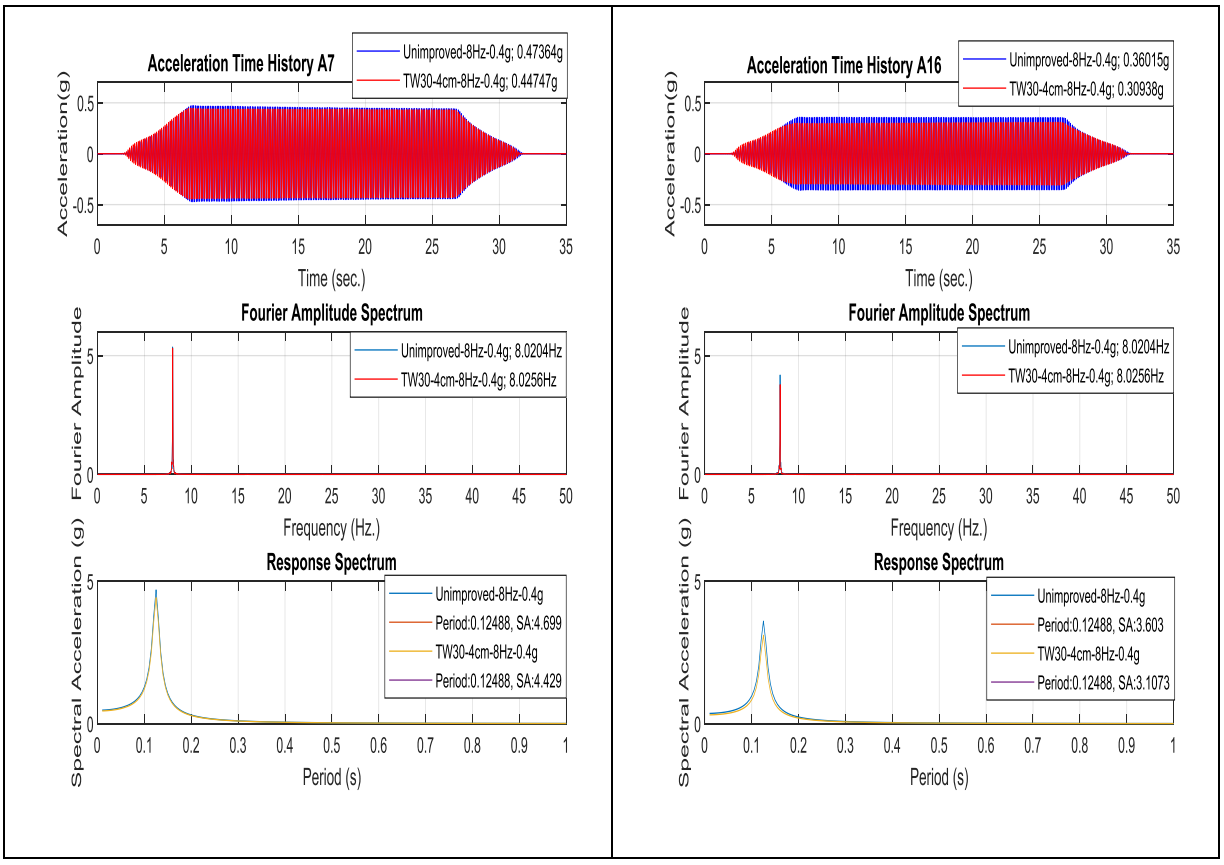


Figure 4.59. The ACCTH, FAS, Response Spectrum at the top of the RWM (A7) and in the backfill (A16) for Case 10 compared to Case 1 under sinusoidal motion at 0.4g amplitude with 8 Hz frequency.

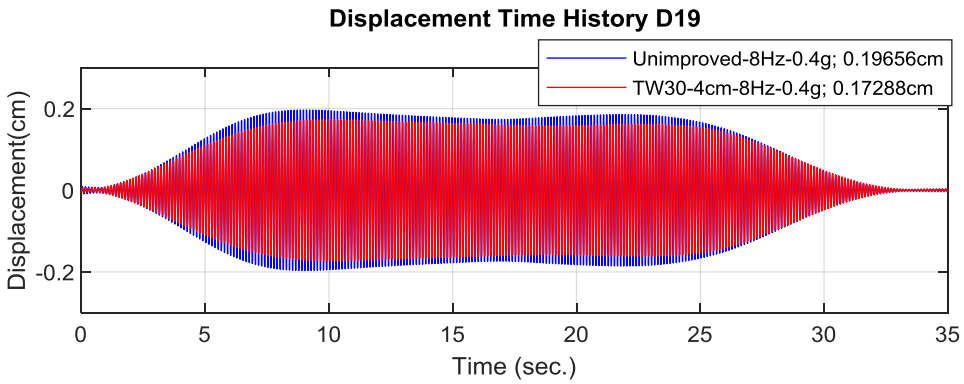


Figure 4.60. The DISTH at the top of the RWM (D19) for Case 10 compared to Case 1 under sinusoidal motion at 0.4g amplitude with 8 Hz frequency.

## 4.11. Results of Case 11 - TW10-8cm

The study examined the effects of using a tire waste and sand mixture cushion with a 10% mixture ratio and 8 cm thickness (TW10-8cm) behind the RWM in Case 11. Figures 4.61 to 4.66 display the results obtained from accelerometer A7, laser displacement sensor D19 at the top of the retaining wall model (RWM), and accelerometer A16 in the backfill, comparing the cushioned Case 11 to the control case. These Figures depict the outcomes for two different earthquake motions and one sinusoidal motion.

Figure 4.61 showcases the Acceleration-Time Histories, Fourier Amplitude Spectrums, and Response Spectrums under the scaled 2020 İzmir EQ Motion-Kuşadası Station excitations for Case 11 compared to the control case. The A7 recorded maximum acceleration values of 0.27g at the top of the RWM for both the control and cushioned cases. Ther A16 measured maximum acceleration values of 0.19g for the control case and 0.24g for the cushioned case. The Fourier amplitudes at the top of the RWM and in the backfill were 9.23 Hz for the control case and 7.35 Hz for the cushioned case. The response spectrums revealed maximum spectral accelerations occurring at period ranges of 0.05 sec and 0.13 sec. Comparing the control case and cushioned cases, it was observed that the maximum spectral acceleration ($S_a$) values decreased from 0.98g to 0.91g at the top of the RWM at a period of 0.06 sec. In the backfill, these values were 0.76g for the control case and 0.88g for the cushioned case at a period of 0.11 sec.

Figure 4.62 demonstrates that under the dynamic motions of the scaled 2020 İzmir EQ Motion-Kuşadası Station, the cushioned model TW10-8cm displaced slightly (0.38 cm) compared to the control case (0.37 cm).

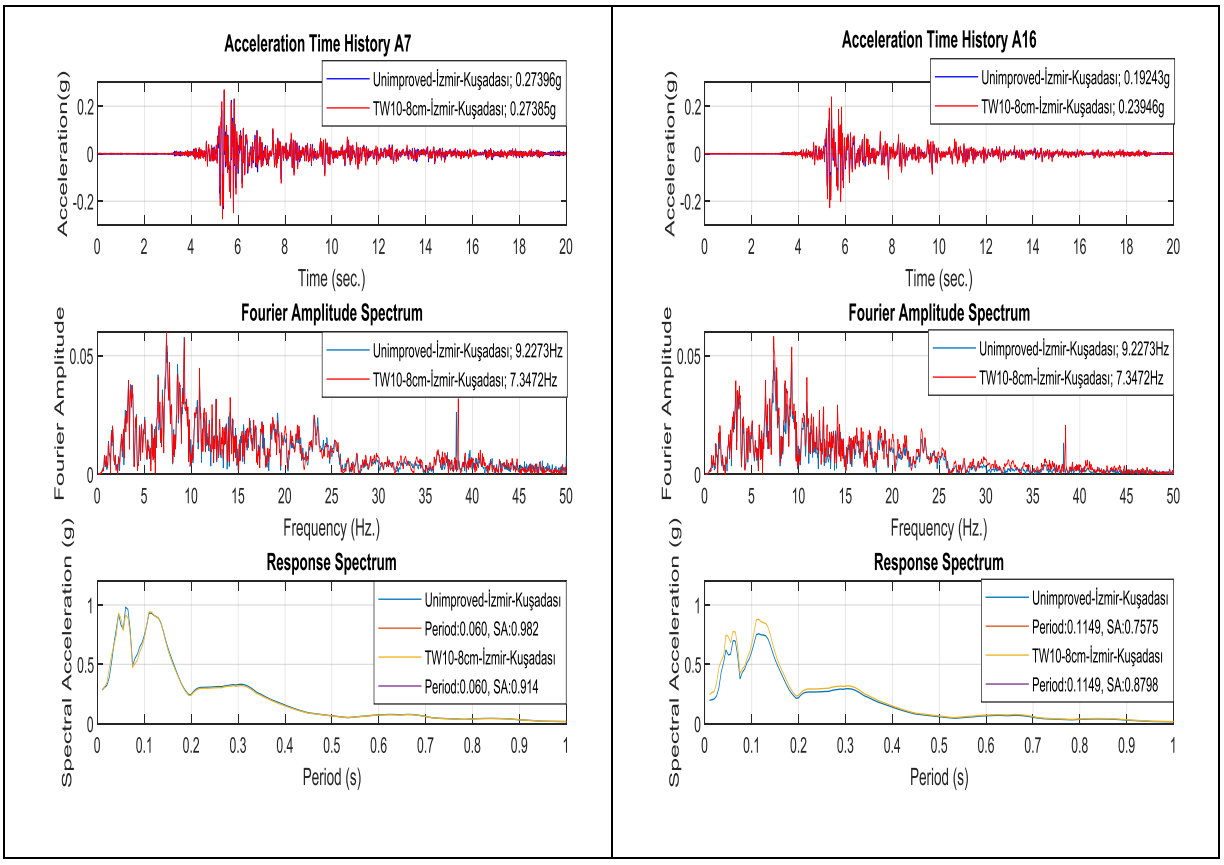


Figure 4.61. The ACCTH, FAS, Response Spectrum at the top of the RWM (A7) and in the backfill (A16) for Case 11 compared to Case 1 under the scaled 2020 İzmir EQ Motion-Kuşadası Station record (FF).

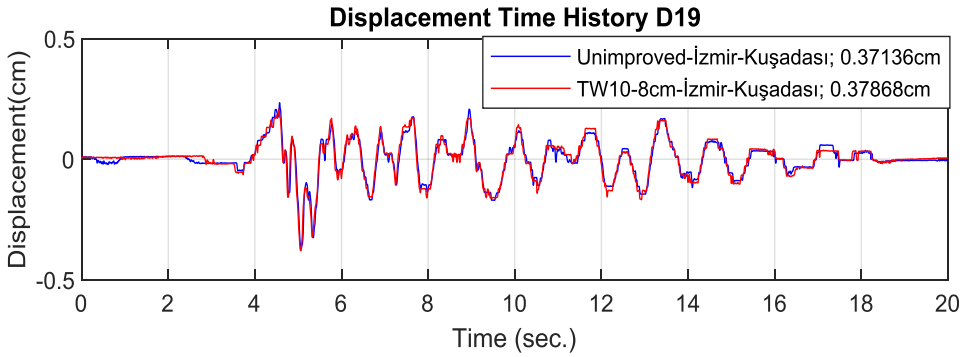


Figure 4.62. The DISTH at the top of the RWM (D19) for Case 11 compared to Case 1 under the scaled 2020 İzmir EQ Motion-Kuşadası Station record (FF).

Figure 4.63 presents the Acceleration-Time Histories, Fourier Amplitude Spectrums, and Response Spectrums under the scaled 1940 Imperial Valley EQ-El Centro Station record. For the control case, the A7 recorded a maximum acceleration value of 0.52g, which decreased to 0.48g for the TW10-8cm cushioned case. The A16 measured a maximum acceleration value of 0.32g for the control case and 0.35g for the cushioned case. It can be obtained that the maximum acceleration values at the top of the RWM decreased when the TW10-8cm cushion was implemented. The Fourier amplitudes peaked around 4.62 Hz at the top of the RWM and in the backfill for both the control and cushioned cases. The response spectrums displayed maximum spectral accelerations at 0.05 and 0.22 sec period ranges. The maximum spectral accelerations ($S_a$) at the top of the RWM were 1.48g for the control case and 1.34g for the cushioned case. In the backfill, these values were 1.26g and 1.49g for the control and cushioned cases, respectively, at a period of 0.22 sec.

Figure 4.64 illustrates the displacement time history for the control case compared to the cushioned case under the scaled 1940 Imperial Valley EQ-El Centro Station record. The cushioned case, TW10-8cm cushion, exhibited a measured maximum displacement of 1.90 cm at the top of the RWM, while the control case had a peak displacement of 1.88 cm.

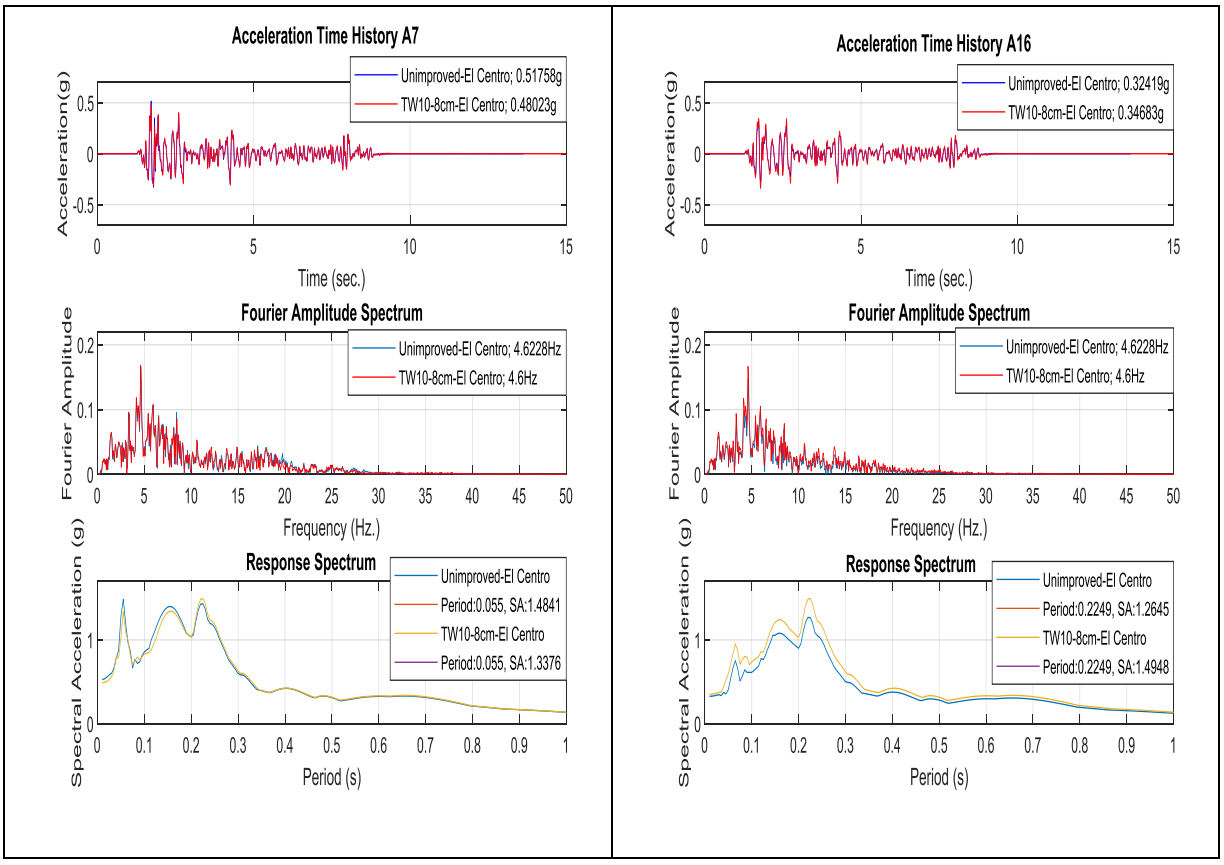


Figure 4.63. The ACCTH, FAS, Response Spectrum at the top of the RWM (A7) and in the backfill (A16) for Case 11 compared to Case 1 under the scaled 1940 Imperial Valley EQ-El Centro Station record (NF).

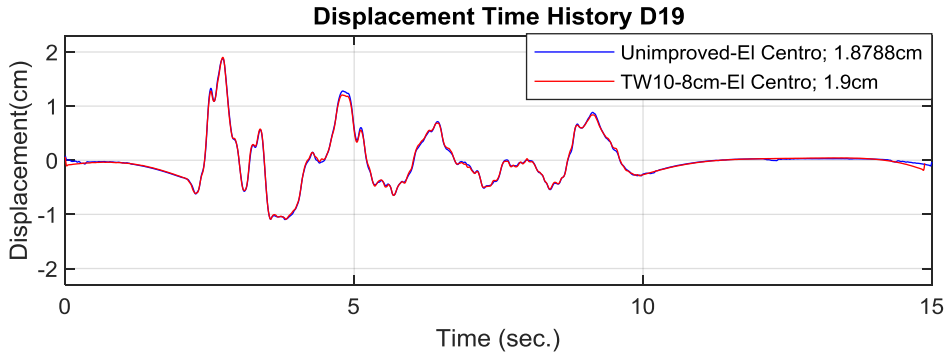


Figure 4.64. The DISTH at the top of the RWM (D19) for Case 11 compared to Case 1 under the scaled 1940 Imperial Valley EQ-El Centro Station record (NF).

Figure 4.65 showcases the Acceleration-Time Histories, Fourier Amplitude Spectrums, and Response Spectrums under a sinusoidal motion at 0.4g amplitude with 8 Hz frequency. For the cushioned case with the TW10-8cm cushion, A7 recorded a maximum acceleration value of 0.43g, whereas the control case recorded a maximum acceleration value of 0.47g. The A16 measured a maximum acceleration value of 0.42g for the cushioned case and 0.36g for the control case. The Fourier amplitudes peaked at 8.03 Hz for both the cushioned and control cases, measured from accelerometers A7 and A16. The maximum spectral accelerations ($S_a$) were at 0.12 sec period, decreasing from 4.7g to 4.32g at the top of the RWM and increasing from 3.60g to 4.21g in the backfill measured from A16 for the control case and cushioned case, respectively.

Figure 4.66 presents the displacement time history of the control case compared to the cushioned case under sinusoidal motion at 0.4g amplitude with 8 Hz frequency. A reduction was observed in displacement measurement. Maximum displacement was measured as 0.17 cm at the top of the RWM for the cushioned case, whereas it was measured as 0.20 cm for the control case.

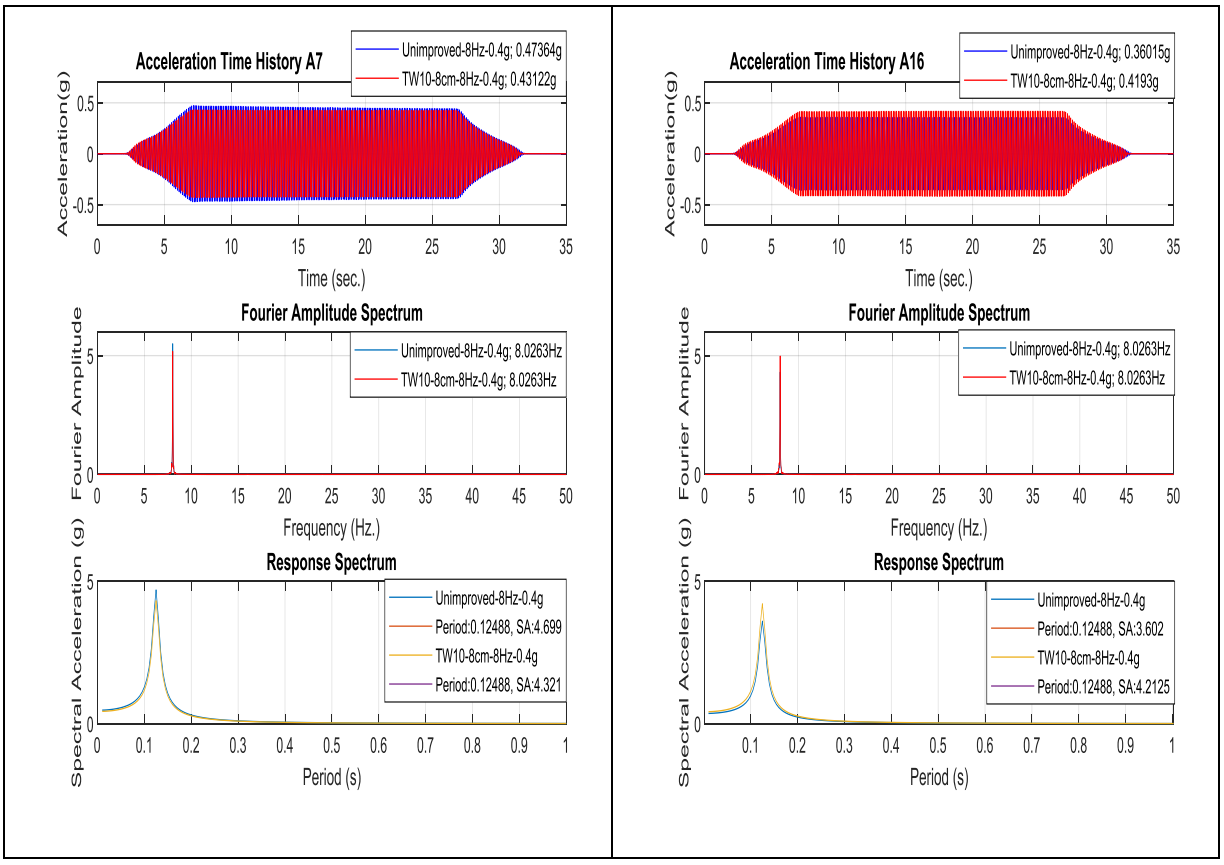


Figure 4.65. The ACCTH, FAS, Response Spectrum at the top of the RWM (A7) and in the backfill (A16) for Case 11 compared to Case 1 under sinusoidal motion at 0.4g amplitude with 8 Hz frequency.

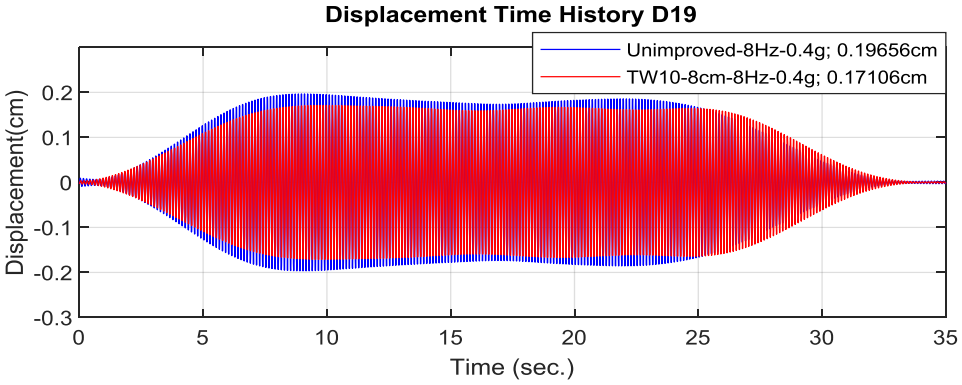


Figure 4.66. The DISTH at the top of the RWM (D19) for Case 11 compared to Case 1 under sinusoidal motion at 0.4g amplitude with 8 Hz frequency.

## 4.12. Results of Case 12 - TW20-8cm

In this study, Case 12 consists of tire waste and sand mixture cushion with 20% mixture ratio and 8 cm thickness (TW20-8cm) behind the RWM. Figures 4.67, 4.68, 4.69, 4.70, 4.71, and 4.72 show the results for two different earthquake motions and one sinusoidal motion as measured by accelerometer A7, laser displacement sensor D19 at the top of the retaining wall model (RWM) and accelerometer A16 in the backfill in comparison to the control case.

Figure 4.67 illustrates the Acceleration-Time Histories, Fourier Amplitude Spectrums, and Response Spectrums under the scaled 2020 İzmir EQ Motion-Kuşadası Station excitations for Case 12 in comparison with the control case. The maximum acceleration was measured as 0.27g and 0.27g at the top of the RWM, and the A16 measured maximum acceleration values as 0.19g and 0.23 for the control case and Case 12, respectively. The Fourier amplitudes for the control and cushioned cases were 9.25 Hz and 7.18 Hz at the top of the RWM, 9.25 Hz and 7.36 Hz, and in the backfill. The maximum spectral accelerations were at 0.05 sec and 0.13 sec period ranges. Compared to the control case and cushioned cases, the maximum spectral acceleration (Sa) values were 0.98g and 0.91g at the top of the RWM at a period of 0.06 sec. The spectral accelerations were 0.75g and 0.83g in the backfill at a period of 0.11 sec for the cushioned case compared to the control case, respectively.

Figure 4.68 shows that, when subjected to the dynamic motions of the scaled 2020 İzmir EQ Motion-Kuşadası Station, the control case displaced 0.37 cm and 0.35 cm for the cushioned model TW20-8cm.

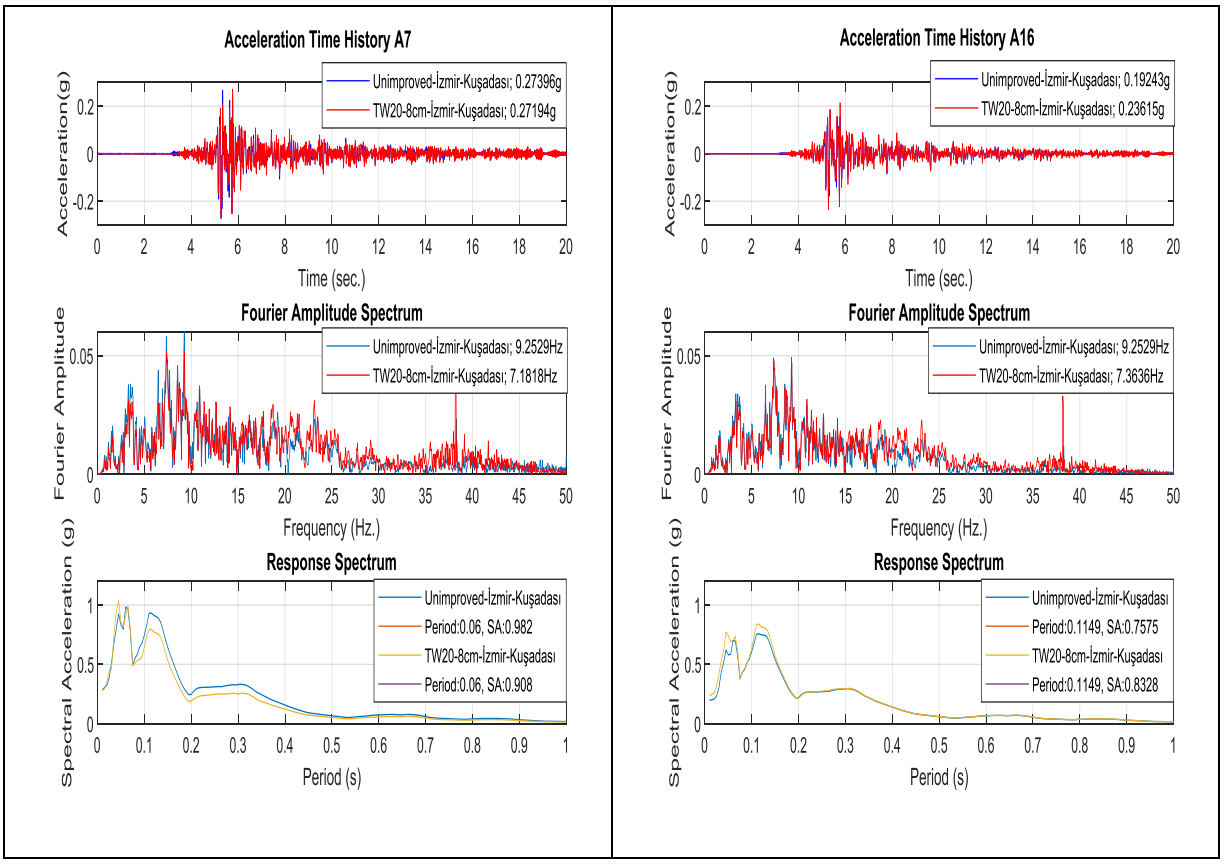


Figure 4.67. The ACCTH, FAS, Response Spectrum at the top of the RWM (A7) and in the backfill (A16) for Case 12 compared to Case 1 under the scaled 2020 İzmir EQ Motion-Kuşadası Station record (FF).

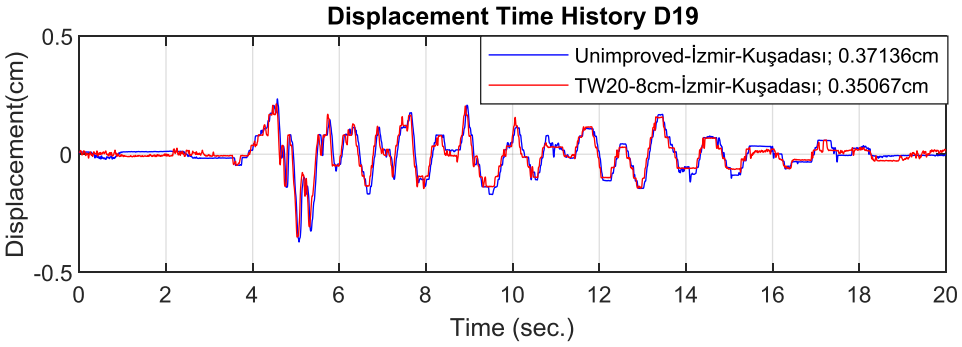


Figure 4.68. The DISTH at the top of the RWM (D19) for Case 12 compared to Case 1 under the scaled 2020 İzmir EQ Motion-Kuşadası Station record (FF).

The Acceleration-Time Histories, Fourier Amplitude Spectrums, and Response Spectrums are illustrated in Figure 4.69 under the scaled 1940 Imperial Valley EQ-El Centro Station record. It was measured 0.52g maximum acceleration for the control case at the top of the RWM decreased to 0.47g maximum acceleration for the TW20-8cm cushioned case. The A16 measured 0.32g maximum acceleration for the control case and 0.36g for the cushioned case. It can be noticed that the maximum acceleration values deceased at the top of the RWM when the TW20-8cm cushion was implemented. Fourier amplitudes peaked around 4.61 Hz at the top of the RWM and in the backfill for the control and cushioned cases. The maximum spectral accelerations were at 0.05 sec and 0.22 sec period ranges for the cushioned and control cases. The maximum spectral accelerations ($S_a$) were 1.48g at 0.055 sec period for the control case, decreasing to 1.37g for the TW20-8cm cushioned case. The spectral accelerations in the backfill were 1.26g and 1.40g at the same periods of 0.22 sec for the control and TW20-8cm cushioned cases, respectively.

Figure 4.70 presents the displacement time history of the control case compared to the cushioned case under the scaled 1940 Imperial Valley EQ-El Centro Station record. The maximum displacement of the TW20-8cm cushioned model was 1.81 cm, while the control case was 1.88 cm at the top of the RWM.

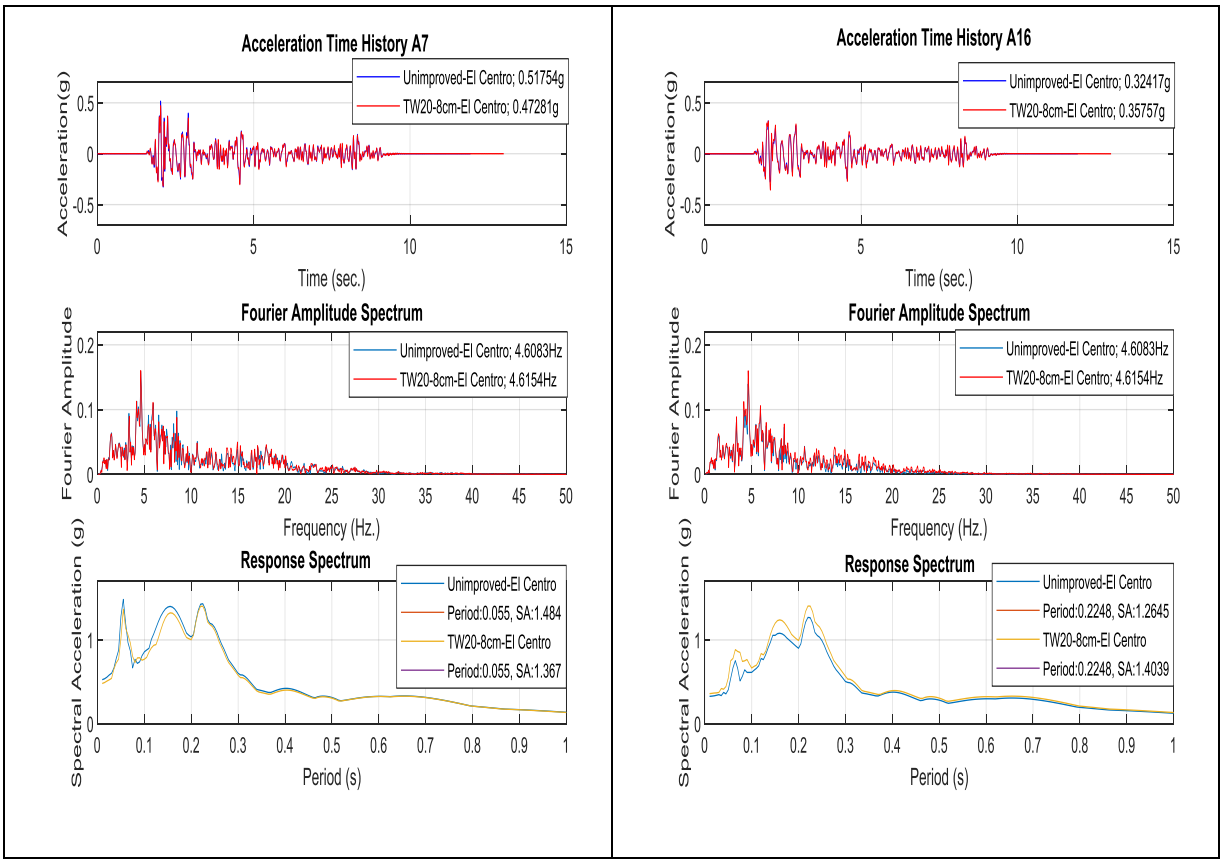


Figure 4.69. The ACCTH, FAS, Response Spectrum at the top of the RWM (A7) and in the backfill (A16) for Case 12 compared to Case 1 under the scaled 1940 Imperial Valley EQ-El Centro Station record (NF).

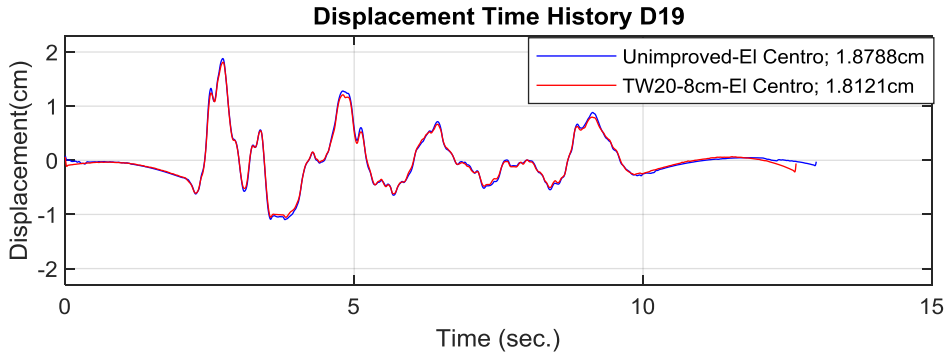


Figure 4.70. The DISTH at the top of the RWM (D19) for Case 12 compared to Case 1 under the scaled 1940 Imperial Valley EQ-El Centro Station record (NF).

The Acceleration-Time Histories, Fourier Amplitude Spectrums, and Response Spectrums under the sinusoidal motion at 0.4g amplitude with 8 Hz frequency are shown in Figure 4.71. It was measured as 0.45g maximum acceleration at the top of the RWM for the TW20-8cm cushioned case compared to the control case of 0.47g, and the A16 measured 0.48g maximum acceleration for the cushioned case compared to the control case as 0.36g. The Fourier amplitude peaks were 8.03 Hz at the top of the RWM and in the backfill for both the cushioned and control cases. The maximum spectral accelerations ($S_a$) were at 0.12 sec period, decreasing from 4.7g to 4.46g at the top of the RWM and increasing from 3.60g to 4.77g in the backfill measured from A16 for the control case and cushioned cases, respectively.

Figure 4.72 presents the displacement time history of the control case compared to the cushioned case. Maximum displacement was measured as 0.20 cm at the top of the RWM acquired from D19 under the sinusoidal motion at 0.4g amplitude with 8 Hz frequency excitation for the cushioned case, whereas it was measured as 0.20 cm for the control case.

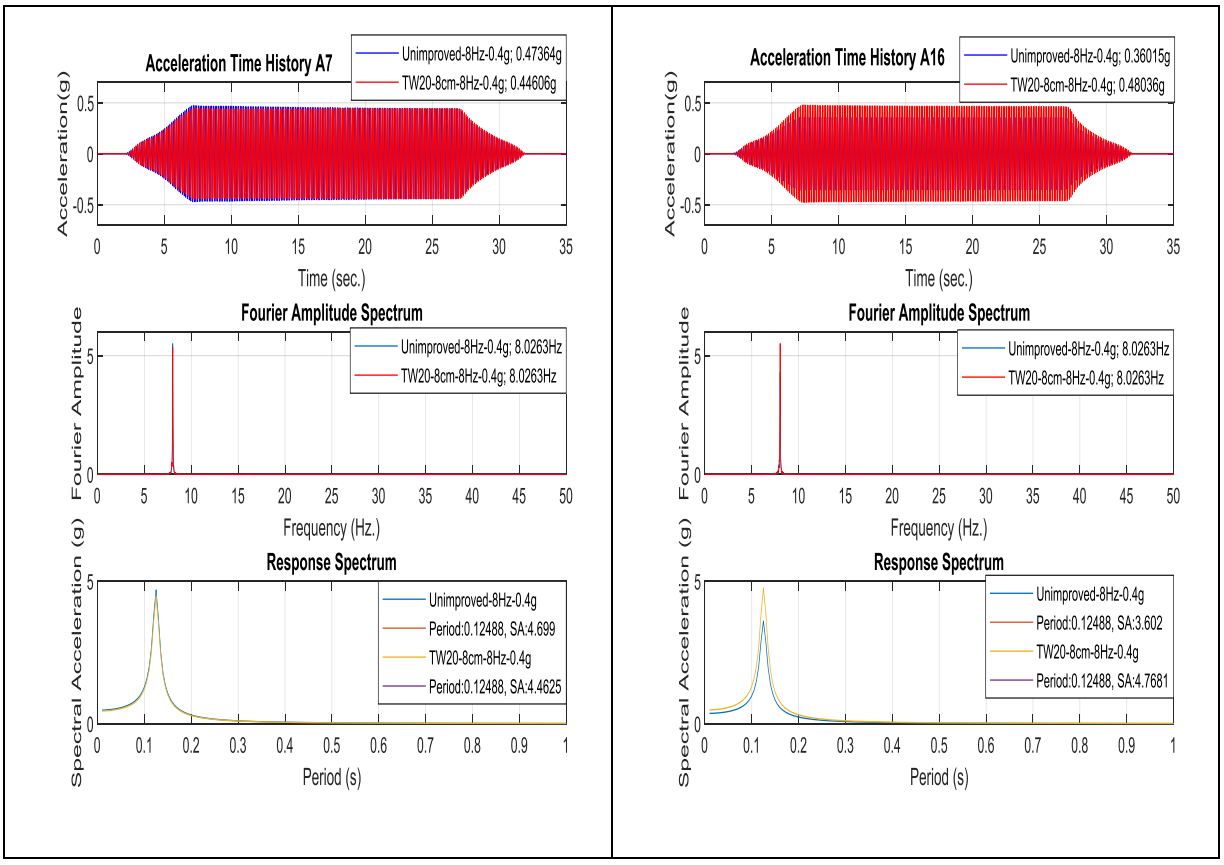


Figure 4.71. The ACCTH, FAS, Response Spectrum at the top of the RWM (A7) and in the backfill (A16) for Case 12 compared to Case 1 under sinusoidal motion at 0.4g amplitude with 8 Hz frequency.

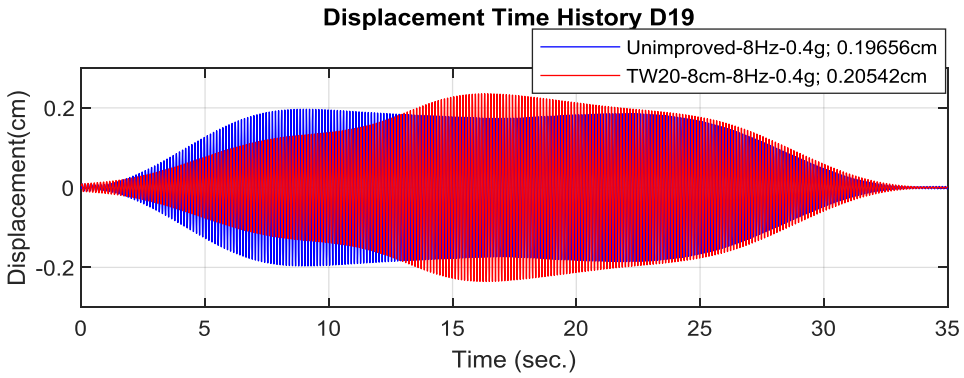


Figure 4.72. The DISTH at the top of the RWM (D19) for Case 12 compared to Case 1 under sinusoidal motion at 0.4g amplitude with 8 Hz frequency.

## 4.13. Results of Case 13 - TW30-8cm

The study includes Case 13, which consists of a cushion made of a mixture of tire waste and sand with a ratio of 30% and a thickness of 8 cm (TW30-8cm) behind the RWM. Figures 4.73, 4.74, 4.75, 4.76, 4.77, and 4.78 present the results for two different earthquake motions and one sinusoidal motion. These results were obtained from accelerometer A7, laser displacement sensor D19 at the top of the retaining wall model (RWM), and accelerometer A16 in the backfill. The results are compared to the control case.

Figure 4.73 displays the Acceleration-Time Histories, Fourier Amplitude Spectrums and Response Spectrums for Case 13 compared to the control case (Case 1) under the scaled 2020 İzmir EQ Motion-Kuşadası Station record. The A7 recorded maximum acceleration values of 0.27g and 0.28g, and A16 recorded 0.19g and 0.23g for the control and cushioned cases, respectively. The Fourier amplitudes for the control and cushioned cases were 9.23 Hz and 7.48 Hz at the top of the RWM, 9.23 Hz and 7.36 Hz and in the backfill. The response spectrums indicated that the maximum spectral accelerations occurred in the 0.05 and 0.13 sec period ranges. Comparing the control and cushioned cases, the maximum spectral acceleration ($S_a$) values increased from 0.98g to 0.99g at the top of the RWM at a period of 0.06 sec. In the backfill, the spectral accelerations were 0.76g and 0.83g at a period of 0.11 sec for the cushioned case compared to the control case, respectively.

Figure 4.74 demonstrates that under the dynamic motions of the scaled 2020 İzmir EQ Motion-Kuşadası Station, the displacement of the control case was 0.37 cm, whereas the cushioned model TW30-8cm was also displaced a maximum of 0.37 cm.

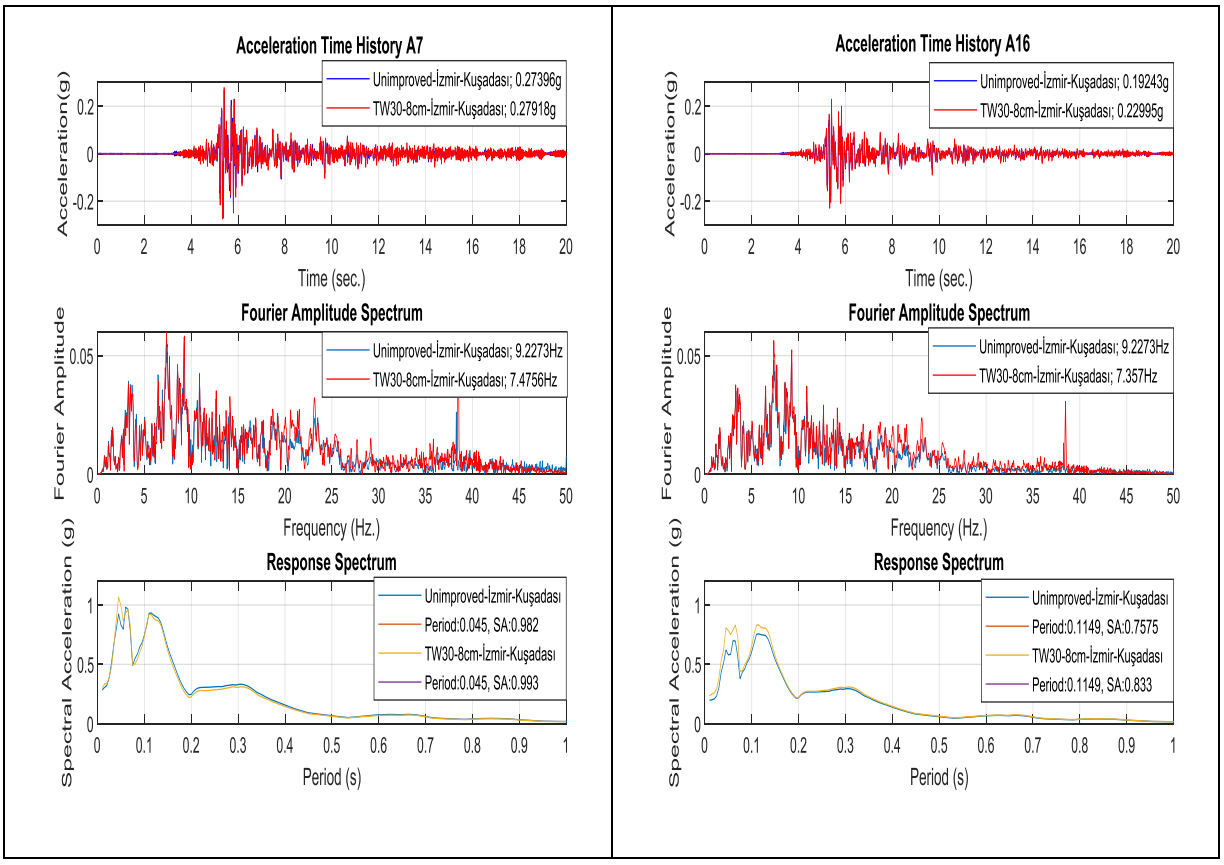


Figure 4.73. The ACCTH, FAS, Response Spectrum at the top of the RWM (A7) and in the backfill (A16) for Case 13 compared to Case 1 under the scaled 2020 İzmir EQ Motion-Kuşadası Station record (FF).

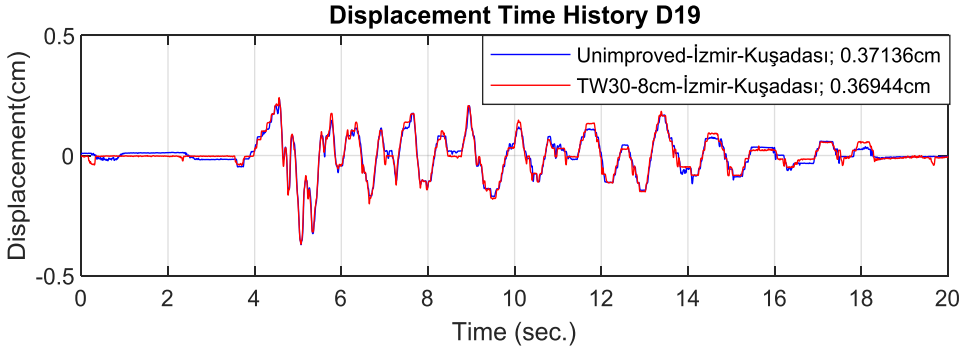


Figure 4.74. The DISTH at the top of the RWM (D19) for Case 13 compared to Case 1 under the scaled 2020 İzmir EQ Motion-Kuşadası Station record (FF).

Figure 4.75 presents the Acceleration-Time Histories, Fourier Amplitude Spectrums, and Response Spectrums under the scaled 1940 Imperial Valley EQ-El Centro Station record. The control case recorded a maximum acceleration of 0.52g at the top of the RWM, which decreased to 0.47g for the TW30-8cm cushioned case. The A16 measured a maximum acceleration of 0.32g for the control case and 0.35g for the cushioned case. It was observed that the maximum acceleration values decreased at the top of the RWM when the cushion TW30-8cm was implemented. The Fourier amplitudes peaked at 4.60 Hz at the top of the RWM and in the backfill for both the control and cushioned cases. The response spectrums indicated that the maximum spectral accelerations occurred in the 0.05 sec and 0.22 sec period ranges. The maximum spectral accelerations ($S_a$) were 1.48g at a period of 0.055 sec at the top of the RWM for the control case, which decreased to 1.17g for the cushioned case. In the backfill, the spectral accelerations were 1.26g for the control case and 1.47g for the cushioned case at the same period of 0.22 sec.

Figure 4.76 displays the displacement time history of the control case compared to the cushioned case under the scaled 1940 Imperial Valley EQ-El Centro Station record. The measured maximum displacement for the cushioned model was 1.84 cm, while it was 1.88 cm for the control case at the top of the RWM.

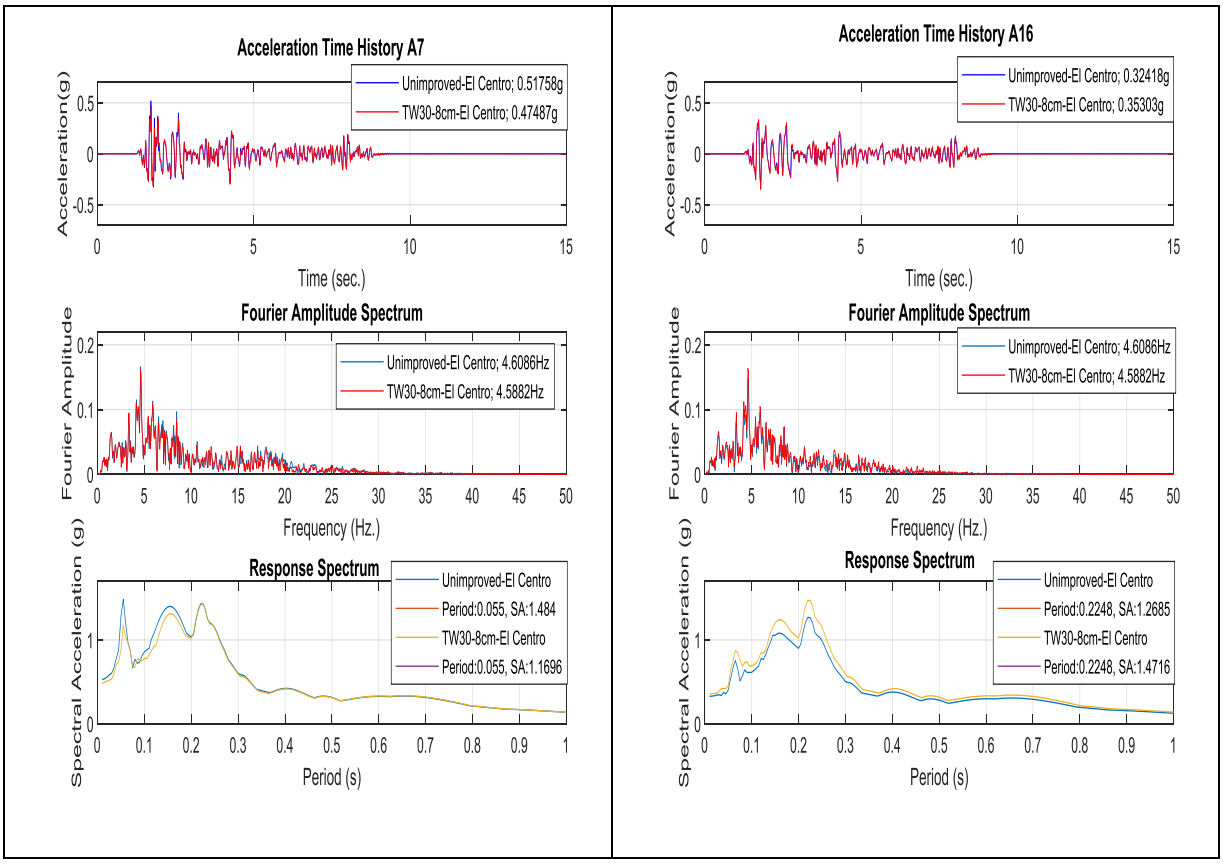


Figure 4.75. The ACCTH, FAS, Response Spectrum at the top of the RWM (A7) and in the backfill (A16) for Case 13 compared to Case 1 under the scaled 1940 Imperial Valley EQ-El Centro Station record (NF).

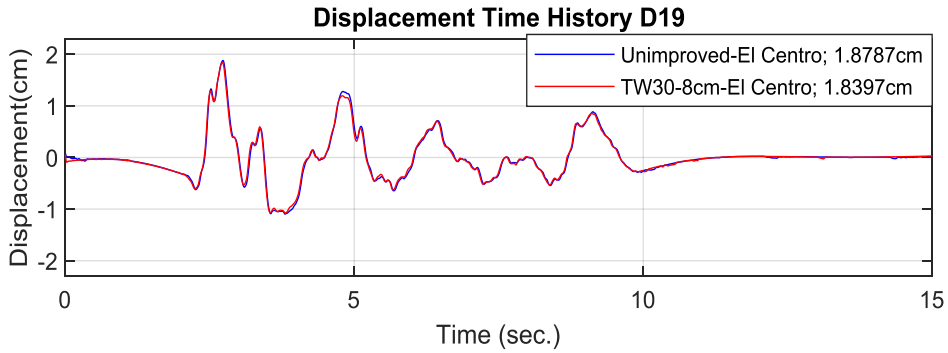


Figure 4.76. The DISTH at the top of the RWM (D19) for Case 13 compared to Case 1 under the scaled 1940 Imperial Valley EQ-El Centro Station record (NF).

Figure 4.77 illustrates the Acceleration-Time Histories, Fourier Amplitude Spectrums, and Response Spectrums under the sinusoidal motion at 0.4g amplitude with 8 Hz frequency. For the TW30-8cm cushioned case, it was recorded a peak acceleration of 0.42g at the top of the RWM, compared to 0.47g for the control case. The A16 measured a maximum acceleration of 0.46g for the cushioned case, compared to 0.36g for the control case. The Fourier amplitudes peaked at 8.01 Hz both at the top of the RWM and in the backfill for both the cushioned and control cases. The maximum spectral accelerations ($S_a$) can be observed at a period of 0.12 seconds and decreased from 4.7g to 4.22g at the top of the RWM. Conversely, it increased from 3.60g to 4.67g in the backfill. These measurements correspond to the control case and cushioned case, respectively.

In Figure 4.78, the displacement time history of the control case is compared to the cushioned case. The peak displacement at the top of the RWM, taken from point D19, was measured as 0.16 cm for the cushioned case under the sinusoidal motion. In contrast, it was measured as 0.20 cm for the control case.

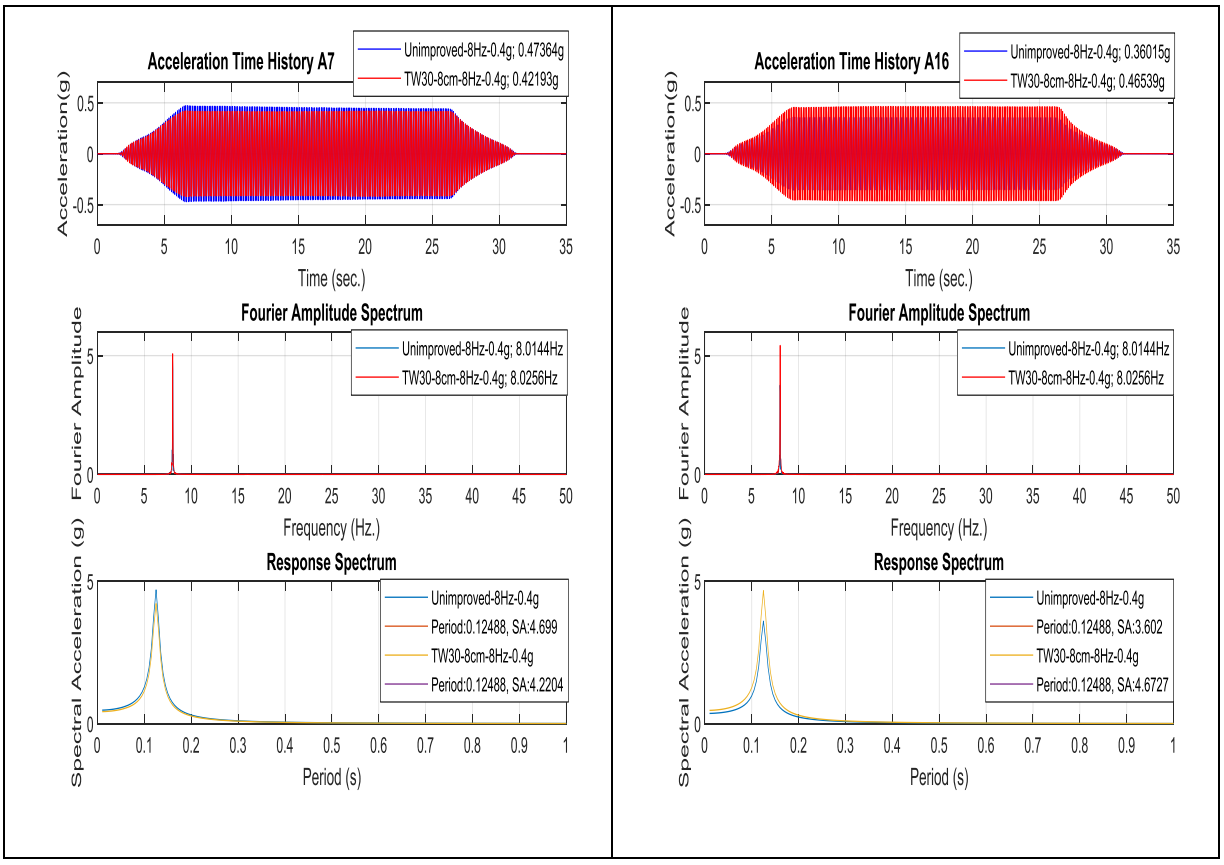


Figure 4.77. The ACCTH, FAS, Response Spectrum at the top of the RWM (A7) and in the backfill (A16) for Case 13 compared to Case 1 under sinusoidal motion at 0.4g amplitude with 8 Hz frequency.

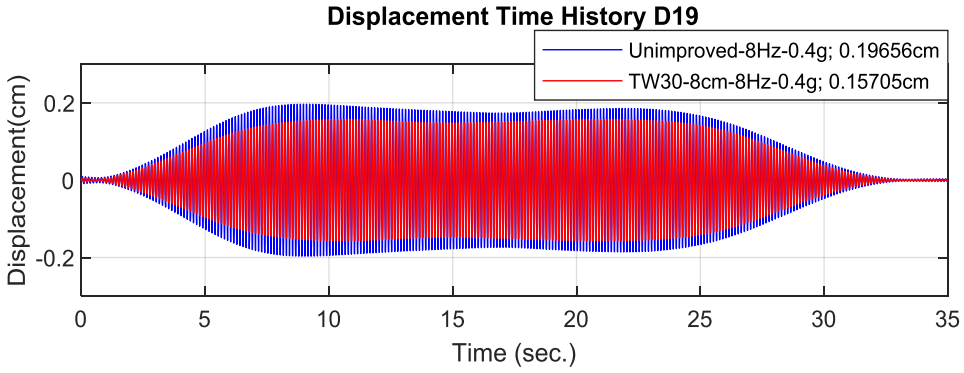


Figure 4.78. The DISTH at the top of the RWM (D19) for Case 13 compared to Case 1 under sinusoidal motion at 0.4g amplitude with 8 Hz frequency.

## 4.14. Results of Case 14 - EPSB10-4cm

In this study, Case 14 was composed of a mixture of EPS beads and sand cushion with a mixture ratio of 10% and a thickness of 4 cm (EPSB10-4cm) behind the RWM. Results were obtained for two different earthquake motions and one sinusoidal motion, as measured by accelerometer A7, laser displacement sensor D19 at the top of the retaining wall model (RWM) and accelerometer A16 in the backfill, in comparison to the control case. Figures 4.79, 4.80, 4.81, 4.82, 4.83, and 4.84 present the data.

Figure 4.79 indicates the Acceleration-Time Histories, Fourier Amplitude Spectrums, and Response Spectrums under the scaled 2020 İzmir EQ Motion-Kuşadası Station excitations for Case 14 compared with the control case. The A7 recorded maximum acceleration values of 0.27g and 0.28g, while the A16 measured maximum acceleration values of 0.19g and 0.20g for the control case and Case 14, respectively. The Fourier amplitudes for the control and cushioned cases were 9.23 Hz and 7.34 Hz at the top of the RWM and in the backfill. The maximum spectral accelerations were at 0.05 sec and 0.13 sec period ranges. The maximum spectral acceleration ($S_a$) values increased from 0.98g to 0.99g at the top of the RWM at a period of 0.06 sec in the case of the cushioned scenario. The spectral accelerations were 0.79g and 0.76g in the backfill at a period of 0.11 sec for the cushioned case compared to the control case.

Figure 4.80 shows that, when subjected to the dynamic motions of the scaled 2020 İzmir EQ Motion-Kuşadası Station, the control case displaced a maximum of 0.37 cm and 0.35 cm for the cushioned model EPSB10-4cm.

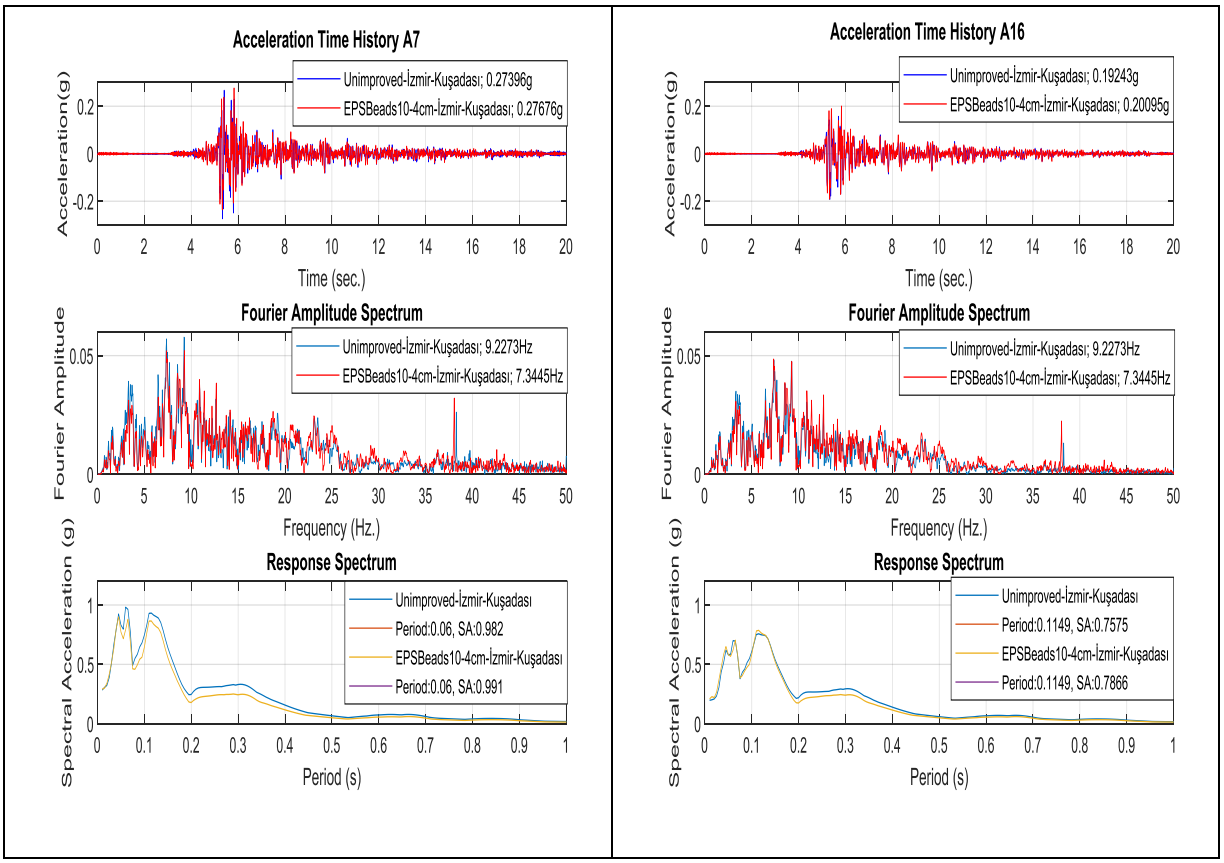


Figure 4.79. The ACCTH, FAS, Response Spectrum at the top of the RWM (A7) and in the backfill (A16) for Case 14 compared to Case 1 under the scaled 2020 İzmir EQ Motion-Kuşadası Station record (FF).

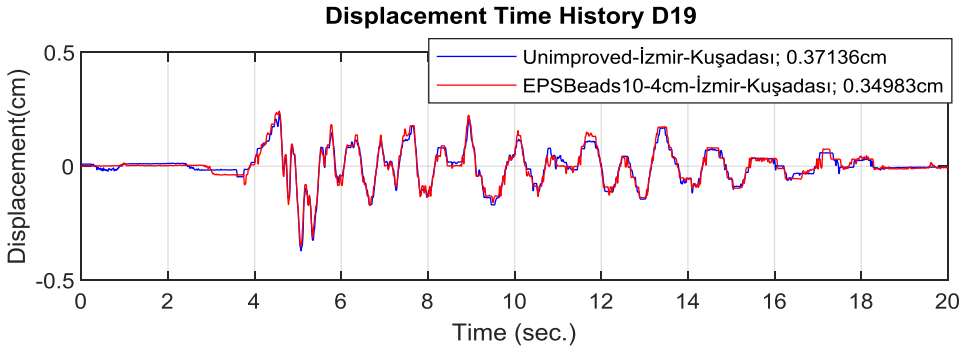


Figure 4.80. The DISTH at the top of the RWM (D19) for Case 14 compared to Case 1 under the scaled 2020 İzmir EQ Motion-Kuşadası Station record (FF).

Figure 4.81 illustrates the Acceleration-Time Histories, Fourier Amplitude Spectrums, and Response Spectrums under the scaled 1940 Imperial Valley EQ-El Centro Station record. The A7 recorded 0.52g maximum acceleration for the control case, which decreased to 0.50g for the cushioned case EPSB10-4cm. The A16 measured a maximum acceleration of 0.32g for the control case and 0.36g for the cushioned case. It was observed that the maximum acceleration values decreased at the top of the RWM when improvement was conducted through the implementation of the EPSB10-4cm cushion. The results showed that the Fourier amplitudes peaked around 4.58 Hz at the top of the RWM and in the backfill for the control and cushioned cases measured from A7 and A16. The maximum spectral accelerations were at 0.05 sec and 0.22 sec period ranges for both the cushioned and control cases. The maximum spectral accelerations ($S_a$) were 1.48g at 0.055 sec period at the top of the RWM for the control case, which decreased to 1.47g for the cushioned case made of EPSB10-4cm. In the backfill, the spectral accelerations were 1.26g and 1.39g at the same periods of 0.22 sec for the control and cushioned cases, respectively.

In Figure 4.82, the displacement time history of the control case was compared to the cushioned case EPSB10-4cm under the scaled 1940 Imperial Valley EQ-El Centro Station record. The measurements showed that the maximum displacement of the cushioned model was 1.93 cm, while the control case was 1.88 cm at the top of the RWM.

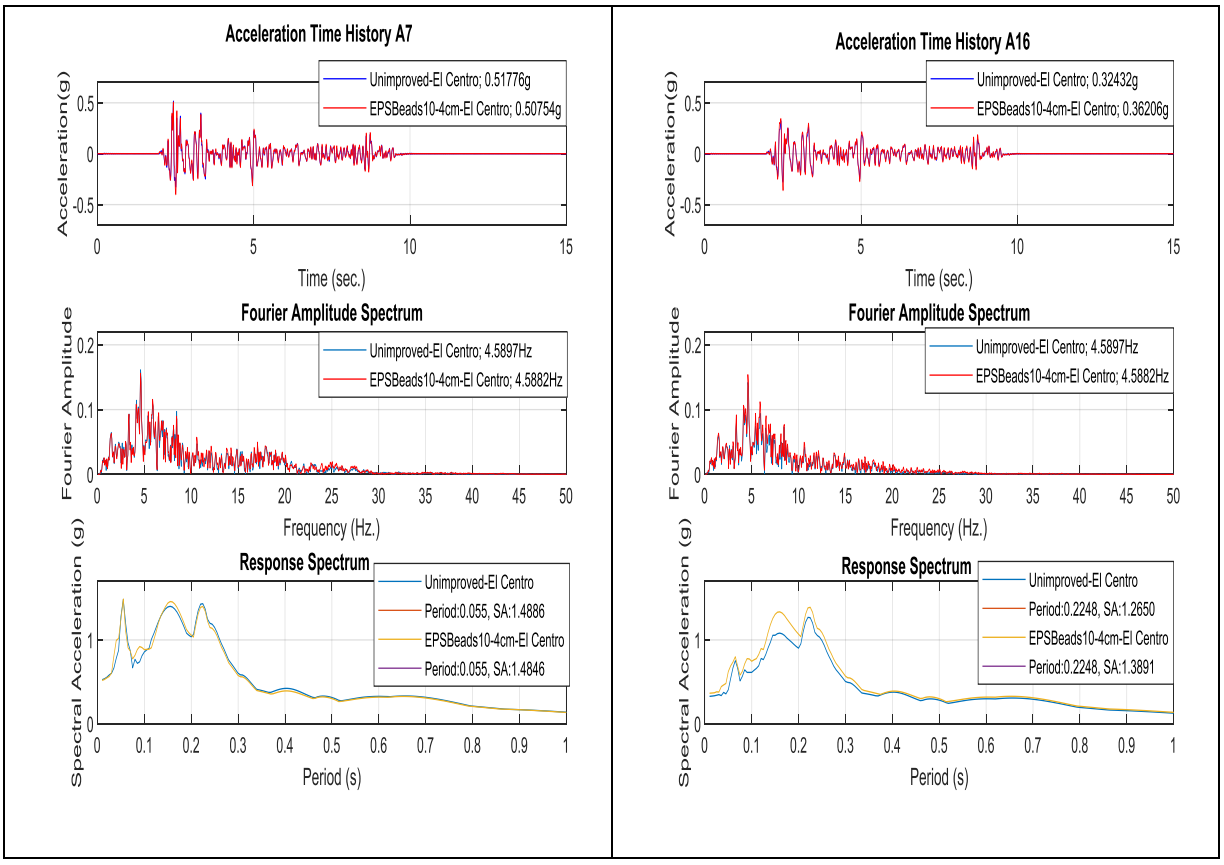


Figure 4.81. The ACCTH, FAS, Response Spectrum at the top of the RWM (A7) and in the backfill (A16) for Case 14 compared to Case 1 under the scaled 1940 Imperial Valley EQ-El Centro Station record (NF).

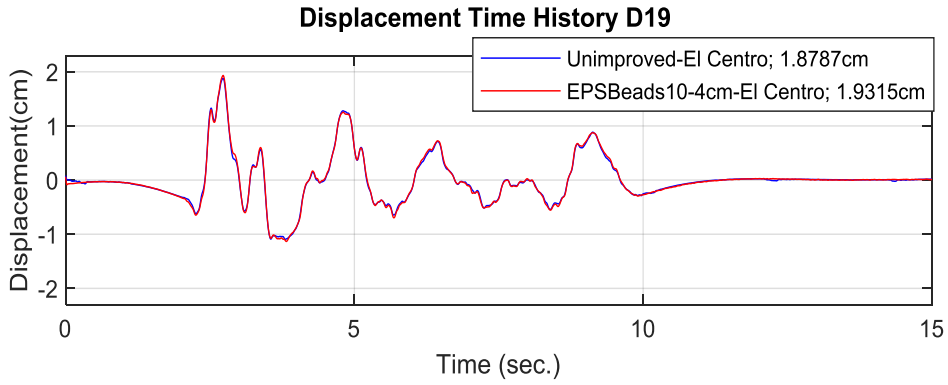


Figure 4.82. The DISTH at the top of the RWM (D19) for Case 14 compared to Case 1 under the scaled 1940 Imperial Valley EQ-El Centro Station record (NF).

Figure 4.83 presents the Acceleration-Time Histories, Fourier Amplitude Spectrums, and Response Spectrums under the sinusoidal motion at 0.4g amplitude with 8 Hz frequency. It was measured 0.45g maximum acceleration at the top of the RWM for the cushioned case EPSB10-4cm compared to 0.47g for the control case. The A16 measured a maximum acceleration of 0.44g for the cushioned case compared to 0.36g for the control case. The results showed that the Fourier amplitudes peaked at 8.02 Hz at the top of the RWM and in the backfill for both the cushioned and control cases. The maximum spectral accelerations ($S_a$) were at 0.12 sec period, decreasing from 4.7g to 4.57g at the top of the RWM and increasing from 3.60g to 4.43g in the backfill for the cushioned case compared to the control case.

In Figure 4.84, the displacement time history of the control case was compared to the cushioned case EPSB10-4cm under sinusoidal motion at 0.4g amplitude with 8 Hz frequency. The measurements showed that the maximum displacement was 0.19 cm at the top of the RWM for the cushioned case, whereas it was 0.20 cm for the control case.

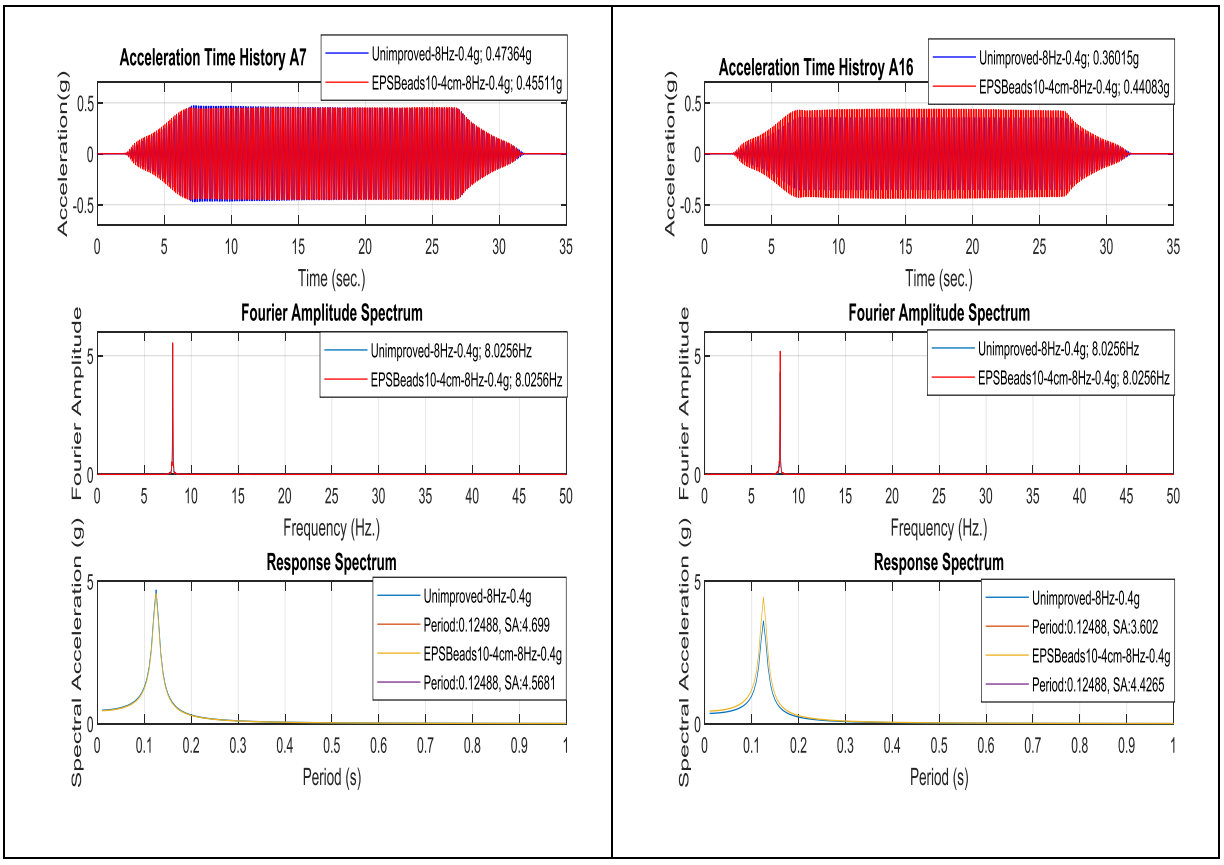


Figure 4.83. The ACCTH, FAS, Response Spectrum at the top of the RWM (A7) and in the backfill (A16) for Case 14 compared to Case 1 under sinusoidal motion at 0.4g amplitude with 8 Hz frequency.

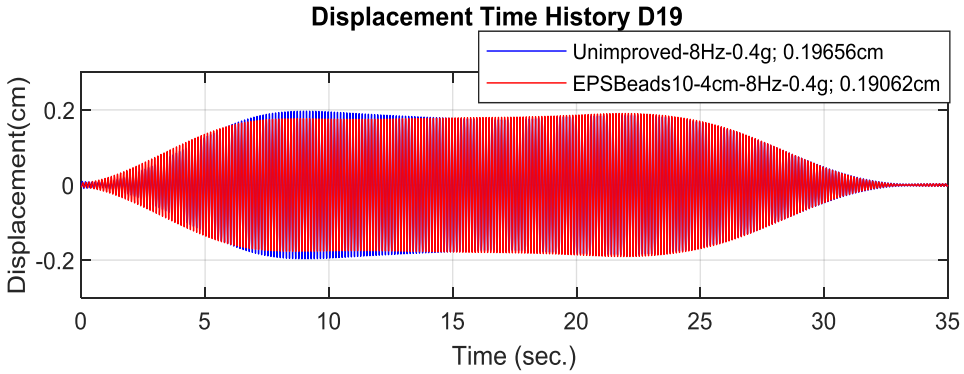


Figure 4.84. The DISTH at the top of the RWM (D19) for Case 14 compared to Case 1 under sinusoidal motion at 0.4g amplitude with 8 Hz frequency.

### 4.15. Results of Case 15 - EPSB20-4cm

In this study, Case 15 consists of EPS beads and sand mixture cushion with a 20% mixture ratio and 4 cm thickness (EPSB20-4cm) behind the RWM. Figures 4.85, 4.86, 4.87, 4.88, 4.89, and 4.90 show the results for two different earthquake motions and one sinusoidal motion as measured by accelerometer A7, laser displacement sensor D19 at the top of the RWM and the accelerometer A16 in the backfill in comparison to the control case.

Figure 4.85 illustrates the Acceleration-Time Histories, Fourier Amplitude Spectrums, and Response Spectrums under the scaled 2020 İzmir EQ Motion-Kuşadası Station excitations for Case 15 compared to the control case Case 1. The maximum acceleration values were measured as 0.27g and 0.27g at the top of the RWM, and 0.19g and 0.20 in the backfill for the control case and cushioned case, Case 15, respectively. The Fourier amplitudes for the control and cushioned cases were 9.26 Hz and 7.33 Hz at the top of the RWM and in the backfill. The maximum spectral accelerations were at 0.05 sec and 0.13 sec period ranges. Compared to the control case and cushioned cases, the maximum spectral acceleration (Sa) values decreased from 0.98g to 0.96g at the top of the RWM at a period of 0.06 sec. The spectral accelerations were 0.78g and 0.76g in the backfill at a period of 0.11 sec for the cushioned case compared to the control case.

Figure 4.86 shows that, when subjected to the dynamic motions of the scaled 2020 İzmir EQ Motion-Kuşadası Station, the control case displaced a maximum of 0.37 cm compared to 0.38 cm for the EPSB20-4cm.

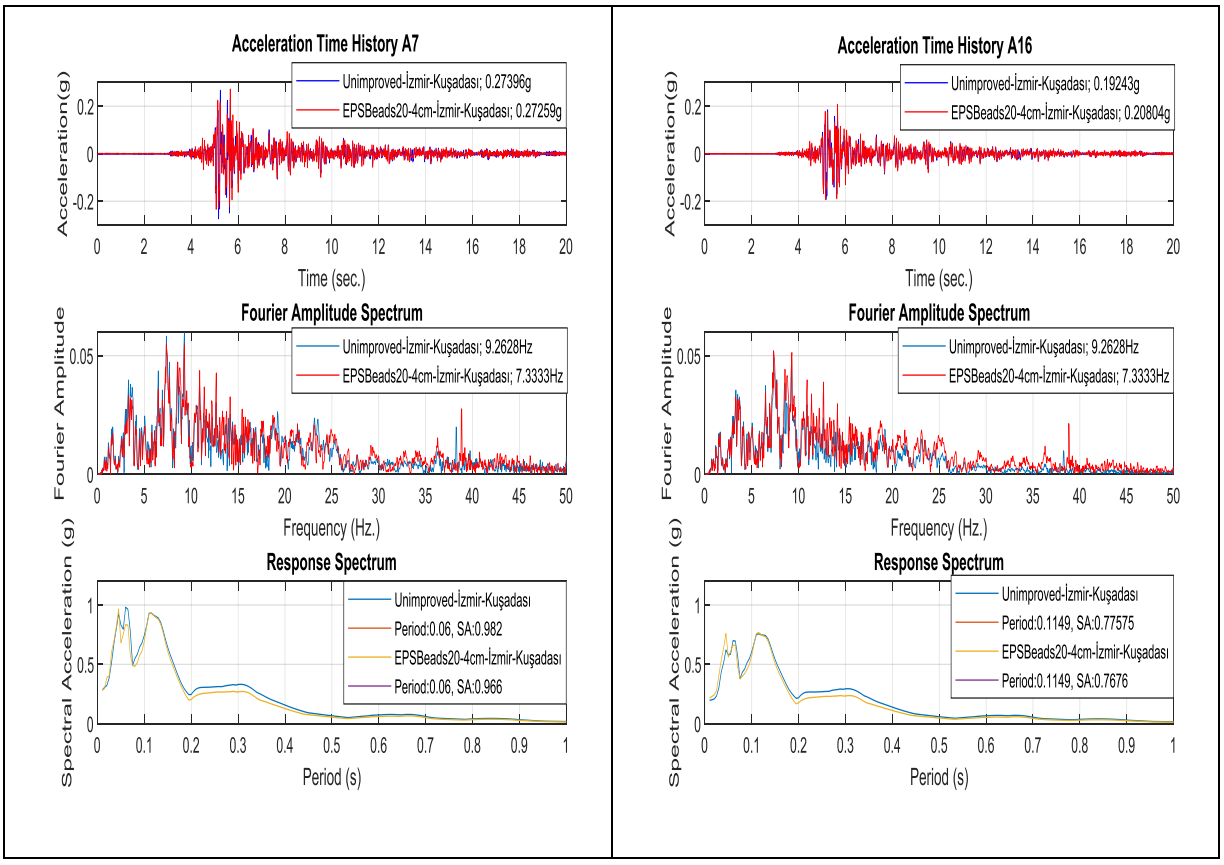


Figure 4.85. The ACCTH, FAS, Response Spectrum at the top of the RWM (A7) and in the backfill (A16) for Case 15 compared to Case 1 under the scaled 2020 İzmir EQ Motion-Kuşadası Station record (FF).

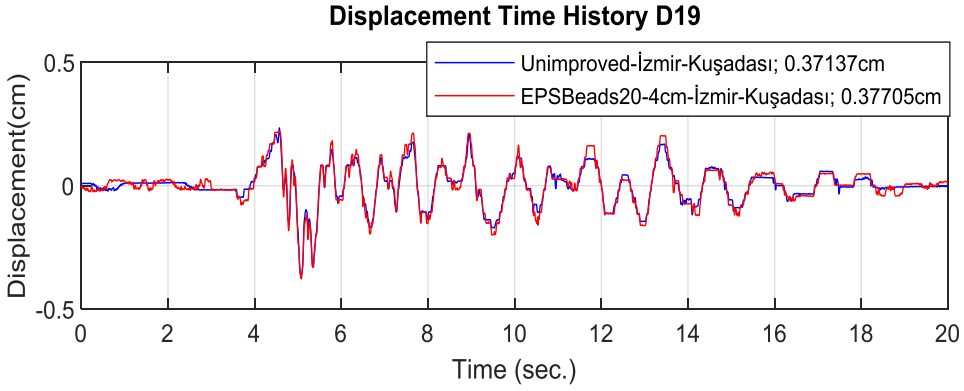


Figure 4.86. The DISTH at the top of the RWM (D19) for Case 15 compared to Case 1 under the scaled 2020 İzmir EQ Motion-Kuşadası Station record (FF).

The Acceleration-Time Histories, Fourier Amplitude Spectrums, and Response Spectrums are illustrated in Figure 4.87 under the scaled 1940 Imperial Valley EQ-El Centro Station record. It was measured that 0.52g maximum acceleration for the control case at the top of the RWM decreased to 0.47g maximum acceleration for the EPSB20-4cm cushioned case. The A16 measured 0.32g maximum acceleration for the control case and 0.39g for the cushioned case. It can be noticed that the maximum acceleration values deceased at the top of the RWM when the EPSB20-4cm cushion was implemented. Fourier amplitudes peaked around 4.64 Hz and 4.61 Hz at the top of the RWM and in the backfill for the control and cushioned cases. The maximum spectral accelerations were at 0.05 sec and 0.22 sec period ranges for the cushioned and control cases. The maximum spectral accelerations ($S_a$) were 1.48g at 0.055 sec period at the top of the RWM for the control case, decreasing to 1.18g for the EPSB20-4cm cushioned case. The spectral accelerations in the backfill were 1.26g and 1.39g at the same periods 0.22 sec for the control case and EPSB20-4cm cushioned cases, respectively.

Figure 4.88 presents the displacement time history of the control case compared to the cushioned case under the scaled 1940 Imperial Valley EQ-El Centro Station record. The maximum displacement of the EPSB20-4cm cushioned model was measured as 1.82 cm, while the control case was measured as 1.88 cm at the top of the RWM.

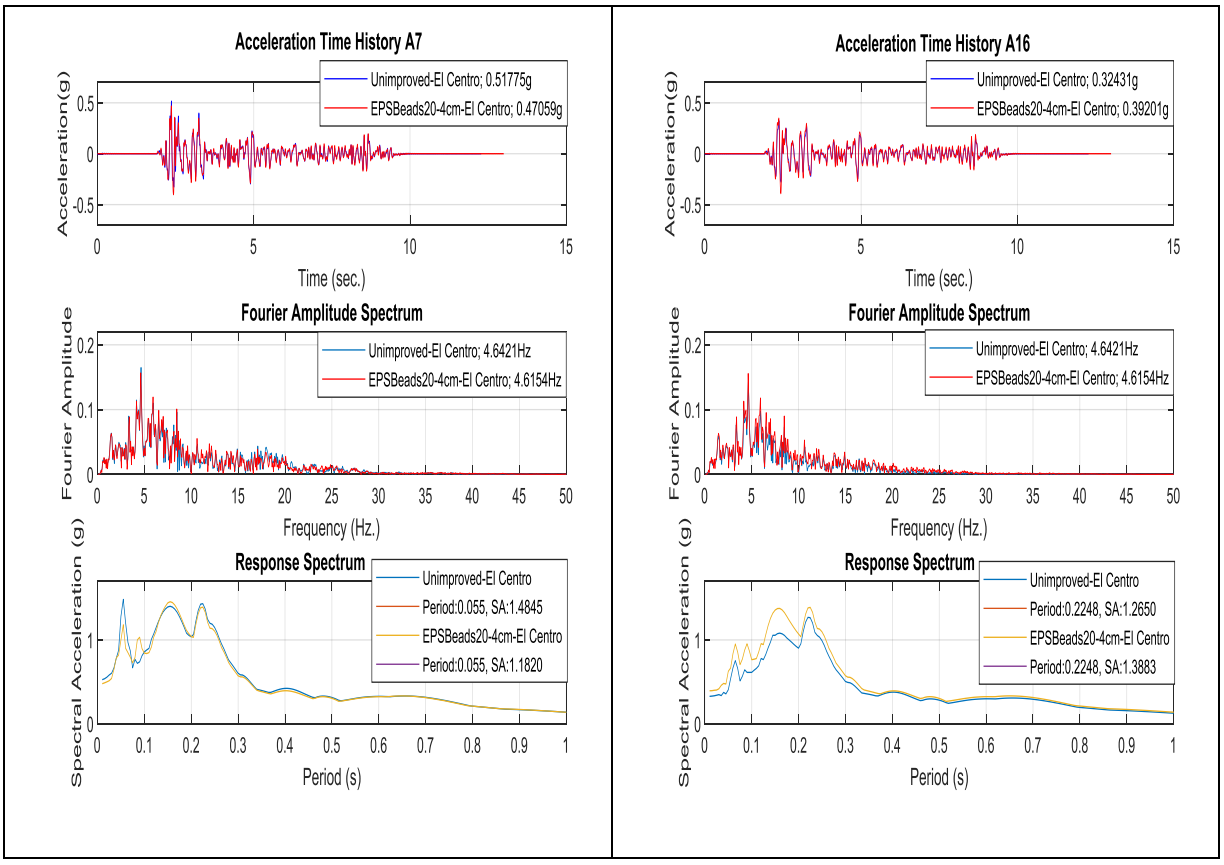


Figure 4.87. The ACCTH, FAS, Response Spectrum at the top of the RWM (A7) and in the backfill (A16) for Case 15 compared to Case 1 under the scaled 1940 Imperial Valley EQ-El Centro Station record (NF).

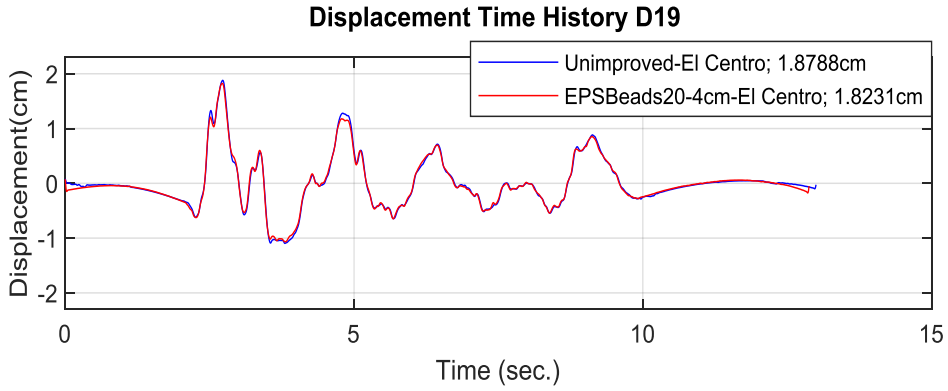


Figure 4.88. The DISTH at the top of the RWM (D19) for Case 15 compared to Case 1 under the scaled 1940 Imperial Valley EQ-El Centro Station record (NF).

The Acceleration-Time Histories, Fourier Amplitude Spectrums, and Response Spectrums under the sinusoidal motion at 0.4g amplitude with 8 Hz frequency are shown in Figure 4.89. The A7 measured 0.47g maximum acceleration for the EPSB20-4cm cushioned case compared to the control case as 0.47g, and the A16 measured 0.49g maximum acceleration for the cushioned case compared to the control case 0.36g. The Fourier amplitudes peaked at 8.02 Hz at the top of the RWM and in the backfill for both the cushioned case and the control case. The maximum spectral accelerations ($S_a$) were at 0.12 sec period, decreasing from 4.7g to 4.6g at the top of the RWM and increasing from 3.60g to 4.86g in the backfill for the control case and cushioned cases, respectively.

Figure 4.90 presents the displacement time history of the control case compared to the cushioned case under sinusoidal motion at 0.4g amplitude with 8 Hz frequency. Maximum displacement was measured as 0.18 cm at the top of the RWM for the cushioned case, whereas it was measured as 0.20 cm for the control case.

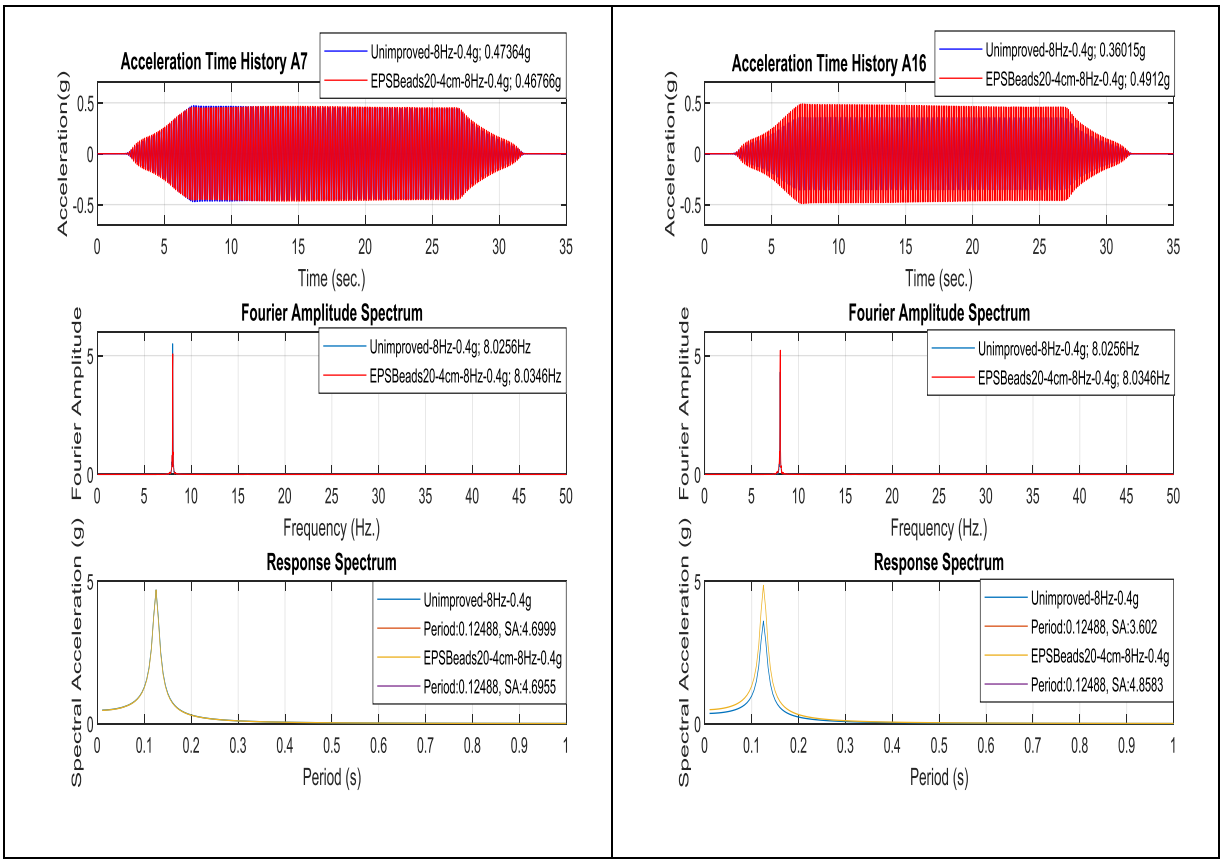


Figure 4.89. The ACCTH, FAS, Response Spectrum at the top of the RWM (A7) and in the backfill (A16) for Case 15 compared to Case 1 under sinusoidal motion at 0.4g amplitude with 8 Hz frequency.

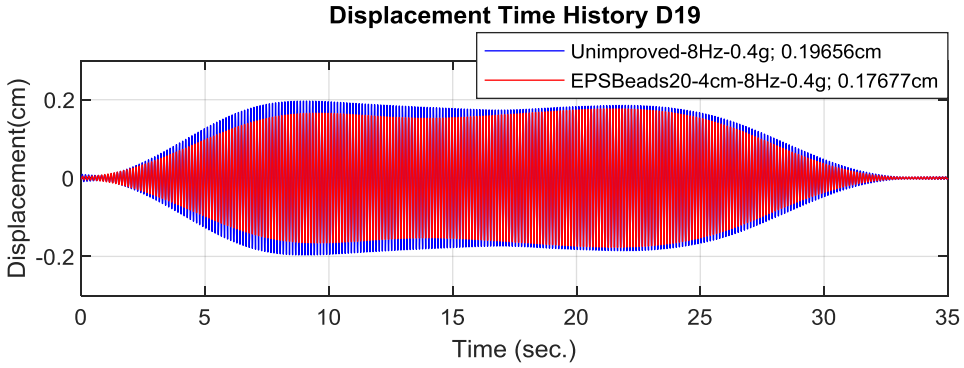


Figure 4.90. The DISTH at the top of the RWM (D19) for Case 15 compared to Case 1 under sinusoidal motion at 0.4g amplitude with 8 Hz frequency.

### 4.16. Results of Case 16 - EPSB30-4cm

Case 16 involves a cushion made of a mixture of EPS beads and sand with a 30% mixture ratio and 4 cm thickness (EPSB30-4cm) behind the RWM. The results obtained from accelerometer A7, laser displacement sensor D19 at the top of the retaining wall model (RWM), and accelerometer A16 in the backfill, compared to the control case, are presented in Figures 4.91, 4.92, 4.93, 4.94, 4.95, and 4.96.

Figure 4.91 shows the Acceleration-Time Histories, Fourier Amplitude Spectrums, and Response Spectrums for the scaled 2020 İzmir EQ Motion-Kuşadası Station excitations in Case 16 and the control case. For the control case, A7 recorded maximum acceleration values of 0.27g and 0.28g, while A16 measured maximum acceleration values of 0.19g and 0.22g. The Fourier amplitudes for the control and cushioned cases were 9.23 Hz and 7.34 Hz at the top of the RWM and in the backfill. The maximum spectral accelerations occur in the period ranges of 0.05 and 0.13 sec. Comparing the control and cushioned cases, there is a slight decrease in the maximum spectral acceleration ($S_a$) values, from 0.98g to 0.96g at the top of the RWM at a period of 0.06 sec. In the backfill, the spectral accelerations were 0.76g and 0.86g at a period of 0.11 sec for the cushioned and control cases, respectively.

Figure 4.92 demonstrates that under the dynamic motions of the scaled 2020 İzmir EQ Motion-Kuşadası Station, the control case was displaced a maximum of 0.37 cm, while the EPSB30-4cm was displaced a maximum of 0.36cm.

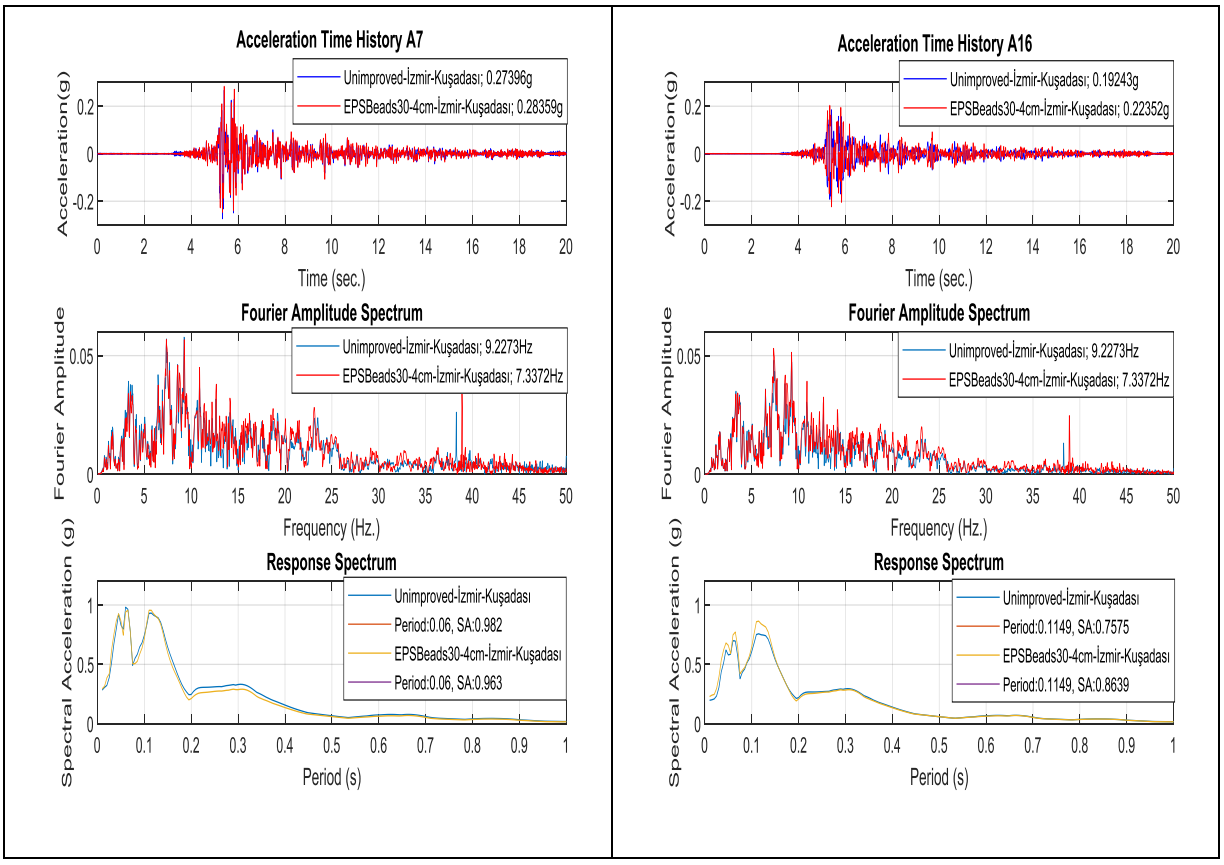


Figure 4.91. The ACCTH, FAS, Response Spectrum at the top of the RWM (A7) and in the backfill (A16) for Case 16 compared to Case 1 under the scaled 2020 İzmir EQ Motion-Kuşadası Station record (FF).

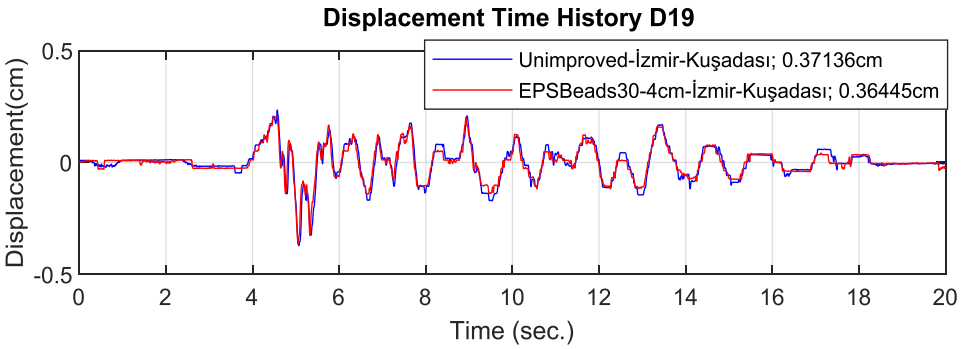


Figure 4.92. The DISTH at the top of the RWM (D19) for Case 16 compared to Case 1 under the scaled 2020 İzmir EQ Motion-Kuşadası Station record (FF).

Figure 4.93 showcases the Acceleration-Time Histories, Fourier Amplitude Spectrums, and Response Spectrums under the scaled 1940 Imperial Valley EQ-El Centro Station record. For the control case, A7 measured a maximum acceleration of 0.52g, which decreased to 0.47g for the cushioned case. The A16 measured a maximum acceleration of 0.32g for the control case and 0.36g for the cushioned case. The implementation of the EPSB cushion led to a decrease in maximum acceleration values at the top of the RWM. The Fourier amplitudes peaked around 4.64 Hz and 4.61 Hz at the top of the RWM and in the backfill for the control and cushioned cases. The maximum spectral accelerations occur at period ranges of 0.05 and 0.22 sec for the cushioned and control cases. At the top of the RWM, the maximum spectral acceleration ($S_a$) decreased from 1.48g to 1.43g for the cushioned case. In the backfill, the spectral accelerations were 1.26g and 1.39g at the same periods of 0.22 sec for the control and cushioned cases, respectively.

Figure 4.94 shows the displacement time history of the control case compared to the cushioned case during the scaled 1940 Imperial Valley EQ-El Centro Station record. The maximum displacement for the cushioned case with EPSB30-4cm was measured as 1.83 cm, while it was measured as 1.88 cm for the control case at the top of the RWM.

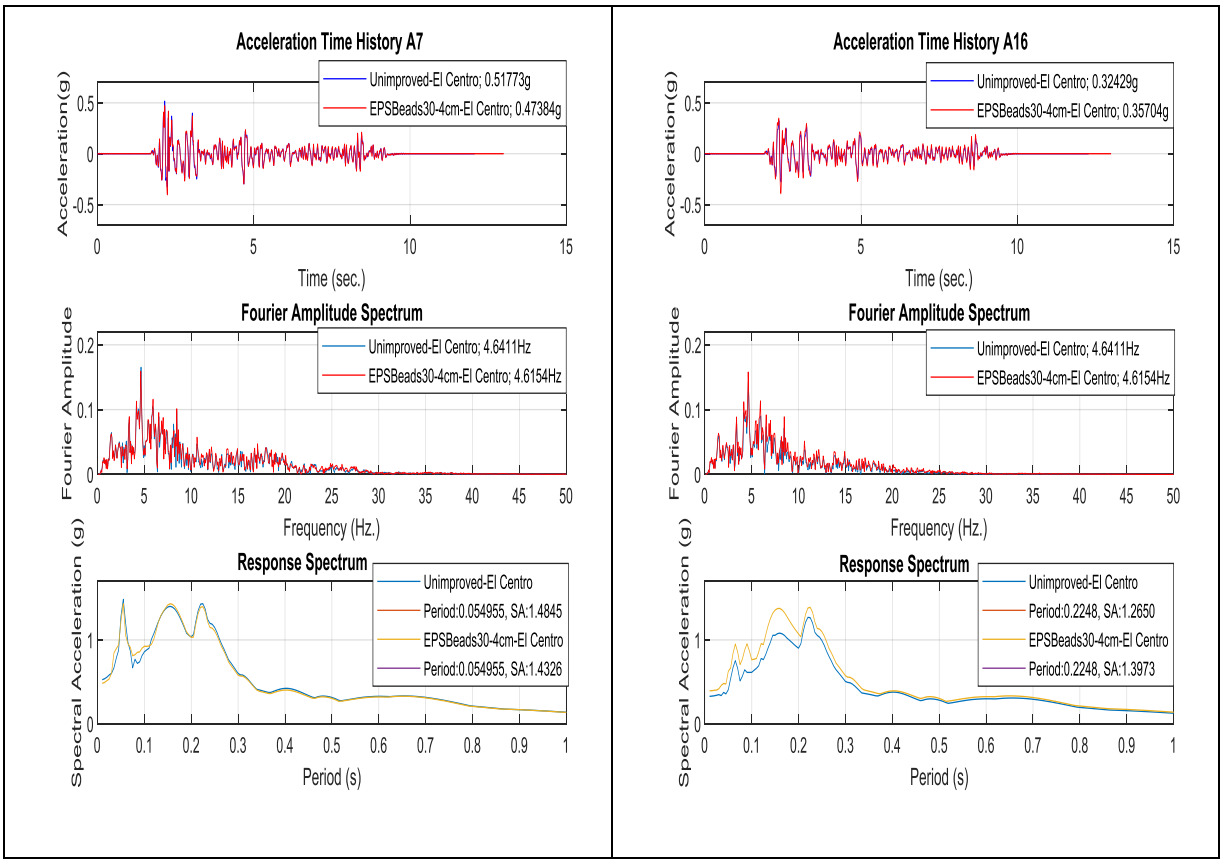


Figure 4.93. The ACCTH, FAS, Response Spectrum at the top of the RWM (A7) and in the backfill (A16) for Case 16 compared to Case 1 under the scaled 1940 Imperial Valley EQ-El Centro Station record (NF).

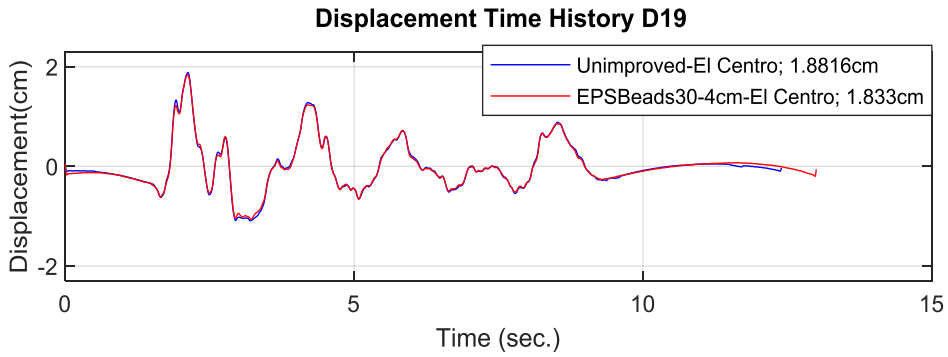


Figure 4.94. The DISTH at the top of the RWM (D19) for Case 16 compared to Case 1 under the scaled 1940 Imperial Valley EQ-El Centro Station record (NF).

Figure 4.95 displays the Acceleration-Time Histories, Fourier Amplitude Spectrums, and Response Spectrums under the sinusoidal motion at 0.4g amplitude with 8 Hz frequency. When this motion was applied, the A7 recorded a peak acceleration of 0.48g for the cushioned case. This is slightly higher compared to the control case, with a maximum acceleration of 0.47g. The A16 recorded a maximum acceleration of 0.47g for the cushioned case, while it was 0.36g for the control case. Both cases exhibit Fourier amplitudes peaking at 8.02 Hz at the top of the RWM and in the backfill. The maximum spectral accelerations ($S_a$) occurred at a period of 0.12 sec. For the control and cushioned cases, these values increased from 4.7g to 4.77g at the top of the RWM and from 3.60g to 4.74g in the backfill, respectively.

Figure 4.96 illustrates the displacement time history of the control case compared to the cushioned case under sinusoidal motion at 0.4g amplitude with 8 Hz frequency. The maximum displacement measured at the top of the RWM was 0.17 cm for the cushioned case, while 0.20 cm for the control case.

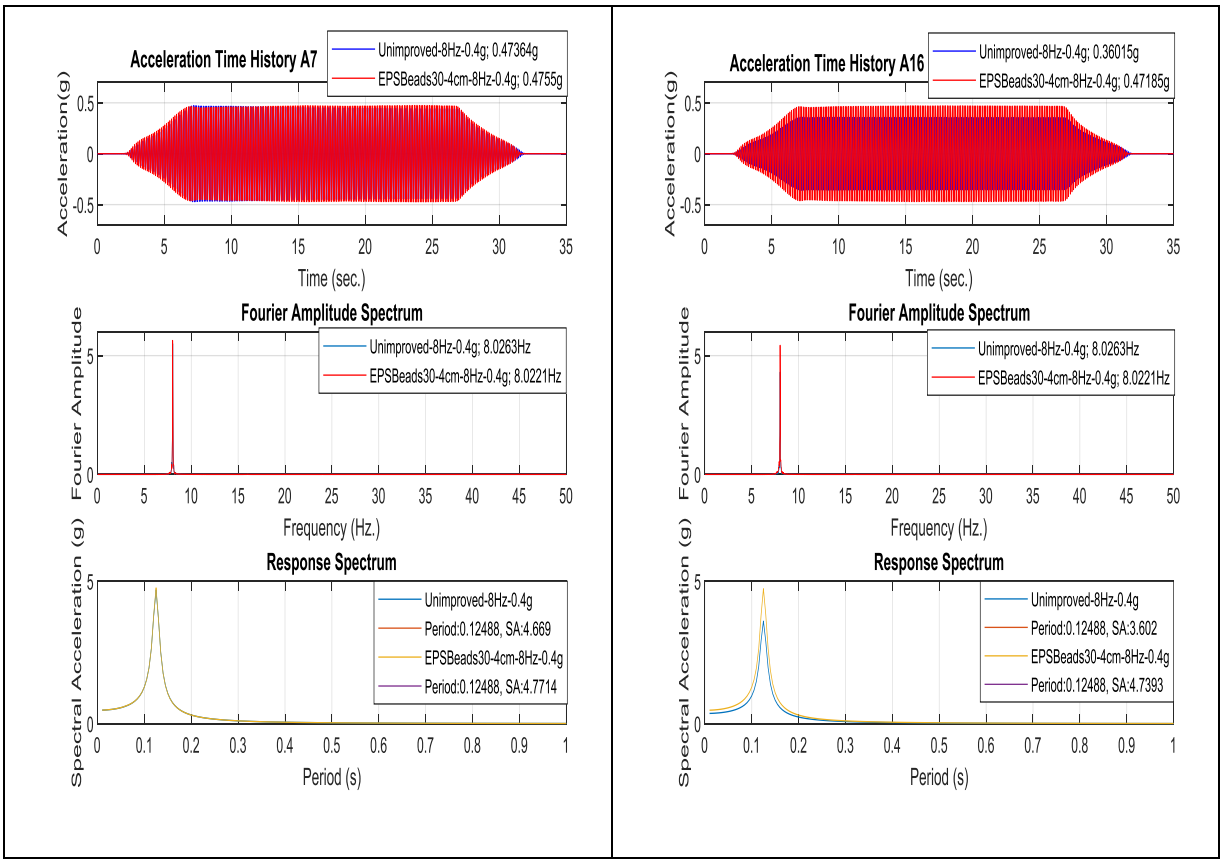


Figure 4.95. The ACCTH, FAS, Response Spectrum at the top of the RWM (A7) and in the backfill (A16) for Case 16 compared to Case 1 under sinusoidal motion at 0.4g amplitude with 8 Hz frequency.

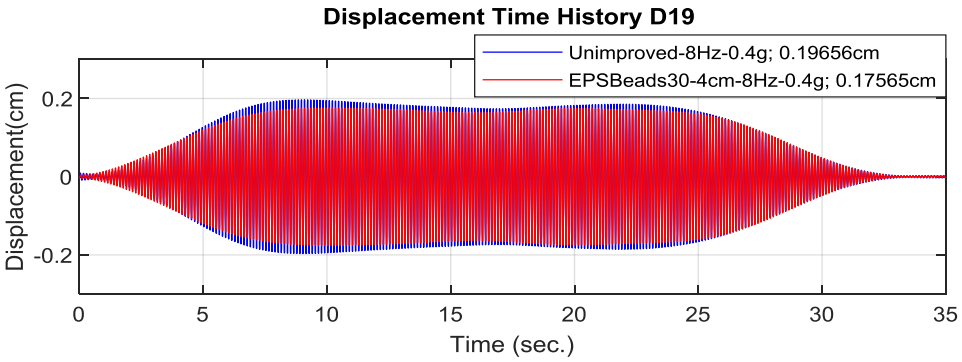


Figure 4.96. The DISTH at the top of the RWM (D19) for Case 16 compared to Case 1 under sinusoidal motion at 0.4g amplitude with 8 Hz frequency.

### 4.17. Results of Case 17 - EPSB10-6cm

In this study, Case 17 involves a cushion made of a mixture of EPS beads and sand with a ratio of 10% and a thickness of 6 cm (EPSB10-6cm) behind the RWM. The results for two different earthquake motions and one sinusoidal motion are presented in Figures 4.97, 4.98, 4.99, 4.100, 4.101, and 4.102. These Figures compare the measurements taken by accelerometer A7, laser displacement sensor D19 at the top of the retaining wall model (RWM), and accelerometer A16 in the backfill against the control case.

Figure 4.97 depicts the Acceleration-Time Histories, Fourier Amplitude Spectrums, and Response Spectrums under the scaled 2020 İzmir EQ Motion-Kuşadası Station excitations for Case 17, compared to the control case. The A7 recorded maximum acceleration values of 0.27g and 0.28g, while the A16 measured maximum acceleration values of 0.19g and 0.23g for the control and cushioned cases, respectively. The Fourier amplitudes for the control and cushioned cases were 9.26 Hz and 7.36 Hz at the top of the RWM and in the backfill. The maximum spectral accelerations occur in the 0.05 sec and 0.13 sec period ranges. Comparing the control and cushioned cases, the maximum spectral acceleration ($S_a$) values decreased from 0.98g to 0.96g at the top of the RWM at a period of 0.06 sec for the cushioned case. In the backfill, the spectral accelerations at a period of 0.11 sec were 0.78g and 0.76g for the cushioned case, compared to the control case, respectively.

Figure 4.98 demonstrates that, when subjected to the dynamic motions of the scaled 2020 İzmir EQ Motion-Kuşadası Station, the control case displaced a maximum of 0.37 cm, while the cushioned model EPSB10-6cm displaced a maximum of 0.32 cm.

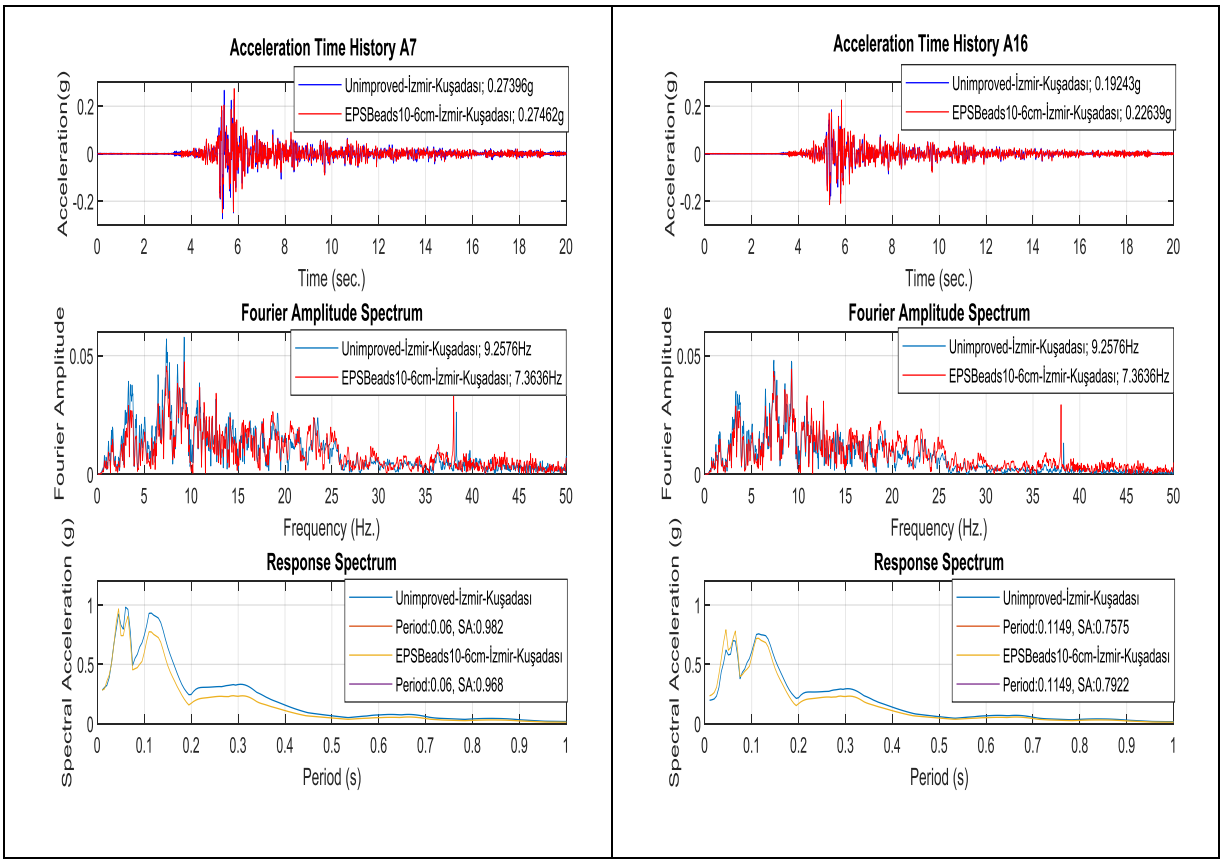


Figure 4.97. The ACCTH, FAS, Response Spectrum at the top of the RWM (A7) and in the backfill (A16) for Case 17 compared to Case 1 under the scaled 2020 İzmir EQ Motion-Kuşadası Station record (FF).

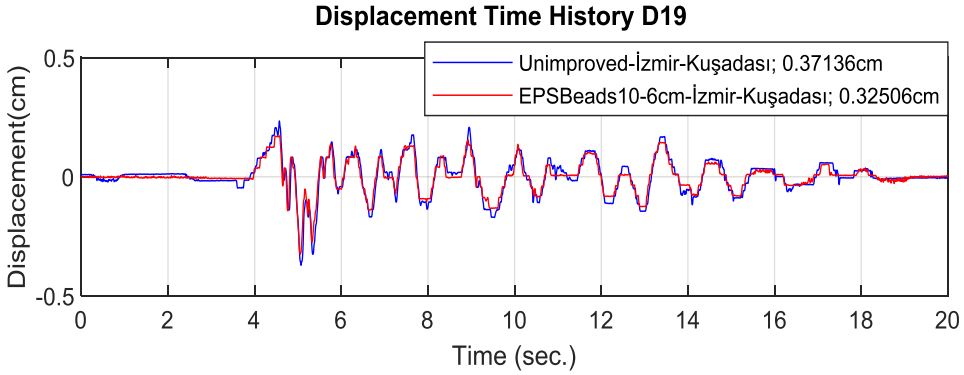


Figure 4.98. The DISTH at the top of the RWM (D19) for Case 17 compared to Case 1 under the scaled 2020 İzmir EQ Motion-Kuşadası Station record (FF).

In Figure 4.99, the Acceleration-Time Histories, Fourier Amplitude Spectrums, and Response Spectrums are depicted under the scaled 1940 Imperial Valley EQ-El Centro Station record. For the control case, the A7 recorded a maximum acceleration of 0.52g. However, with the implementation of EPSB10-6cm, the maximum acceleration decreased to 0.49g. Similarly, A16 measured a maximum acceleration of 0.32g for the control case, which increased to 0.39g for the cushioned case. The Fourier amplitudes peaked at around 4.64 Hz for both the control and cushioned cases, as measured by A7 and A16. The maximum spectral accelerations occurred within the 0.05 and 0.22 sec period ranges for both cases. For the control case, the maximum $S_a$ was 1.48g at a period of 0.055 sec at the top of the RWM. With EPSB10-6cm cushioning, the maximum $S_a$ decreased to 1.45g. Similarly, in the backfill, the spectral accelerations were 1.26g and 1.38g at the same 0.22 sec period for the control and cushioned cases, respectively.

Figure 4.100 presents the displacement time history for the control case compared to the cushioned case under the scaled 1940 Imperial Valley EQ-El Centro Station record. The maximum displacement measured at the top of the RWM was 1.88cm for the control case and 1.76cm for the cushioned case, indicating an improvement in performance.

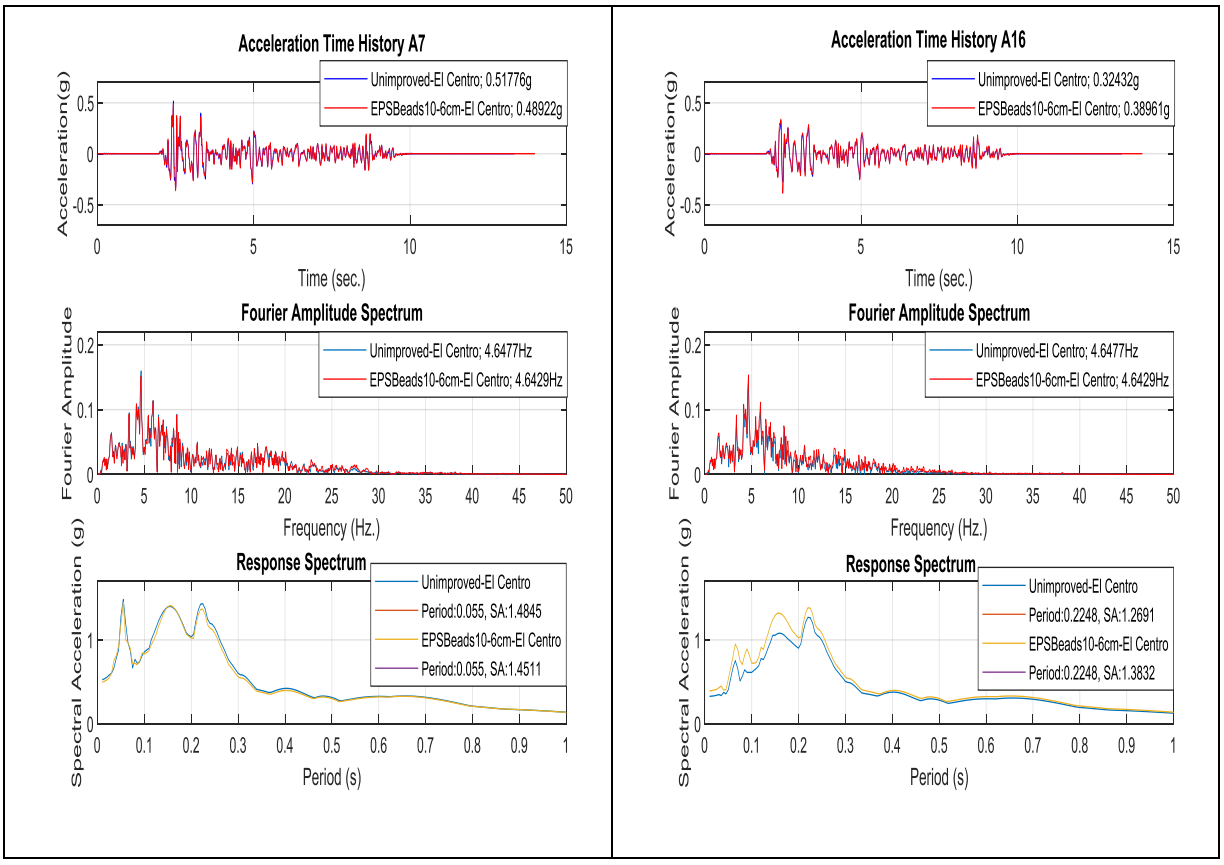


Figure 4.99. The ACCTH, FAS, Response Spectrum at the top of the RWM (A7) and in the backfill (A16) for Case 17 compared to Case 1 under the scaled 1940 Imperial Valley EQ-El Centro Station record (NF).

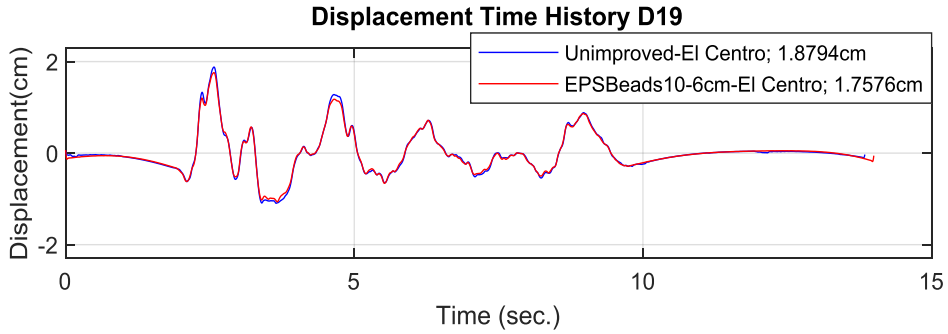


Figure 4.100. The DISTH at the top of the RWM (D19) for Case 17 compared to Case 1 under the scaled 1940 Imperial Valley EQ-El Centro Station record (NF).

Figure 4.101 illustrates the Acceleration-Time Histories, Fourier Amplitude Spectrums, and Response Spectrums under sinusoidal motion at 0.4g amplitude with 8 Hz frequency. It was observed that the EPSB cushioning decreased maximum acceleration values compared to the control case. At the top of the RWM, for the cushioned case, it was recorded a maximum acceleration of 0.44g, while for the control case, a maximum acceleration of 0.47g was recorded. In the backfill, a maximum acceleration of 0.42g was measured for the cushioned case, whereas for the control case, it was 0.36g. In terms of Fourier amplitudes, both cases showed a peak at 8.02 Hz at the top of the RWM and in the backfill. The response spectrum indicated that the maximum spectral accelerations occurred at a period of 0.12 sec. For the control case, the $S_a$ decreased from 4.7g to 4.48g at the top of the RWM and increased from 3.60g to 4.22g in the backfill with the implementation of EPSB cushioning.

Figure 4.102 displays the displacement time history for the control case compared to the cushioned case under sinusoidal motion at 0.4g amplitude with 8 Hz frequency. The cushioned case measured a peak displacement of 0.17cm at the top of the RWM, while for the control case, it was 0.20cm.

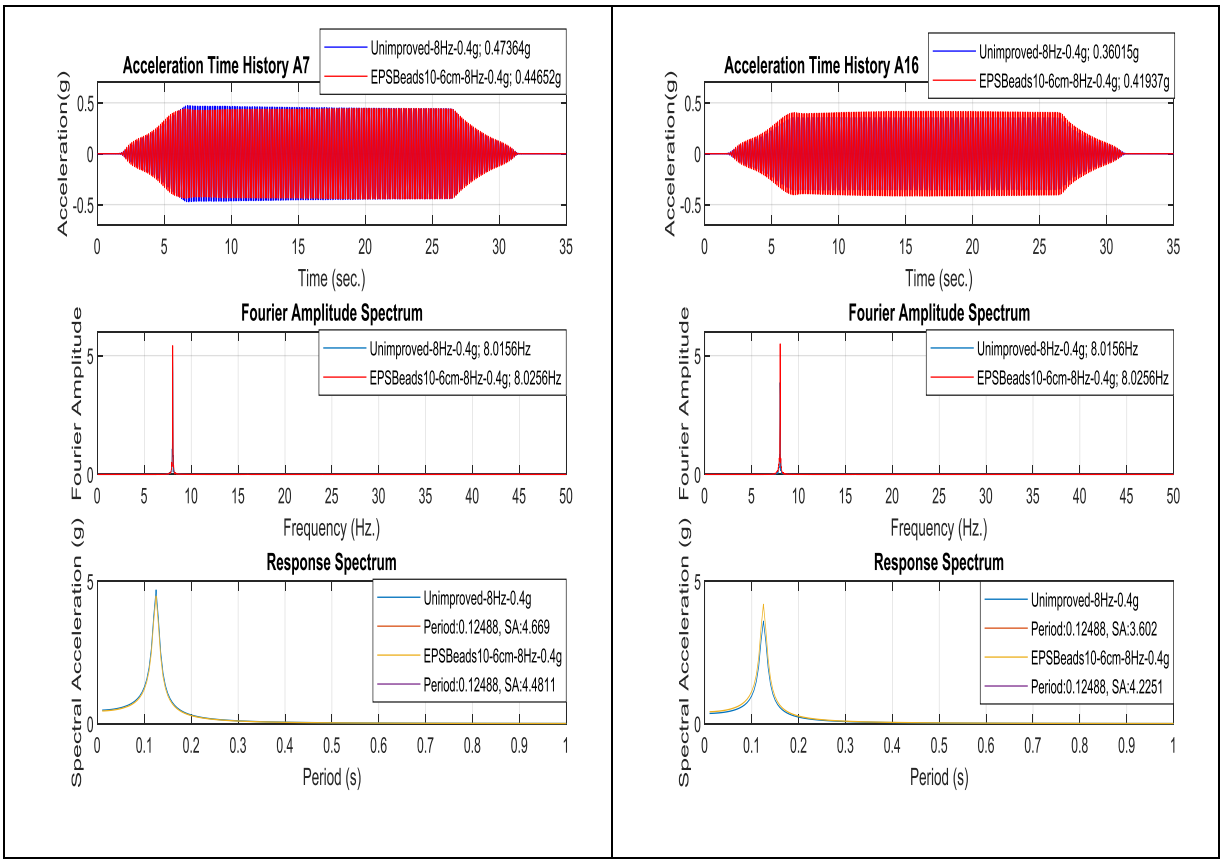


Figure 4.101. The ACCTH, FAS, Response Spectrum at the top of the RWM (A7) and in the backfill (A16) for Case 17 compared to Case 1 under sinusoidal motion at 0.4g amplitude with 8 Hz frequency.

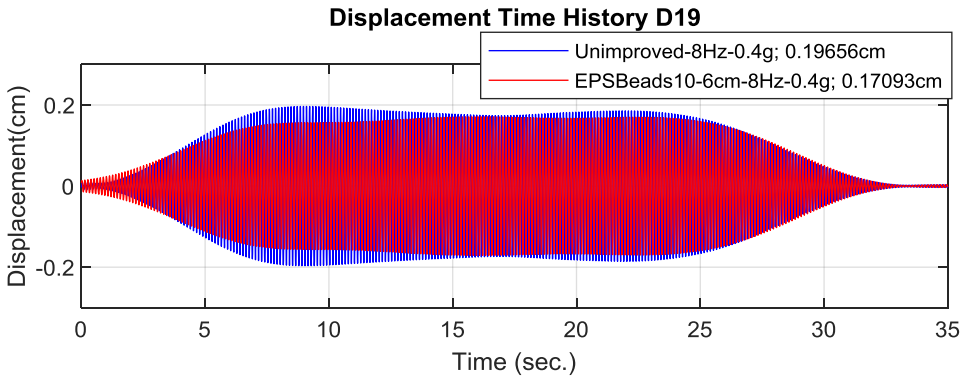


Figure 4.102. The DISTH at the top of the RWM (D19) for Case 17 compared to Case 1 under sinusoidal motion at 0.4g amplitude with 8 Hz frequency.

### 4.18. Results of Case 18 - EPSB20-6cm

Case 18 involves a mixture of EPS beads and sand cushion with a 20% mixture ratio and a thickness of 6 cm (EPSB20-6cm) behind the RWM. The results were compared under two different earthquake motions and one sinusoidal motion measured by accelerometer A7, laser displacement sensor D19 at the top of the retaining wall model (RWM), and accelerometer A16 in the backfill in comparison to the control case shown in Figures 4.103, 4.104, 4.105, 4.106, 4.107, and 4.108.

Figure 4.103 provides information on the Acceleration-Time Histories, Fourier Amplitude Spectrums, and Response Spectrums under the scaled 2020 İzmir EQ Motion-Kuşadası Station excitations for Case 18 compared to the control case. The maximum acceleration values of 0.27g and 0.28g were measured by A7 for the control and cushioned cases, respectively. In the backfill, it was measured maximum acceleration values of 0.19g and 0.22g for the control and cushioned cases, respectively. The Fourier amplitudes for the control and cushioned cases were 9.24 Hz and 7.36 Hz at the top of the RWM and in the backfill. The response spectrums showed maximum spectral accelerations at period ranges of 0.05 and 0.13 sec. Comparing the control case and cushioned cases, it is apparent that the peak spectral acceleration ($S_a$) values were 0.98g and 0.96g at the top of the RWM at a period of 0.06 sec. In the backfill, the spectral accelerations were 0.76g and 0.84g at a period of 0.11 sec for the cushioned case compared to the control case, respectively.

Figure 4.104 highlights the displacement difference between the control case and the cushioned model EPSB20-6cm under the dynamic motions of the scaled 2020 İzmir EQ Motion-Kuşadası Station. The control case had a displacement of 0.37 cm, while the cushioned model had a displacement of 0.33 cm.

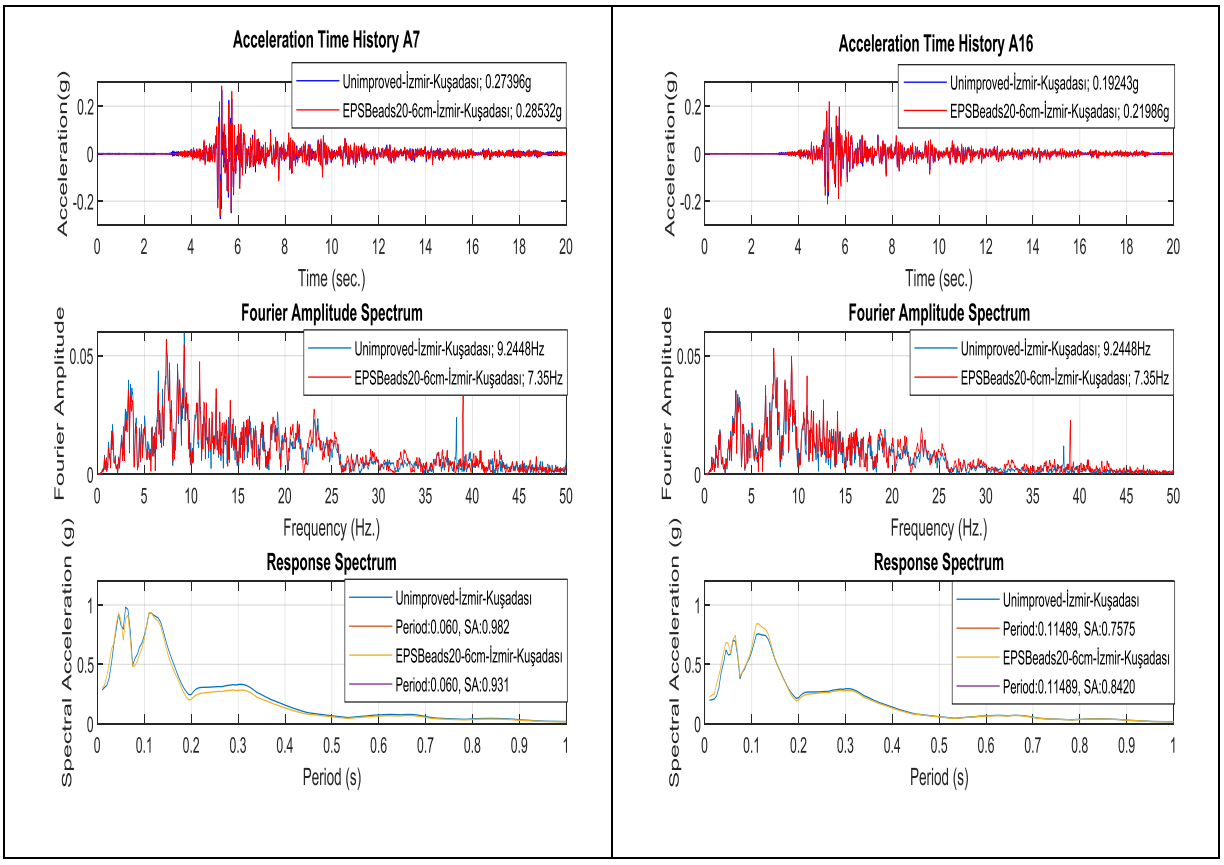


Figure 4.103. The ACCTH, FAS, Response Spectrum at the top of the RWM (A7) and in the backfill (A16) for Case 18 compared to Case 1 under the scaled 2020 İzmir EQ Motion-Kuşadası Station record (FF).

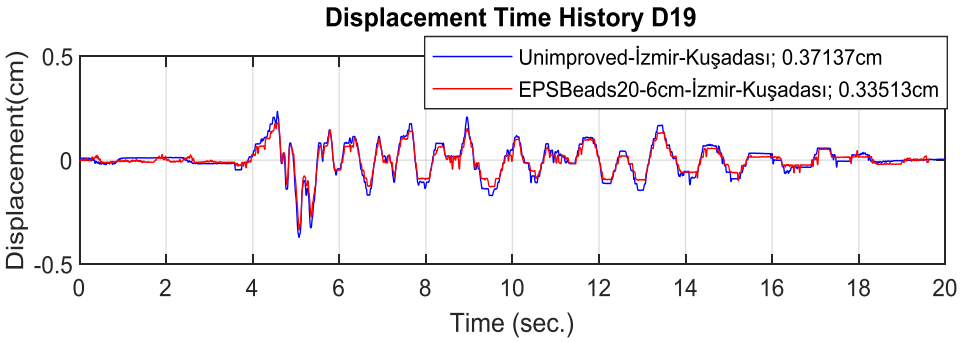


Figure 4.104. The DISTH at the top of the RWM (D19) for Case 18 compared to Case 1 under the scaled 2020 İzmir EQ Motion-Kuşadası Station record (FF).

Figure 4.105 displays the Acceleration-Time Histories, Fourier Amplitude Spectrums, and Response Spectrums under the scaled 1940 Imperial Valley EQ-El Centro Station record. For the control case, the A7 measured a maximum acceleration of 0.52g, which decreased to 0.49g for the cushioned case. The A16 measured a maximum acceleration of 0.32g for the control case and 0.36g for the cushioned case. Fourier amplitudes peaked around 4.60 Hz for both the control and cushioned cases. The response spectrums indicated maximum spectral accelerations at 0.05 and 0.22 sec periods for both the cushioned and control cases. At the top of the RWM, the control case had a maximum spectral acceleration ($S_a$) of 1.48g at a period of 0.055 sec, while the cushioned case had a maximum $S_a$ of 1.46g. In the backfill, the spectral accelerations were 1.26g and 1.39g at a period of 0.22 sec for the control and cushioned cases, respectively.

Figure 4.106 showcases the displacement time history of the control case compared to the cushioned case under the scaled 1940 Imperial Valley EQ-El Centro Station record. The cushioned model had a peak displacement of 1.82 cm at the top of the RWM, whereas the control case had a peak displacement of 1.88 cm.

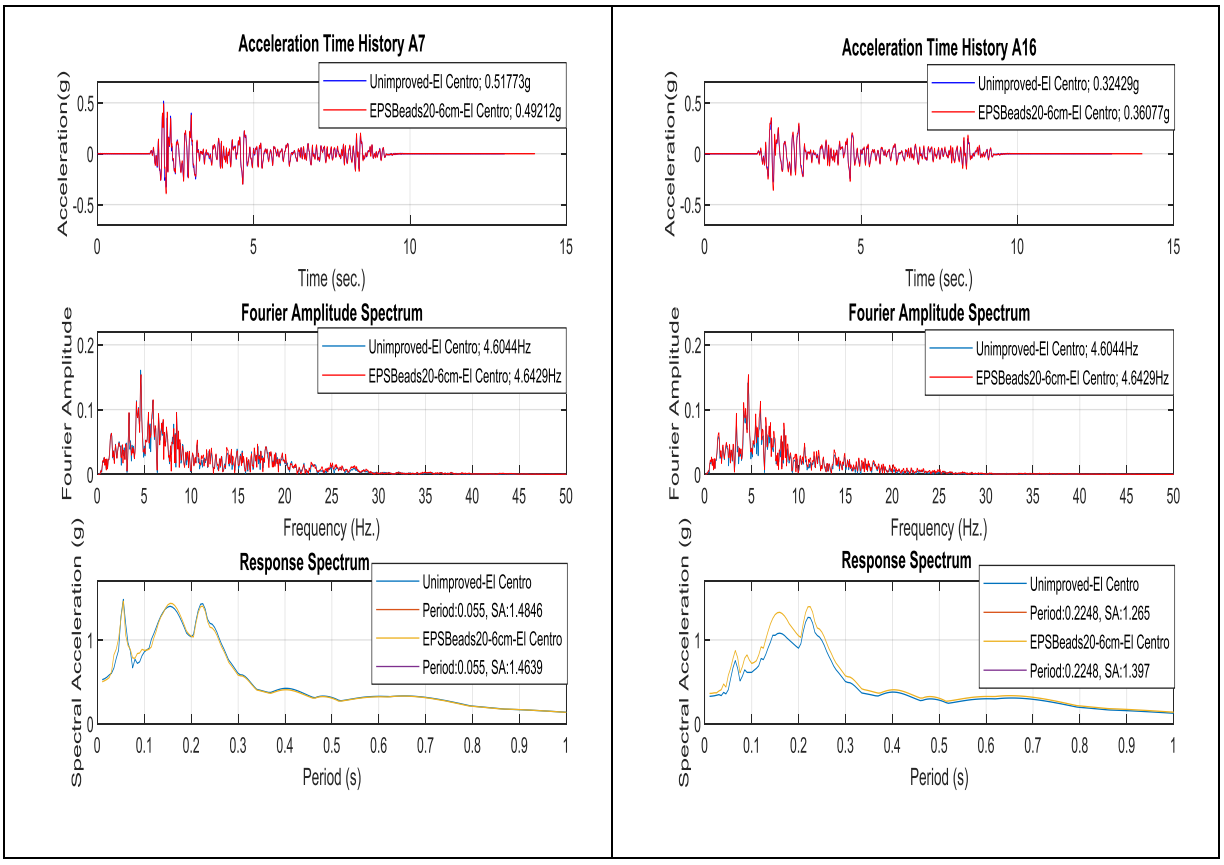


Figure 4.105. The ACCTH, FAS, Response Spectrum at the top of the RWM (A7) and in the backfill (A16) for Case 18 compared to Case 1 under the scaled 1940 Imperial Valley EQ-El Centro Station record (NF).

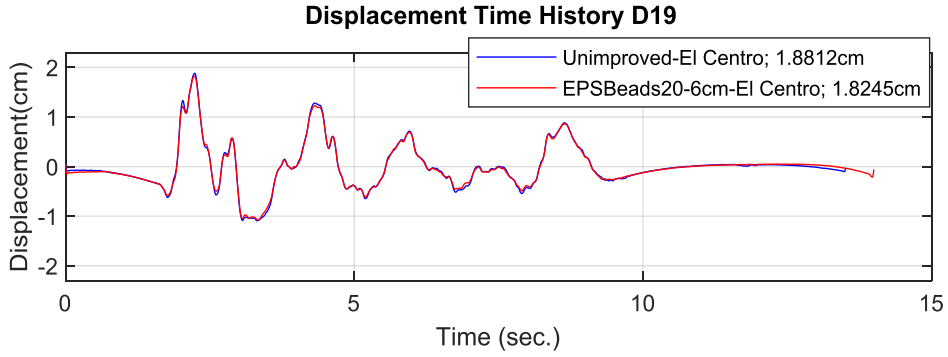


Figure 4.106. The DISTH at the top of the RWM (D19) for Case 18 compared to Case 1 under the scaled 1940 Imperial Valley EQ-El Centro Station record (NF).

Figure 4.107 presents the Acceleration-Time Histories, Fourier Amplitude Spectrums, and Response Spectrums under the sinusoidal motion at 0.4g amplitude with 8 Hz frequency. For the cushioned case, A7 measured a maximum acceleration of 0.45g compared to 0.47g for the control case. The A16 measured a maximum acceleration of 0.45g for the cushioned case and 0.36g for the control case. At the top of the RWM and in the backfill, Fourier amplitudes peaked at 8.02 Hz for both the cushioned and control cases. The maximum spectral accelerations ($S_a$) occurred at a period of 0.12 seconds. These accelerations decreased from 4.7g to 4.50g at the top of the RWM and increased from 3.60g to 4.45g in the backfill for the control and cushioned cases, respectively.

Figure 4.108 shows the displacement time history for both the control and cushioned cases under sinusoidal motion at 0.4g amplitude with 8 Hz frequency. In the cushioned case, the maximum displacement was measured as 0.18 cm at the top of the RWM. In comparison, the control case had a measured maximum displacement of 0.20 cm.

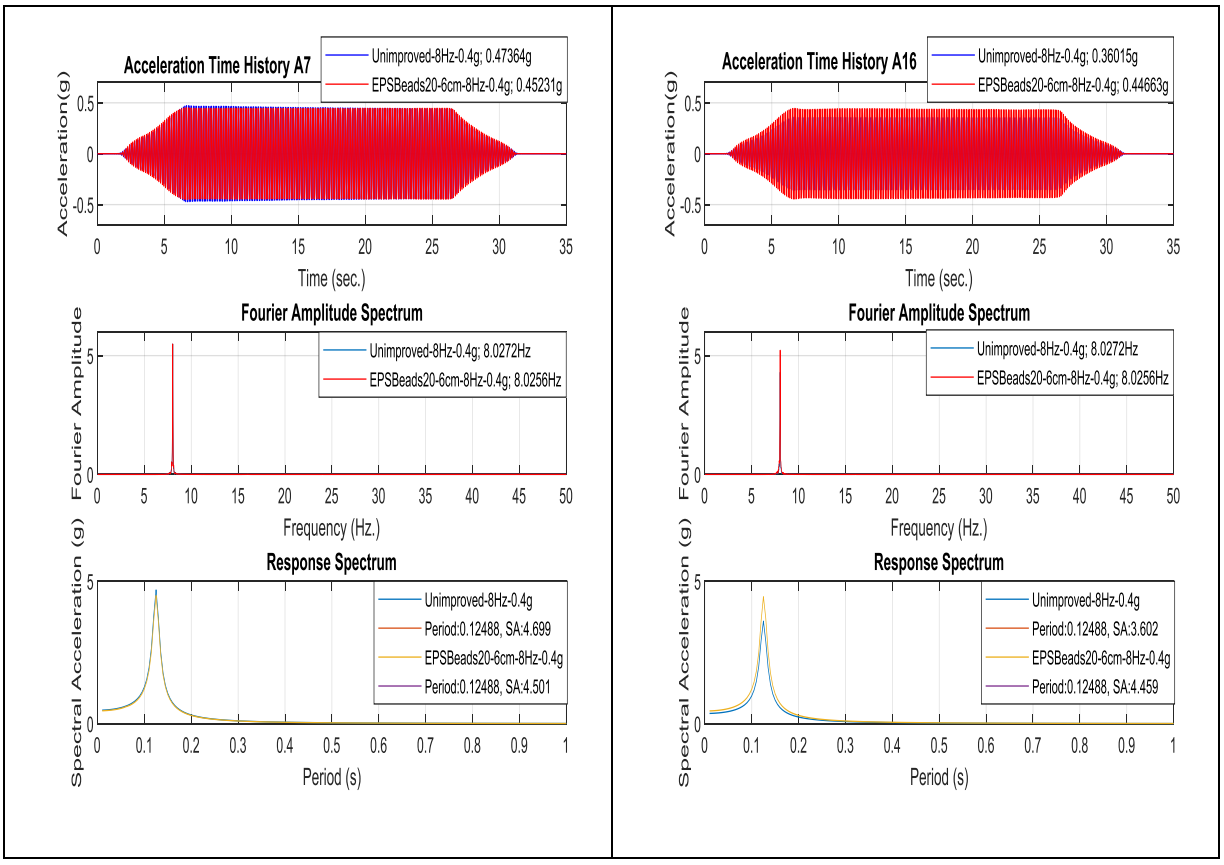


Figure 4.107. The ACCTH, FAS, Response Spectrum at the top of the RWM (A7) and in the backfill (A16) for Case 18 compared to Case 1 under sinusoidal motion at 0.4g amplitude with 8 Hz frequency.

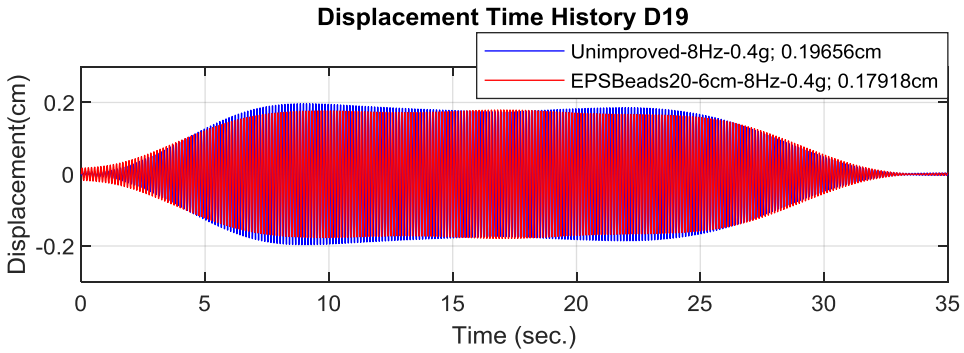


Figure 4.108. The DISTH at the top of the RWM (D19) for Case 18 compared to Case 1 under sinusoidal motion at 0.4g amplitude with 8 Hz frequency.

### 4.19. Results of Case 19 - EPSB30-6cm

Case 19 consists of EPS beads and sand mixture cushion with 30% mixture ratio and 6 cm thickness (EPSB30-6cm) behind the RWM. Figures 4.109, 4.110, 4.111, 4.112, 4.113, and 4.114 show the results for two different earthquake motions and one sinusoidal motion as measured by accelerometer A7, laser displacement sensor D19 at the top of the retaining wall model (RWM) and accelerometer A16 in the backfill in comparison to the control case.

Figure 4.109 illustrates the Acceleration-Time Histories, Fourier Amplitude Spectrums, and Response Spectrums under the scaled 2020 İzmir EQ Motion-Kuşadası Station excitations for Case 19 compared to the control case. The maximum accelerations were measured as 0.27g and 0.28g at the top of the RWM, and 0.19g and 0.22 in the backfill for the control case and Case 19, respectively. The Fourier amplitudes for the control and cushioned cases were 9.23 Hz and 7.36 Hz at the top of the RWM and in the backfill. The maximum spectral accelerations were at 0.05 sec and 0.13 sec period ranges. Compared to the control case and cushioned cases, the maximum spectral acceleration (Sa) values decreased from 0.98g to 0.96g at the top of the RWM at a period of 0.06 sec. The spectral accelerations were 0.76g and 0.84g in the backfill at period of 0.11 sec for the cushioned case compared to the control case, respectively.

Figure 4.110 shows that, when subjected to the dynamic motions of the scaled 2020 İzmir EQ Motion-Kuşadası Station, the control case displaced a maximum of 0.37 cm compared to 0.38cm for the cushioned model EPSB30-6cm.

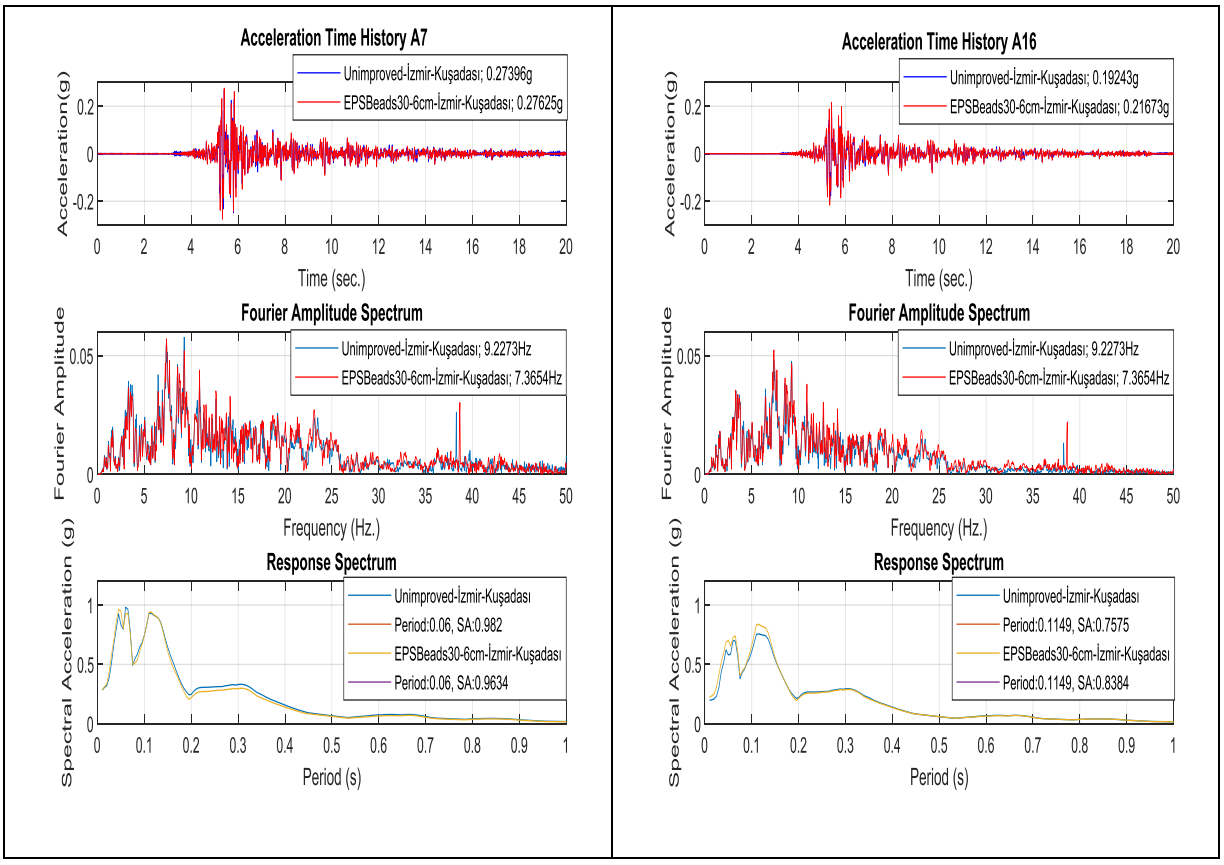


Figure 4.109. The ACCTH, FAS, Response Spectrum at the top of the RWM (A7) and in the backfill (A16) for Case 19 compared to Case 1 under the scaled 2020 İzmir EQ Motion-Kuşadası Station record (FF).

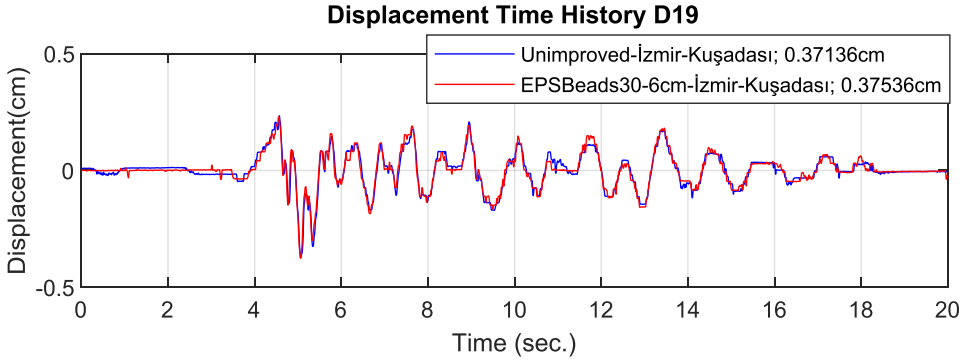


Figure 4.110. The DISTH at the top of the RWM (D19) for Case 19 compared to Case 1 under the scaled 2020 İzmir EQ Motion-Kuşadası Station record (FF).

The Acceleration-Time Histories, Fourier Amplitude Spectrums, and Response Spectrums are illustrated in Figure 4.111 under the scaled 1940 Imperial Valley EQ-El Centro Station record. It was measured 0.52g maximum acceleration for the control case at the top of the RWM decreased to 0.47g for the EPSB30-6cm cushioned case. The A16 measured 0.32g maximum acceleration for the control case and 0.36g for the cushioned case. It can be noticed that the maximum acceleration values deceased at the top of the RWM when the EPSB30-6cm cushion was implemented. Fourier amplitudes peaked around 4.60 Hz at the top of the RWM and in the backfill for the control and cushioned cases measured from A7 and A16. The maximum spectral accelerations were at 0.05 sec and 0.22 sec period ranges for the cushioned and control cases. The maximum spectral accelerations ($S_a$) were 1.48g at 0.055 sec period at the top of the RWM for the control case, decreasing to 1.29g for the EPSB30-6cm cushioned case. The spectral accelerations in the backfill were 1.26g and 1.37g at the same periods 0.22 sec for the control case and EPSB30-6cm cushioned cases, respectively.

Figure 4.112 presents the displacement time history of the control case compared to the cushioned case under the scaled 1940 Imperial Valley EQ-El Centro Station record. The maximum displacement of the EPSB30-6cm cushioned model was measured as 1.81 cm, while the control case was measured as 1.88 cm at the top of the RWM.

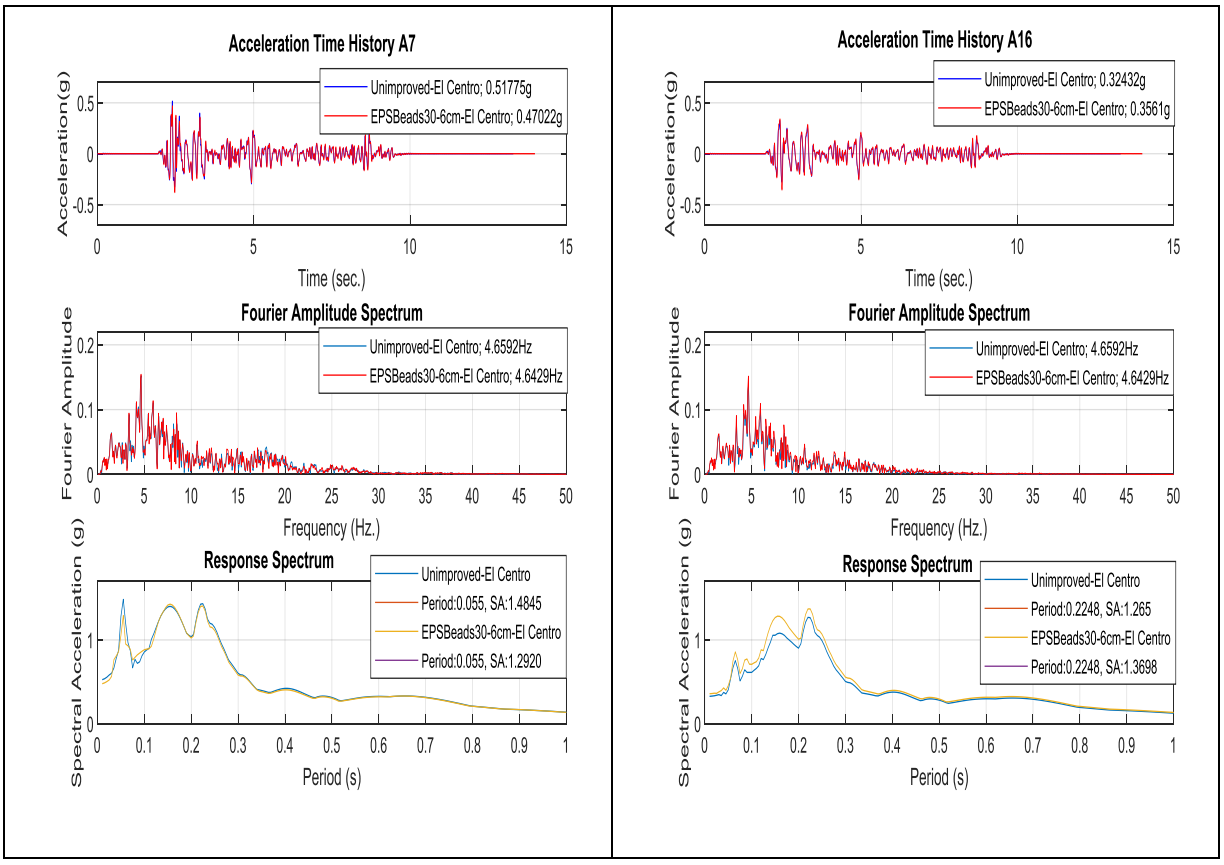


Figure 4.111. The ACCTH, FAS, Response Spectrum at the top of the RWM (A7) and in the backfill (A16) for Case 19 compared to Case 1 under the scaled 1940 Imperial Valley EQ-El Centro Station record (NF).

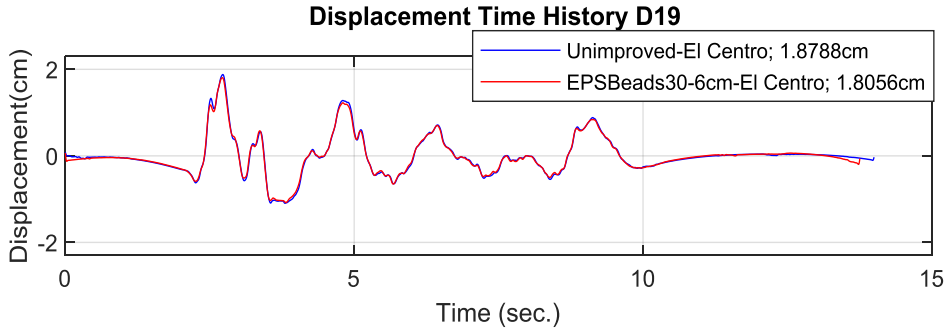


Figure 4.112. The DISTH at the top of the RWM (D19) for Case 19 compared to Case 1 under the scaled 1940 Imperial Valley EQ-El Centro Station record (NF).

The Acceleration-Time Histories, Fourier Amplitude Spectrums, and Response Spectrums under the sinusoidal motion at 0.4g amplitude with 8 Hz frequency are shown in Figure 4.113. The A7 measured 0.46g maximum acceleration for the EPSB30-6cm cushioned case compared to the control case as 0.47g, and the A16 measured 0.44g maximum acceleration for the cushioned case compared to the control case 0.36g. The Fourier amplitudes peaked at 8.02 Hz at the top of the RWM and in the backfill for both the cushioned case and the control case. The maximum spectral accelerations ($S_a$) were at 0.12 sec period, decreased from 4.7g to 4.61g at the top of the RWM, and increased from 3.60g to 4.43g in the backfill for the control and cushioned cases.

Figure 4.114 presents the displacement time history of the control case compared to the cushioned case under sinusoidal motion at 0.4g amplitude with 8 Hz frequency. Maximum displacement was measured as 0.17 cm at the top of the RWM for the cushioned case, whereas it was measured as 0.20 cm for the control case.

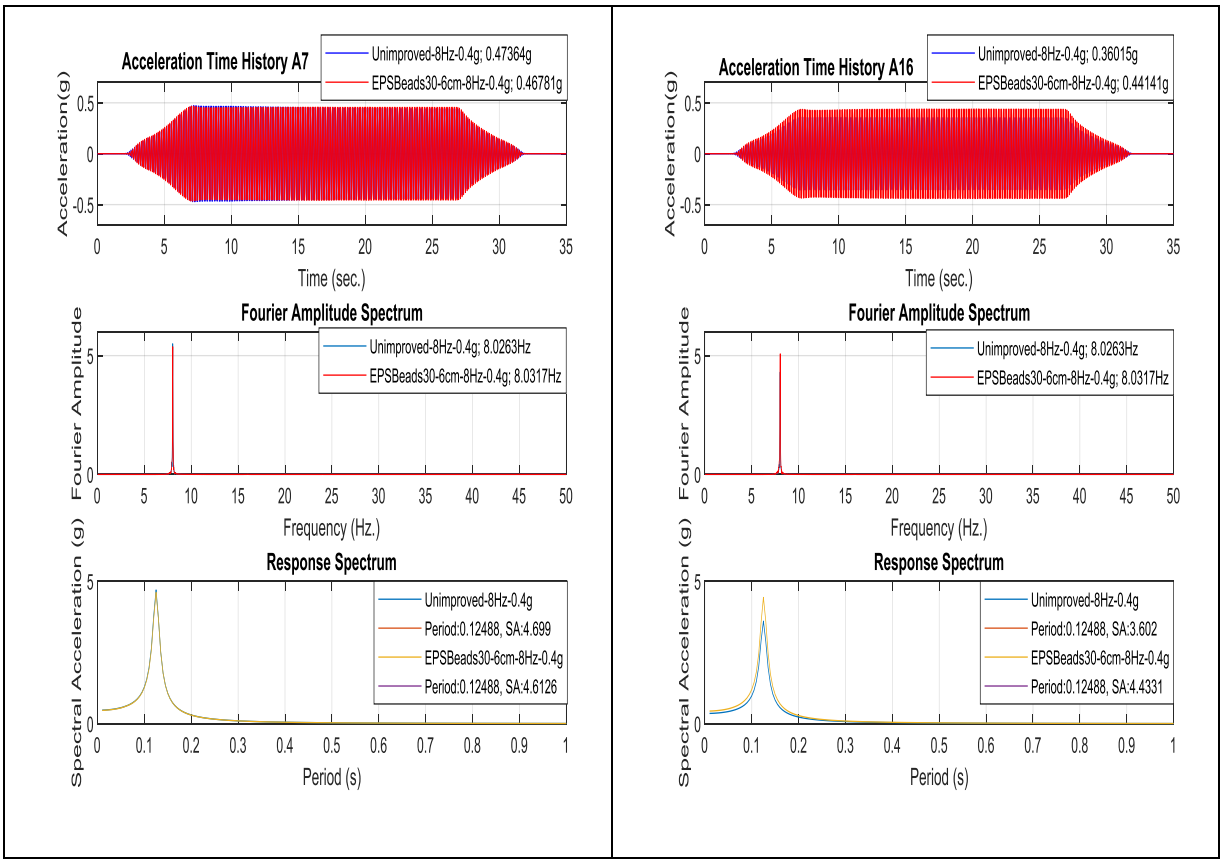


Figure 4.113. The ACCTH, FAS, Response Spectrum at the top of the RWM (A7) and in the backfill (A16) for Case 19 compared to Case 1 under sinusoidal motion at 0.4g amplitude with 8 Hz frequency.

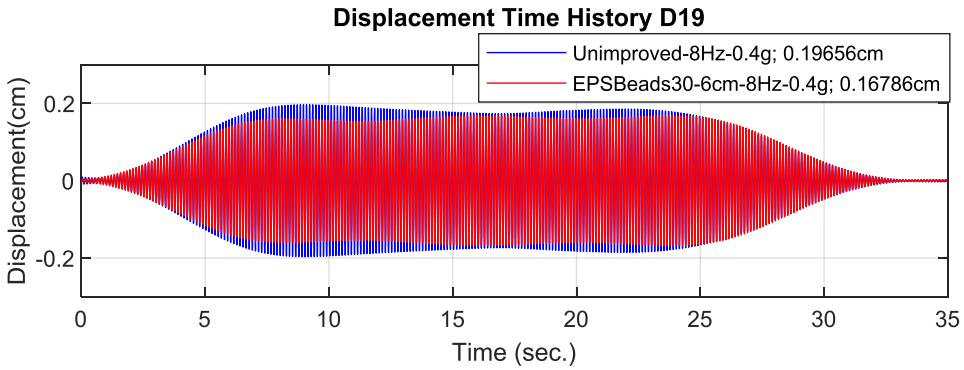


Figure 4.114. The DISTH at the top of the RWM (D19) for Case 19 compared to Case 1 under sinusoidal motion at 0.4g amplitude with 8 Hz frequency.

### 4.20. Results of Case 20 - EPSB10-8cm

Case 20 involved a mixture of EPS beads and sand cushion with a ratio of 10% and a thickness of 8 cm (EPSB10-8cm) behind the RWM. Figures 4.115-.120 present the results for two different earthquake motions and a sinusoidal motion. These results were obtained from measurements taken by accelerometer A7, laser displacement sensor D19 at the top of the retaining wall model (RWM), and accelerometer A16 in the backfill. The measurements were then compared to the findings of the control case.

Figure 4.115 displays the Acceleration-Time Histories, Fourier Amplitude Spectrums, and Response Spectrums for Case 20 under the scaled 2020 İzmir EQ Motion-Kuşadası Station excitations. These results are compared with the control case (Case 1). The A7 recorded maximum acceleration values of 0.27g and 0.28g, while A16 measured maximum acceleration values of 0.19g and 0.21g for the control and cushioned cases, respectively. The Fourier amplitudes for the control and cushioned cases were 9.25 Hz and 7.37 Hz at the top of the RWM and in the backfill. The maximum spectral accelerations occur at periods of 0.05 sec and 0.13 sec. Comparing the control and cushioned cases, a decrease in the maximum spectral acceleration (Sa) values was observed from 0.98g to 0.91g for the cushioned case at the top of the RWM at a period of 0.06 sec. Additionally, the spectral accelerations in the backfill were 0.76g and 0.80g at a period of 0.11 sec for the control and cushioned cases, respectively.

In Figure 4.116, it is seen that when subjected to the dynamic motions of the scaled 2020 İzmir EQ Motion-Kuşadası Station, the control case displaced a maximum of 0.37 cm, whereas the cushioned model EPSB10-8cm displaced a maximum of 0.34 cm.

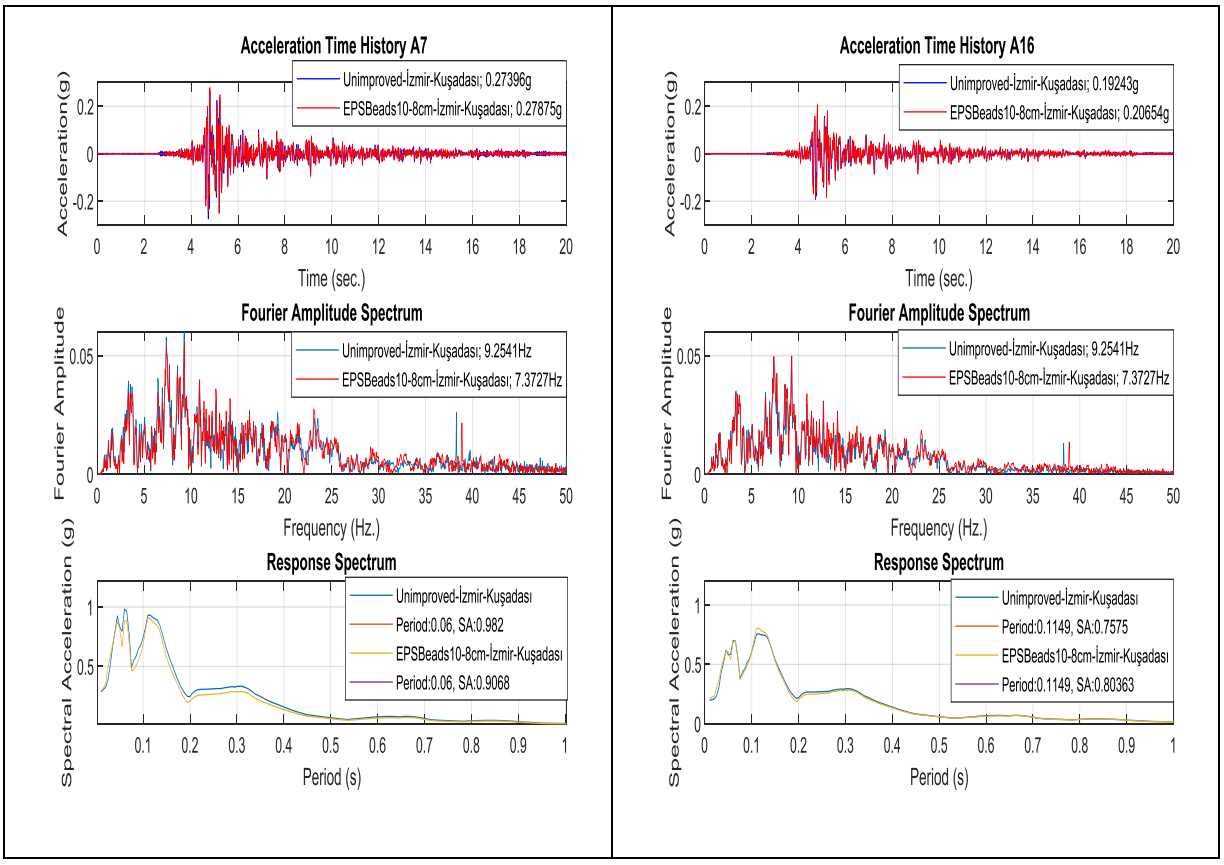


Figure 4.115. The ACCTH, FAS, Response Spectrum at the top of the RWM (A7) and in the backfill (A16) for Case 20 compared to Case 1 under the scaled 2020 İzmir EQ Motion-Kuşadası Station record (FF).

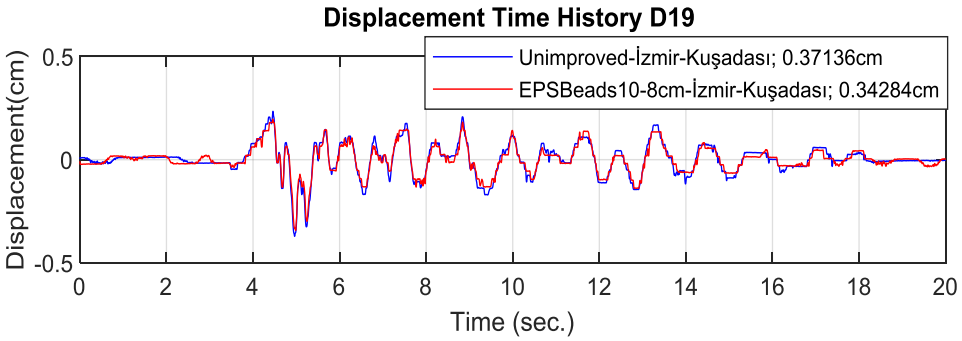


Figure 4.116. The DISTH at the top of the RWM (D19) for Case 21 compared to Case 1 under the scaled 2020 İzmir EQ Motion-Kuşadası Station record (FF).

Figure 4.117 showcases the Acceleration-Time Histories, Fourier Amplitude Spectrums, and Response Spectrums for different cases under the scaled 1940 Imperial Valley EQ-El Centro Station record. The A7 recorded a maximum acceleration of 0.52g for the control case. However, this value decreased to 0.48g when the EPSB10-8cm cushion was implemented. Similarly, the A16 measured a maximum acceleration of 0.32g for the control case, which increased to 0.34g for the cushioned case. The improvement with the EPSB10-8cm cushion caused a decrease in maximum acceleration values at the top of the RWM. The Fourier amplitudes peaked at around 4.62 Hz for both the control and cushioned cases, as measured by A7 and A16. The response spectrums indicate that the maximum spectral accelerations occur at the period ranges of 0.05 and 0.22 sec for both cases. For the control case, the maximum spectral acceleration ($S_a$) at the top of the RWM was 1.48g at a period of 0.055sec, while this value decreased to 1.31g for the cushioned case. In the backfill, the spectral accelerations were 1.26g and 1.36g at a period of 0.22 sec for the control and cushioned cases, respectively.

Figure 4.118 compares the displacement time history of the control case with the cushioned case under the scaled 1940 Imperial Valley EQ-El Centro Station record. The maximum displacement measured at the top of the RWM was 1.92 cm for the EPSB10-8cm cushioned model, while it was 1.88 cm for the control case.

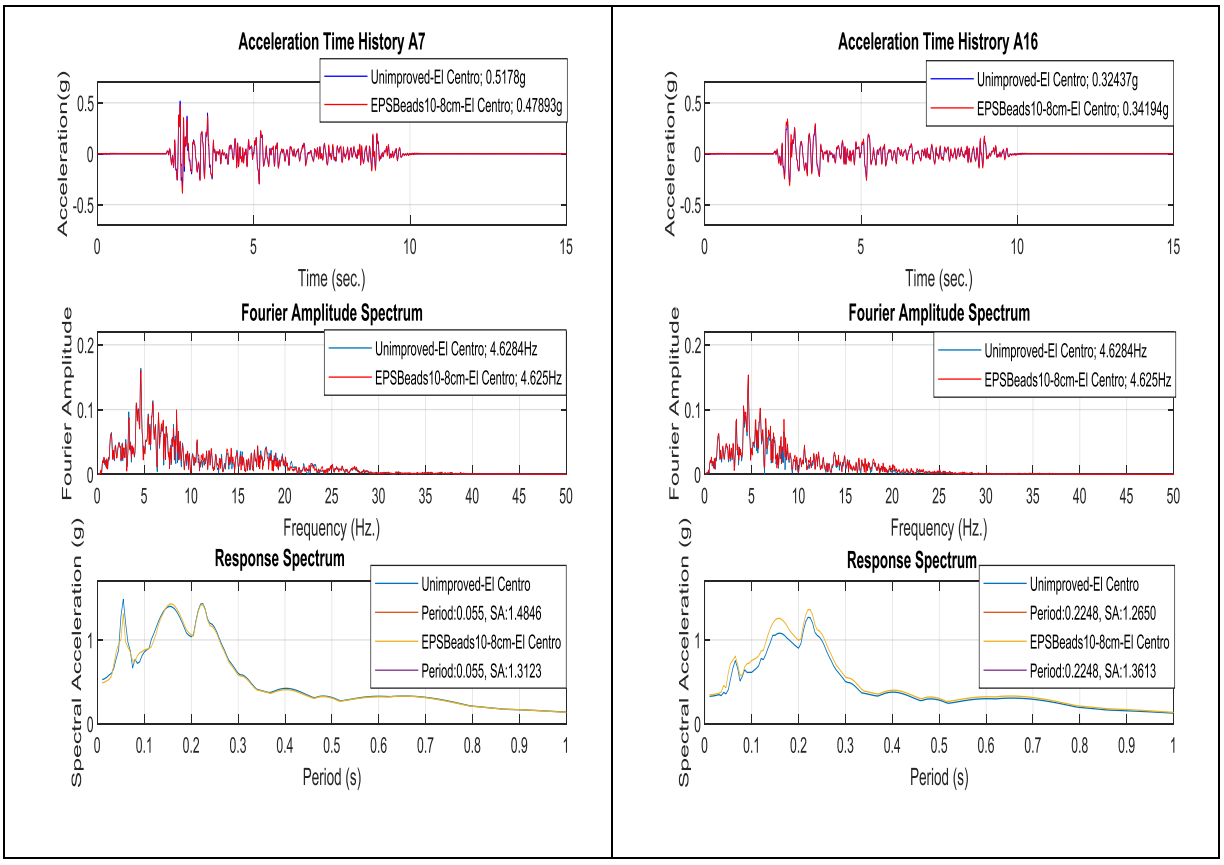


Figure 4.117. The ACCTH, FAS, Response Spectrum at the top of the RWM (A7) and in the backfill (A16) for Case 20 compared to Case 1 under the scaled 1940 Imperial Valley EQ-El Centro Station record (NF).

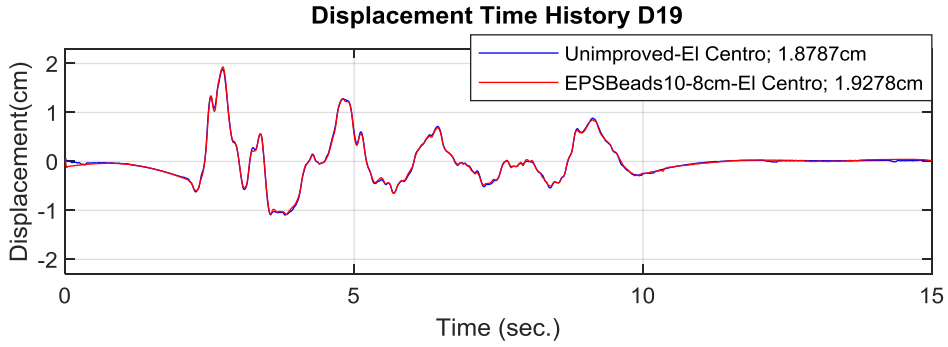


Figure 4.118. The DISTH at the top of the RWM (D19) for Case 20 compared to Case 1 under the scaled 1940 Imperial Valley EQ-El Centro Station record (NF).

In Figure 4.119, the Acceleration-Time Histories, Fourier Amplitude Spectrums, and Response Spectrums under a sinusoidal motion at 0.4g amplitude with 8 Hz frequency are given. When this motion was applied, the A7 recorded a peak acceleration of 0.44g for the cushioned case, whereas it was 0.47g for the control case. In the backfill, it was measured a maximum acceleration of 0.42g for the cushioned case, while it was 0.36g for the control case. Fourier amplitudes for both cases showed a peak at 8.02 Hz at the top of the RWM and in the backfill. The maximum spectral accelerations ($S_a$) were observed at a period of 0.12 sec. The $S_a$ values decreased from 4.7g to 4.38g at the top of the RWM, whereas they increased from 3.60g to 4.19g in the backfill for the cushioned case compared to the control case.

Figure 4.120 illustrates the displacement time history for the same sinusoidal motion at 0.4g amplitude with 8 Hz frequency. In the cushioned case, the maximum displacement measured at the top of the RWM was 0.19 cm, obtained from sensor D19. On the other hand, for the control case, the maximum displacement was measured as 0.20 cm.

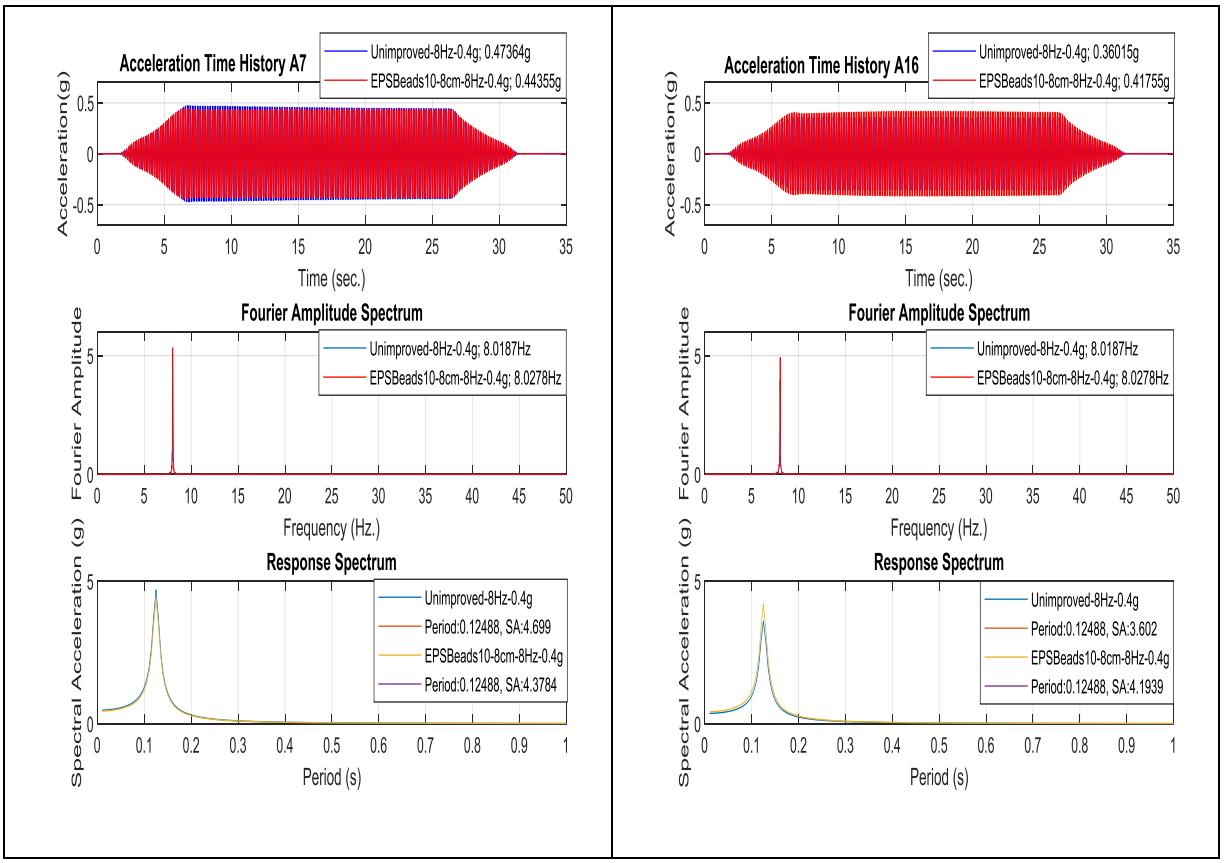


Figure 4.119. The ACCTH, FAS, Response Spectrum at the top of the RWM (A7) and in the backfill (A16) for Case 20 compared to Case 1 under sinusoidal motion at 0.4g amplitude with 8 Hz frequency.

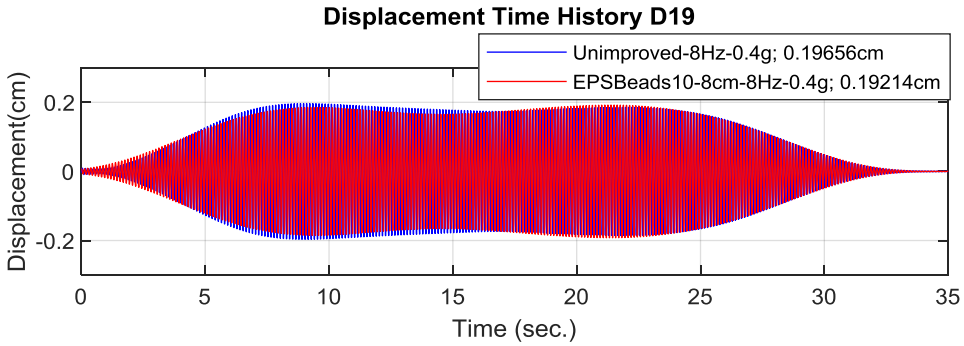


Figure 4.120. The DISTH at the top of the RWM (D19) for Case 20 compared to Case 1 under sinusoidal motion at 0.4g amplitude with 8 Hz frequency.

## 4.21. Results of Case 21 - EPSB20-8cm

In this study, Case 21 involves a cushion made of EPS beads and sand mixture with a ratio of 20% and a thickness of 8 cm (EPSB20-8cm) behind the RWM. The results of two different earthquake motions and one sinusoidal motion are presented in Figures 4.121, 4.122, 4.123, 4.124, 4.125, and 4.126. These results were obtained from measurements taken by accelerometer A7, laser displacement sensor D19 at the top of the retaining wall model (RWM) and accelerometer A16 in the backfill. A comparison is made between these measurements and the control case.

Figure 4.121 displays the Acceleration-Time Histories, Fourier Amplitude Spectrums, and Response Spectrums under the scaled 2020 İzmir EQ Motion-Kuşadası Station excitations for Case 21 in comparison to the control case. The A7 recorded maximum acceleration values of 0.27g and 0.26g, while the A16 measured maximum acceleration values of 0.19g and 0.21g for the control and cushioned cases, respectively. Additionally, the Fourier amplitudes for the control and cushioned cases were 9.24 Hz and 7.35 Hz at the top of the RWM and in the backfill. The maximum spectral accelerations occur in the 0.05 and 0.13 sec period ranges. Comparing the control case and cushioned cases, it is seen a decrease in maximum spectral acceleration ($S_a$) values from 0.98g to 0.83g at the top of the RWM, with a period of 0.06 sec. In the backfill, the cushioned case has spectral accelerations of 0.75g and 0.91g at a period of 0.11 sec, compared to the control case.

In Figure 4.122, it is observed that under the dynamic motions of the scaled 2020 İzmir EQ Motion-Kuşadası Station, the control case displaced a maximum of 0.37 cm, while the cushioned model EPSB20-8cm displaced a maximum of 0.33 cm.

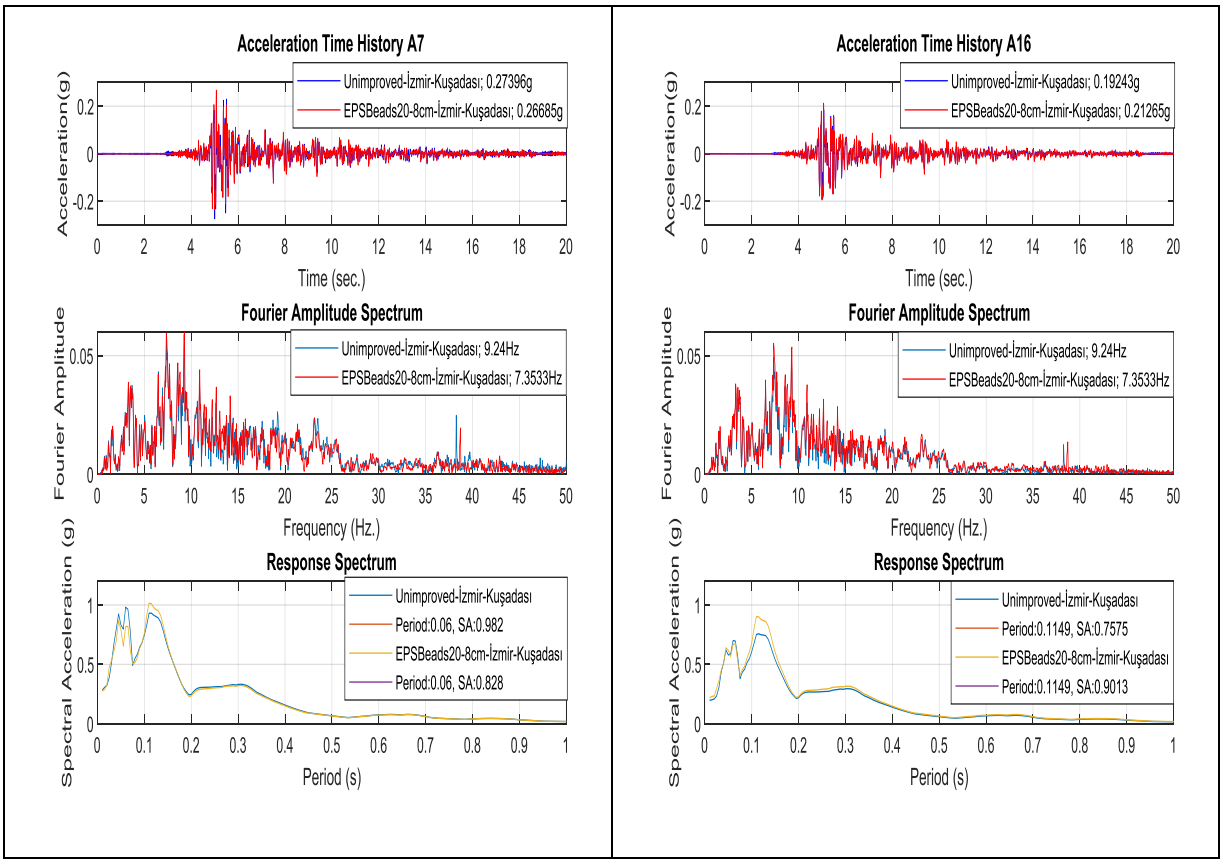


Figure 4.121. The ACCTH, FAS, Response Spectrum at the top of the RWM (A7) and in the backfill (A16) for Case 21 compared to Case 1 under the scaled 2020 İzmir EQ Motion-Kuşadası Station record (FF).

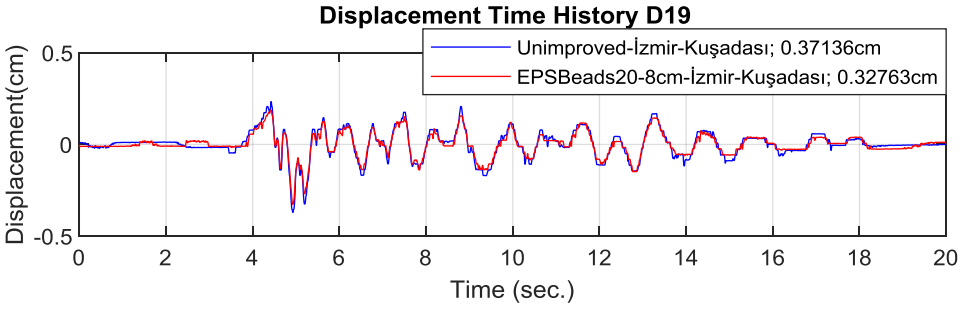


Figure 4.122. The DISTH at the top of the RWM (D19) for Case 22 compared to Case 1 under the scaled 2020 İzmir EQ Motion-Kuşadası Station record (FF).

Figure 4.123 displays the Acceleration-Time Histories, Fourier Amplitude Spectrums, and Response Spectrums under the scaled 1940 Imperial Valley EQ-El Centro Station record. The A7 recorded a maximum acceleration of 0.52g for the control case. This value decreased to 0.51g maximum acceleration when the wall was cushioned with EPSB20-8cm. Similarly, the A16 recorded a maximum acceleration of 0.32g for the control case and a maximum acceleration of 0.37g for the cushioned case. Implementing the EPSB cushion resulted in a decrease in maximum acceleration values at the top of the RWM. The Fourier amplitude peaks were around 4.61 Hz for both the control and cushioned cases, as measured from A7 and A16. The maximum spectral accelerations occur in the 0.05 and 0.22 sec period ranges for both the cushioned and control cases. For the control case, the maximum spectral acceleration ($S_a$) at the top of the RWM was 1.48g at a period of 0.055 sec. However, when the wall was cushioned with the EPSB, this value decreased to 1.06g. In the backfill, the spectral accelerations during the same period of 0.22 sec were 1.26g for the control case and 1.43g for the cushioned case (EPSB20-8cm).

Figure 4.124 presents the displacement time history for both the control and cushioned cases under the scaled 1940 Imperial Valley EQ-El Centro Station record. The maximum displacement was measured as 1.93 cm for the cushioned case and 1.88 cm for the control case.

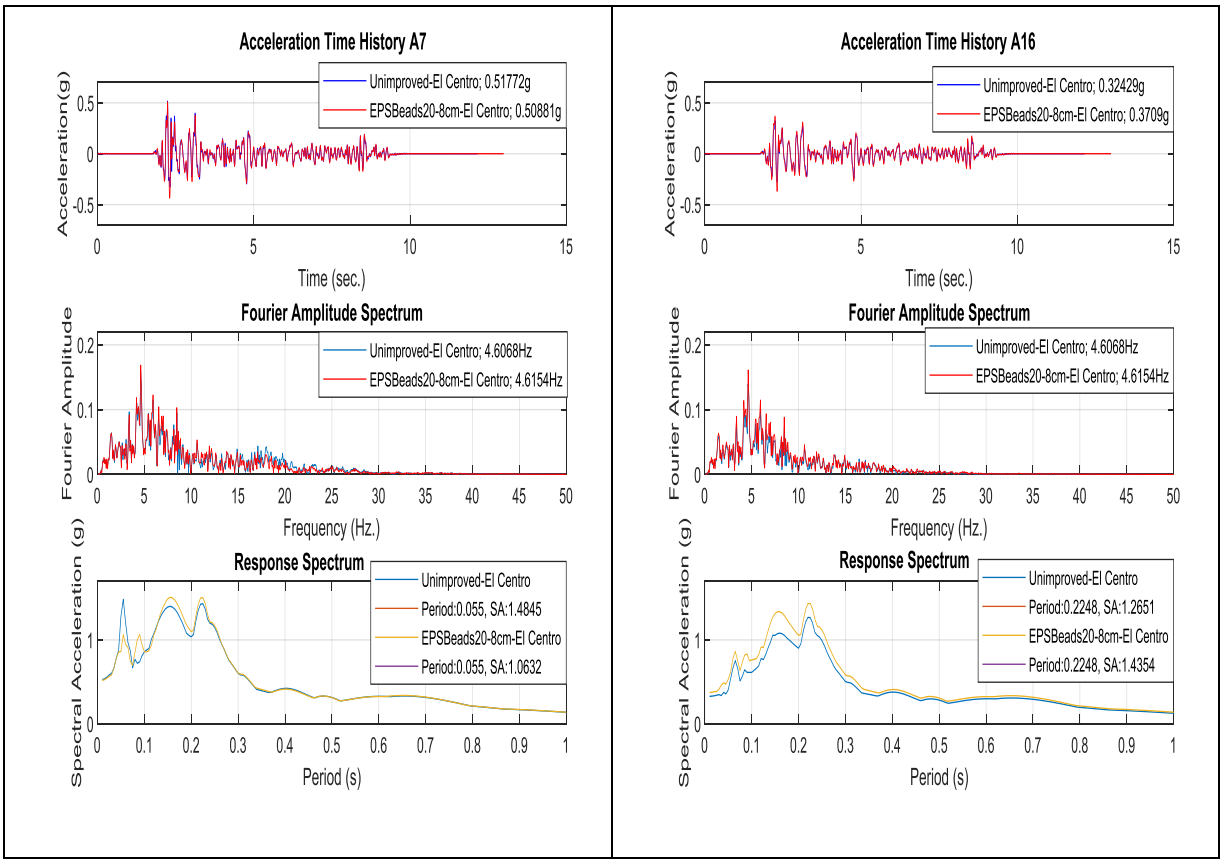


Figure 4.123. The ACCTH, FAS, Response Spectrum at the top of the RWM (A7) and in the backfill (A16) for Case 21 compared to Case 1 under the scaled 1940 Imperial Valley EQ-El Centro Station record (NF).

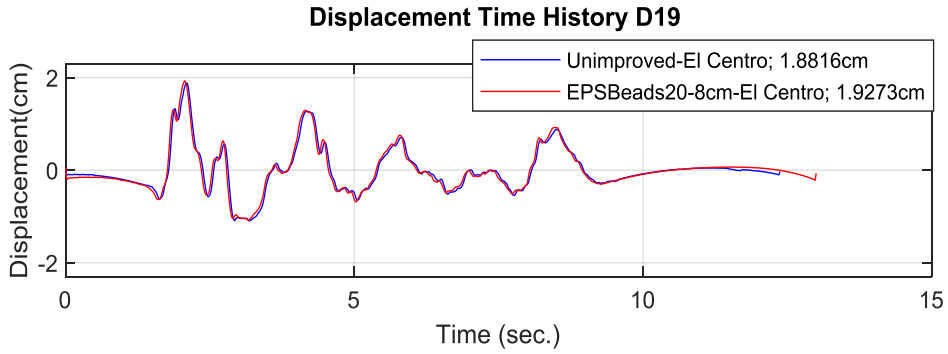


Figure 4.124. The DISTH at the top of the RWM (D19) for Case 21 compared to Case 1 under the scaled 1940 Imperial Valley EQ-El Centro Station record (NF).

Figure 4.125 illustrates the Acceleration-Time Histories, Fourier Amplitude Spectrums, and Response Spectrums when subjected to sinusoidal motion at 8 Hz and 0.4g. The cushioned case, which involved using an EPSB20-8cm cushion, resulted in a lower maximum acceleration of 0.45g at the top of the RWM compared to the control case as 0.47g. The A16 measured a maximum acceleration of 0.44g for the cushioned case, whereas the control case only measured 0.36g. The cushioned and control cases showed Fourier amplitudes peak at 8.02 Hz at the top of the RWM and in the backfill. According to the maximum spectral accelerations, it can be observed that at a period of 0.12 sec, the $S_a$ decreased from 4.7g to 4.45g at the top of the RWM, while it increased from 3.60g to 4.36g in the backfill for the control case and the cushioned case, respectively.

Figure 4.126 displays the displacement time history for both the control and cushioned cases under sinusoidal motion at 8 Hz and 0.4g. In the cushioned case, the maximum displacement was 0.15 cm, whereas it was 0.20 cm for the control case.

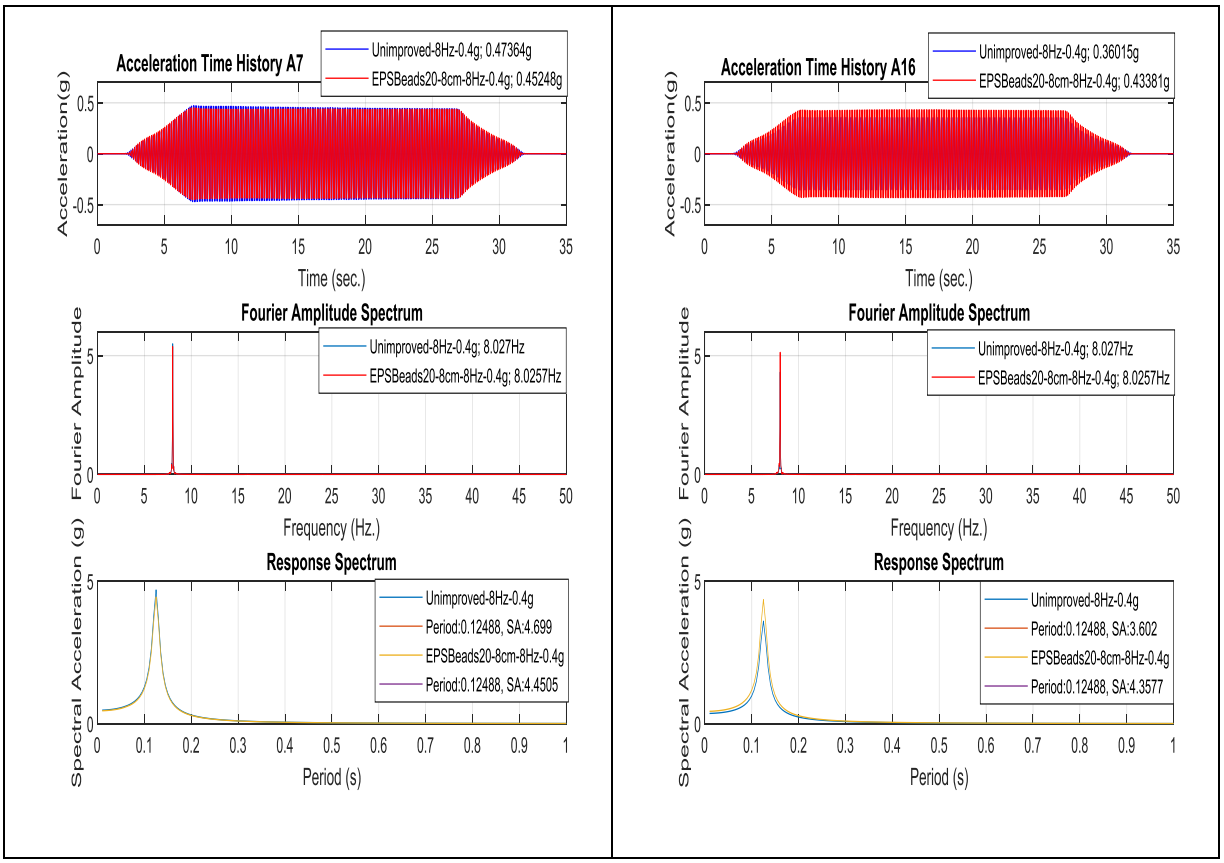


Figure 4.125. The ACCTH, FAS, Response Spectrum at the top of the RWM (A7) and in the backfill (A16) for Case 21 compared to Case 1 under sinusoidal motion at 0.4g amplitude with 8 Hz frequency.

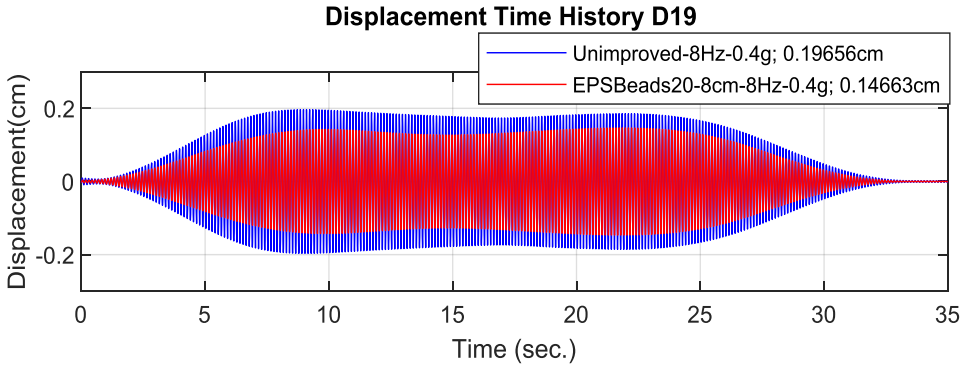


Figure 4.126. The DISTH at the top of the RWM (D19) for Case 21 compared to Case 1 under sinusoidal motion at 0.4g amplitude with 8 Hz frequency.

## 4.22. Results of Case 22 - EPSB30-8cm

In this study, Case 22 consists of EPS beads and sand mixture cushion with a 30% mixture ratio and 8 cm thickness (EPSB30-8cm) behind the RWM. Figures 4.127, 4.128, 4.129, 4.130, 4.131, and 4.132 show the results for two different earthquake motions and one sinusoidal motion as measured by accelerometer A7, laser displacement sensor D19 at the top of the retaining wall model (RWM) and accelerometer A16 in the backfill in comparison to the control case.

Figure 4.127 illustrates the Acceleration-Time Histories, Fourier Amplitude Spectrums, and Response Spectrums under the scaled 2020 İzmir EQ Motion-Kuşadası Station excitations for Case 22 in comparison with the control case Case 1. It was measured maximum acceleration values as 0.27g and 0.29g at the top of the RWM, and 0.19g and 0.24g in the backfill for the control case and Case 22, respectively. The Fourier amplitudes for the control case and cushioned case were 9.26 Hz and 7.33 Hz at the top of the RWM and in the backfill. The maximum spectral accelerations were at 0.05 sec and 0.13 sec period ranges. In comparison of the control case and cushioned cases, the maximum spectral acceleration ($S_a$) values were 0.98g and 0.96g at the top of the RWM at period of 0.06 sec and 0.75g and 0.86g in the backfill at period of 0.11 sec for the cushioned case compared to the control case, respectively.

Figure 4.128 shows that, when subjected to the dynamic motions of the scaled 2020 İzmir EQ Motion-Kuşadası Station, the control case displaced a maximum of 0.37 cm compared to 0.36cm for the cushioned model EPSB30-8cm.

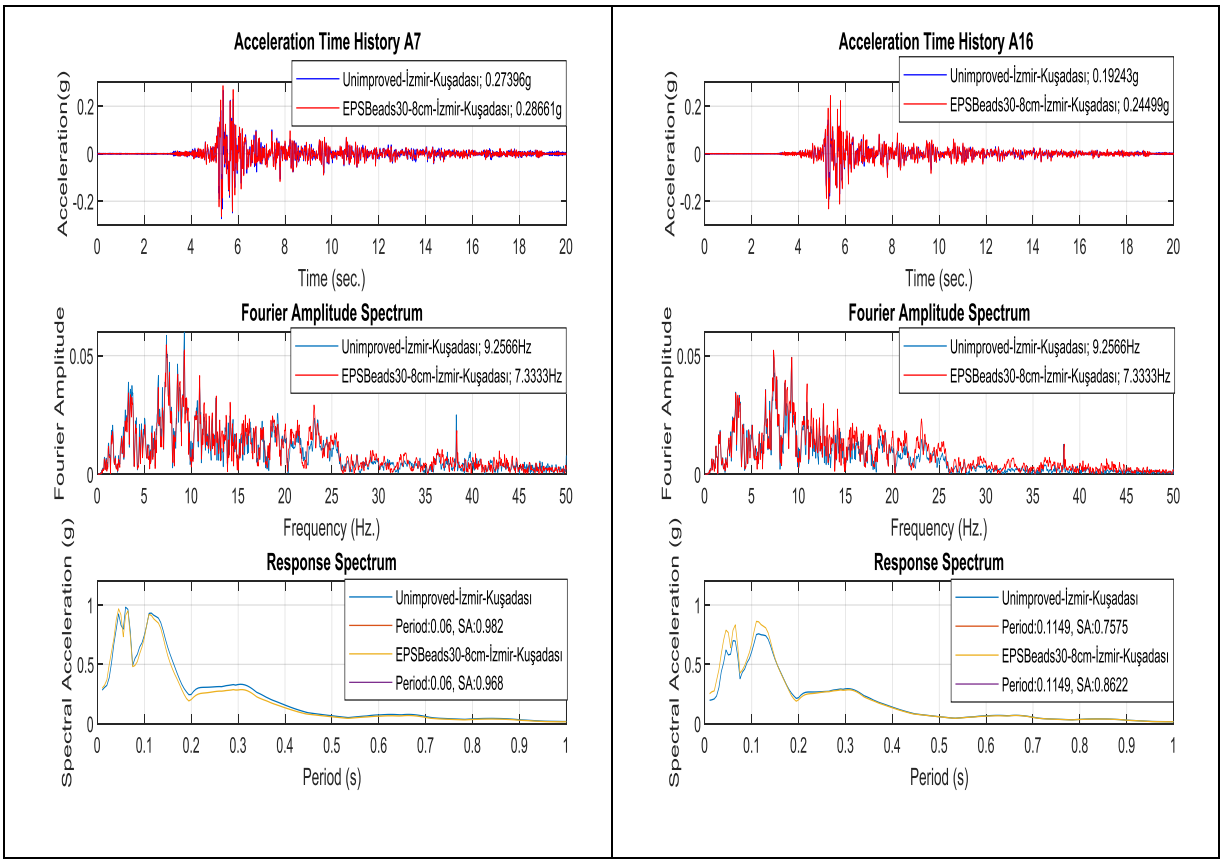


Figure 4.127. The ACCTH, FAS, Response Spectrum at the top of the RWM (A7) and in the backfill (A16) for Case 22 compared to Case 1 under the scaled 2020 İzmir EQ Motion-Kuşadası Station record (FF).

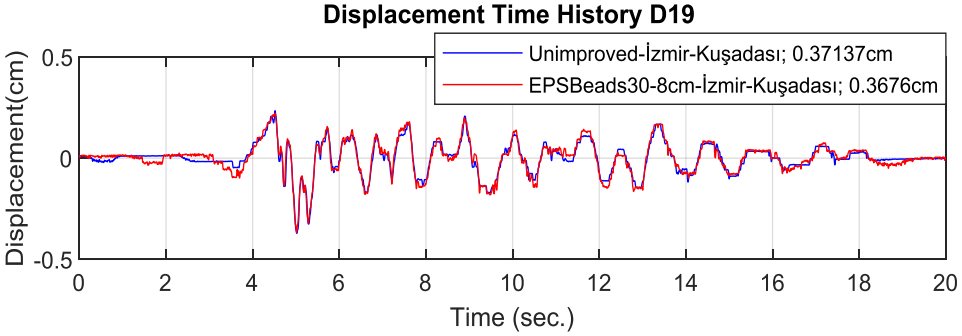


Figure 4.128. The DISTH at the top of the RWM (D19) for Case 22 compared to Case 1 under the scaled 2020 İzmir EQ Motion-Kuşadası Station record (FF).

The Acceleration-Time Histories, Fourier Amplitude Spectrums, and Response Spectrums are illustrated in Figure 4.129 under the scaled 1940 Imperial Valley EQ-El Centro Station record. It was measured 0.52g maximum acceleration for the control case at the top of the RWM decreased to 0.48g maximum acceleration for the EPSB30-8cm cushioned case. The A16 measured 0.32g maximum acceleration for the control case and 0.41g for the cushioned case. It can be noticed that the maximum accelerations decreased at the top of the RWM when the EPSB30-8cm cushion was implemented. Fourier amplitudes peaked around 4.60 Hz at the top of the RWM and in the backfill for the control and cushioned cases. The maximum spectral accelerations were at 0.05 sec and 0.22 sec period ranges for the cushioned and control cases. The maximum spectral accelerations ($S_a$) were 1.48g at 0.055 sec period at the top of the RWM for the control case, decreasing to 1.28g for the EPSB30-8cm cushioned case. The spectral accelerations in the backfill were 1.26g and 1.40g at the same periods 0.22 sec for the control case and EPSB30-8cm cushioned cases, respectively.

Figure 4.130 presents the displacement time history of the control case compared to the cushioned case under the scaled 1940 Imperial Valley EQ-El Centro Station record. The maximum displacement of the EPSB30-8cm cushioned model was measured as 1.87 cm, while the control case was measured as 1.88 cm at the top of the RWM.

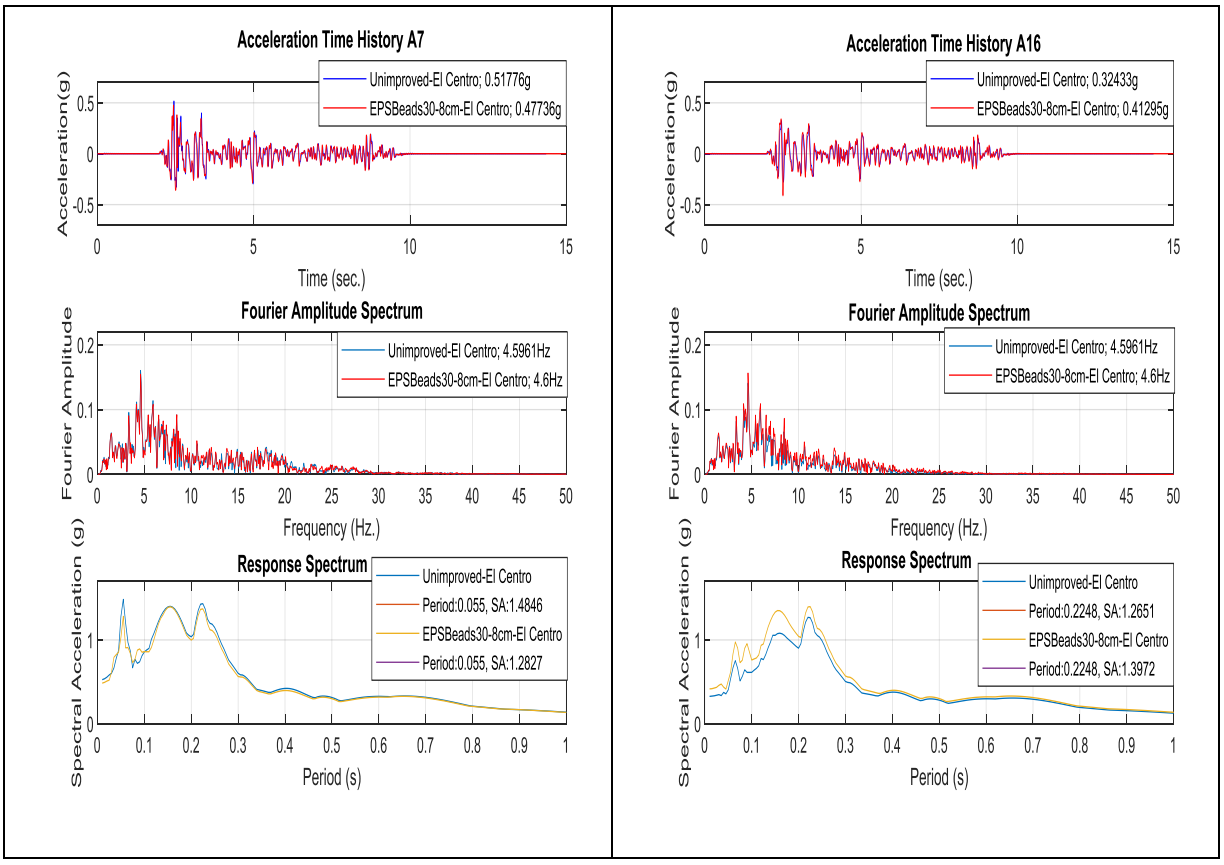


Figure 4.129. The ACCTH, FAS, Response Spectrum at the top of the RWM (A7) and in the backfill (A16) for Case 22 compared to Case 1 under the scaled 1940 Imperial Valley EQ-El Centro Station record (NF).

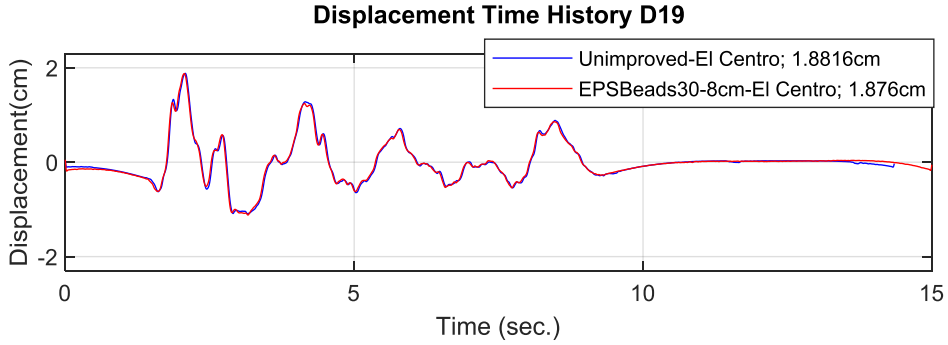


Figure 4.130. The DISTH at the top of the RWM (D19) for Case 22 compared to Case 1 under the scaled 1940 Imperial Valley EQ-El Centro Station record (NF).

The Acceleration-Time Histories, Fourier Amplitude Spectrums, and Response Spectrums under the sinusoidal motion at 0.4g amplitude with 8 Hz frequency are shown in Figure 4.131. It was measured 0.45g maximum acceleration at the top of the RWM for the EPSB30-8cm cushioned model as 0.47g. The A16 measured 0.48g maximum acceleration for the cushioned case compared to the control case 0.36g. For both the cushioned case and the control case the Fourier amplitudes peaked at 8.02 Hz at the top of the RWM and in the backfill. The maximum spectral accelerations ($S_a$) were at 0.12 sec period, decreasing from 4.7g to 4.41g measured from A7 and increasing from 3.60g to 4.92g in the backfill measured from A16 for the control case and cushioned cases, respectively.

Figure 4.132 presents the displacement time history of the control case compared to the cushioned case under sinusoidal motion at 0.4g amplitude with 8 Hz frequency. Maximum displacement was measured as 0.18 cm at the top of the RWM for the cushioned case, whereas it was measured as 0.20 cm for the control case.

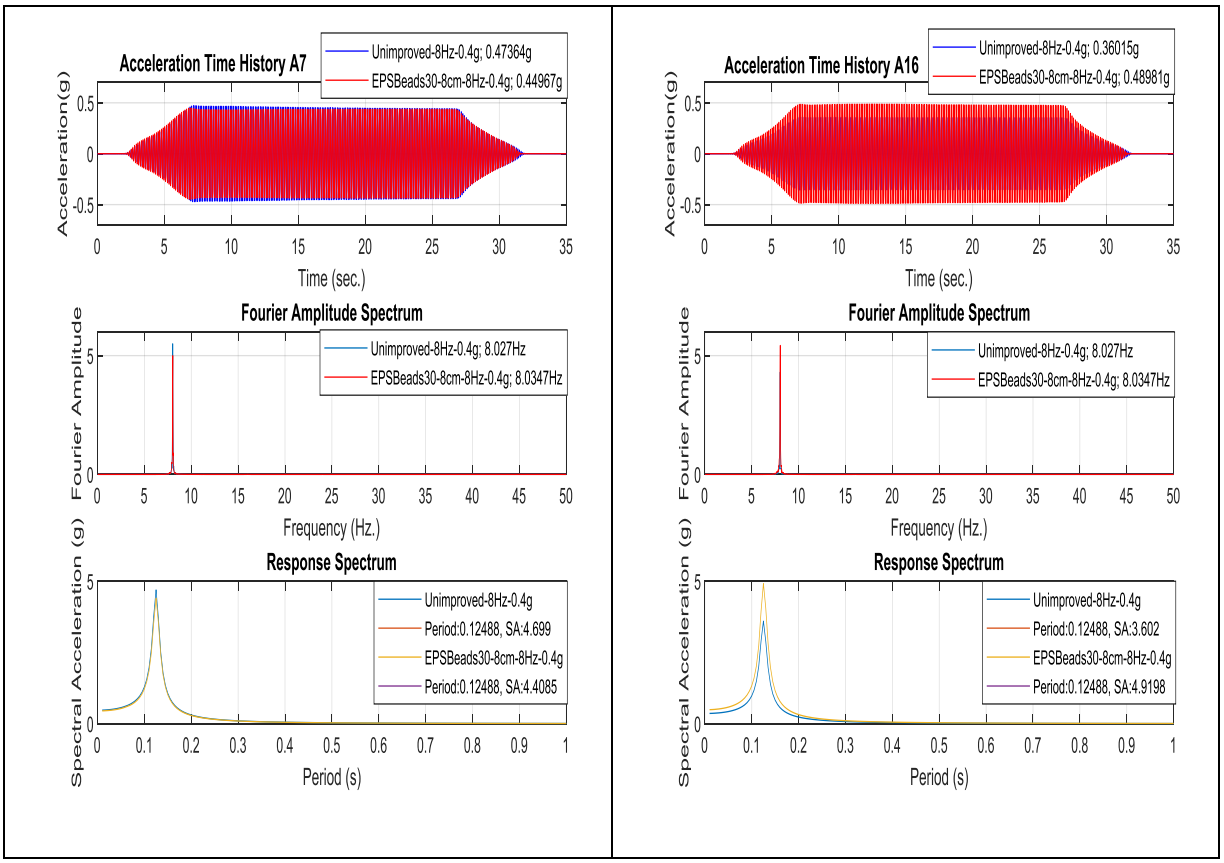


Figure 4.131. The ACCTH, FAS, Response Spectrum at the top of the RWM (A7) and in the backfill (A16) for Case 22 compared to Case 1 under sinusoidal motion at 0.4g amplitude with 8 Hz frequency.

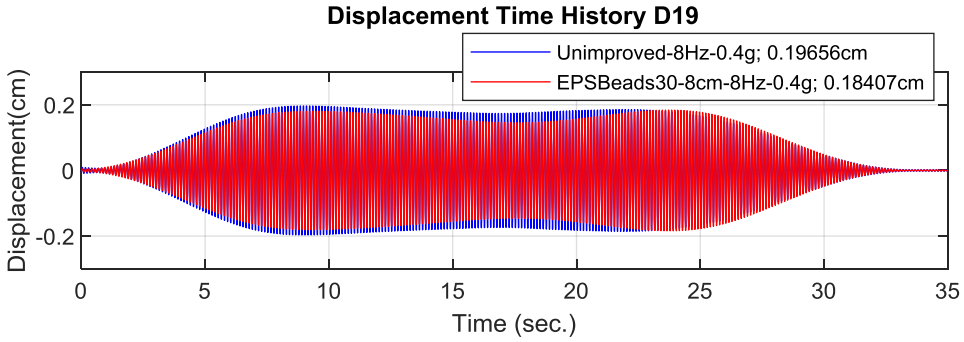


Figure 4.132. The DISTH at the top of the RWM (D19) for Case 22 compared to Case 1 under sinusoidal motion at 0.4g amplitude with 8 Hz frequency.

# 5. DISCUSSION

The main aim of this study is to assess the effectiveness and efficiency of a firstly proposed cushion layer for retaining structures. This cushion layer is composed of a mixture of EPS beads and sand, and the study examines the impact of thickness, mixture ratio, and input motion on its performance. Additionally, the study compares the performance of EPS beads and sand cushions (EPSB) with the performance of two cushion materials as EPS geofoam and tire waste and sand mixture (TW) under the same input motions. To investigate the methods for improving retaining walls, experiments were conducted on a shake table in a laminar box, and three different types of cushion materials were placed respectively behind the 1/15 scaled retaining wall model.

This chapter of the study covers the discussion of the shake table experimental study findings, which include changes in the density and thickness of the EPS geofoam cushion, tire waste and sand mixture cushion, as well as the EPS beads and sand mixture cushions under the same input motions. The effectivenesses of the cushions is discussed in terms of maximum accelerations, maximum lateral displacements, and maximum spectral accelerations under the given far field, near field, and sinusoidal input motions.

The effectiveness of the cushion type in reducing the acceleration response at the retaining wall model can be quantitatively measured using the improvement efficiency. The improvement efficiencies are calculated by comparing the cushioned cases with the control case. This is an important tool in studying the impact of cushions on retaining structures. The improvement efficiency provides a measure of the variation in maximum accelerations on retaining walls by cushions. Therefore, detailed comparisons of the experimental study are evaluated to understand the effectiveness of the cushions. The improvement efficiency percentage increase is indicated by positive values as improving the seismic performance of the RWM, while negative values indicate a percentage decrease.

The improvement efficiency (%) is calculated as:

$$Improvement\ Efficiency\ (\%) = \left(1 - \left(\frac{Maximum\ Acceleration\ of\ the\ Case\ n}{Maximum\ Acceleration\ of\ Case\ 1}\right)\right) * 100 \qquad (5.1)$$

where Case 1 is the control case, Case n is the cushioned case, and "n" is the case number.

## 5.1. The Effects of EPS Geofoam Cushion on the Seismic Performance of the Retaining Wall Model

The effects of thickness and density concerning improvement efficiency and spectral acceleration, the effects of acceleration response, and the comparison of maximum lateral displacements at the top of the RWM under the given near field and far field earthquake and sinusoidal motions are evaluated for EPS geofoam cushion in this part of the study.

### 5.1.1. The Effects of Thickness and Density of EPS Geofoam Cushion

The experimental studies of the cushion type EPS geofoam are conducted for for three different densities as 0.10 kN/m$^3$ (EPS10), 0.20 kN/m$^3$ (EPS20) and 0.30 kN/m$^3$ (EPS30) with two different thicknesses, 4cm and 8cm, regarding 0.10 and 0.20 t/H ratios, respectively. These cases are listed from Case 2 to Case 7, as explained in Table 3.11 in Chapter 3. Each of these cases was compared with the control case (unimproved case) of Case 1, and the improvement efficiency was calculated for each.

In this part of the study, the results of improvement efficiency (%) for each cushion thickness ratio (t/H) and density under all input motions are given. The influence of density, thickness, and input excitation on seismic performance of the EPS geofoam cushioned RWM are also investigated based on the improvement efficiencies and spectral accelerations in comparison to Case 1. The EPS geofoam cushioned cases, Cases 2 to Case 7, with comparisons to Case 1, have been reported under the given input motions.

5.1.1.1. Comparison of Improvement Efficiency under Far Field and Near Field Earthquake Motions

The improvement efficiency at the top of the RWM with respect to cushion thickness ratio and EPS geofoam density of the EPS Geofoam cushioned cases compared to the control case under far field and near field earthquakes is discussed by evaluating Figure 5.1.

The improvement efficiency under the scaled 1999 Kocaeli EQ Motion-İznik Station record is represented in Figure 5.1.a. Evaluation of the results indicates that the improvement efficiency for the EPS geofoam cushioned case was limited to 3% for the EPS10-4cm. Acceleration reduction was not observed for the rest of the EPS geofoam densities and the cushion thickness ratios. In this case, the results were obtained under the far field earthquake record at a frequency of 2.6 Hz and an amplitude of 0.12g.

Figure 5.1.b shows the improvement efficiency under the scaled 2014 Gökçeada EQ Motion-Çanakkale Station record. Evaluation of the shake table results shows that the improvement efficiency for the EPS geofoam cushioned case was 18% when the EPS30-8cm was used. For the EPS geofoam densities and the cushion thickness ratios, improvement efficiency ranged between 5% and 12%. The results were obtained under the far field earthquake record at 3.2 Hz predominant frequency 0.14g amplitude.

The improvement efficiency under the scaled 2020 İzmir EQ Motion-Kuşadası Station record is represented in Figure 5.1.c. The obtained results show that the improvement efficiency for the EPS geofoam cushioned case was up to 28% when the EPS20-8cm was used. For the rest of the EPS geofoam cushioned cases, maximum improvement efficiency ranged between 12% and 20%. This behaviour is a direct result of the input motion characteristic under the far field earthquake record at 24.4 Hz predominant frequency 0.18g amplitude in this case.

Under the scaled 1999 Kocaeli EQ Motion-İzmit Station record, the improvement efficiency is represented in Figure 5.1.d. Obtained results show that the improvement efficiency for the EPS geofoam cushioned case was up to 10% when the EPS10 was used with

the cushion thickness ratio of 0.2. For the rest of the EPS geofoam densities and the cushion thickness ratios, improvement efficiency was slightly observed, ranging between 2% and 5%. In this case, the results were obtained from the near field earthquake record with a frequency of 13 Hz and an amplitude of 0.22g.

The improvement efficiency under the scaled 1940 Imperial Valley EQ-El Centro Station record is represented in Figure 5.1.e. The maximum improvement efficiency was obtained to be around 23% for EPS20 with a cushion thickness ratio of 0.1. For the rest of the EPS geofoam densities and the cushion thickness ratios, improvement efficiency was clearly observed, ranging between 6% and 21%. The results were obtained under the near field earthquake record at 6 Hz frequency, 0.32g amplitude in this case.

Under the scaled 1995 Kobe EQ record, the improvement efficiency is represented in Figure 5.1.f. The obtained results showed that the improvement efficiency for the EPS Geofoam case was up to 30% when EPS20 was used with the cushion thickness ratio of 0.1. For the rest of the EPS geofoam densities and the cushion thickness ratios, improvement efficiency was clearly observed, ranging between 6% and 23%. There was no clear influence of cushion thickness over height ratio (t/H) on the improvement efficiencies of EPS geofoam cushioned cases. This behaviour is a direct result of the input motion characteristic under the near field earthquake record at 5.7 Hz frequency, 0.82g amplitude in this case.

The general evaluation of the results based on improvement efficiency at the top of the RWM for the EPS Geofoam cushioned cases under far field and near field earthquakes are given in the following explanations:

- In consideration of the scaled real earthquakes executed, the cushioned model EPS20-4cm provides significant improvement compared to the control model in reducing maximum acceleration under the scaled 1940 Imperial Valley EQ-El Centro Station record and the scaled 1995 Kobe EQ record (Figure 5.1.e-f). On the other hand, the improvement efficiency is limited to 3% under the scaled 1999 Kocaeli EQ Motion-İznik Station record (Figure 5.1.a). The evaluation of the results clearly shows that the

EPS geofoam type demonstrates improvement for most of the cushion thicknesses and mixture ratios of this study.

- At maximum acceleration amplitudes greater than 0.3g for the near field earthquakes, the EPS geofoam can be supposed as a promising solution to improve the seismic performance of retaining walls. This result can be interpreted as the high amplitude effect under the near field earthquakes. In the evaluation of the far field earthquakes, the maximum improvement efficiency was obtained as 28% under the scaled 2020 İzmir EQ Motion-Kuşadası Station record (Figure 5.1.c). This finding demonstrates the effectiveness of the EPS geofoam cushioned model under high-frequency input motion, which is regarded as a far field earthquake record with a predominant frequency of 24.4Hz.

- Increasing cushion thickness positively affects the calculated improvement efficiencies for most of the EPS geofoam cases. As represented in Figure 5.1, improvement efficiencies show an increasing trend for some of the cases with respect to cushion thickness.

- Considering various EPS geofoam densities, the effect of EPS geofoam density on the calculated improvement efficiency results highly depends on the applied dynamic motion. As shown in Figure 5.1, the maximum improvement efficiencies are generally calculated for the EPS20 cases.

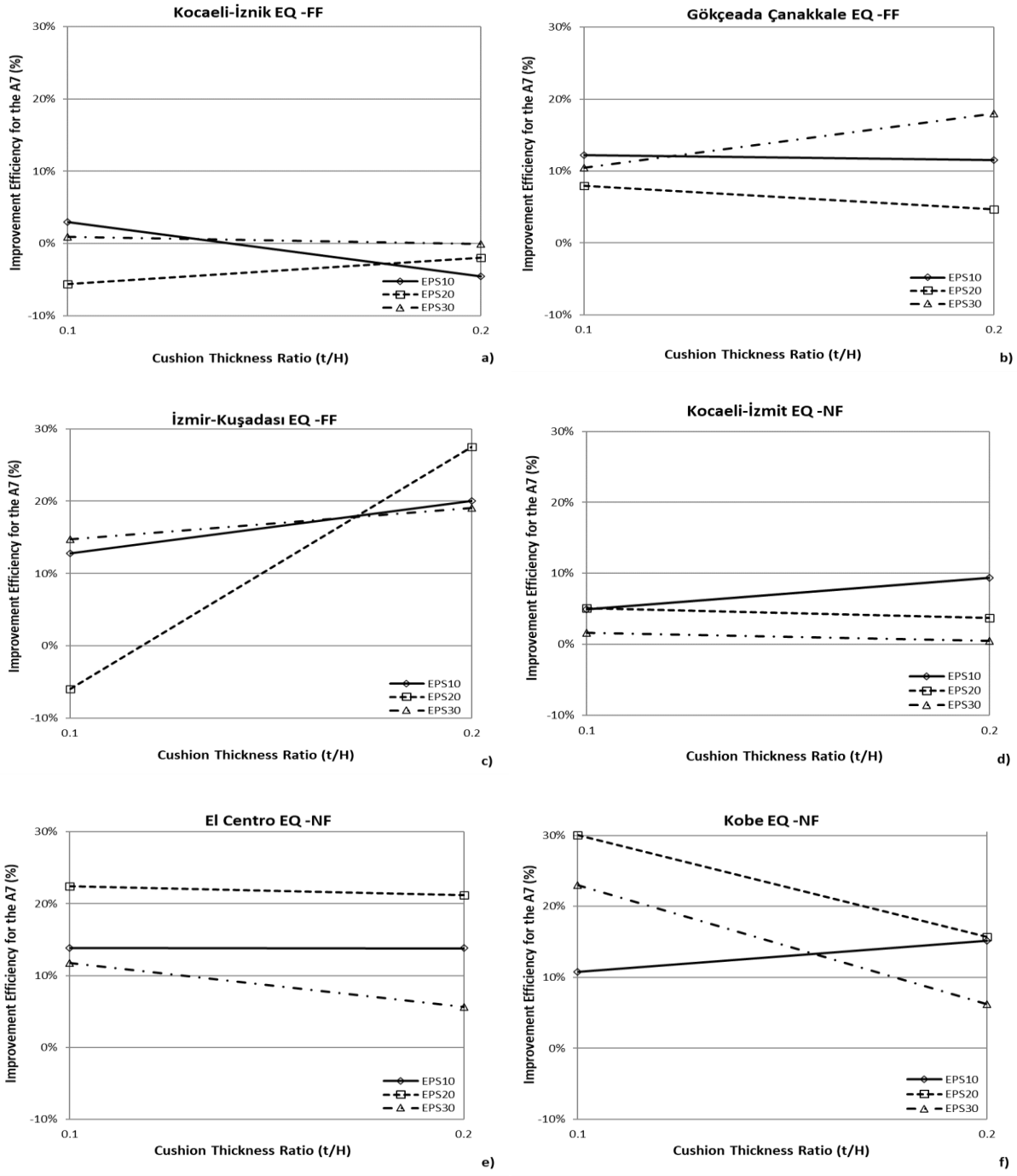


Figure 5.1. Improvement efficiencies for all EPS Geofoam cushioned cases with respect to A7 under a) the scaled 1999 Kocaeli EQ Motion-İznik Station Record-FF, b) the scaled 2014 Gökçeada EQ Motion-Çanakkale Station Record-FF, c) the scaled 2020 İzmir EQ Motion-Kuşadası Station Record-FF, d) the scaled 1999 Kocaeli EQ Motion-İzmit Station Record-NF, e) the scaled 1940 Imperial Valley EQ-El Centro Station record-NF, f) the scaled 1995 Kobe EQ Record-NF.

5.1.1.2. Comparison of Maximum Spectral Accelerations under Far Field and Near Field Earthquake Motions

The response spectrums at the top of the RWM with respect to cushion thickness ratio and EPS geofoam density of the EPS Geofoam cushioned cases compared to the control case under far field earthquakes are discussed by evaluating Figure 5.2.

The response spectrums for the EPS10, EPS20, and EPS30 cases with cushion thicknesses of 4 cm and 8 cm and the control case under the scaled 1999 Kocaeli EQ Motion-İznik Station record are shown in Figure 5.2.a, 5.2.b, and 5.2.c, respectively. At a period of 0.12 seconds, the maximum $S_a$ values increased from 0.39g to 0.44g and 0.43g for EPS10-4cm (Case 2) and EPS10-8cm (Case 5) cushioned cases, respectively, and from 0.39g to 0.49g and 0.44g for EPS20-4cm (Case 3) and EPS20-8cm (Case 6) cushioned cases, respectively, and from 0.39g to 0.49g and 0.48g for EPS30-4cm (Case 4) and EPS30-8cm (Case 7) cushioned cases, respectively. At a period of 0.30 seconds, the maximum $S_a$ values increased from 0.42g to 0.43g and 0.44g for EPS10-4cm (Case 2) and EPS10-8cm (Case 5) cushioned cases, respectively, and from 0.42g to 0.45g and 0.44g for EPS20-4cm (Case 3) and EPS20-8cm (Case 6) cushioned cases, respectively, and from 0.42g to 0.45g and 0.44g for EPS30-4cm (Case 4) and EPS30-8cm (Case 7) cushioned cases, respectively.

The response spectrums for the EPS10, EPS20, and EPS30 cases with cushion thicknesses of 4 cm and 8 cm and the control case under the scaled 2014 Gökçeada EQ Motion-Çanakkale Station record are given in Figures 5.2.d, 5.2.e, and 5.2.f. The figures show the maximum spectral accelerations ($S_a$) evaluated at two different periods for the control case and cushioned cases with EPS10, EPS20, and EPS30 for 4 cm and 8 cm thicknesses. The results indicate that the maximum $S_a$ values decreased for all cushioned cases at a period of 0.11 seconds, the maximum $S_a$ values decreased from 0.67g to 0.64g and 0.63g for EPS10-4cm (Case 2) and EPS10-8cm (Case 5), respectively. At a period of 0.22 seconds, the maximum $S_a$ values decreased from 0.52g to 0.47g and 0.50g for EPS10-4cm (Case 2) and EPS10-8cm (Case 5), respectively. Similarly, for EPS20 and EPS30 cushioned cases, the maximum $S_a$ values decreased at both periods.

The response spectrums for the EPS10, EPS20, and EPS30 cases with cushion thicknesses of 4 cm and 8 cm, and the control case under the scaled 2020 İzmir EQ Motion-Kuşadası Station record are shown in Figures 5.2.g, 5.2.h, and 5.2.i. In Figure 5.2.g, the maximum $S_a$ values decreased at periods of 0.06 seconds and 0.11 seconds for the EPS10 cushioned cases. In Figure 5.2.h, the maximum $S_a$ values changed at periods of 0.06 seconds and 0.11 seconds for the EPS20 cushioned cases. In Figure 5.2.i, the maximum $S_a$ values decreased at periods of 0.06 seconds and 0.11 seconds for the EPS30 cushioned cases.

The general evaluation of results with respect to maximum spectral accelerations at the top of the RWM for the EPS Geofoam cushioned cases under far field earthquakes are given in the following:

- The response spectrum analysis shows that EPS geofoam cushioned cases can reduce the maximum $S_a$ values, depending on the thickness of the EPS geofoam cushion and the input motion. The maximum spectral accelerations increased more in the 0.05-0.15 sec period range under the scaled 1999 Kocaeli EQ Motion-İznik Station record, while there was less increase in the 0.25-0.35 sec period range. Under the scaled 2014 Gökçeada EQ Motion-Çanakkale Station record, the spectral acceleration in the 0.05-0.15 sec period range decreased by 10% for EPS10-4cm (Case 2) and EPS30-8cm (Case 7) and in the 0.25-0.35 sec period range, it decreased by a maximum of 15% for EPS20-4cm (Case 3) and EPS30-8cm. The maximum spectral acceleration in the 0.05-0.10 sec period range decreased by a maximum of 38% for EPS20-8cm (Case 6), and in the 0.10-0.15 sec period range, it decreased by a maximum of 28% for EPS30-8cm. The decrease in maximum spectral acceleration continued up to the 0.5 sec period under the scaled 2020 İzmir EQ Motion-Kuşadası Station record. Considering the far field earthquakes, it is clear that the period interval is important since higher frequencies within the 10 Hz to 20 Hz range have a significant impact on reducing the spectral acceleration.

- Thickness ratio was observed to be more effective in the period range of 0.05-0-15 sec, while it was observed to be less effective in the period range of 0.25-0.35 sec under the far field earthquakes as the scaled 1999 Kocaeli EQ Motion-İznik Station record and the scaled 2014 Gökçeada EQ Motion-Çanakkale Station record. The scaled 2020 İzmir EQ Motion-Kuşadası Station record having earthquake characteristics with 24.4 Hz predominant frequency 0.18g amplitude shows a reduction in maximum spectral accelerations most clearly due to cushion thickness ratio showing the maximum reduction as 38% for 8 cm thickness. Increasing cushion thickness positively affects the calculated spectral accelerations for most of the EPS geofoam cases. As represented in Figure 5.2, maximum spectral accelerations generally decreased with respect to the increase in cushion thickness.

- The effect of EPS geofoam density on the maximum spectral acceleration results highly depends on the applied dynamic motion. In general, the EPS20 density has the maximum decrease in spectral accelerations observed in the study under the far field earthquakes.

- A detailed evaluation of the results indicates that the EPS geofoam as a cushion type generally exhibits improvement in spectral accelerations for all cushion thicknesses and mixture ratios examined in this study under far field earthquakes, as given in Figure 5.2. In consideration of the scaled earthquakes executed, the study shows that the EPS30-8cm provides a significant improvement compared to the control model in reducing maximum spectral accelerations under the scaled 2020 İzmir EQ Motion-Kuşadası Station record with 38% reduction (Figure 5.2.g-h-i). The results show that the EPS geofoam cushion can reduce the maximum $S_a$ values at given periods, which could improve the seismic performance of the retaining wall. On the other hand, the improvement efficiency is limited to 10% under the scaled 2014 Gökçeada EQ Motion-Çanakkale Station record (Figure 5.2.d-e-f).

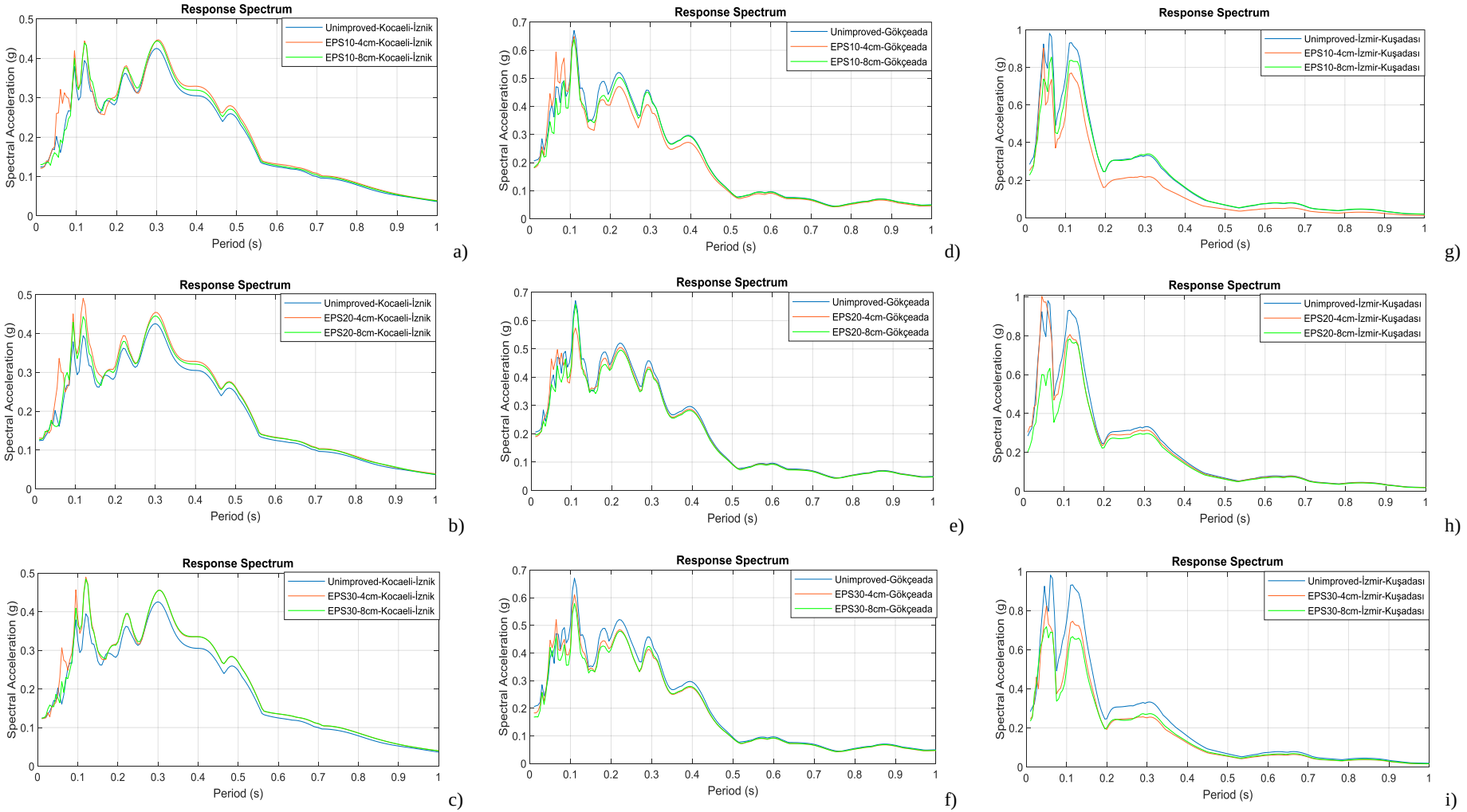


Figure 5.2 Response Spectrums of all EPS Geofoam cushioned cases with respect to A7 under a-b-c) the scaled 1999 Kocaeli EQ Motion-İznik Station Record-FF, d-e-f) the scaled 2014 Gökçeada EQ Motion-Çanakkale Station Record-FF, g-h-i) the scaled 2020 İzmir EQ Motion-Kuşadası Station Record-FF.

The response spectrums at the top of the RWM with respect to cushion thickness ratio and EPS geofoam density of the EPS Geofoam cushioned cases compared to the control case under near field earthquakes are discussed by evaluating Figure 5.3.

The response spectrums for EPS geofoam cushioned cases and the control case under the scaled 1999 Kocaeli EQ Motion-İzmit Station record are shown in Figure 5.3.a, 5.3.b, 5.3.c. The maximum spectral accelerations ($S_a$) were evaluated at two different periods. At a period of 0.07 seconds, the maximum $S_a$ values decreased from 1.13g to 1.11g and 0.83g for EPS10-4cm and EPS10-8cm cushioned cases, respectively, and from 1.13g to 1.12g and 0.84g for EPS20-4cm and EPS20-8cm cushioned cases, respectively. For EPS30-4cm and EPS30-8cm cushioned cases, the maximum $S_a$ values decreased from 1.13g to 1.02g and 0.83g, respectively. At a period of 0.15 seconds, the maximum $S_a$ values decreased from 0.96g to 0.86g and 0.83g for EPS10-4cm and EPS10-8cm cushioned cases, respectively, and from 0.96g to 0.88g and 0.93g for EPS20-4cm and EPS20-8cm cushioned cases, respectively. For EPS30-4cm and EPS30-8cm cushioned cases, the maximum $S_a$ values decreased from 0.96g to 0.90g and 0.95g, respectively.

The response spectrums for EPS10, ESP20, EPS30 with thicknesses of 4 cm and 8 cm and the control case under the scaled 1940 Imperial Valley EQ-El Centro Station record are shown in Figures 5.3.d, 5.3.e, and 5.3.f. The maximum spectral accelerations ($S_a$) were evaluated at two different periods as 0.055 sec and 0.15 sec, and the maximum $S_a$ values decreased for the cushioned cases. At a period of 0.055 seconds, the maximum $S_a$ values decreased from 1.48g to 1.27g and 1.06g for EPS10-4cm and EPS10-8cm, respectively, and from 1.48g to 1.03g and 0.88g for EPS20-4cm and EPS20-8cm, respectively. Additionally, the maximum $S_a$ values decreased by lengthening the period from 0.055 sec to 0.065 sec for EPS10-8cm and from 0.055 sec to 0.070 sec for EPS20-4cm. The maximum $S_a$ values decreased for EPS30-4cm and EPS30-8cm at both periods.

The response spectrums for the EPS10, EPS20, and EPS30 cases with cushion thicknesses of 4 cm and 8 cm and the control case under the scaled 1995 Kobe EQ record are shown in Figures 5.3.g, 5.3.h, and 5.3.i. The maximum spectral accelerations ($S_a$) were

evaluated at two different periods. In Figure 5.3.g, at a period of 0.08 seconds, the maximum $S_a$ values decreased from 3.33g to 2.76g and 2.34g, and at a period of 0.25 seconds, the maximum $S_a$ values decreased from 2.29g to 2.11g and 1.87g for the EPS10-4cm (Case 2) and EPS10-8cm (Case 5) cushioned cases, respectively. In Figure 5.3.h, at a period of 0.08 seconds, the maximum $S_a$ values changed from 3.33g to 1.45g and 1.98g, and at a period of 0.25 seconds, the maximum $S_a$ values decreased from 2.29g to 1.77g and 2.18g for the EPS20-4cm (Case 3) and EPS20-8cm (Case 6) cushioned cases, respectively. In Figure 5.3.i, at a period of 0.08 seconds, the maximum $S_a$ values decreased from 3.33g to 2.90g and 2.61g, and at a period of 0.25 seconds, the maximum $S_a$ values decreased from 2.29g to 2.04g and 2.14g for the EPS30-4cm (Case 4) and EPS30-8cm (Case 7) cushioned cases, respectively.

Observed general results with respect to maximum spectral accelerations at the top of the RWM for the EPS Geofoam cushioned cases under near field earthquakes are given in the following:

- It was found that the maximum spectral accelerations decreased more in the 0.05-0.10 sec period range with maximum 27% reduction ratio for the cases EPS10-8cm, EPS20-8cm, EPS30-8cm, while there was less decrease in the 0.10-0.20 sec period range with maximum 14% reduction ratio for the case EPS10-8cm under the scaled 1999 Kocaeli EQ Motion-İzmit Station record. Under the scaled 1940 Imperial Valley EQ-El Centro Station record, the spectral acceleration in the 0.05-0.10 sec period range decreased by 40% for EPS20-8cm, and at that period range, the reduction ranged between 15%-40%, and in the 0.10-0.20 sec period range, it decreased by a maximum of 33% for EPS20-4cm. The maximum spectral acceleration in the 0.05-0.10 sec period range decreased by a maximum of 56% for EPS20-4cm, and in the 0.20-0.30 sec period range, it decreased by a maximum of 23% for EPS20-4cm under the scaled 1995 Kobe EQ record and the decrease in maximum $S_a$ continued up to the 0.4 sec period. The cushioned cases showed a decrease in maximum $S_a$ values, indicating that the use of EPS cushions can improve the seismic performance of the wall.

- Thickness ratio was observed to be more effective in decreasing the maximum spectral accelerations with increasing cushion thickness ratio in the period range of 0.05-0.10 sec, while it was observed to be less effective in the period range of 0.10-0.20 sec under the near field earthquakes as the scaled 1999 Kocaeli EQ Motion-İzmit Station record, the scaled 1940 Imperial Valley EQ-El Centro Station record and the scaled 1995 Kobe EQ record. Increasing cushion thickness positively affects the calculated spectral accelerations for most of the EPS geofoam cases. As represented in Figure 5.3, maximum spectral accelerations mostly decreased with respect to the increase of cushion thickness, cushion thickness ratio 0.2H.

- The effect of EPS geofoam density on the maximum spectral acceleration results is highly dependent on the applied dynamic motion. The effect of density was observed to be more effective in the period range of 0.05-0.10 sec with increasing density decreases the maximum spectral accelerations, while it was observed to be less effective in the period range of 0.10-0.20 sec under the near field earthquakes. In general, the EPS20 exhibits the maximum decrease in spectral accelerations observed in the study under the near field earthquakes.

- The EPS geofoam cushion generally exhibits improvement by reducing spectral accelerations across all cushion thicknesses and densities examined in this study under near field earthquakes. In consideration of the scaled real earthquakes executed, the study shows that the EPS20-4cm provides significant improvement compared to the control model in reducing maximum spectral accelerations in the 0.05-0.10 sec period range under the scaled 1995 Kobe EQ record with a 56% reduction (Figure 5.3.g-h-i).

- The period interval, which is effective in the period range of 0.05–0.10 sec, is an important factor in decreasing the maximum spectral accelerations under near field earthquakes. As opposed to the control case under the near field earthquakes, higher frequencies in the 10 Hz to 20 Hz range have been shown to reduce the spectrum accelerations significantly.

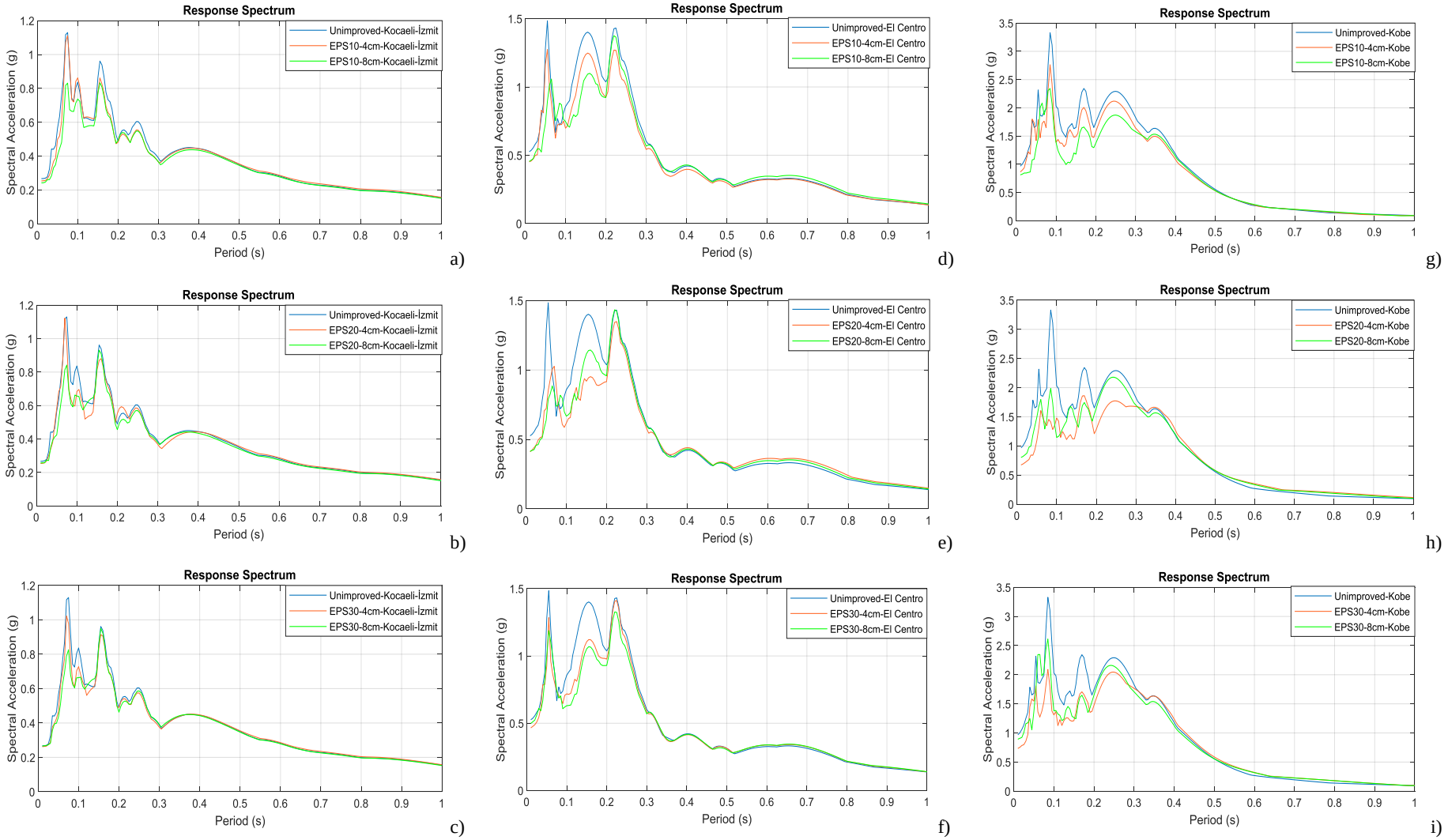


Figure 5.3 Response Spectrums of all EPS Geofoam cushioned cases with respect to A7 under a-b-c) the scaled 1999 Kocaeli EQ Motion-İzmit Station Record-NF, d-e-f) the scaled 1940 Imperial Valley EQ-El Centro Station record-NF, g-h-i) the scaled 1995 Kobe EQ Record-NF.

5.1.1.3. Comparison of Improvement Efficiency under Sinusoidal Motions

The improvement efficiency (%) at the top of the RWM with respect to cushion thickness ratio and EPS geofoam density of the EPS Geofoam cushioned cases compared to the control case under sinusoidal motions is discussed by evaluating Figure 5.4.

The improvement efficiency is given in Figure 5.4.a for all cases of EPS geofoam under sinusoidal motion at 0.3g amplitude with 8 Hz frequency. Evaluation for the cases of EPS geofoam in terms of changing cushion thickness and density indicated that the improvement efficiency of EPS geofoam cushioned case under the given dynamic motion was up to 42% when the EPS30 is used with the cushion thickness ratio of 0.2. For the rest of the cases, the EPS geofoam densities and the cushion thickness ratios maximum improvement efficiency ranged between 17% and 38%.

The improvement efficiencies under sinusoidal motion at 0.4g amplitude with 8 Hz frequency are represented in Figure 5.4.b. Evaluation of the shake table results showed that the improvement efficiency for the EPS geofoam cushioned case was 42% when the EPS30-8cm was used. For the EPS geofoam densities and the cushion thickness ratios, maximum improvement efficiency ranged between 12% and 39%.

The improvement efficiencies are given in Figure 5.4.c for all cases of EPS geofoam under sinusoidal motion at 0.5g amplitude with 8 Hz frequency. Due to the placement of the EPS30-8cm, the maximum decrease in transmitted accelerations at the top of the RWM was 41% under the given dynamic motion, whereas the reductions ranged between 15% and 40% for the other EPS geofoam cushioned cases.

Figure 5.4.d displays the improvement efficiency for all EPS geofoam cases under sinusoidal motion at 0.4g amplitude with 12 Hz frequency. The improvement efficiencies of EPS geofoam cushioned cases ranged from 9% to 42%, with the highest improvement efficiency when the EPS30-8cm was used.

Under the sinusoidal motion at 0.4g amplitude with 14 Hz frequency, the improvement efficiency is represented in Figure 5.4.e. The improvement efficiencies of the EPS geofoam cushioned cases varied from 1% to 28%. The best improvement efficiency for reducing seismic transmission of accelerations in the retaining wall was achieved when using EPS10 with a cushion thickness ratio of 0.2.

The general evaluation of results based on improvement efficiency at the top of the RWM for the EPS Geofoam cushioned cases under sinusoidal motions is given in the following:

- The study demonstrates that the EPS geofoam cushioned cases significantly decreased the maximum acceleration values under various sinusoidal excitations when compared to the control case. Consequently, this EPS geofoam cushioned model could be a good way to improve the seismic performance of retaining walls. In consideration of the sinusoidal motions executed, the study shows that the cushioned model EPS30-8cm provides significant improvement in reducing maximum accelerations up to 42% reduction under the sinusoidal motions range between 8 Hz and 12 Hz and the amplitude range between 0.3g and 0.5g. While 2-3 Hz are the typical main frequencies of medium-to-high frequency earthquakes, the sinusoidal motion frequencies of 8 Hz and 12 Hz of the 1/15 scaled model correspond to 2.1-3.1 Hz in the full-scale model. This result shows us that earthquake characteristics play an important role in the effectiveness of the improvement of retaining walls.

- Increasing cushion thickness positively affects the calculated improvement efficiencies for the EPS geofoam cushioned cases under all input sinusoidal motions. As represented in Figure 5.4, improvement efficiencies generally increase with respect to cushion thickness and may lead to seismic reduction. When the EPS geofoam cushion is placed behind the retaining wall, the maximum accelerations are lowered by around 10%–25% at excitation frequencies of 8 Hz and 12 Hz at a thickness of 4 cm (0.1H). This reduction increased to about 42% if the geofoam thickness is increased to 8 cm

(0.2H). Additionally, as the thickness of the EPS geofoam cushion increases, the acceleration recorded at the top of the RWM decreases for all input sinusoidal input motions. The best improvement results were observed for 8 cm thickness of EPS geofoam under these sinusoidal motions.

- The effect of EPS geofoam density on the calculated maximum improvement efficiency results is highly dependent on the applied dynamic motion. As shown in Figure 5.a-d, EPS geofoam density with 0.30 $kN/m^3$ shows significant acceleration reduction under sinusoidal motions frequency range between 8 Hz and 12 Hz and the amplitude range between 0.3g and 0.5g. This indicates that the increasing EPS geofoam density affects the improvement efficiencies positively.

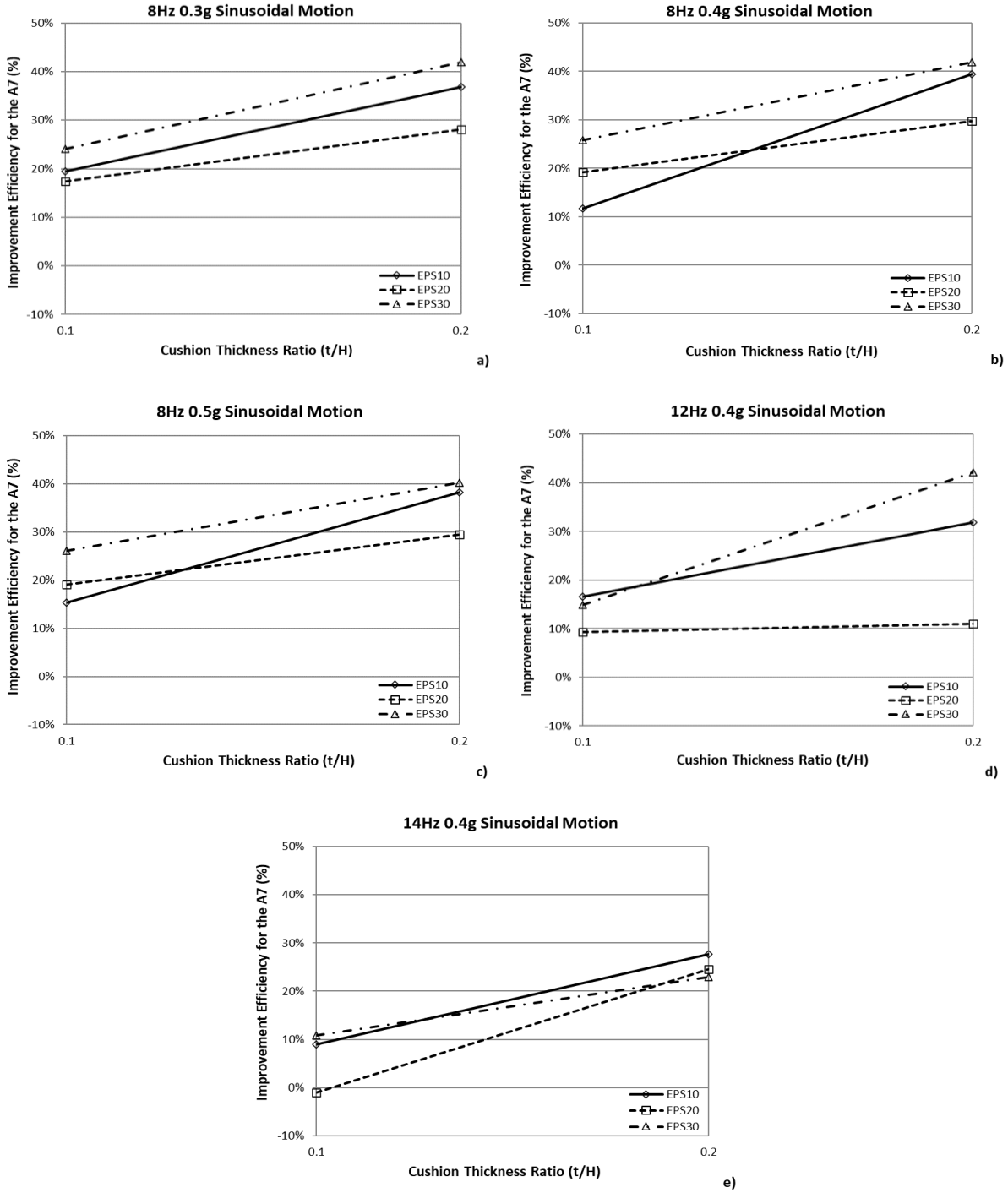


Figure 5.4. Improvement efficiencies for all EPS Geofoam cushioned cases with respect to A7 under a) sinusoidal motion at 0.3g amplitude with 8 Hz frequency, b) sinusoidal motion at 0.4g amplitude with 8 Hz frequency, c) sinusoidal motion at 0.5g amplitude with 8 Hz frequency, d) sinusoidal motion at 0.4g amplitude with 12 Hz frequency, e) sinusoidal motion at 0.4g amplitude with 14 Hz frequency.

5.1.1.4. Comparison of Maximum Spectral Accelerations under Sinusoidal Motions

The response spectrums at the top of the RWM with respect to the cushion thickness ratio and EPS geofoam density of the EPS Geofoam cushioned cases compared to the control case under sinusoidal motions are discussed by evaluating Figures 5.5 and 5.6.

The response spectrums for the EPS10, EPS20, and EPS30 cases with cushion thicknesses of 4 cm and 8 cm and the control case under sinusoidal motion at 0.3g amplitude with 8 Hz frequency are shown in Figure 5.5.a-c. The maximum spectral accelerations ($S_a$) occurred at a period of 0.125 sec and decreased for all cushioned cases. In Figure 5.5.a, the $S_a$ decreased from 3.49g to 2.82g and 2.24g for the EPS10-4cm and EPS10-8cm cases, respectively. In Figure 5.5.b, the $S_a$ decreased from 3.49g to 2.89g and 2.54g for the EPS20-4cm and EPS20-8cm cases, respectively. In Figure 5.5.c, the $S_a$ decreased from 3.49g to 2.67g and 2.04g for the EPS30-4cm and EPS30-8cm cases, respectively. The cushioned cases show a decrease in maximum $S_a$ with increasing cushion thickness, resulting in a higher decrease in $S_a$.

The response spectrums for the control case and for different cushion thicknesses (4 cm and 8 cm) and EPS densities (EPS10, EPS20, and EPS30) under sinusoidal motion at 0.4g amplitude with 8 Hz frequency are represented in Figures 5.5.d, 5.5.e, and 5.5.f. The maximum spectral accelerations ($S_a$) occurred at a period of 0.125 sec and decreased for all cushioned cases. The decrease in $S_a$ is more significant for higher EPS densities and thicknesses. In Figure 5.5.d, the $S_a$ decreased from 4.70g to 4.14g and 2.86g for the control case and EPS10-4cm and EPS10-8cm cushioned cases, respectively. Similarly, in Figure 5.5.e, the $S_a$ decreased from 4.70g to 3.84g and 3.31g for the control case and EPS20-4cm and EPS20-8cm cushioned cases, respectively. In Figure 5.5.f, the $S_a$ decreased from 4.70g to 3.49g and 2.72g for the control case and EPS30-4cm and EPS30-8cm cushioned cases, respectively.

The response spectrums for the EPS10, EPS20, and EPS30 cases with cushion thicknesses of 4 cm and 8 cm and the control case under sinusoidal motion at 0.5g amplitude with 8 Hz frequency are shown in Figure 5.5.g-i. These figures compare the EPS10, EPS20,

and EPS30 with thicknesses of 4 cm and 8 cm to the control case. The maximum spectral accelerations ($S_a$) occurred at a period of 0.125 sec and decreased as the thickness of the cushioning material increased. In Figure 5.5.g, the $S_a$ decreased from 5.73g to 4.85g and 3.57g for the control case and EPS10-4cm and EPS10-8cm cushioned cases, respectively. In Figure 5.5.h, the $S_a$ decreased from 5.73g to 4.68g and 4.10g for the control case and EPS20-4cm and EPS20-8cm cushioned cases, respectively. In Figure 5.5.i, the $S_a$ decreased from 5.73g to 4.30g and 3.44g for the control case and EPS30-4cm and EPS30-8cm cushioned cases, respectively.

The response spectrums for EPS10, EPS20, and EPS30 cases, respectively, with cushion thicknesses of 4 cm and 8 cm and the control case under sinusoidal motion at 0.4g amplitude with 12 Hz are represented in Figures 5.6.a, 5.6.b, and 5.6.c. The maximum spectral accelerations ($S_a$) occurred at a period of 0.085 sec and decreased from 3.79g to 3.17g and 2.48g for EPS10-4cm and EPS10-8cm cushioned cases, respectively. Similarly, for EPS20-4cm and EPS20-8cm cushioned cases, the maximum $S_a$ decreased from 3.79g to 3.34g and 2.85g, respectively. For EPS30-4cm and EPS30-8cm cushioned cases, the maximum $S_a$ decreased from 3.79g to 3.24g and 2.25g, respectively.

Figures 5.6.d-f show the response spectrums of results under sinusoidal motion at 0.4g amplitude with 14 Hz frequency. The figures compare the EPS10, EPS20, and EPS30 cushioned cases with thicknesses of 4 cm and 8 cm to the control case. The maximum spectral accelerations ($S_a$) occurred at a period of 0.07 sec and decreased for all cushioned cases. In Figure 5.6.d, the $S_a$ decreased from 4.22g to 3.60g and 2.96g for the EPS10-4cm and EPS10-8cm cushioned cases, respectively. In Figure 5.6.e, the $S_a$ decreased from 4.22g to 3.89g and 3.11g for the EPS20-4cm and EPS20-8cm cases, respectively. In Figure 5.6.f, the $S_a$ decreased from 4.22g to 3.62g and 3.19g for the EPS30-4cm and EPS30-8cm cushioned cases, respectively.

Observed general results with respect to maximum spectral accelerations for the EPS Geofoam cushioned cases under sinusoidal motions are summarized as follows:

- It was found that the maximum spectral accelerations at 0.125 sec period decreased with a maximum 42% reduction ratio for the case EPS30-8cm (Case 7) under the sinusoidal motion at 0.3g amplitude with 8 Hz frequency, and the reduction ranged between 17%-42%. Under the sinusoidal motion at 0.4g amplitude with 8 Hz frequency, the maximum spectral accelerations at 0.125 sec period decreased with a maximum 42% reduction ratio for the case EPS30-8cm, and the reduction ranged between 12%-42%. The maximum spectral acceleration at 0.125 sec period decreased with a maximum of 40% for the case EPS30-8cm, and the reduction ranged between 15%-40% under the sinusoidal motion at 0.5g amplitude with 8 Hz frequency. Under the sinusoidal motion at 0.4g amplitude with 12 Hz frequency, the maximum spectral accelerations at 0.085 sec period decreased with a maximum 41% reduction ratio for the case EPS30-8cm, and the reduction ranged between 12%-41%. The maximum spectral accelerations at 0.07 sec period decreased with a maximum 30% reduction ratio for the case EPS10-8cm (Case 5) under the sinusoidal motion at 0.3g amplitude with 8 Hz frequency, and the reduction ranged between 8%-30%.

- The thickness ratio was observed to be effective in decreasing the maximum spectral accelerations with increasing cushion thickness ratio at 0.125 sec period under the sinusoidal motion at 0.3g amplitude with 8 Hz frequency and at 0.4g amplitude with 8 Hz frequency and at 0.5g amplitude with 8 Hz frequency. This effect was particularly noticeable at a period of 0.085 seconds when subjected to sinusoidal motion with an amplitude of 0.4g and a frequency of 12 Hz. Similarly, at a period of 0.07 seconds under sinusoidal motion at an amplitude of 0.4g and a frequency of 14 Hz, increasing the cushion thickness ratio also decreased maximum spectral accelerations. Increasing cushion thickness positively affects the calculated spectral accelerations for all of the EPS geofoam cases. As represented in Figure 5.5 and Figure 5.6, maximum spectral accelerations decreased with respect to the increase of cushion thickness.

- The effect of EPS geofoam density on the maximum spectral acceleration results is highly dependent on the applied sinusoidal motion. The effect of density was observed

to be mostly effective at the period of 0.125 sec with increasing density decreasing the maximum spectral accelerations under the sinusoidal motions with 0.3g, 0.4g and 0.5g amplitude, 8 Hz frequency. Additionally, at a period of 0.085 sec when the density increases, it generally reduces the maximum spectral accelerations under sinusoidal motion at 0.4g amplitude with 12 Hz frequency. However, increasing density does not have any impact on decreasing the maximum spectral accelerations under sinusoidal motion at 0.4g amplitude with 14 Hz frequency. In general, the EPS30 has the maximum decrease in spectral accelerations observed in the study under all the input sinusoidal motions.

- It is indicated that the EPS geofoam generally exhibits improvement by reducing the maximum spectral accelerations and can improve the seismic performance of the wall for all cushion thicknesses and densities under all input sinusoidal motions, as given in Figure 5.5 and Figure 5.6. It is shown that the EPS30-8cm provides a significant improvement compared to the control model in reducing maximum spectral accelerations under the sinusoidal motions with 0.3g amplitude, 8 Hz frequency, and the sinusoidal motions with 0.4g amplitude, 8 Hz frequency with 42% reduction (Figure 5.5.a-b).

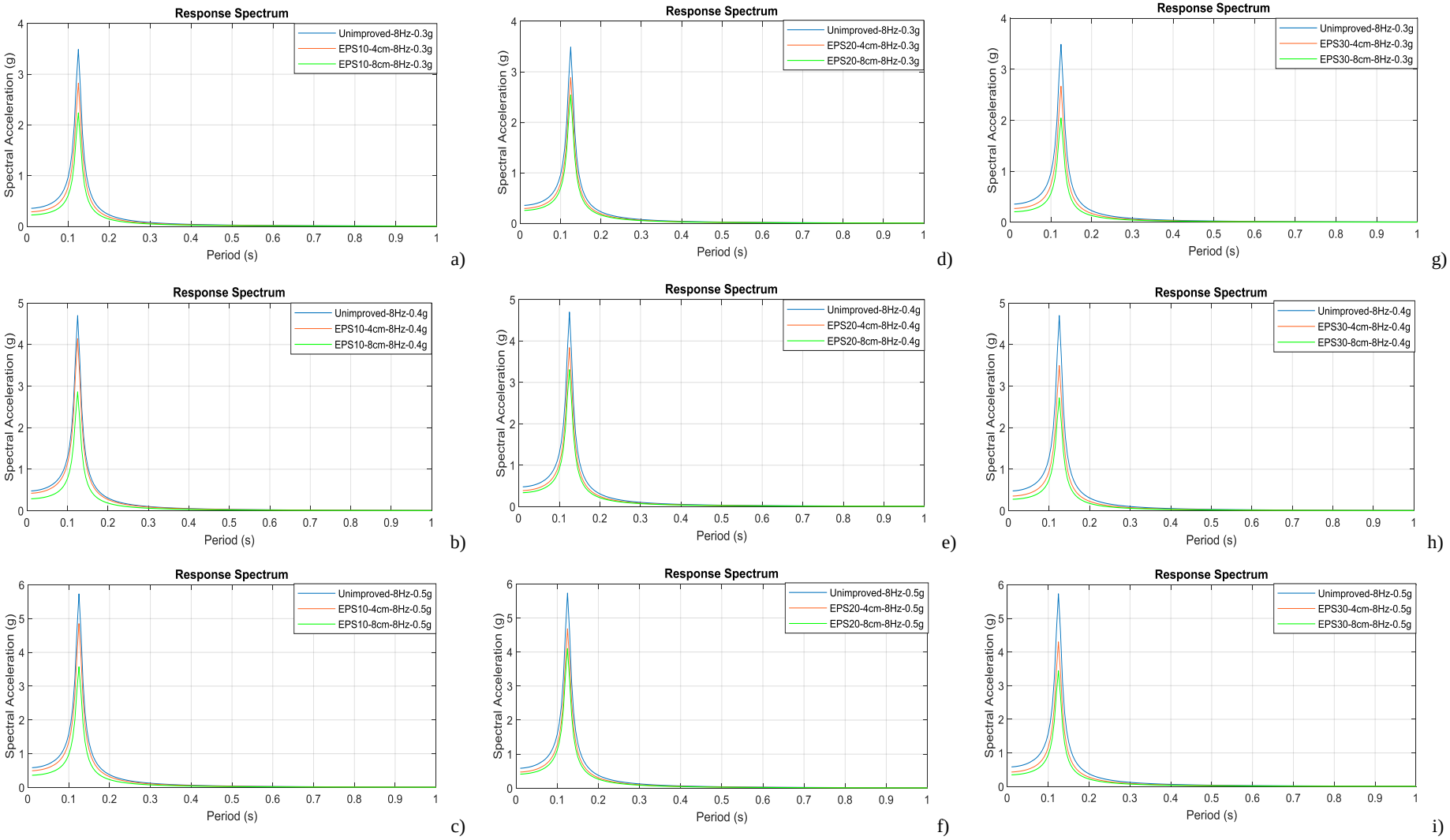


Figure 5.5 Response Spectrums of all EPS Geofoam cushioned cases with respect to A7 under a-b-c) sinusoidal motion at 0.3g amplitude with 8 Hz frequency, d-e-f) sinusoidal motion at 0.4g amplitude with 8 Hz frequency, g-h-i) sinusoidal motion at 0.5g amplitude with 8 Hz frequency.

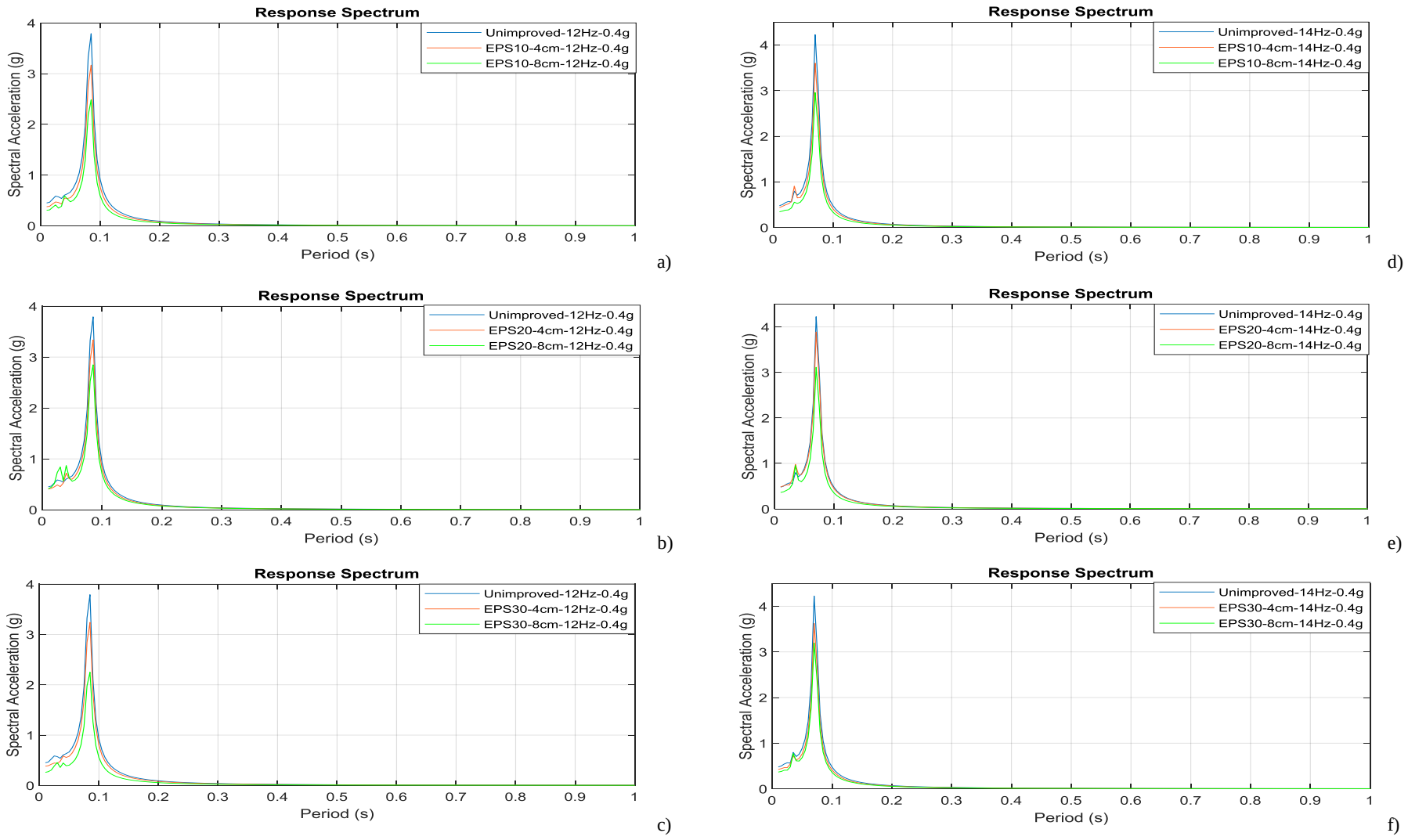


Figure 5.6 Response Spectrums of all EPS Geofoam cushioned cases with respect to A7 under a-b-c) sinusoidal motion at 0.4g amplitude with 12 Hz frequency, d-e-f) sinusoidal motion at 0.4g amplitude with 14 Hz frequency.

### 5.1.2. The Effects of Acceleration Response for EPS Geofoam Cushion under Different Input Motions

The variation of maximum accelerations at the top of the RWM for EPS geofoam cushioned cases at different thicknesses and densities compared with the control case under all input motions is shown in Figures 5.7 and 5.8.

#### 5.1.2.1. Maximum Acceleration Comparison at 4 cm Thickness

The maximum transmitted accelerations of the EPS10-4cm, EPS20-4cm and EPS30-4cm cases at the top of the RWM are compared with the maximum transmitted accelerations of the control case considering the PGA of the input motions. PGA of the input motions are 0.12g, 0.14g, 0.18g, 0.22g, 0.32g, 0.82g, and sinusoidal motions at 0.3g amplitude with 8 Hz frequency, at 0.4g amplitude with 8 Hz frequency, at 0.5g amplitude with 8 Hz frequency, at 0.4g amplitude with 12 Hz frequency, at 0.4g amplitude with 14 Hz frequency (Figure 5.7).

The comparison of maximum transmitted accelerations measured from A7 for the control case and for EPS geofoam cases with 4 cm thickness as Case 2 (EPS10-4cm), Case 3 (EPS20-4cm), and Case 4 (EPS30-4cm) with the PGA of input motions are shown in Figure 5.7. The study conducted using six different earthquake records and five different sinusoidal motions shows that the maximum accelerations of the control case amplify under all earthquake and sinusoidal motions except for the scaled 1999 Kocaeli EQ Motion-İznik Station record, compared to the PGA of input motions. The deamplification in maximum accelerations of EPS Geofoam cushioned cases with 4 cm thickness is observed under both near field earthquakes, far field earthquakes, and sinusoidal motions compared to the control case.

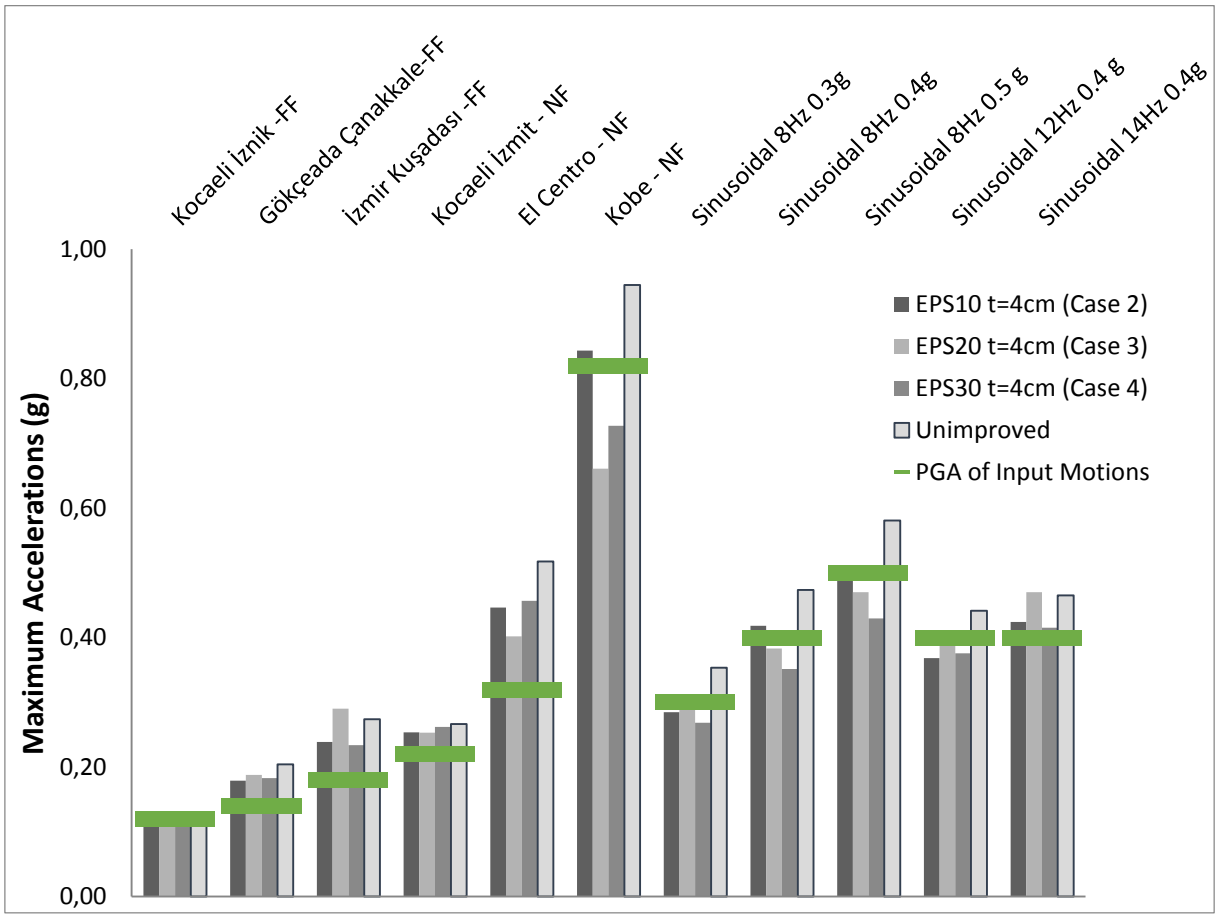


Figure 5.7 Variation of maximum accelerations at the top of the RWM for EPS Geofoam cases with t=4cm compared to the control case under all input motions.

When the maximum accelerations are compared to the control case, the highest decrease in maximum acceleration values is seen under the scaled 1995 Kobe EQ record for EPS20-4cm (Case 3). Under all sinusoidal motions, decrease in maximum accelerations is generally observed for the cushion type EPS30-4cm (Case 4) under the scaled 1995 Kobe EQ record and the scaled 1940 Imperial Valley EQ-El Centro Station record, and it stands out for the cushion type EPS20-4cm, however under the scaled 2020 İzmir EQ Motion-Kuşadası Station record, EPS20-4cm shows the lowest decrease in maximum acceleration value. No significant difference in maximum acceleration values is observed under the scaled 1999 Kocaeli EQ Motion-İznik Station record, the scaled 2014 Gökçeada EQ Motion-Çanakkale Station record, and the scaled 1999 Kocaeli EQ Motion-İzmit Station record.

5.1.2.2. Maximum Acceleration Comparison at 8 cm Thickness

The maximum transmitted accelerations of the EPS10-8cm, EPS20-8cm and EPS30-8cm cases at the top of the RWM are compared with the maximum transmitted accelerations of the control case considering the PGA of the input motions. PGA of the input motions are 0.12g, 0.14g, 0.18g, 0.22g, 0.32g, and 0.82g, followed by sinusoidal motions with amplitudes of 0.3g, 0.4g, and 0.5g at a frequency of 8Hz, and sinusoidal motions with amplitudes of 0.4g at frequencies of 12 Hz and 14 Hz (Figure 5.8).

The comparison of maximum transmitted accelerations measured from A7 for the control case and for EPS geofoam cases with 8cm thickness as Case 5 (EPS10-8cm), Case 6 (EPS20-8cm), and Case 7 (EPS30-8cm) with the PGA of input motions are shown in Figure 5.8. The study was conducted using six different earthquake records and five different sinusoidal motions. It is seen in Figure 5.8 that the maximum accelerations of the control case amplify under all earthquake and sinusoidal motions except for the scaled 1999 Kocaeli EQ Motion-İznik Station record, compared to the PGA of input motions. The deamplification in maximum accelerations of EPS Geofoam cushioned cases with 8 cm thickness is observed under both near field earthquakes, far field earthquakes, and sinusoidal motions compared to the control case.

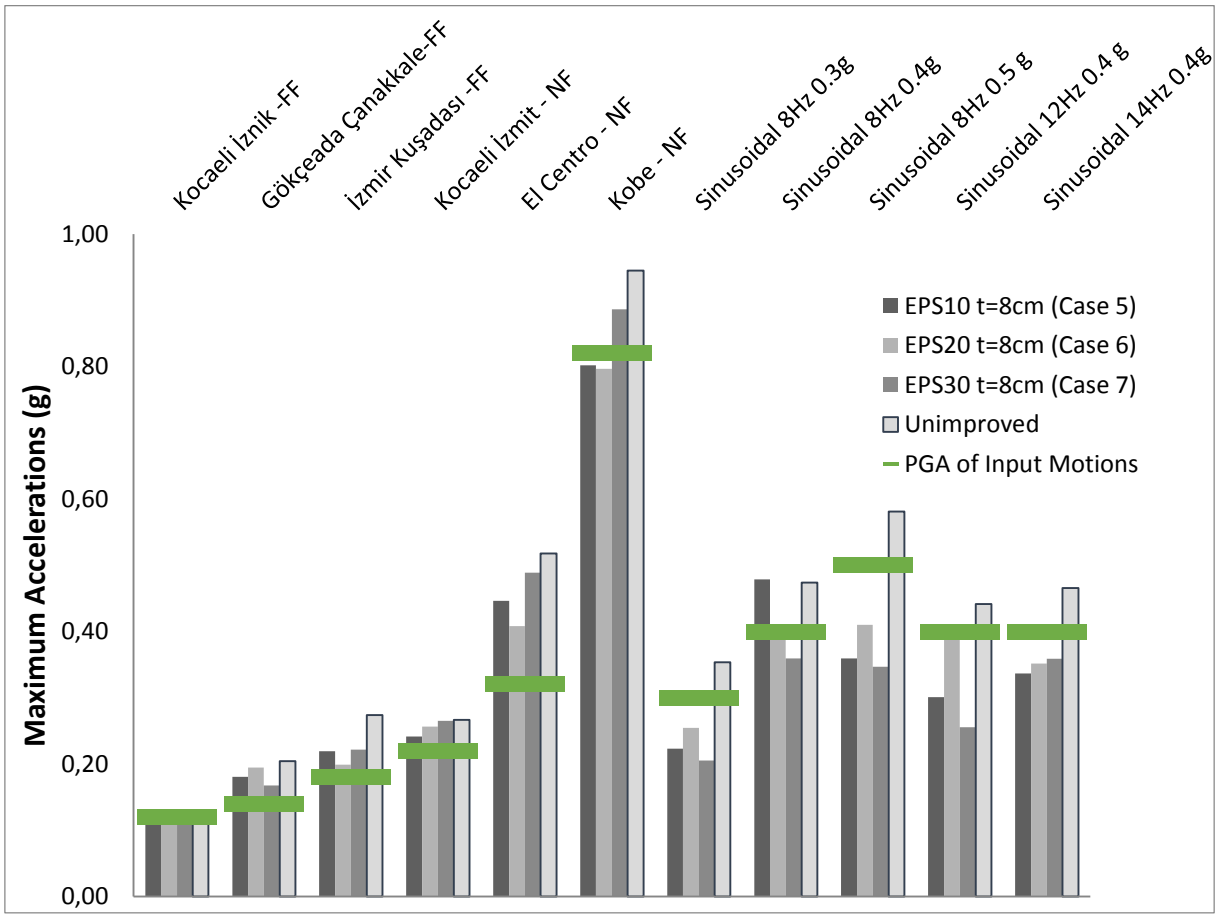


Figure 5.8 Variation of maximum accelerations at the top of the RWM for EPS Geofoam cases with t=8cm compared to the control case under all input motions.

In comparison of the maximum acceleration values to the control case, the highest decrease in maximum acceleration values is seen under the sinusoidal motion at 0.3g amplitude with 8 Hz frequency, sinusoidal motion at 0.4g amplitude with 8 Hz frequency, and sinusoidal motion at 0.5g amplitude with 8 Hz frequency, for cushion type EPS10-8cm (Case 5) and EPS30-8cm (Case 7). Under the scaled 2020 İzmir EQ Motion-Kuşadası Station record, the 1940 El Centro, and the scaled 1995 Kobe EQ record, a significant decrease in maximum accelerations is generally observed for the cushion type EPS20-8cm (Case 6) however, under the scaled 1999 Kocaeli EQ Motion-İzmit Station record, all the cases Case 5, Case 6 and Case 7 shows the lowest decrease in maximum acceleration. No significant difference in maximum acceleration values is observed under the scaled 1999 Kocaeli EQ Motion-İznik Station record.

### 5.1.3. Maximum Lateral Displacements for EPS Geofoam Cushion Cases under All Input Motions

Two laser displacement sensors have been installed on the retaining wall model, one at the height of H as D19 and the other at the height of 0.5H as D18, as shown in Figure 3.27 and Figure 3.29 in Chapter 3. Figure 5.9 shows the comparison of the maximum lateral displacements at the top of the retaining wall model with respect to cushion thickness ratio and EPS geofoam density under different earthquake input motions and sinusoidal motions. The control case is shown in Figure 5.9.a, while the remaining cases are shown in Figures 5.9.b to 5.9.g. Each figure shows the maximum lateral displacements for a particular case under different input motions, including far field and near field earthquakes and sinusoidal motions.

As seen in Figure 5.9. the maximum lateral displacement measured from D19 of the control case (Case 1) was obtained as 1.14 cm under the scaled 1999 Kocaeli EQ Motion-İznik Station record, 0.70 cm under the scaled 2014 Gökçeada EQ Motion-Çanakkale Station record, 0.37 cm under the scaled 2020 İzmir EQ Motion-Kuşadası Station record, 1.85 cm under the scaled 1999 Kocaeli EQ Motion-İzmit Station record, 1.88 cm under the scaled 1940 Imperial Valley EQ-El Centro Station record, 1.50 cm under the scaled 1995 Kobe EQ record, 0.14 cm under the sinusoidal motion at 0.3g amplitude with 8 Hz frequency, 0.20 cm under the sinusoidal motion at 0.4g amplitude with 8 Hz frequency, 0.23 cm under the sinusoidal motion at 0.5g amplitude with 8 Hz frequency, 0.1 cm under the sinusoidal motion at 0.4g amplitude with 12 Hz and 14 Hz frequency.

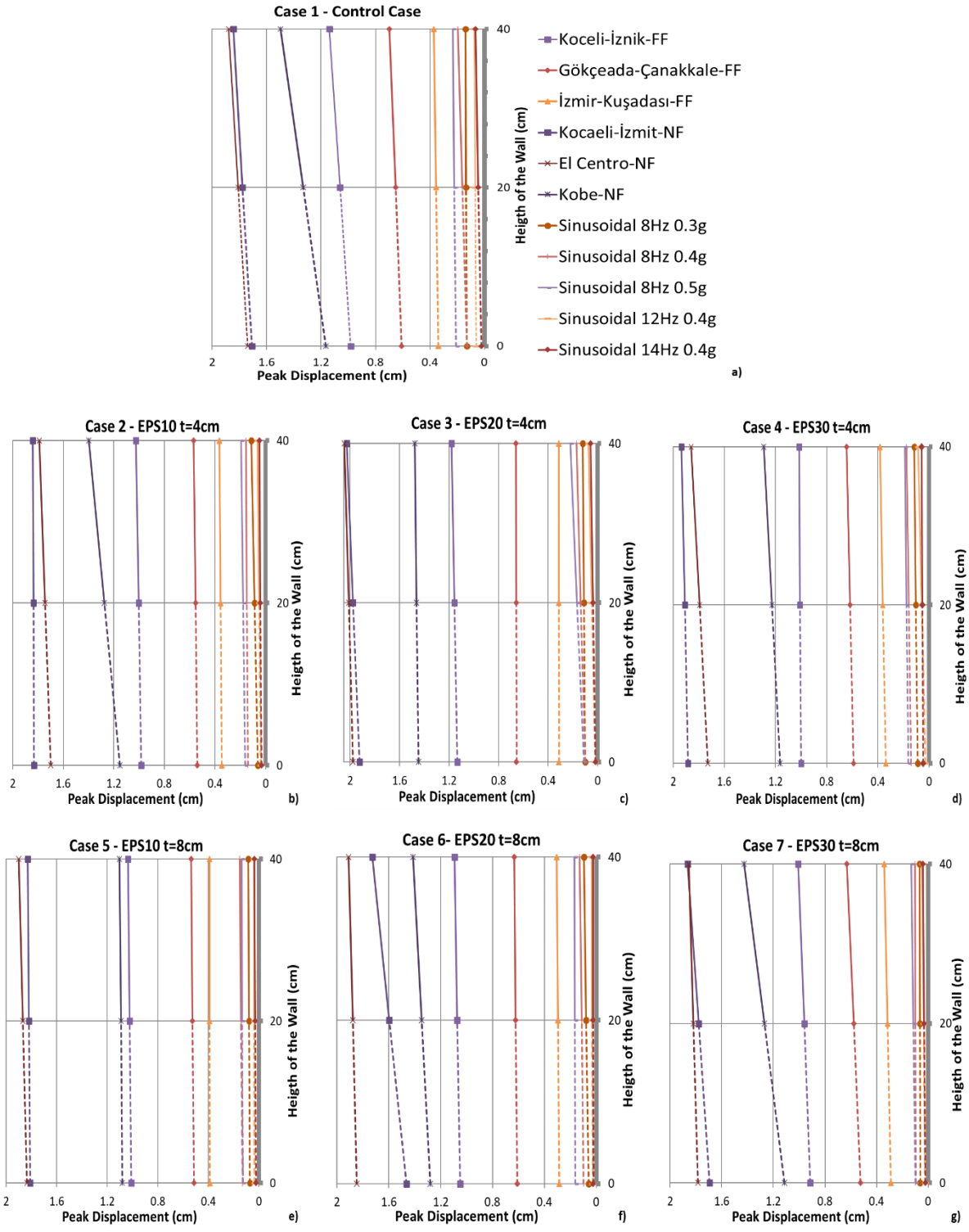


Figure 5.9. Maximum lateral displacements measured from D19 under all input motions a) Case 1, b) Case 2, c) Case 3, d) Case 4, e) Case 5, f) Case 6, g) Case 7.

The evaluation of the results of the maximum lateral displacements at the top of the RWM for the EPS Geofoam cushioned cases compared with the cushioned case under all given input motions is summarized as follows:

- In consideration of the maximum lateral displacements given in Figure 5.9, it has been observed that under sinusoidal motions, the displacements are lower, whereas under the effect of earthquake motions, higher displacements occur. Comparing far field and near field earthquakes reveals that greater displacements occur under near field earthquakes (Figure 5.9.a-g).

- Taking into account thickness and density changes in each case of EPS geofoam, EPS30-8cm (Case 7) is the most effective case that can reduce the maximum lateral displacement values at the top of the RWM by 12% under the scaled 1999 Kocaeli EQ Motion-İznik Station. At the input motion characteristics, it is obtained that EPS geofoam is slightly effective as a cushion for lowering maximum lateral displacement values. The maximum lateral displacement reduction under the scaled 2014 Gökçeada EQ Motion-Çanakkale Station record is up to 23% when the EPS10-8cm (Case 5) is used. Similarly, under the scaled 2020 İzmir EQ Motion-Kuşadası Station record, the maximum lateral displacement reduction is 18% when EPS20-8cm (Case 6) is used. Under the scaled 1999 Kocaeli EQ Motion-İzmit Station record, the maximum lateral displacement reduction is 7% when EPS20-8cm is utilized. The maximum lateral displacement reduction under the scaled 1940 Imperial Valley EQ-El Centro Station record is 5% when EPS10-4cm (Case 2) is used. It is indicated that the maximum lateral displacement reduction for the EPS Geofoam case under the scaled 1995 Kobe EQ record is a maximum of 26% when the EPS10-8cm is used.

- Using EPS geofoam cushion in combination with a sand backfill can significantly reduce maximum lateral displacements under the earthquake input motions. The reduction in maximum lateral displacements varied depending on the earthquake characterization with the highest effect observed for the EPS10-8cm cushioned model

under the scaled 1995 Kobe EQ record. EPS geofoam is effective as a cushion under the input motion characteristics of the scaled 2014 Gökçeada EQ Motion-Çanakkale Station record having 3.2 Hz predominant frequency 0.14g amplitude, the scaled 2020 İzmir EQ Motion-Kuşadası Station record having 24.4 Hz predominant frequency 0.18g amplitude and the scaled 1995 Kobe EQ record having 5.7 Hz predominant frequency 0.82g amplitude in reducing maximum lateral displacement. Considering the results of the scaled earthquake records, it can be clearly examined that increasing cushion thickness positively affects the maximum lateral displacement reduction for the EPS geofoam cushioned cases. Additionally, it can be explained that there was no clear influence of cushion density in reducing the maximum lateral displacements. The most efficient cushion density for EPS geofoam cushioned cases in terms of decreasing displacements is EPS30, which should be highlighted as well.

- The highest reduction in maximum lateral displacements under the sinusoidal motion with 0.3g amplitude with 8 Hz frequency was found to be a maximum of 53%, considering the changes in thickness and density of EPS geofoam. The EPS30-8cm is the most effective case under that sinusoidal motion in reducing the displacement values at the top of the RWM. The maximum lateral displacements are more limited that under sinusoidal motions. Under sinusoidal motion at 0.4g amplitude with 8 Hz frequency, the reduction in displacement is up to 48% applying EPS30-8cm, and the highest reduction in maximum lateral displacement is 44% under sinusoidal motion at 0.5g amplitude with 8 Hz frequency for the case with EPS30-8cm. Under the sinusoidal motion at 0.4g amplitude with 12 Hz frequency, the maximum reduction compared to the control case is up to 56% when the EPS20-8cm (Case 6) is utilized. The maximum reduction based on maximum lateral displacements under the sinusoidal motion at 0.4g amplitude with 14 Hz frequency is maximum 59% when EPS20-8cm (Case 6) is used.

- The study showed that using EPS geofoam cushion can reduce maximum lateral displacements during the excitation of sinusoidal motions. The highest reductions depending on the sinusoidal motions were observed for the EPS30-8cm cushioned

model under the sinusoidal motion at 0.3g amplitude with 8 Hz frequency and sinusoidal motion at 0.4g amplitude with 8 Hz frequency. EPS geofoam is effective as a cushion at the input motion characteristics under sinusoidal motions in the frequency range between 8 Hz and 12 Hz and the amplitude range between 0.3g and 0.5g in reducing maximum lateral displacements for the EPS geofoam cushioned cases. It is evident that EPS geofoam acts as an efficient cushion in reducing maximum lateral displacement values at these input motion characteristics. The results suggest that cushion density has an influence on the improvement effect, with higher density leading to greater improvement in general. Additionally, when considering the sinusoidal motions at 8 Hz frequency, it can be concluded that EPS geofoam with 8 cm thickness is most effective in reducing maximum lateral displacements at the top of the RWM.

## 5.2. The Effects of Tire Waste and Sand Mixture Cushion on the Seismic Performance of the Retaining Wall Model

The effects of thickness and density concerning improvement efficiency and spectral acceleration, the effects of acceleration response, and the comparison of maximum lateral displacements under the given near field and far field earthquake and sinusoidal motions are explained for tire waste and sand mixture cushion in this part of the study.

### 5.2.1. The Effects of Thickness and Mixture Ratio of Tire Waste and Sand Mixture Cushion

The experimental studies of the tire waste and sand mixture (TW) cushioned cases are conducted for three mixture ratios, 10% (TW10), 20% (TW20), and 30% (TW30) tire waste additives with two different thicknesses 4 cm and 8 cm regarding 0.10, and 0.20 t/H ratios, respectively. These cases are listed from Case 8 (TW10-4cm) to Case 13 (TW30-8cm) as explained in Table 3.11 in Chapter 3. Each of these cases was compared with the control case of Case 1, and the improvement efficiency was calculated for each.

The results of the analysis of improvement efficiency for each cushion thickness ratio (t/H) and mixture ratio under each input motion are shown in this section of the study. The influence of density, thickness, and input excitation on the seismic performance of the TW cushioned retaining wall model is also investigated based on the improvement efficiencies and spectral accelerations in comparison to Case 1. The TW cushioned cases, Cases 8 to Case 13, with comparisons to Case 1, have been reported under the given far field, near field, and sinusoidal input motions.

5.2.1.1. Comparison of Improvement Efficiency under Far Field and Near Field Earthquake Motions

The improvement efficiency at the top of the RWM with respect to cushion thickness ratio and tire waste and sand mixture ratio of the TW cushioned cases compared to the control case under far field and near field earthquakes is discussed by evaluating Figure 5.10.

The improvement efficiency values for each case under the scaled 1999 Kocaeli EQ Motion-İznik Station record can be seen in Figure 5.10.a. The improvement efficiencies of TW cushioned cases were limited to 1%, with the maximum improvement efficiency for the cushion type TW10-8cm. This indicates that using a mixture of tire waste and sand as a cushion material was ineffective in reducing the maximum acceleration values under this earthquake motion characteristics.

The improvement efficiency under the scaled 2014 Gökçeada EQ Motion-Çanakkale Station record is represented in Figure 5.10.b. The improvement efficiencies of TW cushioned cases ranged between 2% and 9%, with the highest improvement efficiency for the TW20-8cm. It can be evaluated that TW is slightly effective as a cushion. Additionally, no trend was observed for the seismic reduction effect depending on thickness and density. This situation is a direct result of the input motion characteristics of a far field earthquake record at 3.2 Hz predominant frequency 0.14g amplitude.

Figure 5.10.c shows the maximum improvement efficiency measured from A7 under the scaled 2020 İzmir EQ Motion-Kuşadası Station record. The results indicate that the improvement efficiency for the TW cushioned case was limited to 2% when the TW30-4cm was used. For the rest of the TW cushioned cases, no acceleration reduction was observed.

The improvement efficiencies with respect to the data from A7 under the scaled 1999 Kocaeli EQ Motion-İzmit Station record is represented in Figure 5.10.d. It is indicated that the improvement efficiency for the TW cushioned case is limited to 1% when the TW10 is used with the cushion thickness ratio of 0.2.

The improvement efficiencies of TW cushioned cases ranged between 3% and 12% under the scaled 1940 Imperial Valley EQ-El Centro Station record, as shown in Figure 5.10.e. The maximum improvement efficiency was obtained to be around 12% for TW20 with a cushion thickness ratio of 0.1. It can be evaluated that the TW cushion demonstrated improvement at all cushion thicknesses and mixture ratios and is effective as a cushion at these input motion characteristics at 6 Hz frequency 0.32g amplitude in this case.

Under the scaled 1995 Kobe EQ, the improvement efficiency is represented in Figure 5.10.f. The highest improvement efficiency for the TW cushion type was TW30-8cm with 21%. For the TW ratios and the cushion thickness ratios, improvement efficiency was observed, ranging between 6% and 21%. It can be stated that tire waste sand mixture is effective as a cushion at these input motion characteristics at 5.7 Hz frequency 0.82g amplitude.

The general evaluation of the results based on improvement efficiency at the top of the RWM for the TW cushioned cases under far field and near field earthquakes are given in the following explanations:

- Evaluation of the results indicates that the TW, as a cushion type, exhibits improvement across all cushion thicknesses and mixture ratios, examined in this study under the far field earthquake as the scaled 2014 Gökçeada EQ Motion-Çanakkale Station record and near field earthquakes as the scaled 1940 Imperial Valley EQ El Centro Station record and the scaled 1995 Kobe EQ record as given in Figure 5.10.b,e,f. Considering the real earthquakes executed, the study shows that the cushioned model of TW30-8cm provides significant improvement compared to the control model in reducing maximum acceleration under the scaled 1995 Kobe EQ (Figure 5.10.f). On the other hand, the improvement efficiency is limited to 2% under the scaled 1999 Kocaeli EQ Motion-İznik Station record (Figure 5.10.a), under the scaled 2020 İzmir EQ Motion-Kuşadası Station record (Figure 5.10.c), and under the scaled 1999 Kocaeli EQ Motion-İzmit Station record (Figure 5.10.d).

- The TW cushion might be considered as a solution to improve the seismic performance of retaining walls at the predominant frequency of near field earthquakes, around 6 Hz, and amplitudes higher than 0.30g. In the evaluation of the far field earthquakes, the maximum improvement efficiency was limited to 9% under the scaled 2014 Gökçeada EQ Motion-Çanakkale Station record. This finding demonstrates that the TW cushioned model is slightly effective under far field earthquakes, and low amplitude of the input motion in the range of 0.12g-0.18g can be considered as a result of this behaviour.

- Increasing cushion thickness sightly affects the calculated improvement efficiencies for some of the TW cushioned cases. As represented in Figure 5.10.f, improvement efficiencies under the scaled 1995 Kobe EQ generally increase with respect to cushion thickness.

- The effect of the TW cushion mixture ratio on improvement efficiency results is highly dependent on the applied dynamic motion. The results reveal that TW30 is the most efficient for reaching the highest improvement under the scaled 1995 Kobe EQ, as shown in Figure 5.10.f.

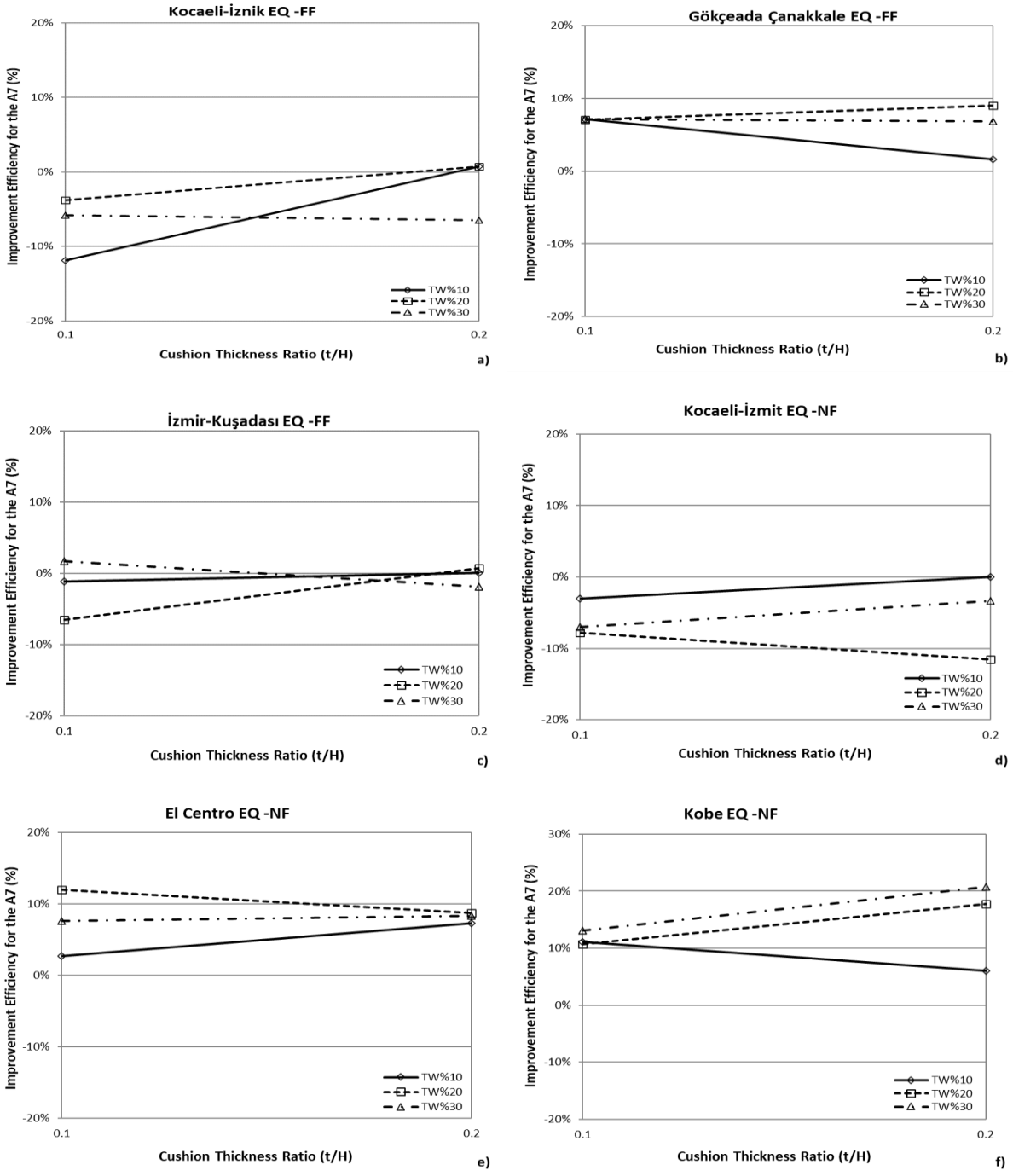


Figure 5.10. Improvement efficiency for all Tire Waste and Sand Mixture cushioned cases with respect to A7 under a) the scaled 1999 Kocaeli EQ Motion-İznik Station Record-FF, b) the scaled 2014 Gökçeada EQ Motion-Çanakkale Station Record-FF, c) the scaled 2020 İzmir EQ Motion-Kuşadası Station Record-FF, d) the scaled 1999 Kocaeli EQ Motion-İzmit Station Record-NF, e) the scaled 1940 Imperial Valley EQ-El Centro Station record-NF, f) the scaled 1995 Kobe EQ record-NF.

5.2.1.2. Comparison of Maximum Spectral Accelerations under Far Field and Near Field Earthquake Motions

The response spectrums at the top of the RWM with respect to the cushion thickness ratio and tire waste and sand mixture ratio of the TW cushioned cases compared to the control case under far field earthquakes are discussed by evaluating Figure 5.11.

The response spectrums for the TW10, TW20, and TW30 cases with cushion thicknesses of 4 cm and 8 cm compared to the control case under the scaled 1999 Kocaeli EQ Motion-İznik Station record are represented in Figures 5.11.a, 5.11.b, and 5.11.c. The maximum spectral accelerations ($S_a$) at the top of the RWM were evaluated at two different time periods. For TW10 cases, the maximum $S_a$ values increased from 0.39g to 0.49g and 0.48g at a period of 0.12 seconds and from 0.42g to 0.44g and 0.45g at a period of 0.30 seconds for the control case and TW10-4cm and TW10-8cm cushioned cases, respectively. For TW20 cases, the maximum $S_a$ values increased from 0.39g to 0.47g and 0.51g at a period of 0.12 seconds and from 0.42g to 0.45g and 0.455g at a period of 0.30 seconds for the control case and TW20-4cm and TW20-8cm cushioned cases, respectively. For TW30 cases, the maximum $S_a$ values increased from 0.39g to 0.47g and 0.53g at a period of 0.12 seconds and from 0.42g to 0.44g and 0.46g at a period of 0.30 seconds for the control case and TW30-4cm and TW30-8cm cushioned cases, respectively.

The response spectrums for the TW10, TW20, and TW30 cases with cushioned thicknesses of 4 cm and 8 cm compared to the control case under the scaled 2014 Gökçeada EQ Motion-Çanakkale Station record are shown in Figures 5.11.d, 5.11.e, and 5.11.f, respectively. The maximum spectral accelerations ($S_a$) were evaluated at two different periods in each case. In Figure 5.11.d, at a period of 0.11 seconds, the maximum $S_a$ values decreased from 0.67g to 0.65g and increased to 0.70g, while at a period of 0.22 seconds, the maximum $S_a$ values decreased from 0.52g to 0.51g and 0.50g for the control case and the TW10-4cm and TW10-8cm cushioned cases, respectively. In Figure 5.11.e, at a period of 0.11 seconds, the maximum $S_a$ values decreased from 0.67g to 0.62g and 0.66g, while at a period of 0.22 seconds, the maximum $S_a$ values decreased from 0.52g to 0.49g and 0.508g for the control case

and the TW20-4cm and TW20-8cm cushioned cases, respectively. In Figure 5.11.f, at a period of 0.11 seconds, the maximum $S_a$ values decreased from 0.67g to 0.66g and increased to 0.69g, while at a period of 0.22 seconds, the maximum $S_a$ values decreased from 0.52g to 0.49g and 0.50g for the control case and the TW30-4cm and TW30-8cm cushioned cases, respectively.

The response spectrums for the TW10, TW20, and TW30 cases with cushioned thicknesses of 4 cm and 8 cm compared to the control case under the scaled 2020 İzmir EQ Motion-Kuşadası Station record are given in Figure 5.11.g, Figure 5.11.h, and Figure 5.11.i. The maximum $S_a$ values were evaluated at two different periods for each case. In Figure 5.11.g, at a period of 0.06 seconds, the maximum $S_a$ values increased from 0.98g to 1.10g and decreased to 0.91g for the control case. At a period of 0.11 seconds, the maximum $S_a$ values decreased from 0.93g to 0.90g and 0.92g for the TW10-4cm and TW10-8cm cushioned cases, respectively. In Figure 5.11.h, at a period of 0.06 seconds, the maximum $S_a$ values changed from 0.98g to 1.02g and 0.91g. At a period of 0.11 seconds, the maximum $S_a$ values decreased from 0.93g to 0.84g and 0.78g for the control case and the TW20-4cm and TW20-8cm cushioned cases, respectively. In Figure 5.11.i, at a period of 0.06 seconds, the maximum $S_a$ values increased from 0.98g to 0.99g and 1.0g and at a period of 0.11 seconds, the maximum $S_a$ values decreased from 0.93g to 0.80g and 0.92g for the control case and the TW30-4cm and TW30-8cm cushioned cases, respectively.

Observed general results with respect to maximum spectral accelerations at the top of the RWM for the TW cushioned cases under far field earthquakes are given in the following:

- According to results under the scaled 1999 Kocaeli EQ Motion-İznik Station record, it was obtained that the maximum spectral accelerations increased more in the 0.05-0.15 sec period range and less in the 0.25-0.35 sec period range. Under the scaled 2014 Gökçeada EQ Motion-Çanakkale Station record, the spectral acceleration in the 0.05-0.15 sec period range decreased by 8% for TW20-4cm (Case 9). No changes were observed for the other cases. Additionally, within the 0.25-0.35 second period range, the maximum decrease in spectral acceleration was 6% for both TW20-4cm and TW30-4cm (Case 10). The maximum spectral acceleration in the 0.05-0.10 sec period range

decreased by a maximum of 10% for TW30-4cm, and in the 0.10-0.15 sec period range, it decreased by a maximum of 16% for TW20-8cm (Case 12). The decrease in maximum spectral acceleration continued up to the 0.5 sec period under the scaled 2020 İzmir EQ Motion-Kuşadası Station record. The period range is clearly an important factor when taking into account far field earthquakes. Higher frequencies in the 10 Hz to 20 Hz range have been shown to significantly reduce the spectral accelerations when compared to the control case.

- The effectiveness of the thickness ratio was found to be insignificant in the period range of both 0.05-0-15 sec and 0.25-0.35 sec under the far field earthquakes as the scaled 1999 Kocaeli EQ Motion-İznik Station record and the scaled 2014 Gökçeada EQ Motion-Çanakkale Station record. The largest decrease in maximum spectral accelerations, as shown by the cushion thickness ratio is 16% for 8 cm thickness under the scaled 2020 İzmir EQ Motion-Kuşadası Station record, which has earthquake characteristics with a 24.4 Hz predominant frequency and 0.18g amplitude. For most of the TW cushioned cases, increasing cushion thickness has a positive impact on the calculated spectral accelerations. Maximum spectral accelerations often decrease as cushion thickness increases, as seen in Figure 5.11, using a t/H=0.2 cushion thickness ratio.

- Considering the effect of the TW ratio on the maximum spectral acceleration results, in general, the TW20 and TW30 have the maximum reduction in spectral accelerations observed in the study under far field earthquakes. This can be drawn from the effect of the TW ratio on the maximum spectral acceleration results. The highest decrease based on maximum spectral accelerations in comparison to the control case is observed when the tire waste mixture ratio is increased.

- According to analysis of the data, all cushion thicknesses and mixture ratios examined in this study under far field earthquakes show a minor reduction in spectral accelerations for the TW cushion type, as shown in Figure 5.11. In consideration of the

scaled real earthquakes executed, the study shows that the TW20-8cm provides a significant improvement compared to the control model in reducing maximum spectral accelerations under the scaled 2020 İzmir EQ Motion-Kuşadası Station record with a 16% reduction (Figure 5.11.g-h-i). On the other hand, the improvement efficiency is limited to 7% under the scaled 2014 Gökçeada EQ Motion-Çanakkale Station record (Figure 5.11.d-e-f).

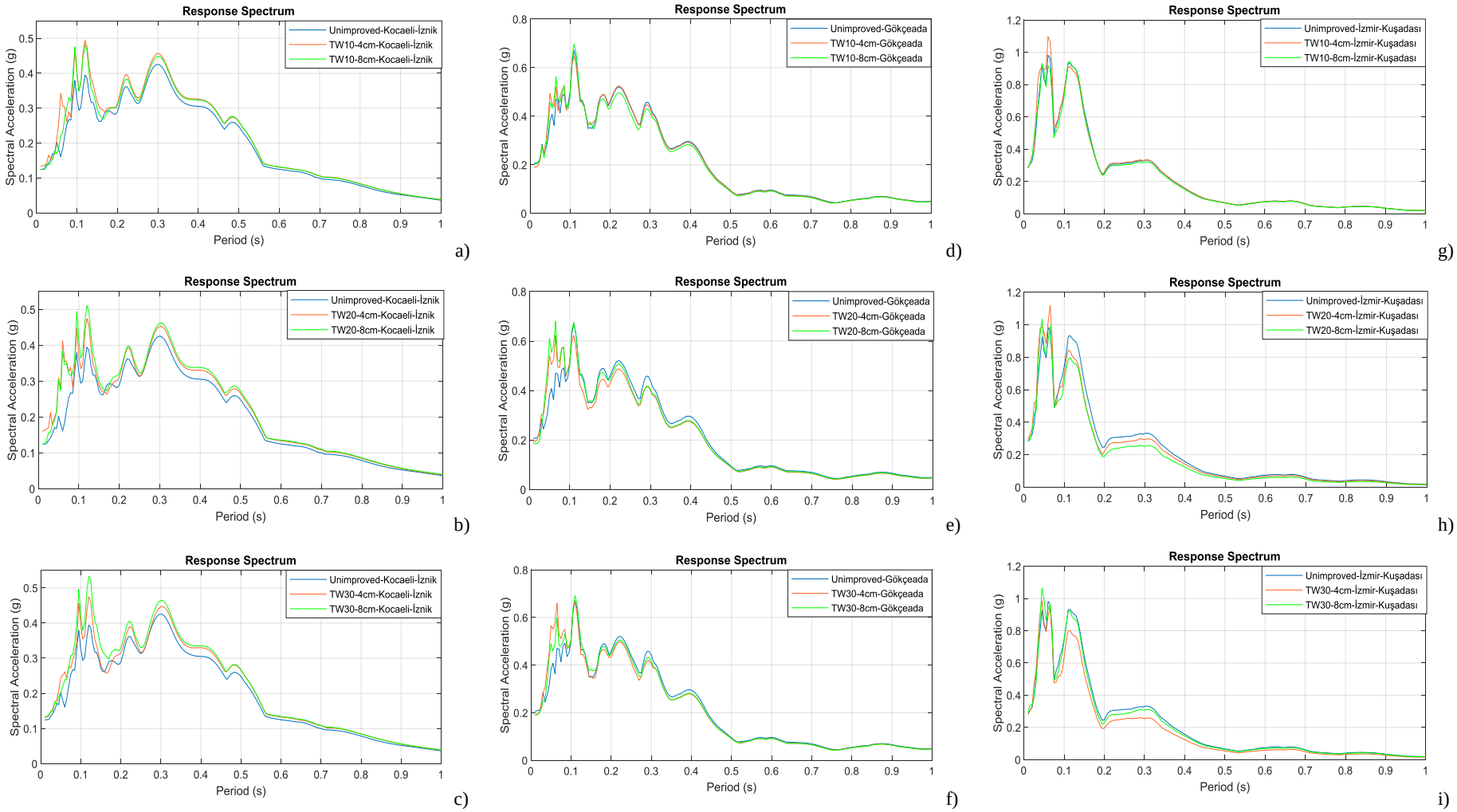


Figure 5.11 Response Spectrums of all Tire Waste and Sand Mixture cushioned cases with respect to A7 under a-b-c) the scaled 1999 Kocaeli EQ Motion-İznik Station Record-FF, d-e-f) the scaled 2014 Gökçeada EQ Motion-Çanakkale Station Record-FF, g-h-i) the scaled 2020 İzmir EQ Motion-Kuşadası Station Record-FF.

The response spectrums at the top of the RWM with respect to cushion thickness ratio and tire waste and sand mixture ratio of the TW cushioned cases compared to the control case under near field earthquakes are discussed by evaluating Figure 5.12.

The response spectrums for the TW10 and TW20 cases with cushion thicknesses of 4 cm and 8 cm under the scaled 1999 Kocaeli EQ Motion-İzmit Station record are shown in Figure 5.12.a, 5.12.b, 5.12.c. The maximum $S_a$ values increased at a period of 0.07 seconds and decreased at a period of 0.15 seconds. In Figure 5.12.c, for the TW30 cases with cushion thicknesses of 4 cm and 8 cm, the maximum $S_a$ values decreased at a period of 0.07 seconds and increased at a period of 0.15 seconds.

The response spectrums for the TW10, TW20, and TW30 cases with cushion thicknesses of 4 cm and 8 cm and the control case under the scaled 1940 Imperial Valley EQ-El Centro Station record are shown in Figures 5.12.d, 5.12.e, and 5.12.f. The maximum spectral accelerations ($S_a$) were evaluated at two different periods for each case. In Figure 5.12.d, at a period of 0.055 seconds, the maximum $S_a$ values decreased from 1.48g to 1.24g and 1.34g, and at a period of 0.15 seconds, the maximum $S_a$ values decreased from 1.40g to 1.23g and 1.34g for the TW10-4cm and TW10-8cm cushioned cases, respectively. Additionally, for the TW10-4cm case, the maximum $S_a$ values decreased from 1.48g to 1.24g by lengthening the period from 0.55 sec to 0.60 sec. In Figure 5.12.e, at a period of 0.055 seconds, the maximum $S_a$ values decreased from 1.48g to 1.18g and 1.37g, and at a period of 0.15 seconds, the maximum $S_a$ values decreased from 1.40g to 1.23g and 1.32g for the TW20-4cm and TW20-8cm cushioned cases, respectively. Furthermore, for the TW20-4cm case, the maximum $S_a$ values decreased from 1.48g to 1.18g by lengthening the period from 0.55 sec to 0.60 sec. In Figure 5.12.f, at a period of 0.055 seconds, the maximum $S_a$ values decreased from 1.48g to 1.40g and 1.17g, and at a period of 0.15 seconds, the maximum $S_a$ values decreased from 1.40g to 1.31g and 1.34g for the TW30-4cm and TW30-8cm cushioned cases, respectively.

The response spectrums for TW10, TW20, and TW30 cases with thicknesses of 4 cm and 8 cm and the control case under the scaled 1995 Kobe EQ record are represented Figures 5.12.g, 5.12.h, and 5.12.i. The maximum spectral accelerations ($S_a$) were evaluated at two

different periods, and the data shows that the maximum $S_a$ values decreased for the cushioned case. The decrease in maximum $S_a$ values was observed at a period of 0.08 seconds and 0.25 seconds for all three cases.

Observed general results with respect to maximum spectral accelerations at the top of the RWM for the TW cushioned cases under near field earthquakes are given in the following:

- According to results under the scaled 1999 Kocaeli EQ Motion-İzmit Station record, it was observed that the maximum spectral accelerations increased more in the 0.05-0.15 sec period range and less in the 0.25-0.35 sec period range. Under the scaled 1940 Imperial Valley EQ-El Centro Station record, the spectral acceleration in the 0.05-0.10 sec period range decreased by 22% for TW30-8cm (Case 13), and at that period range the reduction ratio varied between 6%-22% and in the 0.10-0.20 sec period range, it decreased by a maximum of 12% for the cases TW10-4cm (Case 8) and TW20-4cm (Case 9). The maximum spectral acceleration in the 0.05-0.10 sec period range decreased by a maximum of 38% for TW10-8cm (Case 11), and the reduction varied between 16%-38%. Additionally, in the 0.20-0.30 sec period range, it decreased by a maximum of 8% for TW20-8cm (Case 12) under the scaled 1995 Kobe EQ record.

- The improvement effectiveness of the thickness ratio was found to be insignificant in in the period range of both 0.05-0-15 sec and 0.25-0.35 sec under the far field earthquakes as the scaled 1999 Kocaeli EQ Motion-İzmit Station record. The thickness ratio was observed to be generally effective in decreasing the maximum spectral accelerations with increasing cushion thickness ratio in the period range of 0.05-0.10 sec, while it was observed to be less effective in the period range of 0.10-0.20 sec under the near field earthquakes as the scaled 1940 Imperial Valley EQ-El Centro Station record and the scaled 1995 Kobe EQ record. The results show that TW cushion with different thicknesses can have a significant impact on the response of the retaining wall to seismic activity at different period ranges.

- In general, the maximum reduction in spectral accelerations was observed for the TW20 and TW30 under near field earthquakes.

- Evaluation of the data indicates that the TW as a cushion type generally exhibits improvement in spectral accelerations across all cushion thicknesses and densities examined in this study under near field earthquakes as the scaled 1940 Imperial Valley EQ-El Centro Station record and the scaled 1995 Kobe EQ record as given in Figure 5.12.d-e-f and Figure 5.12.g.h.i. In consideration of the scaled real earthquakes executed, the study shows that the cushioned model TW10-8cm provides a significant improvement compared to the control model in reducing maximum spectral accelerations under the scaled 1995 Kobe EQ record with a 38% reduction (Figure 5.12.g-h-i).

- It is obvious that the period range of 0.05-0.10 sec is effective in decreasing the spectral acceleration values when taking into consideration near field earthquakes. Frequencies in the 10 Hz to 20 Hz range have been demonstrated lower the spectrum accelerations compared to the control case.

In comparison of the far field and near field effect for spectral acceleration reduction, the highest improvement effects were obtained at 0.05-0.10 sec period range in both. Though it improves to 38% under near field earthquakes, the improvement is just 16% under far field earthquakes. The higher acceleration amplitude, which is higher in the near field than the far field, is what causes this improvement impact.

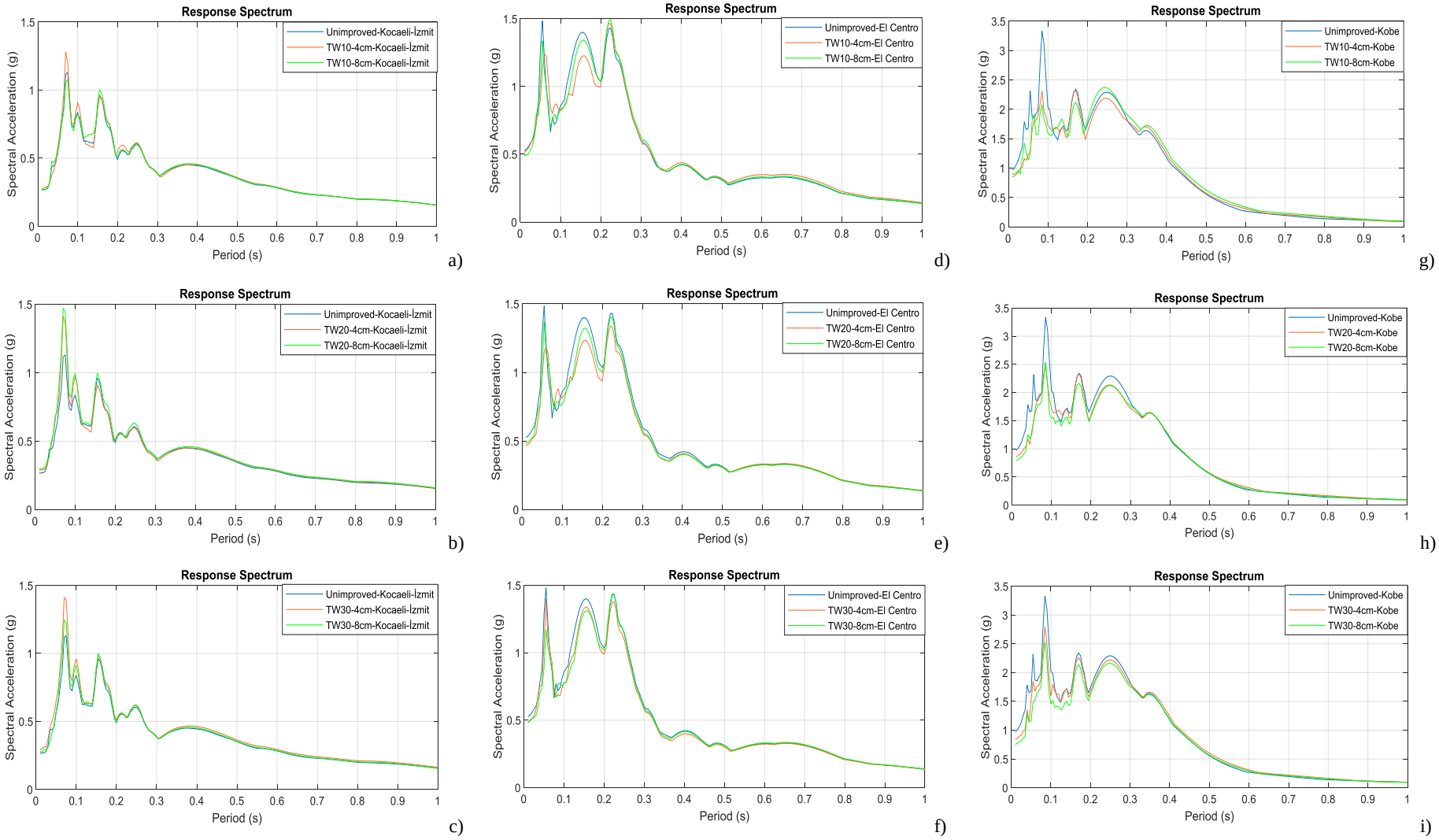


Figure 5.12 Response Spectrums of all Tire Waste and Sand Mixture cushioned cases with respect to A7 under a-b-c) the scaled 1999 Kocaeli EQ Motion-İzmit Station Record-NF, d-e-f) the scaled 1940 Imperial Valley EQ-El Centro Station record-NF, g-h-i) the scaled 1995 Kobe EQ Record-NF.

5.2.1.3. Comparison of Improvement Efficiency under Sinusoidal Motions

The improvement efficiency at the top of the RWM with respect to the cushion thickness ratio and tire waste and sand mixture ratio of the TW cushioned case compared to the control case under sinusoidal motion is discussed by evaluating Figure 5.13.

Figure 5.13.a displays the improvement efficiency for various combinations of TW under sinusoidal motion at 0.3g amplitude with 8 Hz frequency. The improvement efficiencies for cushioned cases of TW ranged from 2% to 8% under these motion characteristics. TW10-8cm showed the highest reduction of the transmitted accelerations of the retaining wall under that sinusoidal motion.

Figure 5.13.b shows the improvement efficiency for TW cushion thickness and mixture ratio under sinusoidal motion at 0.4g amplitude with 8 Hz frequency. The TW cushion type demonstrated improvement at all cushion thicknesses and mixture ratios at these input motion characteristics. The peak improvement efficiency was nearly 11% for the cushion type TW30-8cm and ranged between 5.5% and 9% for all cases of TW cushion under sinusoidal motion at 0.4g amplitude with 8 Hz frequency.

The improvement efficiency is given in Figure 5.13.c for all TW cushioned cases under sinusoidal motion at 0.5g amplitude with 8 Hz frequency. The improvement efficiencies ranged from 2% to 14% when subjected to sinusoidal motion with 0.5g amplitude with 8 Hz frequency, with the highest improvement efficiency of nearly 14% observed for the TW10-4cm. The TW cushion is somewhat effective under that input motion characteristics.

Figure 5.13.d displays the improvement efficiency for all TW cushioned cases under sinusoidal motion at 0.4g amplitude with 12 Hz frequency. The peak improvement efficiency was nearly 8% for the cushion type TW30-4cm. It can be evaluated that TW cushion is low effective at these input motion characteristics.

Under the sinusoidal motion at 0.4g amplitude with 14 Hz frequency, the improvement efficiency for all TW cushioned cases is represented in Figure 5.13.e. The peak improvement efficiency was nearly 5% for the cushion type TW10-4cm under sinusoidal motion at 0.4g amplitude with 14 Hz frequency.

The general evaluation of the results based on improvement efficiency at the top of the RWM for the TW cushioned cases under sinusoidal motions are given in the following explanations:

- The study demonstrates that the TW cushioned cases may decrease the maximum acceleration values under given sinusoidal motions compared to the control model. TW cushioned model is effective in improving the seismic performance of retaining walls. In consideration of the sinusoidal motions executed, the study shows that TW30-8cm provides significant improvement in reducing maximum acceleration up to 14% reduction under the sinusoidal motions range between 8 Hz and 12 Hz and the amplitude range between 0.3g and 0.5g. This result shows us that earthquake characteristics play an important role in improving the retaining wall.

- Increasing cushion thickness mostly affects the calculated improvement efficiencies for the TW cushioned cases under the sinusoidal motion at 0.3g amplitude with 8 Hz frequency and under the sinusoidal motion at 0.4g amplitude with 8 Hz frequency, as represented in Figure 5.13.a and Figure 5.13.b. However, no trend was observed for seismic reduction effect depending on thickness and mixture ratio under sinusoidal motion at 0.4g amplitude with 12 Hz frequency and at 0.4g amplitude with 14 Hz frequency.

- The TW ratio affects the estimated maximum improvement efficiency results depending significantly on the applied dynamic motion. The most effective mixture ratio in reaching the maximum improvement for most of the TW cushioned cases is the mixture ratio of 30% under the input sinusoidal motions, as illustrated in Figure 5.13.

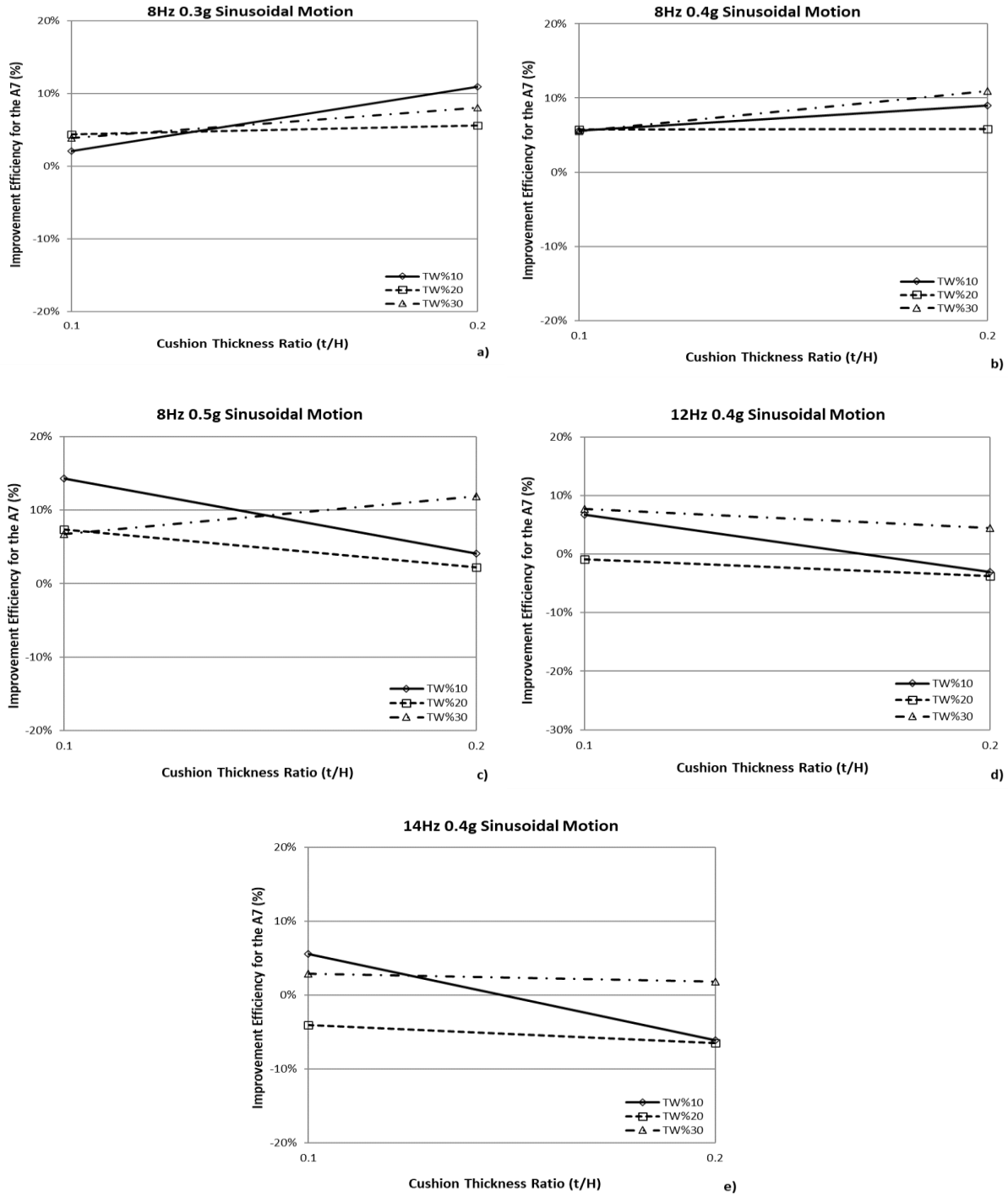


Figure 5.13. Improvement efficiency for all Tire Waste and Sand Mixture cushioned cases with respect to A7 under a) sinusoidal motion at 0.3g amplitude with 8 Hz frequency, b) sinusoidal motion at 0.4g amplitude with 8 Hz frequency, c) sinusoidal motion at 0.5g amplitude with 8 Hz frequency, d) sinusoidal motion at 0.4g amplitude with 12 Hz frequency, e) sinusoidal motion at 0.4g amplitude with 14 Hz frequency.

5.2.1.4. Comparison of Maximum Spectral Accelerations under Sinusoidal Motions

The response spectrums at the top of the RWM with respect to the cushion thickness ratio and tire waste and sand mixture ratio of the TW cushioned cases compared to the control case under sinusoidal motions are discussed by evaluating Figures 5.14 and 5.15.

The response spectrums under sinusoidal motion at 0.3g amplitude with 8 Hz frequency for TW10, TW20, and TW30 cushion with thicknesses of 4 cm and 8 cm and the control case are shown in Figure 5.14.a-c. The maximum spectral accelerations ($S_a$) occurred at a period of 0.125 sec and decreased from 3.49g to 3.42g and 3.12g for TW10-4cm and TW10-8cm, respectively. Similarly, for TW20-4cm and TW20-8cm, the $S_a$ decreased from 3.49g to 3.34g and 3.31g, respectively. For TW30-4cm and TW30-8cm, the $S_a$ decreased from 3.49g to 3.37g and 3.23g, respectively.

The response spectrums under sinusoidal motion at 0.4g amplitude with 8 Hz frequency for TW10, TW20, and TW30 cushion with thicknesses of 4 cm and 8 cm and the control case are shown in Figure 5.14.d-f. The maximum spectral accelerations ($S_a$) occurred at a period of 0.125 sec and decreased from 4.70g to 4.45g, 4.44g, and 4.43g for the TW10-4cm, TW20-4cm, and TW30-4cm cushioned cases decreased from 4.70g to 4.32g, 4.46g, and 4.22g for the TW10-8cm, TW20-8cm, and TW30-8cm cushioned cases, respectively.

The response spectrums under the sinusoidal motion at 0.5g amplitude with 8 Hz frequency for TW10, TW20, and TW30 cushion with thicknesses of 4 cm and 8 cm and the control case are shown in Figure 5.14.g-i. The maximum spectral accelerations ($S_a$) occurred at a period of 0.125 sec and decreased from 5.73g to 4.94g and 5.6g for TW10-4cm and TW10-8cm cushioned cases, respectively. For TW20-4cm and TW20-8cm cushioned cases, the maximum $S_a$ decreased from 5.73g to 5.40g and 5.70g, and for TW30-4cm and TW30-8cm cushioned cases, the maximum $S_a$ decreased from 5.73g to 5.40g and 5.09g, respectively.

The response spectrums under the sinusoidal motion at 0.4g amplitude with 12 Hz frequency for TW10, TW20, and TW30 cushion with thicknesses of 4 cm and 8 cm and the

control case are shown in Figure 5.15.a-c. The maximum spectral accelerations ($S_a$) occurred at a period of 0.085 sec. For the TW10 cases, the maximum $S_a$ decreased from 3.79g to 3.46g for the 4cm cushioned case and increased to 3.99g for the 8cm cushioned case. For the TW20 cases, the maximum $S_a$ increased from 3.79g to 3.84g for the 4cm cushioned case and 3.96g for the 8cm cushioned case. For the TW30 cases, the maximum $S_a$ decreased from 3.79g to 3.54g for the 4cm cushioned case and 3.65g for the 8cm cushioned case.

The response spectrums under the sinusoidal motion at 0.4g amplitude with 14 Hz frequency for TW10, TW20, and TW30 cushion with thicknesses of 4 cm and 8 cm and the control case are shown in Figure 5.15.d-f. The maximum spectral accelerations ($S_a$) occurred at a period of 0.07 sec. In Figure 5.15.d, the $S_a$ decreased from 4.22g to 3.92g for TW10-4cm and increased to 4.37g for TW10-8cm. In Figure 5.15.e, the $S_a$ increased from 4.22g to 4.38g for TW20-4cm and 4.52g for TW20-8cm. In Figure 5.15.f, the $S_a$ decreased from 4.22g to 4.05g for TW30-4cm and 4.07g for TW30-8cm.

Based on the evaluation of the general results with respect to maximum spectral accelerations at the top of the RWM for the TW cushioned cases under sinusoidal motions are given in the following:

- The maximum spectral accelerations at 0.125 sec period decreased with a maximum 11% reduction ratio for the case TW10-8cm (Case 10) under the sinusoidal motion at 0.3g amplitude with 8 Hz frequency, and the reduction ranged between 2%-11%. Under the sinusoidal motion at 0.4g amplitude with 8 Hz frequency, the maximum spectral accelerations at 0.125 sec period decreased with a maximum 10% reduction ratio for the TW30-8cm (Case 13), and the reduction ranged between 6%-10%. The maximum spectral acceleration at 0.125 sec period decreased by 14% for the case TW10-4cm (Case 8) under the sinusoidal motion at 0.5g amplitude with 8 Hz frequency. Under the sinusoidal motion at 0.4g amplitude with 12 Hz frequency, the maximum spectral accelerations at 0.085 sec period decreased with a maximum of 9% for the TW10-4cm. The maximum spectral accelerations at 0.07 sec period decreased by 8% for the case TW10-4cm under the sinusoidal motion at 0.4g amplitude with 14 Hz frequency.

- Thickness ratio was observed to be effective in decreasing the maximum spectral accelerations with increasing cushion thickness ratio at 0.125 sec period under the sinusoidal motion at 0.3g amplitude with 8 Hz frequency and the sinusoidal motion at 0.4g amplitude with 8 Hz frequency for TW cushioned cases. This effect is not noticeable under the rest of the sinusoidal input motions. As represented in Figure 5.14.a-b-c and Figure 5.14.d-e-f, maximum spectral accelerations decreased with respect to the increase of cushion thickness.

- The mixture ratio of TW cushion has a significant impact on the maximum spectral acceleration results. Increasing the mixture ratio of TW material generally leads to a decrease in maximum spectral accelerations under sinusoidal motions with 0.3g, 0.4g, and 0.5g amplitude with 8 Hz frequency, particularly at a period of 0.125 sec. Also, at a period of 0.085 sec and at 0.4g amplitude with 12 Hz frequency, increasing mixture ratio of the TW material generally reduces maximum spectral accelerations. On the other hand, increasing mixture ratio does not affect the maximum spectral accelerations under sinusoidal motion at 0.4g amplitude with 14 Hz frequency. The TW30 had the most significant decrease in spectral accelerations under all input sinusoidal motions, as shown in Figures 5.14 and 5.15.

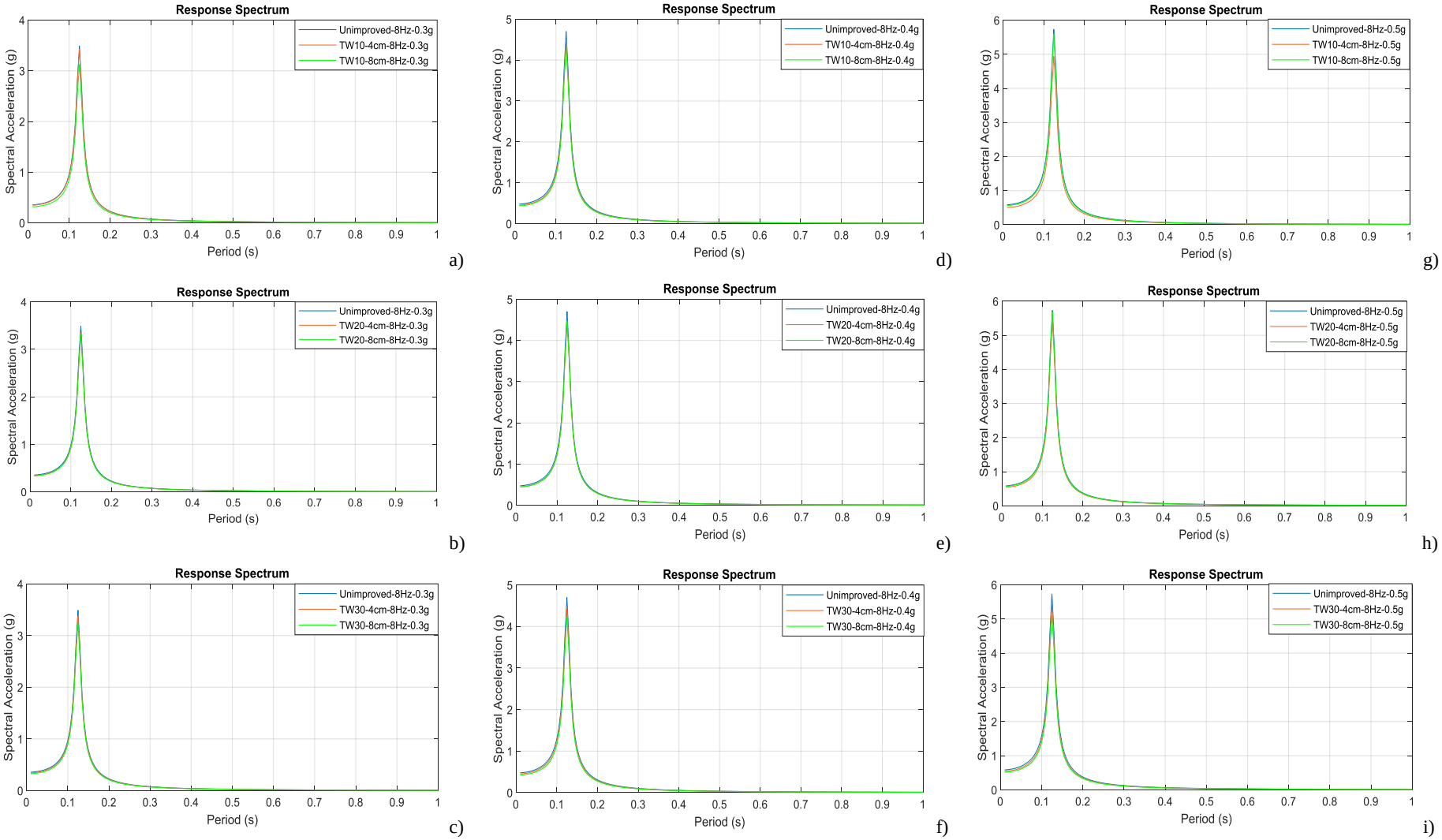


Figure 5.14 Response Spectrums of all Tire Waste and Sand Mixture cushioned cases with respect to A7 under a-b-c) sinusoidal motion at 0.3g amplitude with 8 Hz frequency, d-e-f) sinusoidal motion at 0.4g amplitude with 8 Hz frequency, g-h-i) sinusoidal motion at 0.5g amplitude with 8 Hz frequency.

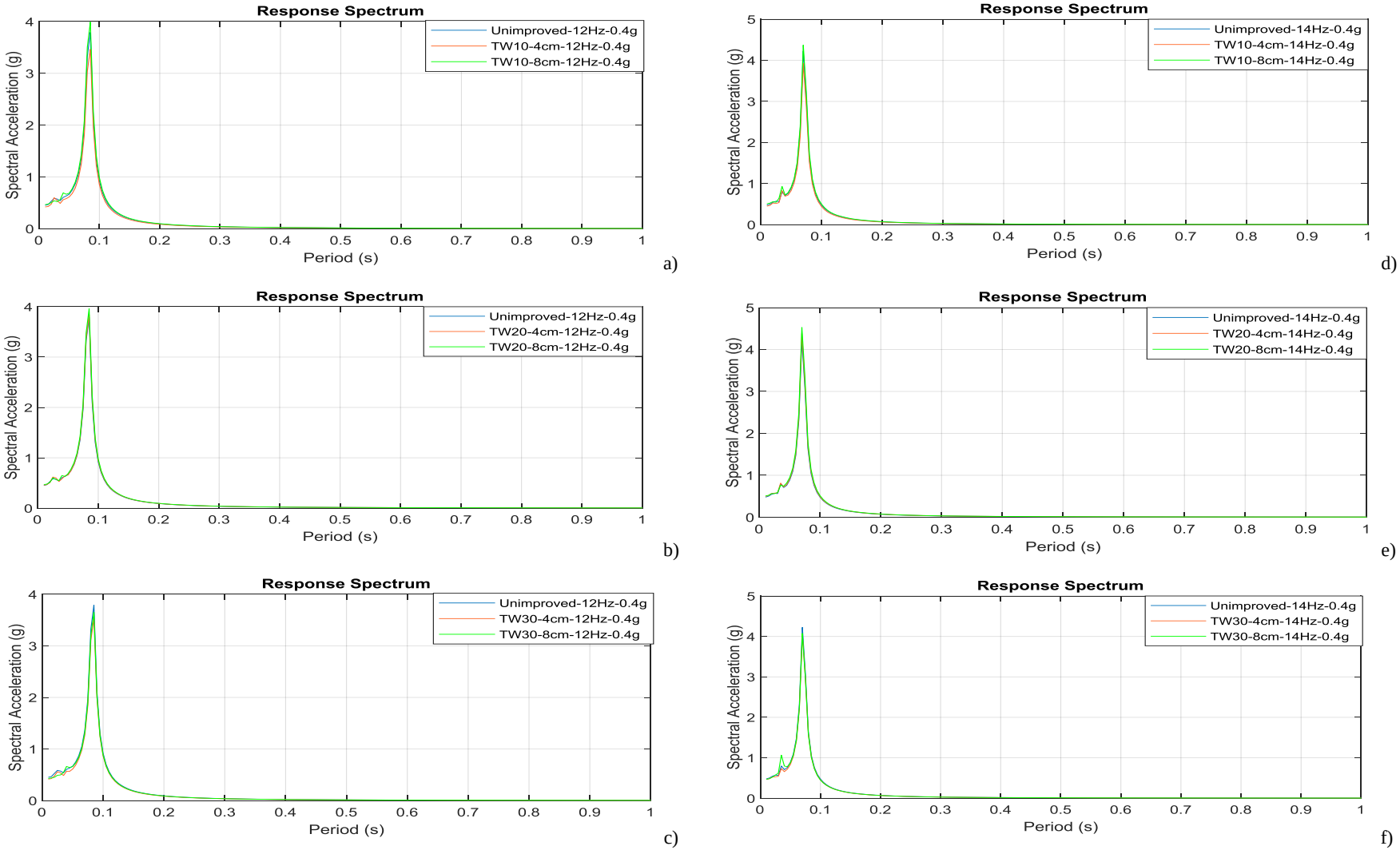


Figure 5.15 Response Spectrums of all Tire Waste and Sand Mixture cushioned cases with respect to A7 under a-b-c) sinusoidal motion at 0.4g amplitude with 12 Hz frequency, d-e-f) sinusoidal motion at 0.4g amplitude with 14 Hz frequency.

### 5.2.2. The Effects of Acceleration Response for Tire Waste and Sand Mixture Cushion under Different Input Motions

The variation of maximum accelerations at the top of the RWM for TW cushioned cases at different thicknesses and mixture ratios compared with the control case under all input motions are shown in Figure 5.16 and Figure 5.17.

#### 5.2.2.1. Maximum Acceleration Comparison at 4 cm Thickness

The maximum transmitted accelerations of the TW10-4cm, TW20-4cm and TW30-4cm cases at the top of the RWM are compared with the maximum transmitted accelerations of the control case considering the PGA of the input motions. PGA of the input motions are 0.12g, 0.14g, 0.18g, 0.22g, 0.32g, 0.82g, and sinusoidal motions at 0.3g amplitude with 8 Hz frequency, at 0.4g amplitude with 8 Hz frequency, at 0.5g amplitude with 8 Hz frequency, at 0.4g amplitude with 12 Hz frequency, at 0.4g amplitude with 14 Hz frequency (Figure 5.16).

The comparisons of the maximum transmitted accelerations measured from A7 for the control case and for TW cushioned cases with 4 cm thickness as Case 8, Case 9, and Case 10 with the PGA of input motions are shown in Figure 5.16. As seen in Figure 5.16, the study conducted using six different earthquake records and five different sinusoidal motions shows that the maximum accelerations of the control case amplify under all earthquake and sinusoidal motions except for the scaled 1999 Kocaeli EQ Motion-İznik Station record, compared to the PGA of input motions. Compared to the control case, the deamplification in maximum accelerations for most of the TW cushioned cases with 4 cm thickness is observed under both near field earthquakes, far field earthquakes and sinusoidal motions.

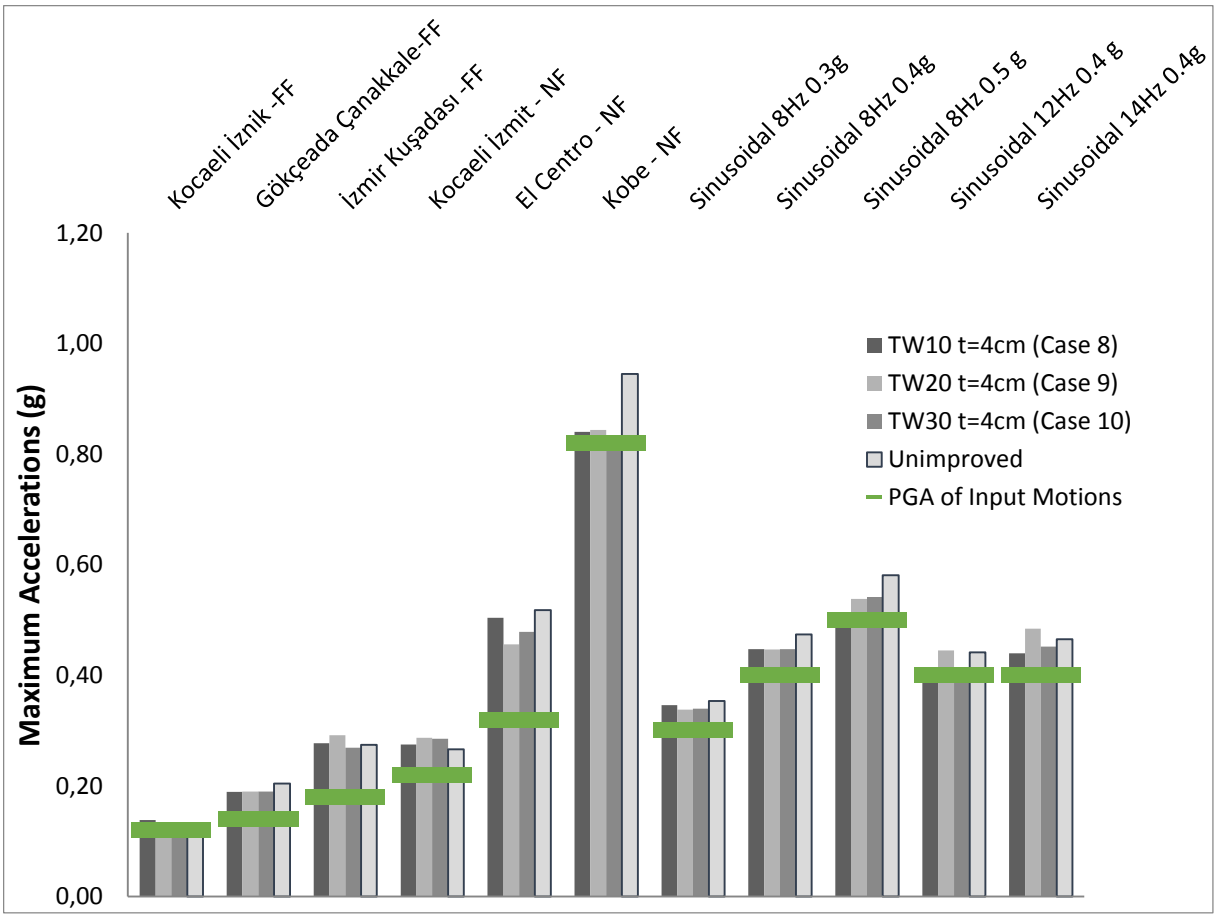


Figure 5.16 Variation of maximum accelerations at the top of the RWM for Tire Waste and Sand Mixture cases with t=4cm compared to the control case under all input motions.

When the maximum acceleration recordings measured from A7 are compared to the control case, the highest decrease in maximum acceleration values is seen under the scaled 1995 Kobe EQ record for cushion type TW30-4cm (Case 10). Under sinusoidal motions, a decrease in maximum acceleration is generally observed for the cushion types TW10-4cm (Case 8) and TW30-4cm compared to the control case. A minor decrease in maximum acceleration values is observed under the scaled 2014 Gökçeada EQ Motion-Çanakkale Station record and the scaled 1940 Imperial Valley EQ-El Centro Station record and no significant difference in maximum accelerations is observed under the scaled 1999 Kocaeli EQ Motion-İznik Station record, the scaled 2020 İzmir EQ Motion-Kuşadası Station record, and the scaled 1999 Kocaeli EQ Motion-İzmit Station record compared to the control case.

5.2.2.2. Maximum Acceleration Comparison at 8 cm Thickness

The maximum transmitted accelerations of the TW10-8cm, TW20-8cm and TW30-8cm cases at the top of the RWM are compared with the maximum transmitted accelerations of the control case considering the PGA of the input motions. PGA of the input motions are 0.12g, 0.14g, 0.18g, 0.22g, 0.32g, 0.82g, and sinusoidal motions at 0.3g amplitude with 8 Hz frequency, at 0.4g amplitude with 8 Hz frequency, at 0.5g amplitude with 8 Hz frequency, at 0.4g amplitude with 12 Hz frequency, at 0.4g amplitude with 14 Hz frequency (Figure 5.17).

The comparisons of maximum transmitted accelerations measured from A7 for the control case and for TW cushioned cases with 8 cm thickness as Case 11, Case 12, Case 13 with the PGA of input motions are shown in Figure 5.17. As seen in Figure 5.17, the study conducted using 6 different earthquake records and 5 different sinusoidal motions shows that the maximum accelerations of the control case amplify under all earthquake and sinusoidal motions except for the scaled 1999 Kocaeli EQ Motion-İznik Station record, compared to the PGA of input motions. The deamplification in maximum accelerations for most of the TW cushioned cases with 8 cm thickness is observed under both near field earthquakes, far field earthquakes and sinusoidal motions compared to the control case.

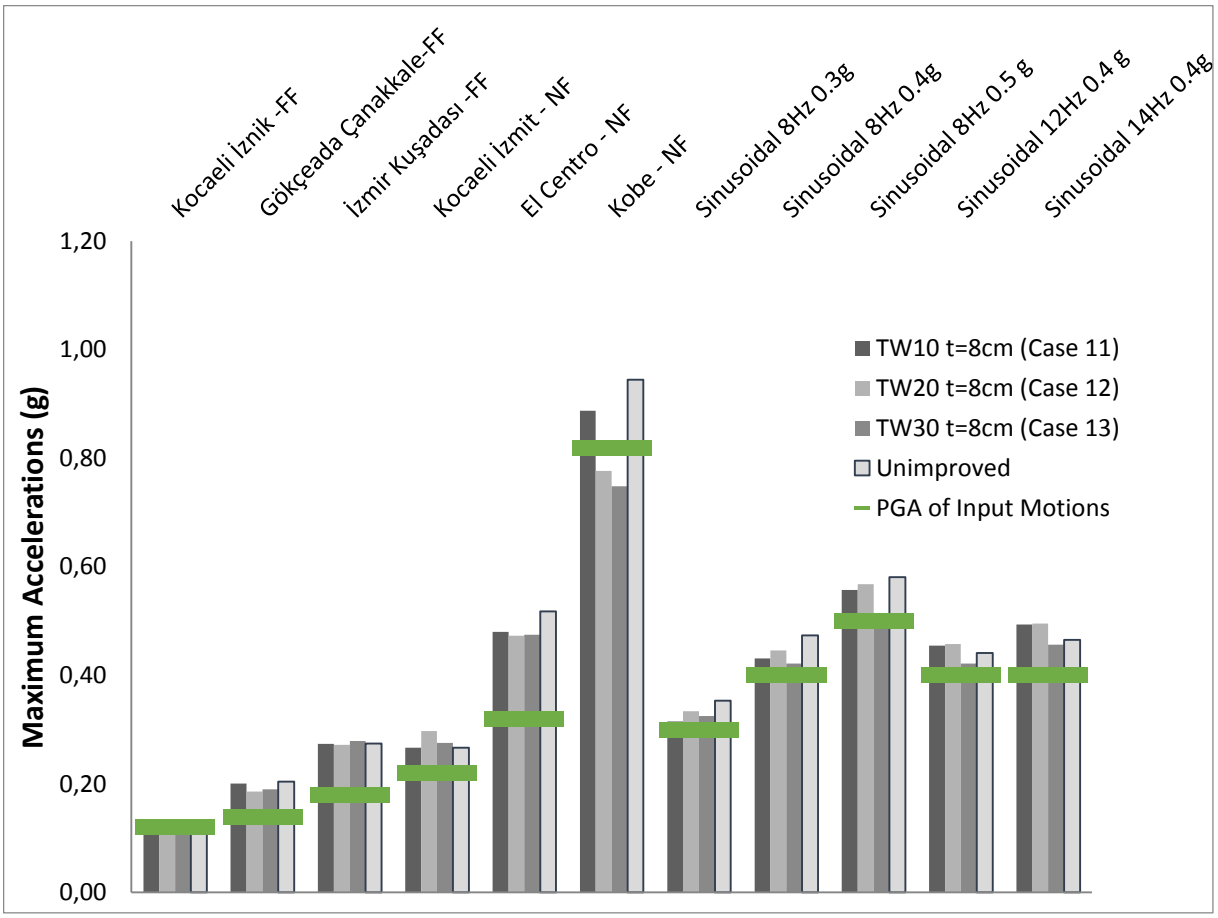


Figure 5.17 Variation of maximum accelerations at the top of the RWM for Tire Waste and Sand Mixture cases with t=8cm compared to the control case under all input motions.

In comparison of the maximum acceleration measurements from A7 to the control case, the highest decrease in maximum acceleration values is seen under the scaled 1995 Kobe EQ record for cushion type TW30-8cm (Case 13). Under sinusoidal motions, a reduction of maximum accelerations is generally observed for the cushion type TW30-8cm. A slight reduction in maximum acceleration values is observed under the scaled 2014 Gökçeada EQ Motion-Çanakkale Station record and the scaled 1940 Imperial Valley EQ-El Centro Station record, and no significant difference in maximum accelerations is observed under the scaled 1999 Kocaeli EQ Motion-İznik Station record, the scaled 2020 İzmir EQ Motion-Kuşadası Station record, and the scaled 1999 Kocaeli EQ Motion-İzmit Station record compared to the control case.

### 5.2.3. Maximum Lateral Displacements for Tire Waste and Sand Mixture Cushion Cases under All Input Motions

Two laser displacement sensors have been installed on the RWM, one at the height of H as D19 and the other at the height of 0.5H as D18, as shown in Figure 3.27 and Figure 3.29 in Chapter 3. Figure 5.18 shows the comparison of the maximum lateral displacements at the top of the retaining wall model with respect to cushion thickness ratio and tire waste and sand mixture ratio for the TW cushioned cases under the given earthquake and sinusoidal motions. The figures include seven different cases (Case 1, Case 8, Case 9, Case 10, Case 11, Case 12, and Case 13) and show the maximum lateral displacements for each case. The control case is shown in Figure 5.9.a, while the remaining cases are shown in Figures 5.9.b to 5.9.g. Each figure shows the maximum lateral displacements for a particular case under different input motions, including far field and near field earthquakes and sinusoidal motions. The maximum lateral displacements for Case 1 under far field and near field earthquakes and sinusoidal motions were explained in Part 5.1.3 and can be seen in Figure 5.18.a.

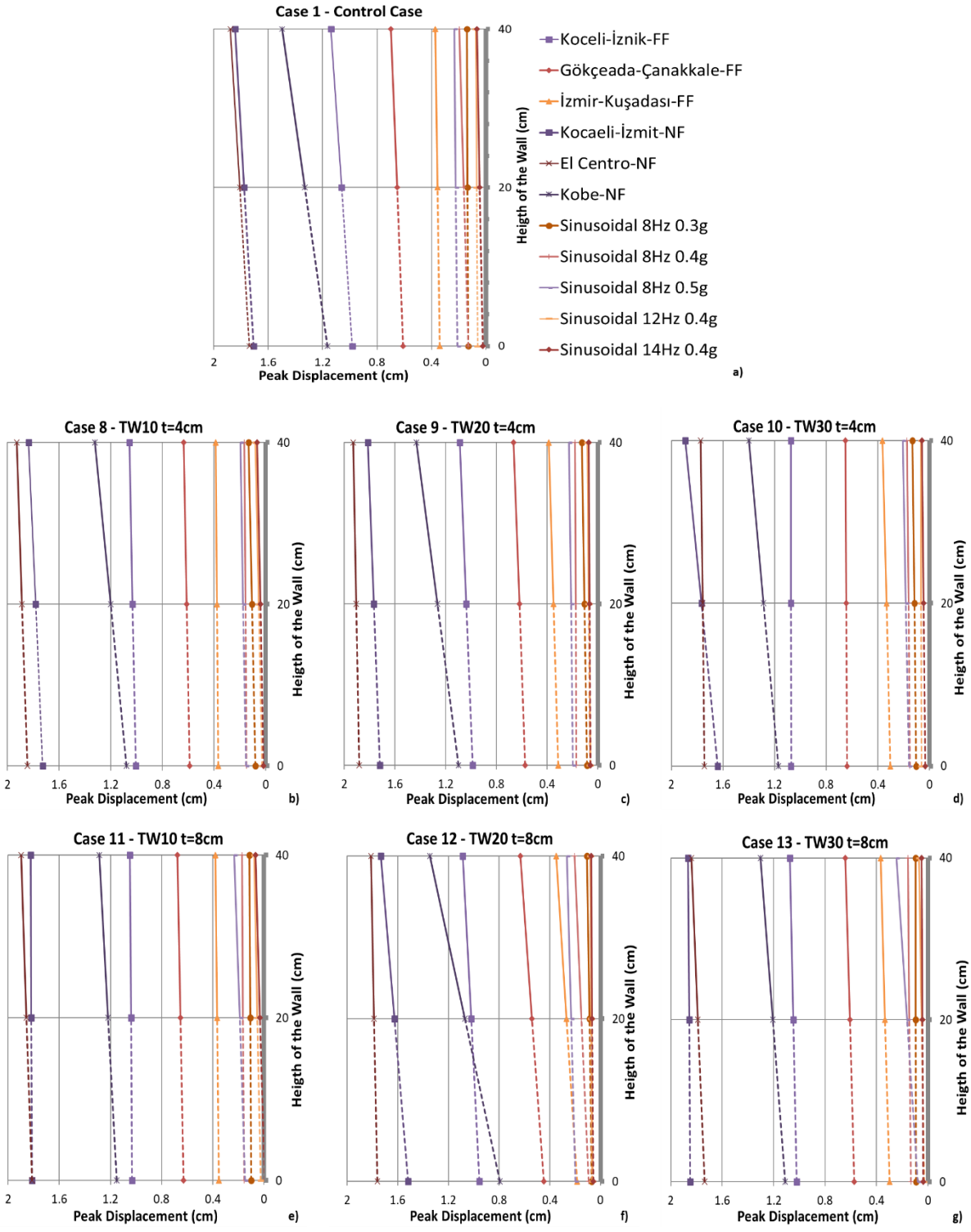


Figure 5.18. Maximum lateral displacements measured from D19 under all input motions a) Case 8, b) Case 9, c) Case 10, d) Case 11, e) Case 12, f) Case 6, g) Case 13.

The evaluation of the results of the maximum lateral displacements at the top of the RWM for the TW cushioned cases compared with the cushioned case under all given input motions is summarized as follows:

- In consideration of the maximum lateral displacements given in Figure 5.18, it has been observed that under sinusoidal motion, the displacements are lower, whereas under the effect of earthquake motions, higher displacements occur. Comparing far field and near field earthquakes reveals that greater displacements occur under near field earthquakes (Figure 5.18.a-g).

- All the TW cushioned cases were compared with the control case, and the results were evaluated under all input motions. Taking into account thickness and mixture ratio changes in each case of TW, the highest and the lowest reduction in displacement were 8% and 6% under the scaled 1999 Kocaeli EQ Motion-İznik Station record, respectively. TW10-8cm is the most effective case that can reduce the amount of displacement values measured at the top of the RWM. The maximum lateral displacement reduction under the scaled 2014 Gökçeada EQ Motion-Çanakkale Station record was 9% and 3%, respectively, and the peak was mitigated for the TW20-8cm application. The highest decrease in maximum lateral displacement was 5.5% under the scaled 2020 İzmir EQ Motion-Kuşadası Station record. The highest reduction for maximum lateral displacement was observed for the TW20-8cm cushioned model. Under the scaled 1999 Kocaeli EQ Motion-İzmit Station record, the highest reduction for displacement was 6% for the case TW20-8 cm. The highest reduction value for the case of TW30-4cm under the scaled 1940 Imperial Valley EQ-El Centro Station record is 5.5%. For the case TW10-8cm, the peak reduction was 13% and for the rest of the cases, it is minimum 4.5% under the scaled 1995 Kobe EQ record. The reduction in maximum lateral displacements varied depending on the far field and near field earthquakes, with the highest reduction ratio observed for the TW10-8cm cushioned model under the scaled 1995 Kobe EQ record and for the TW20-8cm cushioned model under the scaled 2014 Gökçeada EQ Motion-Çanakkale Station record (far field).

- The highest and the lowest reduction in maximum lateral displacements were 31% and 4.5% under sinusoidal motion at 0.3g amplitude with 8 Hz frequency, respectively. TW30-8cm. In this scenario, it was observed that TW30-8cm is the most effective in reducing the displacement values at the top of the RWM. Under sinusoidal motion at 0.4g amplitude with 8 Hz frequency, the reduction in displacement was up to 20% for TW30 with a thickness of 8 cm.

- For sinusoidal motion at 0.5g amplitude with 8 Hz frequency, the highest and lowest reduction in maximum lateral displacement was 15.5% for the model with TW10 and a thickness of 4 cm. Under sinusoidal motion at 0.4g amplitude with 12 Hz frequency, the case with TW30-4cm showed the highest reduction in displacement with a value of 14%. Under sinusoidal motion at 0.4g amplitude with 14 Hz frequency, the highest and lowest reduction in displacement exhibited 59% and 12%, respectively. Considering the changes in thickness and mixture ratios of TW cushion, TW10-8cm is shown to be the most effective case in reducing displacement.

- The study showed that using TW cushioning in combination with a sand backfill can significantly reduce maximum lateral displacements during the excitation of sinusoidal motions. The highest improvement effect was observed for the TW30-8cm cushioned model under the sinusoidal motion at 0.3g and 0.4g amplitudes with 8 Hz frequency. TW cushion is effective as a cushion at the input motion characteristics under sinusoidal motions in the frequency range between 8 Hz and 14 Hz and the amplitude range between 0.3g and 0.5g in reducing the maximum lateral displacement of the model.

## 5.3. The Effects of EPS Beads and Sand Mixture Cushion on the Seismic Performance of the Retaining Wall Model

The effects of thickness and density concerning improvement efficiency and spectral acceleration, the effects of acceleration response, and the comparison of maximum lateral displacements under the given near field and far field earthquake and sinusoidal motions are explained for EPS beads and sand mixture cushion in this part of the study.

### 5.3.1. The Effects of Thickness and Mixture Ratio of EPS Beads and Sand Mixture Cushion

The experimental studies of the EPS beads and sand mixture (EPSB) cushioned cases are conducted for three mixture ratios as 10% (EPSB10), 20% (EPSB20), and 30% (EPSB30) EPS Beads additive for three thicknesses 4 cm, 6 cm, 8 cm regarding 0.10, 0.15, and 0.20 t/H ratios respectively. These cases are listed from Case 14 to Case 22, as explained in Table 6 in Chapter 3. Each of these cases was compared with the control case (Case 1), and the improvement efficiency was calculated for each case.

The improvement efficiency for each cushion thickness ratio (t/H) and mixture ratio under all input motions are given in this part of the study. The influence of mixture ratio, thickness, and input excitation on the seismic performance of the EPSB cushioned retaining wall model is investigated based on the improvement efficiencies and spectral accelerations in comparison to Case 1. The EPSB cushioned cases, Cases 14 to Case 22, with comparisons to Case 1, have been reported under the defined input motions.

5.3.1.1. Comparison of Improvement Efficiency under Far Field and Near Field Earthquake Motions

The improvement efficiency at the top of the RWM with respect to the cushion thickness ratio and EPSB mixture ratio of the EPSB cushioned case compared to the control case under far field and near field earthquakes is discussed by evaluating Figure 5.19.

The improvement efficiency under the scaled 1999 Kocaeli EQ Motion-İznik Station record is represented in Figure 5.19.a. The improvement efficiency for the EPSB cushioned case was limited to 0.1% when the EPSB10 was used with a cushion thickness ratio of 0.2. For the rest of the EPSB ratios and the cushion thickness ratios, the EPSB cushion inclusion was not effective on the seismic performance.

The improvement efficiency under the scaled 2014 Gökçeada EQ Motion-Çanakkale Station record is represented in Figure 5.19.b. The improvement efficiency for the EPSB cushioned case was 1% when the EPSB10 was used with the cushion thickness ratio of 0.15. For the rest of the EPSB ratios and the cushion thickness ratios, the EPSB cushion inclusion was not effective on the seismic performance.

The improvement efficiency under the scaled 2020 İzmir EQ Motion-Kuşadası Station record is represented in Figure 5.19.c. The obtained results show that the improvement efficiency for the EPSB cushioned case was up to 3% when the EPSB20 was used with the cushion thickness ratio of 0.2. For the rest of the EPSB densities and the cushion thicknesses, an improvement effect was not observed.

Under the scaled 1999 Kocaeli EQ Motion-İzmit Station record, the improvement efficiency is represented in Figure 5.19.d. In comparison to the control case, no acceleration reduction was observed for all EPS bead densities and the cushion thickness ratios of the EPSB cushioned cases under this dynamic motion.

The improvement efficiency under the scaled 1940 Imperial Valley EQ-El Centro Station record is represented in Figure 5.19.e. The EPSB cushioned cases demonstrated improvement at all cushion thicknesses and mixture ratios. The maximum improvement efficiency was obtained to be around 10% for EPSB20 with a cushion thickness ratio of 0.1. For the other EPSB cushioned cases, the improvement efficiency values were in the range of 2% to 9%.

Under the scaled 1995 Kobe EQ record, the improvement efficiency is represented in Figure 5.19.f. The improvement efficiency for the EPSB cushioned case was up to 4% when EPSB10-8cm under the given dynamic motion effect.

The general evaluation of the results based on improvement efficiency at the top of the RWM for the EPSB cushioned cases under far field and near field earthquakes are given in the following explanations:

- As given in Figure 5.19, the improvement efficiencies are much higher in near field earthquakes than far field earthquakes. In Figure 5.19.e, the maximum improvement efficiency is calculated as 10% under the scaled 1940 Imperial Valley EQ-El Centro Station record. In Figure 5.19.e, the increase in EPSB ratio and cushion thickness ratio combined leads to higher improvement efficiency values, which highlights the importance of earthquake characteristics on the dynamic response of the retaining wall. On the other hand, the improvement efficiency is limited to 3% under the scaled 2020 İzmir EQ Motion-Kuşadası Station record (Figure 5.19.b).

- Increasing cushion thickness positively affects the calculated improvement efficiencies for EPSB cushioned cases. In Figure 5.19, improvement efficiencies increase with respect to increasing cushion thickness for some of the EPSB cushioned cases.

- The effect of EPSB cushion mixture ratio on the calculated maximum improvement efficiency results is highly dependent on the applied dynamic motion. In Figure 5.19.e,

the maximum improvement efficiency is calculated as 7.5% for EPSB10, 9% for EPSB20, and 9.5% for EPSB30, respectively. This indicates that the increasing EPS beads ratio slightly affects the improvement efficiencies positively.

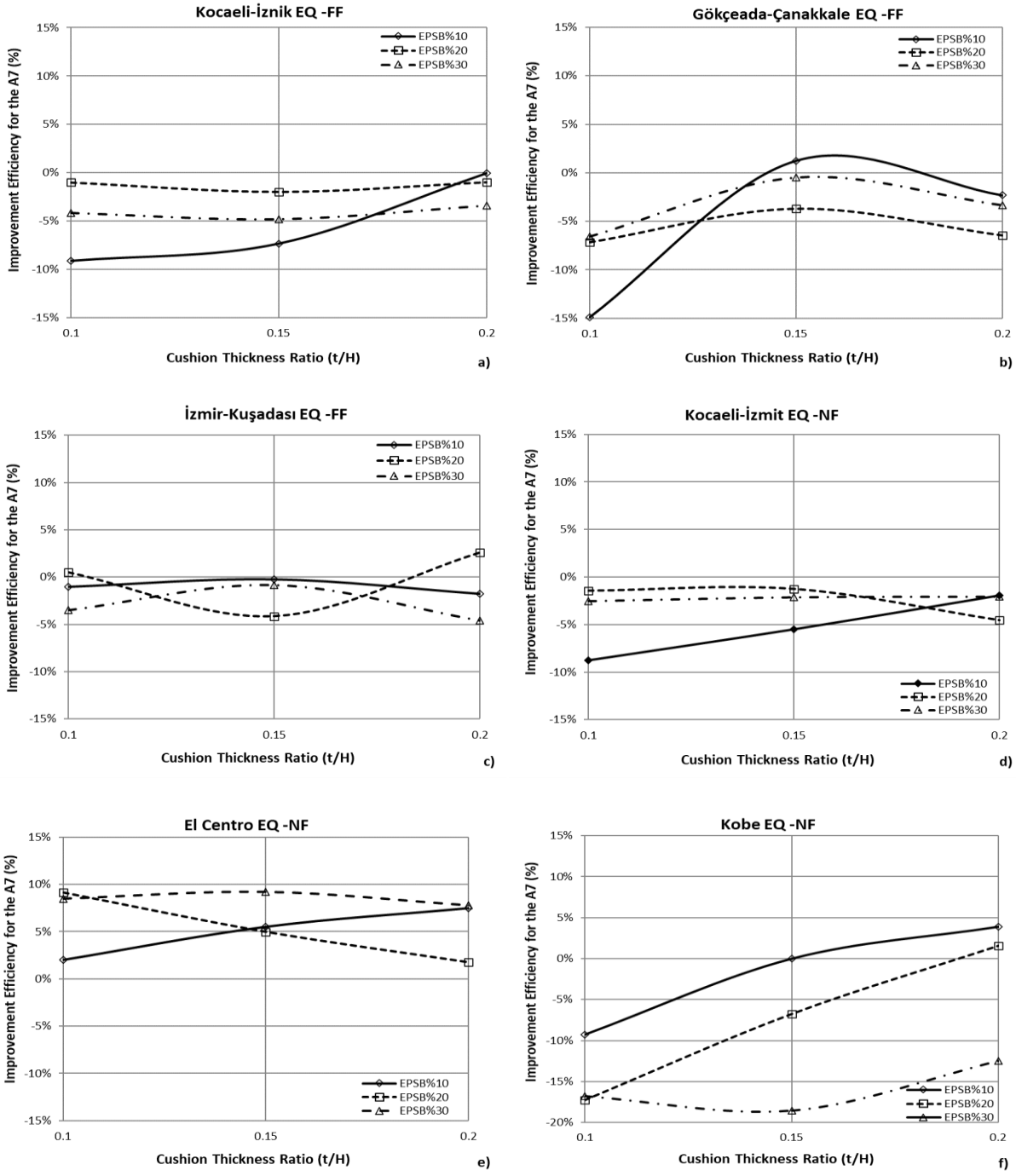


Figure 5.19. Improvement efficiency for all EPS Beads and Sand Mixture cushioned cases with respect to A7 under a) the scaled 1999 Kocaeli EQ Motion-İznik Station Record-FF, b) the scaled 2014 Gökçeada EQ Motion-Çanakkale Station Record-FF, c) the scaled 2020 İzmir EQ Motion-Kuşadası Station Record-FF, d) the scaled 1999 Kocaeli EQ Motion-İzmit Station Record-NF, e) the scaled 1940 Imperial Valley EQ-El Centro Station record-NF, f) the scaled 1995 Kobe EQ Record-NF.

5.3.1.2. Comparison of Maximum Spectral Accelerations under Far Field and Near Field Earthquake Motions

The response spectrums at the top of the RWM with respect to cushion thickness ratio and mixture ratio of the EPSB cushioned cases compared to the control case under far field earthquakes are discussed by evaluating Figure 5.20.

The response spectrums for EPSB10, EPSB20, and EPSB30 with thicknesses 4 cm, 6 cm, and 8 cm and the control case under the scaled 1999 Kocaeli EQ Motion-İznik Station record are presented in Figure 5.20.a, 5.20.b, and 5.20.c. The maximum spectral accelerations ($S_a$) were evaluated at two different time periods, 0.12 and 0.30 seconds, at the top of the RWM. For EPSB10 cushioned cases, the maximum $S_a$ values increased from 0.39g to 0.47g, 0.48g, and 0.51g at a period of 0.12 seconds, and from 0.42g to 0.45g, 0.44g, and 0.46g at a period of 0.30 seconds. For EPSB20 cushioned cases, the maximum $S_a$ values increased from 0.39g to 0.47g, 0.47g, and 0.48g at a period of 0.12 seconds, and from 0.42g to 0.44g, 0.45g, and 0.46g at a period of 0.30 seconds. For EPSB30 cushioned cases, the maximum $S_a$ values increased from 0.39g to 0.52g, 0.47g, and 0.48g at a period of 0.12 seconds, and from 0.42g to 0.46g, 0.46g, and 0.44g at a period of 0.30 seconds.

The response spectrums for EPSB10, EPSB20, and EPSB30 with thicknesses 4 cm, 6 cm, and 8 cm and the control case under the scaled 2014 Gökçeada EQ Motion-Çanakkale Station record are represented in Figure 5.20.d, Figure 5.20.e, and Figure 5.20.f. Evaluating the maximum spectral accelerations ($S_a$) at two different periods for each case. At a period of 0.11 seconds, the maximum $S_a$ values increased for all cushioned cases. At a period of 0.22 seconds, the maximum $S_a$ values decreased for most of the EPSB cushioned cases depending on the thickness of the cushioning material.

The response spectrums for the control case and for EPSB10, EPSB20, and EPSB30 with thicknesses of 4 cm, 6 cm, and 8 cm was evaluated under the scaled 2020 İzmir EQ Motion-Kuşadası Station record. Figure 5.20.g, Figure 5.20.h, and Figure 5.20.i represent the maximum spectral accelerations ($S_a$) at two different periods for each case. At a period of 0.06

seconds, the maximum $S_a$ values for the EPSB10 cases increased from 0.98g to 0.99g and decreased to 0.97g and 0.91g, while for the EPSB20 cases, the maximum $S_a$ values changed from 0.98g to 0.97g, 0.93g, and 0.83g, and for the EPSB30 cases, the maximum $S_a$ values decreased from 0.98g to 0.96g, 0.96g, and 0.97g. At a period of 0.11 seconds, the maximum $S_a$ values for the EPSB10 cases decreased from 0.93g to 0.86g, 0.77g, and 0.91g, while for the EPSB20 cases, the maximum $S_a$ values decreased from 0.93g to 0.92g, 0.92g, and increased to 1.01g, and for the EPSB30 cases, the maximum $S_a$ values increased from 0.93g to 0.95g, 0.94g, and decreased to 0.92g.

Observed general results with respect to maximum spectral accelerations at the top of the RWM for the EPSB cushioned cases under far field earthquakes are given in the following:

- The effect of EPS geofoam density on the maximum spectral acceleration results is highly dependent on the applied dynamic motion. In general, the EPS20 density has the maximum decrease in spectral accelerations observed under the far field earthquakes.

- The maximum spectral accelerations increased more in the 0.05-0.15 sec period range and less in the 0.25-0.35 sec period range, according to results under the scaled 1999 Kocaeli EQ Motion-İznik Station record. Under the scaled 2014 Gökçeada EQ Motion-Çanakkale Station record, an increase in spectral accelerations has been observed for the EPSB cushioned cases in the 0.05-0.15 sec period range. Additionally, within the 0.25-0.35 second period range, the maximum decrease in spectral acceleration was 8% for both EPSB30-6cm (Case 19) and EPSB30-8cm (Case 22). For the rest of the EPSB cushioned cases, it was observed up to 6%. The maximum spectral acceleration in the 0.05-0.10 sec period range decreased by a maximum of 18% for EPSB20-8cm (Case 21), and in the 0.10-0.15 sec period range, decreased by a maximum of 17% for EPSB10-6cm (Case17). For the rest of the EPSB cushioned cases, it was observed up to 8%.

- The effectiveness of the thickness ratio was found to be insignificant in in the period range of both 0.05-0-15 sec and 0.25-0.35 sec under the far field earthquakes as the scaled 1999 Kocaeli EQ Motion-İznik Station record. Under the scaled 2014 Gökçeada EQ Motion-Çanakkale Station record, it was observed that the improvement effectiveness increased as the thickness increased. The largest decrease in maximum spectral accelerations, as shown by the cushion thickness ratio, is 18% for 8 cm thickness under the scaled 2020 İzmir EQ Motion-Kuşadası Station record, which has earthquake characteristics with a 24.4 Hz predominant frequency and 0.18g amplitude.

- In general, the EPSB20 and the EPSB30 have the maximum reduction in spectral accelerations under far field earthquakes. This conclusion can be drawn from the effect of the EPSB ratio on the maximum spectral acceleration results.

- The data analysis indicates that the EPSB cushion type exhibit a little improvement in spectrum accelerations for all cushion thicknesses and mixture ratios for far field earthquakes, as illustrated in Figure 5.20. Considering the scaled real earthquakes that were carried out, the study demonstrates that the cushioned model, which are EPSB20-6cm and EPSB20-8cm improves the RWM in terms of lowering maximum spectral accelerations under the scaled 2020 İzmir EQ Motion-Kuşadası Station record by 18%. However, under the scaled 2014 Gökçeada EQ Motion-Çanakkale Station record, the improvement efficiency is limited to 6% (Figure 5.20.d-e-f).

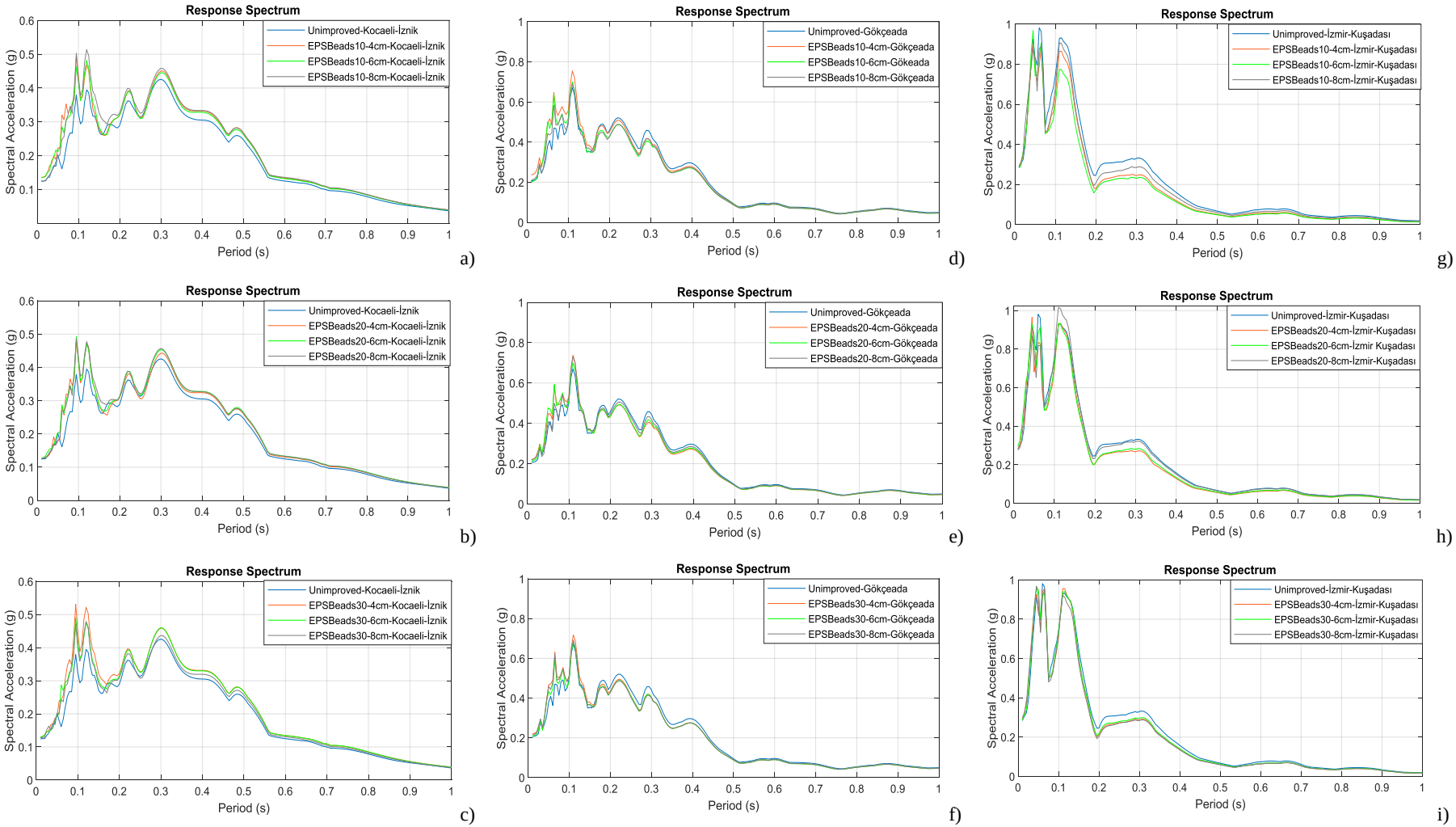


Figure 5.20 Response Spectrums of all EPS Beads and Sand Mixture cushioned cases with respect to A7 under a-b-c) the scaled 1999 Kocaeli EQ Motion-İznik Station Record-FF, d-e-f) the scaled 2014 Gökçeada EQ Motion-Çanakkale Station Record-FF, g-h-i) the scaled 2020 İzmir EQ Motion-Kuşadası Station Record-FF.

The response spectrums at the top of the RWM with respect to cushion thickness ratio and mixture ratio of the EPSB cushioned cases compared to the control case under near field earthquakes are discussed by evaluating Figure 5.21.

The response spectrums for the control case and for EPSB10, EPSB20, and EPSB30 with thicknesses of 4cm, 6cm, and 8cm were evaluated under the scaled 1999 Kocaeli EQ Motion-İzmit Station record. Figures 5.21a, 5.21b, and 5.21c show the maximum spectral accelerations ($S_a$) at two different periods for each case. At a period of 0.07 seconds, the maximum $S_a$ values increased for all cushioned cases. At a period of 0.15 seconds, the maximum $S_a$ values increased for some of the EPSB cushioned cases but decreased for other EPSB cushioned cases.

The response spectrums for the control case and EPSB10, EPSB20, and EPSB30 with cushion thicknesses of 4cm, 6cm, and 8cm under the scaled 1940 Imperial Valley EQ-El Centro Station record are presented in Figures 5.21.d, 5.21.e, and 5.21.f. The maximum spectral accelerations ($S_a$) were evaluated at two different periods. At a period of 0.055 seconds, the maximum $S_a$ values decreased for all cushion thicknesses for the EPSB10 and EPSB20 cases, while for the EPSB30 cases, the maximum $S_a$ values decreased for the cushion thickness of 4cm and increased for the cushion thicknesses of 6cm and 8cm. At a period of 0.15 seconds, the maximum $S_a$ values increased for all cushion thicknesses for the EPSB10 and EPSB20 cases, while for the EPSB30 cases, the maximum $S_a$ values almost remained constant for all cushion thicknesses. The EPSB cushioned cases showed an improvement effect by reducing the maximum $S_a$ values for the EPSB20 cases.

The response spectrums for the control case and for EPSB10, EPSB20, and EPSB30 cushioned cases with thicknesses of 4cm, 6cm, and 8cm under the scaled 1995 Kobe EQ record are shown in Figures 5.21.g, 5.21.h, and 5.21.i. At a period of 0.08 seconds, the maximum $S_a$ values increased for EPSB10-4cm and EPSB10-6cm, decreased for EPSB10-8cm, EPSB20-4cm, and EPSB20-8cm, and increased for EPSB20-6cm and for all EPSB30 cushioned cases. At a period of 0.25 seconds, the maximum $S_a$ values increased for EPSB10-4cm and EPSB20 and EPSB30 cushioned cases and decreased for EPSB-6cm and EPSB-8cm cushion cases.

Observed general results with respect to maximum spectral accelerations at the top of the RWM for the EPSB cushioned cases under near field earthquakes are given in the following:

- According to results under the scaled 1999 Kocaeli EQ Motion-İzmit Station record, it was discovered that the maximum spectral accelerations increased more in the 0.05-0.15 sec period range and less in the 0.25-0.35 sec period range. Under the scaled 1940 Imperial Valley EQ-El Centro Station record, the maximum spectral acceleration in the 0.05-0.10 sec period range decreased by 28% for EPSB20-8cm (Case 21), and at that period range, the reduction varied between 2%-20% for the rest of the EPSB cushioned cases and in the 0.10-0.20 sec period range, no reduction in spectral accelerations was observed. The maximum spectral acceleration in the 0.05-0.10 sec period range decreased by a maximum of 17% for EPSB20-8cm (Case 21). Additionally, in the 0.20-0.30 sec period range, it decreased up to 3% for EPSB10-8cm (Case 20) under the scaled 1995 Kobe EQ record.

- The thickness ratio was found to be insignificant in the 0.05-0.15 sec and 0.25-0.35 sec ranges under the scaled 1999 Kocaeli EQ Motion-İzmit Station record. However, in the 0.05-0.10 sec range, increasing cushion thickness ratio generally decreased maximum spectral accelerations under the scaled 1940 Imperial Valley EQ-El Centro Station record and the scaled 1995 Kobe EQ record. In contrast, the thickness ratio was less effective in the 0.10-0.20 sec range. Increasing cushion thickness had generally impact on reducing spectral accelerations for the EPSB cushioned cases.

- The greatest decrease in maximum spectral accelerations under far field earthquakes is observed for the EPSB20 and EPSB30.

- The EPSB as a cushion type generally exhibits improvement in spectral accelerations across all cushion thicknesses and densities examined under near field earthquakes as the scaled 1940 Imperial Valley EQ-El Centro Station record and the scaled 1995 Kobe

EQ record as given in Figure 5.21.d-e-f and Figure 5.21.g.h.i. In consideration of the scaled real earthquakes executed, the EPSB20-8cm provides significant improvement by reducing the maximum spectral accelerations under the scaled 1940 Imperial Valley Earthquake El Centro Station with 28% reduction and under the scaled 1995 Kobe EQ record with 17% reduction.

- Considering the near field earthquakes, it is evident that the period range of 0.05-0.10 seconds plays a crucial role. Compared to the control case under the near field earthquakes, it has been observed that higher frequencies between 10 Hz and 20 Hz can considerably decrease the maximum spectrum accelerations.

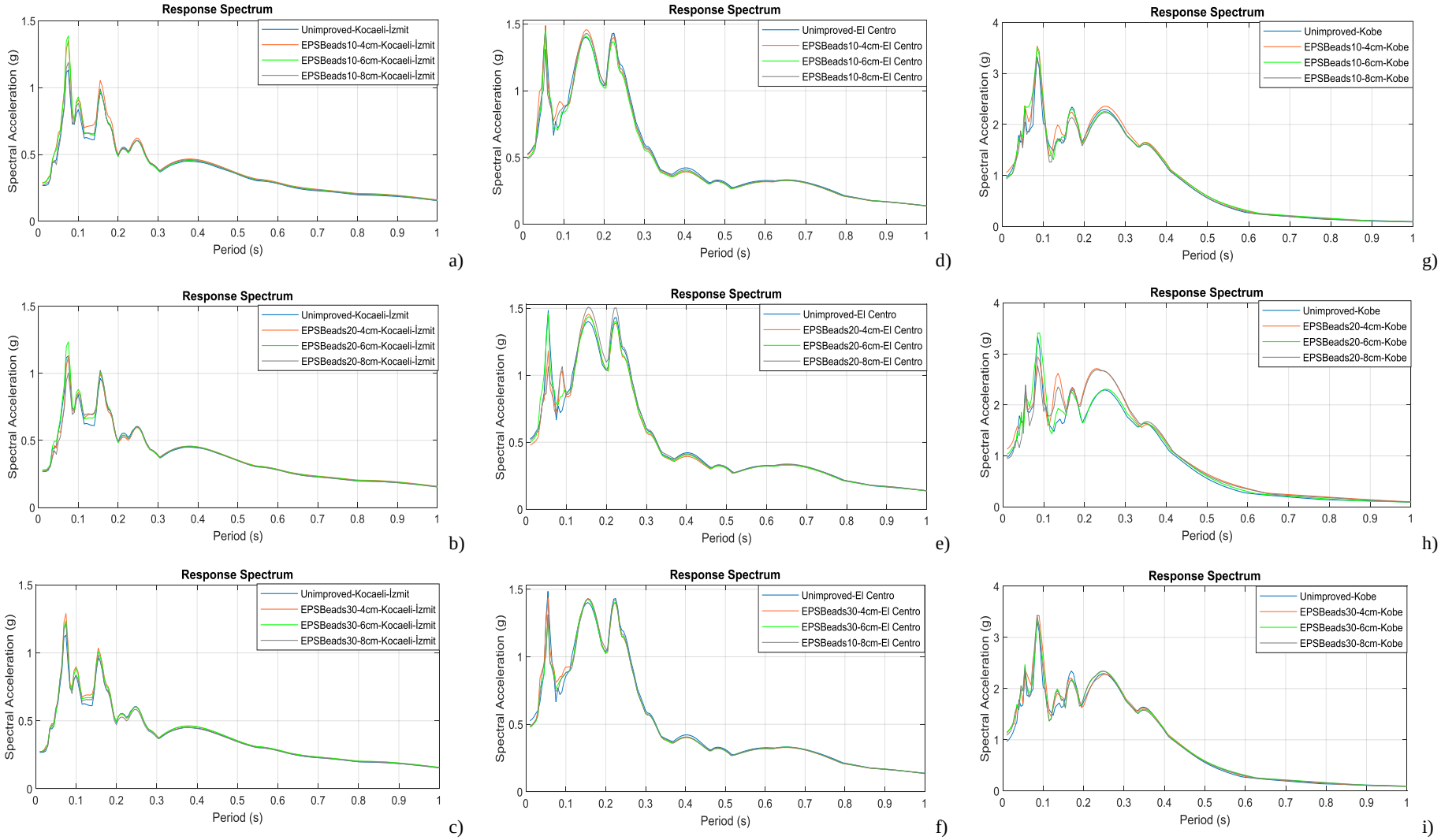


Figure 5.21 Response Spectrums of all EPS Beads and Sand Mixture cushioned cases with respect to A7 under a-b-c) the scaled 1999 Kocaeli EQ Motion-İzmit Station Record-NF, d-e-f) the scaled 1940 Imperial Valley EQ-El Centro Station record-NF, g-h-i) the scaled 1995 Kobe EQ Record-NF.

5.3.1.3. Comparison of Improvement Efficiency under Sinusoidal Motions

The improvement efficiency at the top of the RWM with respect to the cushion thickness ratio and EPSB mixture ratio of the EPSB cushioned case compared to the control case under sinusoidal motions is discussed by evaluating Figure 5.22.

The improvement efficiency under sinusoidal motion at 0.3g amplitude with 8 Hz frequency is given in Figure 5.22.a. The improvement efficiencies of EPSB cushioned cases were limited to 1%. An improvement impact was not seen for the remaining EPSB cushions.

The improvement efficiency under sinusoidal motion at 0.4g amplitude with 8 Hz frequency is given in Figure 5.22.b. The EPSB cushion type demonstrated improvement at all cushion thicknesses, and mixture ratios ranged between 1% and 7%, and the highest improvement efficiency was for EPSB10-8cm. It can be determined that the EPSB cushion is slightly effective as a cushion at these input motion characteristics at 0.4g amplitude with 8 Hz frequency.

The improvement efficiency under sinusoidal motion at 0.5g amplitude with 8 Hz frequency is given in Figure 5.22.c. The EPSB cushion type demonstrated improvement at all cushion thicknesses and mixture ratios. The maximum improvement efficiency was nearly 6%, for the EPSB20-8cm. The EPSB cushion is slightly effective as a cushion at these input motion characteristics of sinusoidal motions at 0.5g amplitude with 8 Hz frequency.

The improvement efficiency under sinusoidal motion at 0.4g amplitude with 12 Hz frequency is given in Figure 5.22.d. The maximum improvement efficiency was nearly 3% for the EPSB10-4cm. The EPSB cushion is not effective as a cushion at these input motion characteristics.

The maximum improvement efficiency was nearly 4% for the case EPSB10-6cm under sinusoidal motion at 0.4g amplitude with 14 Hz frequency, as shown in Figure 5.22.e. The EPS

beads sand mixture is not significantly effective as a cushion at these input motion characteristics. Also, no trend was observed for the seismic reduction effect depending on thickness and mixture ratio.

The general evaluation of the results based on improvement efficiency at the top of the RWM for the EPSB cushioned cases under sinusoidal motions are given in the following explanations:

- The improvement efficiencies are slightly effective under sinusoidal motions, as given in Figure 5.22. In Figure 5.22.b, the maximum improvement efficiency is calculated as nearly 7% under sinusoidal motion at 0.4g and 0.5g amplitude with 8 Hz frequency. On the other hand, the improvement efficiency is limited to 4% under the rest of the sinusoidal motions.

- The improvement efficiencies for EPSB cushioned cases are mostly impacted by the increase in cushion thickness. Figure 5.22 shows the improvement efficiencies tend to increase as the cushion thickness increases. The improvement efficiencies are not positively impacted by the increasing ratio of EPS beads under the input sinusoidal motions.

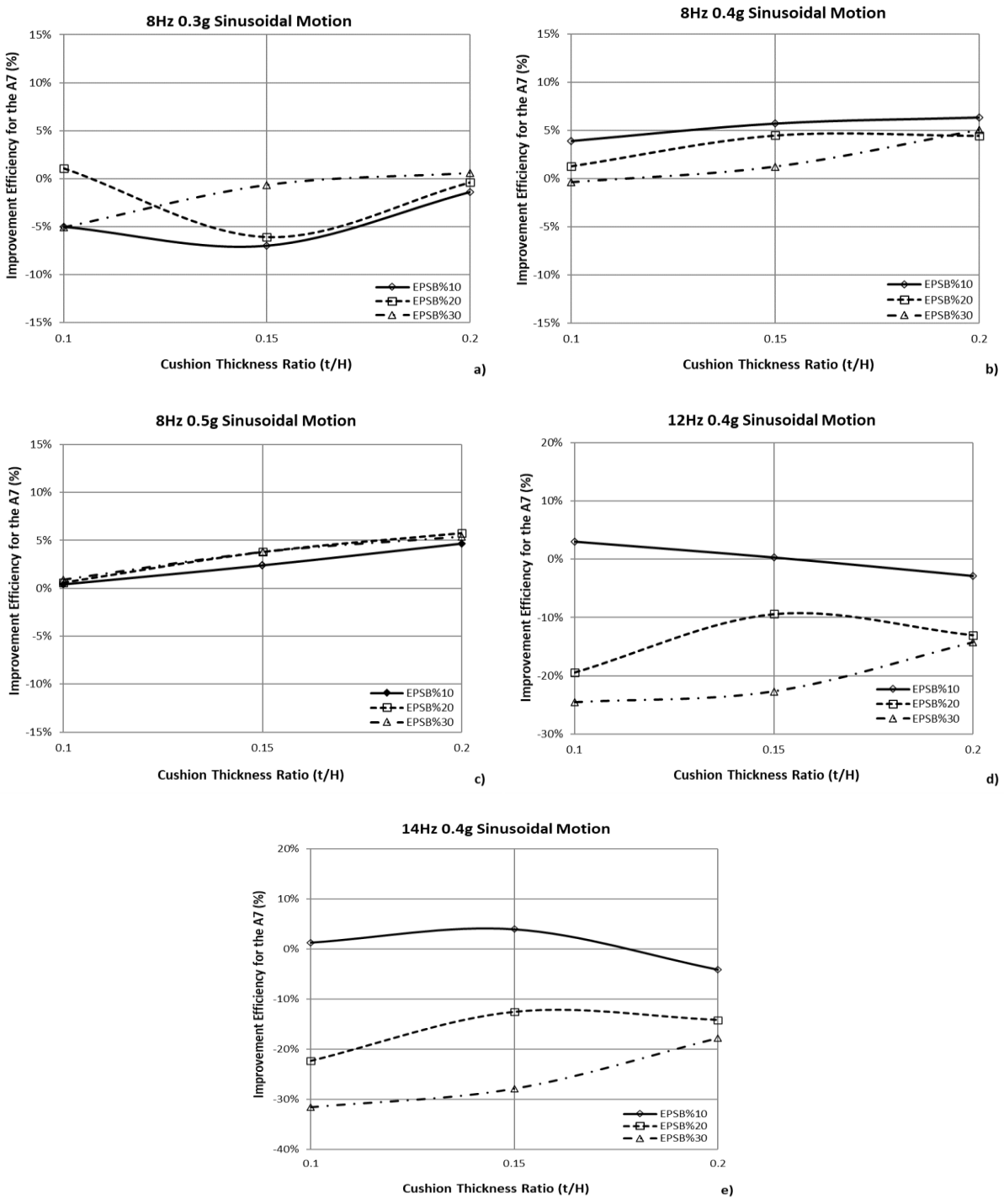


Figure 5.22. Improvement efficiency for all EPS Beads and Sand Mixture cushioned cases with respect to A7 under a) sinusoidal motion at 0.3g amplitude with 8 Hz frequency, b) sinusoidal motion at 0.4g amplitude with 8 Hz frequency, c) sinusoidal motion at 0.5g amplitude with 8 Hz frequency, d) sinusoidal motion at 0.4g amplitude with 12 Hz frequency, e) sinusoidal motion at 0.4g amplitude with 14 Hz frequency.

5.3.1.4. Comparison of Maximum Spectral Accelerations under Sinusoidal Motions

The response spectrums at the top of the RWM with respect to the cushion thickness ratio and mixture ratio of the EPSB cushioned cases compared to the control case under sinusoidal motions are discussed by evaluating Figure 5.23 and Figure 5.24.

The response spectrums for the control case and for EPSB10, EPSB20, and EPSB30 cases with thicknesses 4 cm, 6cm and 8 cm under the sinusoidal motion at 0.3g amplitude with 8 Hz frequency are represented in Figure 5.23.a, 5.23.b, and 5.23.c. The maximum spectral accelerations ($S_a$) occurred at a period of 0.125 sec and changed for each case. For EPSB10, the $S_a$ changed from 3.49g to 3.70g, 3.76g, and 3.50g for cushioned cases with thicknesses of 4 cm, 6 cm, and 8 cm, respectively. For EPSB20, the $S_a$ changed from 3.49g to 3.49g, 3.73g, and 3.53g for cushioned cases with thicknesses of 4 cm, 6 cm, and 8 cm, respectively. For EPSB30, the $S_a$ changed from 3.49g to 3.70g, 3.54g, and 3.49g for cushioned cases with thicknesses of 4 cm, 6 cm, and 8 cm, respectively.

The response spectrums for the control case and for EPSB10, EPSB20, and EPSB30 cases with thicknesses of 4cm, 6cm, and 8cm under the sinusoidal motion at 0.4g amplitude with 8 Hz frequency are represented in Figures 5.23.d, 5.23.e, and 5.23.f. The maximum spectral accelerations ($S_a$) occurred at a period of 0.125 sec and decreased from 4.70g to 4.56g, 4.48g, and 4.37g for EPSB10-4cm, EPSB10-6cm, and EPSB10-8cm cushioned cases, respectively. Similarly, for EPSB20-4cm, EPSB20-6cm, and EPSB20-8cm cushioned cases, the maximum $S_a$ decreased from 4.70g to 4.69g, 4.50g, and 4.45g, respectively. For EPSB30-4cm, EPSB30-6cm, and EPSB30-8cm cushioned cases, the maximum $S_a$ decreased from 4.70g to 4.67g, 4.61g, and 4.48g, respectively. The comparisons indicate that EPSB cushioning reduces the maximum $S_a$ at the top of the RWM.

The response spectrums for the control case and different cushioned cases EPSB10, EPSB20, and EPSB30 with thicknesses of 4 cm, 6cm and 8 cm under the sinusoidal motion at 0.5g amplitude with 8 Hz frequency are shown in Figures 5.23.g, 5.23.h, and 5.23.i. The maximum spectral accelerations ($S_a$) occurred at a period of 0.125 sec and decreased for all

cushioned cases. For EPSB10, the $S_a$ decreased from 5.73g to 5.70g, 5.59g, and 5.55g for cushion thicknesses of 4 cm, 6 cm, and 8 cm, respectively. For EPSB20, the $S_a$ decreased from 5.73g to 5.72g, 5.61g, and 5.50g for cushion thicknesses of 4 cm, 6 cm, and 8 cm, respectively. For EPSB30, the $S_a$ decreased from 5.73g to 5.72g, 5.56g, and 5.52g for cushion thicknesses of 4 cm, 6 cm, and 8 cm, respectively.

The response spectrums for the control case and for EPSB10, EPSB20, and EPSB30 with thicknesses of 4 cm, 6cm, and 8 cm under the sinusoidal motion at 0.4g amplitude with 12 Hz frequency are shown in Figures 5.24.a-c. The maximum spectral accelerations ($S_a$) occurred at a period of 0.085 sec. In Figure 5.24a, the $S_a$ decreased from 3.79g to 3.59g for the EPSB10-4cm case, increased to 3.80g for the EPSB10-8cm case, and remained the same for the EPSB10-6cm case. In Figure 5.24b, the $S_a$ increased from 3.79g to 4.38g, 4.22g, and 4.22g for the EPSB20-4cm, EPSB20-6cm, and EPSB20-8cm cases, respectively. In Figure 5.24c, the $S_a$ increased from 3.79g to 4.59g, 4.41g, and 4.18g for the EPSB30-4cm, EPSB30-6cm, and EPSB30-8cm cases, respectively.

The response spectrums for the control case and for EPSB10, EPSB20, and EPSB30 with thicknesses of 4 cm, 6cm, and 8 cm under the sinusoidal motion at 0.4g amplitude with 14 Hz frequency are shown in Figures 5.24.d-f. The maximum spectral accelerations ($S_a$) occurred at a period of 0.07 sec. In Figure 5.24.d, the $S_a$ decreased from 4.22g to 4.15g, 3.97g, and increased to 4.35g for the control case and EPSB10-4cm, EPSB10-6cm, and EPSB10-8cm cushioned cases, respectively. In Figure 5.24.e, the $S_a$ increased from 4.22g to 4.69g, 4.65g, and 4.43g for the control case and EPSB20-4cm, EPSB20-6cm, and EPSB20-8cm cushioned cases, respectively. In Figure 5.24.f, the $S_a$ increased from 4.22g to 5.11g, 4.81g, and 4.58g for the control case and EPSB30-4cm, EPSB30-6cm, and EPSB30-8cm cushioned cases, respectively.

Based on the evaluation of the general results with respect to maximum spectral accelerations at the top of the RWM for the EPSB cushioned cases under sinusoidal motions are given in the following:

- The maximum spectral acceleration reduction at 0.125 sec period was limited to 1% under the sinusoidal motion at 0.3g amplitude with 8 Hz frequency. Under the sinusoidal motion at 0.4g amplitude with 8 Hz frequency, the maximum spectral accelerations at 0.125 sec period decreased with a maximum 7% reduction ratio for the case EPSB10-8cm (Case 20), and the reduction ranged between 1%-7%. The maximum spectral acceleration at 0.125 sec period decreased by a maximum of 4% for the case EPSB20-8cm (Case 21) under the sinusoidal motion at 0.5g amplitude with 8 Hz frequency. Under the sinusoidal motion at 0.4g amplitude with 12 Hz frequency, the maximum spectral accelerations at 0.085 sec period decreased with a maximum 5% reduction ratio for the case EPSB10-4cm (Case 14). The maximum spectral accelerations at 0.07 sec period decreased with a maximum 2% reduction ratio for the case EPSB10-4cm under the sinusoidal motion at 0.4g amplitude with 14 Hz frequency.

- For the EPSB cushioned cases, it was found that the thickness ratio was effective in reducing the maximum spectral accelerations at 0.125 sec period under the sinusoidal motion with 0.3g-0.4g-0.5g amplitude, 8 Hz frequency. This effect is not noticeable under the rest of the sinusoidal input motions. Maximum spectral accelerations decreased with regard to an increase in cushion thickness, as shown in Figures 5.23.a-b-c and 5.23.d-e-f.

- Increasing the mixture ratio of EPSB cushion generally leads to a decrease in maximum spectral accelerations under sinusoidal motions at 0.3g, 0.4g, and 0.5g amplitude with 8 Hz frequency, particularly at a period of 0.125 sec. On the other hand, increasing mixture ratio does not affect the maximum spectral accelerations under sinusoidal motion at 0.4g amplitude with 12 Hz and 14 Hz frequency. EPSB30 had the most significant decrease in spectral accelerations under all input sinusoidal motions.

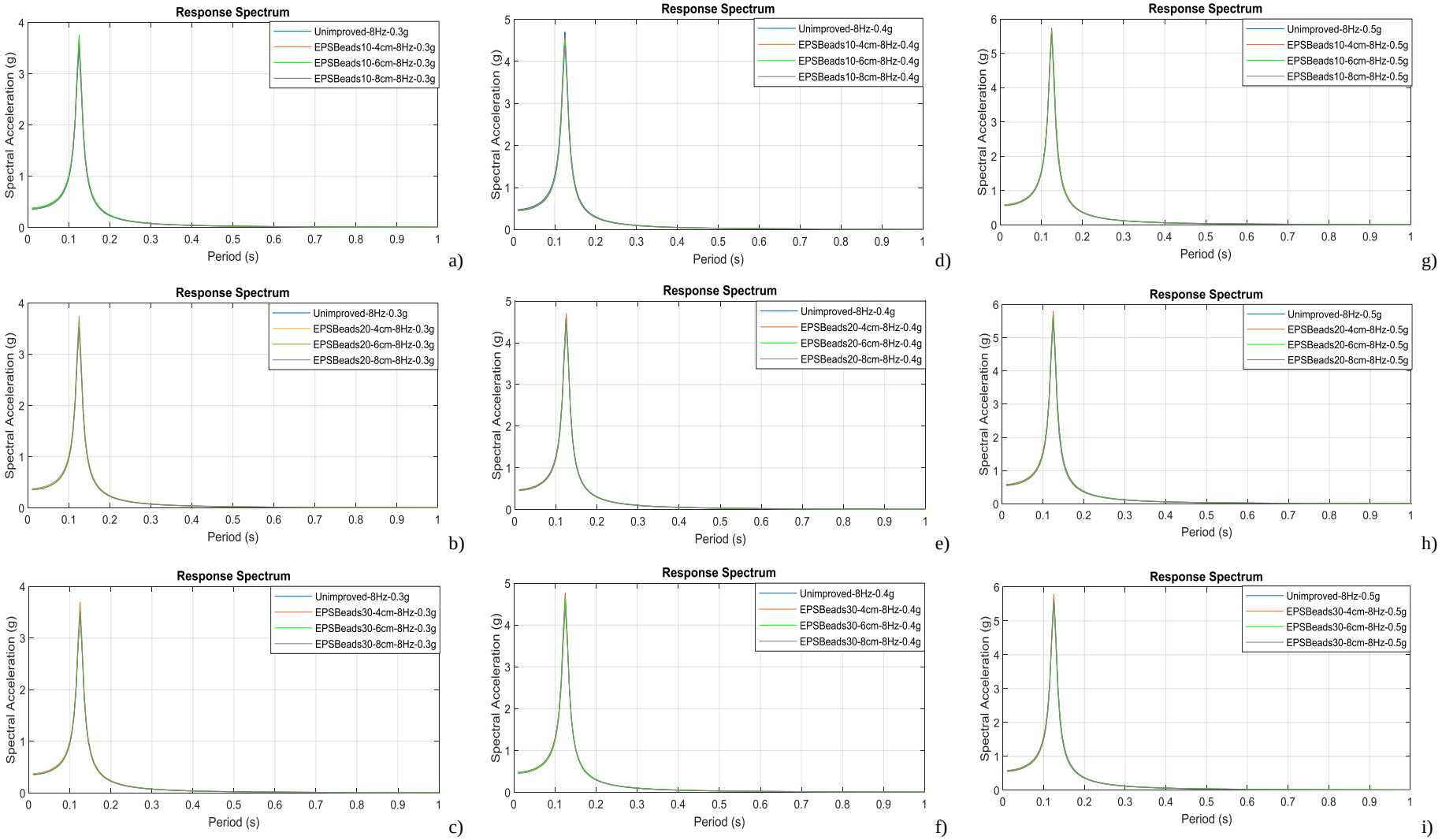


Figure 5.23 Response Spectrums of all EPS Beads and Sand Mixture cushioned cases with respect to A7 under a-b-c) sinusoidal motion at 0.3g amplitude with 8 Hz frequency, d-e-f) sinusoidal motion at 0.4g amplitude with 8 Hz frequency, g-h-i) sinusoidal motion at 0.5g amplitude with 8 Hz frequency.

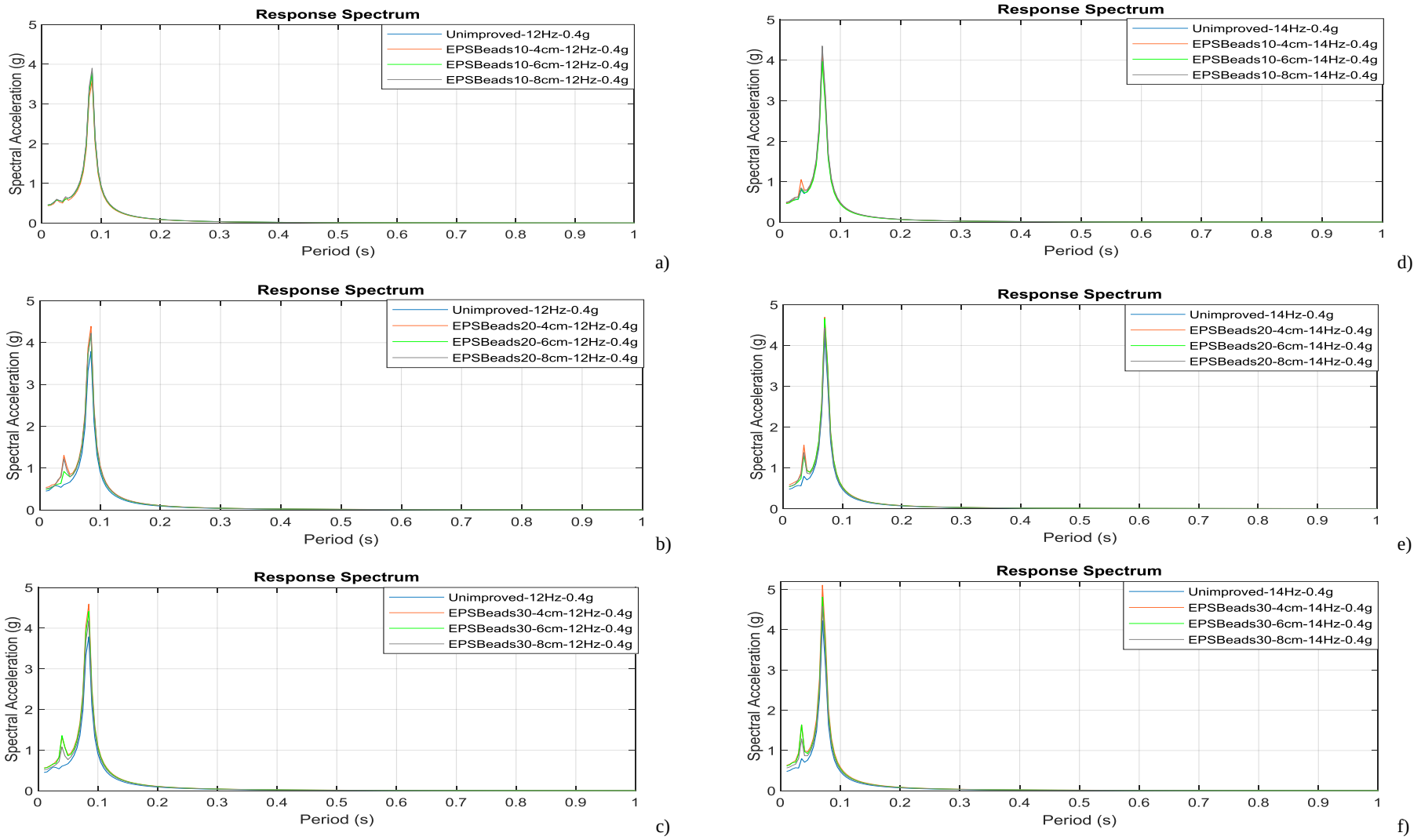


Figure 5.24 Response Spectrums of all EPS Beads and Sand Mixture cushioned cases with respect to A7 under a-b-c) sinusoidal motion at 0.4g amplitude with 12 Hz frequency, d-e-f) sinusoidal motion at 0.4g amplitude with 14 Hz frequency.

### 5.3.2. The Effects of Acceleration Response for EPS Beads and Sand Mixture Cushion under Different Input Motions

The variation of maximum accelerations at the top of the RWM for EPSB cushioned cases at different thicknesses and mixture ratios compared with the control case under all input motions are shown in Figure 5.25 and Figure 5.26.

#### 5.3.2.1. Maximum Acceleration Comparison at 4 cm Thickness

The maximum transmitted accelerations of the EPSB10-4cm, EPSB20-4cm and EPSB30-4cm cases at the top of the RWM are compared with the maximum transmitted accelerations of the control case considering the PGA of the input motions. PGA of the input motions are 0.12g, 0.14g, 0.18g, 0.22g, 0.32g, 0.82g, and sinusoidal motions at 0.3g amplitude with 8 Hz frequency, at 0.4g amplitude with 8 Hz frequency, at 0.5g amplitude with 8 Hz frequency, at 0.4g amplitude with 12 Hz frequency, at 0.4g amplitude with 14 Hz frequency (Figure 5.25).

The comparison of maximum transmitted accelerations measured from A7 for the control case and EPSB cushioned cases with 4 cm thickness as Case 14, Case 15, and Case 16 with the PGA of input motions are shown in Figure 5.25. In Figure 5.25, the maximum accelerations of the control case deamplify under the scaled 1999 Kocaeli EQ Motion-İznik Station record, the scaled 2014 Gökçeada EQ Motion-Çanakkale Station record, the scaled 1999 Kocaeli EQ Motion-İzmit Station record and the scaled 1995 Kobe EQ record and sinusoidal motion at 0.3g amplitude with 8 Hz frequency, sinusoidal motion at 0.4g amplitude with 12 Hz frequency, sinusoidal motion at 0.4g amplitude with 14 Hz frequency compared to the PGA of input motions. However, amplification in the maximum accelerations of the control case is observed under the scaled 2020 İzmir EQ Motion-Kuşadası Station record and the scaled 1940 Imperial Valley EQ-El Centro Station record, and sinusoidal motion at 0.4g amplitude with 8 Hz frequency, sinusoidal motion at 0.5g amplitude with 8 Hz frequency compared to the PGA of input motions. When the acceleration measurements for the EPSB

cases with 4cm thickness from A7 are compared to the control case, the highest decrease in maximum acceleration value was observed for cushion type EPSB20-4cm (Case 15) under the scaled 2020 İzmir EQ Motion-Kuşadası Station record and the scaled 1940 Imperial Valley EQ-El Centro Station record.

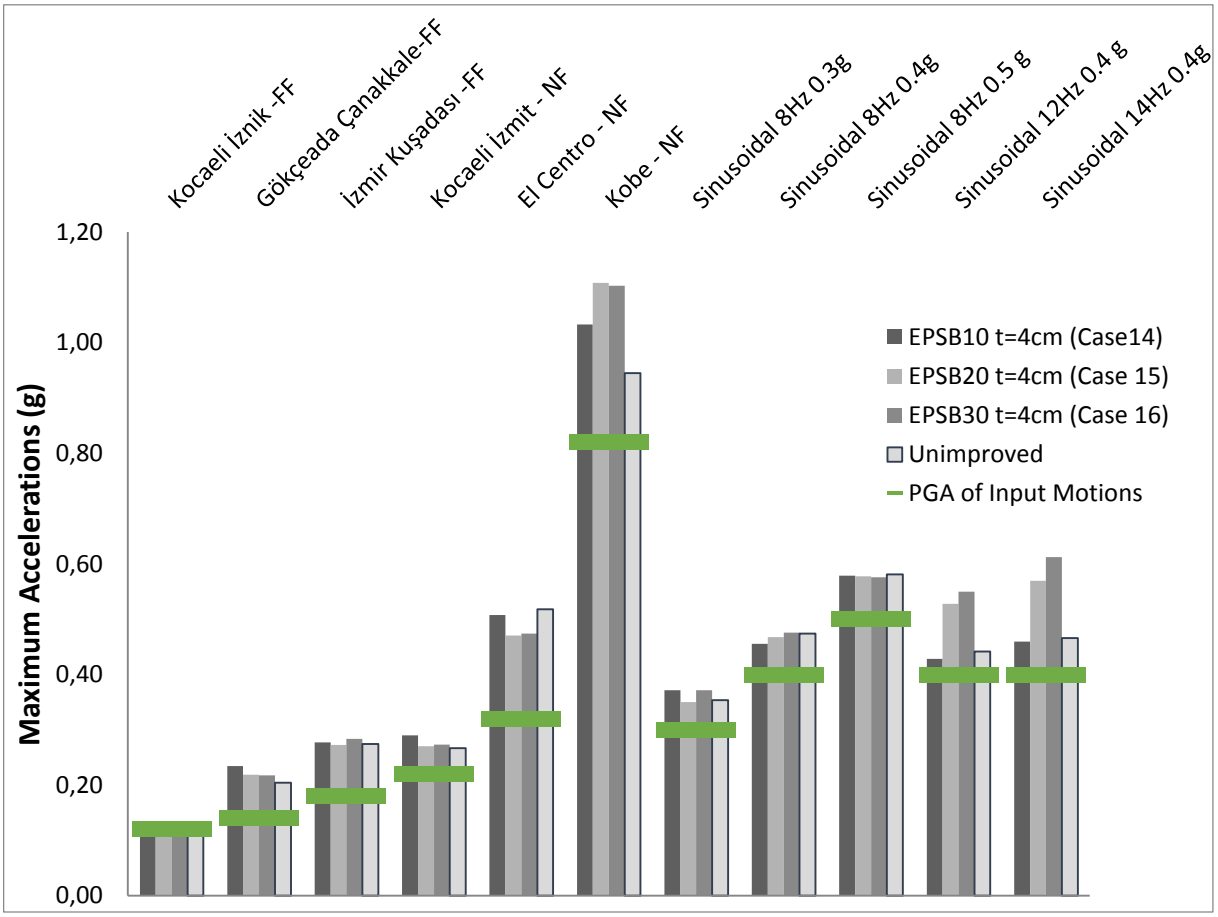


Figure 5.25 Variation of maximum accelerations at the top of the RWM for EPS Beads and Sand Mixture cases with t=4cm compared with the control case under all input motions.

5.3.2.2. Maximum Acceleration Comparison at 6 cm Thickness

The maximum transmitted accelerations measured from A7 for the control case and EPSB cushioned cases with 6 cm thickness as Case 17, Case 18, and Case 19 compared to the PGA of the imput motions are shown in Figure 5.26.

In Figure 5.26, the maximum accelerations of the control case deamplify under the scaled 1999 Kocaeli EQ Motion-İznik Station record, the scaled 2014 Gökçeada EQ Motion-Çanakkale Station record, the scaled 1999 Kocaeli EQ Motion-İzmit Station record and the scaled 1995 Kobe EQ record and sinusoidal motion at 0.3g amplitude with 8 Hz frequency, sinusoidal motion at 0.4g amplitude with 12 Hz frequency, sinusoidal motion at 0.4g amplitude with 14 Hz frequency compared to the control case compared to the PGA of input motions. However, acceleration amplification at the control case is observed under the scaled 1940 Imperial Valley EQ-El Centro Station record and sinusoidal motion at 0.4g amplitude with 8 Hz frequency, sinusoidal motion at 0.5g amplitude with 8 Hz frequency compared to the PGA of input motions. When the acceleration measurements for the EPSB cases with 6cm thickness from A7 are compared to the control case, the highest decrease in maximum acceleration value was observed for EPSB30-6cm (Case 18) under the scaled 1940 Imperial Valley EQ-El Centro Station record, for EPS10-6cm under the sinusoidal motion at 0.4g amplitude with 8 Hz frequency, for EPS30-6cm under sinusoidal motion at 0.5g amplitude with 8 Hz frequency compared to the PGA of input motions.

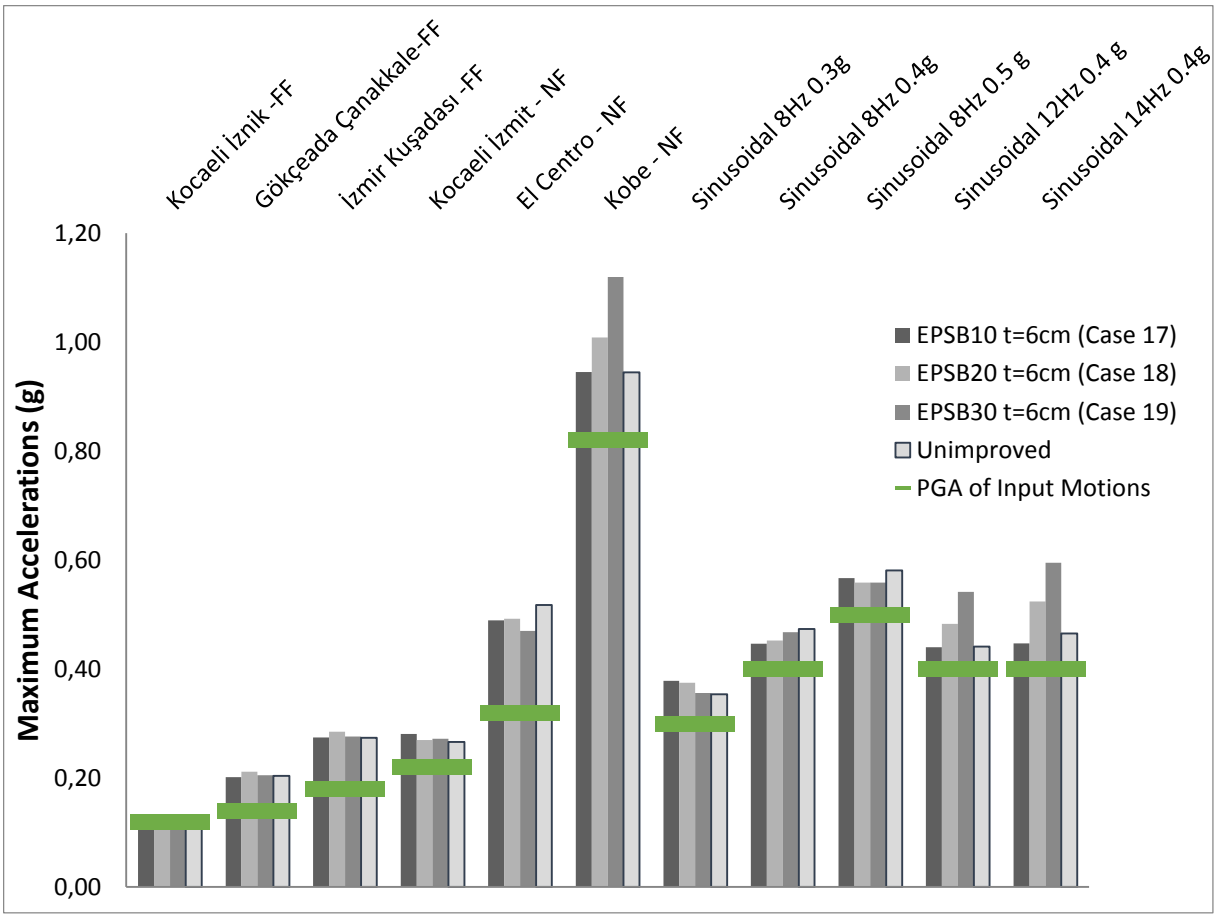


Figure 5.26 Variation of maximum accelerations at the top of the RWM for EPS Beads and Sand Mixture cases with t=6cm compared with the control case under all input motions.

5.3.2.3. Maximum Acceleration Comparison at 8 cm Thickness

The comparisons of input motions maximum transmitted accelerations measured from A7 for the control case and EPSB cushioned cases with 8 cm thickness as Case 20, Case 21, and Case 22, are shown in Figure 5.27.

As seen in Figure 5.27, the maximum accelerations of the control case deamplify under the scaled 1999 Kocaeli EQ Motion-İznik Station record, the scaled 2014 Gökçeada EQ Motion-Çanakkale Station record, the scaled 1999 Kocaeli EQ Motion-İzmit Station record and the scaled 1995 Kobe EQ record and sinusoidal motion at 0.3g amplitude with 8 Hz frequency, sinusoidal motion at 0.4g amplitude with 12 Hz frequency, sinusoidal motion at

0.4g amplitude with 14 Hz frequency compared to the PGA of input motions. However, amplification in the maximum accelerations of the control case is observed under the scaled 1940 Imperial Valley EQ-El Centro Station record and sinusoidal motion at 0.4g and 0.5g amplitude with 8 Hz frequency compared to the PGA of input motions. When the acceleration measurements for the EPSB cases with 8cm thickness are compared to the control case, the highest decrease in maximum acceleration value was observed for EPSB30-8cm (Case 22) under the scaled 1940 Imperial Valley EQ-El Centro Station record.

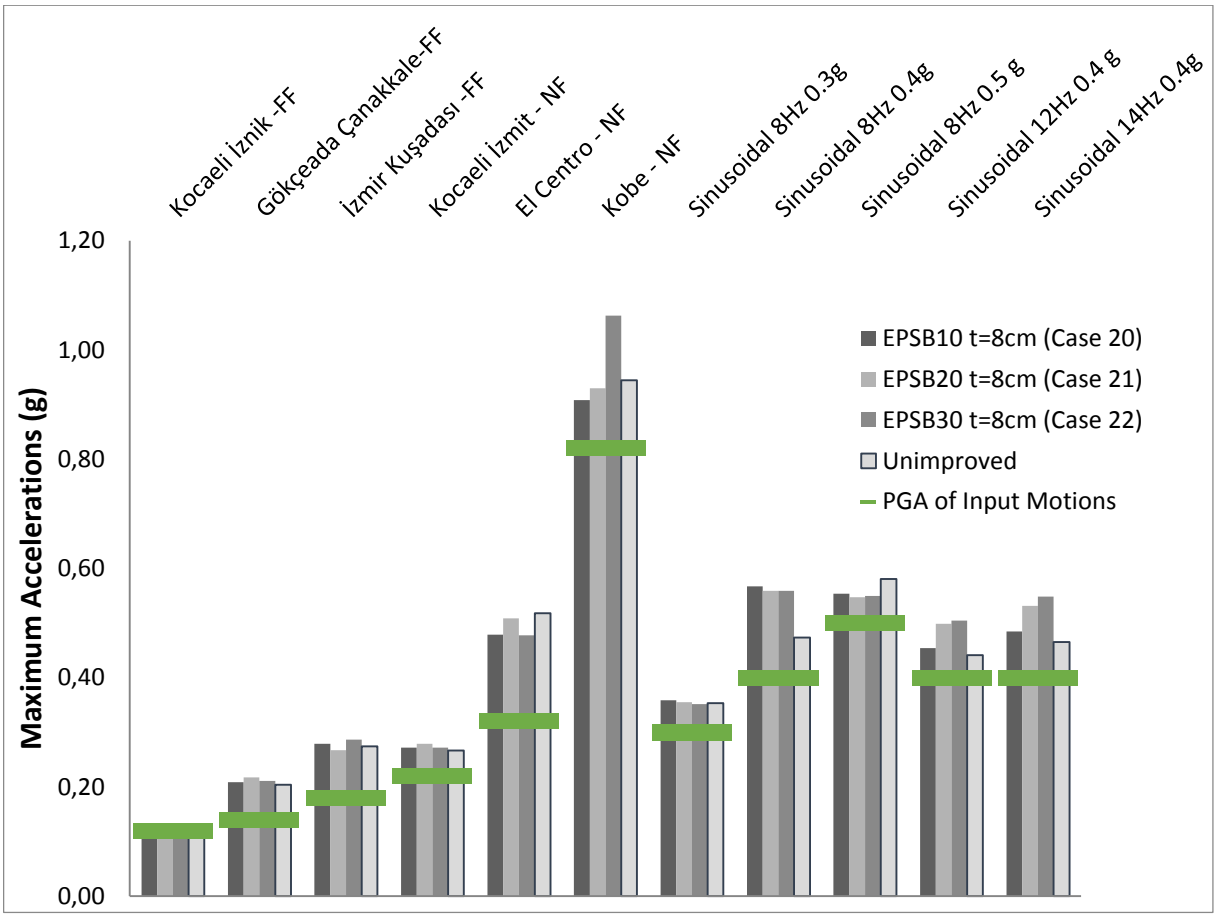


Figure 5.27 Variation of maximum accelerations at the top of the RWM for EPS Beads and Sand Mixture cases with t=8cm compared with the control case under all input motions.

### 5.3.3. Maximum Lateral Displacements for EPS Beads and Sand Mixture Cushion Cases under All Input Motions

Two laser displacement sensors have been installed on the RWM, one at the height of H as D19 and the other at the height of 0.5H as D18, as shown in Figure 3.27 and Figure 3.29 in Chapter 3. Figure 5.28 shows the comparison of the maximum lateral displacements at the top of RWM based on the cushion thickness ratio and mixture ratio of EPSB cushioned cases under different earthquake input motions and sinusoidal motions. The control case is shown in Figure 5.28.a, while the remaining cases are represented in Figures 5.28.b to 5.28.j. Each figure shows the maximum lateral displacements for a particular case under different input motions, including far field and near field earthquakes and sinusoidal motions. The maximum lateral displacements for Case 1 under far field and near field earthquakes and sinusoidal motions were explained in Part 5.1.3 and can be seen in Figure 5.18.a.

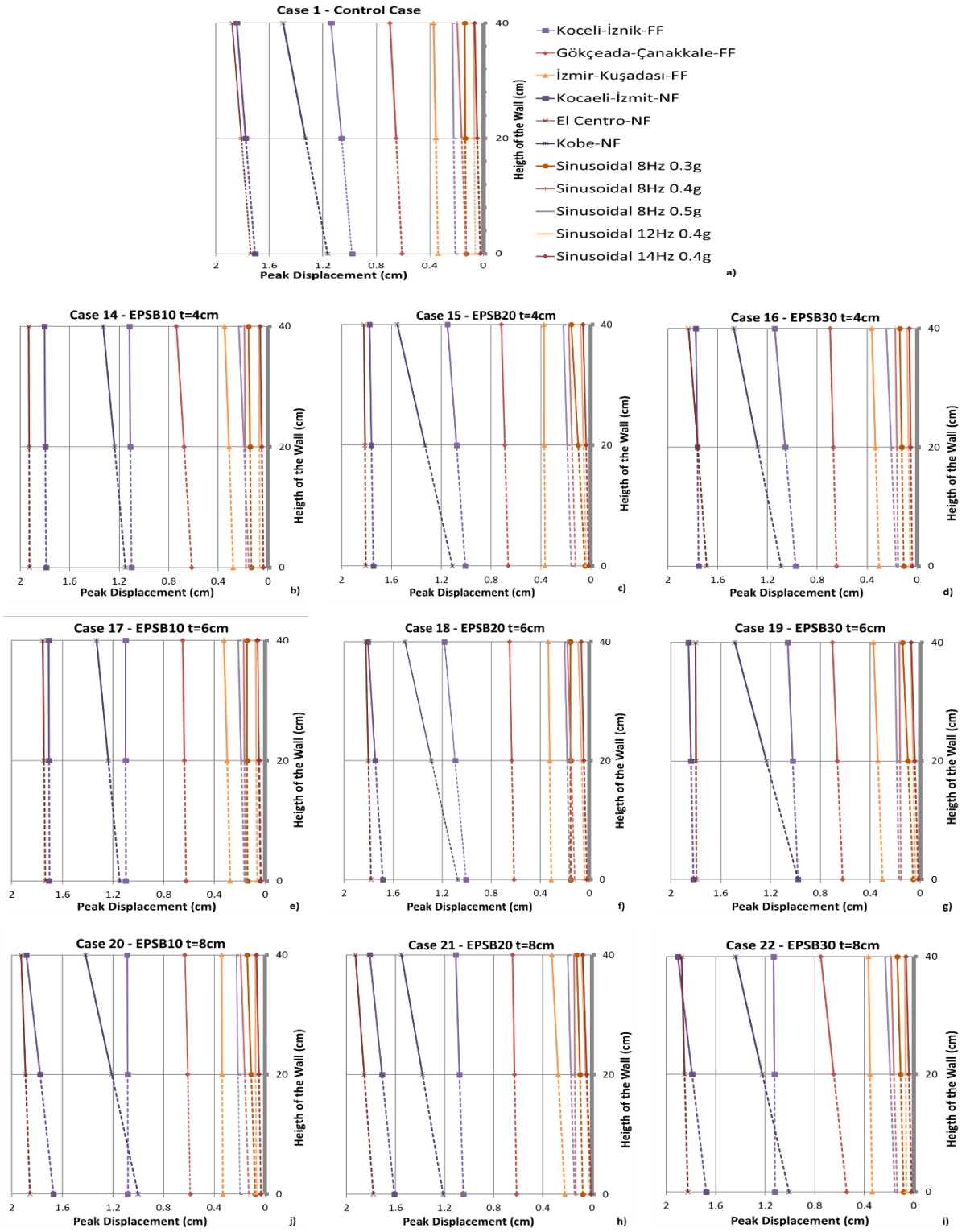


Figure 5.28. Maximum lateral displacements measured from D19 under all input motions a) Case 1, b) Case 14, c) Case 15, d) Case 16, e) Case 17, f) Case 18, g) Case 19, h) Case 20, i) Case 21, j) Case 22.

The evaluation of the results of the maximum lateral displacements at the top of the RWM for the EPSB cushioned cases compared with the cushioned case under all given input motions is summarized as follows:

- When subjected to sinusoidal motion, the maximum lateral displacements are lower compared to the earthquake motions. Near field earthquakes result in higher displacements than far field earthquakes (Figure 5.28.a-g).

- Taking into account thickness and mixture ratio changes in each case of EPSB cushioned cases, EPSB30-6cm is the most effective case that can reduce the maximum lateral displacement values by 7% under the scaled 1999 Kocaeli EQ Motion-İznik Station record. The reduction in maximum lateral displacement under the scaled 2014 Gökçeada EQ Motion-Çanakkale Station is up to 9% with EPSB10-8cm. The highest reduction is 17.5% under the scaled 2020 İzmir EQ Motion-Kuşadası Station record for the case EPSB10-6cm. Under the scaled 1999 Kocaeli EQ Motion-İzmit Station record, the maximum reduction is up to 7% for the EPSB10-6cm. The influence of input motion excitation is for the case EPSB10-6cm under the scaled 1940 Imperial Valley EQ-El Centro Station record, showing the reduction in displacement by 6.5%. For the case EPSB10-6cm, the peak reduction in displacement was 11% under the scaled 1995 Kobe EQ record.

- Using EPSB cushions can reduce maximum lateral displacements under the given earthquake motions. The reduction varied depending on the earthquake, with the highest reduction observed for the EPSB10-6cm cushioned model under the scaled 2020 İzmir EQ Motion-Kuşadası Station record. EPSB cushion is effective as a cushion at the input motion characteristics of the scaled 2014 Gökçeada EQ Motion-Çanakkale Station record, the scaled 2020 İzmir EQ Motion-Kuşadası Station record, and the scaled 1995 Kobe EQ record in reducing maximum lateral displacement of the model.

- Under sinusoidal motion at 0.3g amplitude with 8 Hz frequency, it was observed that EPSB20-8cm is the most effective case in reducing the displacement values at the top of the RWM by 13% reduction. Applying EPSB20-8cm helped mitigate the maximum lateral displacement value, resulting in a 25.5% decrease under the sinusoidal motion at 0.4g amplitude with 8 Hz frequency. The highest reduction by means of maximum lateral displacement was seen in the model with EPSB20-8cm under sinusoidal motion at 0.4g amplitude with 8 Hz frequency with reducing displacement values at these input motion characteristics up to 16%. Under sinusoidal motion at 0.4g amplitude with 12 Hz frequency, the case with EPSB10-4cm reduced the maximum lateral displacement up to 7%. EPSB10-8cm reduced the displacement up to 1% under sinusoidal motion at 0.4g amplitude with 14 Hz frequency.

- Using EPSB cushion can reduce maximum lateral displacements during the excitation of sinusoidal motions. The improvement effects varied depending on the sinusoidal motions, with the highest reduction observed for the EPSB20-t=8cm cushioned model under the sinusoidal motion at 0.4g amplitude with 8 Hz frequency with a 25.50% reduction. EPSB is effective as a cushion at the input motion characteristics under sinusoidal motions at the amplitude range between 0.3g and 0.5g with 8 Hz frequency and in reducing maximum lateral displacements for the EPSB cushioned cases.

## 5.4. Comparison of Maximum Spectral Acceleration of the Backfill and the Top of the Retaining Wall Model

Figure 5.29 represents the maximum spectral acceleration variation ratios for backfill with respect to cushion thickness ratio and density/mixture ratio for the control case and all cushion types under the far field and near field earthquakes at the same thicknesses. The maximum spectral acceleration variation ratio (%) is obtained by dividing the maximum spectral acceleration of A16 by maximum spectral acceleration of A7. Figure 5.29.a, b, c, d, e, and f represent the variation ratio of $S_a$ in percent under the scaled earthquake input motions.

Figure 5.29.a shows the maximum $S_a$ variation ratio for all the cases under the scaled 1999 Kocaeli EQ Motion-İznik Station record. The maximum $S_a$ variation ratio was 11% for the control case. When the cushion was placed, the variation ratio of $S_a$ reduced compared to the control case. This decrease was observed for all cushioned cases, which was most noticeable for EPS30-8cm cushioned case.

Figure 5.29.b displays the maximum $S_a$ variation ratio for all the cases under the scaled 2014 Gökçeada Earthquake Motion-Çanakkale Station record. For the control case, the maximum $S_a$ variation ratio was 13%. When a cushion was placed, the variation ratio of $S_a$ decreased compared to the control case. This decrease was observed for all cushioned cases, with the most significant reduction seen for the EPS20-8cm. The variation ratio of $S_a$ for the cushioned cases was lowest for EPS geofoam and highest for EPSB cushioned cases. It can be noticed that as the thickness ratio increases, the variation ratio of $S_a$ decreases for most of the cushioned cases.

Figure 5.29.c shows the maximum $S_a$ variation ratio for all the cases under the scaled 2020 İzmir Earthquake Motion-Kuşadası Station record. The maximum spectral acceleration variation ratio was 40% for the control case. When a cushion was placed, the variation ratio of $S_a$ decreased compared to the control case. This decrease was observed for all cushioned cases, with the most significant reduction was for the EPS20-8cm cushioned case. The variation ratio of $S_a$ for the cushioned cases was lowest for EPS geofoam cushioned cases and highest for

EPSB cushioned cases. Additionally, it was observed that as the thickness ratio increases, the variation ratio of $S_a$ value decreases.

The maximum spectral accelerations variation ratio for all the cases under the scaled 1999 Kocaeli Earthquake Motion-İzmit Station record is given in Figure 5.29.d. The maximum spectral acceleration variation ratio was 18% for the control case. When the cushion was placed the variation ratio of $S_a$ reduced compared to the control case. This decrease was observed for all cushioned cases, which was most noticeable for EPS30-8cm cushioned case.

Figure 5.29.e shows the maximum $S_a$ variation ratio for all the cases under the scaled 1940 Imperial Valley Earthquake El Centro Station record. The maximum spectral acceleration variation ratio was 31% for the control case. The placement of a cushion was found to decrease the variation ratio of $S_a$ to the control case. This reduction was evident for all cases where a cushion was used. The most significant decrease was observed for the EPS10-4cm.

The maximum $S_a$ variation ratio for all the cases under the scaled 1995 Kobe Earthquake record is shown in Figure 5.29.f. The maximum spectral acceleration variation ratio was 12% for the control case. It was observed that when the cushion was placed, the variation ratio of $S_a$ reduced compared to the control case. This decrease was observed for all cushioned cases and most noticeable for EPS10-8cm.

Evaluation of the results shows that all cushion types were effective in reducing the $S_a$ variation ratio compared to the control case. This behaviour indicates that cushioning has a positive effect by reducing the variation ratio of maximum $S_a$ compared to the control case under the scaled far field and near field earthquakes. Furthermore, for most of the cushion types, the thickness ratio was effective in reducing the variation ratio of maximum $S_a$ for backfill and the top of the RWM as the thickness ratio increases.

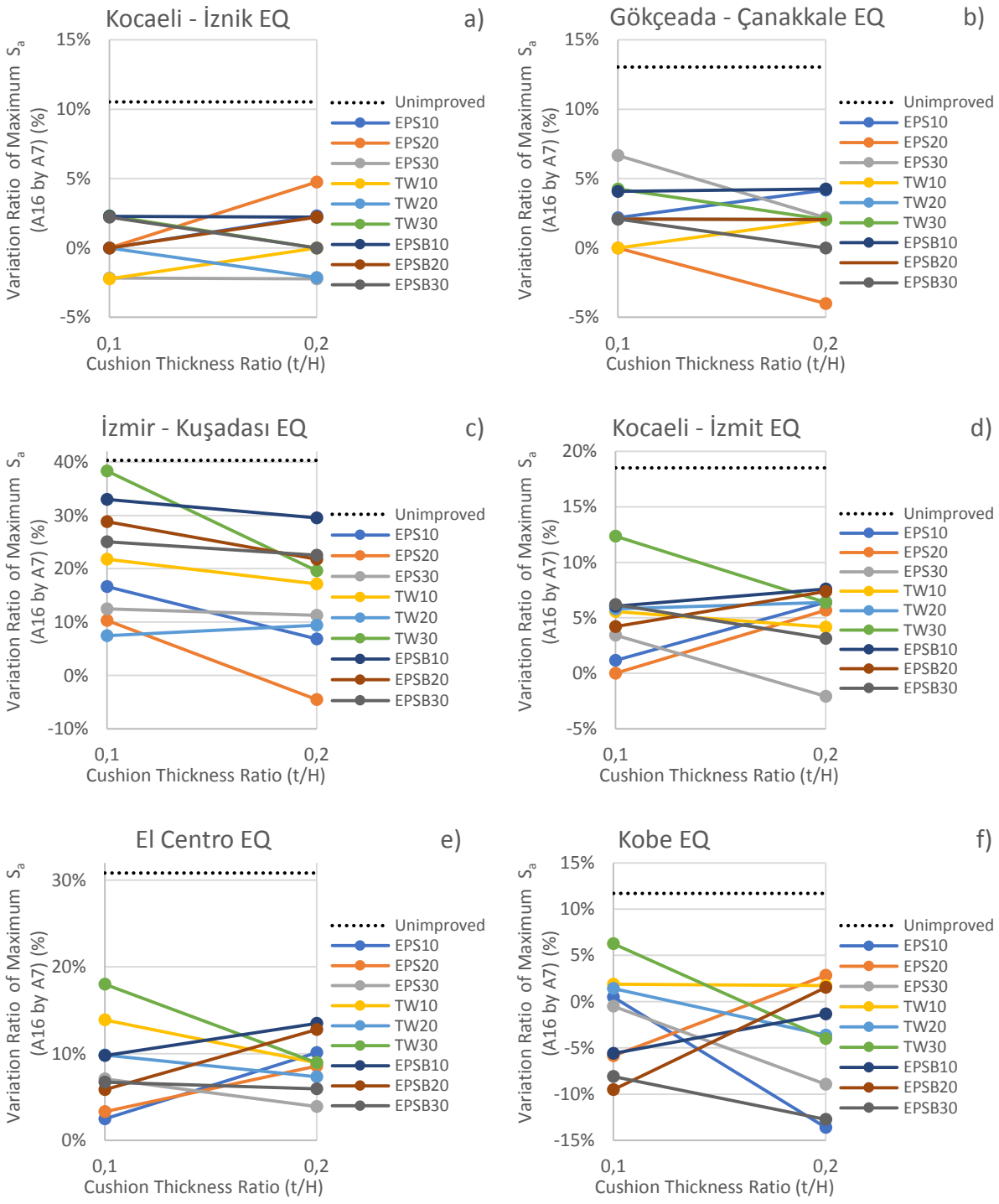


Figure 5.29 The maximum spectral acceleration variation ratio (A16 by A7) for all cushion cases under a) the scaled 1999 Kocaeli EQ Motion-İznik Station Record-FF, b) the scaled 2014 Gökçeada EQ Motion-Çanakkale Station Record-FF, c) the scaled 2020 İzmir EQ Motion-Kuşadası Station Record-FF, d) the scaled 1999 Kocaeli EQ Motion-İzmit Station Record-NF, e) the scaled 1940 Imperial Valley EQ-El Centro Station record-NF, f) the scaled 1995 Kobe EQ Record-NF.

Figure 5.30 shows the maximum spectral acceleration variation ratios with respect to cushion thickness ratio and density/mixture ratio for the control case and all cushion types under sinusoidal motions. Figure 5.29.a, b, c, d, e, and f represent the variation ratio of $S_a$ in percent under the sinusoidal input motions.

Figure 5.30.a shows the maximum $S_a$ variation ratio for all the cases under the sinusoidal motions at 0.3g amplitude with 8 Hz frequency. The maximum spectral acceleration variation ratio was 29% for the control case. When the cushion was placed, the variation ratio of $S_a$ reduced compared to the control case. This decrease was observed for all cushioned cases, which was most noticeable for EPS30-4cm cushioned case. The variation ratio of $S_a$ for the cushioned cases was lowest for EPS geofoam cushioned cases and highest for EPSB cushioned cases.

The maximum $S_a$ variation ratio for all the cases under the sinusoidal motion at 0.4g amplitude with 8 Hz frequency is given in Figure 5.30.b. The maximum spectral acceleration variation ratio was %31 for the control case. The placement of a cushion caused a decrease in the variation ratio of $S_a$ compared to the control case. This decrease was observed for all cushioned cases, with the most significant reduction observed for the EPS30-4cm cushioned case. The study found that the variation ratio of $S_a$ was lowest for the EPS geofoam cushioned cases.

Figure 5.30.c shows the maximum $S_a$ variation ratio for all the cases under the sinusoidal motion at 0.5g amplitude with 8 Hz frequency. The maximum spectral acceleration variation ratio was 26% for the control case. When the cushion was placed, the variation ratio of $S_a$ reduced compared to the control case. This decrease was observed for all cushioned cases, which was most noticeable for EPS30-4cm cushioned case. It was found that the variation ratio of $S_a$ was lowest for EPS geofoam cushioned cases.

The maximum $S_a$ variation ratio for all the cases under the sinusoidal motion at 0.4g amplitude with 12 Hz frequency is shown in Figure 5.30.d. The maximum spectral acceleration variation ratio was 49% for the control case. When the cushion was placed, the variation ratio of $S_a$ reduced compared to the control case. This decrease was observed for all cushioned cases,

which was most noticeable for EPS30-8cm cushioned case. It was found that the variation ratio of $S_a$ was lowest for EPS geofoam cushioned cases.

Figure 5.30.e shows the maximum $S_a$ variation ratio for all the cases under the sinusoidal motion at 0.4g amplitude with 14 Hz frequency. The maximum spectral acceleration variation ratio was 57% for the control case. When the cushion was placed, the variation ratio of $S_a$ reduced compared to the control case. This decrease was observed for all cushioned cases, which was most noticeable for EPS10-8cm cushioned case. It was found that the variation ratio of $S_a$ was lowest for EPS geofoam cushioned cases.

Evaluation of the results shows that all cushion types were effective in reducing the $S_a$ variation ratio compared to the control case. This behaviour indicates that cushion inclusions show a positive effect by reducing the variation ratio of maximum $S_a$ compared to the control case under the sinusoidal motions. Additionally, for most of the cushion types, it can be noticed that the thickness ratio was effective in reducing the variation ratio of maximum $S_a$ as the thickness ratio increases.

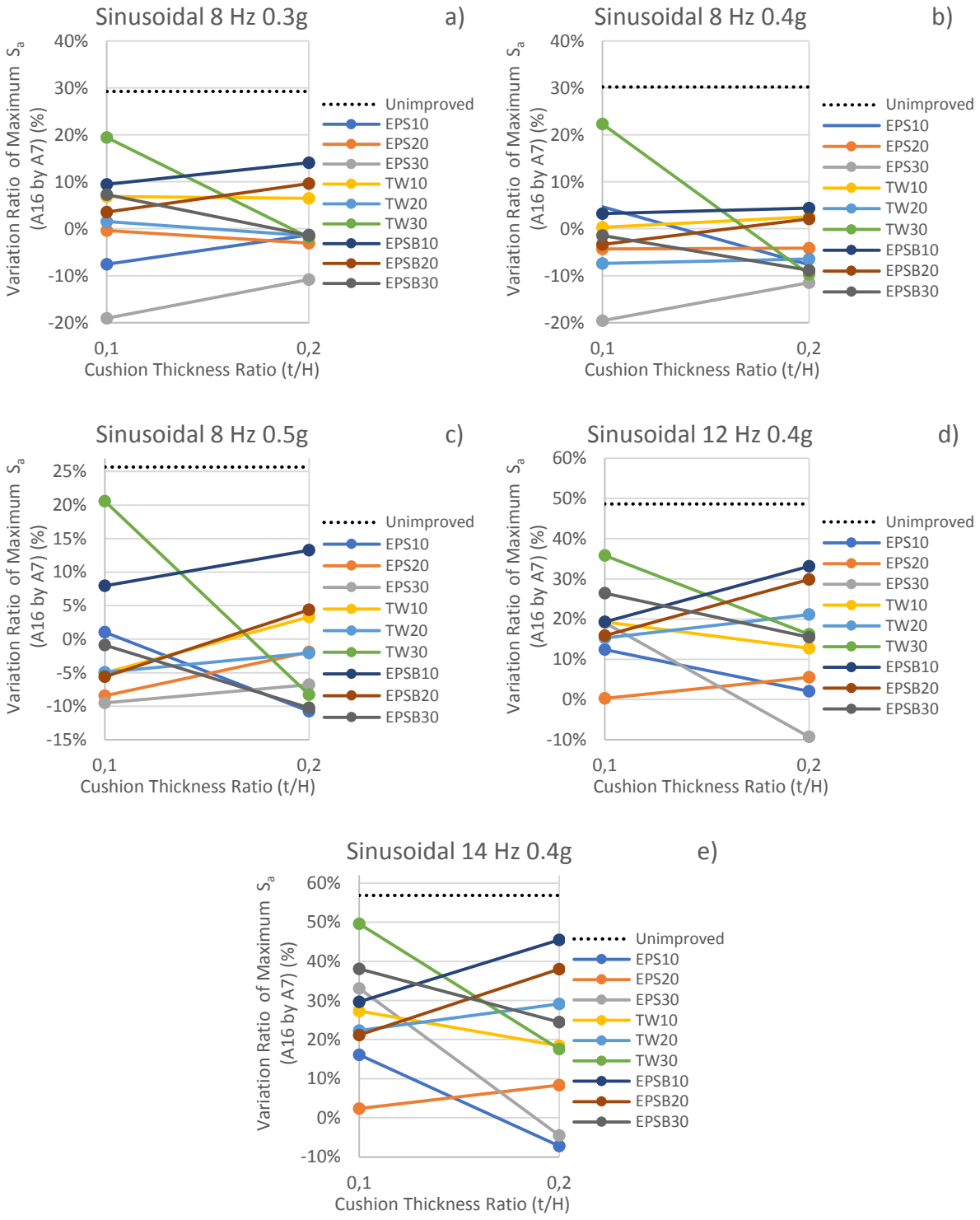


Figure 5.30 The maximum spectral acceleration variation ratio (A16 by A7) for all cushion cases under a) sinusoidal motion at 0.3g amplitude with 8 Hz frequency, b) sinusoidal motion at 0.4g amplitude with 8 Hz frequency, c) sinusoidal motion at 0.5g amplitude with 8 Hz frequency, d) sinusoidal motion at 0.4g amplitude with 12 Hz frequency, e) sinusoidal motion at 0.4g amplitude with 14 Hz frequency.

## 5.5. Discussion on the Effects of Different Cushion Types

In this part of the study, all types of cushions as EPS geofoam, tire waste and sand mixture and EPS beads and sand mixture are compared to each other at the same thicknesses as 4cm and 8cm under all near field earthquakes, far field earthquakes and sinusoidal motions.

### 5.5.1. Comparison of EPS Geofoam, Tire Waste and Sand Mixture, EPS Beads and Sand Mixture Cushioned Cases for t=4cm Thickness

The improvement efficiency comparison based on maximum accelerations measured from A7 for all cushion types with t=4cm thickness under far field earthquake input motions compared to the control case is given in Figure 5.31.

The results showed that the EPS geofoam cushioned case had a limited improvement efficiency of 3% for the EPS10-4cm and 1% for the EPS30-4cm. The TW cushioned cases had a maximum improvement efficiency of 1% for the TW10-4cm. The EPSB cushioned case had a limited improvement efficiency of 0.1% for the EPSB10-4cm under the scaled 1999 Kocaeli EQ Motion-İznik Station record. The improvement efficiencies are limited for the three types of cushion cases, and this may be due to the low amplitude, as the record is 0.12g amplitude.

Under the scaled 2014 Gökçeada EQ Motion-Çanakkale Station record, the EPS geofoam cushioned case has a maximum improvement efficiency of 11% when EPS10-4cm is used. The peak improvement efficiencies of TW cushioned cases are up to 7% for TW30-4cm, and for the EPSB cushioned case, it is limited to 1% when EPSB10-4cm is used.

The EPS Geofoam cushions at 4 cm thickness are mostly effective under the scaled 2020 İzmir EQ Motion-Kuşadası Station record. The EPS geofoam cushioned case has the highest improvement efficiency up to 15% when the EPS30-4cm is used. This behaviour is due to the increasing amplitude and high frequency under the far field earthquake record at 0.18g amplitude with 24.4 Hz predominant frequency. The improvement efficiency for the TW

cushioned case is limited to 2% when the TW30-4cm is used, and for the EPSB cushioned case, it is up to 1% when the EPSB20-4cm is used.

The highest improvement efficiency is observed for the cushion type EPS30-4cm under the scaled 2020 İzmir EQ Motion-Kuşadası Station record as 15%.

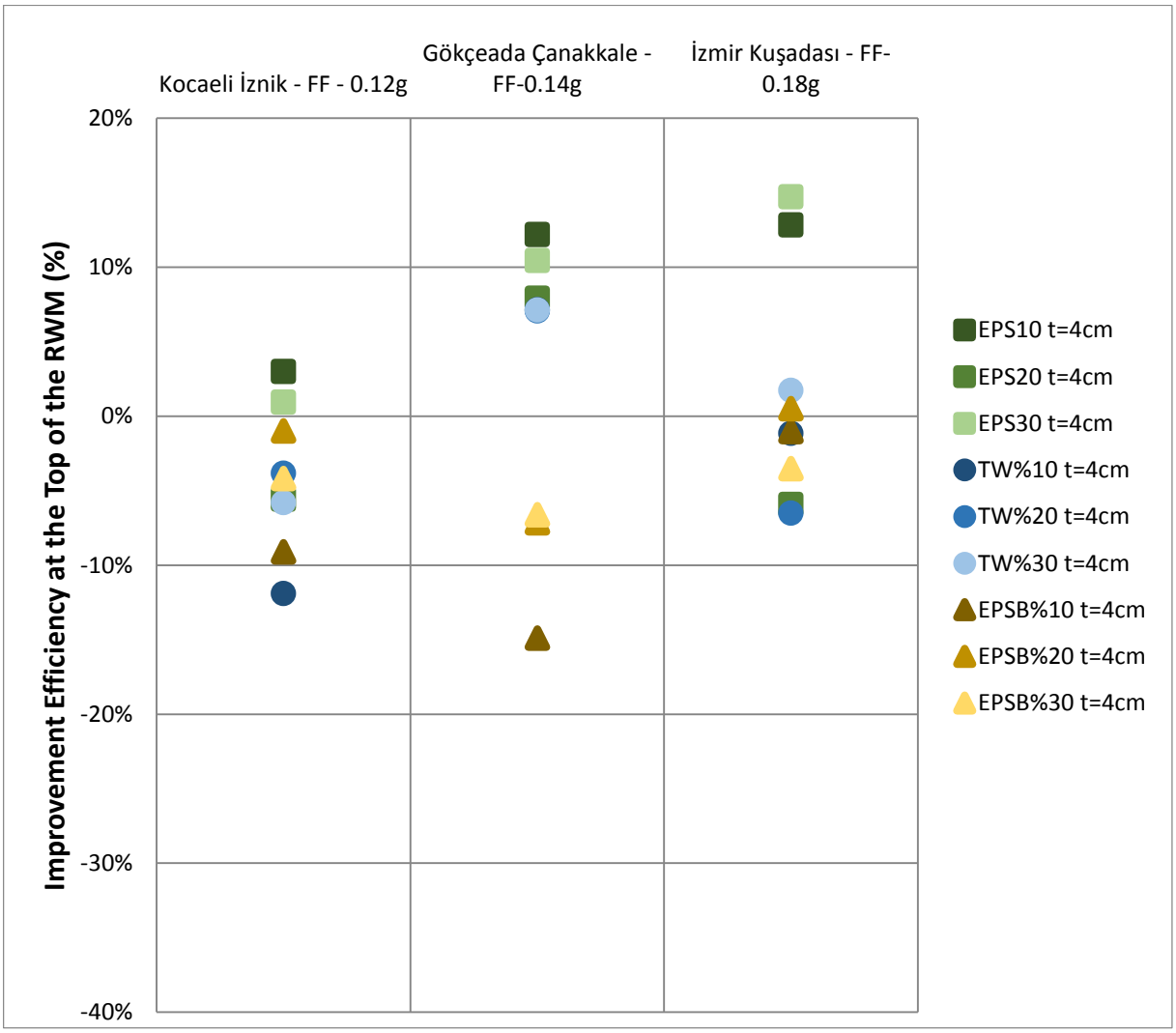


Figure 5.31 Improvement efficiency comparison for all cushion types with t=4cm thickness under far field earthquake input motions.

The improvement efficiency comparison based on maximum accelerations measured from A7 for all cushion types with t=4cm thickness under near field earthquake input motions compared to the control case is given in Figure 5.32.

The EPS geofoam cushioned case has an improvement efficiency of up to 5% when EPS10-4cm is used. For the TW cushion and EPSB cushions, acceleration reduction is not observed at 4 cm thickness under the scaled 1999 Kocaeli EQ Motion-İzmit Station record.

The results showed that all three types of cushion materials demonstrated improvement at all cushion thicknesses and density/mixture ratios. The maximum improvement efficiency was obtained for EPS20-4cm, which showed an improvement efficiency of around 23%. For TW20-4cm, the maximum improvement efficiency was around 12%. For EPSB20-4cm, the maximum improvement efficiency was around 10%. The study suggests that these cushion materials can be effective in improving the performance of retaining walls under the scaled 1940 Imperial Valley EQ-El Centro Station record, having earthquake characteristics at 0.32g with 6 Hz frequency.

Under the scaled 1995 Kobe EQ record, using EPS20-4cm results in a 30% improvement efficiency. The peak improvement efficiency for the TW cushion type is TW30-4cm with 13%. Using EPSB cushion, no acceleration reduction was observed for the 4 cm cushion thickness.

The highest improvement efficiency is observed for the cushion type EPS20-4cm as 30%.

In comparison of far field and near field earthquake records, it is observed that the improvement efficiencies are higher for the near field earthquakes especially for the EPS Geofoam and TW cushion types. This result can be considered as high amplitude effect.

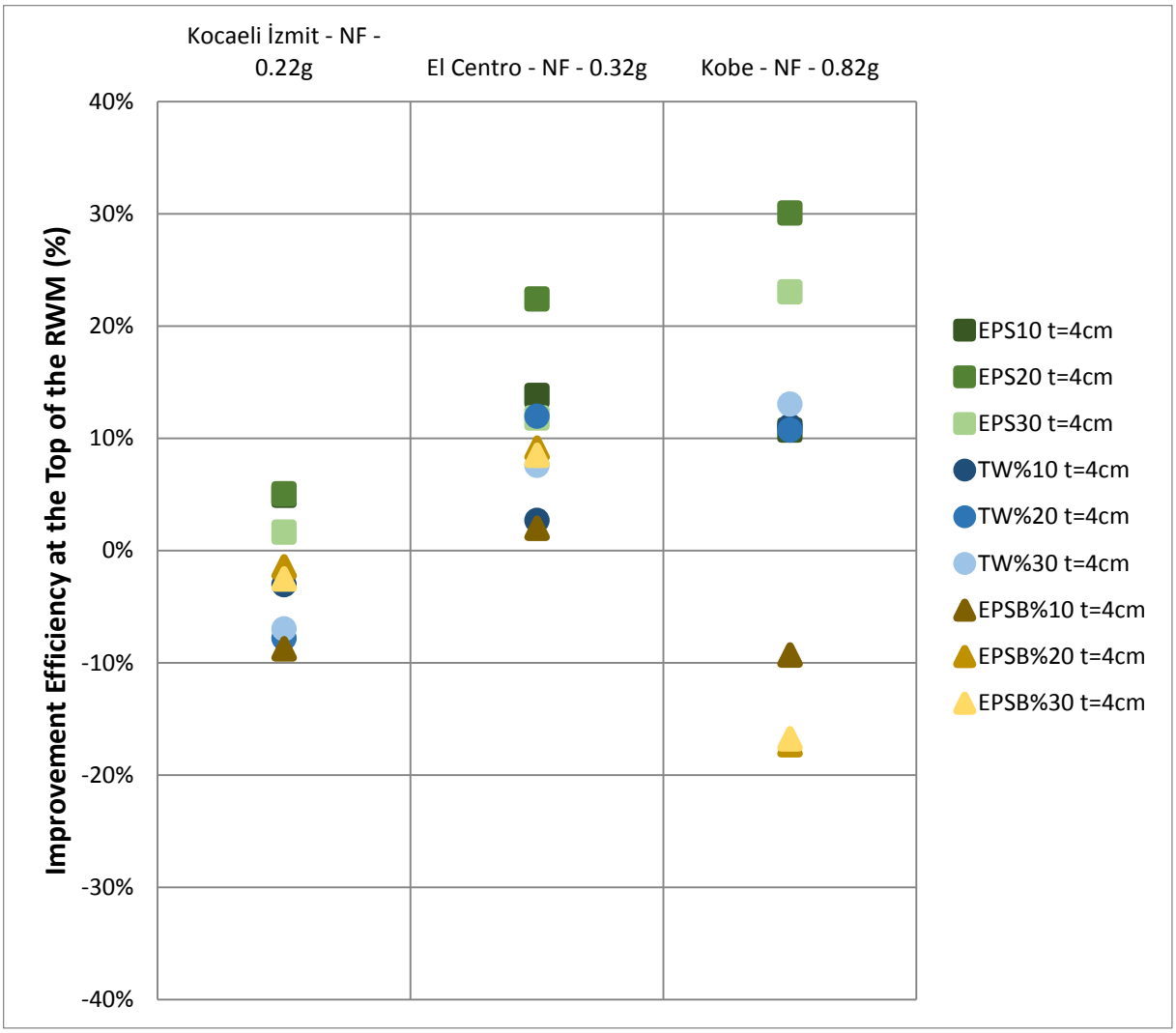


Figure 5.32 Improvement efficiency comparison for all cushion types with t=4cm thickness under near field earthquake input motions.

The improvement efficiency comparison based on maximum accelerations measured from A7 for all cushion types with t=4cm thickness under sinusoidal input motions compared to the control case is given in Figure 5.33.

Under sinusoidal motion at 0.3g amplitude with 8 Hz frequency, the EPS30-4cm has the highest improvement efficiency of up to 24%, resulting in the highest reduction of transmitted accelerations. The cushioned cases of TW have an improvement efficiency up to 4% for TW20-4cm and TW30-4cm, and the improvement efficiency of EPSB cushioned cases is limited to 1% for the EPSB20-4cm.

The EPS geofoam cushioned case has an improvement efficiency of 26% when using EPS30-4cm. The TW cushion type is slightly effective as a cushion with a maximum improvement efficiency of nearly 6% for the cushion types TW20-4cm and TW30-4cm. The EPSB cushioned case with a maximum improvement efficiency of nearly 4% is for the EPSB10-4cm under sinusoidal motion at 0.4g amplitude with 8 Hz frequency.

The use of EPS30-4cm results in a 26% improvement efficiency. Meanwhile, the TW cushion type provides a slightly effective cushion, with the highest improvement efficiency of almost 7% seen for the TW20-4cm and TW30-4cm cushion types. The EPSB cushioned case, on the other hand, shows a maximum improvement efficiency of almost 1% for the EPSB30-4cm under sinusoidal motion at 0.5g amplitude with 8 Hz frequency.

Under sinusoidal motion at 0.4g amplitude with 12 Hz frequency, the highest improvement efficiency is achieved for the EPS10-4cm with the highest value of 17%. The maximum improvement efficiency is nearly 8% for the cushion types TW10-4cm and TW30-4cm and is nearly 3% for EPSB10-4cm.

When subjected to sinusoidal motion at 0.4g amplitude with 12 Hz frequency, the EPS30-4cm cushion type exhibits the highest improvement efficiency at 17%. The cushion type

TW10-4cm shows a peak improvement efficiency of approximately 6%, while the EPSB10-4cm cushion type has a peak improvement efficiency of approximately 1.5%.

The highest improvement efficiency is observed for the cushion type EPS30-4cm under sinusoidal motion at 0.5g amplitude with 8 Hz frequency as 26%.

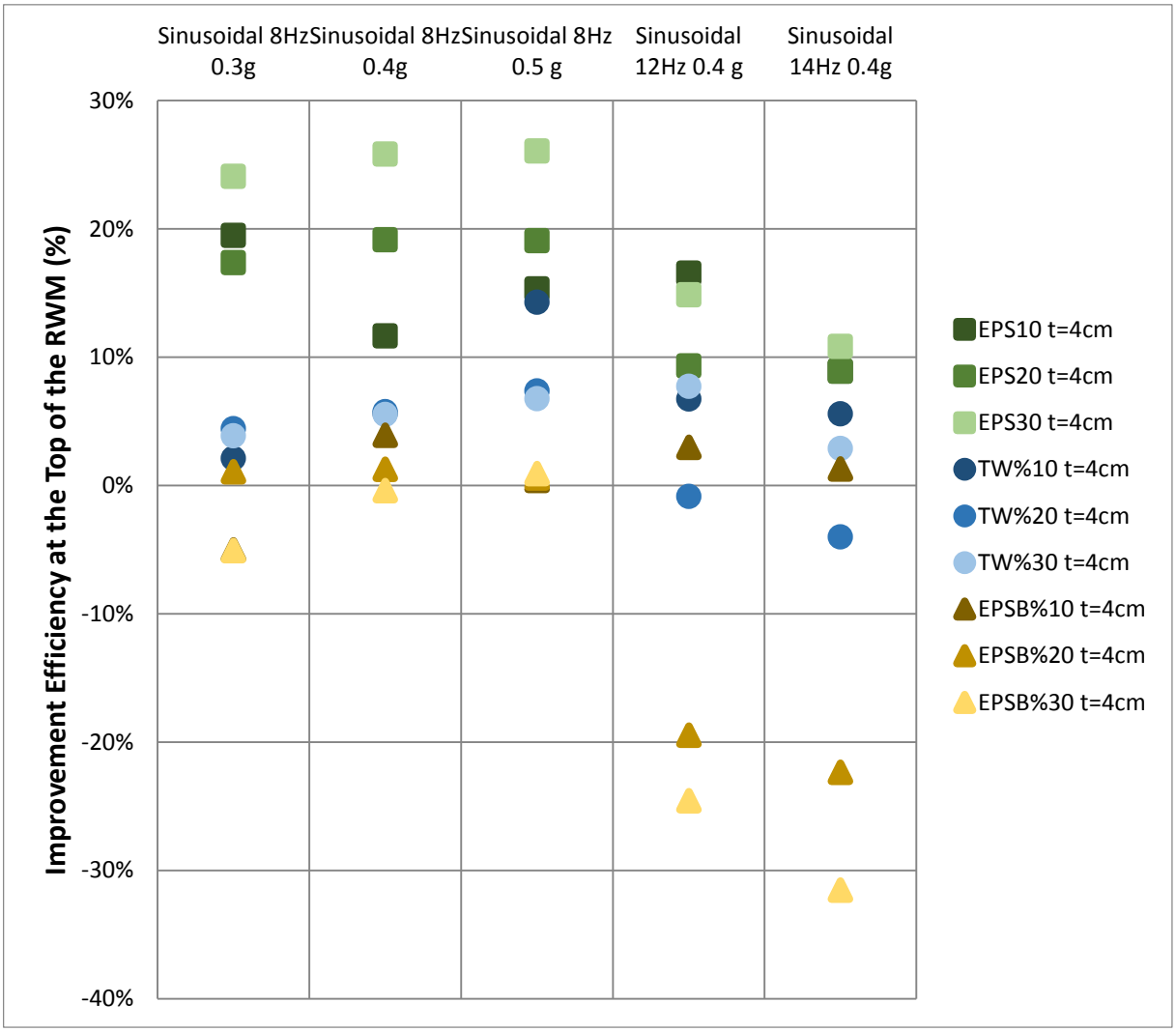


Figure 5.33 Improvement efficiency comparison for all cushion types with t=4cm thickness under sinusoidal input motions.

The improvement efficiency comparison based on maximum accelerations measured from A7 for all cushion types with t=4cm thickness under all input motions compared to the control case is given in Figure 5.34.

Considering all the cushion types for t=4cm, the best improvement values under all input earthquake motions and sinusoidal motions were obtained in the inclusion of EPS geofoam. The highest improvement efficiency values were obtained for the cushion type EPS20-4cm as 30% under the scaled 1995 Kobe EQ record and for the cushion type EPS30-4cm under sinusoidal motion at 0.5g amplitude with 8 Hz frequency and sinusoidal motion at 0.4g amplitude with 8 Hz frequency executions as 26% and 25% respectively. The improvement efficiencies in cushions were observed more significantly under sinusoidal motions than real earthquake motions. The cushions composed of EPS geofoam with t/H=0.1 showed the best improvement efficiency compared to the cushion types consisting of TW and EPSB cushion types.

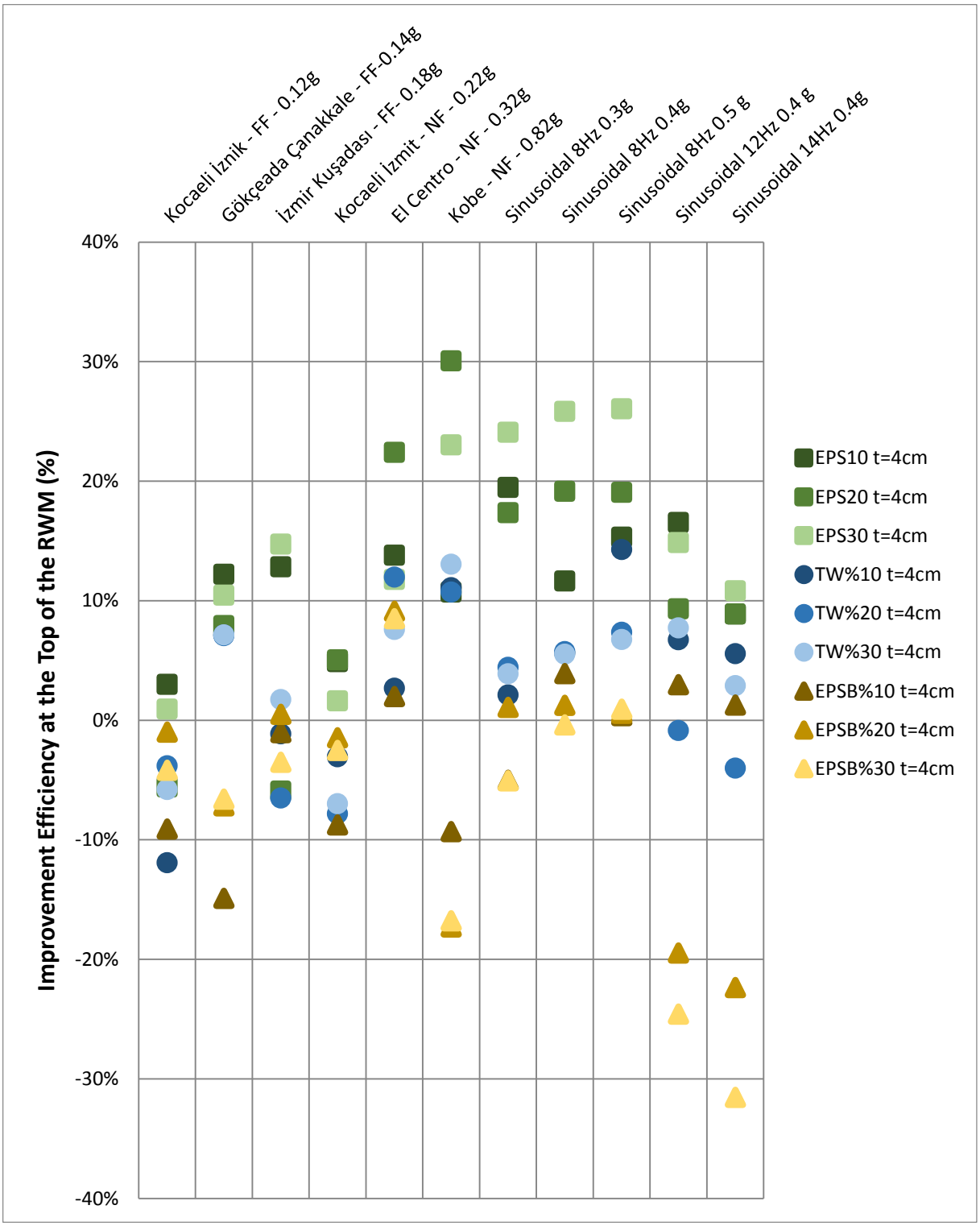


Figure 5.34 Improvement efficiency comparison for all cushion types with t=4cm thickness under all input motions.

### 5.5.2. Comparison of EPS Geofoam, Tire Waste and Sand Mixture, EPS Beads and Sand Mixture Cushioned Cases for t=8cm Thickness

The improvement efficiency comparison based on maximum accelerations measured from A7 for all cushion types with t=8cm thickness under far field earthquake input motions compared to the control case is given in Figure 5.35.

The use of EPS geofoam cushioned cases resulted in a slight improvement efficiency of 1% for the EPS30-8cm, while TW cushioned cases had a maximum improvement efficiency of 1% for the TW20-8cm. The EPSB cushioned case had a limited improvement efficiency of 0.1% for the EPSB10-8cm when subjected to the scaled 1999 Kocaeli EQ Motion-İznik Station record. The improvement efficiencies for all three types of cushion cases were limited, which could be attributed to the low amplitude of the record, which had a 0.12g amplitude.

Under the scaled 2014 Gökçeada EQ Motion-Çanakkale Station record using EPS30-8cm resulted in the highest improvement efficiency of 18%. On the other hand, the peak improvement efficiencies for TW cushioned cases were 9% for TW20-8cm, while no improvement efficiency was observed for the EPSB cushioned case.

The EPS Geofoam cushions at 8 cm thickness are mostly effective under the scaled 2020 İzmir EQ Motion-Kuşadası Station record. Among the different types of EPS geofoam cushioned cases, the EPS30-8cm has demonstrated the highest improvement efficiency, reaching up to 28%. This is because of the earthquake record's increasing amplitude and high frequency, which is more pronounced in the far field at 0.18g amplitude with a predominant frequency of 24.4 Hz. On the other hand, the improvement efficiency for the TW cushioned case is limited to 1% when using TW30-8cm, while for the EPSB cushioned case, it can go up to 3% when using EPSB20-8cm.

The highest improvement efficiency is observed for the cushion type EPS20-8cm under the scaled 2020 İzmir EQ Motion-Kuşadası Station record as 28%.

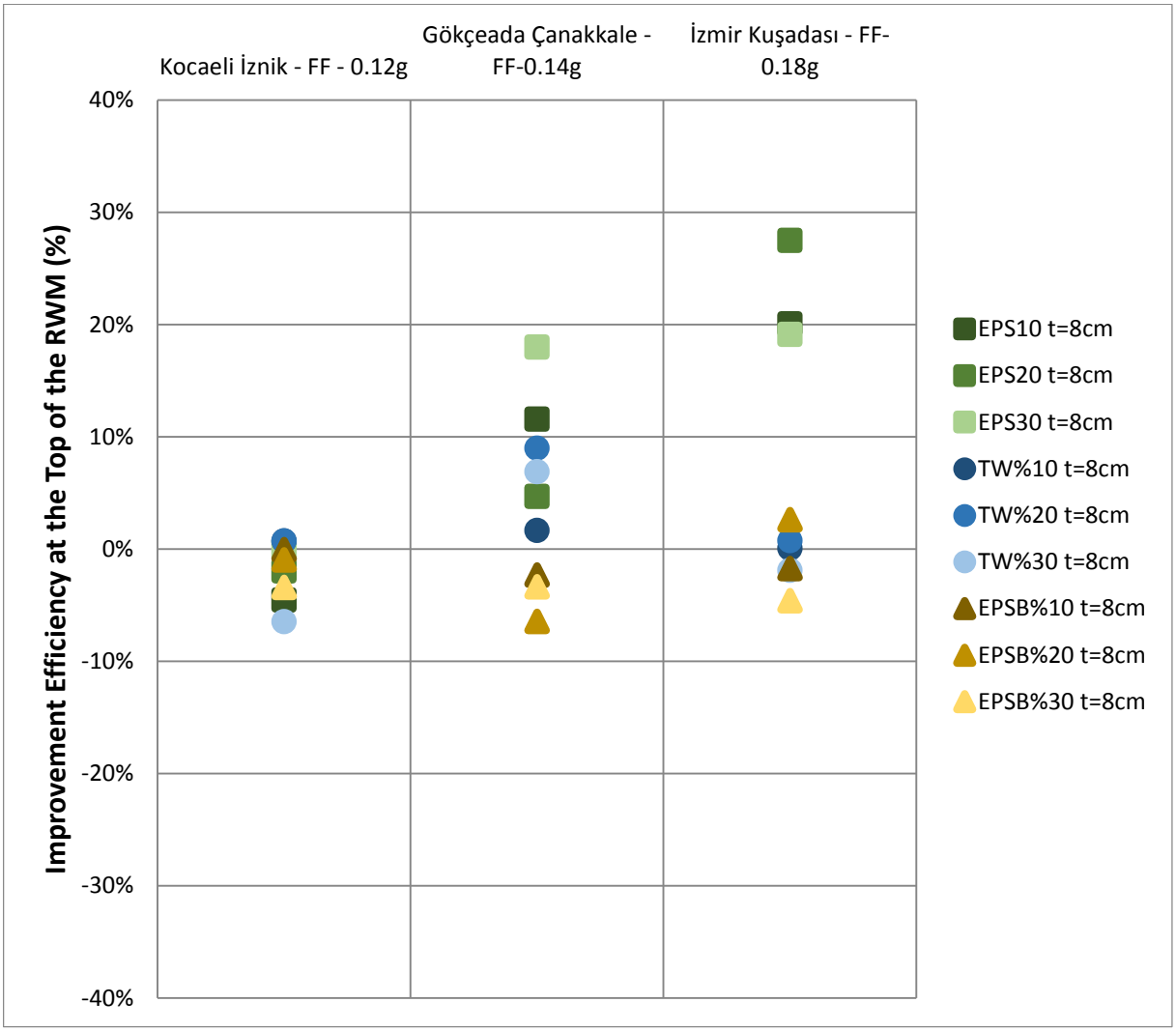


Figure 5.35 Improvement efficiency comparison for all cushion types with t=8cm thickness under far field earthquake input motions.

The improvement efficiency comparison based on maximum accelerations measured from A7 for all cushion types with t=8cm thickness under near field earthquake input motions compared to the control case is given in Figure 5.36.

The use of EPS geofoam cushion results in a 10% improvement in efficiency when EPS10-8cm is utilized. However, there is no acceleration reduction for TW cushion and EPSB cushions at an 8 cm thickness when subjected to the scaled 1999 Kocaeli EQ Motion-İzmit Station record.

The study found that all three cushion materials improved the performance of retaining walls under the scaled 1940 Imperial Valley EQ-El Centro Station record by using 8 cm thickness. The most effective cushion material was EPS20-8cm, which showed an improvement efficiency of approximately 21%. TW20-8cm had a maximum improvement efficiency of around 9%, while EPSB30-8cm had a maximum improvement efficiency of around 7%. The study may indicate that these cushion materials can be useful in enhancing the performance of retaining walls under earthquakes characteristics at 0.32g amplitude with 6 Hz frequency.

Under the scaled 1995 Kobe EQ record, almost all three cushion materials with 8 cm thickness showed improvement by reducing maximum accelerations at the top of the RWM. Using EPS20-8cm results in up to 16% improvement efficiency. The highest improvement efficiency for the TW cushion type is TW30-8cm with 21%. Using the EPSB cushion, the highest improvement efficiency for the EBSB10-8cm with 4%.

The highest improvement efficiency is observed for the cushion type EPS20-8cm under the scaled 1940 Imperial Valley EQ-El Centro Station record as 21%.

It was noticed that improvements are more effective for near field earthquakes, particularly for EPS geofoam and TW cushion types. This outcome can be attributed to the high amplitude effect.

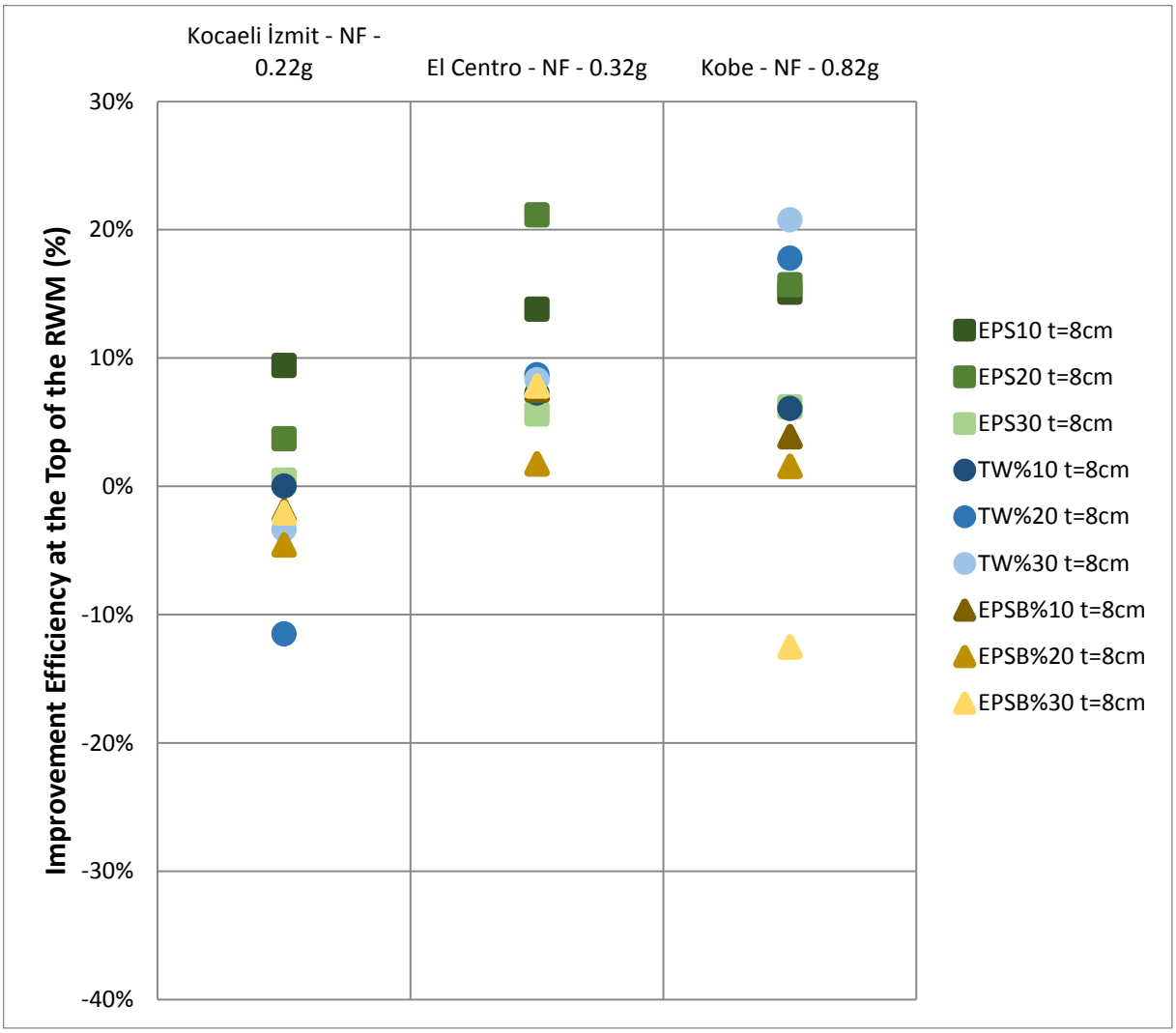


Figure 5.36 Improvement efficiency comparison for all cushion types with t=8cm thickness under near field earthquake input motions.

The improvement efficiency comparison based on maximum accelerations measured from A7 for all cushion types with t=8cm thickness under sinusoidal input motions compared to the control case is given in Figure 5.37.

Under sinusoidal motion at 0.3g amplitude with 8 Hz frequency, the EPS30-8cm material exhibits the most significant improvement efficiency of up to 42%, resulting in the most substantial reduction of transmitted accelerations during seismic activity. On the other hand, the cushioned cases made of TW material have an improvement efficiency of up to 11% for TW10-8 cm, while the improvement efficiency of EPSB cushioned cases is limited to only 1% for the EPSB10-8cm, EPSB20-8cm, and EPSB30-8cm.

The EPS geofoam case provides a 42% improvement in efficiency when using EPS30-8cm. The TW cushion type is somewhat effective as a cushion, with a peak improvement efficiency of almost 11% for the TW30-8cm cushion. The EPSB cushioned case has a peak improvement efficiency of almost 6% for the EPSB10-8cm, EPSB20-8cm, and EPSB30-8cm under sinusoidal motion at 0.4g amplitude with 8 Hz frequency.

The utilization of EPS30-8cm leads to a 40% increase in improvement efficiency. Comparatively, the TW cushion type offers a slightly effective cushion, with the highest improvement efficiency for the TW20-8cm and TW30-8cm cushion types, which show an improvement efficiency of almost 12%. On the other hand, the EPSB cushioned case demonstrated a maximum improvement efficiency of almost 6% for the EPSB10-8cm, EPSB20-8cm, and EPSB30-8cm under sinusoidal motion at 0.5g amplitude with 8 Hz frequency.

The EPS30-8cm exhibits the highest improvement efficiency under sinusoidal motion at 0.4g amplitude with 12 Hz frequency with a peak value of 42%. The cushion type TW30-8cm shows a peak improvement efficiency of nearly 5%, while no acceleration reduction is observed for the EPSB cases.

When subjected to sinusoidal motion at 0.4g amplitude with 12 Hz frequency, the EPS10-8cm cushion type exhibits the highest improvement efficiency at 28%. On the other hand, the TW30-8cm cushion type shows a peak improvement efficiency of around 2%, and no acceleration reduction is observed for the EPSB cases.

The highest improvement efficiency is observed for the cushion type EPS30-8cm under sinusoidal motion at 0.4g amplitude with 12 Hz frequency as 42%.

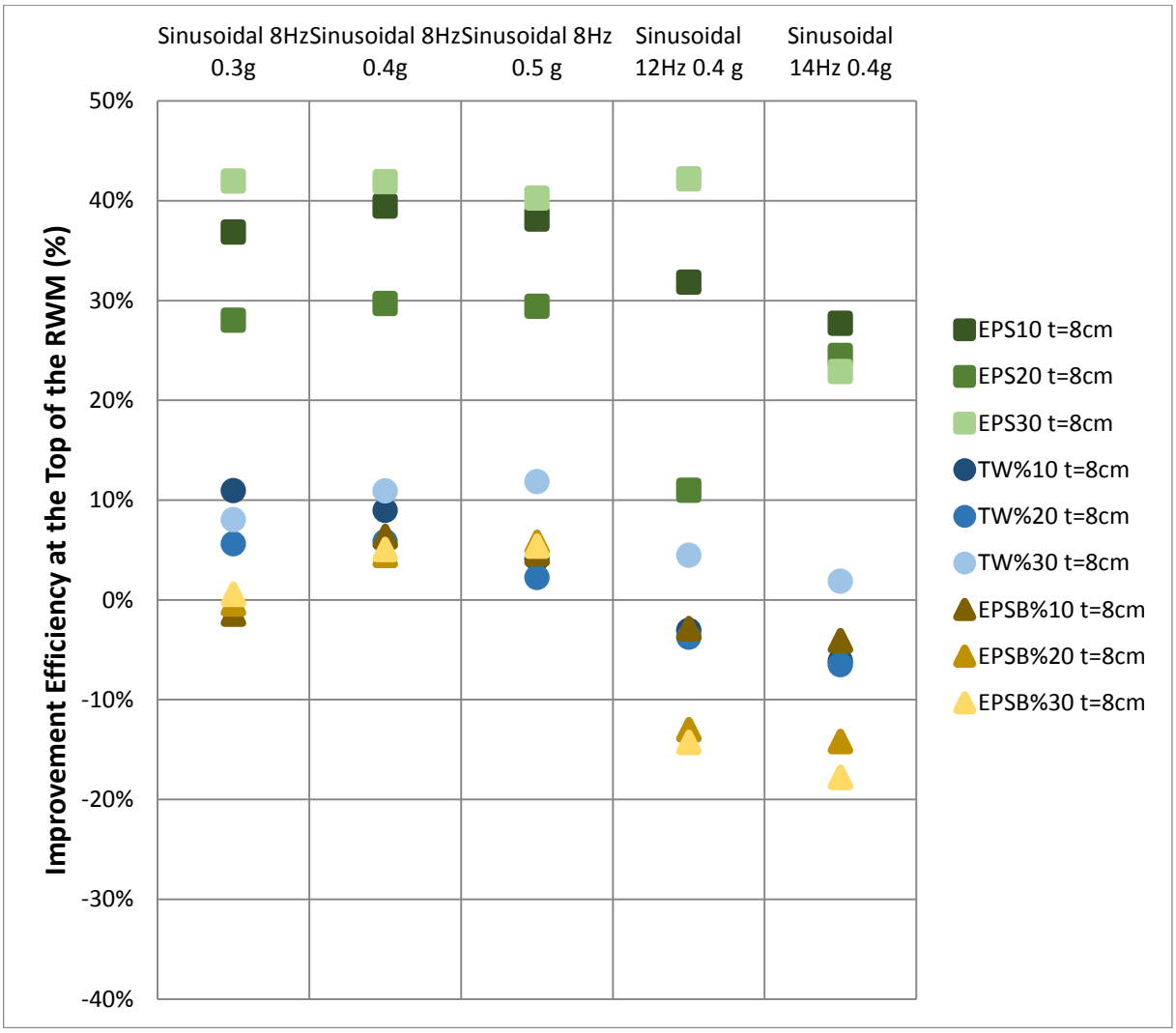


Figure 5.37 Improvement efficiency comparison for all cushion types with t=8cm thickness under sinusoidal input motions.

The improvement efficiency comparison based on maximum accelerations measured from A7 for all cushion types with t=8cm thickness under all input motions compared to the control case is given in Figure 5.37.

Considering all the cushion types for t=8cm, the best improvement values under all input earthquake motions and sinusoidal motions were obtained for the inclusion of the EPS geofoam cushion. The highest improvement efficiency values were obtained for the cushion type EPS30-8cm as 42% under sinusoidal motion at 0.3g amplitude with 8 Hz frequency and for the cushion type EPS30-8cm under sinusoidal motion at 0.5g amplitude with 8 Hz frequency and sinusoidal motion at 0.4g amplitude with 12 Hz frequency executions as 41% and 42% respectively. The improvement efficiencies based on maximum accelerations (A7) of cushioned cases were observed more significantly under sinusoidal motions than real earthquake motions. The cushions composed of EPS geofoam with t/H=0.2 showed the best improvement efficiency compared to those consisting of TW and EPSB cushion types.

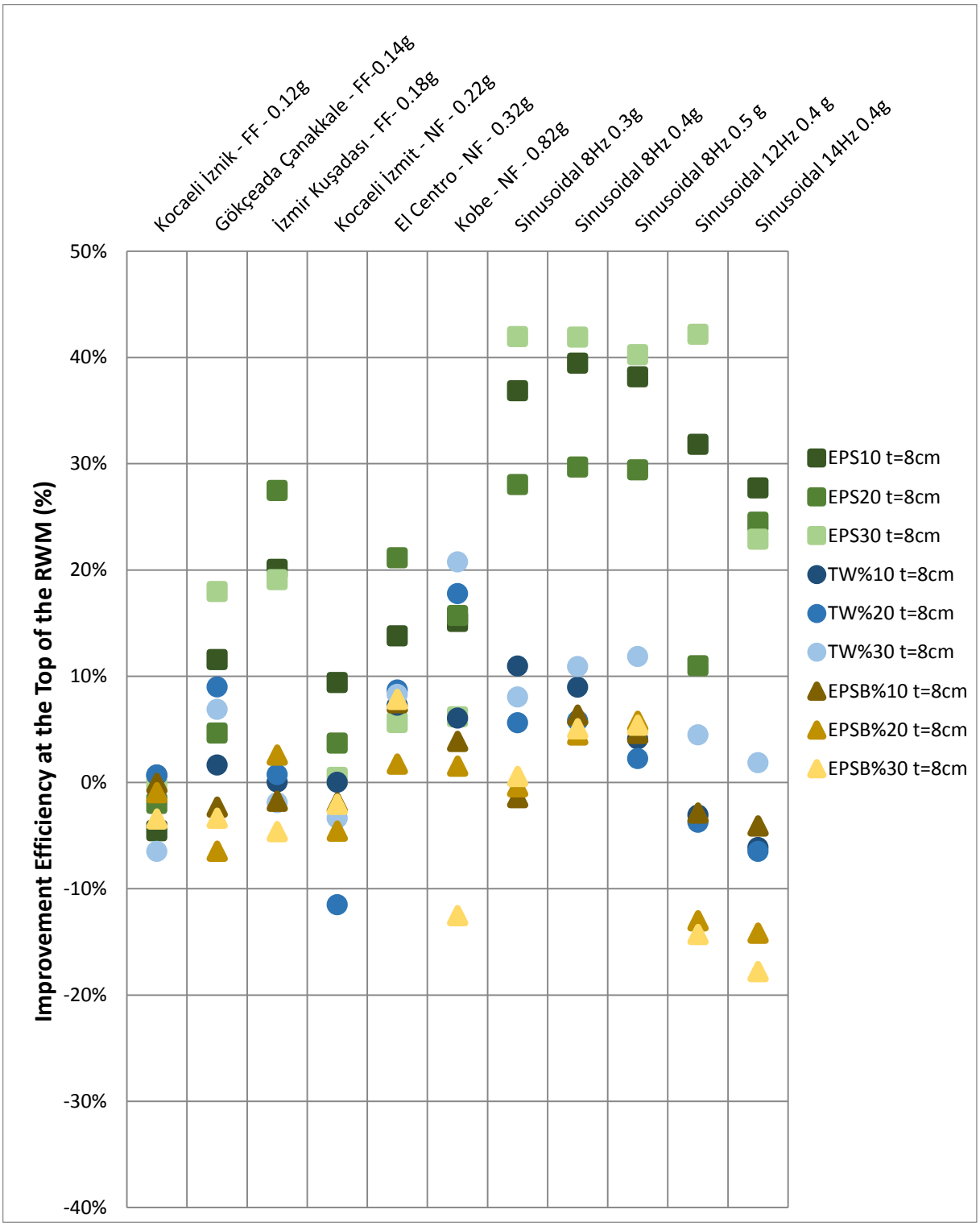


Figure 5.38 Improvement efficiency comparison for all cushion types with t=8cm thickness under all input motions.

Evaluation of the outcomes of various cushion types for 4 cm and 8 cm thicknesses under different scaled earthquake and sinusoidal input motions, it was found that the most significant improvement effect was achieved for cushions made of EPS geofoam. The usage of EPS geofoam cushion may considerably improve the seismic performance of retaining walls. The EPS geofoam's ability of high damping capacity and compressibility acts as a cushion that absorbs seismic energy, thereby reducing the transmitted acceleration and lateral displacement of the retaining wall system and it approaches with the results of this study. The next best option was cushions made of tire waste and sand mixture, which is eco-friendly and cost-effective, while the least improvement was observed in cases where EPSB was used as cushions. The seismic performance of retaining walls may be enhanced by using TW cushions. Tire waste is a more efficient material for absorbing energy than sand because it has greater damping and stiffness properties. Depending on the exact use, each of these materials has its own special qualities that make them suitable for use as cushions. All the three cushion materials as EPS geofoam, tire waste and sand mixtures and EPS beads and sand mixtures are lightweight and resilient, offer high strength, high damping ability, compressibility and deformation properties and can be used to reduce lateral earth pressure on retaining walls. Although all of these materials have similar properties, differences in these similar properties affected the experimental results. EPS geofoam has the lowest density among cushion types. Compared to tire waste, EPS geofoam is stiffer. The effectiveness of these materials as cushions may also influenced by the difference in elasticity modulus.

# 6. CONCLUSIONS

The purpose of the study is to improve the seismic behaviour of the retaining walls by evaluating the effects of different types of cushions considering various parameters, such as thickness and density/mixing ratio, and input motion characteristics. The most notable aspect of this study is that EPS beads and sand mixture was used as a cushion material as the first study in the literature. The impacts of thickness, mixing ratio, earthquake motions and sinusoidal motions were examined for the EPSB cushion. The EPS geofoam and TW cushions were also used as cushion materials, and their performances were compared under the same input motions.

To investigate the cushion effect on the seismic performance of the retaining wall, a model was created at a scale of 1/15. The shake table experiment was started with the control case, where no cushion material was used. The experiments were then continued using three different cushion materials placed behind the retaining wall by adjusting thickness and density/mixture ratio under the same input motions.

The following conclusions have been evaluated for the EPS Geofoam cushioned cases from the experimental studies:

- EPS geofoam as a cushion was ineffective in reducing the maximum accelerations at the top of the RWM under the scaled 1999 Kocaeli EQ Motion-İznik Station record. However, it was effective under the scaled 2014 Gökçeada EQ Motion-Çanakkale Station record and the scaled 2020 İzmir EQ Motion-Kuşadası Station record, with the highest improvement efficiency observed for EPS30-8cm under the scaled 2014 Gökçeada EQ Motion-Çanakkale Station record and for EPS20-8cm under the scaled 2020 İzmir EQ Motion-Kuşadası Station record.

- The EPS geofoam cushioned cases showed the best improvement efficiencies based on maximum accelerations under the scaled 1995 Kobe EQ record and the scaled 1940

Imperial Valley EQ-El Centro Station record for the cushion EPS20-4cm, with improvement efficiencies of 30% and 23%, respectively.

- EPS geofoam was observed to be effective in reducing maximum accelerations at the top of the RWM under the near field records, as the scaled 1940 Imperial Valley EQ-El Centro Station record and the scaled 1995 Kobe EQ record. The thickness and density of the EPS geofoam cushion was found to affect the improvement efficiencies based on maximum accelerations.

- The EPS geofoam cushioned case can significantly reduce the maximum lateral displacements at the top of the RWM under the scaled earthquake input motions. The highest reduction was observed for the EPS10-8cm cushioned model under the scaled 1995 Kobe EQ record. EPS geofoam was effective as a cushion under the scaled 2014 Gökçeada EQ Motion-Çanakkale Station, the scaled 2020 İzmir EQ Motion-Kuşadası Station, and the scaled 1995 Kobe EQ record in reducing the maximum lateral displacement of the model.

- Using EPS geofoam cushioned cases led to an improvement effect by reducing transmitted accelerations under sinusoidal motion at 0.3g amplitude with 8 Hz frequency. The improvement efficiency ranged between 17% and 42% for the EPS30-8cm cushioned case, showing the best improvement effect. Similarly, under sinusoidal motion with 0.4g amplitude with 8 Hz frequency, the improvement efficiency ranged from 12% to 42%. The maximum improvement efficiency was 40% under sinusoidal motion with 0.5g amplitude with 8 Hz frequency, with improvement efficiency ranging from 15% to 40% for all EPS geofoam cushion thicknesses and densities. The EPS geofoam cushioned type demonstrated improvement at all cushion thicknesses and densities under sinusoidal motions.

- As the thickness of the EPS geofoam cushion increased, the acceleration recorded at the top of the RWM decreased compared to the control case under all sinusoidal input motions at 0.3g, 0.4g, and 0.5g amplitude with 8 Hz frequency.

- The maximum improvement efficiency of the transmitted accelerations was found to be the EPS30-8cm cushioned case corresponding to 0.2 t/H ratio under sinusoidal motion at 0.4g amplitude with 12 Hz frequency. Increasing cushion thickness resulted in greater seismic reduction.

- The maximum acceleration measured at the top of the RWM reduced compared to the control case as the thickness of the EPS geofoam cushion increased with a predominant frequency in the range of 12–14 Hz for the EPS10 and EPS30 cushioned cases.

- EPS30-8cm was found to be most effective in reducing displacement values at the top of the RWM under the sinusoidal motion at 0.3g amplitude with 8 Hz frequency and sinusoidal motion at 0.4g amplitude with 8 Hz frequency with the highest reduction up to 53%. EPS geofoam was found to be effective as a cushion under sinusoidal motions in the frequency range between 8 Hz and 12 Hz and the amplitude range between 0.3g and 0.5g in reducing the maximum lateral displacement of the model.

- The EPS20 had the maximum decrease in maximum spectral accelerations under the far field earthquakes. Maximum spectral accelerations under the scaled 2020 İzmir EQ Motion-Kuşadası Station record were reduced by 38% using EPS30-8cm compared to the control model. However, the reduction in maximum $S_a$ was limited to 10% under the scaled 2014 Gökçeada EQ Motion-Çanakkale Station record.

- Increasing cushion thickness positively affected the calculated spectral accelerations, while the effect of density was more effective in the 0.05-0.10 sec period range. The

EPS geofoam cushion type generally exhibited improvement by reducing the spectral accelerations across all cushion thicknesses and densities examined in this study. The best improvement was seen in the 0.05-0.10 sec period range under both far field and near field earthquakes, with a higher improvement effect observed under near field earthquakes due to higher acceleration amplitude.

- Increasing the cushion thickness ratio of the EPS geofoam led to a decrease in maximum spectral accelerations at a period of 0.085 seconds with 12 Hz frequency and at a period of 0.07 seconds with 14 Hz frequency. Additionally, the EPS geofoam density was found to be effective in decreasing maximum spectral accelerations at a period of 0.125 seconds under sinusoidal motions with 0.3g, 0.4g, and 0.5g amplitude with 8 Hz frequency. EPS30 was found to have the maximum decrease in spectral accelerations under all input sinusoidal motions. Overall, the study showed that the cushioned model EPS30-8cm provided significant improvement in reducing maximum spectral accelerations under sinusoidal motions with 0.3g amplitude, 8 Hz frequency, and sinusoidal motions with 0.4g amplitude, 8 Hz frequency with 42% reduction.

- When comparing the far field and near field effect based on spectral acceleration reduction, the best improvements were seen in the 0.05-0.10 sec period range in both. However, the reduction was up to 38% under far field earthquakes, whereas it was up to 56% under near field earthquakes. This better improvement effect can be due to the higher acceleration amplitude, which is higher under the near field than under the far field.

In consideration of the EPS geofoam cushion, it is a type of lightweight material with low density and high stiffness making it an effective buffer. The compressibility and high damping ability of EPS geofoam ensures that the seismic forces acting on retaining walls are considerably reduced. EPS geofoam cushion exhibit an elastic behaviour and can reduce maximum accelerations and lateral displacements. EPS geofoam reduces lateral pressure and

settlements and absorbs seismic energy, minimizing the lateral displacement of the walls. In this study, the decrease in transmitted acceleration of the retaining wall model can be used as a proof of this result depending on the input motion characteristics. EPS geofoam cushion can significantly decrease maximum acceleration values and maximum spectral accelerations under the given input motions, which could enhance the seismic performance of retaining walls. The reduction in transmitted acceleration and displacement of the retaining wall model depends on properties such as thickness, density, and other properties. Furthermore, as the thickness of EPS geofoam increases, the lateral pressures applied to the retaining wall decrease even further, and the maximum accelerations decrease to a greater extent. This reduction in transmitted acceleration and displacement of the retaining wall model is evidence of the effectiveness of EPS geofoam as a cushion.

The following conclusions have been evaluated for the TW cushioned cases from the experimental studies:

- TW cushion was slightly effective in reducing the maximum acceleration values at the top of the RWM under far field earthquakes with a 1% improvement efficiency for the TW10-4cm under the scaled 1999 Kocaeli EQ Motion-İznik Station record, with a 9% improvement efficiency for the TW20-8cm under the scaled 2014 Gökçeada EQ Motion-Çanakkale Station record and with 2% improvement efficiency for the TW30-4cm under the scaled 2020 İzmir EQ Motion-Kuşadası Station record.

- Under the scaled 1940 Imperial Valley EQ-El Centro Station record, the TW cushion type demonstrated improvement at all cushion thicknesses and mixture ratios, with the maximum improvement efficiency nearly 12% for the TW20-4cm. The TW30-8cm had an improvement effect by reducing the transmitted accelerations of the retaining wall under the scaled 1995 Kobe EQ record, with a maximum improvement efficiency of 21%. The tire waste sand mixture is effective as a cushion at these input motion characteristics at 0.32g-0.82g amplitude range and with 6 Hz frequency; however, it is slightly effective at 0.22g with 13 Hz frequency.

- TW cushioned cases can slightly reduce maximum lateral displacements at the top of the RWM during earthquakes, with the highest reduction observed for the TW10-8cm cushioned model under the scaled 1995 Kobe EQ record and for the TW20-8cm cushioned model under the scaled 2014 Gökçeada EQ Motion-Çanakkale Station record.

- Tire waste sand mixture as a cushion considerably reduced accelerations with 10% - 14% improvement efficiency at these input motion characteristics under sinusoidal motion at 0.3g-0.5g amplitude range with 8 Hz frequency.

- Under all sinusoidal input motions at 0.3g, 0.4g, and 0.5g amplitude with 8 Hz frequency, the maximum acceleration recorded at the top of the RWM reduced compared to the control case as the thickness of the TW cushion increased.

- The acceleration measured at the top of the RWM reduced compared to the control case as the thickness of the TW cushion increased with the predominant frequency in the range of 6 Hz–13 Hz and with the amplitude range 0.22g-0.32g for the TW10, TW20 and TW30 cushioned cases.

- TW cushion showed improvement by reducing accelerations in the 5-7% range at the input motion characteristics under sinusoidal motion at 0.4g amplitude with 12 – 14 Hz frequency range.

- TW cushion can effectively reduce the maximum lateral displacement values at the top of the RWM for different input motion characteristics which is up to 31% under sinusoidal motion at 0.3g amplitude with 8 Hz frequency, 20% under sinusoidal motion at 0.4g amplitude with 8 Hz frequency, 16% under sinusoidal motion at 0.5g amplitude with 8 Hz frequency and 14.5% under sinusoidal motion at 0.4g amplitude with 12 Hz frequency.

- TW20 and TW30 showed the maximum reduction in maximum spectral accelerations. The largest decrease in maximum spectral accelerations was observed for 8 cm thickness under the scaled 2020 İzmir EQ Motion-Kuşadası Station record. TW20-8cm corresponding to 0.2 t/H ratio provided a significant improvement compared to the control model in reducing maximum spectral accelerations under the scaled 2020 İzmir EQ Motion-Kuşadası Station record with a 16% reduction. However, the improvement efficiency is limited to 7% under the scaled 2014 Gökçeada EQ Motion-Çanakkale Station record. It highlights the importance of considering the period range when taking into account far field earthquakes and suggests that higher frequencies in the 10 Hz to 20 Hz range can significantly reduce spectral accelerations when compared to the control case.

- The thickness ratio was generally effective in reducing maximum spectral accelerations with increasing cushion thickness ratio in the 0.05-0.10 sec period range, while it was less effective in the 0.10-0.20 sec range under the near field earthquakes. The TW as a cushion type generally exhibited improvement in spectral accelerations across all cushion thicknesses and densities examined in this study under near field earthquakes. The cushioned model TW10-8cm significantly improved compared to the control model in reducing maximum spectral accelerations under the scaled 1995 Kobe EQ record with a 38% reduction.

- The maximum spectral accelerations decreased with increasing cushion thickness ratio at 0.125 sec period under sinusoidal motions with 0.3g and 0.4g amplitude with 8 Hz frequency for the TW cushioned cases. However, this effect was not noticeable under the rest of the sinusoidal input motions. Increasing the mixture ratio of tire waste in the TW cushion generally led to a decrease in maximum spectral accelerations under sinusoidal motions with 0.3g, 0.4g, and 0.5g amplitude with 8 Hz frequency, particularly at a period of 0.125 sec. Additionally, increasing density generally reduced maximum spectral accelerations at a period of 0.085 sec and at 0.4g amplitude with 12 Hz frequency. TW30 had the most significant decrease in spectral accelerations under all

input sinusoidal motions. The maximum spectral accelerations decreased with a maximum reduction ratio of 11%, 10%, and 14% for different cases under different sinusoidal input motions.

- In comparison with the far field and near field earthquake effect, the best improvements for spectral acceleration reduction were obtained in the 0.05-0.10 sec period range in both. However, the reduction was up to 18% under far field earthquakes, whereas it was up to 28% under near field earthquakes. This better improvement effect is due to the higher acceleration amplitude, which is higher in the near field than in the far field.

In consideration of the tire waste material and sand mixture cushion, tire waste is a lightweight and compressible material having superior damping and stiffness characteristics compared to sand making it a more effective material for absorbing energy and improving the seismic performance of retaining walls by reducing maximum accelerations, and maximum lateral displacements. In this study, the decrease in transmitted acceleration of the retaining wall model can be used as a proof of this result depending on the input motion characteristics. TW cushion can decrease maximum accelerations, maximum lateral displacements, and maximum spectral accelerations under the given input motions. The improvement effect may vary depending on factors such as tthe amount of tire waste in the mixture, and the thickness of the tire waste and sand mixture cushion. By increasing the thickness of the tire waste cushion, the lateral forces on the retaining wall decrease, resulting in a decrease in maximum acceleration depending on the input motion characteristics.

The following conclusions have been evaluated for the EPSB cushioned cases from the experimental studies:

- The results showed that the EPSB cushion was not effective in reducing the maximum accelerations at the top of the RWM under the scaled 1999 Kocaeli EQ Motion-İznik

Station record, the scaled 2014 Gökçeada EQ Motion-Çanakkale Station record, the scaled 1999 Kocaeli EQ Motion-İzmit Station record.

- The EPSB10-8cm had an improvement effect based on the transmitted accelerationsat the top of the RWM, reducing by 4% under the scaled 1995 Kobe EQ record.

- The EPSB cushioning was effective in reducing maximum lateral displacement at the top of the RWM under earthquakes with input motion characteristics similar to those of the scaled 2014 Gökçeada EQ Motion-Çanakkale Station record, the scaled 2020 İzmir EQ Motion-Kuşadası Station record and the scaled 1995 Kobe EQ record with the most effective case being EPSB10-6cm among the EPSB cushioned cases.

- The EPSB was not effective as a cushion at frequencies and amplitudes under sinusoidal motion at 0.4g amplitude with 12 Hz frequency and sinusoidal motion at 0.4g amplitude with 14 Hz frequency.

- EPSB20-8cm was the most effective case in reducing the displacement values under sinusoidal motion at 0.3g amplitude with 8 Hz frequency.

- Under the scaled 2020 İzmir EQ Motion-Kuşadası Station record, the highest improvement efficiency was observed for EPSB20-4cm. Under the scaled 1940 Imperial Valley EQ-El Centro Station record, the highest improvement efficiency was nearly 10%, which was observed for EPSB30-6cm. Improvements up to 6% were observed under sinusoidal motion at 0.4g amplitude with 8 Hz frequency.

- According to the EPSB cushion type thickness change results, the highest improvements are at thicknesses 8 cm, corresponding to 0.2 t/H ratio. As the thickness of the EPSB

cushion increased, the improvement efficiency decreased compared to the control case under all sinusoidal input motions with 0.4g-0.5g amplitude with 8 Hz frequency.

- Under the near field earthquakes at 6 Hz – 8 Hz frequency range EPSB cushioned cases showed better improvement impact. Additionally, at the same frequency range under the near field earthquakes, as the thickness increased, the improvement efficiency increased.

- For the EPSB cushioned cases, the transmitted accelerations at the top of the RWM were reduced up to 10% for the EPSB30-6cm and 8% for the EPSB30-8cm, 9% for the EPSB20-4cm under the scaled 1940 Imperial Valley EQ-El Centro Station record, 3% for the EPSB20-8cm under the scaled 2020 İzmir EQ Motion-Kuşadası Station record.

- The maximum lateral displacements for the EPSB cushioned cases measured from the top of the RWM reduced compared to the control case. The maximum reduction by means of maximum lateral displacement was observed 25% for the EPSB20-8cm under sinusoidal motion at 0.4g amplitude with 8 Hz frequency and 18% for the EPSB10-6cm under the scaled 2020 İzmir EQ Motion-Kuşadası Station record. The compressibility of the EPS bead material may lead to a decrease in maximum lateral displacements at the top of the RWM.

- The study found that the EPSB20 and the EPSB30 had the maximum reduction in maximum spectral accelerations under far field earthquakes. The highest decrease in maximum spectral accelerations was observed for the cushion with 8 cm thickness under the scaled 2020 İzmir EQ Motion-Kuşadası Station record. The study concludes that the cushioned model EPSB20-6cm and EPSB20-8cm significantly improve the control model in terms of lowering maximum spectral accelerations under the scaled 2020 İzmir EQ Motion-Kuşadası Station record by 18%. However, under the scaled 2014 Gökçeada EQ Motion-Çanakkale Station record, the reduction is limited to 6%.

- The greatest decrease in maximum spectral accelerations was observed for the EPSB20 and EPSB30 cases. The period range of 0.05-0.10 seconds played a crucial role in reducing spectral accelerations. The improvement efficiency was limited to 18% in far field earthquakes, whereas it increased to 28% in near field earthquakes. Overall, the study suggests that using EPSB20-8cm can provide significant improvement in reducing maximum spectral accelerations under the given earthquake records.

- The increasing cushion thickness and mixture ratio of EPSB generally led to a decrease in maximum spectral accelerations, particularly at a period of 0.125 sec and under sinusoidal motions with 0.3g, 0.4g, and 0.5g amplitude with 8 Hz frequency. However, increasing mixture ratio did not affect maximum spectral accelerations for sinusoidal motions at 0.4g amplitude with 12 Hz and 14 Hz frequencies. The study found that EPSB30 had the most significant decrease in spectral accelerations under all input sinusoidal motions.

- In comparison with the far field and near field earthquake effect the best improvements for spectral acceleration reduction were seen in the 0.05-0.10 sec period range in both. However, the reduction was up to 18% under far field earthquakes, whereas was up to 28% under near field earthquakes. This better improvement effect can be due to the higher acceleration amplitude, which is higher in the near field than in the far field.

In consideration of the EPS beads and sand mixture cushion, EPS beads has characteristics such as a low density, high compressibility, and a high damping capability. The addition of EPS beads to the sand causes a decrease in the transmitted acceleration however this reduction is lower for input motions with less than 0.22g amplitude. The EPS beads to the sand as a cushion material is effective in decreasing the maximum spectral accelerations especially in the frequency ranges 10 Hz – 20 Hz. Increasing the EPS beads content and thickness of the

cushion may decrease lateral pressures on the retaining wall, resulting in a decrease in maximum lateral displacements, depending on the input motion characteristics.

The following conclusions have been evaluated for the general results of all types of cushions from the experimental studies:

Among the different types of cushions, EPS geofoam was found to provide the best improvement efficiency under the defined earthquake and sinusoidal input motions. The highest improvement efficiency values were obtained for the cushion type EPS30-8cm under sinusoidal sinusoidal motion at 0.3g amplitude with 8 Hz frequency, sinusoidal motion at 0.5g amplitude with 8 Hz frequency, and sinusoidal motion at 0.4g amplitude with 12 Hz frequency executions with the heighest improvement efficiency. The improvement efficiencies for cushions were observed more significantly under sinusoidal motions than real earthquake motions. Overall, the improvement effect of the cushions depends on the amplitude and frequency of the input motion and cushion thickness ratio and density/mixture ratio of the cushion materials. In consideration of all the results of all the cushion types the highest improvement effects were obtained for the EPS geofoam cushion type with maximum acceleration reduction up to 42%, maximum spectral acceleration reduction up to 56%, and maximum lateral displacement reduction up to 53%. All results and evaluations in these experimental studies are valid for the parameters as cushion type, thickness and density/mixture ratio and input motion used in this thesis study.

The evaluation of results indicates that all types of cushioned cases were successful in reducing the variation ratio of maximum $S_a$ compared to the control case. This indicates that cushioning has a positive effect by decreasing the maximum $S_a$ variation ratio compared to the control case under the scaled far field and near field earthquakes and sinusoidal motions. Additionally, it was found that for most cushion types, an increase in thickness ratio was effective in reducing the variation of maximum spectral accelerations for backfill and the top of the RWM.

# 7. REFERENCES

Abdullah, A., Hazarika, H., Yasufuku N., and Ishikura, R., 2017, "Numerical Study on the Seismic Response of Waterfront Retaining Wall Reinforced with Cushion", *Geotechnical Hazards from Large Earthquakes and Heavy Rainfalls*, January 2017.

ACI. 2016. 53 The Reinforced Concrete Design Handbook A Companion to ACI 318-14.

Ahn, I. S., Cheng, L., Fox, P. J., Wright, J., Patenaude, S., & Fujii, B., 2015, "Material properties of large-size tire derived aggregate for civil engineering applications", *Journal of Materials in Civil Engineering*, 27(9), 04014258.

Alaie, R. and R. Jamshidi Chenari, 2018, "Cyclic and Post-Cyclic Shear Behaviour of Interface between Geogrid and EPS Beads-Sand Backfill", *KSCE Journal of Civil Engineering*, Vol. 22, No. 9.

Alaie, R., and R. Jamshidi Chenari, 2019, "Dynamic Properties of EPS-Sand Mixtures Using Cyclic Triaxial and Bender Element Tests", *Geosynthetics International*, 26(6): 563–79.

Alaie, R., R. Jamshidi Chenari, and M. Karimpour-Fard, 2021, "Shake Table Study on Sand-EPS Beads-Mixtures Using a Laminar Box", *Geosynthetics International* 28(3): 224–37.

Alliance, E. I., *Expanded Polystyrene (EPS) Geofoam Applications & Technical Data*, Crofton, MD, USA, 2012.

Athanasopoulos, G. A., P. C. Pelekis, and V. C. Xenaki, 1999, "Dynamic Properties of EPS Geofoam: An Experimental Investigation", *Geosynthetics International*, 6(3): 171–94.

Athanasopoulos-Zekkos, A., K. Lamote, and G. Athanasopoulos, 2011, "Seismic Isolation of Earth Retaining Walls Using Eps", *4th International Conference on Geofoam Blocks in Construction Applications*, EPS 2011 Norway: 1–10.

Athanasopoulos - Zekkos, A., K. Lamote, and G.A. Athanasopoulos, 2012, "Use of EPS Geofoam Compressible Inclusions for Reducing the Earthquake Effects on Yielding Earth Retaining Structures", *Soil Dynamics and Earthquake Engineering*, Vol. 41, pp. 59‐71.

Azizi, F., 1999, *Applied Analysis in Geotechnics*, CRC Press, 1999.

Ayuluri, S.R., Ramulu, S., 2017, "Behaviour of Reinforced Soil Retaining Walls under Static Loads by Using Plaxis", *Journal of Research in Science, Technology, Engineering and Management*, 2017, ISSN: 2456-0197.

BASF Aktiengesellschaft, 1997, "Annual Report", P.O. Box, 67056 Ludwigshafen, Germany.

Bathurst, R.J. and Hatami, K., 1998, "Seismic Response Analysis of a Geosynthetic-Reinforced Soil Retaining Wall", *Geosynthetics International*, Vol. 5, Nos. 1-2, pp. 127-166.

Bathurst, R.J., Zarnani, S., Gaskin, A., 2007, "Shaking Table Testing of Geofoam Seismic Buffers", *Soil Dynamics and Earthquake Engineering*, 27(4): 324–32.

Bathurst, R.J., Zarnani, S. and Gaskin, A, 2007a, "Shake table testing of geofoam seismic buffers", *Soil Dynamics and Earthquake Engineering*, 27(4): 324-332.

Bathurst, R. J., and S. Zarnani, 2008, "Numerical Modelling of EPS Seismic Buffers" *12th International Conference on Computer Methods and Advances in Geomechanics*, 2008 1(March): 425–32.

Bathurst, R.J. & Zarnani, S., 2011, "Recent research on EPS geofoam seismic buffer", *4th International Conference on the use of Geofoam Blocks in Construction Applications*, Lillestrom, Norway: 1–10.

Baykal, G. & Doven, GA, 2000, "Utilization of fly ash by pelletization process: theory, application areas and research results", *Resources, Conservation, and Recycling* 30: 59–77.

Cagley, James R et al., 2004, "Building Code Requirements for Structural Concrete (ACI 318-02) and Commentary (ACI 318R-02)"

Changwei, Y., Shixian, Z., Jianjing, Z. and Junwei, B., 2015, "Seismic Stability Time-Frequency Analysis Method of Reinforced Retaining Wall", *Hindawi Publishing Corporation Mathematical Problems in Engineering*, Volume 2015, Article ID 178692.

Chun, Byung Sik, Hae Sik Lim, Myung Sagong, and Kyungmin Kim, 2004, "Development of a Hyperbolic Constitutive Model for Expanded Polystyrene (EPS) Geofoam under Triaxial Compression Tests", *Geotextiles and Geomembranes*, 22(4): 223–37.

Coduto, D.P., *Foundation Design Principles and Practices*, Second Edition, Prentice Hall, 2001.

Dabiri, R., and N. Hasanpouri Notash, 2020, "Evaluation of Geofoam Effects on Seismic Response in Cantilever Retaining Wall", *Geotechnical and Geological Engineering,* Vol. 38, No. 2, pp. 2097–2116.

Dalyan, Ilknur, Muhammed Selahaddin Akin, and Zulal Akbay Arama, 2020, "The Evaluation of the Effective Parameters on the Geotechnical Design of Reinforced Concrete Retaining Walls According to the Turkish Building Earthquake Code 2018", *Turk Deprem Arastirma Dergisi*, 2(2): 176–92.

Das, B.M., *Principles of Geotechnical Engineering,* Fifth Edition, Thompson Learning, 2006.

Dave, T. N., S. M. Dasaka, N. Khan, and Krishna A. Murali, 2013, "Evaluation of Seismic Earth Pressure Reduction Using EPS Geofoam", *18th International Conference on Soil Mechanics and Geotechnical Engineering: Challenges and Innovations in Geotechnics,* ICSMGE 2013 2: 903–6.

Davoodi, M., Sadjadi, M., Goljahani, P., & Kamalian, M., 2012, "Effects of far field and near field earthquakes on seismic response of SDOF system considering soil-structure interaction*", In 15th World Conference on Earthquake Engineering*, Lisbon, Portugal.

Day, R.W., *Geotechnical earthquake engineering handbook*, McGraw-Hill Companies, New York, 2002.

Demirtaş, B.S., *Effects of Site Improvement Technique on Seismic Performance of Geotechnical Structures,* Master's Thesis, Boğaziçi University, 2022.

Ecemis, N., & I. Kahraman, 2012, "Design of Laminar Shear Box for One Dimensional Shake Table Tests", *10th International Congress on Advances in Civil Engineering.*

Edinçliler, A., Baykal, G. and Dengili, K., 2004, "Determination of Static and Dynamic Behavior of Recycled Materials for Highways", *Resources, Conservation and Recycling*, 42(3): 223–37.

Edinçliler A., 2007, "Using waste tire-soil mixtures for embankment construction", *Proceedings of the international workshop on scrap tire derived geomaterials—opportunities and challenges,* Yokosuka, Japan, 2007.

Edinçliler, A., 2008, "Using Waste Tire-Soil Mixtures for Embankment Construction", *Proceedings of the International Workshop on Scrap Tire Derived Geomaterials - Opportunities and Challenges,* IW-TDGM 2007: 319–28.

Edinçliler, A., Baykal, G. and Saygili, A., 2010, "Influence of Different Processing Techniques on the Mechanical Properties of Used Tires in Embankment Construction", *Waste Management,* 30(6): 1073–80.

Edinçliler, A. & Toksoy Y.S., 2014, "Investigation on Effects of Tire Crumb Cushion on Seismic Performance of Retaining Wall", *TC207 Soil-Structure Interaction and Retaining Walls,* 16-18 June, St. Petersburg, Russia.

Edinçliler, A., and A. T. Özer, 2014, "Effects of EPS Bead Inclusions on Stress-Strain Behaviour of Sand", *Geosynthetics International,* 21(2): 89–102.

Edinçliler, A. & Toksoy Y.S., 2017, "Effects of Ground Motion Characteristics on the Seismic Performance of Retaining Walls with Tire Waste Cushion", *16th World Conference on Earthquake Engineering,* 16WCEE 2017 Santiago Chile.

Edinçliler, A., & Toksoy, Y. S., 2018, "Effects of Dimensions of Tire Waste Cushion on Seismic Performance of Retaining Wall", *Eurasian Journal of Civil Engineering and Architecture,* 2(2), 69-78.

Edinçliler, A., & Toksoy, Y. S., 2018, "Effects of improvement techniques on seismic performance of highway embankments", *In 16th European Conference on Earthquake Engineering (16ECEE) proceedings*, (pp. 18-21).

Edinçliler, A., and Ö. Yıldız, 2022, "Effects of Processing Type on Shear Modulus and Damping Ratio of Waste Tire-Sand Mixtures", *Geosynthetics International*, 29(4): 389–408.

Edinçliler, A., and Yıldız, Ö., 2023, "Shake Table Tests on Geotechnical Seismic Isolation for Medium-Rise Buildings Using EPS Beads-Sand Mixtures", *Bulletin of Earthquake Engineering*, 21(8): 3851–77. https://doi.org/10.1007/s10518-022-01587-6.

El-Sherbiny, R. M., S. H. Ramadan, and M. A. El-Khouly, 2018, "Dynamic Properties of Sand-EPS Bead Mixtures", *Geosynthetics International* 25(4): 456–70.

Ertugrul, O. L., and Trandafir, A. C., 2011, "Reduction of lateral earth forces acting on rigid nonyielding retaining walls by EPS geofoam inclusions", *Journal of Materials in Civil Engineering*, 23(12), 1711-1718.

Fang, Y.S., Yang, Y.C. and Chen, T.J., 2003, "Retaining walls damaged in the Chi-Chi earthquake", Published on the NRC Research Press Web site at http://cgj.nrc.ca on 31 October 2003.

Feng, Zheng Yi, and Kevin G. Sutter, 2000, "Dynamic Properties of Granulated Rubber/Sand Mixtures", *Geotechnical Testing Journal*, 23(3): 338–44.

Hasanpouri Notash N, Dabiri R, 2018, "Effects of geofoam panels on static behavior of cantilever retaining wall", *Adv Civ Eng*, 2018(6):1–16.

Hazarika, H., Nakazawa, J., Matsuzawa, H., & Negussey, D., 2001, "On the seismic earth pressure reduction against retaining structures using lightweight geofoam fill".

Hazarika, H. and Sugano, T., 2004, "Combined Use of EPS and Tire Chips as Compressible Cushion behind Retaining Structure - A Field Test", *Proceedings of the International Conference on Geosynthetics and Geoenvironmental Engineering (ICGGE - 2004),* Mumbai, India, pp. 229-234.

Hazarika, H., & Okuzono, S., 2004, "Modeling the behavior of a hybrid interactive system involving soil, structure and EPS geofoam" *Soils and Foundations,* 44(5), 149-162.

Hazarika, H., Kohama, E., & Sugano T., 2008, "Underwater Shake Table Tests on Waterfront Structures Protected with Tire Chips Cushion", *Journal of Geotechnical and Environmental Engineering,* ASCE, 134-11.

Heydari, M., & Mousavi, M., 2015, "The comparison of seismic effects of far field and near field earthquakes on relative displacement of seven-storey concrete building with shear wall", *Current World Environment,* 10(Special Issue), 40.

Horvath, J. S. 1994, "Expanded Polystyrene (EPS) Geofoam: An Introduction to Material Behavior", *Geotextiles and Geomembranes* 13(4): 263–80.

Horvath, J.S., *Geofoam Geosynthetic,* Horvath Engineering, P.C. Scarsdale, New York, USA, 217 p., 1995.

Horvath, J.S., 1997, "Compressible inclusion function of EPS geofoam", *Geotextiles and Geomembranes,* 15(1-3), 77–120.

Horvath, J.S., 2005, "Expanding the Use of Expanded Polystyrene (EPS) Geofoam in Practice", *Boston Society of Civil Engineers Section/American Society of Civil*

*Engineers Geo-Institute 2005 Geotechnical Engineering Seminar*, Waltham, MA, U.S.A. · 29 October 2005.

Hylands, K. N., and Shulman, V., 2003, *Civil engineering applications of tires, Viridis Report VR5.*

Hyodo, M. et al., 2008, "Undrained Cyclic Shear Properties of Tire Chip-Sand Mixtures", *Proceedings of the International Workshop on Scrap Tire Derived Geomaterials - Opportunities and Challenges,* IW-TDGM 2007: 187–96.

Iai, Susumu, 1989, "Similitude for Shake Table Tests on Soil-Structure-Fluid Model in 1g Gravitational Field" *Soils and Foundations,* 29(1): 105–18.

Institute, Turkish Standard, 1990, "Soil Retaining Structures; Properties and Guidelines for Design (TS 7994)", Turkish Standard (112).

Ismeik, Muhannad Idsham, *Full Scale Modeling of Geotextile Reinforced Lime Stabilized Cohesive Soil Retaining Wall,* Doctor of Philosophy Thesis, Boğaziçi University, 1996.

J.J. Tweedie, D.N. Humphrey, T.C. Sandford, 1998, "Full-Scale Field Trials of Tire Shreds as Lightweight Retaining Wall Backfill, at-rest Conditions", *Transportation Research Record No. 1619 Transportation Research Board*, Washington DC, USA (1998) pp. 64–71.

Jafarzadeh, F., 2004, "Design and Evaluation Concepts of Laminar Shear Box for 1g Shake Table Tests", *13th World Conference on Earthquake Engineering.*

Jamshidi Chenari, Reza et al., 2016, "An Investigation on the Geotechnical Properties of Sand-EPS Mixture Using Large Oedometer Apparatus", *Construction and Building Materials* 113:773–82.

Jan, J., *Principles and Practice of Ground Improvement,* John Wiley & Sons, Inc., Hoboken, New Jersey, 2015.

Kandilli Observatory and Earthquake Research Institute Ground Motion Database (KOERI).

Karimpour Fard, M., R. Jamshidi Chenari, and F. Soheili, 2015, "Shear Strength Characteristics of Sand Mixed with EPS Beads Using Large Direct Shear Apparatus" *Electronic Journal of Geotechnical Engineering*, 20(8): 2205–20.

Karpurapu, R. & Bathurst R.J., 1992, "Numerical investigation of controlled yielding of soil-retaining wall structures", *Geotextiles and Geomembranes,* 11, 115–31.

K Kaneda, H Yamazaki, S Ohtsuka, 2017, "Numerical Simulations with Cushioning Material Installed Behind the Retaining Wall for Resilient Structures", *COMPDYN 2017 6th ECCOMAS Thematic Conference on Computational Methods in Structural Dynamics and Earthquake Engineering,* M. Papadrakakis, M. Fragiadakis (eds.) Rhodes Island, Greece, 15–17 June 2017.

Khan, M. I., & Meguid, M. A., 2021, "A numerical study on the role of EPS geofoam in reducing earth pressure on retaining structures under dynamic loading", *International Journal of Geosynthetics and Ground Engineering*, 7(3), 57.

Khushefati, W, N Ahmed, and M Alim, 2015, "Review on the Potential Applications of Geofoam Material in Saudi Arabia for Highways and Building Construction", *Journal of King Abdulaziz University-Engineering Sciences,* 26(2): 23–47.

Koerner, R. M., *Designing with geosynthetics*-Vol. 1 (Vol. 1). Xlibris Corporation, 2012.

Kramer, S.L., *Geotechnical Earthquake Engineering,* Prentice Hall, Upper Saddle River, NJ, 1996.

Kumar, K., *Basic geotechnical earthquake engineering*, 2008.

Lepcha, K. H., Agnihotri, A. K., Priyadarshee, A., Yadav, M., 2014, "Application of Tire chips in reinforcement of soil: A review Journal of Civil Engineering and Environmental Technology", *Print ISSN: 2349-8404; Online ISSN: 2349-879X*, Volume 1, Number 5; August, the 2014 pp. 51 – 53 © Krishi Sanskriti Publications.

Lim, A., 2018, "Lesson Learned from Retaining Wall Failures: A Geotechnical Disaster", *MATEC Web of Conferences 229.*

Lutenegger, A.J. and Ciufetti, M., 2009, "Full-Scale Pilot Study to Reduce Lateral Stresses in Retaining Structures Using GeoFoam", *Final Report Project -no. Rsch010-983 Vermont Department of Transportation.*

M. Matsuo, S. Kenmochi, H. Yagi, 1978, "Experimental study on earth pressure of retaining wall by field tests" *Soils Found,* 18 (3), pp. 27-41.

Majumder, M., Ghosh, P. and Rajesh, S., 2017b, "An innovative vibration barrier by intermittent geofoam-a numerical study", *Geomech. Eng.,* 13(2), 269-284.

Murthy, V. N. S., *Geotechnical engineering: principles and practices of soil mechanics and foundation engineering,* CRC Press, 2002.

Nadim, F., 1982, "A Numerical Model for Evaluation of Seismic Behavior of Gravity Retaining Walls", *Research Report R82-33.* Department of Civil Engineering, Massachusetts Institute of Technology, Cambridge.

Nadim, F., and Whitman, R. V., 1984, "Coupled Sliding and Tilting of Gravity Retaining Walls During Earthquakes", *Proceedings, 8th World Conference on Earthquake Engineering*, vol. 3, San Francisco, pp. 477–484.

Partos, A.M. & Kazaniwsky P.M., 1987, “Geoboard reduces lateral earth pressures”, Proceedings *of Geosynthetics’87, Industrial Fabrics Association International.* New Orleans, LA, USA, 628–39.

Pacific Earthquake Engineering Research Center Ground Motion Database (PEER).

Prasad, S.K., I. Towhata, G.P. Chandradhara, & P. Nanjundaswamy, 2004, “Shake Table Tests in Earthquake Geotechnical Engineering", *Current Science,* Vol. 78, pp. 1398-1404.

Reddy, S.B., and Krishna, A.M., 2017, “Tyre chips as compressible inclusions in earth-retaining walls”, *Article in Proceedings of the Institution of Civil Engineers Ground Improvement,* June 2017.

Reddy, S. Bali, and A. Murali Krishna. 2019, “Sand–Scrap Tyre Chip Mixtures for Improving the Dynamic Behaviour of Retaining Walls”, *International Journal of Geotechnical Engineering,* 15(9): 1093–1105.

Republic of Turkey Ministry of Interior Disaster and Emergency Management Presidency Earthquake Department Ground Motion Database (AFAD).

Saran, S., Garg, K. G., & Bhandari, R. K., 1992, “Retaining wall with reinforced cohesionless backfill”, *Journal of Geotechnical Engineering,* 118(12), 1869-1888.

Schaefer, V.R., Mitchell, J.R., Berg, R.R., Filz, G.M., and Douglas, S.C., 2012, “Ground improvement in the 21st century: A comprehensive web-based information system”, *Geotechnical Engineering State of the Art and Practice, Keynote Lectures from GeoCongress 2012,* Geotechnical Special Publication No. 226, 272−293.

Scrap Tires: *Handbook on Recycling Applications and Management for the U.S. and Mexico EPA United States Environmental Protection Agency (2010),* p. 134 EPA530-R-10-010

Sekman, M., *Experimental Study on Mitigation of Earthquake Hazards Using Geosynthetics,* Master's Thesis, Boğaziçi University, 2016.

Sherif, M. A., Ishibashi, I., and Lee, C. D., 1982, "Earth Pressures Against Rigid Retaining Walls", *Journal of the Geotechnical Engineering Division, ASCE,* vol. 108, no. GT5, pp. 679–695.

Sherif, M. A., and Fang, Y. S., 1984a, "Dynamic Earth Pressures on Wall Rotating About the Base", *Proceedings, 8th World Conference on Earthquake Engineering,* vol. 6, San Francisco, pp. 993–1000.

Sherif, M. A., and Fang, Y. S., 1984b, "Dynamic Earth Pressures on Wall Rotating About the Top", *Soils and Foundations,* vol. 24, no. 4, pp. 109–117.

Shrestha, S, and Ravichandran, N., 2018, "Performance of Retaining Wall Backfilled with Tire Aggregate under Static and Dynamic Loading Conditions: Conventional Designs and Finite Element Simulations", *International Journal of Geotechnical Engineering,* (April 17, 2018): 1–13. doi:10.1080/19386362.2018.1460963.

Shukla, S. K., *An introduction to geosynthetic engineering,* CRC Press, 2017.

Siddharthan, R., Ara, S., and Norris, G. M., 1992, "Simple Rigid Plastic Model for Seismic Tilting of Rigid Walls", *Journal of Structural Engineering,* ASCE, vol. 118, no. 2, pp. 469–487.

Sitar, N., Mikola, R.G., and Candia, G., 2012, "Seismically Induced Lateral Earth Pressures on Retaining Structures and Basement Walls", *Conference Paper in Geotechnical Special Publication* May 2012.

Sodom, Bali Reddy, Murali Krishna Adapa, and S. Murty Dasaka, 2015, "Seismic Resilience of Retaining Walls Backfilled with Sand–Tire Chips Mixtures", *Japanese Geotechnical Society Special Publication* 3(2): 20–23.

Somantri, A. K., & Febriansya, A., 2019, "The effect of EPS addition to soil stabilized with fly ash as lightweight fill materials for embankment construction", *In Journal of Physics: Conference Series* (Vol. 1364, No. 1, p. 012077). IOP Publishing.

Steedman, R. S., and Zeng, X., 1990, "The Seismic Response of Waterfront Retaining Walls", *Proceedings, ASCE Specialty Conference on Design and Performance of Earth Retaining Structures,* Special Technical Publication 25, Cornell University, Ithaca, NY, pp. 872–886.

Whitman, R. V., 1990, "Seismic Design Behavior of Gravity Retaining Walls", *Proceedings, ASCE Specialty Conference on Design and Performance of Earth Retaining Structures,* Geotechnical Special Publication 25. ASCE, New York, pp. 817–842.

Wang, Fei, and Linchang Miao, 2009, "A Proposed Lightweight Fill for Embankments Using Cement-Treated Yangzi River Sand and Expanded Polystyrene (EPS) Beads", *Bulletin of Engineering Geology and the Environment*, 68(4): 517–24.

Wang, D., and R.J. Bathurst, 2012, "Numerical Analysis of Earthquake Load Mitigation on Rigid Retaining Walls Using EPS Geofoam", *The Open Civil Engineering Journal,* Vol. 6, No. 1, pp. 21–25.

Whitman, R.V., & P.C. Lambe, 1986, “Effect of Boundary Conditions Upon Centrifuge Experiments Using Ground Motion Simulation", *The American Society for Testing and Materials*, Vol 90, pp. 61-71.

Wood, David Muir, *Geotechnical Modelling*, Geotechnical Modelling (April): 1–488, 2017.

Wu, G., 1994, *Dynamic Soil-Structure Interaction: Pile Foundations and Retaining Structures*, Ph.D. Thesis, Department of Civil Engineering, University of British Columbia, Vancouver, British Columbia, Canada, 213 p.

Xiao M, Bowmen J, Graham M, Larralde J., 2012, “Comparison of seismic responses of geosynthetically reinforced walls with tire-derived aggregates and granular backfills”, *Mater Civ Eng (ASCE)*, 24:1368–1377.

Yadav, P.A., Singh, D.K., Dahale, P.P., Padade, A.H., 2018, “Analysis of retaining wall in static and seismic condition with inclusion of geofoam using Plaxis 2D”, *Indian Geotechnical Conference*, Indian Institute of Science Bengaluru.

Yewalekar, Mohini B et al., 2020, “Causes of Failure of Retaining Wall and It’s Prevention: A Review”, *Ijesc*, 10(3): 1–4.

Yıldız, Ö., *Investigation on the Mitigation of Earthquake Hazards with Inclusion of Tire Wastes into the Sand*, Master’s Thesis, Boğaziçi University, 2011.

Yıldız, Ö., 2022., “Use of EPS in Geotechnical Engineering”, *Architectural and Engineering Research and Practice*, 179,202.

Yoo, Chungsik, H. S. Jung, and H. Y. Jung, 2004, “Lessons Learned from a Failure of Geosynthetics-Reinforced Segmental Retaining Wall”, *3rd Asian Regional Conf. on Geosynthetics:* 265–74.

Yünkül, K., Gürbüz, A., 2022, "Shaking table study on seismic behavior of MSE wall with inclined backfill soils reinforced by polymeric geostrips", *Geotextiles and Geomembranes,* 50 (2022) 116–136.

Zamiran, S., Osouli, A., 2016, "Seismic Earth Pressure Variations in Retaining Walls with Cohesive Backfill Material", *ASCE G-I Case History Night,* April 28, 2016.

Zarnani S, Bathurst RJ, Gaskin A., 2005, "Experimental investigation of geofoam seismic buffer using a shaking table", *In: Proceedings of the North American geosynthetics society (NAGS)/GRI19 conference,* Las Vegas, NV, USA, 2005, 11pp.

Zarnani, S. and Bathurst, R.J., 2005, "Numerical Investigation of Geofoam Seismic Buffers Using Flac", *In Proceedings of the North American Geosynthetics Society (NAGS)/GRI19 Conference,* 2005, Las Vegas, NV, USA. 8p.

Zarnani, S. and Bathurst, R.J., 2006, "Application of EPS Geofoam as A Seismic Buffer: Numerical Study Using Flac", *Sea to Sky Geotechnique,* 2006.

Zarnani, S. and Bathurst, R.J., 2007, "Experimental investigation of EPS geofoam seismic buffers using shaking table tests", *Geosynthetics International,* 2007, 14, No. 3.

Zarnani, S., Bathurst, R.J., 2008a, "Numerical modeling of EPS seismic buffer shaking table tests", *Geotextiles and Geomembranes,* 26 (5), 371–383.

Zarnani, Saman, and Richard J. Bathurst., 2009, "Influence of Constitutive Model on Numerical Simulation of EPS Seismic Buffer Shake Table Tests", *Geotextiles and Geomembranes,* 27(4): 308–12.

Zarnani, S. and Bathurst, R.J., 2009, "Numerical parametric study of expanded polystyrene (EPS) geofoam seismic buffers", *Canadian Geotechnical Journal,* March 2009.

Zarnani, S. and Bathurst, R.J., 2010, "Numerical parametric study of geofoam seismic buffers with different constitutive models", *9th International Conference on Geosynthetics*, Brazil, 2010.